

**METAL-ORGANIC FRAMEWORK PLATFORMS: DIVERSITY-ORIENTED  
SYNTHESIS AND APPLICATION-DIRECTED CUSTOM DESIGN**

by

**Tianyi Luo**

B.S., Sichuan University, 2012

Submitted to the Graduate Faculty of the  
Dietrich School of Arts and Sciences in partial fulfillment  
of the requirements for the degree of  
Doctor of Philosophy

University of Pittsburgh

2019

UNIVERSITY OF PITTSBURGH  
DIETRICH SCHOOL OF ARTS AND SCIENCES

This dissertation was presented

by

**Tianyi Luo**

It was defended on

October 28, 2019

and approved by

Haitao Liu, PhD, Associate Professor, Department of Chemistry

Jill E. Millstone, PhD, Associate Professor, Department of Chemistry

Christopher E. Wilmer, PhD, Assistant Professor, Department of Chemical & Petroleum Engineering

Thesis Advisor: Nathaniel L. Rosi, PhD, Professor, Department of Chemistry

Copyright © by Tianyi Luo

2019

**METAL-ORGANIC FRAMEWORK PLATFORMS: DIVERSITY-ORIENTED  
SYNTHESIS AND APPLICATION-DIRECTED CUSTOM DESIGN**

Tianyi Luo, PhD

University of Pittsburgh, 2019

This dissertation describes diversity-oriented development of metal-organic framework (MOF) platforms and their custom design for specific applications. The three aims of this dissertation include: 1) construct MOF material platforms with exceptional amenability to systematic variations via de novo design; 2) develop new strategies to further increase the diversity and complexity of established MOF platforms; 3) custom-design MOF materials for target applications based on judiciously adjustment on structural parameters of established MOF platforms.

The work in Chapter 2 describes the de novo design of a diverse series of rare earth MOF materials amenable to rational and systematic control of topology, structural metrics, functionalization and inorganic compositions. The optical properties of these MOFs can be customized for potential near infrared (NIR) biological imaging. Chapter 3 describes the custom-design of lanthanide MOF materials as luminescence “turn-on” sensors for gossypol, a natural toxin concerning the cotton industry. The ability to judiciously control the inorganic composition, structural metrics as well as functionalities with the employed lanthanide MOF platform allows for the observed sensing performance and insight into the sensing mechanism. Chapter 4 introduces the concept of domain building blocks (DBBs) as an effective approach to create additional levels of diversity and complexity in MOF platforms. DBBs are defined as distinct structural or compositional regions within a MOF material. I demonstrate that the DBB strategy

can be used in conjunction with post-synthetic modification and nanoparticle encapsulation to construct a rich library of UiO-67 stratified MOF (sMOF) particles consisting of multiple concentric DBBs. I further discuss the negative consequences of linker exchange reactions during sMOFs synthesis on the compositional integrity of DBBs in the UiO-67 sMOFs and propose mitigation strategies. In Chapter 5, the application of MOFs as adsorbent materials for chemical warfare agents (CWAs) is explored. A combined experimental and computational study shows that tailoring the functional groups of UiO-67 MOFs can influence their binding energy for dimethyl methylphosphonate (DMMP), a CWA adsorption simulant.

## TABLE OF CONTENTS

<b>ACKNOWLEDGEMENT</b> .....	<b>xxxiii</b>
<b>1.0 INTRODUCTION</b> .....	<b>1</b>
<b>1.1 MATERIAL PLATFORMS</b> .....	<b>1</b>
<b>1.2 METAL-ORGANIC FRAMEWORKS</b> .....	<b>4</b>
<b>1.3 MOF PLATFORMS</b> .....	<b>6</b>
<b>1.4 TOPOLOGY</b> .....	<b>8</b>
<b>1.4.1 What is topology?</b> .....	<b>8</b>
<b>1.4.2 Rational and systematic control of MOF topologies</b> .....	<b>10</b>
<b>1.5 STRUCTURE METRICS</b> .....	<b>14</b>
<b>1.6 FUNCTIONALITIES</b> .....	<b>17</b>
<b>1.7 INORGANIC COMPOSITION</b> .....	<b>22</b>
<b>1.7.1 Luminescent lanthanide MOFs</b> .....	<b>24</b>
<b>1.8 OBJECTIVES OF THIS DISSERTATION</b> .....	<b>26</b>
<b>2.0 RARE EARTH PCU MOF PLATFORM BASED ON <math>RE_4(\mu_3-OH)_4(COO)_6^{2+}</math></b> <b>CLUSTERS: RATIONAL DESIGN, DIRECTED SYNTHESIS, AND</b> <b>DELIBERATE TUNING OF EXCITATION WAVELENGTHS</b> .....	<b>29</b>
<b>2.1 INTRODUCTION</b> .....	<b>29</b>
<b>2.2 RESULTS AND DISCUSSION</b> .....	<b>33</b>
<b>2.3 CONCLUSIONS</b> .....	<b>66</b>
<b>2.4 EXPERIMENTAL SECTION</b> .....	<b>67</b>
<b>2.4.1 General methods</b> .....	<b>67</b>

<b>2.4.2 Syntheses and characterization of ligands .....</b>	<b>69</b>
<b>2.4.2.1 Synthesis of 3-amino-4-methoxycarbonyl-phenylboronic acid pinacol ester .....</b>	<b>69</b>
<b>2.4.2.2 Synthesis of dimethyl 3,3'-diamino-1,1'-biphenyl-4,4'-dicarboxylate</b>	<b>70</b>
<b>2.4.2.3 Synthesis of 3, 3'-diamino-1, 1'-biphenyl-4,4'-dicarboxylic acid .....</b>	<b>70</b>
<b>2.4.2.4 Synthesis of dimethyl 3, 3''-diamino-1,1':4',1''-terphenyl-4,4''-dicarboxylate .....</b>	<b>71</b>
<b>2.4.2.5 Synthesis of 3, 3''-diamino-1, 1': 4', 1''-terphenyl-4, 4''-dicarboxylic acid .....</b>	<b>72</b>
<b>2.4.2.6 Synthesis of 9,10-anthracenediboronic acid bis(pinacol) ester .....</b>	<b>73</b>
<b>2.4.2.7 Synthesis of dimethyl 4,4'-(9,10-anthracenediyl)bis(2-aminobenzoate) .....</b>	<b>74</b>
<b>2.4.2.8 1.8 Synthesis of 4,4'-(9,10-anthracenediyl)bis(2-aminobenzoic acid)</b>	<b>75</b>
<b>2.4.3 Solvothermal syntheses and CHN elemental analyses of MOF-1114.....</b>	<b>76</b>
<b>2.4.3.1 MOF-1114(Y) .....</b>	<b>76</b>
<b>2.4.3.2 MOF-1114(Gd).....</b>	<b>76</b>
<b>2.4.3.3 MOF-1114(Tb) .....</b>	<b>76</b>
<b>2.4.3.4 MOF-1114(Dy) .....</b>	<b>77</b>
<b>2.4.3.5 MOF-1114(Ho).....</b>	<b>77</b>
<b>2.4.3.6 MOF-1114(Er).....</b>	<b>78</b>
<b>2.4.3.7 MOF-1114(Tm) .....</b>	<b>78</b>
<b>2.4.3.8 MOF-1114(Yb).....</b>	<b>78</b>

<b>2.4.4 Solvothermal syntheses and CHN elemental analyses of MOF-1130 and MOF-1131 .....</b>	<b>79</b>
<b>2.4.4.1 MOF-1130(Y) .....</b>	<b>79</b>
<b>2.4.4.2 MOF-1130(Gd).....</b>	<b>79</b>
<b>2.4.4.3 MOF-1130(Tb) .....</b>	<b>80</b>
<b>2.4.4.4 MOF-1130(Dy) .....</b>	<b>80</b>
<b>2.4.4.5 MOF-1130(Ho).....</b>	<b>80</b>
<b>2.4.4.6 MOF-1131(Er).....</b>	<b>81</b>
<b>2.4.4.7 MOF-1131(Yb).....</b>	<b>81</b>
<b>2.4.5 Solvothermal synthesis and CHN elemental analyses of MOF-1115.....</b>	<b>82</b>
<b>2.4.5.1 MOF-1115(Sm) .....</b>	<b>82</b>
<b>2.4.5.2 MOF-1115(Eu) .....</b>	<b>82</b>
<b>2.4.5.3 MOF-1115(Gd).....</b>	<b>82</b>
<b>2.4.5.4 MOF-1115(Tb) .....</b>	<b>83</b>
<b>2.4.5.5 MOF-1115(Dy) .....</b>	<b>83</b>
<b>2.4.5.6 MOF-1115(Ho).....</b>	<b>84</b>
<b>2.4.5.7 MOF-1115(Er).....</b>	<b>84</b>
<b>2.4.6 Anion exchange of MOF-1114(Tb) with NMe<sub>4</sub>BF<sub>4</sub> .....</b>	<b>84</b>
<b>2.4.7 N<sub>2</sub> adsorption experiments .....</b>	<b>85</b>
<b>2.4.8 Covalent postsynthetic modification of MOF-1114(Yb) experiments.....</b>	<b>86</b>
<b>2.4.8.1 Preparation and characterization of MOF-1114(Yb)<sub>1</sub> .....</b>	<b>86</b>
<b>2.4.8.2 Preparation and characterization of MOF-1114(Yb)<sub>2</sub> .....</b>	<b>86</b>

<b>3.0 LUMINESCENCE “TURN-ON” DETECTION OF GOSSYPOL USING LANTHANIDE(III)-BASED METAL-ORGANIC FRAMEWORKS AND LANTHANIDE SALTS.....</b>	<b>88</b>
<b>3.1 INTRODUCTION .....</b>	<b>88</b>
<b>3.2 RESULTS AND DISCUSSION.....</b>	<b>90</b>
<b>3.3 CONCLUSIONS.....</b>	<b>109</b>
<b>3.4 EXPERIMENTAL SECTION .....</b>	<b>109</b>
<b>3.4.1 General materials and methods.....</b>	<b>109</b>
<b>3.4.2 Synthesis of 3,3''-diamino-1,1':4',1''-terphenyl-4,4''-dicarboxylic acid (H<sub>2</sub>-NH<sub>2</sub>-TPDC).....</b>	<b>110</b>
<b>3.4.3 Synthesis of 2'-nitro-1,1':4',1''-terphenyl-4,4''-dicarboxylic acid (H<sub>2</sub>-NO<sub>2</sub>-TPDC) .....</b>	<b>111</b>
<b>3.4.4 Synthesis of Yb-NH<sub>2</sub>-TPDC .....</b>	<b>111</b>
<b>3.4.5 Sample activation and N<sub>2</sub> gas adsorption experiment of Yb-NH<sub>2</sub>-TPDC..</b>	<b>111</b>
<b>3.4.6 Excitation-Emission maps of Yb-NH<sub>2</sub>-TPDC samples .....</b>	<b>112</b>
<b>3.4.7 Sensing experiments using Yb-NH<sub>2</sub>-TPDC.....</b>	<b>113</b>
<b>3.4.8 Synthesis of Yb-NO<sub>2</sub>-TPDC .....</b>	<b>114</b>
<b>3.4.9 Excitation-Emission maps of Yb-NO<sub>2</sub>-TPDC samples .....</b>	<b>115</b>
<b>3.4.10 LC-MS experiments.....</b>	<b>115</b>
<b>3.4.11 Excitation-Emission map of YbCl<sub>3</sub>•6H<sub>2</sub>O sample in the presence of gossypol ..</b>	<b>117</b>
<b>3.4.12 Gossypol sensing experiments using YbCl<sub>3</sub> .....</b>	<b>118</b>
<b>3.4.13 Gossypol sensing experiments using NdCl<sub>3</sub> .....</b>	<b>119</b>

<b>4.0 MULTIVARIATE STRATIFIED METAL-ORGANIC FRAMEWORKS: DIVERSIFICATION USING DOMAIN BUILDING BLOCKS .....</b>	<b>120</b>
<b>4.1 INTRODUCTION .....</b>	<b>120</b>
<b>4.2 RESULTS AND DISCUSSION.....</b>	<b>125</b>
<b>4.3 CONCLUSIONS.....</b>	<b>149</b>
<b>4.4 EXPERIMENTAL SECTION .....</b>	<b>150</b>
<b>4.4.1 General methods .....</b>	<b>150</b>
<b>4.4.2 Syntheses and characterization of MOF linkers .....</b>	<b>152</b>
<b>4.4.2.1 Dimethyl 2-nitro-1, 1'-biphenyl-4,4'-dicarboxylate (1) .....</b>	<b>152</b>
<b>4.4.2.2 Dimethyl 2-amino-1, 1'-biphenyl-4,4'-dicarboxylate (2) .....</b>	<b>153</b>
<b>4.4.2.3 2-Amino-1, 1'-biphenyl-4,4'-dicarboxylic acid (3) .....</b>	<b>153</b>
<b>4.4.2.4 Dimethyl 2-iodo-1, 1'-biphenyl-4,4'-dicarboxylate (4) .....</b>	<b>154</b>
<b>4.4.2.5 2-Iodo-1, 1'-biphenyl-4,4'-dicarboxylic acid (5).....</b>	<b>154</b>
<b>4.4.2.6 2,2'-Bipyridine-5,5'-dicarboxylic acid (6).....</b>	<b>155</b>
<b>4.4.2.7 (S)-2-(1-(tert-butoxycarbonyl)pyrrolidine-2-carboxamido)-1,1'- biphenyl-4,4'-dicarboxylic acid (7).....</b>	<b>155</b>
<b>4.4.3 Syntheses and characterization of stratified MOFs.....</b>	<b>156</b>
<b>4.4.3.1 Synthesis of UiO-67(Zr) seed crystallites.....</b>	<b>156</b>
<b>4.4.3.2 Synthesis of UiO-67(Zr)⊂UiO-67(Hf).....</b>	<b>157</b>
<b>4.4.3.3 Synthesis of UiO-67(Hf) seed crystallites.....</b>	<b>158</b>
<b>4.4.3.4 Synthesis of UiO-67(Hf)⊂UiO-67(Zr).....</b>	<b>159</b>
<b>4.4.3.5 Synthesis of I-UiO-67(Zr) seed crystallites.....</b>	<b>160</b>
<b>4.4.3.6 Synthesis of I-UiO-67(Zr)⊂UiO-67(Hf).....</b>	<b>161</b>

4.4.3.7 Synthesis of NH <sub>2</sub> -UiO-67(Zr) seed crystallites .....	163
4.4.3.8 Synthesis of NH <sub>2</sub> -UiO-67(Zr)⊂I-UiO-67(Zr) .....	164
4.4.3.9 Linker exchange experiment using NH <sub>2</sub> -UiO-67(Zr) and H <sub>2</sub> -I-BPDC .....	166
4.4.3.10 Synthesis of UiO-67(Zr)⊂UiO-67(Hf)⊂UiO-67(Zr) .....	167
4.4.3.11 Synthesis of I-UiO-67(Zr)⊂UiO-67(Hf)⊂NH <sub>2</sub> -UiO-67(Zr).....	168
4.4.3.12 Synthesis of Bpy-UiO-67(Zr) seed crystallites .....	170
4.4.3.13 Synthesis of Bpy-UiO-67(Zr)⊂UiO-67(Zr).....	171
4.4.3.14 Synthesis of Bpy-UiO-67(Zr)⊂Pro-UiO-67(Zr) .....	172
4.4.3.15 UiO-67(Zr) metalation control experiment.....	174
4.4.3.16 Pro-UiO-67(Zr) metalation control experiment .....	175
4.4.3.17 Synthesis of BpyPd-UiO-67(Zr)⊂UiO-67(Zr) .....	177
4.4.3.18 Synthesis of BpyPd-UiO-67(Zr)⊂Pro-UiO-67(Zr) .....	178
4.4.4 Characterization of nanoparticle samples .....	180
4.4.4.1 Au nanoparticles with 55 kDa PVP.....	180
4.4.4.2 40 kDa PVP capped Ag nanoparticles .....	180
4.4.4.3 55 kDa PVP capped Cu <sub>2-x</sub> Se (x=0.75) nanoparticles .....	182
4.4.5 Syntheses and characterization of NPs⊂MOF composites .....	182
4.4.5.1 Synthesis of Au⊂UiO-67.....	182
4.4.5.2 Synthesis of Au⊂UiO-67(Zr)⊂UiO-67(Hf).....	185
4.4.5.3 Synthesis of Ag⊂UiO-67(Zr).....	186
4.4.5.4 Synthesis of Ag⊂UiO-67(Zr)⊂UiO-67(Hf) .....	187
4.4.5.5 Synthesis of Cu <sub>2-x</sub> Se⊂UiO-67(Zr).....	188

4.4.5.6 Synthesis of $\text{Cu}_{2-x}\text{Se}@\text{UiO-67}(\text{Zr})@\text{UiO-67}(\text{Hf})$ .....	190
<b>5.0 DESIGN, SYNTHESIS AND CHARACTERIZATION OF METAL-ORGANIC FRAMEWORKS FOR ENHANCED SORPTION OF CHEMICAL WARFARE AGENT SIMULANTS.....</b>	<b>192</b>
<b>5.1 INTRODUCTION .....</b>	<b>192</b>
<b>5.2 RESULTS AND DISCUSSION.....</b>	<b>195</b>
5.2.1 Functional group selection .....	195
5.2.2 DFT calculations .....	196
5.2.3 MOF synthesis and characterization.....	198
5.2.4 Experimental binding of DMMP to the UiO-67-X series MOFs .....	205
<b>5.3 CONCLUSIONS.....</b>	<b>212</b>
<b>5.4 EXPERIMENTAL SECTION .....</b>	<b>213</b>
5.4.1 DFT calculations of DMMP binding energies .....	213
5.4.2 MOF synthesis and characterization.....	214
5.4.2.1 Synthesis of 2-amino-1,1'-biphenyl-4,4'-dicarboxylic acid.....	214
5.4.2.2 Synthesis of 2-methyl-1,1'-biphenyl-4,4'-dicarboxylic acid.....	214
5.4.2.3 Synthesis of UiO-67.....	214
5.4.2.4 Synthesis of UiO-67- $\text{CH}_3$ .....	215
5.4.2.5 Synthesis of UiO-67- $\text{NH}_2$ .....	215
5.4.2.6 Powder x-ray diffraction.....	216
5.4.2.7 $\text{N}_2$ gas adsorption .....	216
5.4.2.8 C, H, N elemental microanalyses.....	216
5.4.2.9 Thermogravimetric analyses .....	217

5.4.2.10 Simulated surface areas .....	217
5.4.2.11 TPD-MS and TP-IR.....	217
<b>APPENDIX A CRYSTALLOGRAPHIC TABLES FOR CHAPTER 2 .....</b>	<b>220</b>
<b>APPENDIX B CRYSTALLOGRAPHIC TABLES FOR CHAPTER 3.....</b>	<b>278</b>
<b>BIBLIOGRAPHY .....</b>	<b>282</b>

## LIST OF TABLES

Table 5.1 Kinetic parameters extracted from desorption profiles following 1000 L DMMP on UiO-67-X, along with DFT predictions of the negative of the binding energies. ....	209
Table A1 Fractional atomic coordinates ( $\times 10^4$ ) and equivalent isotropic displacement parameters ( $\text{\AA}^2 \times 10^3$ ) for MOF-1114(Gd). $U_{eq}$ is defined as 1/3 of the trace of the orthogonalised UIJ tensor. ....	220
Table A2 Anisotropic displacement parameters ( $\text{\AA}^2 \times 10^3$ ) for MOF-1114(Gd). The anisotropic displacement factor exponent takes the form: $-2\pi^2[h2a^*2U11+2hka^*b^*U12+\dots]$ .....	221
Table A3 Bond lengths for MOF-1114(Gd). ....	221
Table A4 Bond angles for MOF-1114(Gd). ....	222
Table A5 Torsion angles for MOF-1114(Gd).....	223
Table A6 Hydrogen atom coordinates ( $\text{\AA} \times 10^4$ ) and isotropic displacement parameters ( $\text{\AA}^2 \times 10^3$ ) for MOF-1114(Gd). ....	223
Table A7 Atomic occupancy for MOF-1114(Gd). ....	223
Table A8 Fractional atomic coordinates ( $\times 10^4$ ) and equivalent isotropic displacement parameters ( $\text{\AA}^2 \times 10^3$ ) for MOF-1130(Dy). $U_{eq}$ is defined as 1/3 of the trace of the orthogonalised UIJ tensor. ....	224
Table A9 Anisotropic displacement parameters ( $\text{\AA}^2 \times 10^3$ ) for MOF-1130(Dy). The anisotropic displacement factor exponent takes the form: $-2\pi^2[h2a^*2U11+2hka^*b^*U12+\dots]$ .....	227
Table A10 Bond lengths for MOF-1130(Dy). ....	230
Table A11 Bond angles for MOF-1130(Dy). ....	233
Table A12 Torsion angles for MOF-1130(Dy).....	239

Table A13 Hydrogen atom coordinates ( $\text{\AA}\times 10^4$ ) and isotropic displacement parameters ( $\text{\AA}^2\times 10^3$ ) for MOF-1130(Dy). .....	242
Table A14 Atomic Occupancy for MOF-1130(Dy). .....	244
Table A15 Fractional atomic coordinates ( $\times 10^4$ ) and equivalent isotropic displacement parameters ( $\text{\AA}^2\times 10^3$ ) for MOF-1131(Yb). Ueq is defined as 1/3 of the trace of the orthogonalised UIJ tensor. ....	245
Table A16 Anisotropic displacement parameters ( $\text{\AA}^2\times 10^3$ ) for MOF-1131(Yb). The anisotropic displacement factor exponent takes the form: $-2\pi^2[h_2a^*2U_{11}+2hka^*b^*U_{12}+\dots]$ .....	249
Table A17 Bond lengths for MOF-1131(Yb). .....	253
Table A18 Bond angles for MOF-1131(Yb). .....	256
Table A19 Torsion angles for MOF-1131(Yb).....	263
Table A20 Hydrogen atom coordinates ( $\text{\AA}\times 10^4$ ) and isotropic displacement parameters ( $\text{\AA}^2\times 10^3$ ) for MOF-1131(Yb). .....	267
Table A21 Atomic occupancy for MOF-1131(Yb). .....	269
Table A22 Fractional atomic coordinates ( $\times 10^4$ ) and equivalent isotropic displacement parameters ( $\text{\AA}^2\times 10^3$ ) for MOF-1115(Tb). Ueq is defined as 1/3 of the trace of the orthogonalised UIJ tensor. ....	270
Table A23 Anisotropic displacement parameters ( $\text{\AA}^2\times 10^3$ ) for MOF-1115(Tb). The anisotropic displacement factor exponent takes the form: $-2\pi^2[h_2a^*2U_{11}+2hka^*b^*U_{12}+\dots]$ .....	271
Table A24 Bond lengths for MOF-1115(Tb).....	272
Table A25 Bond angles for MOF-1115(Tb).....	273
Table A26 Torsion angles for MOF-1115(Tb). .....	276

Table A27 Hydrogen atom coordinates ( $\text{\AA}\times 10^4$ ) and isotropic displacement parameters ( $\text{\AA}^2\times 10^3$ ) for MOF-1115(Tb).....	277
Table A28 Atomic occupancy for MOF-1115(Tb).....	277
Table B1 Fractional atomic coordinates ( $\times 10^4$ ) and equivalent isotropic displacement parameters ( $\text{\AA}^2\times 10^3$ ) for Yb-NH <sub>2</sub> -TPDC. U <sub>eq</sub> is defined as 1/3 of the trace of the orthogonalised UIJ tensor. .....	278
Table B2 Anisotropic displacement parameters ( $\text{\AA}^2\times 10^3$ ) for Yb-NH <sub>2</sub> -TPDC. The anisotropic displacement factor exponent takes the form: $-2\pi^2[h^2a^2U_{11}+2hka^*b^*U_{12}+\dots]$ .....	278
Table B3 Bond lengths for Yb-NH <sub>2</sub> -TPDC.....	279
Table B4 Bond angles for Yb-NH <sub>2</sub> -TPDC. ....	279
Table B5 Torsion angles for Yb-NH <sub>2</sub> -TPDC.....	280
Table B6 Hydrogen atom coordinates ( $\text{\AA}\times 10^4$ ) and isotropic displacement parameters ( $\text{\AA}^2\times 10^3$ ) for Yb-NH <sub>2</sub> -TPDC.....	281
Table B7 Atomic occupancy for Yb-NH <sub>2</sub> -TPDC.....	281

## LIST OF FIGURES

Figure 1.1 (A) molecular structures of selected commercial Grubbs Catalysts for olefin matathesis; <sup>1</sup> (B) photoluminescence and transmission electron micrographs of halide perovskite nanocrystals with variable halide anion compositions (adapted from ref. 2 with permission); <sup>2</sup> (C) solutions of various singled walled carbon nanotubes with different chirality index (adapted from ref. 3 with permission); <sup>3</sup> (D) Tunable localized surface plasmon resonance of gold nanorods with different aspect ratios (adapted from ref. 4 with permission). <sup>4</sup> .....	3
Figure 1.2 The inorganic SBUs, organic linkers and extended structures of MOF-5 and HKUST-1. <sup>10-11</sup> .....	5
Figure 1.3 Examples of inorganic, organic building blocks and their abstract shapes defined by points of extension (reprinted from ref.12). <sup>12</sup> .....	10
Figure 1.4 Structures and topologies of PCN-222 and NU-902. <sup>33-34</sup> .....	11
Figure 1.5 Selected MOF examples of different topologies composed of $Zn_4O(COO)_6$ SBUs. <sup>10, 37, 43-44</sup> .....	13
Figure 1.6 Effects of the size of buliding blocks on MOF structural metrics. (A) augmented diamond net composed of small tetrahedra and short rods; (B) augmented diamond net composed of large tetrahedra and short rods; (A) augmented diamond net composed of small tetrahedra and long rods.....	15
Figure 1.7 Organic linkers and crystal structures of IRMOF-74 series (adapted from ref. 46). <sup>46</sup>	16
Figure 1.8 Isorecticular synthesis of UiO-67 MOFs with a select list of functinalized linkers. ....	18
Figure 1.9 Schematics of (A) post-synthetic linker exchange reactions; and (B) covalent post-synthetic modification reactions. ....	19

Figure 1.10 Examples of covalent post-synthetic modification of MOFs. <sup>62-65</sup> .....	19
Figure 1.11 Examples of multivariated MOFs containing multiple functional groups synthesized via (A) solvothermal synthesis(adapted from ref. 66 ); <sup>66</sup> (B) linker exchange (adapted from ref. 67); <sup>67</sup> and (C) covalent post-synthetic modification (adapted from ref. 68). <sup>68</sup> .....	21
Figure 1.12 MOF-5 crystals after metal ion metathesis reactions with a series of metal ions (reprint from ref. 70). <sup>70</sup> .....	23
Figure 1.13 Isostructural inorganic SBUs with different metal ion compositions. <sup>11, 35-36, 73-98</sup> ....	24
Figure 1.14 Isorecticular synthesis of MIL-78 using a series of Ln(NO <sub>3</sub> ) <sub>3</sub> •5H <sub>2</sub> O (Ln = Pr, Nd, Sm, Eu, Gd, Tb, Dy, Er). C, grey spheres; O, red spheres; Ln, teal polyhedra.....	25
Figure 1.15 Emission spectra of slected Ln <sup>3+</sup> ions. <sup>105-106</sup> .....	26
Figure 2.1 Structure of the RE <sub>4</sub> (μ <sub>3</sub> -OH) <sub>4</sub> (COO) <sub>6</sub> <sup>2+</sup> SBU and construction of the pcu net (RE <sup>3+</sup> , green spheres; C, grey spheres; O, red spheres; green tetrahedron defines RE <sup>3+</sup> core; H atoms omitted for clarity; teal octahedron defines structure of SBU).....	32
Figure 2.2 Construction of MOF-1114. (A) Organic linker and inorganic SBU in MOF-1114; (B) crystal structure of MOF-1114 (RE <sup>3+</sup> , green spheres; C, grey spheres; O, red spheres; RE <sub>4</sub> (μ <sub>3</sub> -OH) <sub>4</sub> , green tetrahedra; teal octahedron defines structure of SBU; coordinated water molecules, μ <sub>1</sub> -OH groups, and H atoms have been omitted for clarity; only one of the possible positions is illustrated for each disordered -NH <sub>2</sub> group); (C) 1-D ~10 Å × 10 Å channels along the <i>a</i> , <i>b</i> , and <i>c</i> crystallographic axes in MOF-1114.....	35
Figure 2.3 [RE <sub>4</sub> (μ <sub>3</sub> -OH) <sub>4</sub> (COO) <sub>6</sub> (H <sub>2</sub> O) <sub>8-x</sub> (μ <sub>1</sub> -OH) <sub>x</sub> ] <sup>(2-x)+</sup> SBU (RE <sup>3+</sup> , green spheres; C, grey spheres; O atoms on carboxylates and μ <sub>3</sub> -OH, red spheres; O atoms on H <sub>2</sub> O or μ <sub>1</sub> -OH, pink spheres; green tetrahedra define RE <sup>3+</sup> cores; teal octahedron defines structure of SBU; H atoms omitted for clarity).....	35

Figure 2.4 PXRD patterns of MOF-1114 synthesized with different RE <sup>3+</sup> (front to back: simulated, Y <sup>3+</sup> , Gd <sup>3+</sup> , Tb <sup>3+</sup> , Dy <sup>3+</sup> , Ho <sup>3+</sup> , Er <sup>3+</sup> , Tm <sup>3+</sup> , Yb <sup>3+</sup> ). .....	36
Figure 2.5 SEM/EDS spectrum of as-synthesized MOF-1114(Tb) (spectrum was collected at the ‘Spectrum 1’ area in top figure). .....	38
Figure 2.6 SEM/EDS spectrum of MOF-1114(Tb) after ion exchange with NMe <sub>4</sub> BF <sub>4</sub> (spectrum was collected at the ‘Spectrum 1’ area in top figure). .....	39
Figure 2.7 Solution <sup>1</sup> H NMR spectra of NH <sub>4</sub> BF <sub>4</sub> (top) and acid dissolved MOF-1114(Tb) after NH <sub>4</sub> BF <sub>4</sub> ion exchange with α,α,α-trifluorotoluene added as internal standard (bottom). .....	40
Figure 2.8 Solution <sup>19</sup> F NMR of acid dissolved MOF-1114(Tb) after NH <sub>4</sub> BF <sub>4</sub> ion exchange with α,α,α-trifluorotoluene added as internal standard. ....	41
Figure 2.9 Solution <sup>1</sup> H NMR of acid digested as-synthesized MOF-1114(Tb) showing approximately 3 : 1 ratio of DMF : NH <sub>2</sub> -BDC ligand. ....	42
Figure 2.10 Simulated PXRD pattern based on MOF-1114(Gd) crystal structure (black), PXRD patterns of as-synthesized MOF-1114(Tb) (red) and NMe <sub>4</sub> BF <sub>4</sub> exchanged MOF-1114(Tb) (navy). .....	43
Figure 2.11 Thermogravimetric Analyses (TGA) of as-synthesized MOF-1114(Tb) (black) and MOF-1114(Tb) after anion exchange with NMe <sub>4</sub> BF <sub>4</sub> (red). ....	43
Figure 2.12 N <sub>2</sub> isotherm at 77 K of MOF-1114(Tb) after anion exchanged with NMe <sub>4</sub> BF <sub>4</sub> . Based on this isotherm, the Brunauer-Emmett-Teller (BET) surface area is estimated to be 264 m <sup>2</sup> /g. ....	44
Figure 2.13 (A) organic linkers and inorganic SBU in MOF-1130 and MOF-1131 (light-orange spheres highlight O atoms on chelating carboxylates); (B) crystal structure of MOF-1130 (for clarity, the identical interpenetrating framework is omitted; only one of the possible positions is illustrated for each disordered –NH <sub>2</sub> group); (C) crystal structure of MOF-1131 (for clarity, the	

identical interpenetrating framework is omitted; only one of the possible positions is illustrated for each disordered  $\text{-NH}_2$  group); ..... 46

Figure 2.14 Interpenetrated crystal structure of (A) MOF-1130 and (B) MOF-1131 ( $\text{RE}^{3+}$ , green spheres; C, grey spheres; O, red spheres; N, blue spheres; green tetrahedra define  $\text{RE}^{3+}$  cores; H atoms and coordinating solvent molecules omitted for clarity). ..... 47

Figure 2.15 PXRD patterns of MOF-1130 synthesized with different  $\text{RE}^{3+}$  ( simulated, black;  $\text{Gd}^{3+}$ , green;  $\text{Dy}^{3+}$ , blue;  $\text{Tb}^{3+}$ , orange;  $\text{Ho}^{3+}$ , wine;  $\text{Y}^{3+}$ , violet). ..... 48

Figure 2.16 PXRD patterns of MOF-1131 synthesized with different  $\text{RE}^{3+}$  ( simulated, black;  $\text{Yb}^{3+}$ , orange;  $\text{Er}^{3+}$ , wine). ..... 49

Figure 2.17 SEM image (top) and EDS spectrum (bottom) of as-synthesized MOF-1130( $\text{Dy}$ ) crystals (spectrum was collected at the ‘Spectrum 1’ area in top image). ..... 50

Figure 2.18 SEM image (top) and EDS spectrum (bottom) of as-synthesized MOF-1131( $\text{Er}$ ) crystals (spectrum was collected at the ‘Spectrum 1’ area in top image). ..... 51

Figure 2.19 (A) organic linker and inorganic SBU in MOF-1115; (B) crystal structure of MOF-1115 ( $\text{RE}^{3+}$ , green spheres; C, gray spheres; O, red spheres;  $\text{RE}_4(\mu_3\text{-OH})_4$ , green tetrahedra; teal octahedron defines structure of SBU; coordinated water molecules,  $\mu_1\text{-OH}$  groups, and H atoms have been omitted for clarity; only one of the possible positions is illustrated for each disordered  $\text{-NH}_2$  group). ..... 53

Figure 2.20 PXRD patterns of MOF-1115 synthesized with different  $\text{RE}^{3+}$  (front to back: simulated,  $\text{Y}^{3+}$ ,  $\text{Gd}^{3+}$ ,  $\text{Tb}^{3+}$ ,  $\text{Dy}^{3+}$ ,  $\text{Ho}^{3+}$ ,  $\text{Er}^{3+}$ ,  $\text{Tm}^{3+}$ ,  $\text{Yb}^{3+}$ ). ..... 54

Figure 2.21 SEM image (top) and EDS spectrum (bottom) of as-synthesized MOF-1115( $\text{Tb}$ ) (spectrum was taken at the ‘Spectrum 1’ area in top image). ..... 55

Figure 2.22 SEM image (top) and EDS spectrum (bottom) of as-synthesized MOF-1115(Tb) after ion exchange with $\text{NMe}_4\text{BF}_4$ . (spectrum was taken at the ‘Spectrum 1’ area in top image).....	56
Figure 2.23 Solution $^1\text{H}$ NMR of acid dissolved MOF-1115(Tb) after $\text{NMe}_4\text{BF}_4$ ion exchange with $\alpha,\alpha,\alpha$ -trifluorotoluene added as internal standard. The molar ratio is calculated based on peak integrations.....	57
Figure 2.24 Solution $^{19}\text{F}$ NMR of acid dissolved MOF-1115(Tb) after $\text{NMe}_4\text{BF}_4$ ion exchange with $\alpha,\alpha,\alpha$ -trifluorotoluene added as internal standard. The molar ratio is calculated based on peak integrations.....	57
Figure 2.25 CPSM reactions in MOF-1114(Yb) (Scale bars = 100 $\mu\text{m}$ ).....	59
Figure 2.26 Simulated PXRD based on MOF-1114(Gd) crystal structure (black), experimental PXRD pattern of as-synthesized MOF-1114(Yb) (red) and MOF-1114(Yb) <sub>1</sub> (navy) and MOF-1114(Yb) <sub>2</sub> (green). .....	60
Figure 2.27 Solution $^1\text{H}$ NMR of acid digested MOF-1114(Yb) <sub>1</sub> (top), and MOF-1114 (Yb) <sub>2</sub> (bottom) in $\text{DMSO-}d_6$ . .....	61
Figure 2.28 Solution $^1\text{H}$ NMR in $\text{D}_2\text{O}$ of digested MOF-1114(Yb) <sub>1</sub> after $\text{NaBH}_4$ reduction. ....	62
Figure 2.29 Mass spectrum (ESI-) of digested MOF-1114(Yb) <sub>1</sub> after $\text{NaBH}_4$ reduction. ....	62
Figure 2.30 Solution $^1\text{H}$ NMR in $\text{D}_2\text{O}$ of digested MOF-1114(Yb) <sub>2</sub> after $\text{NaBH}_4$ reduction. ....	63
Figure 2.31 Mass spectrum (ESI-) of digested MOF-1114(Yb) <sub>1</sub> after $\text{NaBH}_4$ reduction. ....	63
Figure 2.32 . (A) Normalized absorption spectra of single crystalline MOF-1114(Yb) (black), MOF-1114(Yb) <sub>1</sub> (navy) and MOF-1114(Yb) <sub>2</sub> (red); (B) normalized absorption spectra of salicylaldehyde (green) and 3-hydroxy-naphthalene-2-carboxaldehyde (grey) in solution (10 $\mu\text{M}$ in dichloromethane); corrected and normalized (C) emission spectra ( $\lambda_{\text{ex}} = 380 \text{ nm}$ ) and (D) excitation spectra ( $\lambda_{\text{em}} = 980 \text{ nm}$ ) of MOF-1114(Yb), MOF-1114(Yb) <sub>1</sub> and MOF-1114(Yb) <sub>2</sub> ;	65

Figure 2.33 Luminescence lifetimes ( $\tau_{\text{obs}}$ ) and quantum yields ( $Q_{\text{Yb}}$ ) of MOFs at room temperature (crystals under DMF; $2\sigma$ values between parentheses; lifetimes measured under excitation at 355 nm).....	66
Figure 3.1 The molecular structure of gossypol. ....	90
Figure 3.2 Crystal structures of Yb-NH <sub>2</sub> -TPDC and gossypol. <sup>176</sup> (A) synthesis scheme of Yb-NH <sub>2</sub> -TPDC (C, gray spheres; O, red spheres; N, blue spheres, Yb, teal polyhedra; H, omitted for clarity); (B) an octahedral cavity of Yb-NH <sub>2</sub> -TPDC with triangular apertures (all atoms are shown with Van der Waals radii; C, gray spheres; O, red spheres; N, blue spheres, Yb, teal spheres; H, white spheres); (C) a gossypol molecule viewed in two different orientations (all atoms are shown with Van der Waals radii; C, gray spheres; O, red spheres; H, white spheres). ....	92
Figure 3.3 Experimental PXRD pattern of as-synthesized Yb-NH <sub>2</sub> -TPDC (red), and Simulated PXRD pattern of Yb-NH <sub>2</sub> -TPDC (black) base on its crystal structure.....	93
Figure 3.4 Solution <sup>1</sup> H NMR spectrum of acid digested Yb-NH <sub>2</sub> -TPDC sample. Singlet peaks at 1.78 ppm and 8.15 ppm indicate the presence of dimethyl ammonium(DMA). The ratio of DMA:NH <sub>2</sub> -TPDC is determined to be 1:3.....	94
Figure 3.5 [Yb <sub>6</sub> (OH) <sub>8</sub> (COO) <sub>12</sub> (Solvent) <sub>6</sub> ] <sup>2-</sup> SBU (Yb <sup>3+</sup> , teal spheres; C, grey spheres; O atoms on carboxylates and $\mu_3$ -OH groups, red spheres; O atoms from coordinating solvent molecules, yellow spheres). ....	94
Figure 3.6 TGA curve of as-synthesized Yb-NH <sub>2</sub> -TPDC. ....	95
Figure 3.7 Experimental PXRD pattern of activated Yb-NH <sub>2</sub> -TPDC and simulated PXRD pattern of Yb-NH <sub>2</sub> -TPDC (black). ....	96
Figure 3.8 N <sub>2</sub> isotherm at 77K of activated Yb-NH <sub>2</sub> -TPDC. Brunauer–Emmett–Teller (BET) surface area: 2370 m <sup>2</sup> /g.....	96

Figure 3.9 Excitation-Emission maps of Yb-NH<sub>2</sub>-TPDC (A) in the absence of gossypol and (B) in the presence of gossypol. .... 98

Figure 3.10 UV-vis spectra of H<sub>2</sub>-NH<sub>2</sub>-TPDC/DMF solution (0.01 mg/mL, black), and gossypol/acetone solution (0.025 mg/mL, orange). The noisy feature from 270-300 nm of gossypol spectrum is due to acetone absorption. .... 98

Figure 3.11 Gossypol sensing experiments using Yb-NH<sub>2</sub>-TPDC. (A) kinetics of Yb<sup>3+</sup> PL of Yb-NH<sub>2</sub>-TPDC in response to gossypol solutions of different concentrations (100 μg/mL, green; 75 μg/mL, orange; 50 μg/mL, blue; 25 μg/mL, black); (B) emission spectra of Yb-NH<sub>2</sub>-TPDC samples in response to different gossypol concentrations at 300 min (100 μg/mL, green; 75 μg/mL, orange; 50 μg/mL, blue; 25 μg/mL, black; blank, grey; calibration curve, inset). .... 100

Figure 3.12 Yb<sup>3+</sup> PL of Yb-NH<sub>2</sub>-TPDC samples in the presence of interferants (with gossypol, grey bars; without gossypol, white bars). .... 101

Figure 3.13 UV-vis spectra of gossypol/ethanol (0.8 μg/mL, blue), α-tocopherol/ethanol (4 μg/mL, orange), palmitic acid/ethanol (1000 μg/mL, grey) and linoleic acid/ethanol (50 μg/mL, green). Spectrum of cottonseed oil/ethanol was not collected because cottonseed oil is insoluble in ethanol. .... 102

Figure 3.14 UV-Vis spectra of cottonseed oil/acetone solution (33000 μg/mL, red), gossypol/acetone (25 μg/mL, blue), α-tocopherol/acetone (13 μg/mL, orange), palmitic acid/acetone (333 μg/mL, grey) and linoleic acid/acetone (333 μg/mL, green). The noisy features between 280 nm and 330 nm are due to acetone absorption. .... 102

Figure 3.15 Experimental PXRD pattern of as-synthesized Yb-NO<sub>2</sub>-TPDC (red), and Simulated PXRD pattern of Yb-NH<sub>2</sub>-TPDC (black) base on its crystal structure. The close match between the two PXRD patterns indicates Yb-NO<sub>2</sub>-TPDC is a isoreticular MOF of Yb-NH<sub>2</sub>-TPDC. .... 104

Figure 3.16 Excitation-Emission Maps of Yb-NO <sub>2</sub> -TPDC (A) in the absence of gossypol and (B) in the presence of gossypol.....	104
Figure 3.17 Excitation-Emission map of YbCl <sub>3</sub> •6H <sub>2</sub> O solution in the presence of gossypol. ...	105
Figure 3.18 Emission spectra of YbCl <sub>3</sub> solution in the presence of gossypol at various concentrations. Excitation: 400 nm.....	106
Figure 3.19 Emission intensities at 976 nm of YbCl <sub>3</sub> solution in the presence of various gossypol concentration.....	107
Figure 3.20 Emission spectra of NdCl <sub>3</sub> solution in the presence of gossypol at various concentrations. Excitation: 400 nm.....	108
Figure 3.21 Emission intensities at 1056 nm of NdCl <sub>3</sub> solution in the presence of various gossypol concentration.....	108
Figure 3.22 Mass spectrum (ESI+). The [M+H] <sup>+</sup> peak for NH <sub>2</sub> -TPDC linker (m/z = 349) was observed along with additional peaks. However, no peaks corresponding to the two possible reduced Schiff base products were identified. ....	116
Figure 3.23 Mass spectrum (ESI-) of gossypol solution after incubating with MOF Yb-NH <sub>2</sub> -TPDC. The three peaks with m/z = 517, m/z =557, m/z = 597 correspond respectively to [M-H] <sup>-</sup> , [M+acetone-H <sub>2</sub> O-H] <sup>-</sup> and [M+2(acetone-H <sub>2</sub> O)-H] <sup>-</sup> .....	117
Figure 4.1 Illustration of increased diversity and complexity in MTV sMOFs using domain building blocks.....	124
Figure 4.2 (A) TEM image of UiO-67(Zr) seed crystallites with an average diameter of 351±51 nm; (B) TEM image of UiO-67(Zr)⊂UiO-67(Hf) crystallites with an diameter of 555±70 nm ; (C) size distributions (based on 300 counts) of UiO-67(Zr) seed crystallites (black) and UiO-67(Zr)⊂UiO-67(Hf) crystallites (red).....	127

Figure 4.3 SEM-EDS line-scan and mapping data of UiO-67(Zr)⊂UiO-67(Hf) (Zr, green; Hf, red). EDS line-scan and map data were generated using Zr Lα1 line at 2.0 keV, Hf Mα1 line at 1.6 keV. .... 128

Figure 4.4 SEM-EDS line-scan and mapping data of UiO-67(Hf)⊂UiO-67(Zr) (Zr, green; Hf, red). EDS line-scan and map data were generated using Zr Lα1 line at 2.0 keV, Hf Mα1 line at 1.6 keV. .... 130

Figure 4.5 (A) TEM image of octahedral I-UiO-67(Zr) seed crystallites with an average edge length of 290±19 nm; (B) TEM image of octahedral I-UiO-67(Zr)⊂UiO-67(Hf) crystallites with an average edge length of 371±20 nm; (C) size distributions (based on 100 counts) of I-UiO-67(Zr) seed crystallites (black) and I-UiO-67(Zr)⊂UiO-67(Hf) crystallites (red). .... 132

Figure 4.6 SEM-EDS line-scan and mapping data of I-UiO-67(Zr)⊂UiO-67(Hf) (Zr, green; I, orange; Hf, red). EDS line-scan and map data were generated using Zr Lα1 line at 2.0 keV, Hf Mα1 line at 1.6 keV, and I Lα1 at 3.9 keV. .... 133

Figure 4.7 SEM-EDS line-scan and mapping data of NH<sub>2</sub>-UiO-67(Zr)⊂I-UiO-67(Zr) (Zr, green; I, orange). EDS line-scan and map data were generated using Zr Lα1 line at 2.0 keV, and I Lα1 at 3.9 keV. .... 135

Figure 4.8 SEM-EDS line-scan and mapping data of crystallites formed after a linker exchange reaction between NH<sub>2</sub>-UiO-67(Zr) and H<sub>2</sub>-I-BPDC (Zr, green; I, orange). EDS line-scan and map data were generated using Zr Lα1 line at 2.0 keV, and I Lα1 at 3.9 keV. .... 136

Figure 4.9 SEM-EDS characterization of UiO-67(Zr)⊂UiO-67(Hf)⊂UiO-67(Zr) (Zr, green; Hf, red). EDS line-scan and map data were generated using Zr Lα1 line at 2.0 keV, and Hf Mα1 line at 1.6 keV. .... 138

Figure 4.10 SEM-EDS characterization of I-UiO-67(Zr)⊂UiO-67(Hf)⊂NH<sub>2</sub>-UiO-67(Zr) (Zr, green; I, orange; Hf, red). EDS line-scan and map data were generated using Zr Lα<sub>1</sub> line at 2.0 keV, Hf Mα<sub>1</sub> line at 1.6 keV, and I Lα<sub>1</sub> at 3.9 keV. .... 139

Figure 4.11 Characterization of BpyPd-UiO-67(Zr)⊂UiO-67(Zr) and BpyPd-UiO-67(Zr)⊂Pro-UiO-67(Zr). STEM-HAADF image of BpyPd-UiO-67(Zr)⊂UiO-67(Zr) (A); STEM-EDS line-scan data of BpyPd-UiO-67(Zr)⊂UiO-67(Zr) (B); STEM-HAADF image of BpyPd-UiO-67(Zr)⊂Pro-UiO-67(Zr) (C); STEM-EDS line-scan data of BpyPd-UiO-67(Zr)⊂Pro-UiO-67(Zr) (D). EDS line-scan data were generated using Zr Kα<sub>1</sub> line at 15.7 keV and Pd Lα<sub>1</sub> line at 2.8 keV. .... 142

Figure 4.12 Zr:Pd ratios at different points in a BpyPd-UiO-67(Zr)⊂UiO-67(Zr) crystal determined from STEM-EDS spectra using Zr Kα<sub>1</sub> at 15.7 keV and Pd Lα<sub>1</sub> at 2.8 keV..... 143

Figure 4.13 Pd:Zr ratios at different points in a BpyPd-UiO-67(Zr)⊂UiO-67(Zr) crystal determined from STEM-EDS spectra using Zr Kα<sub>1</sub> at 15.7 keV and Pd Lα<sub>1</sub> at 2.8 keV..... 144

Figure 4.14 Characterization of Cu<sub>2-x</sub>⊂UiO-67(Zr)⊂UiO-67(Hf). TEM image of Cu<sub>2-x</sub>Se nanoparticles (A); TEM image of Cu<sub>2-x</sub>Se⊂UiO-67(Zr) (B); STEM-EDS mapping of Cu<sub>2-x</sub>Se⊂UiO-67(Zr)⊂UiO-67(Hf) (C). EDS Maps were generated using Zr Kα<sub>1</sub> line at 15.7 keV, Hf Mα<sub>1</sub> line at 1.6 keV, Cu Lα<sub>1</sub> line at 0.9 keV and Se Kα<sub>1</sub> line at 11.2 keV. .... 146

Figure 4.15 STEM-EDS characterization of Au⊂UiO-67(Zr)⊂UiO-67(Hf). EDS map data were generated using Zr Kα<sub>1</sub> line at 15.7 keV, Hf Mα<sub>1</sub> line at 1.6 keV, and Au Lα<sub>1</sub> line at 9.7 keV. .... 147

Figure 4.16 STEM-EDS characterization of Ag⊂UiO-67(Zr)⊂UiO-67(Hf). EDS map data were generated using Zr Kα<sub>1</sub> line at 15.7 keV, Hf Mα<sub>1</sub> line at 1.6 keV, and Ag Lα<sub>1</sub> line at 3.0 keV. .... 148

Figure 4.17 Extinction spectra of UiO-67(Zr) (black), Au@UiO-67(Zr) (red), Au@UiO-67(Zr)@UiO-67(Hf) (green), Ag@UiO-67(Zr) (orange) and Ag@UiO-67(Zr)@UiO-67(Hf) (grey) samples drop cast on glass slides.....	149
Figure 4.18 Simulated PXRD pattern of UiO-67(Zr) (black) and experimental PXRD pattern of as-synthesized UiO-67(Zr) seed crystallites (red). .....	156
Figure 4.19 Simulated PXRD pattern of UiO-67(Zr) (black) and experimental PXRD pattern of as-synthesized UiO-67(Zr)@UiO-67(Hf) (red).....	157
Figure 4.20 Simulated PXRD pattern of UiO-67(Zr) (black) and experimental PXRD pattern of as-synthesized UiO-67(Hf) seed crystallites (red).....	158
Figure 4.21 Simulated PXRD pattern of UiO-67(Zr) (black) and experimental PXRD pattern of as-synthesized UiO-67(Hf)@UiO-67(Zr) (red).....	159
Figure 4.22 Simulated PXRD pattern of UiO-67(Zr) (black) and experimental PXRD pattern of as-synthesized I-UiO-67(Zr) seed crystallites (red).....	160
Figure 4.23 Simulated PXRD pattern of UiO-67(Zr) (black) and PXRD pattern of as-synthesized I-UiO-67(Zr)@UiO-67(Hf) (red). .....	161
Figure 4.24 <sup>1</sup> H NMR of acid digested I-UiO-67(Zr)@UiO-67(Hf) in DMSO-d <sub>6</sub> showing an approximate I-BPDC : BPDC ratio of 1:1.25. ....	162
Figure 4.25 Simulated PXRD pattern based on UiO-67(Zr) (black) and experimental PXRD pattern of as-synthesized NH <sub>2</sub> -UiO-67(Zr) seed crystallites (red).....	163
Figure 4.26 Simulated PXRD pattern of UiO-67(Zr) (black) and experimental PXRD pattern of as-synthesized NH <sub>2</sub> -UiO-67(Zr)@I-UiO-67(Zr) (red).....	164
Figure 4.27 <sup>1</sup> H NMR of acid digested NH <sub>2</sub> -UiO-67(Zr)@I-UiO-67(Zr) in DMSO-d <sub>6</sub> showing an approximate I-BPDC : NH <sub>2</sub> -BPDC ratio of 1:1.15.....	165

Figure 4.28 $^1\text{H}$ NMR of acid digested $\text{NH}_2\text{-UiO-67(Zr)}\text{cI-UiO-67(Zr)}$ in $\text{DMSO-d}_6$ showing an approximate I-BPDC : $\text{NH}_2\text{-BPDC}$ ratio of 1:1.2.....	166
Figure 4.29 Simulated PXRD pattern of $\text{UiO-67(Zr)}$ (black) and experimental PXRD pattern of as-synthesized $\text{UiO-67(Zr)}\text{cUiO-67(Hf)}\text{cUiO-67(Zr)}$ (red).....	167
Figure 4.30 Simulated PXRD pattern of $\text{UiO-67(Zr)}$ (black) and experimental PXRD pattern of as-synthesized $\text{I-UiO-67(Zr)}\text{cUiO-67(Hf)}\text{cNH}_2\text{-UiO-67(Zr)}$ (red).....	168
Figure 4.31 $^1\text{H}$ NMR of acid digested $\text{I-UiO-67(Zr)}\text{cUiO-67(Hf)}\text{cNH}_2\text{-UiO-67(Zr)}$ in $\text{DMSO-d}_6$ showing an approximate I-BPDC : BPDC : $\text{NH}_2\text{-BPDC}$ ratio of 1 : 2.29 : 2.....	169
Figure 4.32 Simulated PXRD pattern of $\text{UiO-67(Zr)}$ (black) and experimental PXRD pattern of as-synthesized Bpy- $\text{UiO-67(Zr)}$ seed crystallites (red).....	170
Figure 4.33 Simulated PXRD pattern of $\text{UiO-67(Zr)}$ (black) and experimental PXRD pattern of as-synthesized Bpy- $\text{UiO-67(Zr)}\text{cUiO-67(Zr)}$ (red).....	171
Figure 4.34 Simulated PXRD pattern of $\text{UiO-67(Zr)}$ (black) and experimental PXRD pattern of as-synthesized Bpy- $\text{UiO-67(Zr)}\text{cPro-UiO-67(Zr)}$ (red).....	172
Figure 4.35 $^1\text{H}$ NMR of digested Bpy- $\text{UiO-67(Zr)}\text{cPro-UiO-67(Hf)}$ in $\text{K}_3\text{PO}_4/\text{D}_2\text{O}$ showing an approximate BpyDC : Pro-BPDC ratio of 1:1.25.....	173
Figure 4.36 TEM image (A) and STEM-HAADF image (B) of Bpy- $\text{UiO-67(Zr)}\text{cPro-UiO-67(Zr)}$ . .....	173
Figure 4.37 STEM-HAADF Image of $\text{UiO-67(Zr)}$ (top) and EDS sum spectrum (bottom) of the entire image area after soaking with $\text{PdCl}_2(\text{CH}_3\text{CN})_2$ solution and thorough washing.....	174
Figure 4.38 STEM-HAADF Image of Pro- $\text{UiO-67(Zr)}$ (top) and EDS sum spectrum (bottom) of the surveyed area after soaking with $\text{PdCl}_2(\text{CH}_3\text{CN})_2$ solution and thorough washing.....	176

Figure 4.39 Simulated PXRD pattern of UiO-67(Zr) (black) and experimental PXRD pattern of as-synthesized BpyPd-UiO-67(Zr)⊂UiO-67(Zr) (red).....	177
Figure 4.40 Simulated PXRD pattern of UiO-67(Zr) and experimental PXRD pattern of as-synthesized BpyPd-UiO-67(Zr)⊂Pro-UiO-67(Zr) (red).....	178
Figure 4.41 TEM and STEM-HAADF images of BpyPd-UiO-67(Zr)⊂Pro-UiO-67(Zr).....	179
Figure 4.42 STEM-EDS mapping data of BpyPd-UiO-67(Zr)⊂Pro-UiO-67(Zr).....	179
Figure 4.43 TEM images of 13 nm 55 kDa PVP capped Au nanoparticles. ....	180
Figure 4.44 TEM image of 40 nm Ag nanoparticles capped with 40 kDa PVP.....	181
Figure 4.45 TEM image of Cu <sub>2-x</sub> Se nanoparticles capped with 55 kDa.....	182
Figure 4.46 Simulated PXRD pattern of UiO-67(Zr) (black) and PXRD pattern of as-synthesized Au⊂UiO-67(Zr) (red). ....	183
Figure 4.47 TEM images of Au⊂UiO-67(Zr). ....	184
Figure 4.48 Simulated PXRD pattern of UiO-67(Zr) (black) and experimental PXRD pattern of as-synthesized Au⊂UiO-67(Zr)⊂UiO-67(Hf) (red).....	185
Figure 4.49 Simulated PXRD pattern based on UiO-67(Zr) crystal structure and PXRD pattern of as-synthesized Ag⊂UiO-67(Zr) (red).....	186
Figure 4.50 TEM images of Ag⊂UiO-67(Zr). ....	187
Figure 4.51 Simulated PXRD pattern based on UiO-67(Zr) crystal structure (black) and PXRD pattern of as-synthesized Ag⊂UiO-67(Zr)⊂UiO-67(Hf) (red). ....	188
Figure 4.52 Simulated PXRD pattern based on UiO-67(Zr) crystal structure and PXRD pattern of as-synthesized Cu <sub>2-x</sub> Se⊂UiO-67(Zr) (red).....	189
Figure 4.53 TEM images of Cu <sub>2-x</sub> Se⊂UiO-67(Zr).....	190

Figure 4.54 Simulated PXRD pattern based on UiO-67(Zr) crystal structure and PXRD pattern of as-synthesized  $\text{Cu}_{2-x}\text{Se}\subset\text{UiO-67(Zr)}\subset\text{UiO-67(Hf)}$  (red). ..... 191

Figure 5.1 Ligands computationally screened to create a UiO-67 family MOF (from left to right: BPDC,  $\text{CH}_3\text{-BPDC}$ ,  $\text{SH-BPDC}$ ,  $\text{NH}_2\text{-BPDC}$ ,  $\text{N}_3\text{-BPDC}$ ,  $\text{NO}_2\text{-BPDC}$ ,  $\text{Br-BPDC}$ ,  $\text{Cl-BPDC}$ ). 195

Figure 5.2 (a) Crystal binding energies computed from CP2K DFT calculations. (b) Optimal binding geometry of DMMP with UiO-67- $\text{NH}_2$ . Dashed lines indicate hydrogen bonds of 2.34 Å (top) and 2.45 Å (bottom). (c) Optimal binding geometry of DMMP with UiO-67- $\text{CH}_3$ . Dashed lines indicate hydrogen bonds of 2.28 Å (vertical) and 2.40 Å (horizontal). (d) Optimal binding geometry of DMMP with UiO-67. Dashed line indicates hydrogen bond of 2.76 Å. For panels (b), (c), and (d), Zr shown in light blue, oxygen shown in red, carbon shown in gray, nitrogen shown in blue, hydrogen shown in white. Visualizations created with OVITO.<sup>242</sup> ..... 197

Figure 5.3 TEM images of (A) UiO-67 crystals, (B) UiO-67- $\text{CH}_3$  crystals and (C) UiO-67- $\text{NH}_2$  crystals. .... 200

Figure 5.4 PXRD patterns of as-synthesized UiO-67 (black), as-synthesized UiO-67- $\text{NH}_2$  (orange) and as-synthesized UiO-67- $\text{CH}_3$  (red) in comparison with simulated PXRD pattern based on the UiO-67 crystal structure (blue). .... 200

Figure 5.5 Thermogravimetric analyses of as-synthesized UiO-67 (black), UiO-67- $\text{CH}_3$  (red), and UiO-67- $\text{NH}_2$  (orange). .... 201

Figure 5.6 Experimental  $\text{N}_2$  isotherms at 77 K of UiO-67 (black), UiO-67-Me (red) and UiO- $\text{NH}_2$  (blue). Solid circle and open circles represent adsorption and desorption data points respectively. .... 202

Figure 5.7 Reproducible N<sub>2</sub> adsorption isotherms at 77 K collected with multiple independent sample batches of (a) UiO-67, (b) UiO-67-Me and (c) UiO-67-NH<sub>2</sub>. Orange, black and green data points represent different sample batches. .... 203

Figure 5.8 Surface areas for the synthesized MOFs computed from simulations and from experimental BET measurements based on N<sub>2</sub> isotherms at 77 K. The data shown as black bars were computed from a geometric algorithm involving rolling an argon atom over the surface of the MOF. The data shown as red bars were computed from applying the BET equation to simulated N<sub>2</sub> isotherms at 77 K. The blue bars represent BET surface areas from experimental N<sub>2</sub> isotherms at 77 K (Figure 6.5). Overall, the agreement is very good between the experiments and simulations. .... 204

Figure 5.9 DFT pore size distribution of UiO-67 (black), UiO-67-Me (red), and UiO-67-NH<sub>2</sub> (blue) simulated using experimental isotherm data in Figure 5.6. .... 204

Figure 5.10 Mass spectra temperature profiles showing all mass fragments: m/z = 15 (green), m/z = 79 (red), m/z = 94 (blue) and m/z = 109 (gray). All DMMP fragments share similar profiles indicating molecular desorption of DMMP. Note: m/z = 109 was multiplied by 3 for improved resolution..... 206

Figure 5.11 Thermal desorption profiles as a function of DMMP exposure for (a) UiO-67-NH<sub>2</sub>, (b) UiO-67-CH<sub>3</sub> and (c) UiO-67. Spectra are shown for increasing exposure from 1000 L (gray) to 8000 L (red). Desorption sites are characterized by increasing temperature: (M) multilayer, (W) weakly physisorbed and (S) strongly physisorbed..... 208

Figure 5.12 Thermal desorption profiles at 1000 L DMMP exposure for UiO-67-NH<sub>2</sub> (green), UiO-67-CH<sub>3</sub> (blue) and UiO-67 (black). .... 209

Figure 5.13 FTIR spectra of the fingerprint region for (a) UiO-67-NH<sub>2</sub>, (b) UiO-67-CH<sub>3</sub> and (c) UiO-67 showing the initial MOF before DMMP exposure (black), after 9000 L DMMP exposure (red), and after thermal treatment to 473 K (blue). All spectra were collected at 100 K and baseline corrected..... 210

Figure 5.14 Full DMMP mass spectrum after purification via consecutive freeze-pump-thaw cycles..... 219

## ACKNOWLEDGEMENT

With graduate school coming to an end, I feel immensely lucky and grateful for the inspiration, support, help, and love from my mentors, colleagues, friends, and family that has sustained me through the trials and tribulations of this journey.

I want to begin by thanking my advisor, Professor Nathaniel Rosi, for taking me into his research group and allowing me the freedom to explore my own research interests, for his mentoring and encouragement during my difficult times, and, most importantly, for being a role model for me to emulate every day. I am also grateful to my dissertation committee members – Professors Jill Millstone, Haitao Liu and Christopher Wilmer – for their help, guidance and recommendation letters. I have greatly benefited from meetings with them as well as taking their classes.

The work in this dissertation would not have been possible without the contribution of my collaborators outside the Rosi group. I want to thank Dr. Svetlana Eliseeva and Professor Stephane Petoud for their help with photoluminescence experiments. I also thank my friend and colleague David White, who generously spent many hours with me conducting photoluminescence experiments. I very much enjoyed our conversation amid those experiments. I am grateful to my friend and colleague Xing Yee Gan for her nanoparticle samples and for what I have learned from her in our discussions. I am also grateful to Nathan Diemler, who was kind enough to teach me how to use STEM-EDS. In addition, I would like to thank Jonathan Ruffley, Isabella Goodenough, Prof. Karl Johnson, and Prof. Eric Borguet for our successful collaboration over the past 3 years. Prof. Karl Johnson, with his rigorous attitude toward science, and passionate work ethic, has been an inspiration. I thank him for his guidance, criticism and recommendation letter. Also, I would

like to thank, Professor Rongchao Jin, Dr. Qi Li, Yingwei Li and Tatsuya Higaki, for the opportunity to participate in their projects that greatly broadened my research experience. Finally, I acknowledge the research facility staff members at Pitt – Dr. Susheng Tan, Dr. Steven Geib, Dr. Esta Abelev, Dr. Bhaskar Godugu, Mr. Michael McDonald, and Mr. Thomas Harper – for their assistance and training on many scientific instruments.

Many thanks to the past and present members of the Rosi group near and dear to my heart – Dr. Chong Liu, Dr. Andrea Merg, Dr. Soumitra Punekar, Dr. Alexander Spore, Dr. Chen Zhang, Dr. Mona Mohamed, Dr. Yeon Hye Kwon, Patrick Muldoon, Yicheng Zhou, Zachary Schulte, Mattheus De Souza and Sydney Brooks – for their generous help and friendship. I am especially grateful to Chong for his guidance in lab, and to Patrick for teaching me how to fish on the Allegheny River.

The research experience, and life lessons I received from the Floreancig group has greatly influenced me as a chemist. I am thankful for what Professor Paul Floreancig and his group have done for me. I thank Xun and GR for their encouragement over the years long after they have graduated.

Finally, I thank my family for their unconditional love. Mom and dad have been supportive in almost every important decision I have made. No words can do justice to what they have done for me over the years. I fondly remember my late grandparents. In the trying times, I often think of them and my carefree childhood with them. I am tremendously grateful for the joy and warmth my wife, Xinyue, has brought into my life, and the lovely memories we share in both Pittsburgh and State College. I look forward to reading her dissertation soon.

## 1.0 INTRODUCTION

### 1.1 MATERIAL PLATFORMS

One of the most ambitious efforts of modern chemistry is to precisely control and manipulate matter through chemical transformation at the atomic, molecular and, more recently, nanometer scales. Structural and compositional parameters of materials in these microscopic regimes, such as the topology, structure metrics, and functional group placement as well as their intricate interplay, are often instrumental in determining the properties and functions of materials. Conceivably, a powerful and logical approach to novel materials entails systematic control over one or more of these important structural parameters. As a result, a series of new materials, instead of a single material, can be efficiently developed and their structure-property relationships thoroughly evaluated. In this dissertation, I define systematically obtained series of materials such as these as “material platforms”.

A material platform typically consists of one or several prototype material(s) and an ever-expanding library of materials derived from the prototype(s). While individual materials within a material platform are often closely related and share many common features in their chemical structures, step changes in properties/functions may occur due to small variations in critical structural parameters that can be carefully and systematically controlled. In this sense, material platforms offer an efficient approach to diverse properties and sophisticated functions in materials, especially when the corresponding parameters can be readily customized. Also, precise correlation between the systematically manipulated structural parameters with the resulting distinct properties/functions in a material platform may provide critical insights into the mechanisms that

dictate the properties of interest and allow for rational and continuous improvement in material design. Several well-established material platforms are illustrated in Figure 1.1 as examples to demonstrate how their important properties can be improved or diversified by systematically tailoring key structural and compositional parameters. The stability, reaction selectivity, and turnover frequency of Grubbs' catalysts are optimized by modifying molecular structures of their ligands (Figure 1.1A).<sup>1</sup> The photoluminescence spectra of halide perovskite nanocrystals (Figure 1.1B) are tuned by adjusting their halide composition.<sup>2</sup> Electronic and optical properties of single-walled carbon nanotubes (Figure 1.1C) are governed by controlling their "twist", also known as the chirality index.<sup>3</sup> The localized surface plasmon resonance of gold nanorods (Figure 1.1D) is tailored by tuning their aspect ratios.<sup>4</sup>

From a viewpoint of synthetic chemistry, developing novel material platforms includes the following steps: 1) identification or design of prototype materials with exciting properties/functions and tunable structural parameters, and 2) uncovering novel chemistry, or implementing known methodologies to effectively and systematically control or tailor important structural parameters in the prototype materials and, as a result, generate a large number of new materials with diverse properties/functions. *The diversity and complexity of materials within a materials platform are positively correlated to: 1) the variety of their systematically tunable structural parameters, 2) the versatility of applicable chemical methodologies to alter their structural parameters, and 3) the impacts of structure variation on their properties/function. In all of the above aspects, metal-organic frameworks (MOFs) have exceptional potential as platforms where materials with diverse and complex properties and functions can be systematically and rationally custom designed and synthesized.*

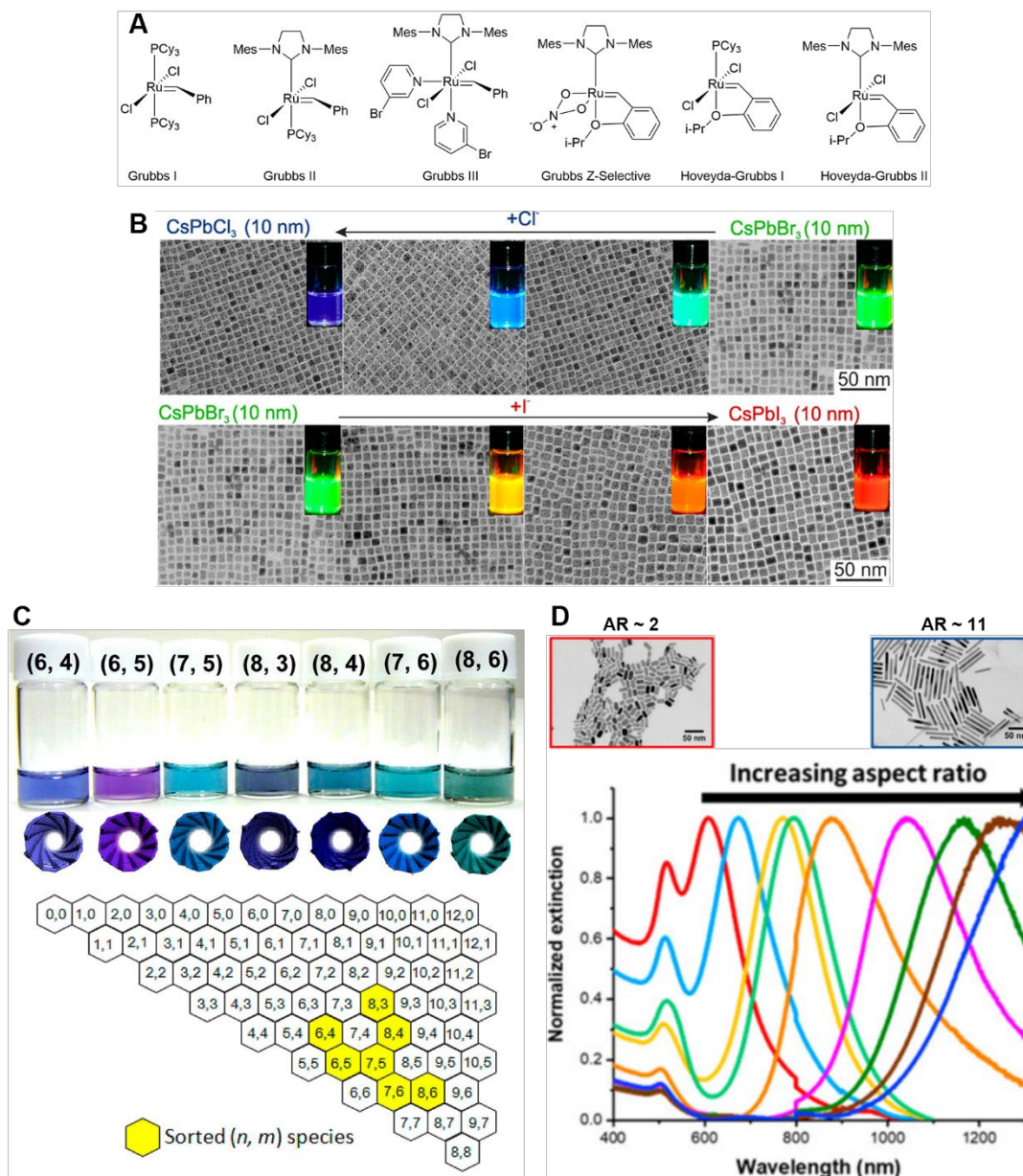


**Figure 1.1** (A) molecular structures of selected commercial Grubbs Catalysts for olefin metathesis;<sup>1</sup> (B) photoluminescence and transmission electron micrographs of halide perovskite nanocrystals with variable halide anion compositions (adapted from ref. 2 with permission);<sup>2</sup> (C) solutions of various single-walled carbon nanotubes with different chirality index (adapted from ref. 3 with permission);<sup>3</sup> (D) Tunable localized surface plasmon resonance of gold nanorods with different aspect ratios (adapted from ref. 4 with permission).<sup>4</sup>

## 1.2 METAL-ORGANIC FRAMEWORKS

The term “metal-organic framework”, coined and popularized by Yaghi et al. in the 1990s,<sup>5-6</sup> refers to a class of crystalline materials featuring extended 2D or 3D networks formed by linking well-defined inorganic metal complexes/clusters - also known as secondary building units (SBUs) - with polytopic organic ligands.<sup>7-9</sup> The structures of two iconic MOFs, MOF-5 and HKUST-1, and their molecular building blocks are shown in Figure 1.2.<sup>10-11</sup> As crystalline extended solid materials, an unprecedented structural feature of MOFs is the simultaneous presence of both organic and inorganic building blocks having molecular characteristics, instead of simple atoms or ions in traditional solid-state materials. This drastically changed the perception that all crystalline extended solids are purely inorganic and non-molecular. For the pioneers of this field, what immediately came into sight was an uncharted materials space waiting to be mined: the possible combinations of organic and inorganic building blocks are virtually infinite. Furthermore, these well-defined molecular building blocks, which can be either pre-synthesized or predictably assembled *in situ* under clearly identified synthetic conditions, allow for careful design of MOF structures, which is in stark contrast to the unpredictable discovery of traditional inorganic solids.<sup>12</sup>

To be truly designable, the atomic structure of MOFs must be thoroughly understood. Due to their crystallinity, complex yet well-defined MOF structures can be unambiguously elucidated with atomic precision using diffraction techniques. Precise correlation of MOFs’ molecular structures to their synthetic conditions and properties offers in-depth knowledge that, in turn, guides and improves material design.

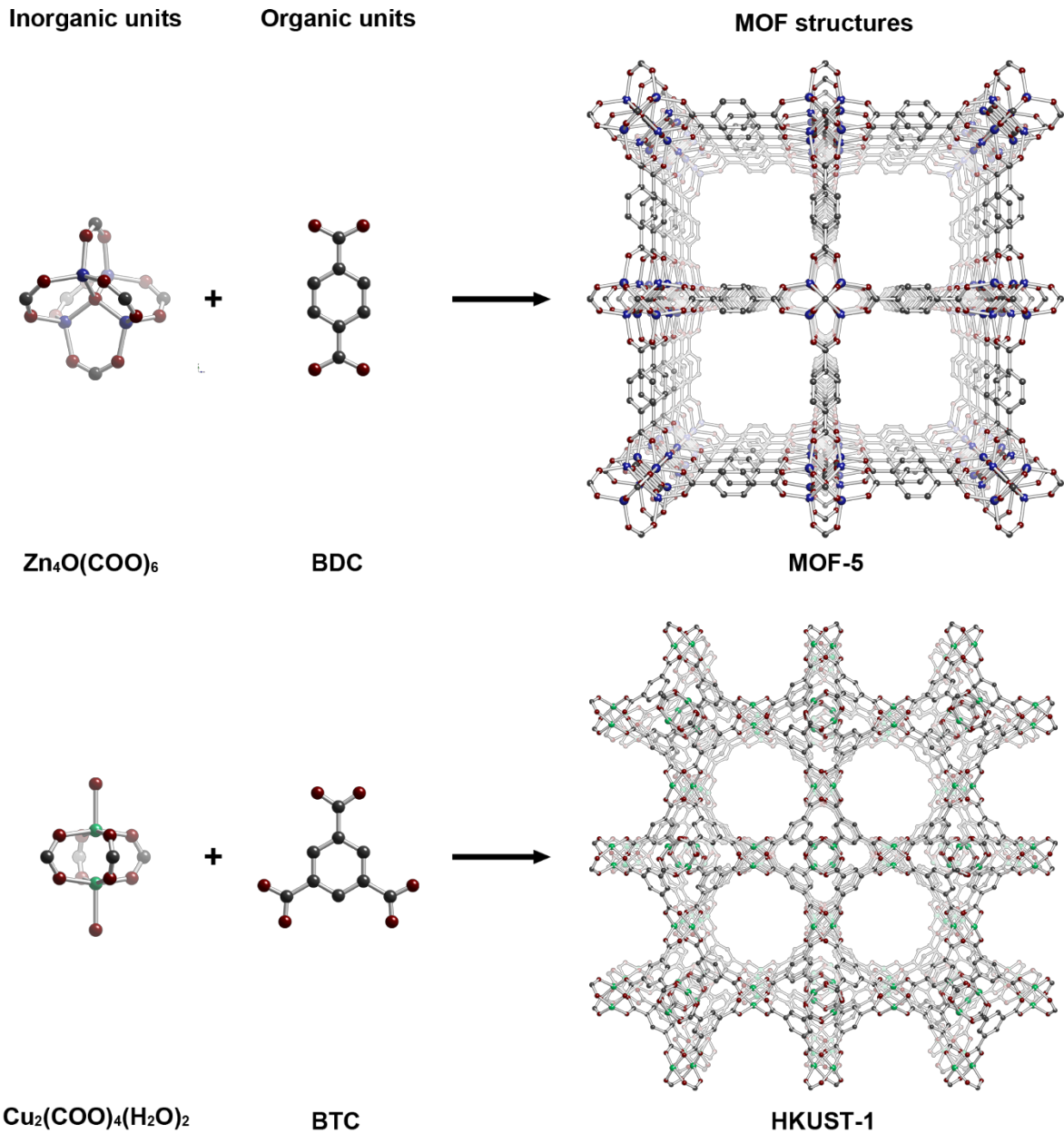


**Figure 1.2** The inorganic SBUs, organic linkers and extended structures of MOF-5 and HKUST-1.<sup>10-11</sup>

Porosity is another important attribute of MOFs. When molecular building blocks are linked together into MOF scaffolds, interstitial cavities can form with diameters ranging from several angstroms to several nanometers. Since MOFs are crystalline, their pores have well-defined size and shape. The large amount of void space in MOFs, including both micropores (< 2 nm in diameter) and mesopores (2 – 50 nm in diameter), not only are suitable for storage and

separations of molecular species,<sup>13-15</sup> but also give rise to substantially large surface areas between MOFs and their environment where interesting phenomena can occur, such as molecular adsorption, catalysis, and molecular recognition.<sup>15-21</sup> MOFs are the most porous materials known, with a host of MOFs having specific surface areas exceeding 4000 m<sup>2</sup>/g.<sup>22-24</sup> The current world record MOF surface area is 7839 m<sup>2</sup>/g.<sup>23</sup>

### 1.3 MOF PLATFORMS

The convergence of three disparate structure elements – inorganic complexes/clusters, organic molecules, and porosity – in the well-defined MOF structures presents a unique opportunity to synergistically integrate a broad range of properties and functions. Most of the properties and functions achievable in MOFs fall into two categories. The first type includes those directly imparted by the inorganic and organic building blocks, or the overall scaffolds, such as catalytic properties,<sup>17</sup> optical properties,<sup>25</sup> magnetic properties,<sup>26</sup> and electroconductive properties.<sup>27</sup> Such properties of MOFs are extremely diverse and are largely determined by the detailed molecular structures, functional groups, and elemental compositions of the organic and inorganic building blocks. Equally important is the second type of properties in MOFs that derive from their interstitial pore space, such as surface area, pore size, and pore geometry. These properties greatly influence the diffusion, transport, and adsorption of molecules in MOFs and are primarily determined by the dimensions, geometry, and connectivity of the organic and inorganic building blocks.<sup>28-29</sup> It is worth noting that the geometry and connectivity of building blocks together determines the underlying topology of a MOF, which is an important structural parameter that will be introduced in the next section.

One can imagine that MOF materials with diverse properties can be custom-designed and optimized for specific needs. To achieve this, developing versatile MOF platforms is fundamentally important where the various structural parameters of a MOF can be rationally and systematically tailored to impart and integrate a broad scope of properties and functions. Ideally, a MOF platform will enable continuous rational design and lead to an ever-expanding library of MOF materials with increasingly diverse and complex properties/functions. The versatility of a MOF platform, to a large degree, is contingent upon the ease with which its various structural parameters can be systematically tailored. At the molecular scale, four structural parameters are of predominant importance in determining the properties and functions of MOFs, including topology, structure metrics, organic functional groups, and inorganic composition. Although tens of thousands of MOF structures have been discovered with most of them tunable in certain aspects of their structures to various degrees, only a small fraction of them are exceptionally amenable to systematic control and modification over several, if not all, of these four structural parameters. Arguably, it is primarily the latter small set of MOFs, collectively as powerful platforms, that truly inspire rational design of MOF materials to achieve diverse properties and complex functions.

The remainder of Chapter 1 serves as an introduction to some of the most important methods and strategies available to control and modify MOF topology, structure metrics, organic functional groups, and inorganic composition. Examples are used to demonstrate how these powerful methods have successfully led to some ever-growing platforms containing MOF materials with increasingly diverse and sophisticated structures and functions.

## 1.4 TOPOLOGY

### 1.4.1 What is topology?

For extended solid materials, a topology, or net, is an abstract graph that describes how building blocks are assembled into a periodic structure. It consists of vertices that are linked together by edges in 2D or 3D space.<sup>30</sup> If a vertex is connected to  $N$  neighboring vertices via  $N$  edges, it is called an  $N$ -connected vertex.<sup>31</sup> The vertices and edges in a net are abstract representations of chemical motifs in an extended structure. In many crystal structures of non-molecular solids, the atoms and bonds coincide, respectively, with the vertices and edges of their underlying nets. For example, the carbon atoms and carbon-carbon covalent bonds in diamond superimpose respectively on the vertices and edges of its underlying topology. Since a net is an abstract graph of the underlying connectivity of building blocks of an extended solid, the same net may be found in different materials. For example, the same net found in diamond is also observed in the crystal structure of silicon. In addition, the vertices and edges in a net may also represent structural motifs beyond atoms and chemical bonds. One can imagine that an  $N$ -connected vertex in a net can be replaced by a polygon or polyhedron building block with  $N$  vertices and, ideally, the same point group symmetry as the original vertex. This operation is referred to as augmentation.<sup>31</sup> For instance, the 4-connected vertices in diamond net can be augmented by tetrahedral building blocks.

Knowledge of topology is fundamentally important for rational design and prediction of MOF structures. The molecular building blocks in MOFs – both polytopic organic linkers and inorganic clusters – can be viewed as polygons or polyhedra defined by atoms representing points of extension to other building blocks.<sup>9</sup> For example, the carbon atoms from the carboxylates are

typically the points of extension for the inorganic SBUs (Figure 1.3). Selected examples of organic/inorganic building blocks with their corresponding polygons/polyhedra are shown in Figure 1.3.<sup>12</sup> Essentially, a MOF structure can be abstracted as an augmented net where well-defined polygons and/or polyhedra are linked together by edges. Conceivably, the topological possibilities for linking different shapes together is a mathematical problem and can be systematically enumerated. MOF structures can then be precisely designed by judiciously linking selected molecular building blocks into targeted topology.

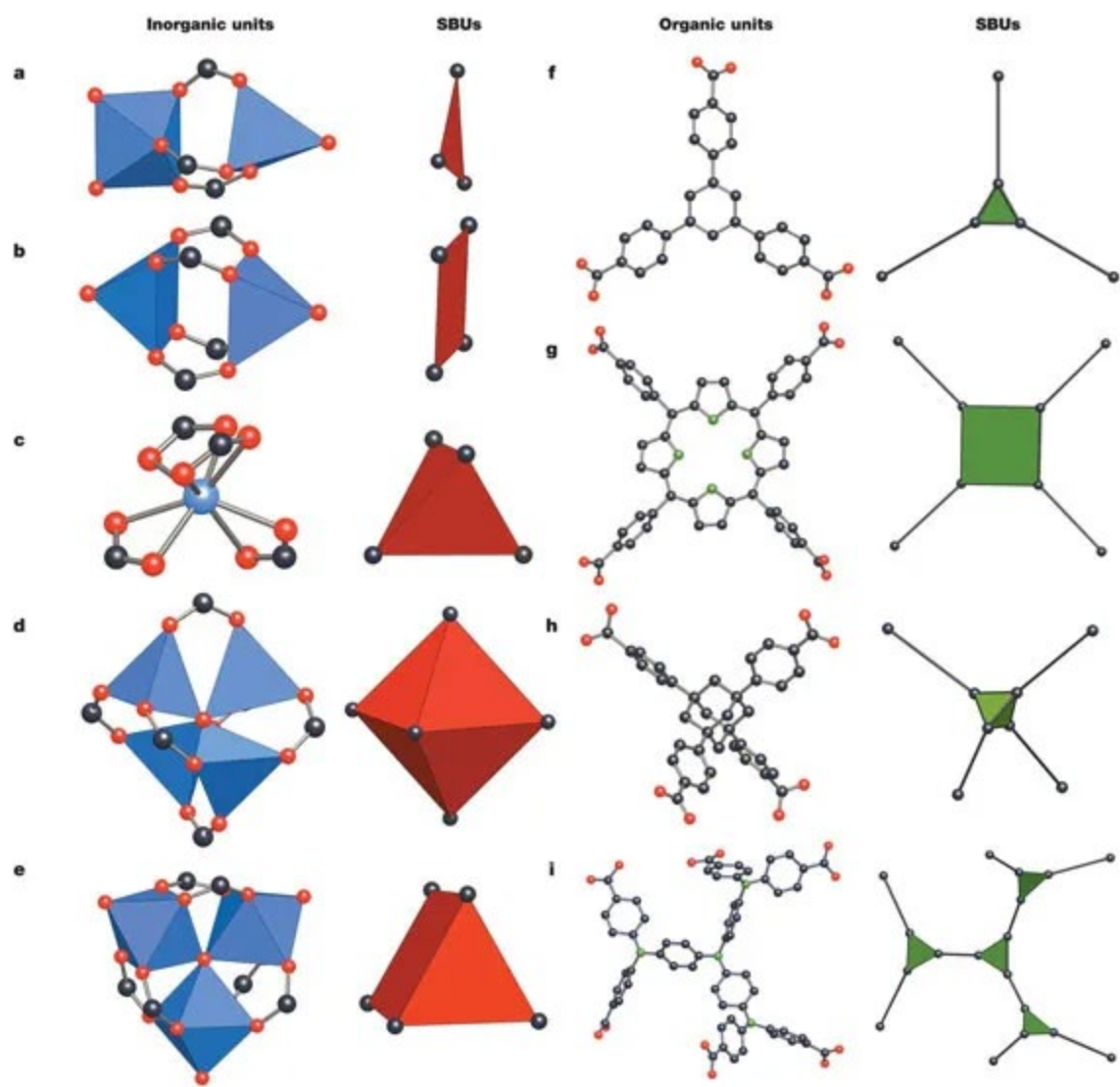


**Figure 1.3** Examples of inorganic, organic building blocks and their abstract shapes defined by points of extension (reprinted from ref.12).<sup>12</sup>

### 1.4.2 Rational and systematic control of MOF topologies

MOF platforms that permit rational and systematic control over MOF topologies are highly desirable, as the underlying topology of a MOF is highly relevant to many important properties, including mechanical properties,<sup>32</sup> internal surface area, and the size and shape of apertures and

cavities.<sup>33-34</sup> These properties may in turn further impact other MOF properties such as stability, adsorption, and transport properties. To demonstrate the impact of topology on properties, we can compare PCN-222 with NU-902 (Figure 1.4),<sup>33-34</sup> two topologically different MOFs with the same building blocks and chemical formula. Because of their different topologies, PCN-222 and NU-902 exhibit different pore sizes and gas adsorption properties. PCN-222 is mesoporous MOF with type IV N<sub>2</sub> adsorption isotherm at 77 K, whereas NU-902 is a microporous MOF with type I N<sub>2</sub> adsorption isotherms at 77 K. When PCN-222 and NU-902 are tested for heterogeneous catalysis, their difference in topology translates to distinct reaction kinetics.<sup>34</sup>

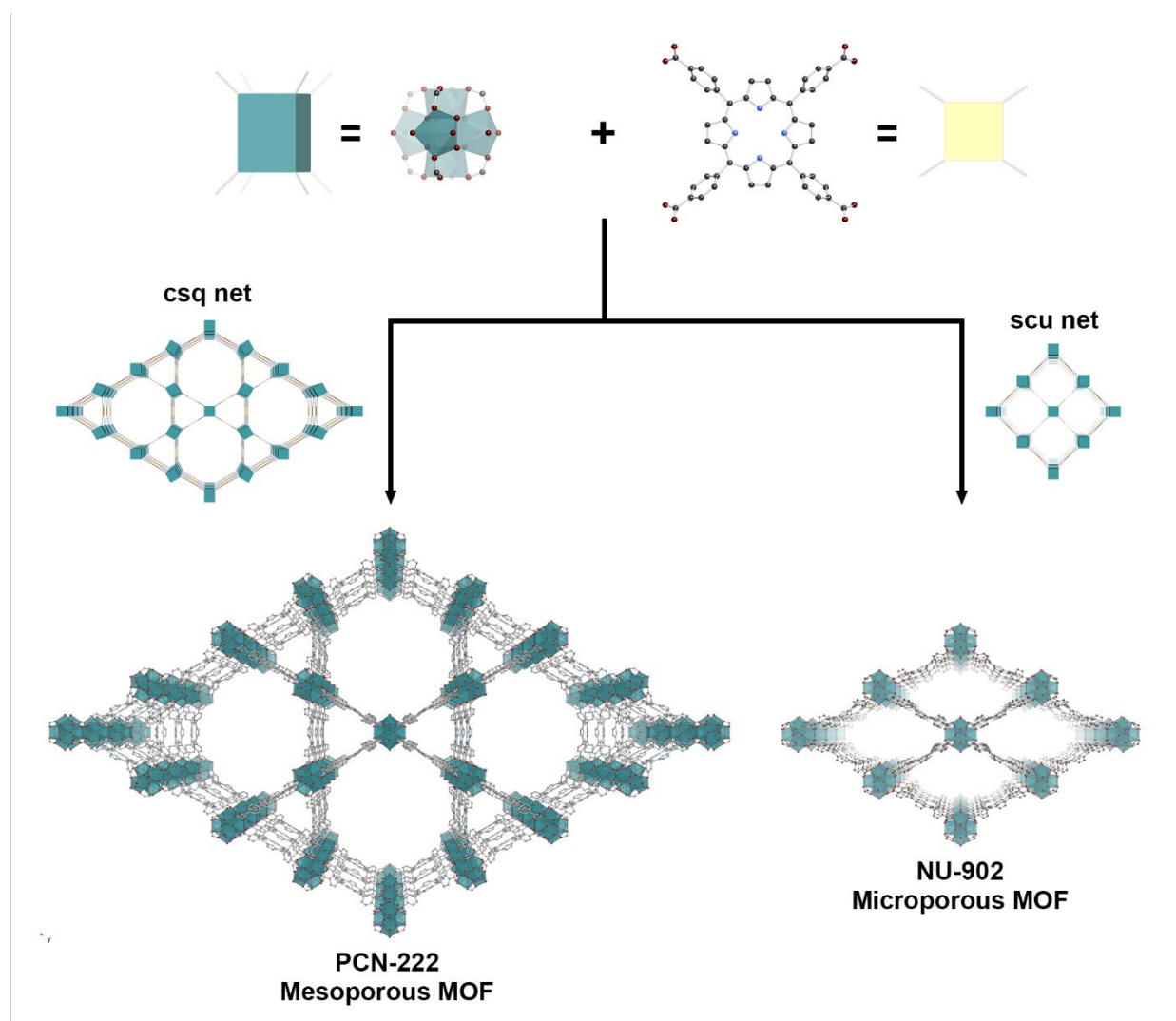


**Figure 1.4** Structures and topologies of PCN-222 and NU-902.<sup>33-34</sup>

Besides serious consideration of topological outcomes from connecting different shapes, achieving MOF structures by design requires non-trivial chemistry. A planned MOF structure will by no means be achievable unless feasible chemistry is in place to form and assemble the devised molecular building blocks. Although pre-synthesized organic linkers are routinely used as starting materials and can maintain their structure integrity in MOF synthesis, tremendous challenges exist in precisely controlling the structures of inorganic building blocks in MOFs. Most inorganic clusters in MOFs, although conceptually considered molecular entities, are not employed as the starting materials in the MOF synthesis. Instead, they are typically assembled *in situ* in solvothermal reactions between metal ion precursors and coordination groups of organic linkers. For MOFs to be truly designable materials, inorganic building blocks must be reliably accessible through clearly-defined reaction conditions.

In practice, only a limited number of inorganic clusters in MOF structures have been found accessible *in situ* through well-defined reaction conditions. Some of these inorganic SBUs with high point group symmetry are extremely versatile building blocks for accessing a large number of nets achievable by design.<sup>10-11, 35-36</sup> These inorganic clusters are indispensable building blocks for developing MOF platforms that are amenable to topological control and variation. In these MOF platforms, MOFs composed of the same building blocks can adopt distinct topologies, like PCN-222 and NU-902 in Figure 1.4.<sup>33-34</sup> More commonly, MOF structures with diverse topologies are achieved by systematic combination of a highly symmetric inorganic cluster with various symmetric organic linkers of different geometries. A prominent example is a family of topologically diverse MOF structures composed of the iconic  $Zn_4O(COO)_6$  cluster.<sup>10, 22, 37-44</sup> Selected examples are shown in Figure 1.5.

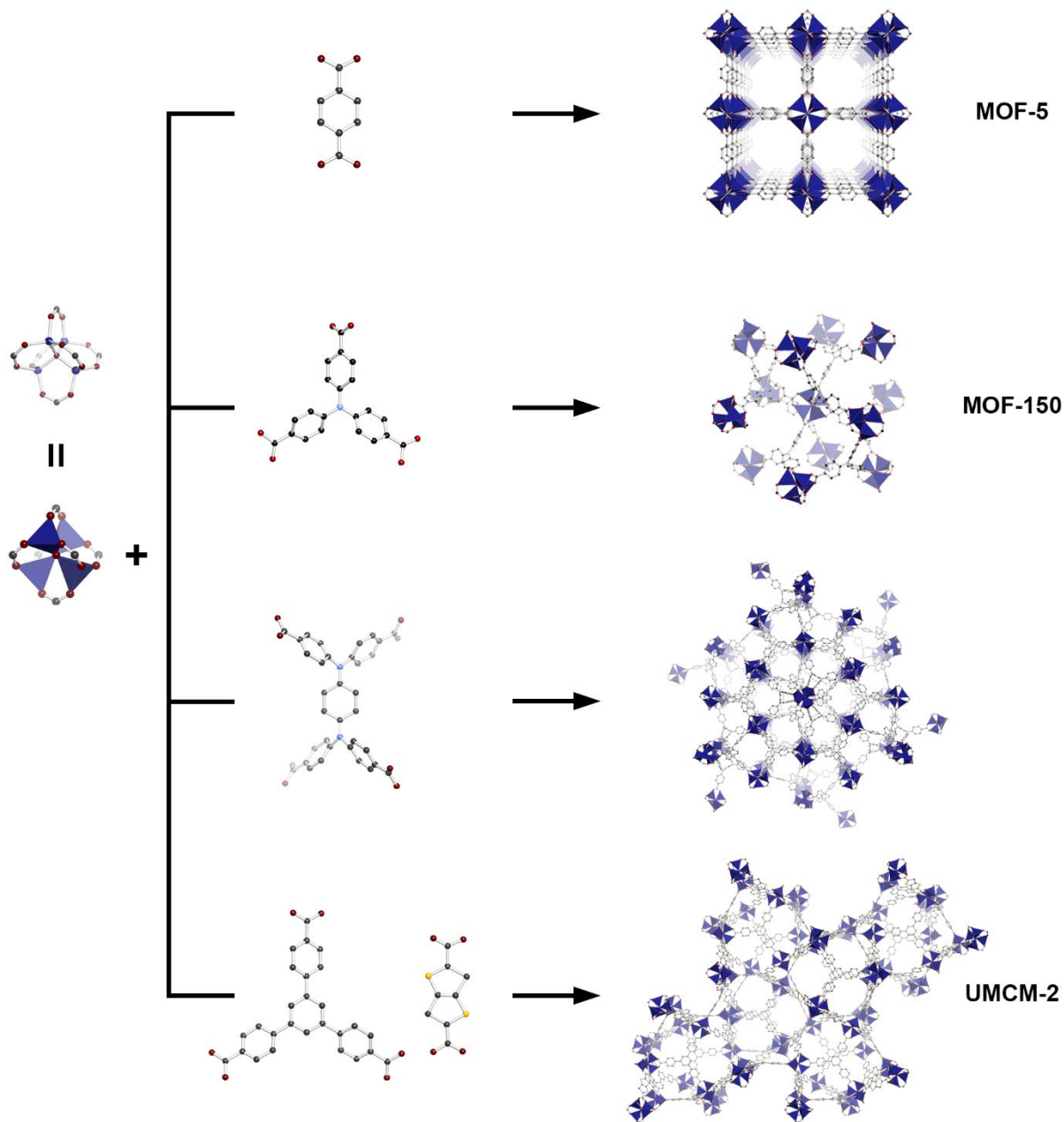


**Figure 1.5** Selected MOF examples of different topologies composed of  $Zn_4O(COO)_6$  SBUs.<sup>10, 37, 43-44</sup>

## 1.5 STRUCTURE METRICS

The preceding section demonstrated that topological diversity within a MOF platform can be rationally and systematically achieved and lead to MOF materials with drastically different properties. Once a MOF with desired topology is obtained, important properties can be further fine-tuned by careful modification of other MOF structural parameters without altering MOF topology. The MOF materials obtained in this fashion are referred to as “isoreticular” to one another for sharing the same underlying net.<sup>45</sup>

One such tunable parameters in MOFs is their structure metrics, which concerns the dimensions of MOF scaffolds and pores. Adjustment of MOF structure metrics is mostly motivated by the desire to precisely control of the pore size of MOFs for various applications and can be accomplished by controlling the dimensions of the molecular building blocks lining the pores. One can simply consider the three structures sharing the same diamond topology that consist of tetrahedra and rod building blocks of different dimensions in Figure 1.6. Compare to the structure in Figure 1.6A, structures in Figure 1.6B and C have expanded scaffolds and cavities that are achieved by increasing size of tetrahedra or the lengths of rods.

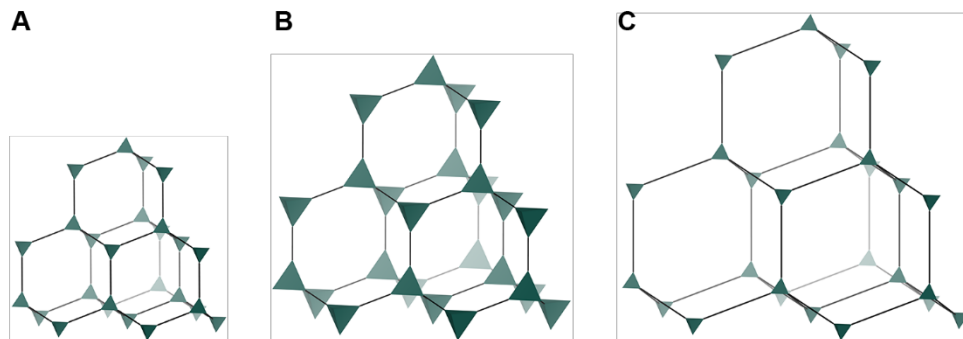


**Figure 1.6** Effects of the size of building blocks on MOF structural metrics. (A) augmented diamond net composed of small tetrahedra and short rods; (B) augmented diamond net composed of large tetrahedra and short rods; (C) augmented diamond net composed of small tetrahedra and long rods.

Realistically, the inorganic building blocks of MOFs are typically indispensable for controlling the topology of a MOF, while organic linkers employed can be readily customized to have different dimensions but the same geometry. Therefore, isorecticular MOFs featuring identical inorganic SBUs and different organic linkers of various dimensions are typically targeted. Specifically, the coordination motifs at the ends of polytopic linkers are held constant to guarantee the assembly of target inorganic clusters under well-defined solvothermal reactions conditions with metal ion precursors, while the spacer groups in between these coordination motifs are varied to control the dimension of linkers. Since rational synthesis like this gives rise to a family of isorecticular MOFs, this approach is termed as “isorecticular synthesis”. A representative example is the IRMOF-74 series (Figure 1.7).<sup>46</sup> Organic linkers of different lengths ranging from 7.0 Å to 50 Å were employed to systematically yield a family of isorecticular MOFs with hexagonal pore apertures tunable from ~ 1 nm to ~10 nm in diameter.

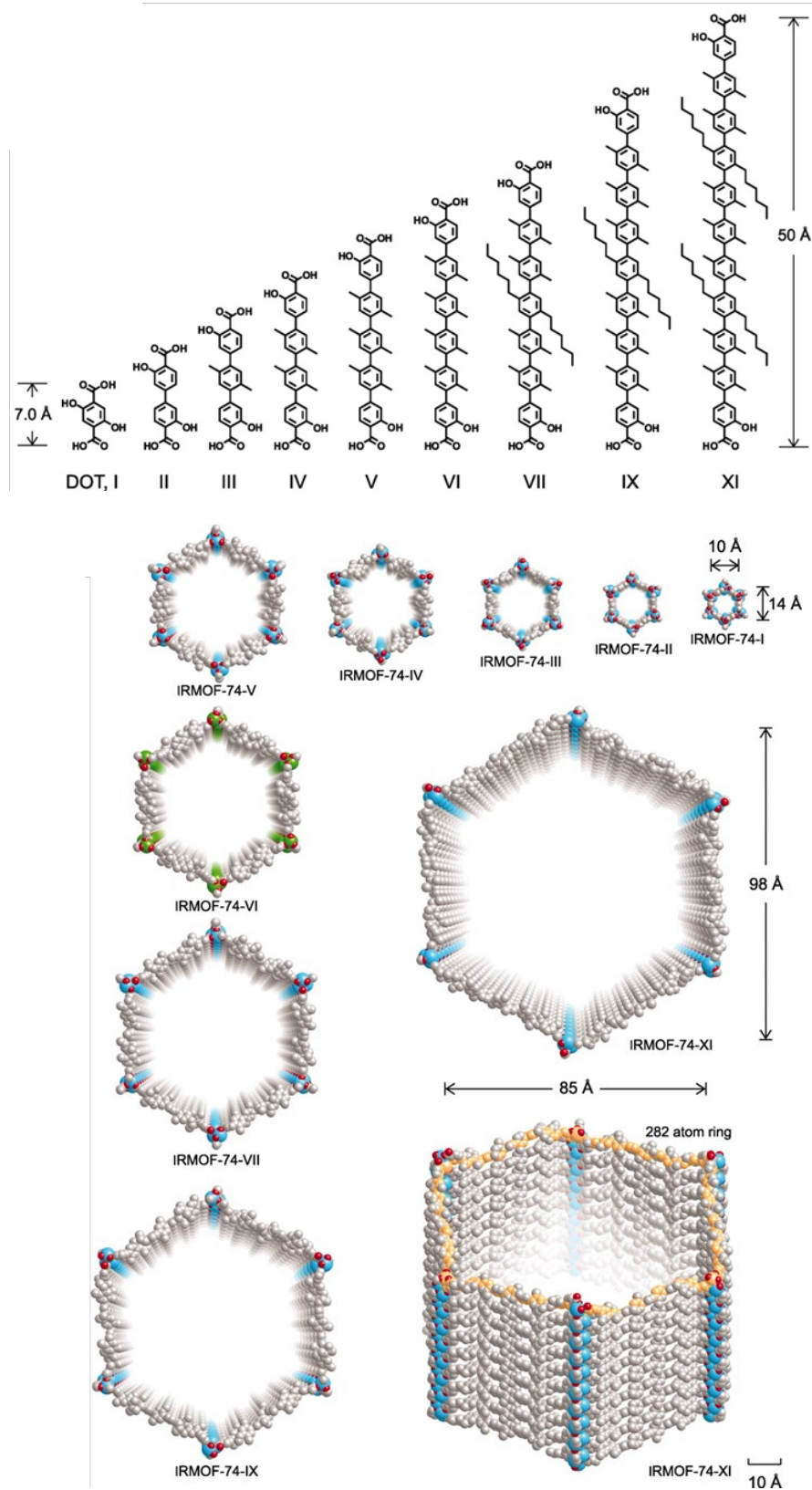


**Figure 1.7** Organic linkers and crystal structures of IRMOF-74 series (adapted from ref. 46).<sup>46</sup>

## 1.6 FUNCTIONALITIES

Apart from readily adjustable structure metrics, the organic building blocks in MOFs can be customized with different functional groups, providing a powerful avenue to incorporating additional functionalities to MOF structures. As extended solids, MOFs' amenability to functionalization is unprecedented. A particularly attractive aspect of this amenability is that the types of functional groups in MOFs can be controlled orthogonally to other structural parameters within a MOF platform, such as the topology and structure metrics. Functional groups in MOFs play multifaceted roles in controlling MOF properties, including: 1) modulation of different aspects of the pore environments, such as size, shape and hydrophobicity, to influence the interactions between the MOF surface and guest molecules; and 2) imparting additional functions such as catalysis, sensing, and reactivity.

Solvothermal synthesis is the most popular approach to obtain isorecticular MOFs containing different functional groups. This approach is often successful when the functional groups in the pre-synthesized organic linkers are stable under MOF synthesis conditions and do not interfere with the *in situ* formation of inorganic SBUs. An exemplary MOF platform achieved using this approach is the UiO-67 MOFs where a host of functionalized ditopic linkers have been employed to obtain isorecticular UiO-67 analogues through solvothermal synthesis (Figure 1.8).<sup>47-</sup>

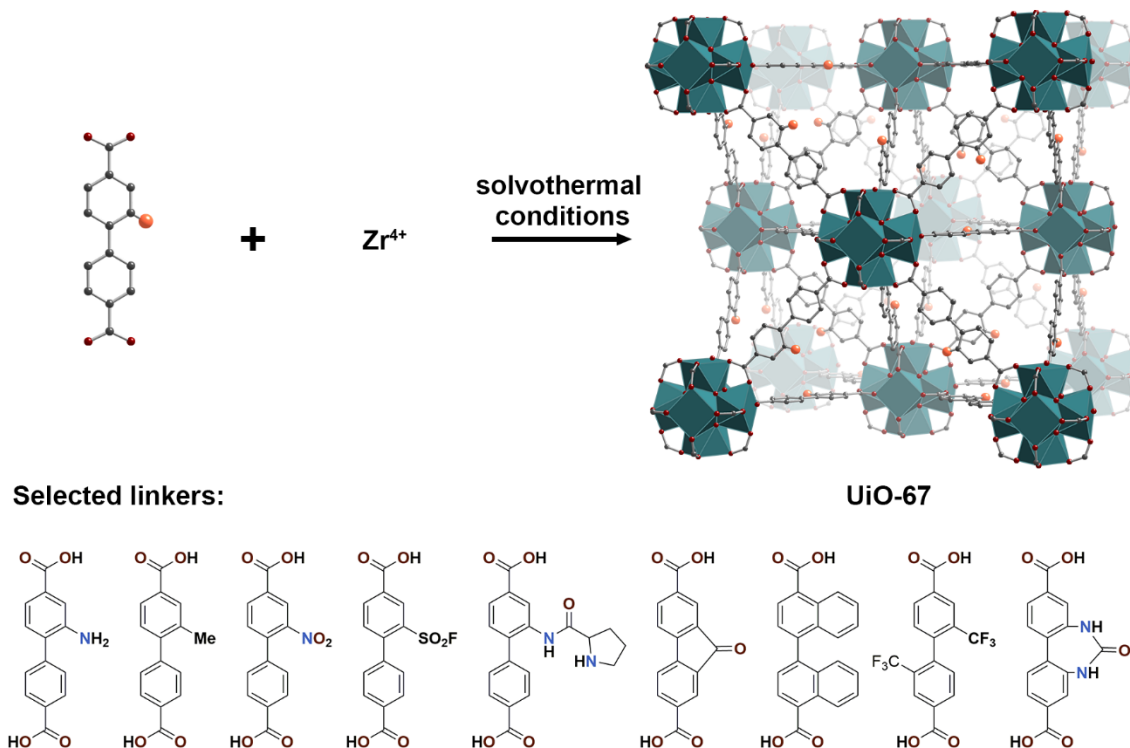


**Figure 1.8** Isoreticular synthesis of UiO-67 MOFs with a select list of functionalized linkers.

Certain functional groups in MOF linkers may interfere with the formation of target inorganic SBUs or suffer from decomposition during solvothermal MOF synthesis, resulting in failure in obtaining functionalized isoreticular MOFs through solvothermal synthesis. Alternatively, post-synthetic linker exchange and covalent post-synthetic modification reactions may be considered.<sup>55-56</sup> For post-synthetic linker exchange, MOF crystals with desired topology and structure metrics are first synthesized and then exposed to a solution containing a second linker carrying a desired functional group (Figure 1.9A). This allows for linker molecules with desired functional groups to swap with linkers in MOF crystals without altering the topology and structure metrics of the MOF. This approach has been broadly employed to introduce functional groups to a variety of different MOFs.<sup>57-61</sup> In post-synthetic modification reactions, MOFs crystals, usually with reactive functional groups, such as primary amine,<sup>62</sup> aldehyde,<sup>63</sup> alkyne and azide,<sup>64-65</sup> can

undergo further covalent reactions to introduce a greater variety of functionalities to their structures (Figure 1.9B, Figure 1.10).

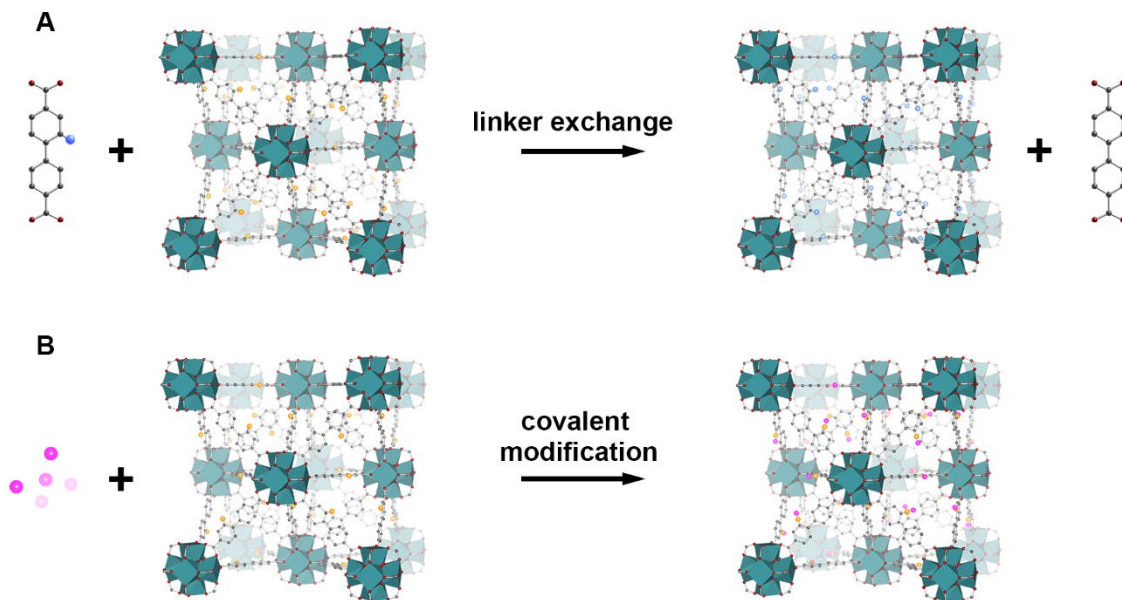


**Figure 1.9** Schematics of (A) post-synthetic linker exchange reactions; and (B) covalent post-synthetic modification reactions.

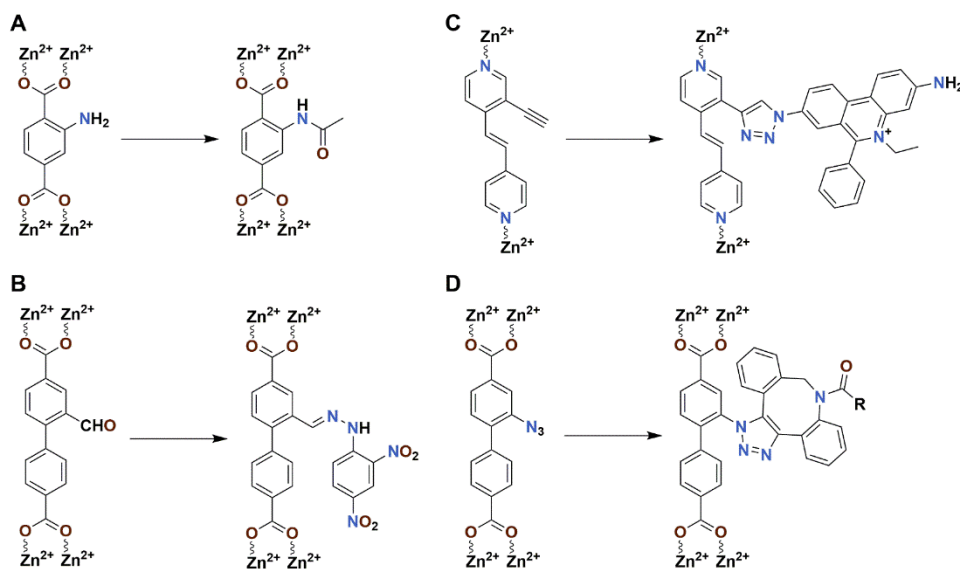


**Figure 1.10** Examples of covalent post-synthetic modification of MOFs.<sup>62-65</sup>

The above synthetic methods also allow for a mixture of different functional groups to be incorporated in single-phase MOF materials, which brings additional levels of diversity and

complexity to MOF materials. For example, isorecticular analogues of MOF-5 containing up to eight different functional groups have been achieved through direct solvothermal synthesis (Figure 1.11 A).<sup>66</sup> Our group also showed that up to three different functional groups can be introduced to bMOF-100 via tandem postsynthetic linker exchange reactions (Figure 1.11 B).<sup>67</sup> Similarly, covalent postsynthetic modification reactions can also be performed in tandem to functionalize a parent MOF material with a mixture of groups (Figure 1.11 C).<sup>68</sup> These types of MOFs are often referred to as multivariate MOFs (MTV MOFs),<sup>66</sup> because with a mixture of functionalities present, several additional variables - including the ratio, combination, and sequence of different functionalities - are now at one's disposal to control and affect MOF properties. Exciting synergies between different functionalities may emerge and vary as a function of their ratio, combination and sequence in MTV MOFs. As a result, the property of an MTV MOF does not simply equal to the sum of the properties of corresponding single-functionality MOFs.<sup>66</sup> As to the three variables in MTV MOFs mentioned above, controlling the ratio and combination of functionalities is relatively straightforward, while controlling and understanding the sequence or spatial arrangement of functionalities in MOF crystals is more challenging, but gives rise to new opportunities in this area. The work described in Chapter 4 of this dissertation represents efforts to address some of the challenges in this domain.

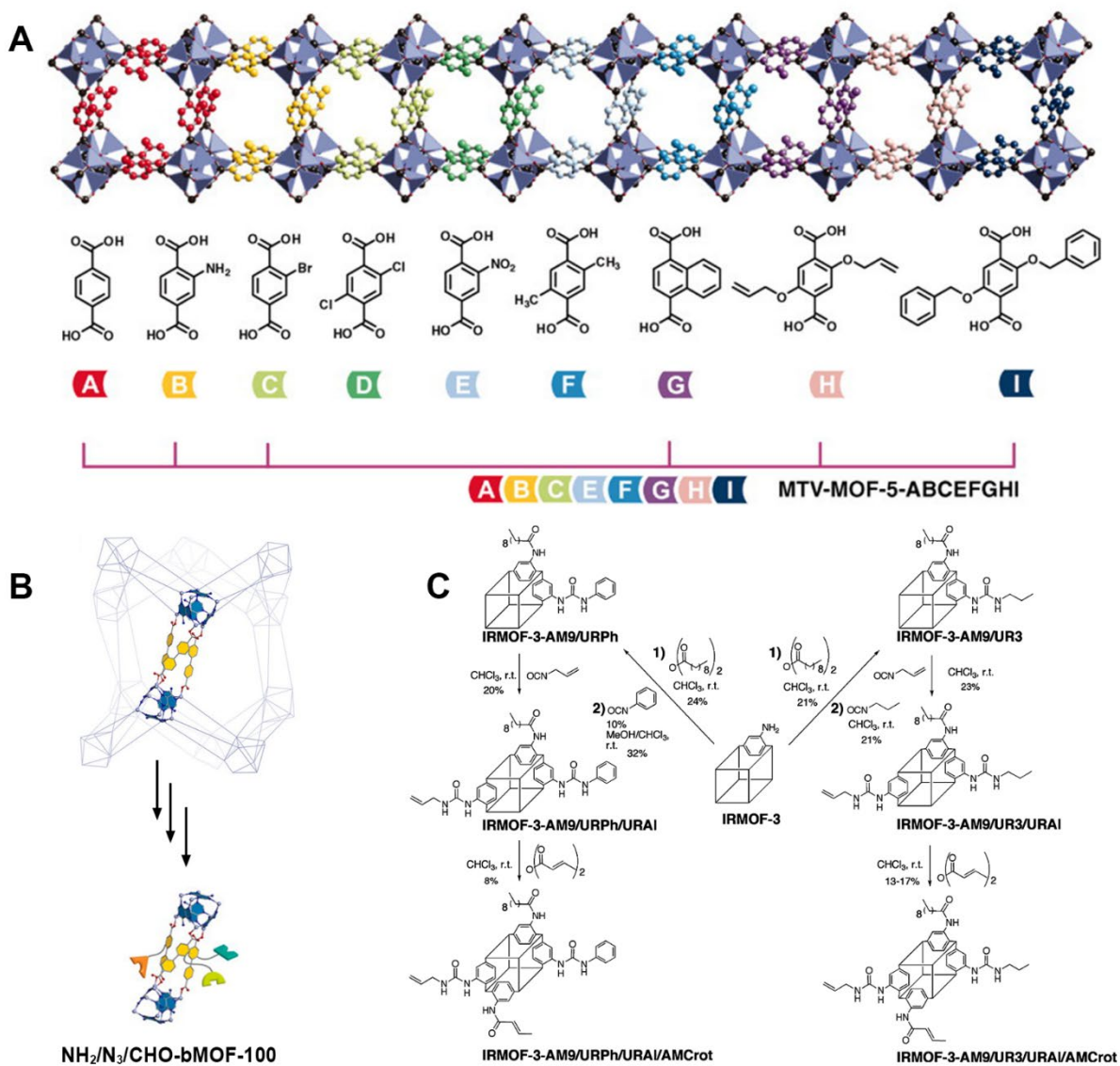


**Figure 1.11** Examples of multivariate MOFs containing multiple functional groups synthesized via (A) solvothermal synthesis (adapted from ref. 66);<sup>66</sup> (B) linker exchange (adapted from ref. 67);<sup>67</sup> and (C) covalent post-synthetic modification (adapted from ref. 68).<sup>68</sup>

## 1.7 INORGANIC COMPOSITION

A broad range of MOFs' physical and chemical properties are significantly affected by or attributable to their inorganic SBUs. Deconvoluting the impacts of the molecular structure and composition of inorganic SBUs on observed MOF properties allows for rational design of materials with optimized performance for various applications. This requires orthogonal control over the inorganic composition, especially the metal composition of MOF SBUs, to their structures as well as other MOF structural parameters discussed above.

Metal ion metathesis is an important post-synthetic modification method to control metal composition in MOF SBUs without changing their structures.<sup>69-70</sup> Metal ion metathesis reactions are typically conducted by soaking the parent MOF samples in a solution of metal salt. During these reactions, metal ions in the SBUs are replaced by a different kind of metal ion in solution that are not present in the parent MOF, leaving the structure of the parent MOF unaltered. This strategy often gives access to materials that are inaccessible through solvothermal reactions. For example, a series of transition metal ions can undergo metathesis reactions with the  $Zn_4O(COO)_6$  SBU and form  $MZn_3O(COO)_6$  ( $M = Ti^{3+}, V^{2+}, V^{3+}, Cr^{2+}, Cr^{3+}, Mn^{2+}$  and  $Fe^{2+}$ ) inorganic clusters in the MOF-5 structure (Figure 1.12).<sup>70</sup> In addition, by carefully controlling metathesis reaction conditions, MTV MOFs containing a mixture of metal ions can be obtained, where the ratio, combination and sequences of metal ions can be deliberately varied.<sup>70-72</sup>

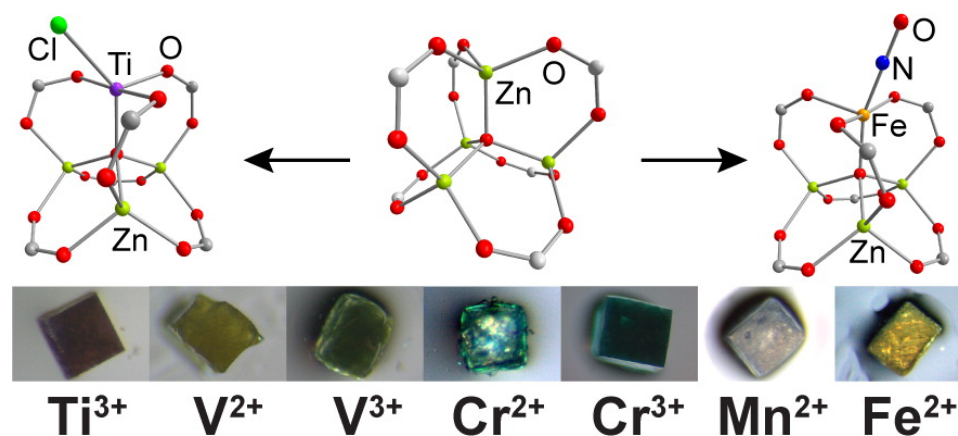


**Figure 1.12** MOF-5 crystals after metal ion metathesis reactions with a series of metal ions (reprint from ref. 70).<sup>70</sup>

Alternatively, solvothermal synthesis can also be utilized to access isostructural MOF materials containing different metal ions, including MTV-MOF with a mixture of metal ions. A few examples of isostructural inorganic SBUs with variable inorganic compositions are shown in Figure 1.13.<sup>11, 35-36, 73-98</sup> Despite having the same molecular structure, isorecticular MOFs containing different transition metal ions may require different solvothermal conditions due to their distinct reactivities, while varying lanthanide metal ions in isorecticular lanthanide MOFs are usually straightforward. In Chapters 2 and 3, I describe the development of a novel lanthanide MOF platform and application of lanthanide MOFs in chemical sensing. In the ensuing section, the synthesis of lanthanide MOFs and their relevant properties are briefly introduced to provide the readers with adequate context for Chapters 2 and 3.

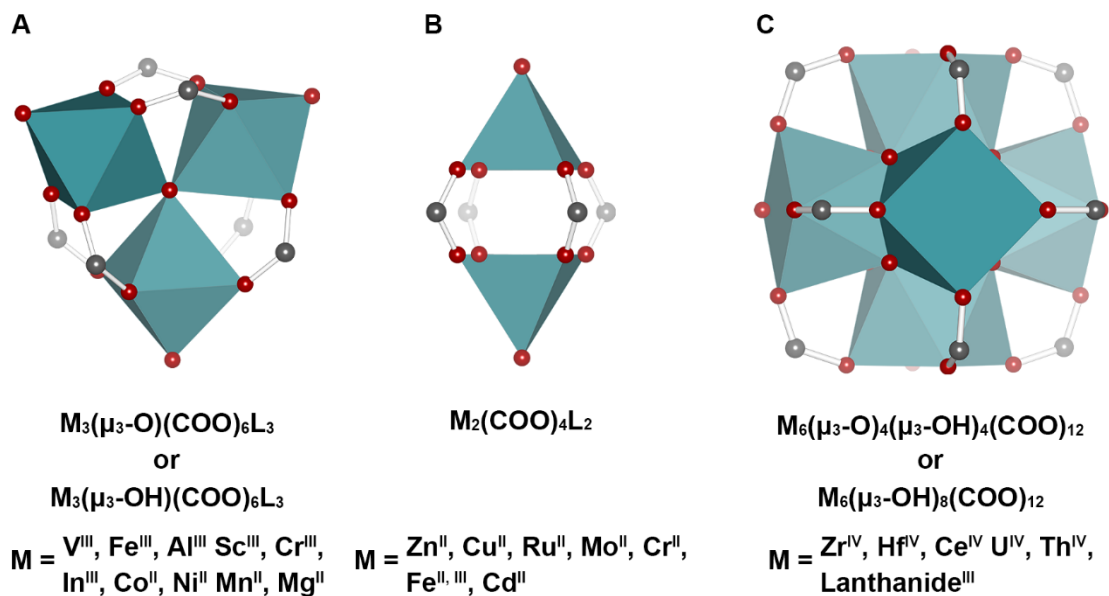


**Figure 1.13** Isostructural inorganic SBUs with different metal ion compositions. <sup>11, 35-36, 73-98</sup>

### 1.7.1 Luminescent lanthanide MOFs

Lanthanide (Ln) elements refer to fifteen f block elements in the 6<sup>th</sup> period of the periodic table, including La, Ce, Pr, Nd, Pm, Sm, Eu, Gd, Tb, Dy, Ho, Er, Tm, Yb and Lu. Together with Y and Sc, they are also known as rare earth elements. The most stable oxidation state of Ln is their trivalent state  $\text{Ln}^{3+}$  with the electronic configuration of  $[\text{Xe}]4f^n$  ( $n = 14$ , with  $n = 0$  for  $\text{La}^{3+}$ , and 14 for  $\text{Lu}^{3+}$ ).  $\text{Ln}^{3+}$  ions are strong Lewis acids and can form stable complexes with oxygen-containing coordination groups. Reacting polytopic organic linkers with  $\text{Ln}^{3+}$  have successfully produced numerous Ln MOF materials. Due to the similar chemical reactivities of different  $\text{Ln}^{3+}$ , isostructural Ln MOFs and complexes can often be synthesized with variable Ln compositions under the same or similar solvothermal conditions. For example, a series of isorecticular MOF known as MIL-78 was synthesized by reacting trimesic acid with various  $\text{Ln}(\text{NO}_3)_3 \cdot 5\text{H}_2\text{O}$  ( $\text{Ln} = \text{Pr}, \text{Nd}, \text{Sm}, \text{Eu}, \text{Gd}, \text{Tb}, \text{Dy}, \text{Er}$ ) under similar conditions (Figure 1.14).<sup>99</sup>

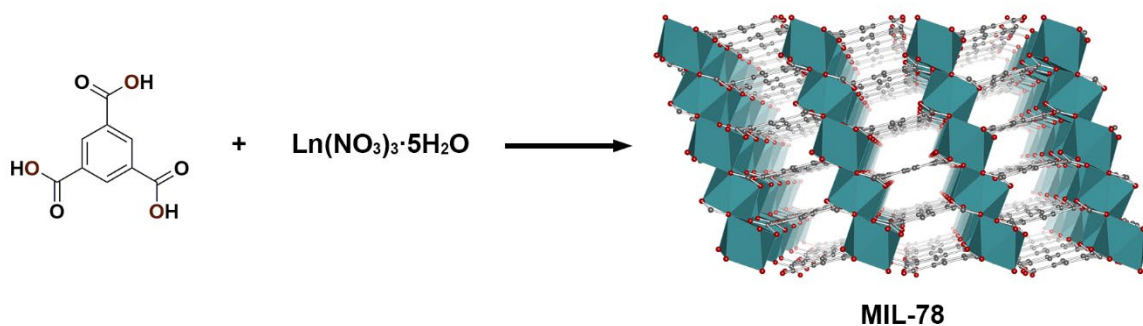


**Figure 1.14** Isorecticular synthesis of MIL-78 using a series of  $\text{Ln}(\text{NO}_3)_3 \cdot 5\text{H}_2\text{O}$  ( $\text{Ln} = \text{Pr}, \text{Nd}, \text{Sm}, \text{Eu}, \text{Gd}, \text{Tb}, \text{Dy}, \text{Er}$ ). C, grey spheres; O, red spheres; Ln, teal polyhedra.

In stark contrast to the similarity in synthetic conditions for isorecticular Ln MOFs containing different  $\text{Ln}^{3+}$  ions are the diverse properties, especially magnetic and luminescence properties,<sup>100-101</sup> attainable by simply altering the Ln composition. These two features, in conjunction with other attributes of Ln MOFs including porosity and high density of emitting  $\text{Ln}^{3+}$  ions in the solid state, make Ln MOFs attractive materials for various applications, such as optical sensing, biological imaging, and single molecular magnets.<sup>102-104</sup> The Rosi group is particularly interested in optimizing the photoluminescence properties of Ln MOFs for optical imaging and sensing applications. For these applications, all  $\text{Ln}^{3+}$  ions, except for  $\text{La}^{3+}$  and  $\text{Lu}^{3+}$ , have sharp emission bands whose positions in the spectrum are insensitive to the environment due to their emissive  $4f \rightarrow 4f$  electronic transitions.<sup>100</sup> These emission bands are characteristic for each  $\text{Ln}^{3+}$  and located across the entire visible and near infrared (NIR) spectrum (Figure 1.15).<sup>105-106</sup> Since the  $4f \rightarrow 4f$  electronic transitions of  $\text{Ln}^{3+}$  are forbidden by the Laporte selection rule, the direct excitation of  $\text{Ln}^{3+}$  luminescence is usually prohibited by their extremely low molar absorption coefficients ( typically  $< 3 \text{ M}^{-1} \text{ s}^{-1}$ ).<sup>107</sup> However, the aromatic linkers or other guest molecules within Ln MOFs can indirectly excite Ln luminescence via the “antenna effect”,<sup>108</sup> a sensitization process in which chromophore molecules with large molar absorption coefficients harvest light

and transfer energy to excite 4f electrons of the nearby  $\text{Ln}^{3+}$  center. To optimize the Ln sensitization process, it is highly desirable to develop Ln MOF platforms with variable topology, structure metrics, functionalities, and guest species in addition to tunable Ln compositions.

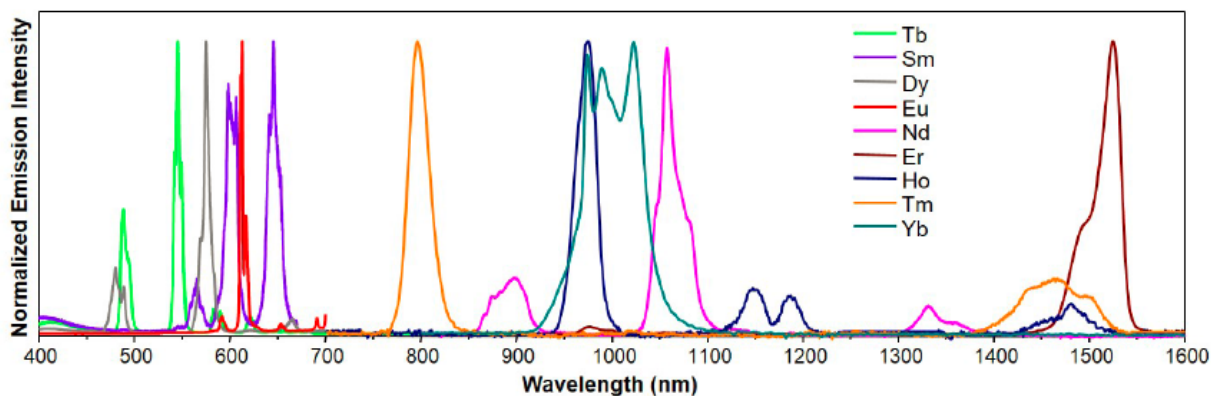


**Figure 1.15** Emission spectra of selected  $\text{Ln}^{3+}$  ions. <sup>105-106</sup>

## 1.8 OBJECTIVES OF THIS DISSERTATION

This dissertation describes diversity-oriented development of metal-organic framework (MOFs) platforms and their custom design for specific applications. The three aims of this dissertation include: 1) construct MOF platforms that are amenable to systematic variations through de novo design; 2) advance new concepts and strategies to further increase the diversity and complexity of MOF materials within established MOF platforms; 3) develop novel MOF materials by judiciously adjusting structural parameters of established MOF platforms for target applications.

The work in Chapter 2 drew inspiration from previously established knowledge in Ln cluster chemistry and serves as an exceptional example to showcase the power of the rational design in MOF chemistry. In this chapter, I describe the de novo development of a diverse library

of rare earth MOF materials as a platform that is amenable to rational and systematic control of their structural parameters including topology, structural metrics, functionalization, and inorganic compositions. I further show that systematic control over functionalities of the linkers via covalent post-synthetic modification reactions allow for careful adjustment of excitation wavelengths for Ln NIR luminescence, making this MOF platform promising materials for NIR biological imaging.

Chapter 3, built upon the work in Chapter 2, describes the development of new Ln MOF materials as luminescence “turn-on” sensors. The Ln MOFs developed in this work are based on the judicious control over the structure metrics and functionalities of a previously established Ln MOF platform with **fcu** topology. The developed Ln MOF materials can detect the presence of gossypol, a toxic molecule concerning the cotton industry, via turn-on responses of Yb<sup>3+</sup> NIR photoluminescence from a non-emissive state. Independent variation of the functional groups in the MOF materials shed light on the sensing mechanism.

In Chapter 4, I introduce the concept of domain building blocks (DBBs) as an effective approach to further increasing the diversity and complexity of metal–organic framework platforms. DBBs are defined as distinct structural or compositional regions within a MOF material. Using the DBB approach, I illustrate how an immense number of MOF materials can be prepared from a small collection of molecular building blocks comprising the distinct domains. This approach was successfully applied to construct a rich library of UiO-67 stratified MOF (sMOF) particles consisting of multiple concentric DBBs. I discuss and highlight the negative consequences of linker exchange reactions on the compositional integrity of DBBs in the UiO-67 sMOFs and propose and demonstrate mitigation strategies. I also demonstrate that individual strata can be specifically postsynthetically addressed and manipulated. Finally, I demonstrate the versatility of these synthetic strategies through the preparation of sMOF–nanoparticle composite materials.

In Chapter 5, the application of MOFs as adsorbent materials for chemical warfare agents (CWAs) is explored. we present a combined experimental and computational study of the adsorption of dimethyl methylphosphonate (DMMP), a CWA adsorption simulant, using a family of UiO-67 MOF materials with systematically controlled functionalities. We demonstrate both computationally and experimentally that the binding energy between the MOF and DMMP can be fine-tuned by adjusting the functional groups of MOF platform.

## 2.0 RARE EARTH PCU MOF PLATFORM BASED ON $\text{RE}_4(\mu_3\text{-OH})_4(\text{COO})_6^{2+}$ CLUSTERS: RATIONAL DESIGN, DIRECTED SYNTHESIS, AND DELIBERATE TUNING OF EXCITATION WAVELENGTHS

This chapter is adapted and reprinted in part with permission from: **Tian-Yi Luo**; Chong Liu; Svetlana V. Eliseeva; Patrick F. Muldoon; Stéphane Petoud; Nathaniel L. Rosi. Rare Earth pcu Metal–Organic Framework Platform Based on  $\text{RE}_4(\mu_3\text{-OH})_4(\text{COO})_6^{2+}$  Clusters: Rational Design, Directed Synthesis, and Deliberate Tuning of Excitation Wavelengths. *Journal of the American Chemical Society* **2017**, *139* (27), 9333-9340. Copyright 2017 American Chemical Society.

Tian-Yi Luo (Tianyi Luo) designed most of the experiments and carried out most of the experiments in MOF synthesis and characterization. Chong Liu collected microspectrophotometry data of MOF samples and helped collect single crystal X-ray diffraction data of some MOF materials. Svetlana V. Eliseeva and Patrick F. Muldoon measured photoluminescence properties of the MOF samples. All authors participated in experiment design. Tian-Yi Luo, Nathaniel L. Rosi, Svetlana V. Eliseeva and Stéphane Petoud wrote the manuscript. All authors made comments on the manuscript.

### 2.1 INTRODUCTION

We have a long-standing interest in creating rare earth ( $\text{RE}^{3+}$ )-based emissive materials,<sup>103, 109-111</sup> with a focus on tuning their excitation properties for optical biological imaging applications.

RE<sup>3+</sup> emitters have several inherent features that make them attractive for biological imaging: i) sharp, non-overlapping emission bands that range from the visible to the near infrared (NIR); ii) long luminescence lifetimes that allow for temporal discrimination from background autofluorescence, which leads to enhanced signal-to-noise ratios and improved sensitivity of detection; iii) continuous, stable emission signals that are highly resistant to photo-bleaching; and iv) the positions of their emission bands, based on atomic  $f \rightarrow f$  transitions, are independent of solution or environmental conditions, such as pH, solvent, etc. However,  $f \rightarrow f$  transitions are Laporte forbidden, causing direct excitation to be prohibitively inefficient. Further, overtones of C-H, O-H, and N-H vibrations from solvent or other neighboring molecules can quench RE<sup>3+</sup> emission. To overcome these challenges, RE<sup>3+</sup> excited states must be indirectly sensitized by appropriate chromophores that have large molar absorption coefficients and are capable of converting the excitation light into energy to feed the electronic structures of RE<sup>3+</sup>. This process is called the ‘antenna effect’.<sup>108, 112</sup> Many examples of classical molecular antennae are typically coordinated to the RE<sup>3+</sup>, providing efficient sensitization and protection to the RE<sup>3+</sup> from sources of non-radiative deactivation. For biological imaging applications, especially in vivo, it is crucial that the antennae absorb low energy visible or NIR light: biological tissues possess low autofluorescence and have much lower absorption in this region known as the biological window (650 - 1450 nm),<sup>113-115</sup> which allows for enhanced sensitivity of detection and deeper penetration of the excitation radiation.

RE<sup>3+</sup>-based metal-organic frameworks<sup>116-118</sup> (MOFs) are highly promising for biological imaging applications.<sup>103, 119-120</sup> RE<sup>3+</sup>-MOFs can be designed to incorporate a high density of both chromophoric ligands and RE<sup>3+</sup>, which renders them sufficiently bright. Further, different RE<sup>3+</sup> can be incorporated into a single MOF, enabling the creation of luminescent ‘barcoded’

materials<sup>110</sup> that would be uniquely attractive for multiplex measurements. To date, we have prepared numerous NIR-emitting MOFs<sup>111</sup> and shown for the first time that they can be used for biological imaging in living cells.<sup>103</sup> Having demonstrated the applicability of NIR-emitting RE<sup>3+</sup>-MOFs, we are now motivated to design RE<sup>3+</sup>-MOF platform materials that will allow for systematic control over structure and careful optimization of photophysical properties. In particular, an ideal MOF platform would accommodate a wide range of RE<sup>3+</sup>, would be easily post-synthetically modified to tune the RE<sup>3+</sup> environment and the photophysical properties, and would serve as the basis for myriad structure-property studies.

Salient features of prototypical MOF platforms include: i) high symmetry and predictable topology imparted by rigid, well-defined secondary building units (SBUs);<sup>9,15</sup> ii) ease of structural modification and formation of isorecticular analogues by employing different metal and ligand precursors; and iii) amenability to functionalization. Multiple MOF platforms have been developed using transition metal ion-based SBUs, including Zn<sub>4</sub>O(COO)<sub>6</sub>- and Zr<sub>6</sub>(OH)<sub>4</sub>O<sub>4</sub>(COO)<sub>n</sub>-based MOFs.<sup>10, 36, 45, 121</sup> While numerous RE<sup>3+</sup>-based MOFs have been reported and studied,<sup>102, 117-118</sup> RE<sup>3+</sup>-based platforms suitable for systematic modification and study are scarce, with notable exceptions,<sup>98, 122-123</sup> despite the presence of many well-defined discrete RE<sup>3+</sup>-carboxylate clusters in the literature.<sup>124-129</sup> RE<sub>4</sub>(μ<sub>3</sub>-OH)<sub>4</sub>(COO)<sub>6</sub><sup>2+</sup> clusters exhibiting the RE<sub>4</sub>(μ<sub>3</sub>-OH)<sub>4</sub> cubane-like core (Figure 2.1) are particularly attractive building blocks due to their symmetry, connectivity, and similarity to the ubiquitous Zn<sub>4</sub>O(COO)<sub>6</sub> SBU. Like Zn<sub>4</sub>O(COO)<sub>6</sub>, RE<sub>4</sub>(μ<sub>3</sub>-OH)<sub>4</sub>(COO)<sub>6</sub><sup>2+</sup> can be viewed as an octahedral SBU which can theoretically lead to a wide variety of network topologies through rational design.<sup>12</sup> For example, connecting RE<sub>4</sub>(μ<sub>3</sub>-OH)<sub>4</sub>(COO)<sub>6</sub><sup>2+</sup> with linear linkers should afford the **pcu** net (Figure 2.1). However, it has been difficult to carefully control carboxylate coordination to the RE<sub>4</sub>(μ<sub>3</sub>-OH)<sub>4</sub> core, in part because the RE<sup>3+</sup> can accommodate

varying numbers of carboxylate ligands and coordinating solvent molecules.<sup>128</sup> Further, syntheses are dependent on solvent, temperature, and pH, as well as on the nature of carboxylate ligands employed. Although a few MOFs containing  $RE_4(\mu_3-OH)_4(\text{ligand})_n$  clusters have been discovered,<sup>130-133</sup> constructing a MOF platform through deliberate and predictable formation of the  $RE_4(\mu_3-OH)_4(\text{COO})_6^{2+}$  cluster has not been achieved to date.

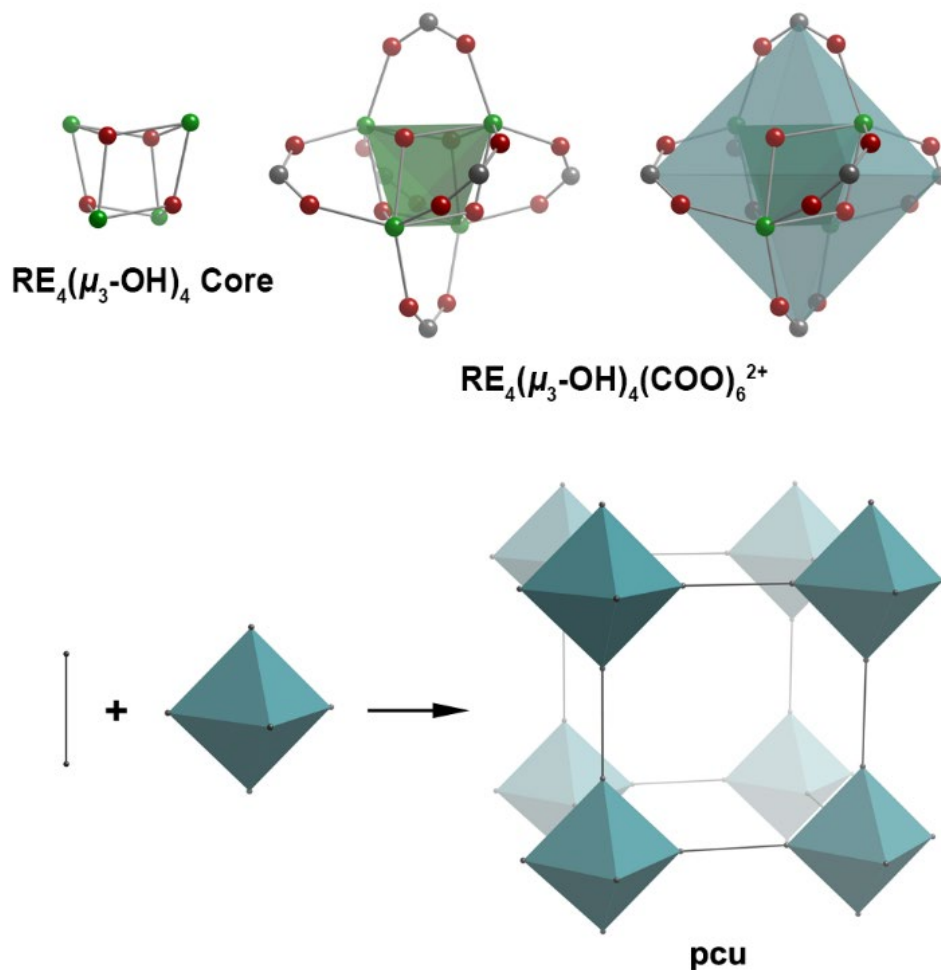


**Figure 2.1** Structure of the  $RE_4(\mu_3-OH)_4(\text{COO})_6^{2+}$  SBU and construction of the pcu net ( $RE^{3+}$ , green spheres; C, grey spheres; O, red spheres; green tetrahedron defines  $RE^{3+}$  core; H atoms omitted for clarity; teal octahedron defines structure of SBU).

Herein, we present the rational design and synthesis of a new porous **pcu** MOF platform based on the  $RE_4(\mu_3-OH)_4(\text{COO})_6^{2+}$  cluster. We determine strategies for constructing an

isorecticular family of MOFs based on this SBU and present, in total, 22 new MOF materials with varying structures and compositions. Finally, we demonstrate that these materials are amenable to post-synthetic modification (PSM) via both ion exchange and covalent chemistry.<sup>56</sup> In one representative example, we show for the first time that covalent PSM can be used to systematically optimize the photophysical properties of an Yb<sup>3+</sup>-based MOF in this series. More specifically, we shift the excitation wavelengths of this MOF towards lower energy in order to create more biologically adapted luminescent probes that would possess excitation and emission wavelengths within the biological window.<sup>113-115</sup>

## 2.2 RESULTS AND DISCUSSION

Formation of RE<sub>4</sub>(μ<sub>3</sub>-OH)<sub>4</sub>-related complexes relies on well-controlled hydrolysis or alcoholysis of RE<sup>3+</sup> where both solution conditions and suitable supporting ligands play essential roles. Several studies<sup>126-128</sup> have reported the formation and crystallization of various complexes with RE<sub>4</sub>(μ<sub>3</sub>-OH)<sub>4</sub> cores from aqueous or alcoholic solutions in the presence of a variety of α-amino acids as supporting ligands. In these examples, the α-amino groups in proximity to the coordinating carboxylates may play an important role in regulating the RE<sup>3+</sup> hydrolysis/alcoholysis processes by temporarily coordinating the RE<sup>3+</sup> centers at intermediate stages of reaction and/or by affecting the local pH environment surrounding the cluster.<sup>128</sup> We therefore hypothesized that target MOFs based on the RE<sub>4</sub>(μ<sub>3</sub>-OH)<sub>4</sub>(COO)<sub>6</sub><sup>2+</sup> cluster should require carboxylate linkers having a primary amino group located at the ortho position to the coordinating carboxylate. To implement this design strategy, we reacted 2-amino-1,4-benzenedicarboxylic acid (H<sub>2</sub>-NH<sub>2</sub>-BDC) with

GdCl<sub>3</sub>·6H<sub>2</sub>O in mixed dimethylformamide (DMF) and water solution at 100 °C. This reaction yielded clear, colorless cubic crystals, MOF-1114(Gd).<sup>134</sup>

Single crystal X-ray diffraction (SCXRD) of MOF-1114(Gd) revealed that it crystallizes in the cubic space group *Fm-3m* with the unit cell dimensions  $a = b = c = 27.860$  Å. The inorganic SBU has the distorted cubane Gd<sub>4</sub>(μ<sub>3</sub>-OH)<sub>4</sub> polymetallic core with T<sub>d</sub> symmetry (Figure 2.2A and Figure 2.3). The four Gd<sup>3+</sup> ions located at the vertices of the tetrahedron (shown in green in Figure 2.2A) are bridged by four μ<sub>3</sub>-OH which protrude slightly from the four triangular faces. Each Gd<sup>3+</sup> pair is bridged by one carboxylate group along each edge of the tetrahedron. In addition, two other O atoms are bound to each Gd<sup>3+</sup>; one is located on the 3-fold axis and the other is disordered among 3 symmetry equivalent positions around the 3-fold axis with equal 1/3 occupancy (Figure 2.3 pink spheres). We speculate that these O atoms could be either water molecules or μ<sub>1</sub>-OH coordinating to Gd<sup>3+</sup> ions. The inorganic SBUs, formulated as [Gd<sub>4</sub>(μ<sub>3</sub>-OH)<sub>4</sub>(COO)<sub>6</sub>(H<sub>2</sub>O)<sub>8-x</sub>(μ<sub>1</sub>-OH)<sub>x</sub>]<sup>(2-x)+</sup>, are connected by the linear aminophenylene linkers into a **pcu** 3-D framework (Figure 2.2A-C). Interconnected ~10 Å × 10 Å 1-D channels run along the *a*, *b*, and *c* crystallographic axes. In addition to Gd<sup>3+</sup>, isorecticular MOFs were prepared using Y<sup>3+</sup>, Tb<sup>3+</sup>, Dy<sup>3+</sup>, Ho<sup>3+</sup>, Er<sup>3+</sup>, Tm<sup>3+</sup>, and Yb<sup>3+</sup>, as evidenced by comparing their powder X-ray diffraction (PXRD) patterns to that collected for MOF-1114(Gd) and that simulated from single crystal diffraction data (Figure 2.4). Attempts to make isorecticular MOFs by reacting RECl<sub>3</sub>·6H<sub>2</sub>O with 1,4-benzenedicarboxylic acid (H<sub>2</sub>-BDC) or other functionalized variants of H<sub>2</sub>-BDC (e.g. -Br, -NO<sub>2</sub>, -OH) yielded MOFs containing infinite RE<sup>3+</sup>-carboxylate SBUs, pointing toward the potential importance of the primary amino group in influencing SBU formation. Collectively, this series of new MOFs represents a platform for different studies and applications based on the unique optical, magnetic, and catalytic properties of RE<sup>3+</sup>.

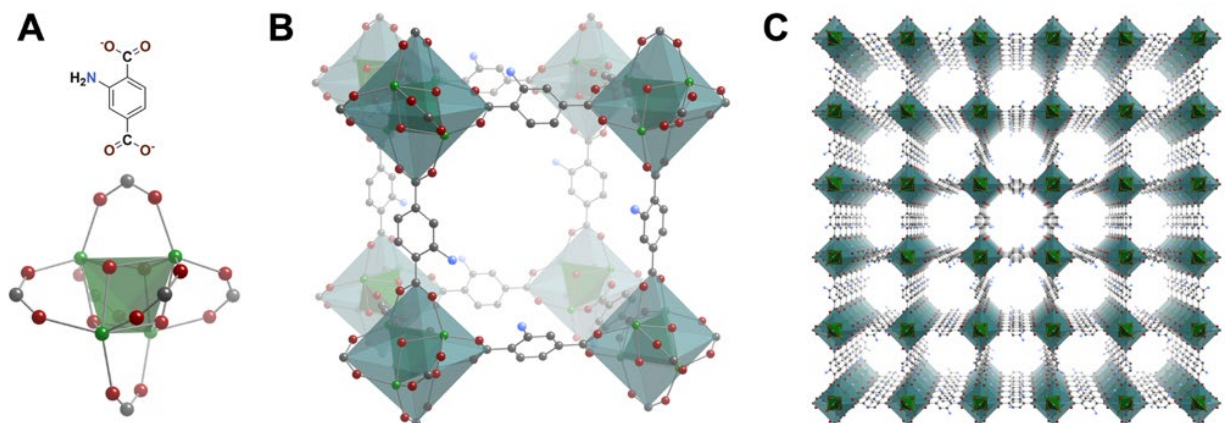


**Figure 2.2** Construction of MOF-1114. (A) Organic linker and inorganic SBU in MOF-1114; (B) crystal structure of MOF-1114 (RE<sup>3+</sup>, green spheres; C, grey spheres; O, red spheres; RE<sub>4</sub>(μ<sub>3</sub>-OH)<sub>4</sub>, green tetrahedra; teal octahedron defines structure of SBU; coordinated water molecules, μ<sub>1</sub>-OH groups, and H atoms have been omitted for clarity; only one of the possible positions is illustrated for each disordered -NH<sub>2</sub> group); (C) 1-D ~10 Å × 10 Å channels along the *a*, *b*, and *c* crystallographic axes in MOF-1114.

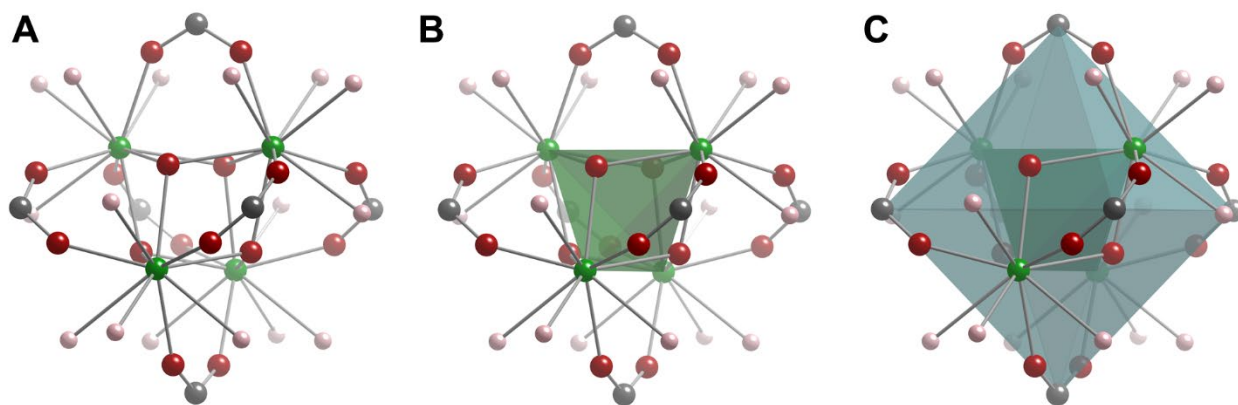


**Figure 2.3** [RE<sub>4</sub>(μ<sub>3</sub>-OH)<sub>4</sub>(COO)<sub>6</sub>(H<sub>2</sub>O)<sub>8-x</sub>(μ<sub>1</sub>-OH)<sub>x</sub>]<sup>(2-x)+</sup> SBU (RE<sup>3+</sup>, green spheres; C, grey spheres; O atoms on carboxylates and μ<sub>3</sub>-OH, red spheres; O atoms on H<sub>2</sub>O or μ<sub>1</sub>-OH, pink spheres; green tetrahedra define RE<sup>3+</sup> cores; teal octahedron defines structure of SBU; H atoms omitted for clarity).

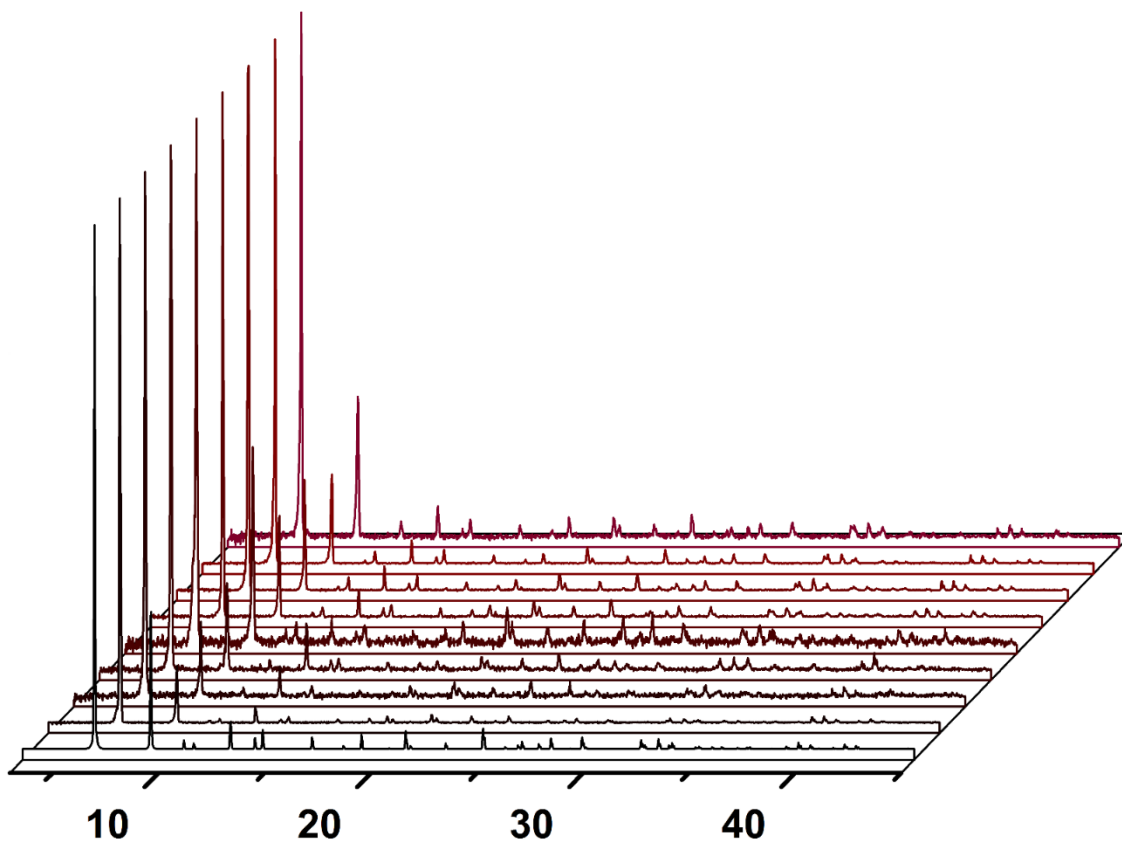


**Figure 2.4** PXRD patterns of MOF-1114 synthesized with different  $\text{RE}^{3+}$  (front to back: simulated,  $\text{Y}^{3+}$ ,  $\text{Gd}^{3+}$ ,  $\text{Tb}^{3+}$ ,  $\text{Dy}^{3+}$ ,  $\text{Ho}^{3+}$ ,  $\text{Er}^{3+}$ ,  $\text{Tm}^{3+}$ ,  $\text{Yb}^{3+}$ ).

MOF-1114 could be charged depending on  $x$ , the number of  $\mu_1$ -OH groups per SBU. For example, if  $x$  is less than 2, the framework would be positively charged. The positive charges would likely be balanced by anions, such as  $\text{Cl}^-$ , randomly disordered in the MOF cavities. Qualitative scanning electron microscopy energy-dispersive X-ray spectroscopy (SEM/EDS) analysis on the as-synthesized MOF-1114(Tb) (Figures 2.5) revealed the presence of Cl in the MOF crystals, likely in the form of mobile  $\text{Cl}^-$  ions, as confirmed by ion exchange experiments. MOF-1114(Tb) was soaked in a 0.1 M DMF solution of  $\text{NMe}_4\text{BF}_4$  for 5 days. Thereafter, the crystalline material was thoroughly washed with fresh DMF and analyzed using SEM/EDS, which shows nearly complete removal of  $\text{Cl}^-$  and appearance of F from  $\text{BF}_4^-$  (Figures 2.6). The number of mobile anions per formula unit in MOF-1114 was quantified by solution nuclear magnetic

resonance (NMR) spectroscopy. An ion-exchanged MOF-1114(Tb) sample was digested with acidified DMSO- $d_6$  and analyzed using both solution  $^1\text{H}$  and  $^{19}\text{F}$  NMR with the internal standard  $\alpha,\alpha,\alpha$ -trifluorotoluene (Figures 2.7 and 2.8).  $\text{NMe}_4^+$  was not observed via  $^1\text{H}$  NMR (Figure 2.7 bottom spectrum), while 0.5  $\text{BF}_4^-$  per  $\text{NH}_2\text{-BDC}$ , were observed via  $^{19}\text{F}$  NMR (Figures 2.8), indicating 1.5  $\text{Cl}^-$  per SBU in the as-synthesized MOF-1114(Tb). The as-synthesized MOF-1114 is therefore formulated as  $[\text{RE}_4(\mu_3\text{-OH})_4(\text{NH}_2\text{-BDC})_3(\text{H}_2\text{O})_{7.5}(\mu_1\text{-OH})_{0.5}] \cdot 1.5\text{Cl}, 9\text{DMF}$  according to elemental microanalysis (see section 2.4.3 for details) and solution  $^1\text{H}$  NMR (Figure 2.9). We note that each MOF analogue may have elemental compositions that deviate slightly from this formula. These data indicate that: i) the framework is cationic, and ii) the anions are mobile and can be readily exchanged without loss of framework crystallinity (Figure 2.10). Therefore, ion exchange could advantageously be used to tailor the MOF pore space and adjust MOF properties. Thermogravimetric analyses of both as-synthesized and  $\text{BF}_4^-$  anion-exchanged MOF-1114(Tb) samples (Figure 2.11) show a steep weight loss corresponding to solvent removal between 25 °C and ~150 °C followed by a steady gradual weight loss up to 650 °C. We have not yet determined the experimental conditions for activating the as-synthesized MOF to obtain permanent porosity. However, after anion exchange with  $\text{BF}_4^-$ , MOF-1114(Tb) can be activated. Despite a loss of crystallinity after activation,  $\text{N}_2$  adsorption analysis (77 K) yields a type I isotherm (Figure 2.12), characteristic of a microporous material.

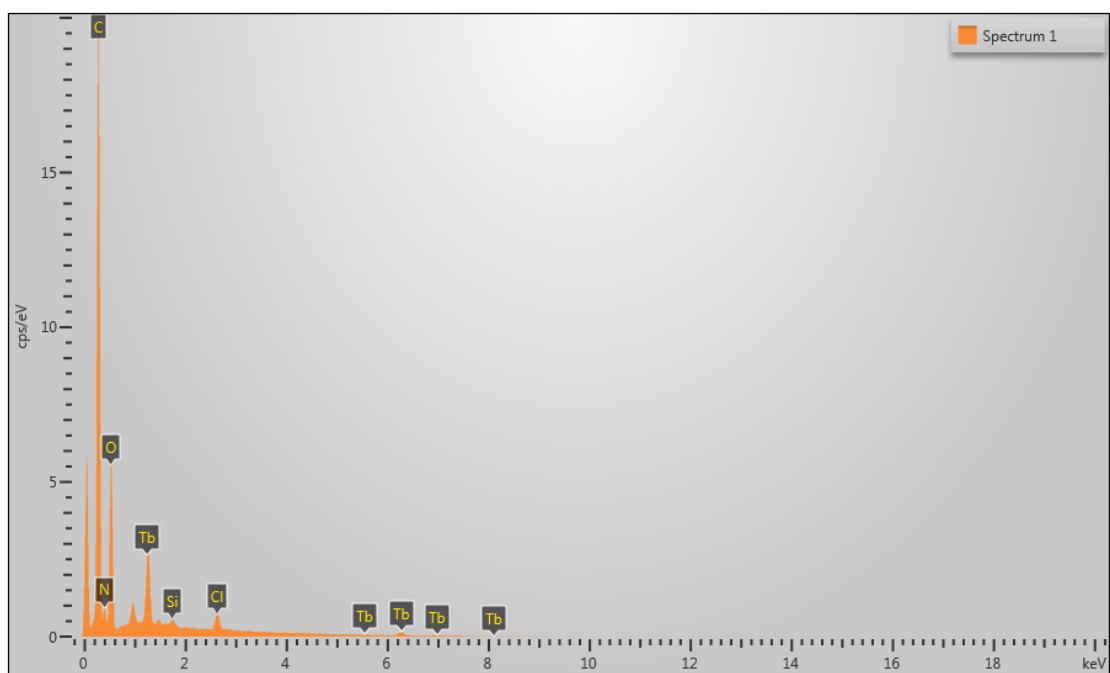
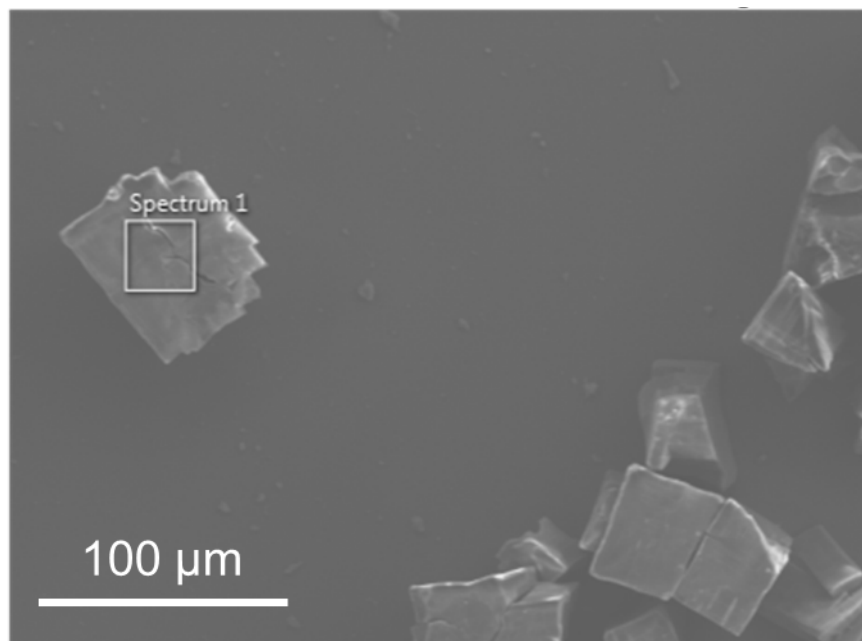


**Figure 2.5** SEM/EDS spectrum of as-synthesized MOF-114(Tb) (spectrum was collected at the 'Spectrum 1' area in top figure).

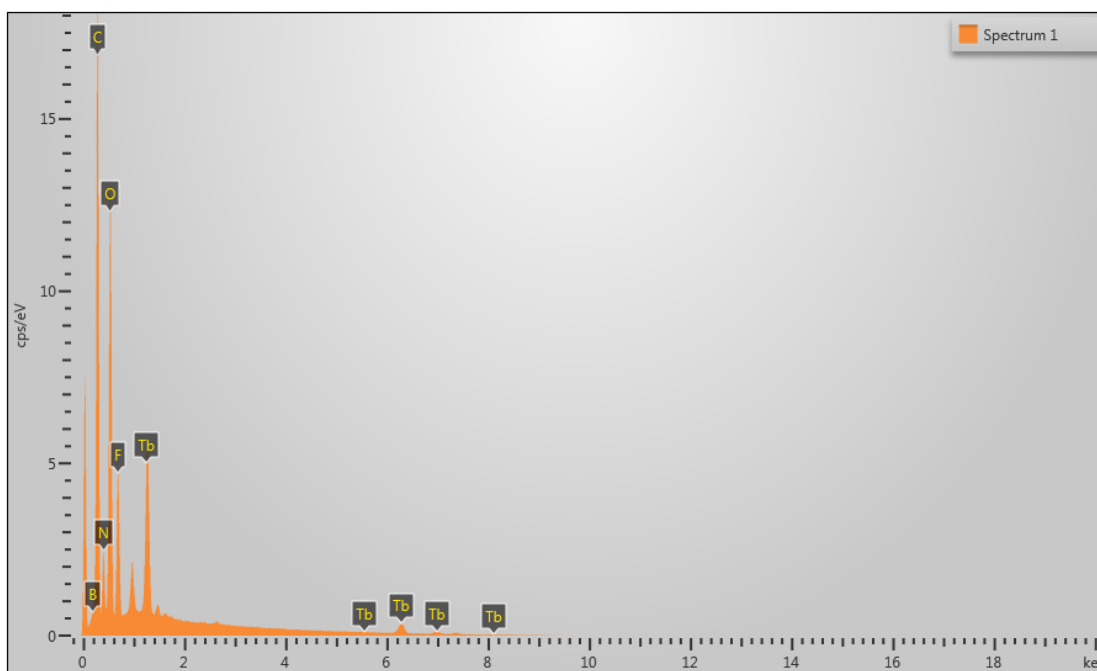
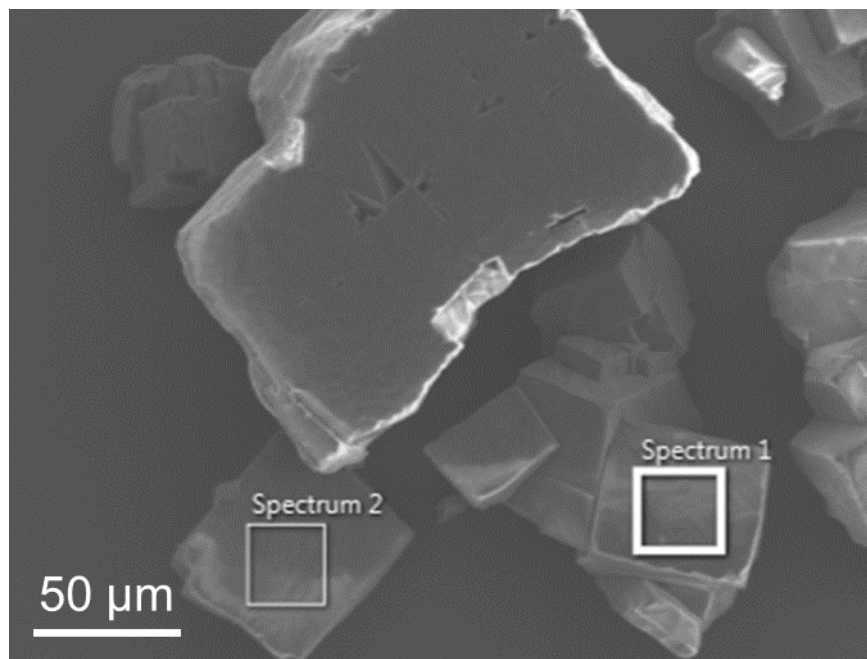


**Figure 2.6** SEM/EDS spectrum of MOF-1114(Tb) after ion exchange with  $\text{NMe}_4\text{BF}_4$  (spectrum was collected at the ‘Spectrum 1’ area in top figure).

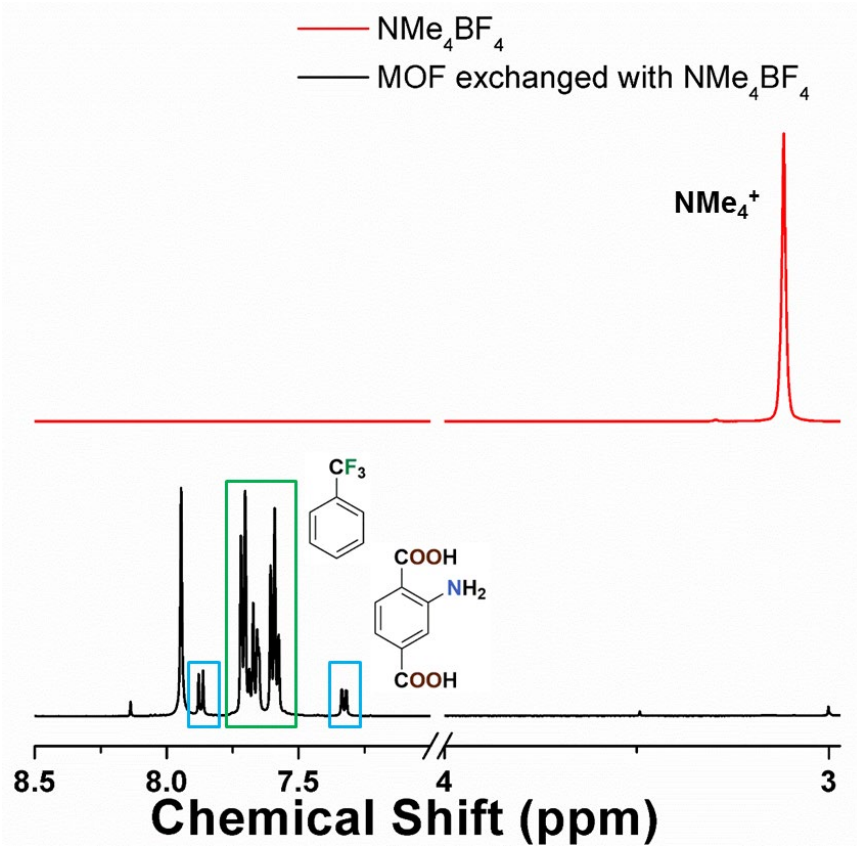


**Figure 2.7** Solution  $^1\text{H}$  NMR spectra of  $\text{NH}_4\text{BF}_4$  (top) and acid dissolved MOF-1114(Tb) after  $\text{NH}_4\text{BF}_4$  ion exchange with  $\alpha,\alpha,\alpha$ -trifluorotoluene added as internal standard (bottom).

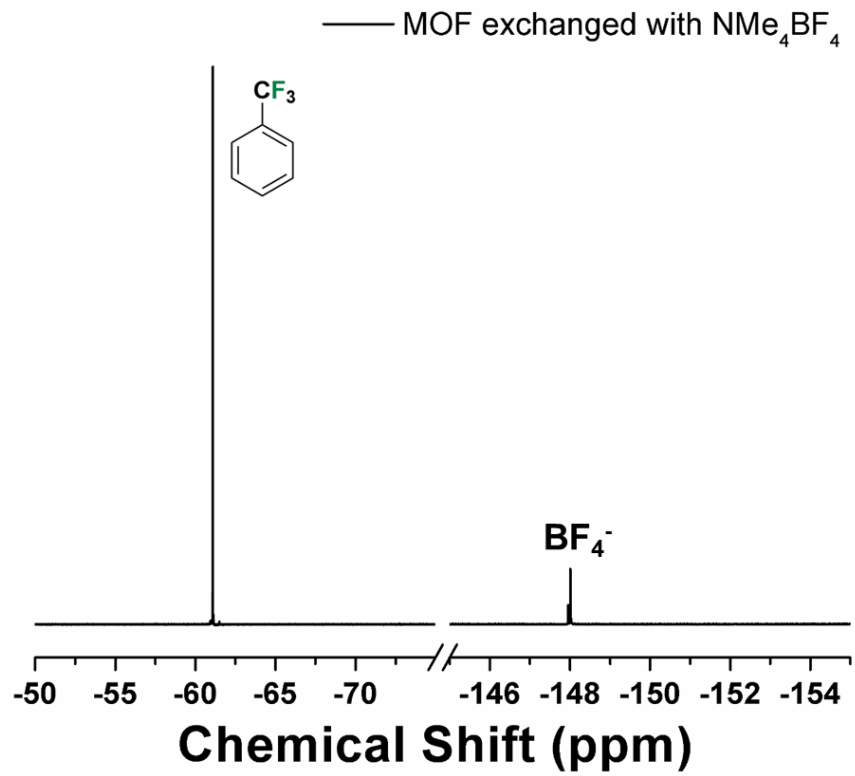


**Figure 2.8** Solution  $^{19}\text{F}$  NMR of acid dissolved MOF-1114(Tb) after  $\text{NH}_4\text{BF}_4$  ion exchange with  $\alpha,\alpha,\alpha$ -trifluorotoluene added as internal standard.

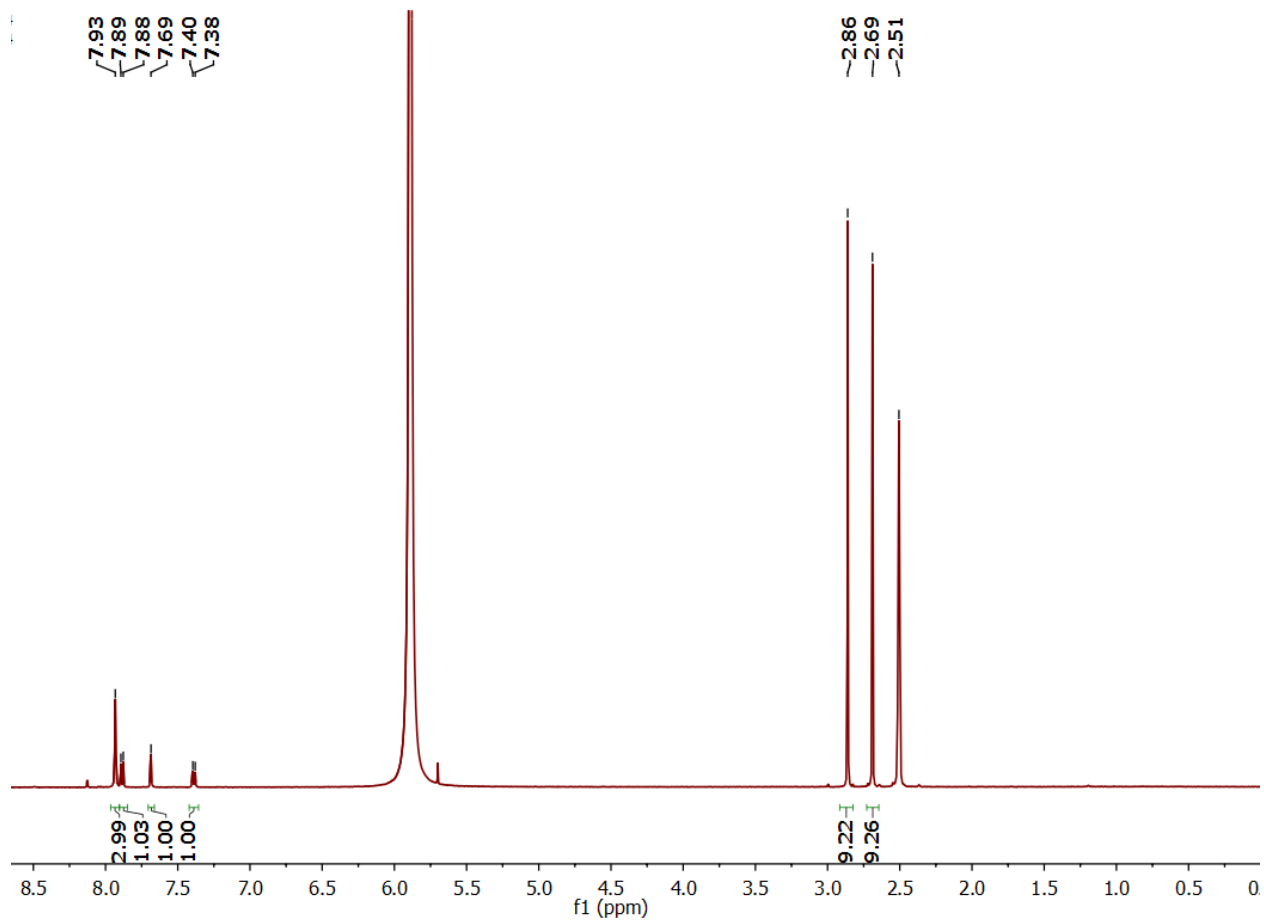


**Figure 2.9** Solution <sup>1</sup>H NMR of acid digested as-synthesized MOF-1114(Tb) showing approximately 3 : 1 ratio of DMF : NH<sub>2</sub>-BDC ligand.

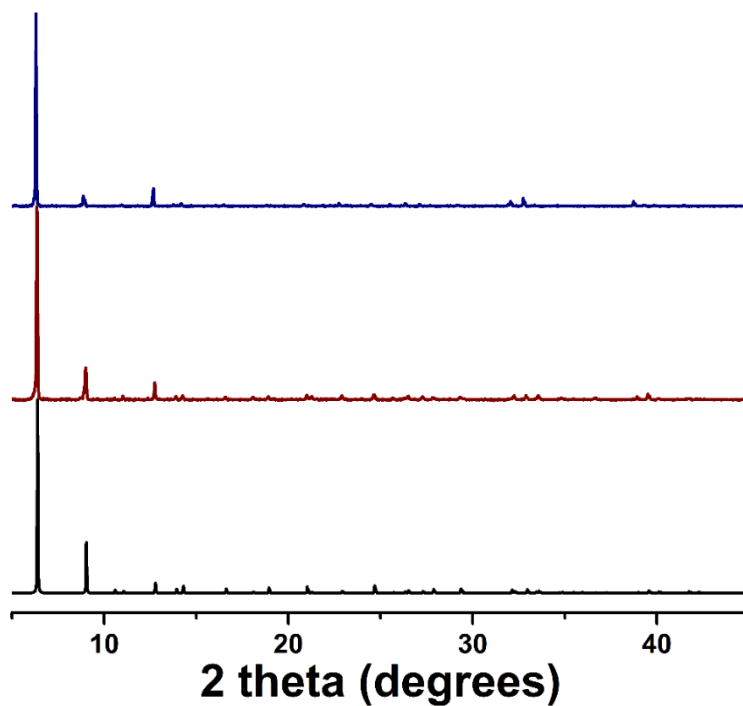


**Figure 2.10** Simulated PXRD pattern based on MOF-1114(Gd) crystal structure (black), PXRD patterns of as-synthesized MOF-1114(Tb) (red) and NMe<sub>4</sub>BF<sub>4</sub> exchanged MOF-1114(Tb) (navy).

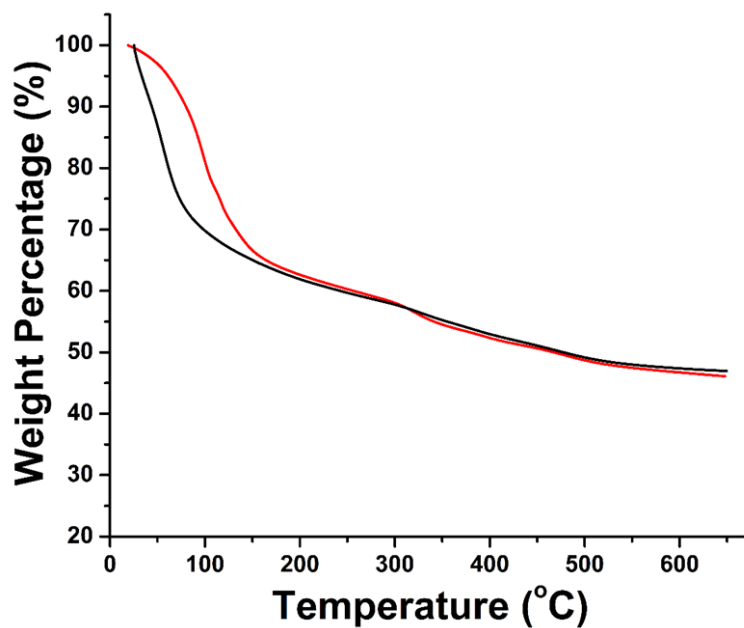


**Figure 2.11** Thermogravimetric Analyses (TGA) of as-synthesized MOF-1114(Tb) (black) and MOF-1114(Tb) after anion exchange with NMe<sub>4</sub>BF<sub>4</sub> (red).

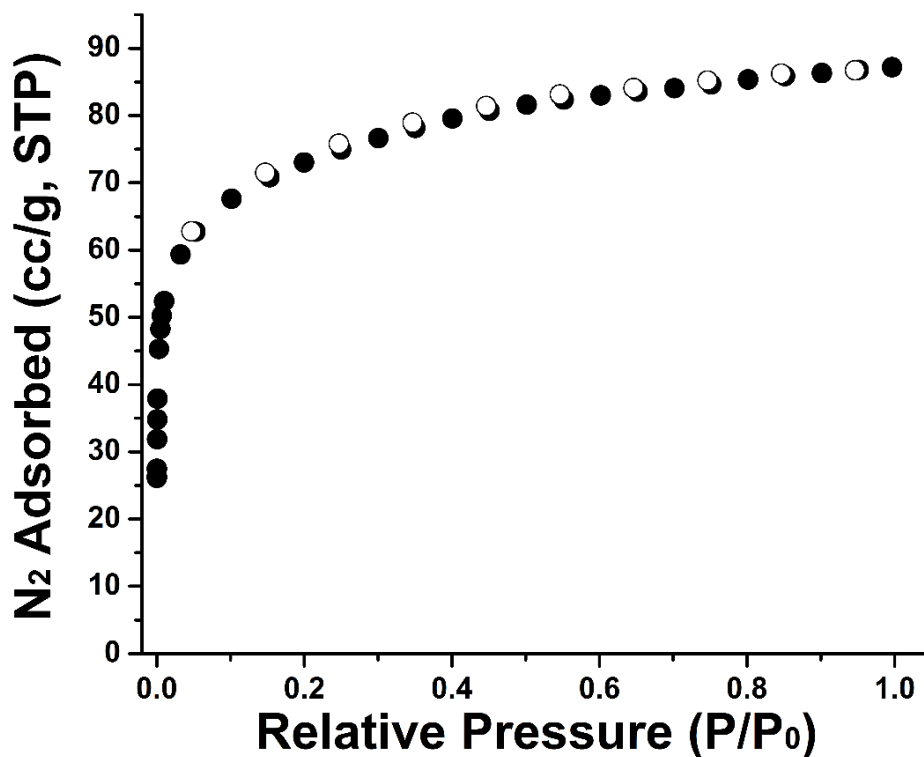


**Figure 2.12** N<sub>2</sub> isotherm at 77 K of MOF-1114(Tb) after anion exchanged with NMe<sub>4</sub>BF<sub>4</sub>. Based on this isotherm, the Brunauer-Emmett-Teller (BET) surface area is estimated to be 264 m<sup>2</sup>/g.

Having successfully prepared MOF-1114 via deliberate design and directed synthesis, we next sought to build a family of isorecticular analogues using biphenyl- and terphenyl-based amino-functionalized carboxylate linkers: 3,3'-diamino-1,1'-biphenyl-4,4'-dicarboxylate (NH<sub>2</sub>-BPDC) and 3,3''-diamino-1,1':4',1''-terphenyl-4,4''-dicarboxylate (NH<sub>2</sub>-TPDC) (Figure 2.13A). Using similar solvothermal conditions that yielded MOF-1114 but substituting either H<sub>2</sub>-NH<sub>2</sub>-BPDC or H<sub>2</sub>-NH<sub>2</sub>-TPDC for H<sub>2</sub>-NH<sub>2</sub>-BDC, two new twofold interpenetrated MOF structures were formed: MOF-1130(Y,Gd,Tb,Dy,Ho) and MOF-1131(Er,Yb). MOF-1130 and MOF-1131 are isorecticular. MOF-1130 crystallizes in the monoclinic space group  $P2_1/n$  ( $a = 18.0453 \text{ \AA}$ ,  $b = 18.1800 \text{ \AA}$ ,  $c = 32.5984 \text{ \AA}$ ;  $\alpha = 90^\circ$ ,  $\beta = 95.864^\circ$ ,  $\gamma = 90^\circ$ ); MOF-1131 crystallizes in the same space group with different unit cell dimensions ( $a = 23.6058 \text{ \AA}$ ,  $b = 22.2824 \text{ \AA}$ ,  $c = 37.1223 \text{ \AA}$ ;  $\alpha = 90^\circ$ ,  $\beta = 90.222^\circ$ ,  $\gamma = 90^\circ$ ) (Figure 2.13B,C, Figures 2.14 to 2.16). The inorganic SBU for both MOF-1130 and MOF-

1131 (Figure 2.13A) consists of the  $\text{RE}_4(\mu_3\text{-OH})_4$  polymetallic core observed in MOF-1114. This result confirms our hypothesis that the primary amino group adjacent to the carboxylate facilitates formation of  $\text{RE}_4(\mu_3\text{-OH})_4$ . However, in addition to the six carboxylates that bridge the edges of the  $\text{RE}^{3+}$  tetrahedron, two additional carboxylate groups coordinate in a chelating mode to two of the  $\text{RE}^{3+}$  in the cluster, resulting in a total of eight carboxylates per SBU present in two different coordination modes (Figure 2.13A; O on chelating carboxylates highlighted in orange). This new SBU, formulated as  $[\text{RE}_4(\mu_3\text{-OH})_4(\text{COO})_8(\text{solvent})_4]$  (solvent = DMF or  $\text{H}_2\text{O}$ ) according to SCXRD data, should be a neutral moiety, which is supported by the absence of Cl peaks in the SEM/EDS spectra (Figures 2.17 to 2.18). To visualize the crystal structures of MOF-1130 and MOF-1131, a single, non-interpenetrated framework is shown for each MOF in Figure 2.13B and Figure 2.13C, respectively (the interpenetrated frameworks are shown in Figure 2.14). Cages within the MOF are defined by eight neighboring inorganic SBUs that no longer sit at the corners of a cube, as in MOF-1114. Instead, the cages are distorted with two parallel faces along (010), each having one additional ligand crosslinking two SBUs on the face diagonal. The carboxylates from these diagonal crosslinkers coordinate to the single  $\text{RE}^{3+}$ , while the carboxylates on the linkers on the edges of the cage all bridge two  $\text{RE}^{3+}$  ions.

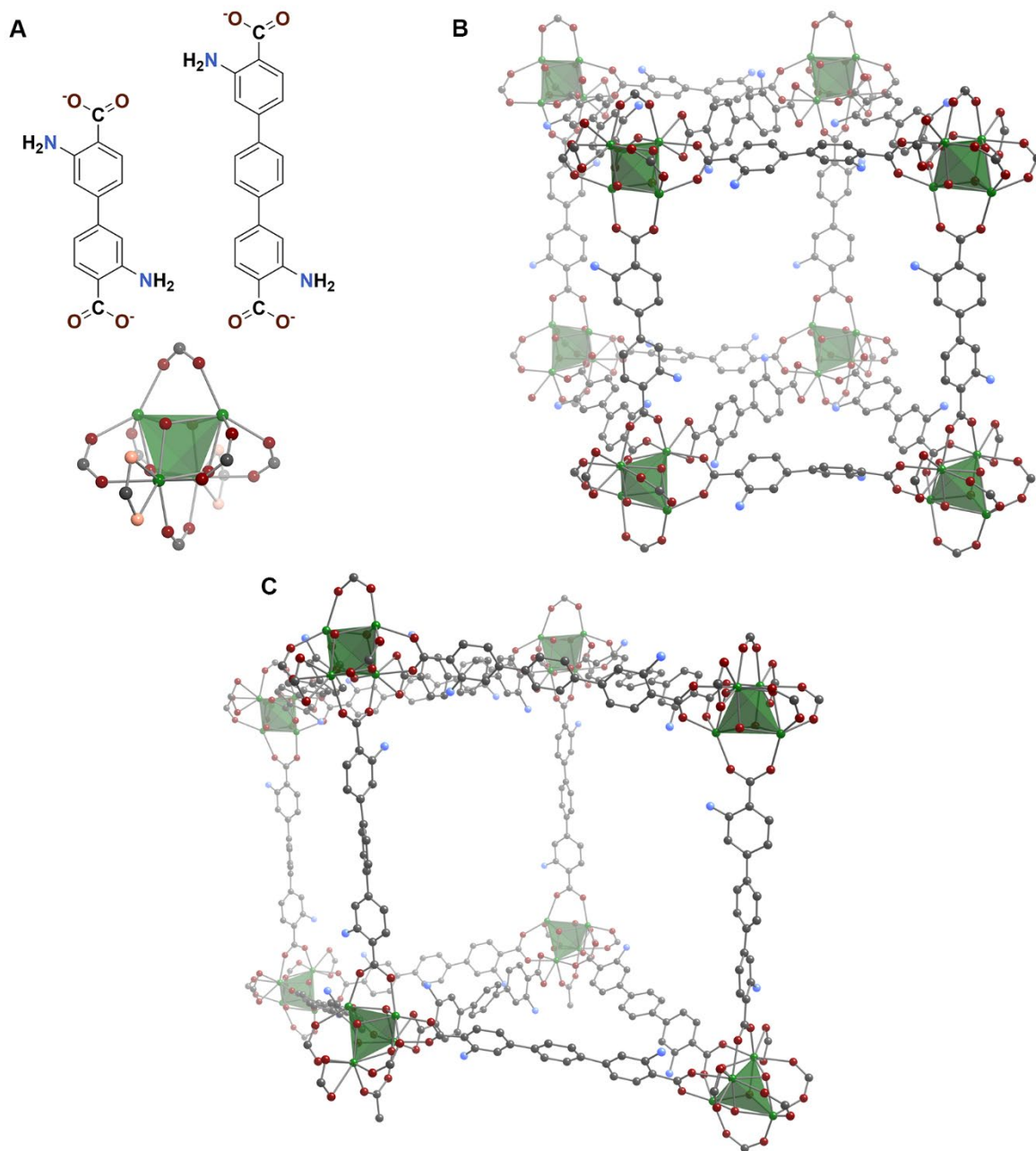


**Figure 2.13** (A) organic linkers and inorganic SBU in MOF-1130 and MOF-1131 (light-orange spheres highlight O atoms on chelating carboxylates); (B) crystal structure of MOF-1130 (for clarity, the identical interpenetrating framework is omitted; only one of the possible positions is illustrated for each disordered  $\text{-NH}_2$  group); (C) crystal structure of MOF-1131 (for clarity, the identical interpenetrating framework is omitted; only one of the possible positions is illustrated for each disordered  $\text{-NH}_2$  group);

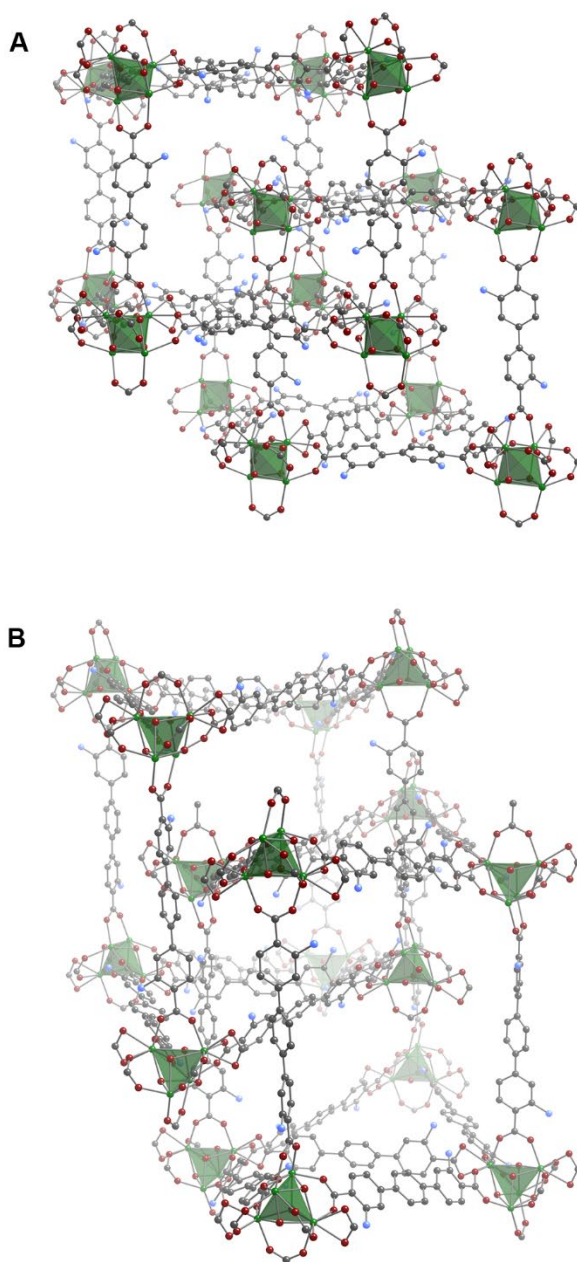


**Figure 2.14** Interpenetrated crystal structure of (A) MOF-1130 and (B) MOF-1131 ( $\text{RE}^{3+}$ , green spheres; C, grey spheres; O, red spheres; N, blue spheres; green tetrahedra define  $\text{RE}^{3+}$  cores; H atoms and coordinating solvent molecules omitted for clarity).

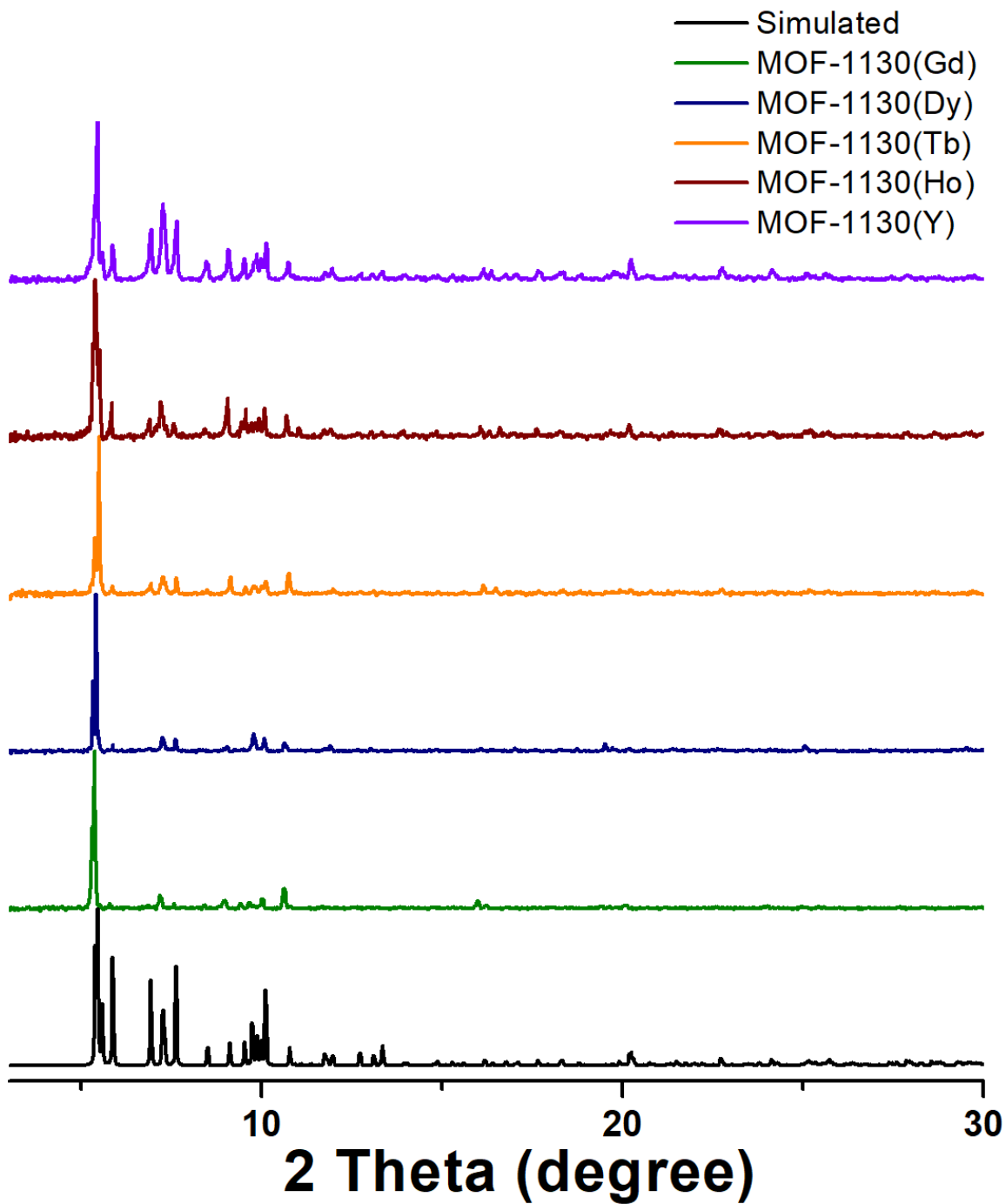


**Figure 2.15** PXRD patterns of MOF-1130 synthesized with different RE<sup>3+</sup> ( simulated, black; Gd<sup>3+</sup>, green; Dy<sup>3+</sup>, blue; Tb<sup>3+</sup>, orange; Ho<sup>3+</sup>, wine; Y<sup>3+</sup>, violet).

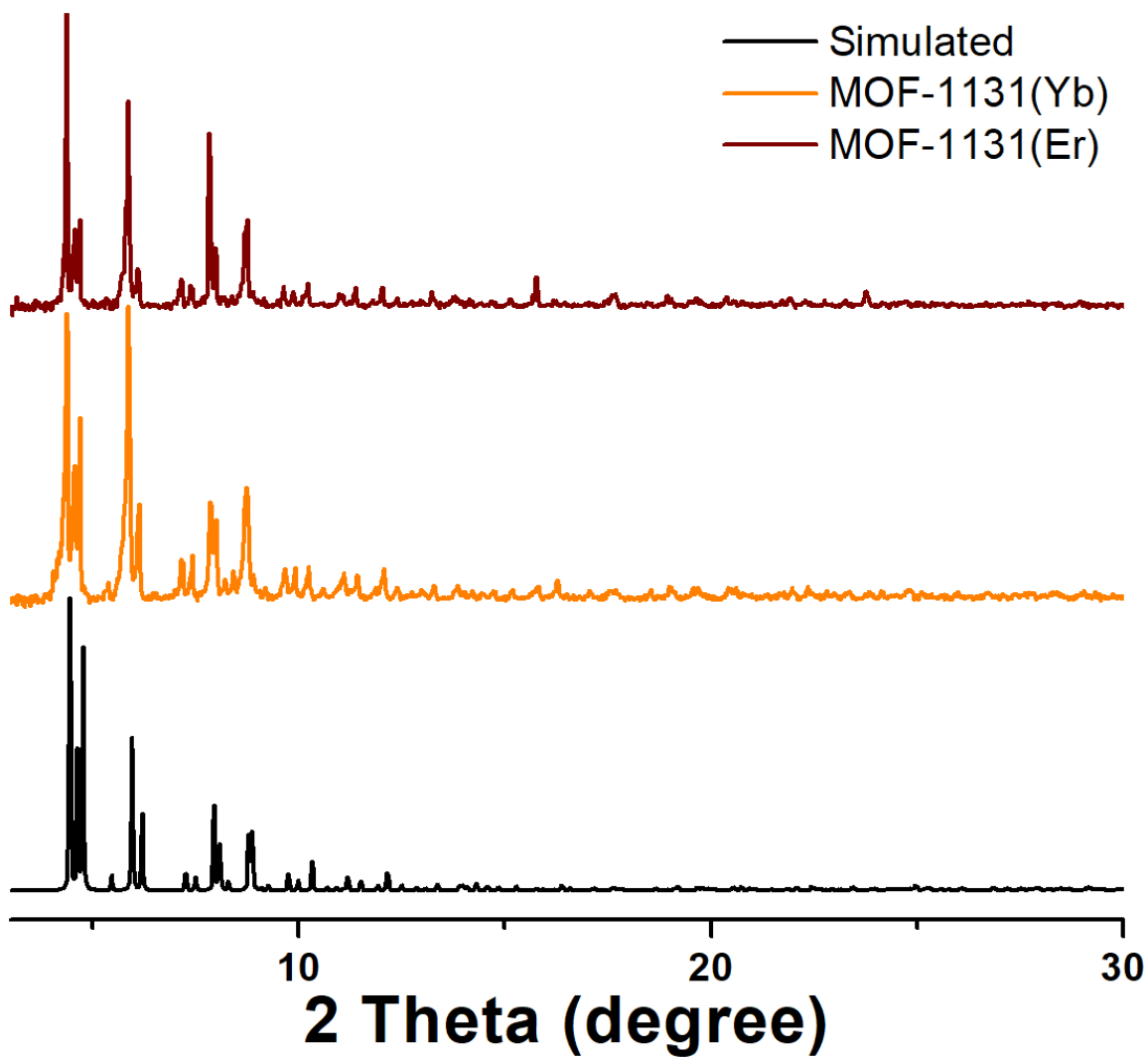


**Figure 2.16** PXRD patterns of MOF-1131 synthesized with different RE<sup>3+</sup> ( simulated, black; Yb<sup>3+</sup>, orange; Er<sup>3+</sup>, wine).

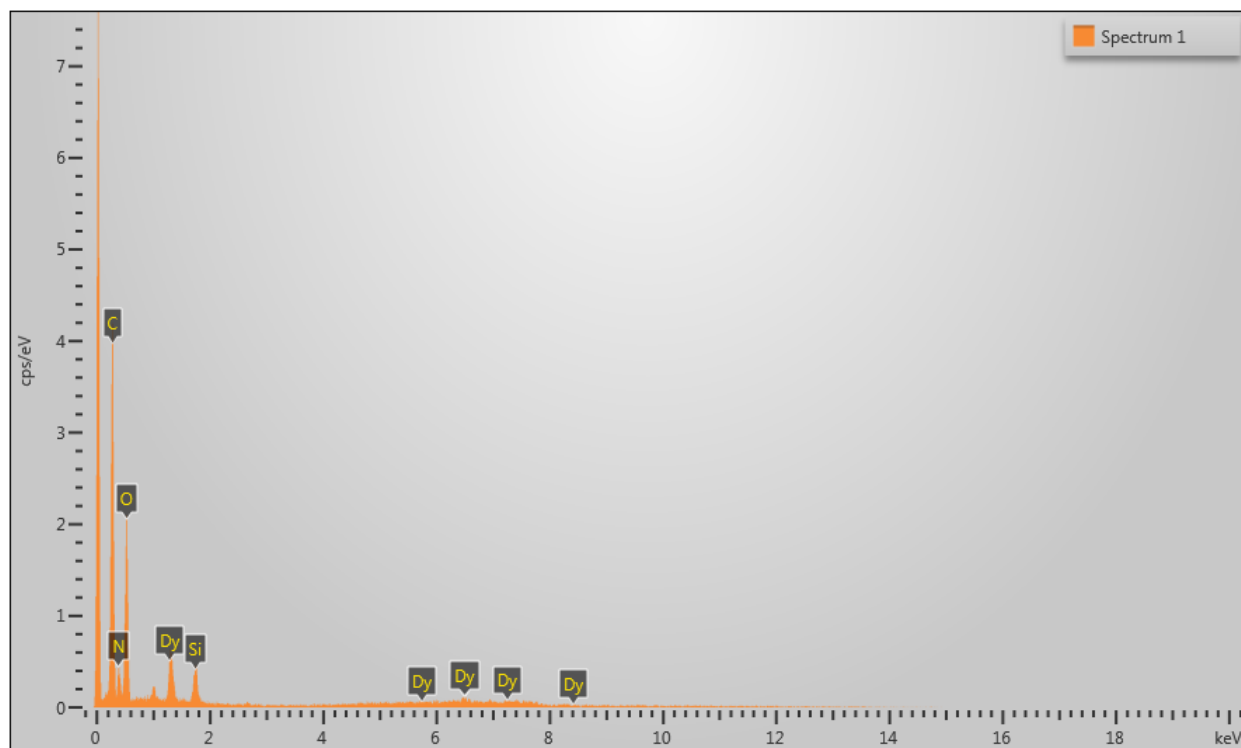
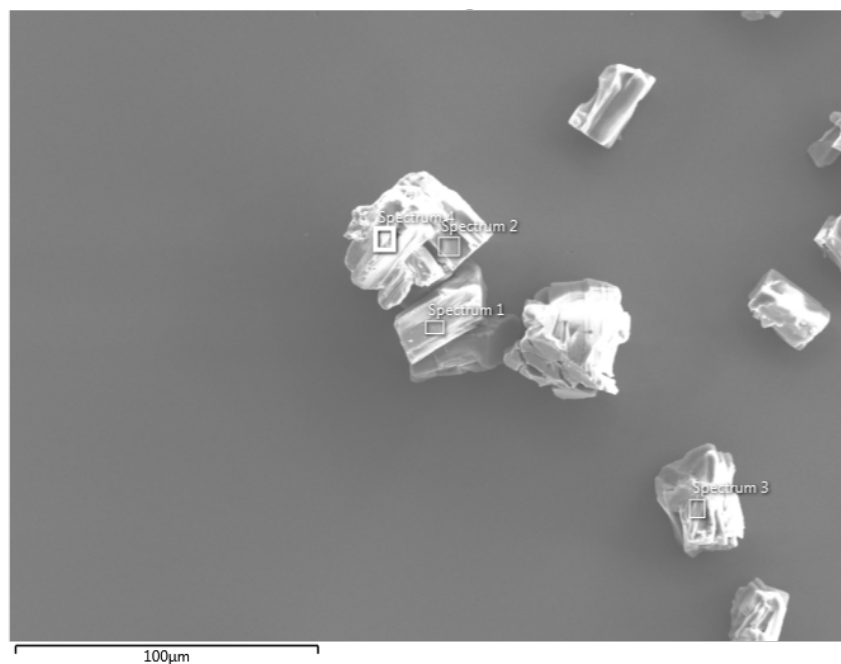


**Figure 2.17** SEM image (top) and EDS spectrum (bottom) of as-synthesized MOF-1130(Dy) crystals (spectrum was collected at the ‘Spectrum 1’ area in top image).

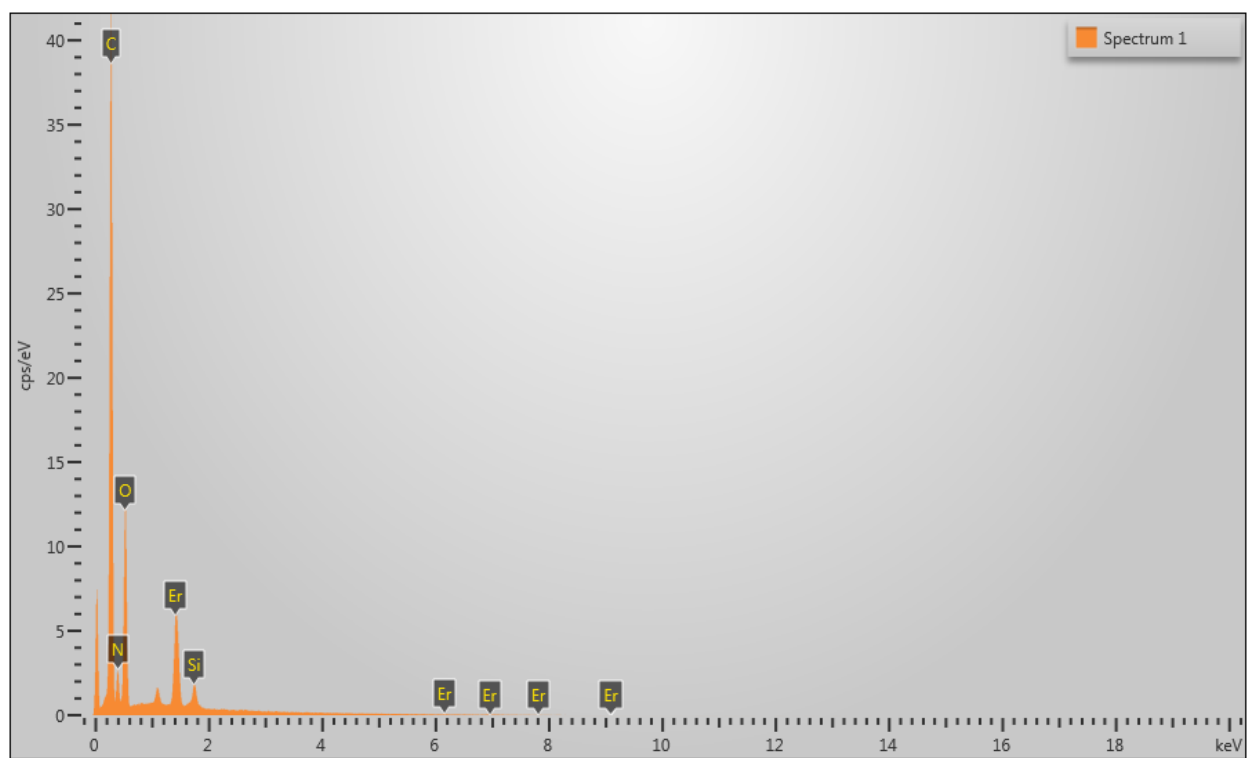
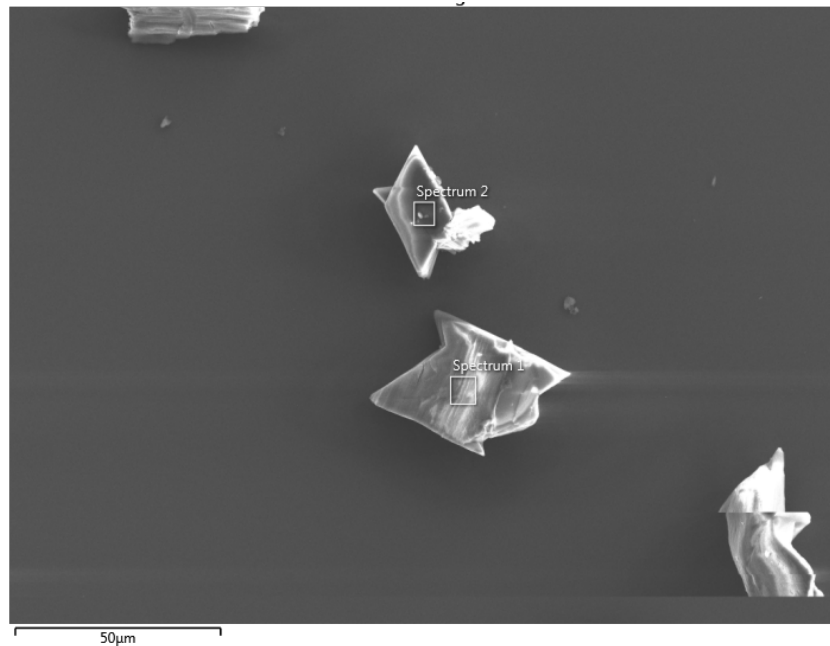


**Figure 2.18** SEM image (top) and EDS spectrum (bottom) of as-synthesized MOF-1131(Er) crystals (spectrum was collected at the ‘Spectrum 1’ area in top image).

If the crosslinking ligands in MOF-1130 and MOF-1131 were removed and replaced with terminal aqua ligands, the resulting structures would be isorecticular to MOF-1114. In MOF-1114, the positive charges of the  $\text{RE}_4(\mu_3\text{-OH})_4(\text{COO})_6^{2+}$  cluster are balanced by  $\mu_1\text{-OH}$  groups bound to the  $\text{RE}^{3+}$  centers and  $\text{Cl}^-$  ions in the cavities. MOF-1130 and MOF-1131 have a different means to achieve charge balance: two additional carboxylates bind to the inorganic SBUs. The longer biphenyl and terphenyl struts in MOF-1130 and MOF-1131 may yield void space that is sufficient to accommodate the additional diagonal crosslinking ligands that provide charge balance. We postulated that a sterically bulky ligand, such as 4,4'-(9,10-anthracenediyl)bis(2-aminobenzoate) ( $\text{NH}_2\text{-ABB}$ ) (Figure 2.19A), may prevent the incorporation of the diagonal cross-linker and lead to the target expanded version of the **pcu** net. Using similar reaction conditions that produced MOF-1114, MOF-1130, and MOF-1131,  $\text{H}_2\text{-NH}_2\text{-ABB}$  and  $\text{RECl}_3 \cdot 6\text{H}_2\text{O}$  were reacted to yield MOF-1115, which crystallizes in the cubic space group  $Fd\bar{3}m$  with the unit cell dimensions  $a = b = c = 44.8598 \text{ \AA}$ . MOF-1115 consists of two maximally displaced interpenetrated frameworks that are isorecticular to MOF-1114 (Figure 2.19B). Seven different  $\text{RE}^{3+}$  ( $\text{Sm}^{3+}$ ,  $\text{Eu}^{3+}$ ,  $\text{Gd}^{3+}$ ,  $\text{Tb}^{3+}$ ,  $\text{Dy}^{3+}$ ,  $\text{Ho}^{3+}$ ,  $\text{Er}^{3+}$ ) can form MOF-1115, as confirmed by comparing their PXRD patterns with that simulated from crystal structure data of MOF-1115(Tb) (Figure 2.20). Similar to MOF-1114, MOF-1115 has a positively charged framework with mobile charge balancing  $\text{Cl}^-$  anions in its cavities as confirmed by SEM/EDS data before and after ion exchange with  $\text{NMe}_4\text{BF}_4$  (Figure 2.21 and 2.22). MOF-1115 is formulated as  $[\text{RE}_4(\mu_3\text{-OH})_4(\text{NH}_2\text{-ABB})_3(\text{H}_2\text{O})_8] \cdot 2\text{Cl}, 11.5\text{DEF}$  (DEF = diethylformamide) based on solution  $^1\text{H}$  and  $^{19}\text{F}$  NMR spectra of anion-exchanged MOF-1115(Tb) (Figure 2.23 and 2.24) and CHN elemental microanalysis of as-synthesized MOF-1115(Tb) (see section 2.4.5 for details). In this example, we demonstrate the importance of ligand steric demand

in influencing MOF topology. In summary, we have achieved, via design and rational, directed syntheses, a family of new pcu MOFs based on the  $\text{RE}_4(\mu_3\text{-OH})_4(\text{COO})_6^{2+}$  cluster.

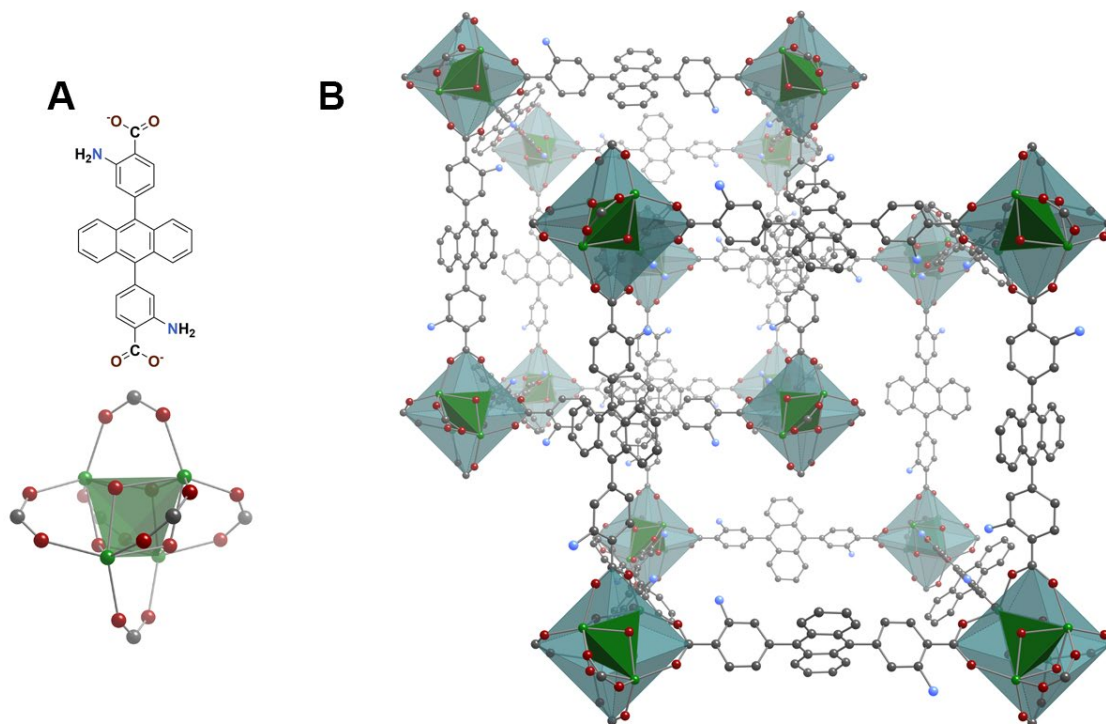


**Figure 2.19** (A) organic linker and inorganic SBU in MOF-1115; (B) crystal structure of MOF-1115 ( $\text{RE}^{3+}$ , green spheres; C, gray spheres; O, red spheres;  $\text{RE}_4(\mu_3\text{-OH})_4$ , green tetrahedra; teal octahedron defines structure of SBU; coordinated water molecules,  $\mu_1$ -OH groups, and H atoms have been omitted for clarity; only one of the possible positions is illustrated for each disordered  $-\text{NH}_2$  group).

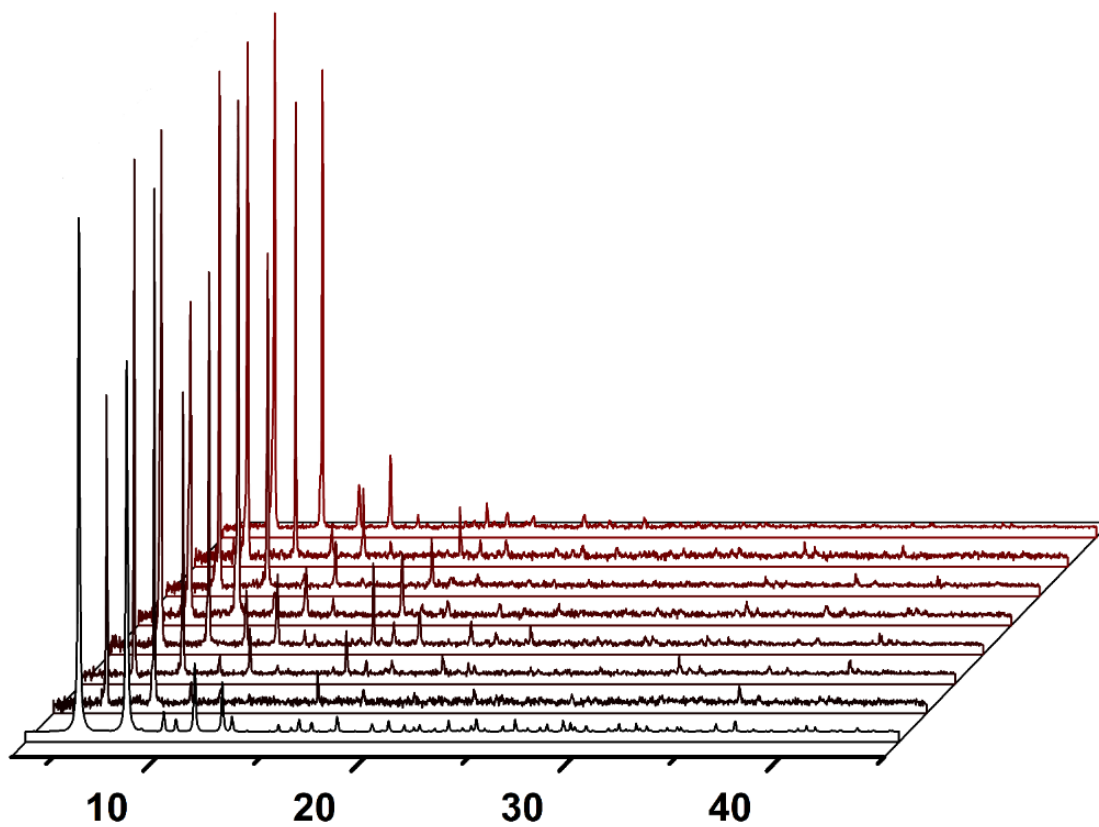


**Figure 2.20** PXRD patterns of MOF-1115 synthesized with different RE<sup>3+</sup> (front to back: simulated, Y<sup>3+</sup>, Gd<sup>3+</sup>, Tb<sup>3+</sup>, Dy<sup>3+</sup>, Ho<sup>3+</sup>, Er<sup>3+</sup>, Tm<sup>3+</sup>, Yb<sup>3+</sup>).

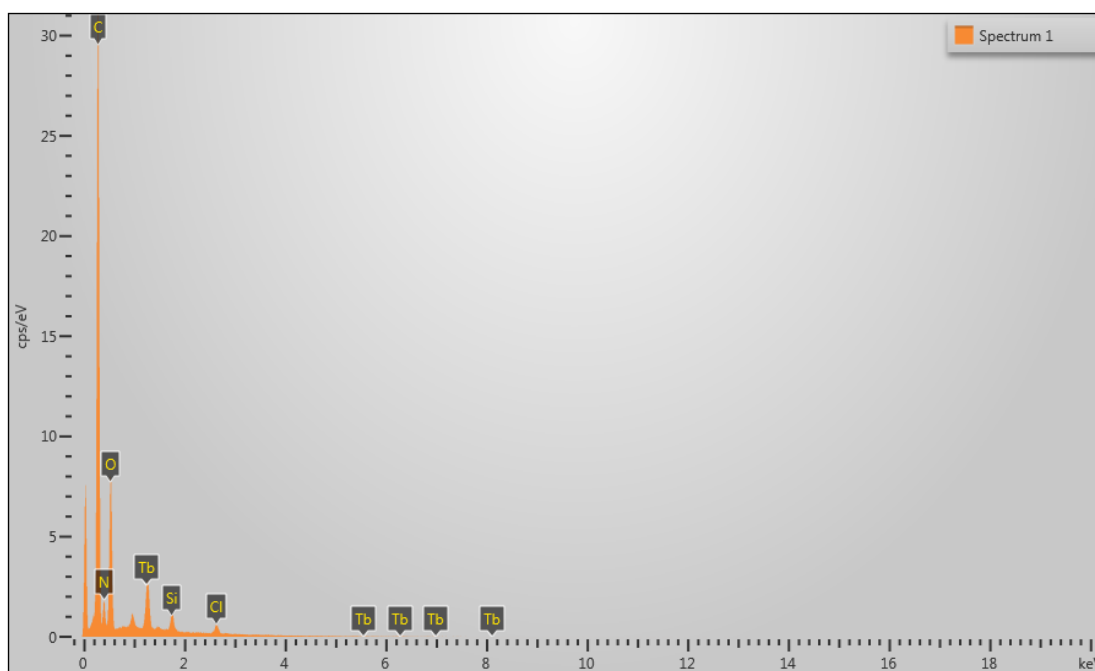
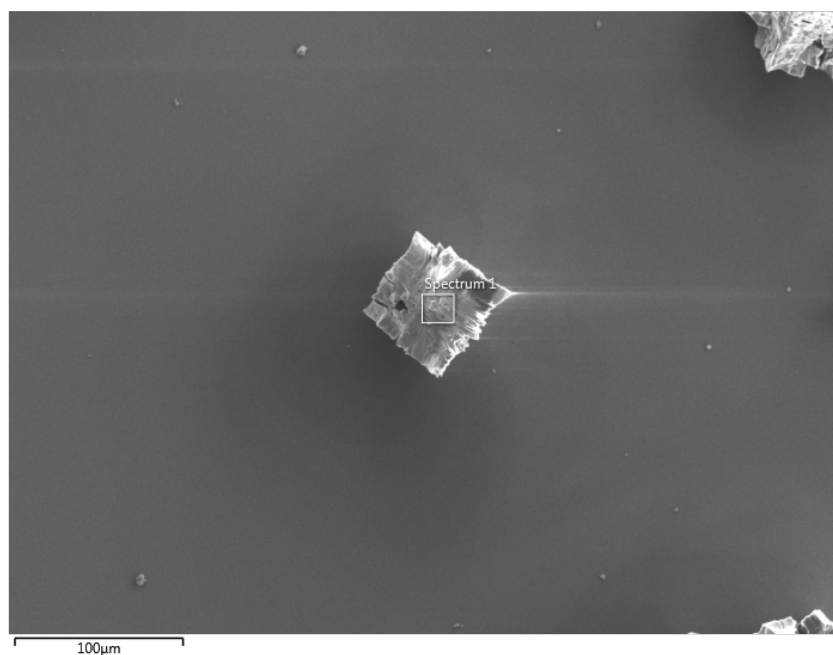


**Figure 2.21** SEM image (top) and EDS spectrum (bottom) of as-synthesized MOF-1115(Tb) (spectrum was taken at the 'Spectrum 1' area in top image).

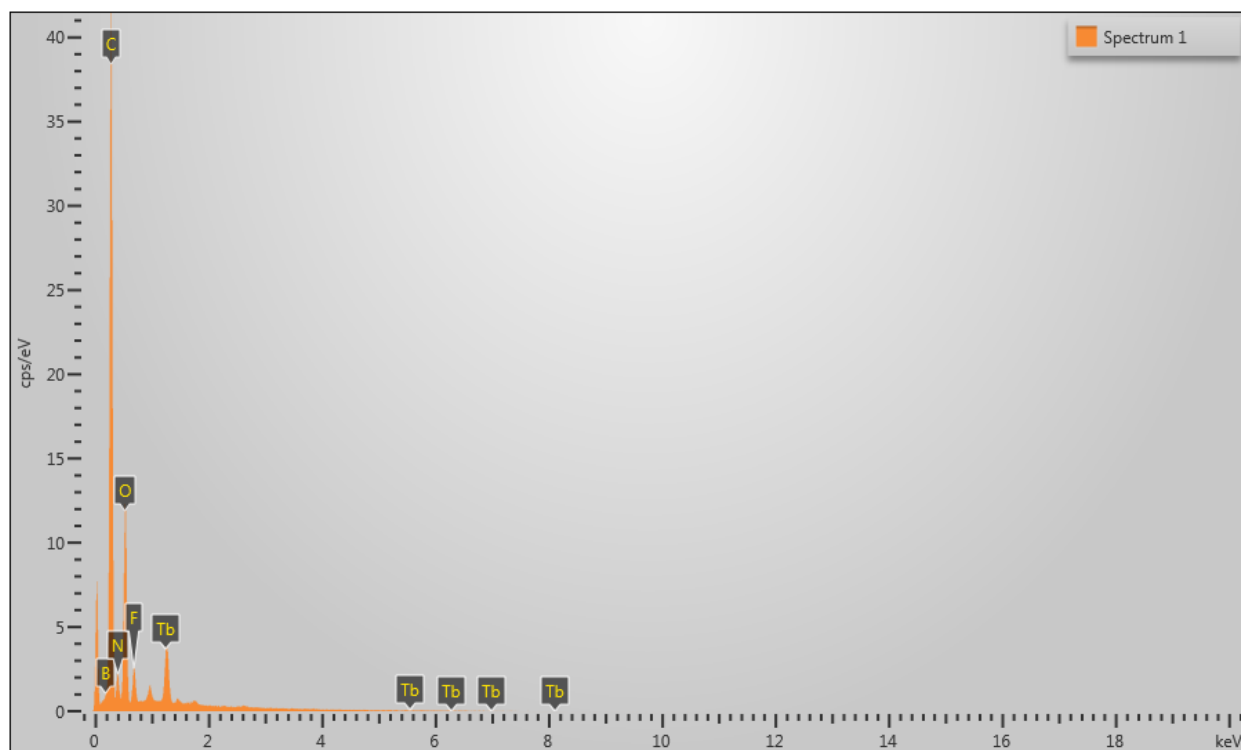
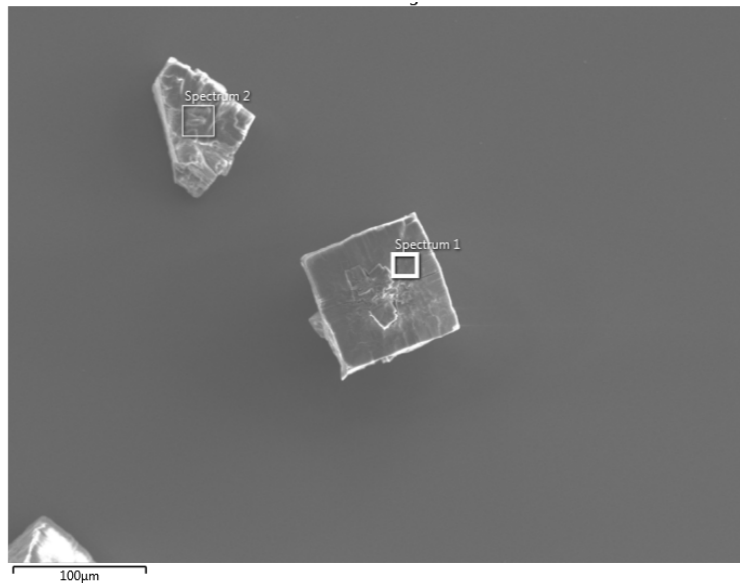


**Figure 2.22** SEM image (top) and EDS spectrum (bottom) of as-synthesized MOF-1115(Tb) after ion exchange with  $\text{NMe}_4\text{BF}_4$ . (spectrum was taken at the ‘Spectrum 1’ area in top image).

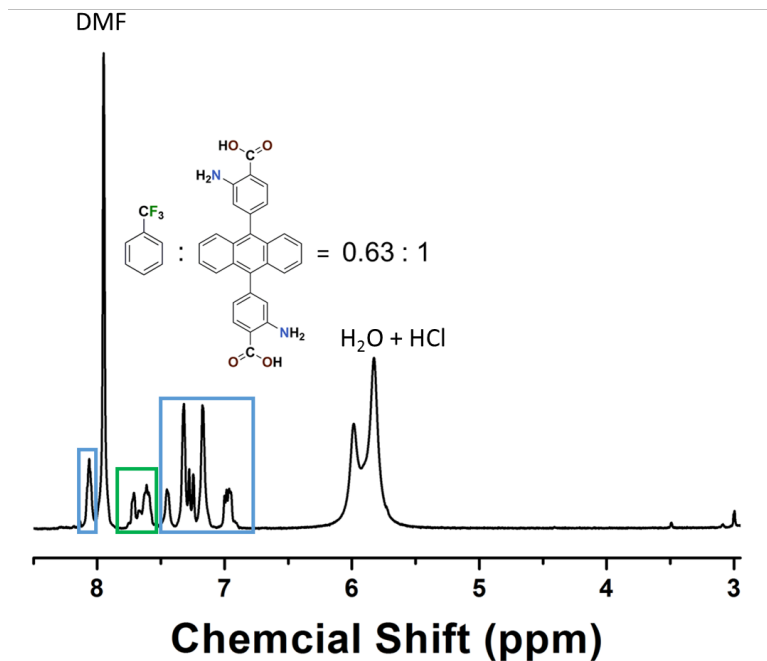


**Figure 2.23** Solution  $^1\text{H}$  NMR of acid dissolved MOF-1115(Tb) after  $\text{NMe}_4\text{BF}_4$  ion exchange with  $\alpha,\alpha,\alpha$ -trifluorotoluene added as internal standard. The molar ratio is calculated based on peak integrations.

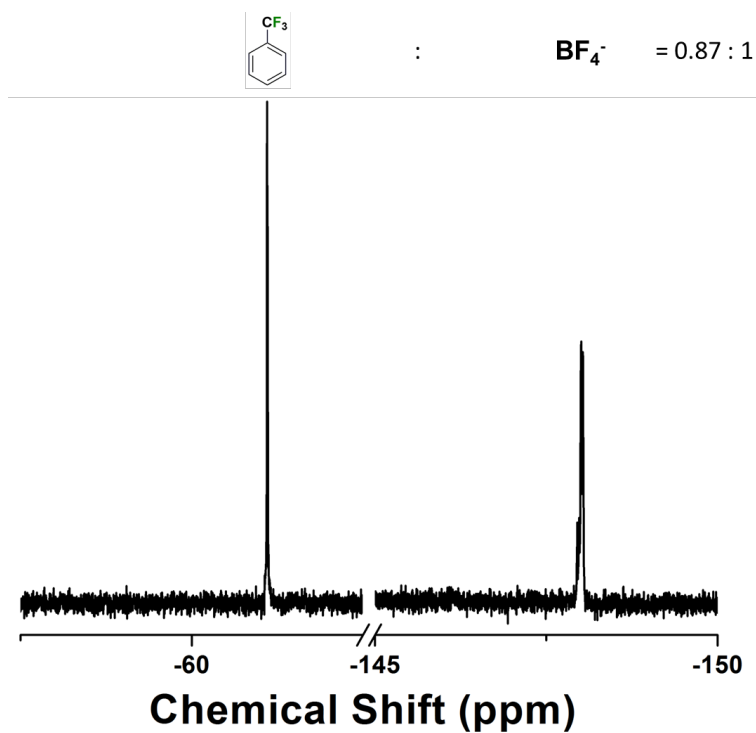


**Figure 2.24** Solution  $^{19}\text{F}$  NMR of acid dissolved MOF-1115(Tb) after  $\text{NMe}_4\text{BF}_4$  ion exchange with  $\alpha,\alpha,\alpha$ -trifluorotoluene added as internal standard. The molar ratio is calculated based on peak integrations.

An ideal material for optical biological imaging should have excitation and emitting wavelengths within the biological window (*vide supra*). Many RE<sup>3+</sup> emit in the NIR, yet typical MOF ligands that serve as the antennae absorb in the UV or high energy visible regions.<sup>135</sup> In order to lower the excitation energy, ligands having extended  $\pi$  systems are often used.<sup>111</sup> One common consequence of this approach is formation of lower density MOFs that have fewer RE<sup>3+</sup> emitters per unit volume. We suggest that covalent post-synthetic modification (CPSM) of MOF linkers (antennae)<sup>136</sup> is one way to systematically shift their excitation wavelengths to lower energy while maintaining a high density of RE<sup>3+</sup> emitters.

The MOF-1114 platform is ideal for investigating this approach: i) the amino groups can serve as sites for CPSM reactions used to extend the  $\pi$  system, and ii) the pore space is sufficient for facile diffusion of precursor molecules for CPSM and for accommodating the product extended antennae. MOF-1114(Yb) was selected because Yb<sup>3+</sup> emits exclusively in the NIR range ( $\lambda_{em} = 940 - 1100$  nm). We hypothesized that condensation reactions between primary amines of NH<sub>2</sub>-BDC and aromatic aldehydes would result in the expansion of the conjugated  $\pi$  system, leading to a red-shift of the excitation band. To test this hypothesis, colorless as-synthesized MOF-1114(Yb) crystals were soaked in DMF solutions of either salicylaldehyde or 3-hydroxynaphthalene-2-carboxaldehyde to yield orange MOF-1114(Yb)<sub>1</sub> crystals and red MOF-1114(Yb)<sub>2</sub> crystals, respectively (Figure 2.25). PXRD patterns after CPSM reactions indicate that both MOF-1114(Yb)<sub>1</sub> and MOF-1114(Yb)<sub>2</sub> retain their original crystallinity after modification (Figure 2.26). <sup>1</sup>H NMR of acid digested MOF samples suggested the inclusion of approximately 1 equivalent of salicylaldehyde in MOF-1114(Yb)<sub>1</sub> and 0.41 equivalent of 3-hydroxynaphthalene-2-carboxaldehyde in MOF-1114(Yb)<sub>2</sub> per NH<sub>2</sub>-BDC ligand (Figure 2.27). To confirm covalent attachment of the aldehydes to the framework prior to acid digestion, NaBH<sub>4</sub> in ethanol was used

to reduce the imine to the stable C-N single bond. The reduced MOF samples were then digested for  $^1\text{H}$  NMR analysis and liquid chromatography-mass spectrometry (LC-MS), which showed that ~70% of the  $\text{NH}_2\text{-BDC}$  in  $\text{MOF-1114}(\text{Yb})_1$  were converted into the Schiff base product (Figures 2.28 and 2.29). Reduced alcohol product from salicylaldehyde and unmodified  $\text{NH}_2\text{-BDC}$  were also observed, indicating the presence of free salicylaldehyde trapped in MOF pores after CPSM. Similarly, for  $\text{MOF-1114}(\text{Yb})_2$ , 22% of the  $\text{NH}_2\text{-BDC}$  were converted to a Schiff base product. Again, reduced alcohol product and unmodified  $\text{NH}_2\text{-BDC}$  were observed, indicating free 3-hydroxynaphthalene-2-carboxaldehyde trapped in the pore after CPSM (Figures 2.30 and 2.31).

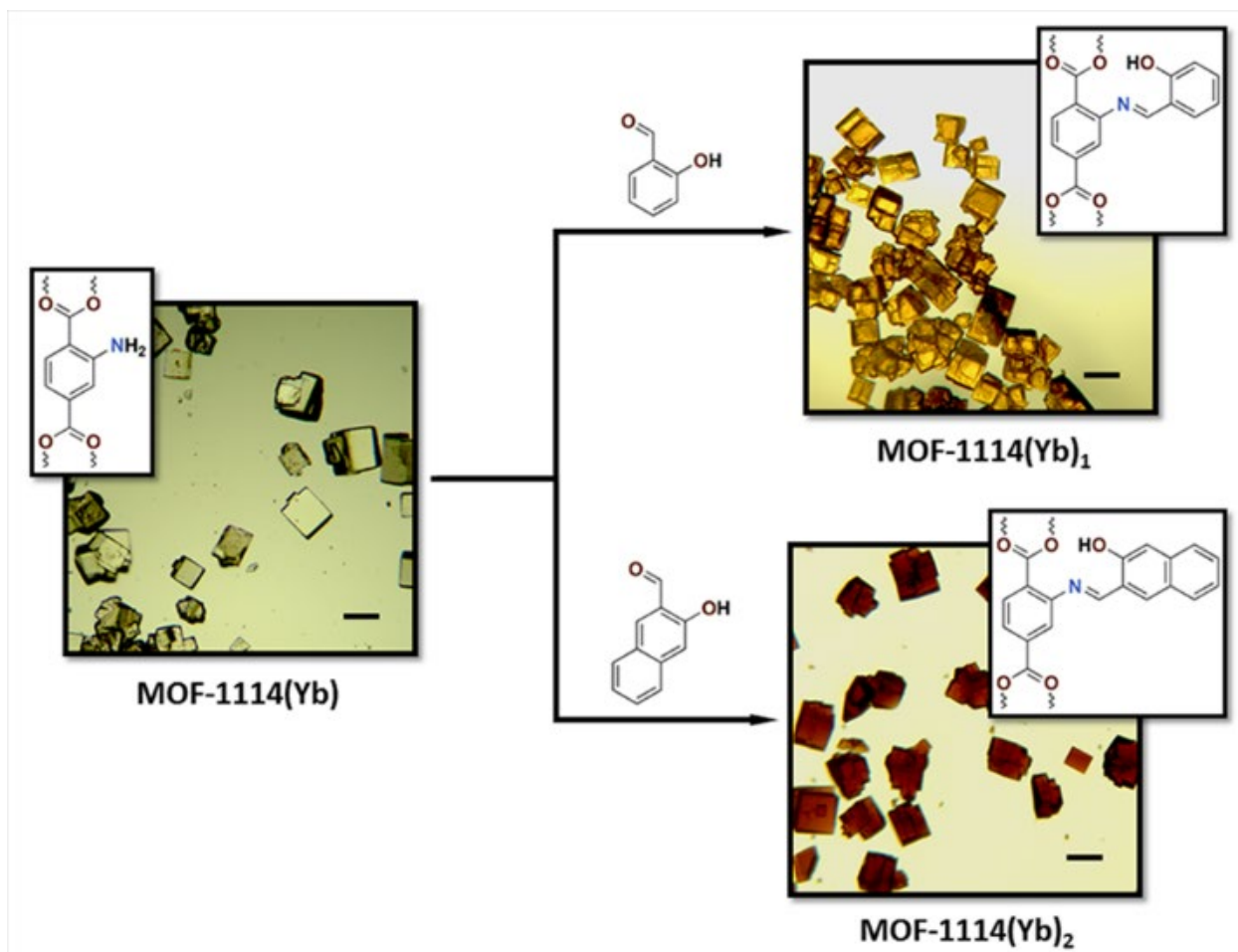
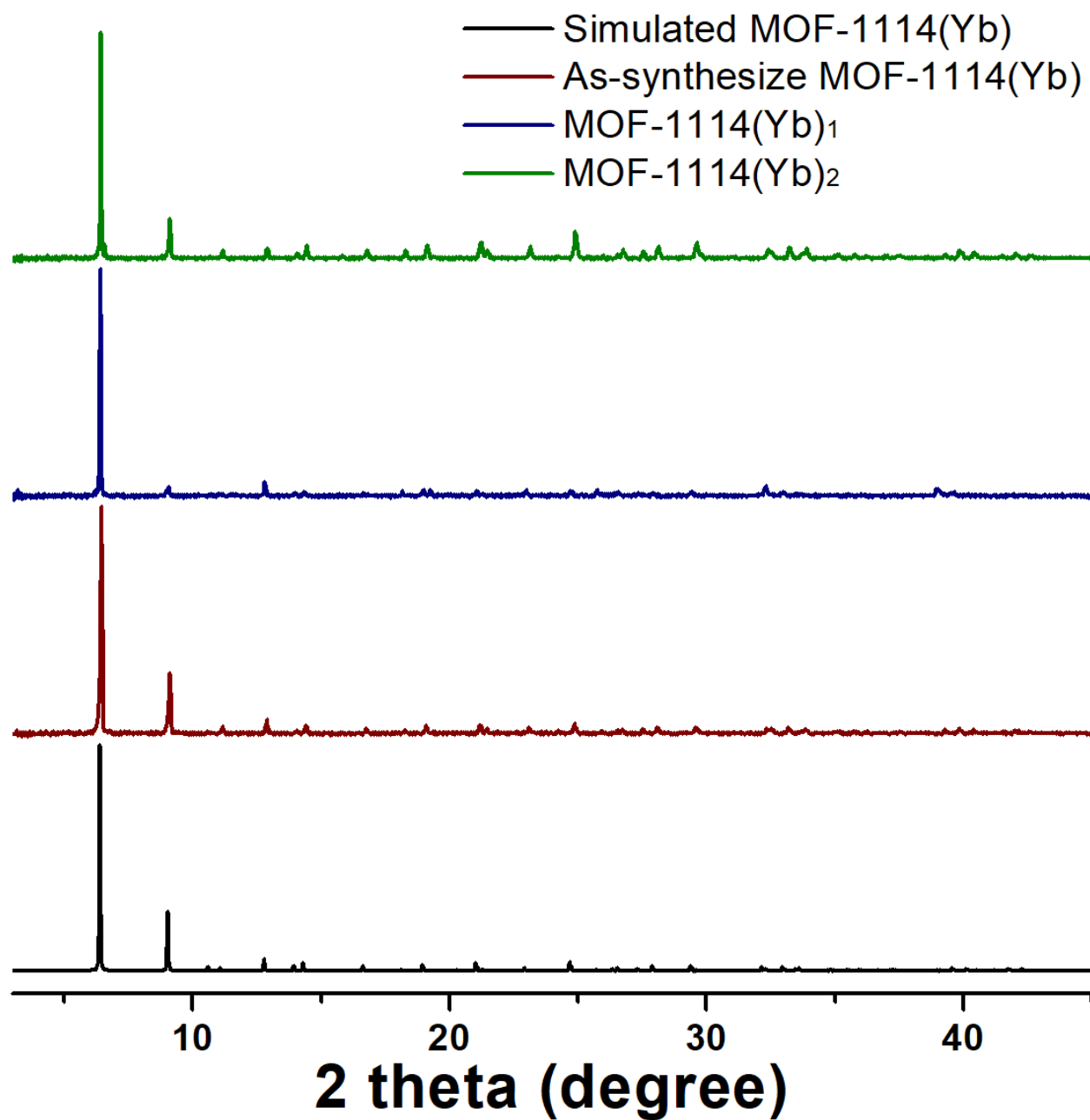
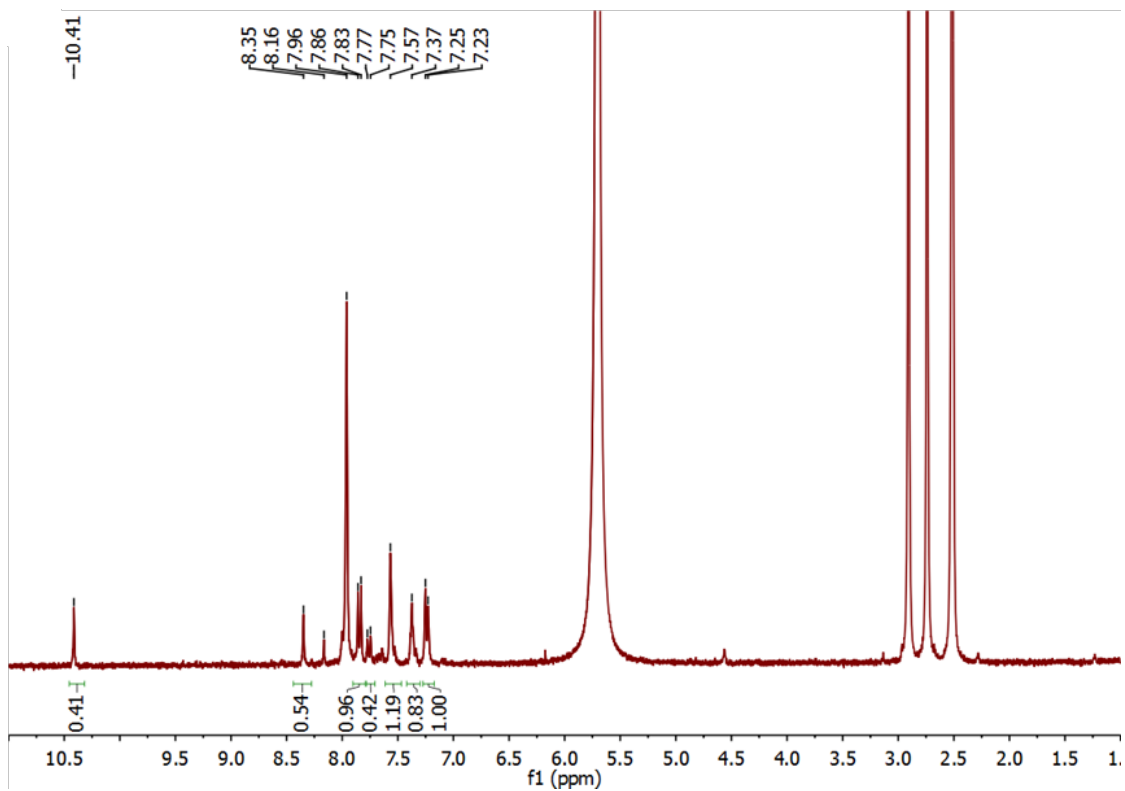
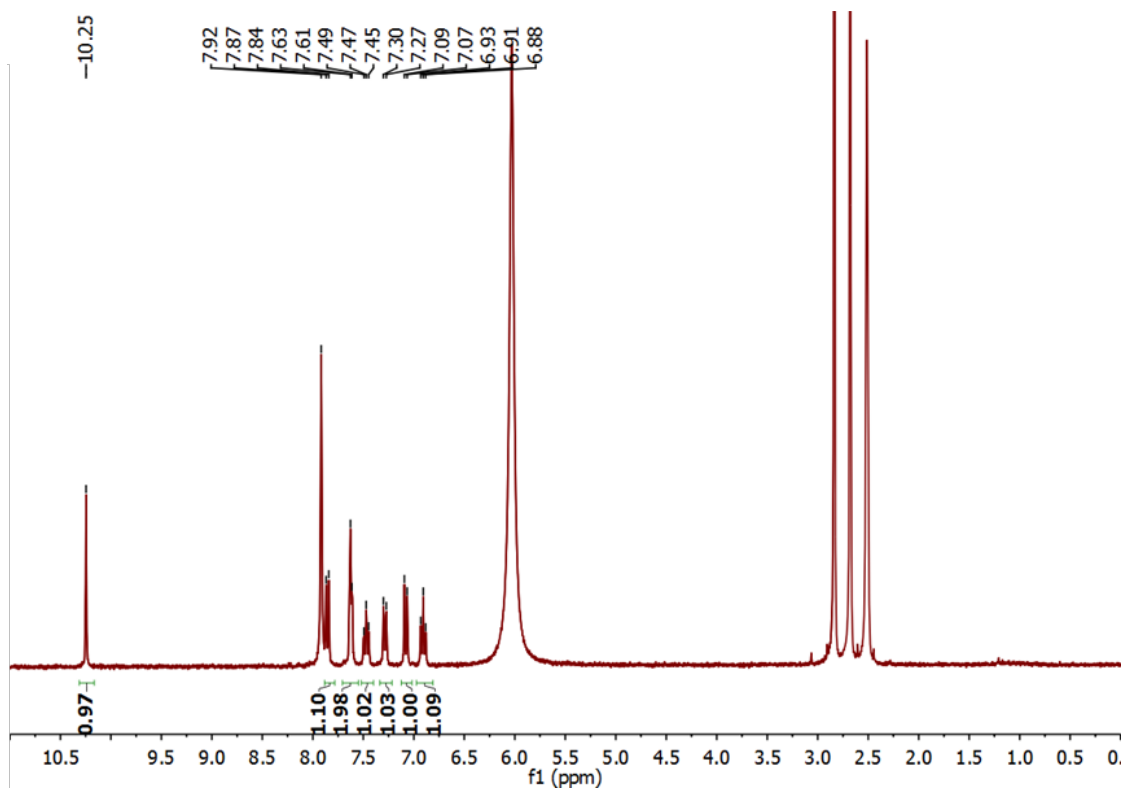


Figure 2.25 CPSM reactions in  $\text{MOF-1114}(\text{Yb})$  (Scale bars = 100  $\mu\text{m}$ ).



**Figure 2.26** Simulated PXRD based on MOF-1114(Gd) crystal structure (black), experimental PXRD pattern of as-synthesized MOF-1114(Yb) (red) and MOF-1114(Yb)<sub>1</sub> (navy) and MOF-1114(Yb)<sub>2</sub> (green).



**Figure 2.27** Solution  $^1\text{H}$  NMR of acid digested MOF-1114( $\text{Yb}$ )<sub>1</sub> (top), and MOF-1114 ( $\text{Yb}$ )<sub>2</sub> (bottom) in  $\text{DMSO-}d_6$ .

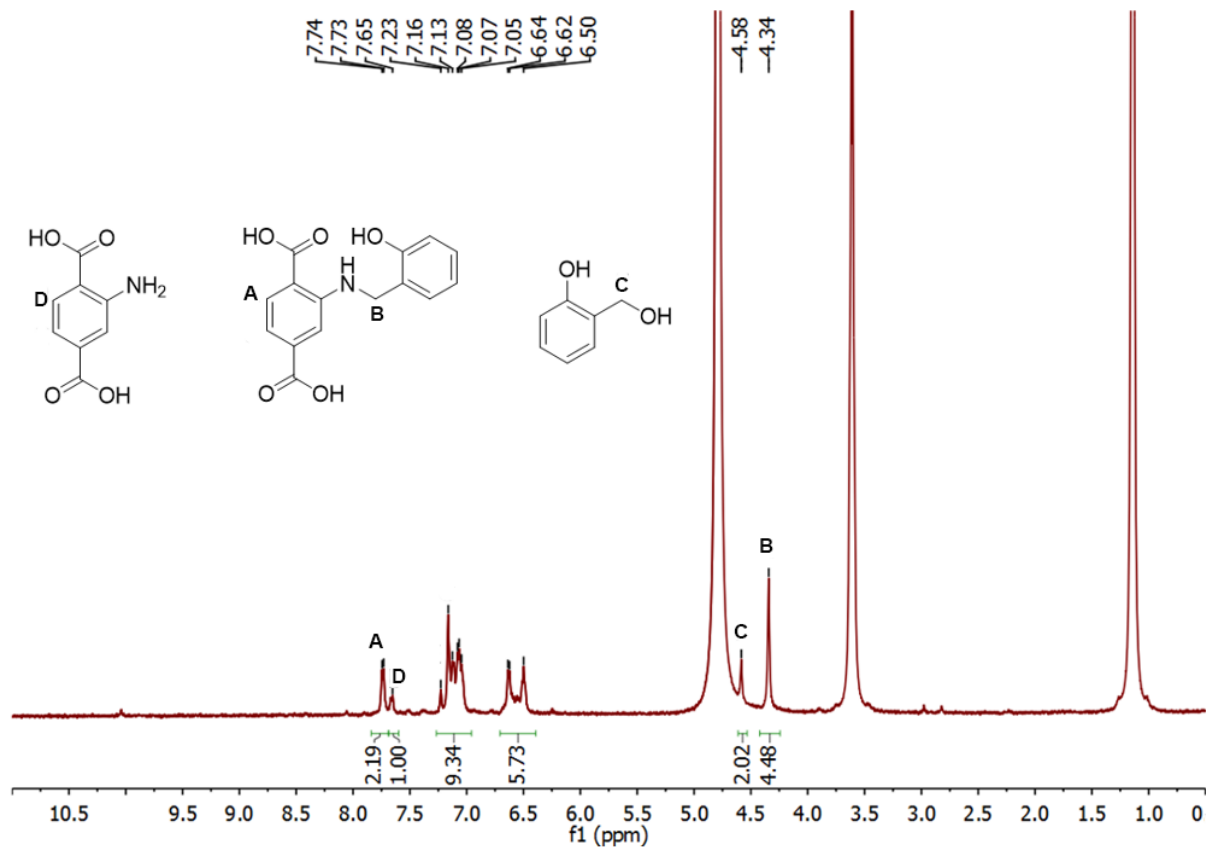


**Figure 2.28** Solution <sup>1</sup>H NMR in D<sub>2</sub>O of digested MOF-1114(Yb)<sub>1</sub> after NaBH<sub>4</sub> reduction.

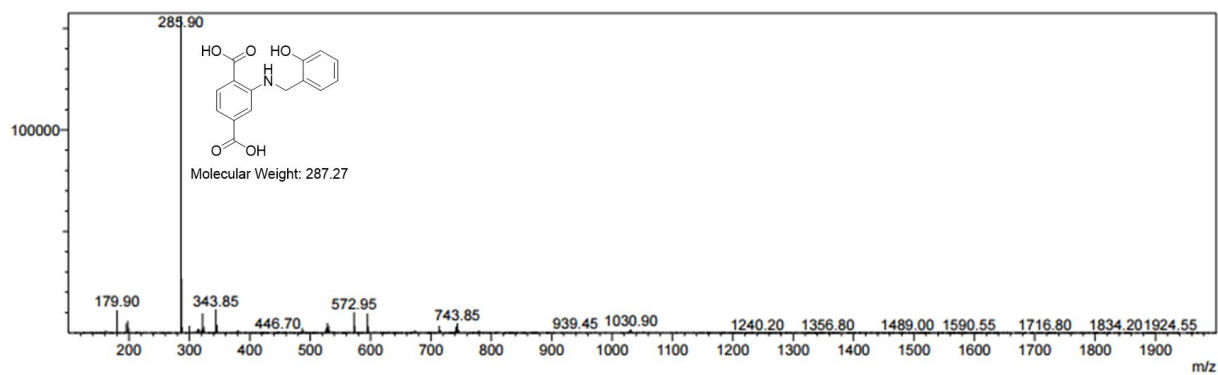


**Figure 2.29** Mass spectrum (ESI-) of digested MOF-1114(Yb)<sub>1</sub> after NaBH<sub>4</sub> reduction.

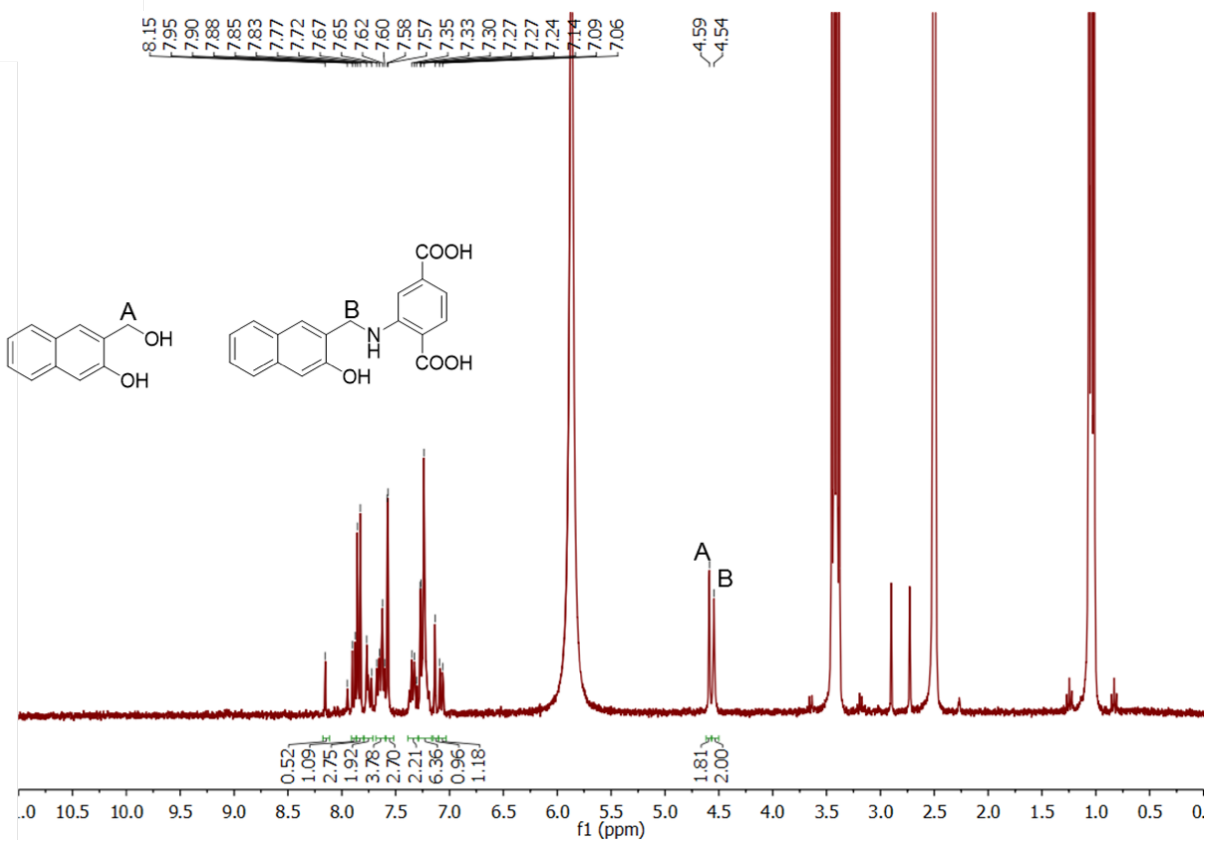


**Figure 2.30** Solution  $^1\text{H}$  NMR in  $\text{D}_2\text{O}$  of digested MOF-1114( $\text{Yb}$ )<sub>2</sub> after  $\text{NaBH}_4$  reduction.

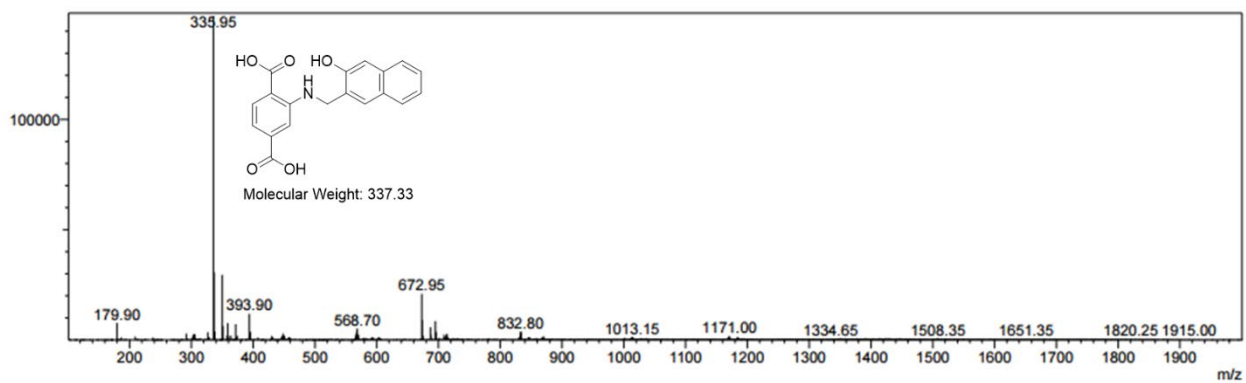


**Figure 2.31** Mass spectrum (ESI-) of digested MOF-1114( $\text{Yb}$ )<sub>1</sub> after  $\text{NaBH}_4$  reduction.

Absorption spectra collected on single crystalline samples of MOF-1114(Yb), MOF-1114(Yb)<sub>1</sub>, and MOF-1114(Yb)<sub>2</sub> are sequentially red-shifted. The as-synthesized MOF-1114(Yb) only absorbs below 450 nm, while the absorption bands of MOF-1114(Yb)<sub>1</sub> and MOF-1114(Yb)<sub>2</sub> extend to 550 nm and 650 nm, respectively (Figure 2.32A). To rule out the possibility that the red-shift of absorption bands is caused by the presence of free aldehyde molecules in the pores, solution UV-Vis spectra were collected for each of the free aldehydes (Figure 2.32B). Both molecules only absorb at wavelengths below 500 nm. Therefore, the red-shift of absorption spectra and the crystal color change after CPSM reactions can be ascribed to the imine products featuring extended conjugated  $\pi$  systems.

Photoluminescence studies were then performed. The characteristic Yb<sup>3+</sup> NIR emission band in the range 940 - 1100 nm due to the  $^2F_{5/2} \rightarrow ^2F_{7/2}$  transition can be observed for MOF-1114(Yb), MOF-1114(Yb)<sub>1</sub> and MOF-1114(Yb)<sub>2</sub> upon excitation through the ligands' bands at 380 nm (Figure 2.32C). This is an indication that an 'antenna effect' is operating between the organic sensitizers and Yb<sup>3+</sup> for all samples: because Yb<sup>3+</sup> does not possess an electronic level in the UV or in the visible, the sensitization of Yb<sup>3+</sup> has to occur through the electronic levels of the chromophoric entities. The excitation spectra of MOF-1114(Yb), MOF-1114(Yb)<sub>1</sub>, and MOF-1114(Yb)<sub>2</sub> upon monitoring the Yb<sup>3+</sup> emission show sequential red-shifts, consistent with the absorption spectra (Figure 2.32A vs. 2.32D). Yb<sup>3+</sup> emission in MOF-1114(Yb) can only be excited by light with wavelengths shorter than 460 nm. In contrast, the excitation spectra are significantly red-shifted after CPSM to 570 nm for MOF-1114(Yb)<sub>1</sub> and to 670 nm for MOF-1114(Yb)<sub>2</sub>. This red-shift of excitation bands can be attributed to sensitizers with large conjugated  $\pi$  systems upon CPSM of RE<sup>3+</sup>-MOFs. It is worth mentioning that for MOF-1114(Yb)<sub>2</sub>, the longest edge of the excitation wavelengths lies within the biological window (650 - 1450 nm). This advantage in

combination with  $\text{Yb}^{3+}$  emission in the NIR range makes  $\text{MOF-1114}(\text{Yb})_2$  a promising candidate for biological applications including in vivo imaging.

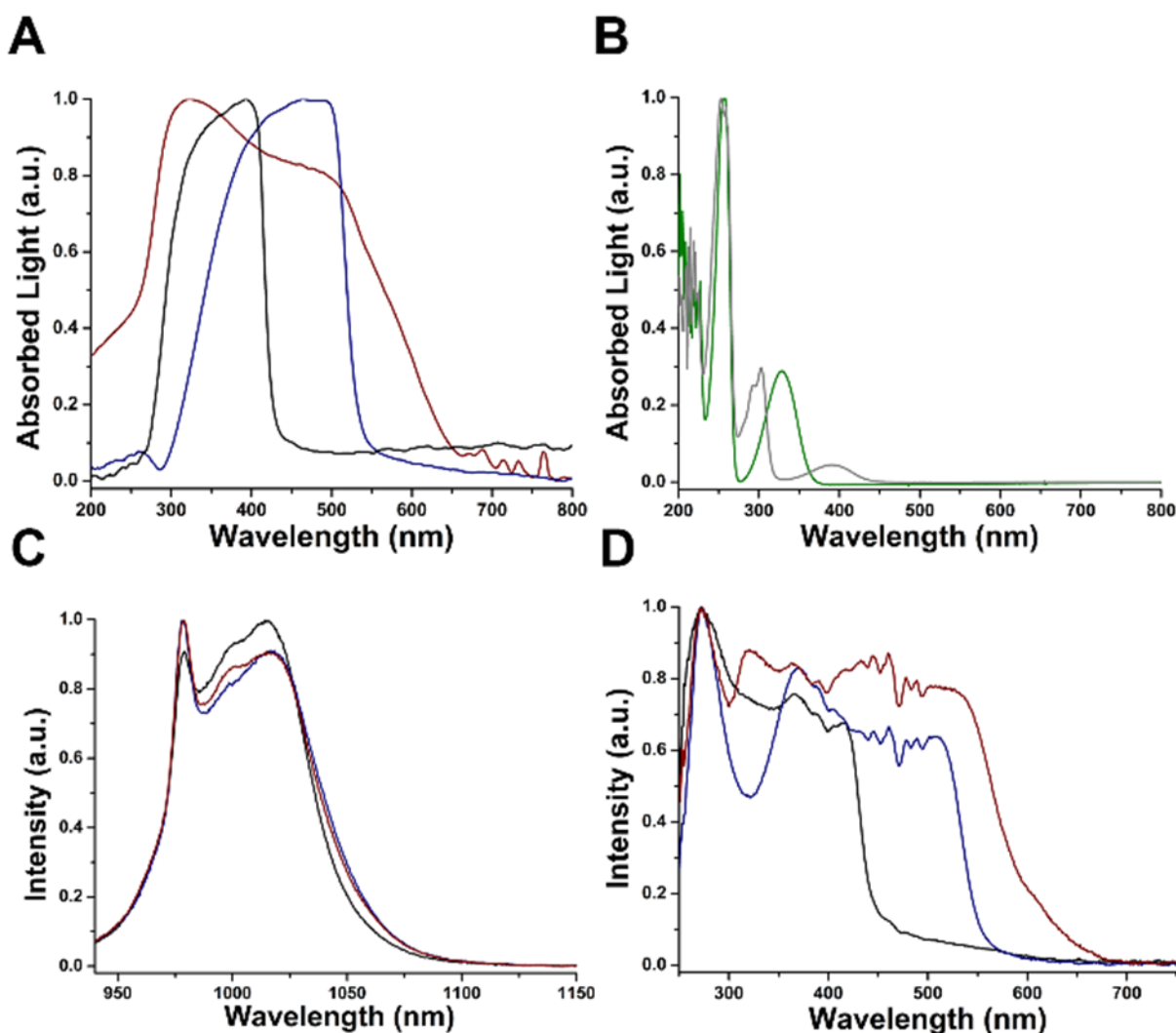


**Figure 2.32 .** (A) Normalized absorption spectra of single crystalline  $\text{MOF-1114}(\text{Yb})$  (black),  $\text{MOF-1114}(\text{Yb})_1$  (navy) and  $\text{MOF-1114}(\text{Yb})_2$  (red); (B) normalized absorption spectra of salicylaldehyde (green) and 3-hydroxy-naphthalene-2-carboxaldehyde (grey) in solution ( $10 \mu\text{M}$  in dichloromethane); corrected and normalized (C) emission spectra ( $\lambda_{\text{ex}} = 380 \text{ nm}$ ) and (D) excitation spectra ( $\lambda_{\text{em}} = 980 \text{ nm}$ ) of  $\text{MOF-1114}(\text{Yb})$ ,  $\text{MOF-1114}(\text{Yb})_1$  and  $\text{MOF-1114}(\text{Yb})_2$ ;

Quantum yields of NIR  $\text{Yb}^{3+}$  emission ( $\text{QYb}$ ) were determined under excitation at 380 and 500 nm (Figure 2.33).  $\text{QYb}$  values for  $\text{MOF-1114}(\text{Yb})_1$  and  $\text{MOF-1114}(\text{Yb})_2$  under 380 nm excitation were found to be similar to that of unmodified  $\text{MOF-1114}(\text{Yb})$ . On the other hand,

CPSM significantly improves  $\text{Yb}^{3+}$  quantum yields under higher excitation wavelength, resulting in up to 4.4 times increase compared to the unmodified MOF-1114(Yb). Also worth noting is that the  $\text{Yb}^{3+}$  quantum yields of these three MOF materials vary under different excitation wavelengths. Especially desirable for biological imaging is that MOF-1114(Yb)<sub>2</sub> exhibits better quantum yield under long-wavelength excitation than short-wavelength excitation. Luminescence lifetimes of  $\text{Yb}^{3+}$  MOFs upon monitoring the  ${}^2\text{F}_{5/2} \rightarrow {}^2\text{F}_{7/2}$  transition lie in the range 620 - 670 ns, indicating that CPSM does not significantly affect the coordination environment around  $\text{Yb}^{3+}$ .

Sample	$\tau_{\text{obs}} / \text{ns}$	$Q_{\text{Yb}} \%$	
		$\lambda_{\text{ex}} = 380 \text{ nm}$	$\lambda_{\text{ex}} = 500 \text{ nm}$
MOF-1114(Yb)	644(7)	$2.9(2) \cdot 10^{-2}$	$1.03(8) \cdot 10^{-2}$
MOF-1114(Yb) <sub>1</sub>	619(4)	$4.27(7) \cdot 10^{-2}$	$3.9(1) \cdot 10^{-2}$
MOF-1114(Yb) <sub>2</sub>	669(5)	$2.8(2) \cdot 10^{-2}$	$4.55(6) \cdot 10^{-2}$

**Figure 2.33** Luminescence lifetimes ( $\tau_{\text{obs}}$ ) and quantum yields ( $Q_{\text{Yb}}$ ) of MOFs at room temperature (crystals under DMF;  $2\sigma$  values between parentheses; lifetimes measured under excitation at 355 nm).

## 2.3 CONCLUSIONS

We successfully designed and synthesized a new class of MOFs based on the  $\text{RE}_4(\mu_3\text{-OH})_4$  cluster motif. A new **pcu** MOF platform was created using the highly symmetric  $\text{RE}_4(\mu_3\text{-OH})_4(\text{COO})_6^{2+}$  cluster as the inorganic SBU. We demonstrated that this MOF platform is highly tunable in terms of  $\text{RE}^{3+}$  composition and structure metrics. It can be systematically modified via either postsynthetic anion exchange or covalent modification. Finally, CPSM was used to

deliberately red-shift the excitation wavelengths of a representative NIR emitting MOF, MOF-1114(Yb), into the range suitable for biological imaging applications.

## 2.4 EXPERIMENTAL SECTION

### 2.4.1 General methods

All purchased chemicals were used without further purification except where otherwise noted. Nanopure water (18.1 M $\Omega$ ) was obtained from a Barnstead Diamond<sup>TM</sup> water purification system.

Powder X-ray diffraction patterns were collected using a Bruker AXS D8 Discover powder diffractometer at 40 kV, 40 mA for Cu K $\alpha$ , ( $\lambda = 1.5406 \text{ \AA}$ ) with a scan speed of 0.10 sec/step from 3 to 45° at a step size of 0.02°. The data were analyzed using the EVA program from the Bruker Powder Analysis Software package. The simulated powder patterns were calculated using Mercury 3.8 based on crystal structures of corresponding MOFs.

Single crystal X-ray diffraction experiments were performed on a Bruker X8 Prospector Ultra diffractometer equipped with an Apex II CCD detector and an I $\mu$ S micro-focus Cu K $\alpha$  X-ray source ( $\lambda = 1.54178 \text{ \AA}$ ). Data were collected at 230 K or 240 K under N<sub>2</sub> flow and processed using the Bruker APEX II software package and refined with Olex2 program.<sup>137-138</sup>

<sup>1</sup>H, <sup>13</sup>C and <sup>19</sup>F NMR spectra were obtained using Bruker Avance III 300/400/500 MHz spectrometers. Chemical shifts are in parts per million (ppm) using the residual solvent peak (CDCl<sub>3</sub>, D<sub>2</sub>O, or DMSO-d<sub>6</sub>) as references.

Thermogravimetric analyses were performed using a TGA Q500 thermal analysis system under a N<sub>2</sub> atmosphere from room temperature to 650 °C at a ramping rate of 5 °C/min.

CHN Elemental microanalyses (EA) were performed by the University of Illinois, Department of Chemistry Microanalytical Laboratory using a Perkin-Elmer 240 Elemental Analyzer and an Exeter Analytical CE440.

LC-MS analyses were performed on a Shimadzu LCMS-2020 instrument using a 6 minute running time with a constant 1:1 ratio of acetonitrile : water at a constant flow rate of 0.2 mL/min without passing through a column.

SEM/EDS analyses were conducted using ZEISS Sigma 500 VP SEM with Oxford Aztec X-EDS. The crystal samples were washed with ethanol and drop cast on silicon wafers and dried under ambient condition before SEM/EDS analyses.

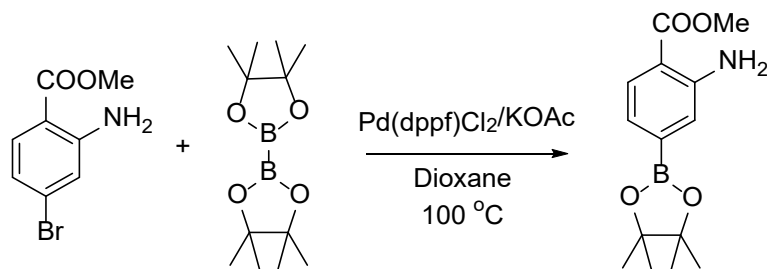
Solution UV-Vis absorption spectra were collected using an Agilent 8453 UV-Vis spectrometer equipped with deuterium and tungsten lamps. Solid state UV-Vis absorption spectra were collected on individual crystals on glass slide using a CRAIC QDI 2010 microspectrophotometer in transmission mode. The sampling area was fixed at  $37 \times 37 \mu\text{m}^2$ .

Photoluminescence properties were measured in an integration sphere using a Horiba Jobin-Yvon Fluorolog-3 spectrofluorometer equipped with a 450 W xenon excitation source and a visible photomultiplier tube (PMT) (220 - 800 nm, R928P; Hamamatsu), and a NIR PMT (950 - 1650 nm, H10330-75; Hamamatsu) on solid MOF samples stored under DMF in quartz capillary tubes. All spectra were corrected for the instrumental functions. Luminescence lifetimes were determined under 355 nm excitation provided by the third harmonic of a YG 980 Quantel Nd-YAG laser; emission signals were selected using a Horiba Scientific iHR-320 monochromator, detected using a Hamamatsu H10330-75 NIR PMT, fed into a 500 MHz bandpass digital

oscilloscope (TDS 754C; Tektronix), transferred to a PC in which data were processed with the Origin 8® program. Quantum yields were determined with a Horiba Scientific Fluorolog-3 spectrofluorimeter based on an absolute method (Model G8, GMP SA, Renens, Switzerland). Each sample was measured several times under comparable experimental conditions, varying the position of samples. Estimated experimental error for the quantum yield determination is ~10 %.

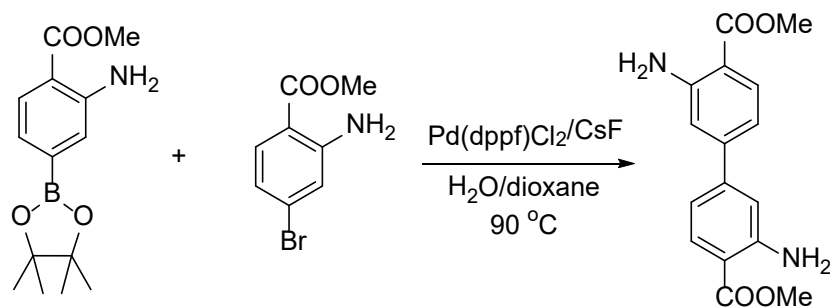
## 2.4.2 Syntheses and characterization of ligands

### 2.4.2.1 Synthesis of 3-amino-4-methoxycarbonyl-phenylboronic acid pinacol ester



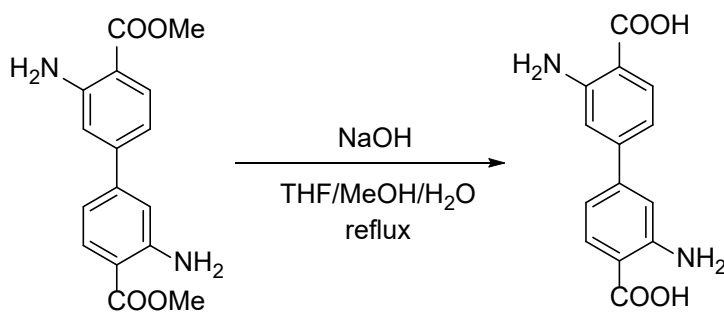
To dioxane (20 mL) were added methyl 2-amino-4-bromobenzoate (1.08 g, 5.0 mmol), bis(pinacolato)diboron (1.27g, 5.0 mmol) and potassium acetate (1.47 g, 15 mmol). The mixture was purged with argon flow for 30 min. Pd(dppf)Cl<sub>2</sub> (200 mg, 0.27 mmol) was then added to the mixture. The reaction was stirred at 100 °C for 6 hours under argon. Once cooled down to room temperature, the reaction was diluted with CH<sub>2</sub>Cl<sub>2</sub> (50 mL). The organic phase was then washed with H<sub>2</sub>O (400 mL, 2x) and saturated NaCl solution (200 mL). After dried over Na<sub>2</sub>SO<sub>4</sub>, the organic solvent was removed in vacuo. The crude product was purified via column chromatography (hexanes : ethyl acetate 10 : 1) to yield white solid (1.0g, 72 %). <sup>1</sup>H NMR (500 MHz, CDCl<sub>3</sub>) δ 7.85 (d, J = 8.0 Hz, 1H), 7.21 (d, J = 1.0 Hz, 1H), 7.11 (dd, J = 8.0, 1.0 Hz, 1H), 3.88 (s, 3H), 1.34 (s, 12H). <sup>13</sup>C NMR (125 MHz, CDCl<sub>3</sub>) δ 168.41, 147.47, 130.26, 124.28, 123.34, 113.95, 84.16, 51.78, 24.87.

### 2.4.2.2 Synthesis of dimethyl 3,3'-diamino-1,1'-biphenyl-4,4'-dicarboxylate



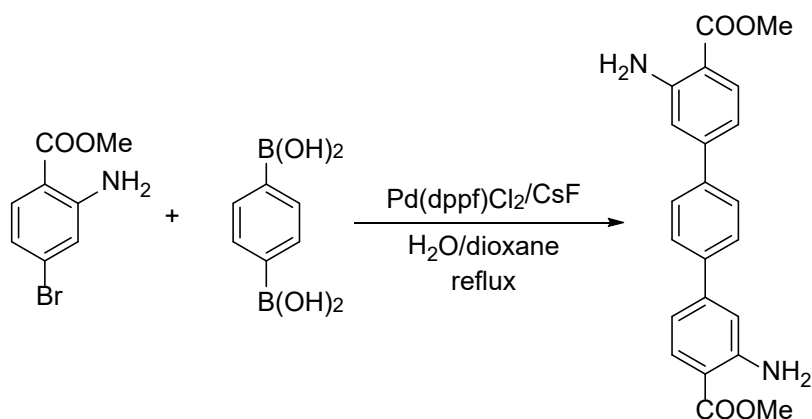
To a 1 : 1 mixture of dioxane/H<sub>2</sub>O (30 mL) were added 3-amino-4-methoxycarbonylphenylboronic acid pinacol ester (1 g, 3.8 mmol), methyl 2-amino-4-bromobenzoate (0.98 g, 4.56 mmol) and cesium fluoride (1.75 g, 11.4 mmol). The mixture was purged with argon for 30 min followed by addition of Pd(dppf)Cl<sub>2</sub> (150 mg, 0.21 mmol). The reaction was then stirred at 90 °C under argon for 18 hours. Once cooled down to room temperature, the reaction mixture was diluted with CH<sub>2</sub>Cl<sub>2</sub> (50 mL). The organic solution was then washed with H<sub>2</sub>O (500 mL, 2x) and saturated NaCl solution (200 mL). After dried over Na<sub>2</sub>SO<sub>4</sub>, the organic solvent was removed in vacuo. The crude product was purified via column chromatography (CH<sub>2</sub>Cl<sub>2</sub> : hexanes 4 : 1) to yield yellow solid (723 mg, 64 %). <sup>1</sup>H NMR (300 MHz, DMSO-d<sub>6</sub>) δ 7.78 (d, J = 5.4 Hz, 2H), 7.03 (d, J = 1.8 Hz, 2H), 6.76 (dd, J = 5.4 Hz, 1.8 Hz, 2H), 3.80 (s, 3H). <sup>13</sup>C NMR (125 MHz, DMSO-d<sub>6</sub>) δ 168.05, 151.89, 145.28, 131.80, 114.87, 113.99, 108.94, 60.20.

### 2.4.2.3 Synthesis of 3,3'-diamino-1,1'-biphenyl-4,4'-dicarboxylic acid



Dimethyl 3,3'-diamino-1,1'-biphenyl-4,4'-dicarboxylate (700 mg, 2.33 mmol) was dissolved in a 1:1 mixture of THF/MeOH (40 mL). To the mixture was added NaOH (1.1 g, 27 mmol) dissolved in water (20 mL). The reaction was stirred under reflux for 24 hours. Once cooled to room temperature, the organic solvent was removed in vacuo. 1 M HCl solution was added to the aqueous residue until the pH of the solution reached 5 to obtain a light yellow paste. The mixture was then centrifuged followed by the removal of supernatant. The precipitate was washed with H<sub>2</sub>O (50 mL, 3x) and dried under vacuum (580 mg, 93%). <sup>1</sup>H NMR (300 MHz, DMSO-d<sub>6</sub>) δ 7.76 (d, J = 8.1 Hz, 2H), 6.98 (d, J = 1.8 Hz, 2H), 6.73 (dd, J = 8.1 Hz, 1.8 Hz, 2H). <sup>13</sup>C NMR (100 MHz, DMSO-d<sub>6</sub>) δ 169.27, 151.60, 144.70, 131.80, 114.15, 113.29, 109.19.

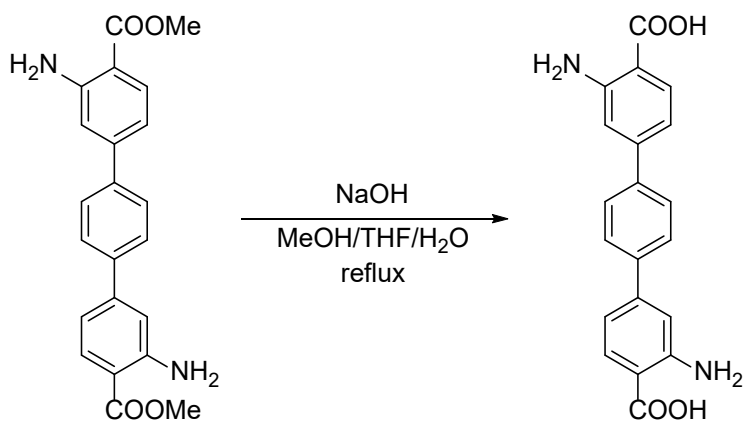
#### 2.4.2.4 Synthesis of dimethyl 3, 3''-diamino-1,1':4',1''-terphenyl-4,4''-dicarboxylate



To a 1:1 mixture of H<sub>2</sub>O/dioxane (80 mL) were added methyl 2-amino-4-bromobenzoate (2.3 g, 10 mmol), 1,4-phenylenediboronic acid (663 mg, 4 mmol) and cesium fluoride 3.6 g, 23.6 mmol). The mixture was purged with argon for 30 min followed by addition of Pd(dppf)Cl<sub>2</sub> (200 mg, 0.27 mmol). The reaction mixture was stirred and refluxed under argon for 24 hours. Once cooled down to room temperature, the reaction mixture was diluted with CH<sub>2</sub>Cl<sub>2</sub> (200 mL). The organic solution was then washed with H<sub>2</sub>O (500 mL, 2x) and saturated NaCl solution (200 mL).

After dried over Na<sub>2</sub>SO<sub>4</sub>, the organic solvent was removed in vacuo. The product was purified via silica gel column chromatography (CH<sub>2</sub>Cl<sub>2</sub> : Ethyl Acetate 40 : 1) to yield yellow solid (1.1g, 73 %). <sup>1</sup>H NMR (400 MHz, DMSO-d<sub>6</sub>) δ 7.89 (d, J = 8.4 Hz, 2H), 7.73 (s, 4H), 7.14 (d, J = 1.6 Hz, 2H), 6.89 (dd, J = 8.4 Hz, 1.6 Hz, 2H), 6.76 (s, 4H). <sup>13</sup>C NMR (100 MHz, DMSO-d<sub>6</sub>) δ 168.11, 152.10, 145.09, 139.53, 131.89, 127.62, 114.55, 113.94, 108.50, 51.90.

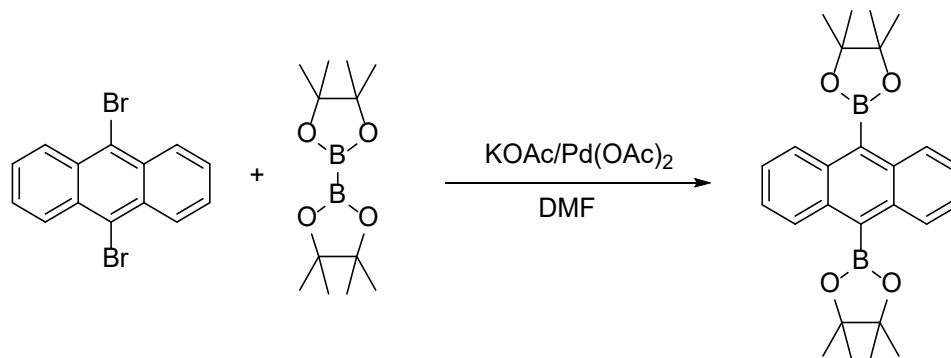
#### 2.4.2.5 Synthesis of 3, 3''-diamino-1, 1': 4', 1''-terphenyl-4, 4''-dicarboxylic acid



Dimethyl 3, 3''-diamino-1, 1': 4', 1''-terphenyl-4, 4''-dicarboxylate (1.1 g, 2.9 mmol) was dissolved in a 1:1 mixture of THF/MeOH (60 mL). To the mixture was added NaOH (1.2 g, 30 mmol) dissolved in H<sub>2</sub>O (30 mL). The reaction mixture was stirred under reflux for 24 hours. Once cooled to room temperature, the organic solvent was removed in vacuo. 1 M HCl solution was added to the aqueous residue until the pH reached 5 to obtain a light yellow paste. After the mixture was centrifuged, supernatant was removed. The precipitate was washed with H<sub>2</sub>O (40 mL, 3x) and then dried under vacuum to yield yellow solid (940 mg, 92%). <sup>1</sup>H NMR (300 MHz, DMSO-d<sub>6</sub>) δ 7.78 (d, J = 8.4 Hz, 2H), 7.72 (s, 4H), 7.09 (d, J = 1.5 Hz, 2H), 6.87 (dd, J = 8.4 Hz, 1.5 Hz, 2H).

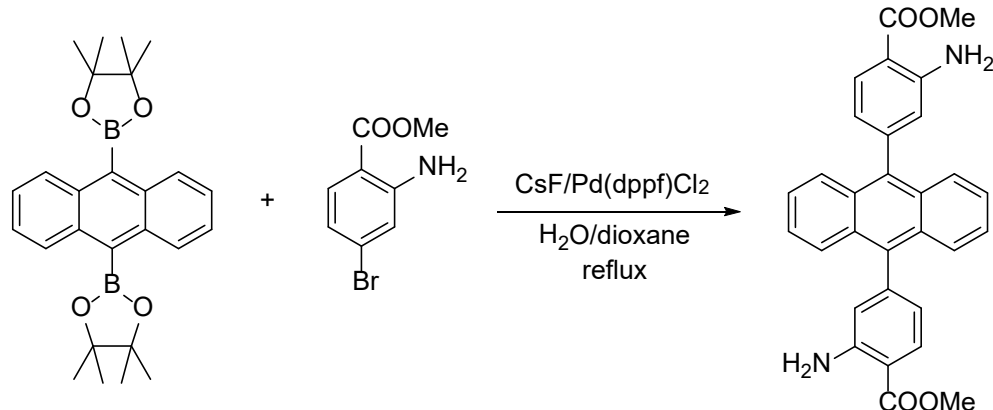
$^{13}\text{C}$  NMR (100 MHz, DMSO- $d_6$ )  $\delta$  169.86, 152.28, 144.90, 139.64, 132.46, 127.60, 114.39, 113.76, 109.38.

#### 2.4.2.6 Synthesis of 9,10-anthracenediboronic acid bis(pinacol) ester



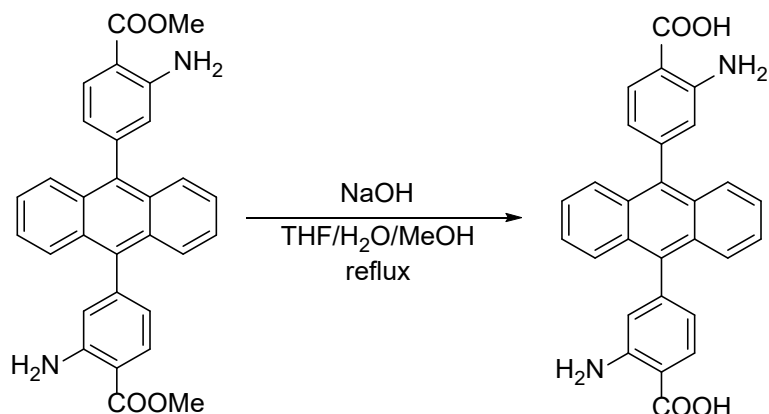
To DMF (35 mL) were added 9,10-dibromoanthracene (4.2 g, 12.5 mmol), bis(pinacolato)diboron (7.75 g, 30.5 mmol) and KOAc (7.35 g, 75 mmol). After the mixture was purged with argon gas for 30 min, Pd(OAc)<sub>2</sub> (166 mg, 0.74 mmol) was added. The reaction was stirred at 70 °C under argon for 18 h. The reaction was then cooled down to room temperature and diluted with CH<sub>2</sub>Cl<sub>2</sub> (100 mL). The organic phase was then washed with water (500 mL, 2x). The aqueous was extracted with CH<sub>2</sub>Cl<sub>2</sub> (100 mL, 2x). The combined organic phase was then washed with brine (50 mL) and dried over Na<sub>2</sub>SO<sub>4</sub>. The organic solvent was removed in vacuo. The product was then purified via silica gel column chromatography (hexanes : ethyl acetate 20 : 1) to yield off-white solid (1.7 g, 31.6 %).  $^1\text{H}$  NMR (400 MHz, CDCl<sub>3</sub>)  $\delta$  8.35 (dd,  $J$  = 6.4 Hz, 2.4 Hz, 4H), 7.45 (dd,  $J$  = 6.4 Hz, 2.4 Hz, 4H), 1.58 (s, 24H).  $^{13}\text{C}$  NMR (100 MHz, DMSO- $d_6$ )  $\delta$  134.95, 128.82, 125.19, 84.50, 25.23.

### 2.4.2.7 Synthesis of dimethyl 4,4'-(9,10-anthracenediyl)bis(2-aminobenzoate)



To a 1:1 mixture of H<sub>2</sub>O/dioxane (80 mL) were added 9,10-anthracenediboronic acid bis(pinacolate) ester (1.7 g, 3.9 mmol), methyl 2-amino-4-bromobenzoate (2.3 g, 10 mmol) and CsF (3.7 g, 24 mmol). The mixture was purged with argon for 30 min. Pd(dppf)Cl<sub>2</sub> (230 mg, 0.3 mmol) was then added. The reaction was stirred and refluxed under argon for 24 h. The reaction was then cooled down to room temperature and diluted with CH<sub>2</sub>Cl<sub>2</sub> (200 mL). The organic phase was then washed with water (500 mL, 2x). The aqueous was extracted with CH<sub>2</sub>Cl<sub>2</sub> (100 mL, 2x). The combined organic phase was then washed with brine (50 mL) and dried over Na<sub>2</sub>SO<sub>4</sub>. The organic solvent was removed in vacuo. The product was purified via column chromatography to yield yellow solid (1.35 g, 76.9 %). <sup>1</sup>H NMR (400 MHz, CDCl<sub>3</sub>) δ 8.11 (dd, J = 8.0 Hz, 2.4 Hz, 2H), 7.78 (dd, J = 6.8 Hz, 3.2 Hz, 4H), 7.37 (dd, J = 6.8 Hz, 3.2 Hz, 4H), 6.86 (s, 2H), 6.82 (dd, J = 8.0 Hz, 1.6 Hz, 2H), 4.09 (s, 6H). <sup>13</sup>C NMR (100 MHz, DMSO-d<sub>6</sub>) δ 168.23, 151.73, 144.58, 136.58, 131.46, 128.93, 126.77, 126.18, 119.23, 118.31, 108.76, 52.03.

#### 2.4.2.8 1.8 Synthesis of 4,4'-(9,10-anthracenediyl)bis(2-aminobenzoic acid)



Dimethyl 4,4'-(9,10-anthracenediyl)bis(2-aminobenzoate) (1.35 g, 3 mmol) was dissolved in a 1:1 mixture of THF/MeOH (60 mL). To the mixture was added NaOH (1.2 g, 30 mL) dissolved in H<sub>2</sub>O (30 mL). The reaction mixture was stirred and refluxed for 24 hours. Once cooled to room temperature, the organic solvent was removed in vacuo. 1 M HCl solution was added to the aqueous residue until the pH reached 5 to obtain a light yellow paste. After centrifugation, the supernatant was removed. The precipitate was washed with H<sub>2</sub>O (40 mL, 3x) and dried under vacuum to yield light brown solid (1.2 g, 90%). <sup>1</sup>H NMR (400 MHz, DMSO-d<sub>6</sub>) δ 7.94 (d, J = 8.0 Hz, 2H), 7.68 (dd, J = 6.8 Hz, 3.2 Hz, 4H), 7.45 (dd, J = 6.8 Hz, 3.2 Hz, 4H), 6.82 (m, 2H), 6.60 (m, 2H). <sup>13</sup>C NMR (100 MHz, DMSO-d<sub>6</sub>) δ 169.99, 151.93, 144.29, 136.70, 131.99, 128.97, 126.84, 126.12, 119.04, 118.10, 109.60.

### 2.4.3 Solvothermal syntheses and CHN elemental analyses of MOF-1114

#### 2.4.3.1 MOF-1114(Y)

2-Amino-1,4-benzenedicarboxylic acid (13.6 mg, 0.075 mmol) and  $\text{YCl}_3 \cdot 6\text{H}_2\text{O}$  (91.0 mg, 0.3 mmol) were dissolved in DMF (5 mL) in a 20 mL Pyrex vial. To the DMF solution was added nanopure water (0.25 mL). The vial was then capped and placed in a 100 °C oven for 12 h to yield colorless cubic block crystals. After the reaction was cooled down to room temperature, the mother liquor was decanted. The crystals were then washed with fresh DMF (3x) (25 mg, 62 %). Formula:  $[\text{Y}_4(\mu_3\text{-OH})_4(\text{C}_8\text{H}_5\text{NO}_4)_3(\text{H}_2\text{O})_{7.5}(\mu_1\text{-OH})_{0.5}] \cdot 1.5\text{Cl}_3 \cdot 6.7\text{DMF}$ ; Anal. calcd. (%): C, 33.05; H, 4.81; N, 8.48; Found (%): C, 32.98; H, 4.23; N, 8.84.

#### 2.4.3.2 MOF-1114(Gd)

2-Amino-1,4-benzenedicarboxylic acid (18.1 mg, 0.1 mmol) and  $\text{GdCl}_3 \cdot 6\text{H}_2\text{O}$  (148.8 mg, 0.4 mmol) were dissolved in DMF (6 mL) in a 20 mL Pyrex vial. To the DMF solution was added nanopure water (0.67 mL). The vial was then capped and placed in a 100 °C oven for 12 h to yield colorless cubic block crystals. Once the reaction cooled down to room temperature, the mother liquor was decanted. The crystals were washed with fresh DMF (3x) (53 mg, 74 %). Formula:  $[\text{Gd}_4(\mu_3\text{-OH})_4(\text{C}_8\text{H}_5\text{NO}_4)_3(\text{H}_2\text{O})_{7.5}(\mu_1\text{-OH})_{0.5}] \cdot 1.5\text{Cl}_3 \cdot 9\text{DMF}$ ; Anal. calcd. (%): C, 30.00; H, 4.87; N, 8.42; Found (%): C, 29.69; H, 4.62; N, 8.49.

#### 2.4.3.3 MOF-1114(Tb)

2-Amino-1,4-benzenedicarboxylic acid (18.1 mg, 0.1 mmol) and  $\text{TbCl}_3 \cdot 6\text{H}_2\text{O}$  (150.0 mg, 0.4 mmol) were dissolved in DMF (6 mL) in a 20 mL Pyrex vial. To the DMF solution was added nanopure water (0.33 mL). The vial was then capped and placed in a 100 °C oven for 12 h to yield

colorless cubic block crystals. After the reaction was cooled down to room temperature, the mother liquor was decanted. The crystals were then washed with fresh DMF (3x) (60 mg, 85 %). Formula:  $[\text{Tb}_4(\mu_3\text{-OH})_4(\text{C}_8\text{H}_5\text{NO}_4)_3(\text{H}_2\text{O})_{7.5}(\mu_1\text{-OH})_{0.5}] \cdot 1.5\text{Cl}, 9\text{DMF}$ ; Anal. calcd. (%): C, 29.23; H, 4.69; N, 8.02; Found (%): C, 29.12; H, 4.15; N, 8.2.

#### 2.4.3.4 MOF-1114(Dy)

2-Amino-1,4-benzenedicarboxylic acid (18.1 mg, 0.1 mmol) and  $\text{DyCl}_3 \cdot 6\text{H}_2\text{O}$  (113.0 mg, 0.3 mmol) were dissolved in DMF (5 mL) in a 20 mL Pyrex vial. To the DMF solution was added nanopure water (0.5 mL). The vial was then capped and placed in a 100 °C oven for 12 h to yield light yellow cubic block crystals. After the reaction was cooled down to room temperature, the mother liquor was decanted. The crystals were then washed with fresh DMF (3x) (41 mg, 52 %). Formula:  $[\text{Dy}_4(\mu_3\text{-OH})_4(\text{C}_8\text{H}_5\text{NO}_4)_3(\text{H}_2\text{O})_{7.5}(\mu_1\text{-OH})_{0.5}] \cdot 1.5\text{Cl}, 11\text{DMF}$  Anal. calcd. (%): C, 30.34; H, 4.98; N, 8.69; Cl, 2.36; Found (%): C, 30.26; H, 4.62; N, 8.66; Cl, 2.16.

#### 2.4.3.5 MOF-1114(Ho)

2-Amino-1,4-benzenedicarboxylic acid (18.1 mg, 0.1 mmol) and  $\text{HoCl}_3 \cdot 6\text{H}_2\text{O}$  (114.1 mg, 0.3 mmol) were dissolved in DMF (5 mL) in a 20 mL Pyrex vial. To the DMF solution was added nanopure water (0.25 mL). The vial was then capped and placed in a 100 °C oven for 12 h to yield light pink cubic block crystals. After the reaction was cooled down to room temperature, the mother liquor was decanted. The crystals were then washed with fresh DMF (3x) (43 mg, 66 %). Formula:  $[\text{Ho}_4(\mu_3\text{-OH})_4(\text{C}_8\text{H}_5\text{NO}_4)_3(\text{H}_2\text{O})_{7.5}(\mu_1\text{-OH})_{0.5}] \cdot 1.5\text{Cl}, 7.5\text{DMF}$ ; Anal. calcd. (%): C, 27.78; H, 4.36; N, 7.32; Found (%): C, 27.6; H, 3.68; N, 7.62.

#### 2.4.3.6 MOF-1114(Er)

2-Amino-1,4-benzenedicarboxylic acid (18.1 mg, 0.1 mmol) and  $\text{ErCl}_3 \cdot 6\text{H}_2\text{O}$  (114.5 mg, 0.3 mmol) were dissolved in DMF (5 mL) in a 20 mL Pyrex vial. To the DMF solution was added nanopure water (0.25 mL). The vial was then capped and placed in a 100 °C oven for 12 h to yield light pink cubic block crystals. After the reaction was cooled down to room temperature, the mother liquor was decanted. The crystals were then washed with fresh DMF (3x) (48 mg, 67 %). Formula:  $[\text{Er}_4(\mu_3\text{-OH})_4(\text{C}_8\text{H}_5\text{NO}_4)_3(\text{H}_2\text{O})_{7.5}(\mu_1\text{-OH})_{0.5}] \cdot 1.5\text{Cl}, 9.4\text{DMF}$ ; Anal. calcd. (%): C, 29.05; H, 4.68; N, 8.05; Found (%): C, 29.04; H, 4.22; N, 8.2.

#### 2.4.3.7 MOF-1114(Tm)

2-Amino-1,4-benzenedicarboxylic acid (13.6 mg, 0.075 mmol) and  $\text{TmCl}_3 \cdot 6\text{H}_2\text{O}$  (114.1mg, 0.3 mmol) were dissolved in DMF (5 mL) in a 20 mL Pyrex vial. To the DMF solution was added nanopure water (0.25 mL). The vial was then capped and placed in a 100 °C oven for 12 h to yield colorless cubic block crystals. After the reaction was cooled down to room temperature, the mother liquor was decanted. The crystals were then washed with fresh DMF (3x) (31 mg, 74%). Formula:  $[\text{Tm}_4(\mu_3\text{-OH})_4(\text{C}_8\text{H}_5\text{NO}_4)_3(\text{H}_2\text{O})_{7.5}(\mu_1\text{-OH})_{0.5}] \cdot 1.5\text{Cl}, 6\text{DMF}, 2\text{H}_2\text{O}$  Anal. calcd. (%): C, 25.84; H, 4.16; N, 6.46; Found (%): C, 25.52; H, 3.90; N, 6.85.

#### 2.4.3.8 MOF-1114(Yb)

2-Amino-1,4-benzenedicarboxylic acid (13.6 mg, 0.075 mmol) and  $\text{YbCl}_3 \cdot 6\text{H}_2\text{O}$  (116.5mg, 0.3 mmol) were dissolved in DMF (4.5 mL) in a 20 mL Pyrex vial. To the DMF solution was added nanopure water (0.25 mL). The vial was then capped and placed in a 100 °C oven for 12 h to yield colorless cubic block crystals. After the reaction was cooled down to room temperature, the mother liquor was decanted. The crystals were then washed with fresh DMF (3x)

(35 mg, 80%). Formula:  $[\text{Yb}_4(\mu_3\text{-OH})_4(\text{C}_8\text{H}_5\text{NO}_4)_3(\text{H}_2\text{O})_{7.5}(\mu_1\text{-OH})_{0.5}] \cdot 1.5\text{Cl}, 11\text{DMF}$ ; Anal. calcd. (%): C, 29.79; H, 4.89; N, 8.53; Found (%): C, 29.88; H, 4.15; N, 8.41.

## 2.4.4 Solvothermal syntheses and CHN elemental analyses of MOF-1130 and MOF-1131

### 2.4.4.1 MOF-1130(Y)

3,3'-diamino-1,1'-biphenyl-4,4'-dicarboxylic acid (20.4 mg, 0.075 mmol) and  $\text{YCl}_3 \cdot 6\text{H}_2\text{O}$  (91.0 mg, 0.3 mmol) were dissolved in DMF (4.5 mL) in a 20 mL Pyrex vial. To the DMF solution was added nanopure water (0.25 mL). The vial was then capped and placed in a 100 °C oven for 12 h to yield colorless crystals. After the reactions was cooled down to room temperature, the mother liquor was decanted. Crystals were then washed with fresh DMF (3x) (23 mg, 56%). Formula:  $[\text{Y}_4(\mu_3\text{-OH})_4(\text{C}_{14}\text{H}_{10}\text{N}_2\text{O}_4)_4(\text{DMF})_3(\text{H}_2\text{O})] \cdot 8\text{H}_2\text{O}, 4.2\text{DMF}$ ; Anal. calcd. (%): C, 42.27; H, 5.50; N, 9.65; Found (%): C, 42.16; H, 4.64; N, 10.34.

### 2.4.4.2 MOF-1130(Gd)

3,3'-diamino-1,1'-biphenyl-4,4'-dicarboxylic acid (20.4 mg, 0.075 mmol) and  $\text{GdCl}_3 \cdot 6\text{H}_2\text{O}$  (111.3 mg, 0.3 mmol) were dissolved in DMF (4.5 mL) in a 20 mL Pyrex vial. To the DMF solution was added nanopure water (0.50 mL). The vial was then capped and placed in a 100 °C oven for 12 h to yield colorless crystals. After the reactions was cooled down to room temperature, the mother liquor was decanted. Crystals were then washed with fresh DMF (3x) (31 mg, 66%). Formula:  $[\text{Gd}_4(\mu_3\text{-OH})_4(\text{C}_{14}\text{H}_{10}\text{N}_2\text{O}_4)_4(\text{DMF})_3(\text{H}_2\text{O})] \cdot 6.3\text{H}_2\text{O}, 5\text{DMF}$ ; Anal. calcd. (%): C, 38.34; H, 4.93; N, 8.94; Found (%): C, 38.30; H, 4.44; N, 9.44.

#### 2.4.4.3 MOF-1130(Tb)

3,3'-diamino-1,1'-biphenyl-4,4'-dicarboxylic acid (20.4 mg, 0.075 mmol) and TbCl<sub>3</sub>·6H<sub>2</sub>O (112 mg, 0.3 mmol) were dissolved in DMF (4.5 mL) in a 20 mL Pyrex vial. To the DMF solution was added nanopure water (0.50 mL). The vial was then capped and placed in a 100 °C oven for 12 h to yield colorless crystals. After the reactions was cooled down to room temperature, the mother liquor was decanted. Crystals were then washed with fresh DMF (3x) (28 mg, 60%). Formula: [Tb<sub>4</sub>(μ<sub>3</sub>-OH)<sub>4</sub>(C<sub>14</sub>H<sub>10</sub>N<sub>2</sub>O<sub>4</sub>)<sub>4</sub>(DMF)<sub>3</sub>(H<sub>2</sub>O)]·5.8H<sub>2</sub>O,4.9DMF; Anal. calcd. (%): C, 38.34; H, 4.88; N, 8.92; Found (%): C, 38.34; H, 4.42; N, 9.34.

#### 2.4.4.4 MOF-1130(Dy)

3,3'-diamino-1,1'-biphenyl-4,4'-dicarboxylic acid (20.4 mg, 0.075 mmol) and DyCl<sub>3</sub>·6H<sub>2</sub>O (113.1 mg, 0.3 mmol) were dissolved in DMF (4.5 mL) in a 20 mL Pyrex vial. To the DMF solution was added nanopure water (0.50 mL). The vial was then capped and placed in a 100 °C oven for 12 h to yield colorless crystals. After the reactions was cooled down to room temperature, the mother liquor was decanted. Crystals were then washed with fresh DMF (3x) (23 mg, 49%). Formula: [Dy<sub>4</sub>(μ<sub>3</sub>-OH)<sub>4</sub>(C<sub>14</sub>H<sub>10</sub>N<sub>2</sub>O<sub>4</sub>)<sub>4</sub>(DMF)<sub>3</sub>(H<sub>2</sub>O)]·6.8H<sub>2</sub>O,3.8DMF; Anal. calcd. (%): C, 38.09; H, 4.84; N, 8.84; Found (%): C, 37.98; H, 4.34; N, 9.32.

#### 2.4.4.5 MOF-1130(Ho)

3,3'-diamino-1,1'-biphenyl-4,4'-dicarboxylic acid (20.4 mg, 0.075 mmol) and HoCl<sub>3</sub>·6H<sub>2</sub>O (113.9 mg, 0.3 mmol) were dissolved in DMF (4.5 mL) in a 20 mL Pyrex vial. To the DMF solution was added nanopure water (0.5 mL). The vial was then capped and placed in a 100 °C oven for 12 h to yield colorless crystals. After the reactions was cooled down to room temperature, the mother liquor was decanted. Crystals were then washed with fresh DMF (3x) (25

mg, 55%). Formula:  $[\text{Ho}_4(\mu_3\text{-OH})_4(\text{C}_{14}\text{H}_{10}\text{N}_2\text{O}_4)_4(\text{DMF})_3(\text{H}_2\text{O})] \cdot 3.7\text{H}_2\text{O}, 4.1\text{DMF}$ ; Anal. calcd. (%): C, 38.30; H, 4.62; N, 8.72; Found (%): C, 37.82; H, 4.28; N, 9.22.

#### 2.4.4.6 MOF-1131(Er)

3,3"-diamino-1,1':4',1"-terphenyl-4,4"-dicarboxylic acid (26.1 mg, 0.075 mmol) and  $\text{ErCl}_3 \cdot 6\text{H}_2\text{O}$  (57.3 mg, 0.15 mmol) were dissolved in DMF (3 mL) in a 20 mL Pyrex vial. To the DMF solution, was added nanopure water (0.125 ml). The vial was then capped and placed in 100 °C oven for 12 h to yield light yellow crystals. After the reactions cooled down to room temperature, the mother liquor was decanted. Crystals were then washed with fresh DMF (3x) (21 mg, 31%). Formula:  $[\text{Er}_4(\mu_3\text{-OH})_4(\text{C}_{20}\text{H}_{14}\text{N}_2\text{O}_4)_4(\text{DMF})(\text{H}_2\text{O})_3] \cdot 16.6\text{H}_2\text{O}, 15.2\text{DMF}$ ; Anal. calcd. (%): C, 42.16; H, 5.85; N, 9.25; Found (%): C, 41.70; H, 5.05; N, 9.78.

#### 2.4.4.7 MOF-1131(Yb)

3,3"-diamino-1,1':4',1"-terphenyl-4,4"-dicarboxylic acid (26.1 mg, 0.075 mmol) and  $\text{YbCl}_3 \cdot 6\text{H}_2\text{O}$  (58.1 mg, 0.15 mmol) were dissolved in DMF (3 mL) in a 20 mL Pyrex vial. To the DMF solution was added nanopure water (0.25 mL). The vial was then capped and placed in 85 °C oven for 24 h to yield light yellow crystals. After the reactions cooled down to room temperature, the mother liquor was decanted. Crystals were then washed with fresh DMF (3x) (32 mg, 48%). Formula:  $[\text{Yb}_4(\mu_3\text{-OH})_4(\text{C}_{20}\text{H}_{14}\text{N}_2\text{O}_4)_4(\text{DMF})(\text{H}_2\text{O})_3] \cdot 11.7\text{H}_2\text{O}, 15\text{DMF}$ ; Anal. calcd. (%): C, 42.95; H, 5.67; N, 9.39; Found (%): C, 41.59; H, 4.80; N, 9.38.

## 2.4.5 Solvothermal synthesis and CHN elemental analyses of MOF-1115

### 2.4.5.1 MOF-1115(Sm)

4,4'-(9,10-Anthracenediyl)bis(2-aminobenzoic acid) (13.5 mg, 0.03 mmol) and SmCl<sub>3</sub>·6H<sub>2</sub>O (54.7 mg, 0.15 mmol) were dissolved in DEF (4.5 mL) in a 20 mL Pyrex vial. To the DEF solution was added nanopure water (0.15 mL). The vial was then capped and placed in 100 °C oven for 24 h to yield light yellow crystals. After the reaction cooled down to room temperature, the mother liquor was decanted. The crystals were washed with fresh DEF (3x) (23 mg, 84%). Formula: [Sm<sub>4</sub>(μ<sub>3</sub>-OH)<sub>4</sub>(C<sub>28</sub>H<sub>18</sub>N<sub>2</sub>O<sub>4</sub>)<sub>3</sub>(H<sub>2</sub>O)<sub>8</sub>]<sub>2</sub>Cl<sub>16</sub>DEF; Anal. calcd. (%): C, 51.27, H, 6.56; N, 8.02; Found (%): C, 51.88; H, 5.94; N, 7.79.

### 2.4.5.2 MOF-1115(Eu)

4,4'-(9,10-Anthracenediyl)bis(2-aminobenzoic acid) (13.5 mg, 0.03 mmol) and EuCl<sub>3</sub>·6H<sub>2</sub>O (55.0 mg, 0.15 mmol) were dissolved in DEF (4.5 mL) in a 20 mL Pyrex vial. To the DEF solution was added nanopure water (0.15 mL). The vial was then capped and placed in 100 °C oven for 24 h to yield light yellow crystals. After the reaction cooled down to room temperature, the mother liquor was decanted. The crystals were washed with fresh DEF (3x) (18 mg, 76%). Formula: [Er<sub>4</sub>(μ<sub>3</sub>-OH)<sub>4</sub>(C<sub>28</sub>H<sub>18</sub>N<sub>2</sub>O<sub>4</sub>)<sub>3</sub>(H<sub>2</sub>O)<sub>8</sub>]<sub>2</sub>Cl<sub>13</sub>DEF; Anal. calcd. (%): C, 50.48; H, 6.17; N, 7.51; Found (%): C, 50.88; H, 5.63; N, 7.33.

### 2.4.5.3 MOF-1115(Gd)

4,4'-(9,10-Anthracenediyl)bis(2-aminobenzoic acid) (13.5 mg, 0.03 mmol) and GdCl<sub>3</sub>·6H<sub>2</sub>O (55.7 mg, 0.15 mmol) were dissolved in DEF (4.5 mL) in a 20 mL Pyrex vial. To the DEF solution was added nanopure water (0.15 mL). The vial was then capped and placed in 100

°C oven for 24 h to yield light yellow crystals. After the reaction cooled down to room temperature, the mother liquor was decanted. The crystals were washed with fresh DEF (3x) (11 mg, 40%). Formula:  $[\text{Gd}_4(\mu_3\text{-OH})_4(\text{C}_{28}\text{H}_{18}\text{N}_2\text{O}_4)_3(\text{H}_2\text{O})_8]\cdot 2\text{Cl}, 13\text{DEF}$ ; Anal. calcd. (%): C, 50.18; H, 6.13; N, 7.46; Found (%): C, 50.84; H, 5.42; N, 7.21.

#### 2.4.5.4 MOF-1115(Tb)

4,4'-(9,10-Anthracenediyl)bis(2-aminobenzoic acid) (13.5 mg, 0.03 mmol) and  $\text{TbCl}_3\cdot 6\text{H}_2\text{O}$  (56.1 mg, 0.15 mmol) were dissolved in DEF (4.5 mL) in a 20 mL Pyrex vial. To the DEF solution was added nanopure water 0.15 mL. The vial was then capped and placed in 100 °C oven for 24 h to yield light yellow crystals. After the reaction cooled down to room temperature, the mother liquor was decanted. The crystals were washed with fresh DEF (3x) (21 mg, 62%). Formula:  $[\text{Tb}_4(\mu_3\text{-OH})_4(\text{C}_{28}\text{H}_{18}\text{N}_2\text{O}_4)_3(\text{H}_2\text{O})_8]\cdot 2\text{Cl}, 11.5\text{DEF}$ ; Anal. calcd. (%): C, 49.67; H, 5.91; N, 7.16; Found (%): C, 49.92; H, 5.49; N, 7.14.

#### 2.4.5.5 MOF-1115(Dy)

4,4'-(9,10-Anthracenediyl)bis(2-aminobenzoic acid) (13.5 mg, 0.03 mmol) and  $\text{DyCl}_3\cdot 6\text{H}_2\text{O}$  (56.5 mg, 0.15 mmol) were dissolved in DEF (4.5 mL) in a 20 mL Pyrex vial. To the DEF solution was added nanopure water (0.15 mL). The vial was then capped and placed in 100 °C oven for 24 h to yield light yellow crystals. After the reaction cooled down to room temperature, the mother liquor was decanted. The crystals were washed with fresh DEF (3x) (18 mg, 74%). Formula:  $[\text{Dy}_4(\mu_3\text{-OH})_4(\text{C}_{28}\text{H}_{18}\text{N}_2\text{O}_4)_3(\text{H}_2\text{O})_8]\cdot 2\text{Cl}, 14\text{DEF}$ ; Anal. calcd. (%): C, 50.15; H, 6.23; N, 7.59; Found (%): C, 50.50; H, 5.48; N, 7.19.

#### 2.4.5.6 MOF-1115(Ho)

4,4'-(9,10-Anthracenediyl)bis(2-aminobenzoic acid) (13.5 mg, 0.03 mmol) and  $\text{HoCl}_3 \cdot 6\text{H}_2\text{O}$  (56.5 mg, 0.15 mmol) were dissolved in DEF (4.5 mL) in a 20 mL Pyrex vial. To the DEF solution was added nanopure water (0.15 mL). The vial was then capped and placed in 100 °C oven for 24 h to yield light yellow crystals. After the reaction cooled down to room temperature, the mother liquor was decanted. The crystals were washed with fresh DEF (3x) (22 mg, 75%). Formula:  $[\text{Ho}_4(\mu_3\text{-OH})_4(\text{C}_{28}\text{H}_{18}\text{N}_2\text{O}_4)_3(\text{H}_2\text{O})_8] \cdot 2\text{Cl}, 16\text{DEF}$ ; Anal. calcd. (%): C, 50.50; H, 6.46; N, 7.90; Found (%): C, 50.68, H, 6.24, N, 7.93.

#### 2.4.5.7 MOF-1115(Er)

4,4'-(9,10-Anthracenediyl)bis(2-aminobenzoic acid) (13.5 mg, 0.03 mmol) and of  $\text{ErCl}_3 \cdot 6\text{H}_2\text{O}$  (56.5 mg, 0.15 mmol) were dissolved in DEF (4.5 mL) in a 20 mL Pyrex vial. To the DEF solution was added nanopure water (0.15 mL). The vial was then capped and placed in 100 °C oven for 24 h to yield light yellow crystals. After the reaction cooled down to room temperature, the mother liquor was decanted. The crystals were washed with fresh DEF (3x) (15 mg, 55%). Formula:  $[\text{Er}_4(\mu_3\text{-OH})_4(\text{C}_{28}\text{H}_{18}\text{N}_2\text{O}_4)_3(\text{H}_2\text{O})_8] \cdot 2\text{Cl}, 17\text{DEF}$ ; Anal. calcd. (%): C, 50.61; H, 6.56; N, 8.03; Found (%): C, 50.95; H, 6.04; N, 7.82.

#### 2.4.6 Anion exchange of MOF-1114(Tb) with $\text{NMe}_4\text{BF}_4$

Approximately 100 mg of as-synthesized MOF-1114(Tb) crystals were soaked in 10 mL of a 0.1 M DMF solution of  $\text{NMe}_4\text{BF}_4$  in a vial. The  $\text{NMe}_4\text{BF}_4$  solution was removed and the crystals were washed with fresh DMF (3x) every 24 h before the vial was replenished with fresh

NMe<sub>4</sub>BF<sub>4</sub> solution. After 5 days, the crystals were copiously washed with DMF and dried on a Schlenk line before solution <sup>1</sup>H and <sup>19</sup>F NMR analysis. About 5 mg of crystals were dissolved in 500 μL of DMSO-*d*<sub>6</sub> and 15 μL of DCl in D<sub>2</sub>O (36%). 1 μL of α,α,α-trifluorotoluene was added as internal standard in the sample before <sup>1</sup>H and <sup>19</sup>F NMR.

#### 2.4.7 N<sub>2</sub> adsorption experiments

After anion exchange, ~50 mg of MOF-1114(Tb) crystals were exchanged in dry EtOH for 3 days in a 20 mL vial. EtOH was removed every 24 h followed by replenishment with fresh EtOH until no DMF peak was observed by solution <sup>1</sup>H NMR of an acid digested MOF sample. The crystals were then transferred to the activation chamber of a Tousimis SAMDRI-PVT-3B supercritical drier where supercritical CO<sub>2</sub> activation experiment was performed. During the entire transfer process, all the crystals were soaked under dry EtOH. After cooling to 0 °C, the chamber was filled with liquid CO<sub>2</sub>. Every 30 min, the chamber was purged for 5 min while the CO<sub>2</sub> filling rate was kept above the purge rate to ensure that the MOF sample remains soaked under liquid CO<sub>2</sub>. The chamber temperature was kept between 0 - 10 °C. After 6 h, the chamber filled with liquid CO<sub>2</sub> was heated to 40 °C to transform CO<sub>2</sub> from liquid state to supercritical state. The chamber was then vented slowly for the next 18 h until the pressure dropped down to 1 atm. The MOF sample was then degassed at 50 °C under dynamic vacuum for 24 h before the N<sub>2</sub> adsorption experiment was performed on a Quantachrome Autosorb-1 instrument at 77 K.

## 2.4.8 Covalent postsynthetic modification of MOF-1114(Yb) experiments

### 2.4.8.1 Preparation and characterization of MOF-1114(Yb)<sub>1</sub>

5 mg of as-synthesized MOF-1114(Yb) were soaked in 1 mL 0.5 M DMF solution of salicylaldehyde for 48 h at room temperature to yield orange MOF-1114(Yb)<sub>1</sub> crystals. The orange crystals were then copiously washed with anhydrous DMF (5x). The MOF crystals were dried under vacuum for 10 min and dissolved in a mixture of 500  $\mu$ L DMSO-*d*<sub>6</sub> and 15  $\mu$ L 36% D<sub>2</sub>O solution of DCl. The solution was used for <sup>1</sup>H NMR experiment. To confirm the formation of imine bond, MOF-1114(Yb)<sub>1</sub> was then reacted with 1 mL of 0.3 M ethanol solution of NaBH<sub>4</sub> in a 4 mL vial. After 24 h, the solid sample was washed with MeOH (3x) and dried under a Schlenk line vacuum for 10 min. To the dried crystal sample were added 500  $\mu$ L D<sub>2</sub>O and 10  $\mu$ L 10% D<sub>2</sub>O solution of NaOD. The mixture was sonicated for 30 min and centrifuged. The supernatant was used for <sup>1</sup>H NMR. 3 mg of the reduced product from MOF-1114(Yb)<sub>1</sub> were dissolved in 1 mL MeOH and 15  $\mu$ L of 36 % HCl in H<sub>2</sub>O. The solution was used for LC-MS experiment.

### 2.4.8.2 Preparation and characterization of MOF-1114(Yb)<sub>2</sub>

5 mg of as-synthesized compound MOF-1114(Yb) were soaked in 1 mL 0.5 M DMF solution of 3-hydroxynaphthalene-2-carboxaldehyde for 48 h at room temperature to yield red MOF-1114(Yb)<sub>2</sub> crystals. The red crystals were copiously washed with anhydrous DMF (5x) and dried under Schlenk line vacuum for 10 min. the sample was then dissolved with 500  $\mu$ L DMSO-*d*<sub>6</sub> and 15  $\mu$ L of 36% D<sub>2</sub>O solution of DCl. The solution was used for <sup>1</sup>H NMR experiment. To confirm the formation of imine bond, MOF-1114(Yb)<sub>2</sub> was then reacted with 1 mL 0.3 M ethanol solution of NaBH<sub>4</sub>. After 24 h, the solid sample was washed with MeOH (3x) and dried under Schlenk line vacuum for 10 min. The dried sample was then dissolved in 500  $\mu$ L DMSO-*d*<sub>6</sub> and

15  $\mu\text{L}$  of 36%  $\text{D}_2\text{O}$  solution of  $\text{DCl}$  for  $^1\text{H}$  NMR. 3 mg of reduced product from  $\text{MOF-1114}(\text{Yb})_2$  were dissolved in 1 mL  $\text{MeOH}$  and 15  $\mu\text{L}$  of 36 %  $\text{HCl}$  in  $\text{H}_2\text{O}$ . The solution was used for LC-MS experiment.

### **3.0 LUMINESCENCE “TURN-ON” DETECTION OF GOSSYPOL USING LANTHANIDE(III)-BASED METAL-ORGANIC FRAMEWORKS AND LANTHANIDE SALTS**

The work presented in this chapter has been submitted for publication.

This work was conducted in collaboration with David White, Chong Liu, Alexander Star and Nathaniel L. Rosi\*. David White helped collect the photoluminescence data. Chong Liu helped collect the single crystal X-ray diffraction data.

#### **3.1 INTRODUCTION**

Luminescence-based methods are highly attractive for chemical sensing and offer several potential advantages such as low limit of detection, high sensitivity, and fast response. Particularly desirable, yet still challenging to achieve, are “turn-on” sensors that luminesce only in the presence of analyte and are non-emissive in the absence of analyte.<sup>139</sup> “Turn-on” sensors, in contrast to luminescence “turn-off” sensors where the presence of analyte attenuates an existing luminescence intensity, have significantly less luminescence background, and are therefore potentially more sensitive and reliable.

The metal-centered photoluminescence (PL) of lanthanide ( $\text{Ln}^{3+}$ ) compounds, such as metal-organic frameworks (MOFs), complexes, and simple salts, offers unique opportunities for chemical sensing in both solid state and solution.<sup>102, 116, 118, 140</sup> “Turn-on” sensing mechanisms,<sup>141-148</sup> though under-tapped for Ln compounds, are especially attractive. Since the 4f-4f electron

transitions associated with  $\text{Ln}^{3+}$  PL are Laporte forbidden, direct excitation of  $\text{Ln}^{3+}$  4f electron transitions is prohibitively inefficient. The excitation of  $\text{Ln}^{3+}$  PL is typically achieved via the “antenna effect”,<sup>108</sup> a sensitization process in which chromophore molecules with large molar absorption coefficients harvest light and transfer energy to excite 4f electrons of the nearby  $\text{Ln}^{3+}$  center. Leveraging the “antenna” effect, luminescence “turn-on” sensing with high specificity are possible for analytes that can either 1) directly function as an antenna,<sup>141-142</sup> or 2) effectively modulate the sensitization of the integral sensitizer,<sup>149</sup> such that with a properly selected excitation wavelength  $\text{Ln}^{3+}$  PL is off in the absence of the analyte and switched on only in the presence of the analyte. Despite the pressing need for facile methods to detect a large variety of organic compounds, including pharmaceutical contaminants,<sup>150-151</sup> industrial chemicals,<sup>152</sup> polycyclic aromatic hydrocarbons,<sup>153</sup> biomarkers,<sup>154</sup> and naturally occurring toxins,<sup>151</sup> and the fact that many of these target analytes are aromatic chromophores that could be effective sensitizers for  $\text{Ln}^{3+}$  PL,  $\text{Ln}^{3+}$ -based luminescence “turn-on” sensors have only been seldomly explored for sensing organic molecules, with few successful examples reported.<sup>141-142</sup>

In this work, we aimed to develop  $\text{Ln}^{3+}$ -based luminescence “turn-on” sensors for gossypol (Figure 3.1), a polyphenolic toxin concentrated in cottonseeds. The presence of gossypol causes great concerns for the safe consumption of cottonseed products, including edible vegetable oil and animal feed materials. A series of detrimental effects of gossypol have been observed in humans and animals, including acute poisoning, hepatotoxicity, infertility, and immunotoxicity.<sup>155</sup> Therefore, cottonseed products must be refined to remove gossypol. Facile and sensitive detection methods are necessary to ensure that gossypol concentration is at a safe level in various cottonseed products, such as cottonseed oil, used commonly in the food industry, and animal feed materials. Chinese Ministry of Health requires that the concentration of free gossypol in edible cottonseed

oil should not exceed 200 ppm.<sup>156</sup> The maximum free gossypol concentrations permitted by the European Union for various animal feed materials and complete feedingstuffs range from 20 ppm to 5000 ppm.<sup>157</sup> Ultraviolet (UV) spectrophotometry methods<sup>158-162</sup> have been extensively studied and broadly used for the detection and quantification of gossypol. These methods, however, are nonspecific and light absorption of impurities can present interference. To improve selectivity for gossypol detection, UV spectrophotometry is often coupled with high-performance liquid chromatography (HPLC).<sup>163-167</sup> Recently, a variety of other methods have also been explored, including Fourier-transform infrared spectroscopy (FTIR),<sup>168</sup> near infrared spectroscopy<sup>169</sup>, piezoelectric imprinting,<sup>170</sup> and luminescence “turn-off” sensing.<sup>171</sup> Luminescence “turn-on” sensors for gossypol, to the best of our knowledge, have not been reported previously. Herein, we demonstrate the first luminescence “turn-on” sensors for gossypol using Ln<sup>3+</sup> MOFs and simple Ln<sup>3+</sup> salts.

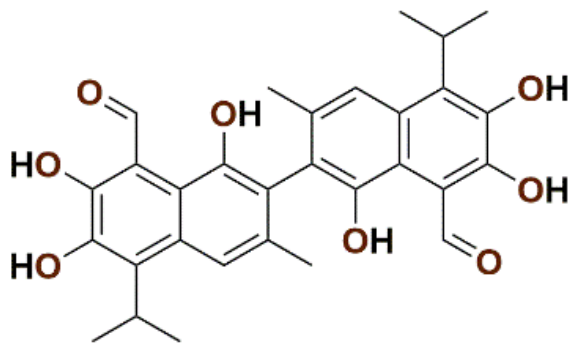


**Figure 3.1** The molecular structure of gossypol.

### 3.2 RESULTS AND DISCUSSION

At the outset of this study, we surmised that Ln<sup>3+</sup> PL could potentially be turned on by gossypol via two possible pathways. Despite no previous report, two salient features of gossypol

make it a promising antenna molecule for sensitizing  $\text{Ln}^{3+}$  PL: 1) gossypol is a yellow pigment with strong absorption of UV and visible light,<sup>172</sup> 2) the multiple hydroxyl substituents and aldehyde groups of the two naphthalene cores are potential polydentate binding sites for  $\text{Ln}^{3+}$ .<sup>173</sup> Furthermore, aromatic aldehyde groups, like those in gossypol, could, according to our previous discovery,<sup>174</sup> react with aromatic amine-functionalized linkers in  $\text{Ln}^{3+}$  MOFs, the integral antennae, to form Schiff base products and effectively red-shift the sensitization wavelength. Both scenarios would allow for the sensitization of  $\text{Ln}^{3+}$  PL at longer wavelengths in the presence of gossypol.

Based on the above hypotheses, we synthesized a MOF analogue of the well-established  $\text{Ln}^{3+}$  **fcu** MOF platform<sup>98</sup> using 3,3''-diamino-1,1':4',1''-terphenyl-4,4''-dicarboxylic acid ( $\text{H}_2\text{-NH}_2\text{-TPDC}$ ) and  $\text{YbCl}_3 \cdot 6\text{H}_2\text{O}$ , denoted as  $\text{Yb-NH}_2\text{-TPDC}$  (Figure 3.2A). We contend that  $\text{Yb}^{3+}$ -centered near infrared (NIR) emission is advantageous for molecular sensing,<sup>175</sup> as it does not overlap with sample fluorescence in the visible spectrum. The anticipated crystal structure of  $\text{Yb-NH}_2\text{-TPDC}$  with **fcu** topology was confirmed by single crystal X-ray diffraction data (Figure 3.2A). The experimental powder X-ray diffraction (PXRD) pattern of the  $\text{Yb-NH}_2\text{-TPDC}$  bulk sample closely matched the simulated PXRD pattern of  $\text{Yb-NH}_2\text{-TPDC}$ , indicating high phase purity (Figure 3.3). The  $[\text{Yb}_6(\text{OH})_8(\text{COO})_{12}]^{2-}$  secondary building units (SBUs) make  $\text{Yb-NH}_2\text{-TPDC}$  a negatively charged framework. The charge balancing cation, dimethylammonium, was observed from  $^1\text{H}$  NMR of the digested  $\text{Yb-NH}_2\text{-TPDC}$  sample (Figure 3.4). With equilateral triangular pore apertures having an altitude of 13.5 Å, when accounting for Van der Waals radii (Figure 3.2B),  $\text{Yb-NH}_2\text{-TPDC}$  should allow entry of gossypol, which measures approximately 10.4 Å x 10.7 Å x 16.9 Å (Figure 3.2C). A coordinating oxygen atom, likely either from a water

or dimethyl formamide (DMF) molecule, was observed near each  $\text{Yb}^{3+}$  ion of the SBU (Figure 3.5), indicating a possible coordination site for gossypol molecules.

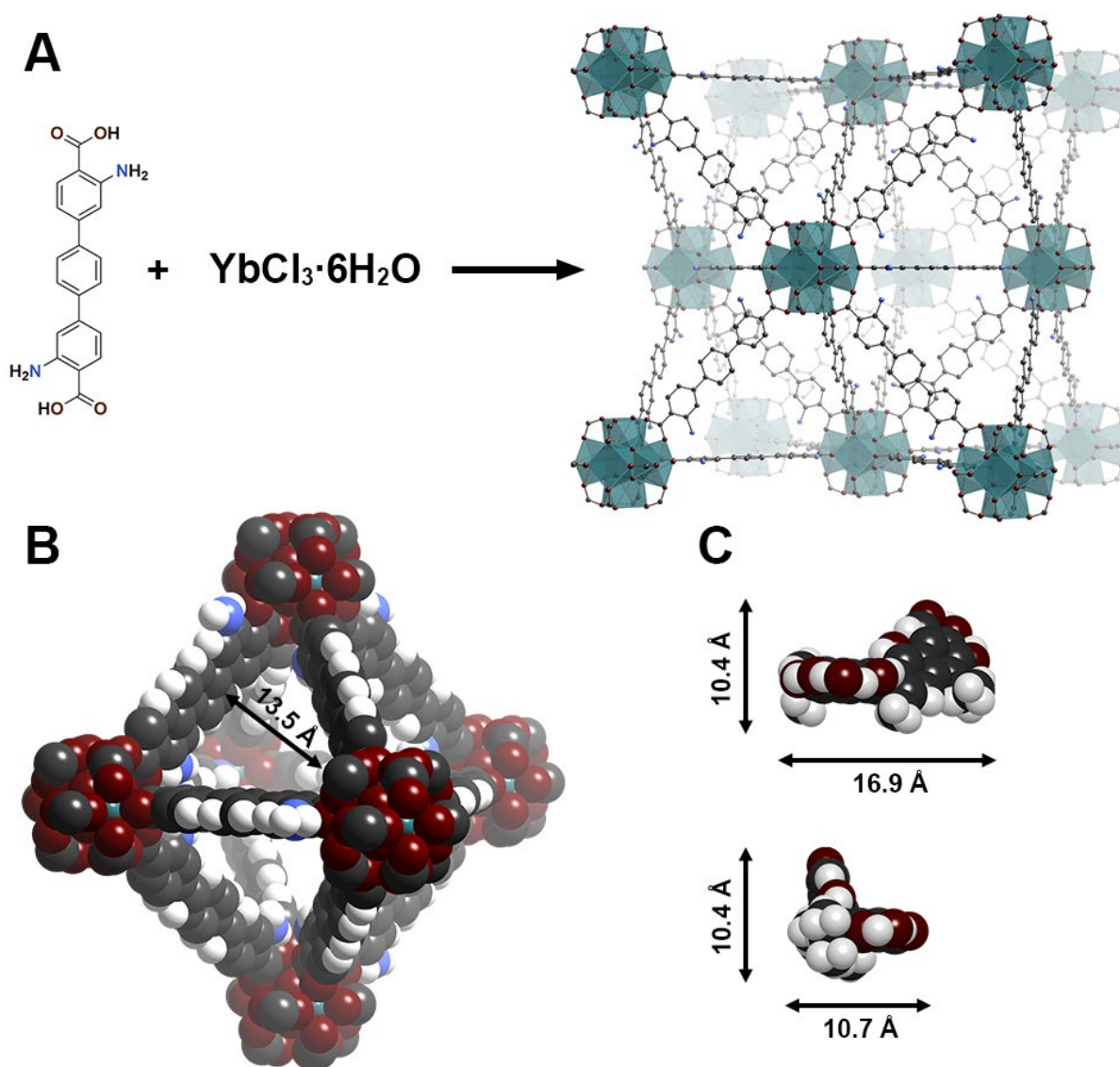


**Figure 3.2** Crystal structures of Yb-NH<sub>2</sub>-TPDC and gossypol.<sup>176</sup> (A) synthesis scheme of Yb-NH<sub>2</sub>-TPDC (C, gray spheres; O, red spheres; N, blue spheres, Yb, teal polyhedra; H, omitted for clarity); (B) an octahedral cavity of Yb-NH<sub>2</sub>-TPDC with triangular apertures (all atoms are shown with Van der Waals radii; C, gray spheres; O, red spheres; N, blue spheres, Yb, teal spheres; H, white spheres); (C) a gossypol molecule viewed in two different orientations (all atoms are shown with Van der Waals radii; C, gray spheres; O, red spheres; H, white spheres).

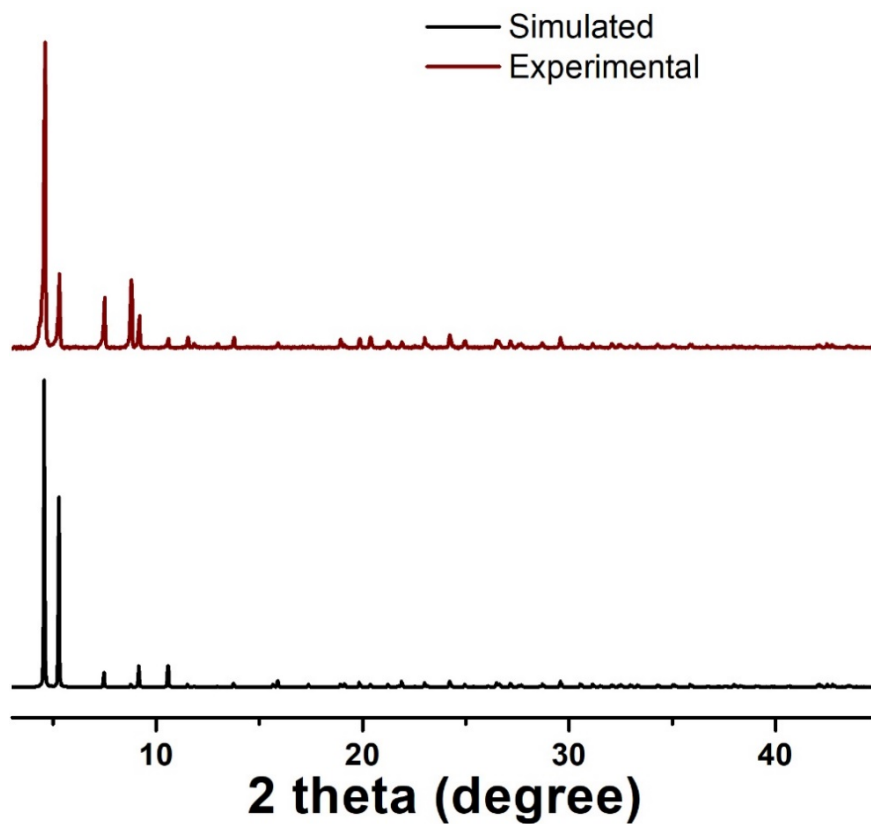


**Figure 3.3** Experimental PXRD pattern of as-synthesized Yb-NH<sub>2</sub>-TPDC (red), and Simulated PXRD pattern of Yb-NH<sub>2</sub>-TPDC (black) base on its crystal structure.

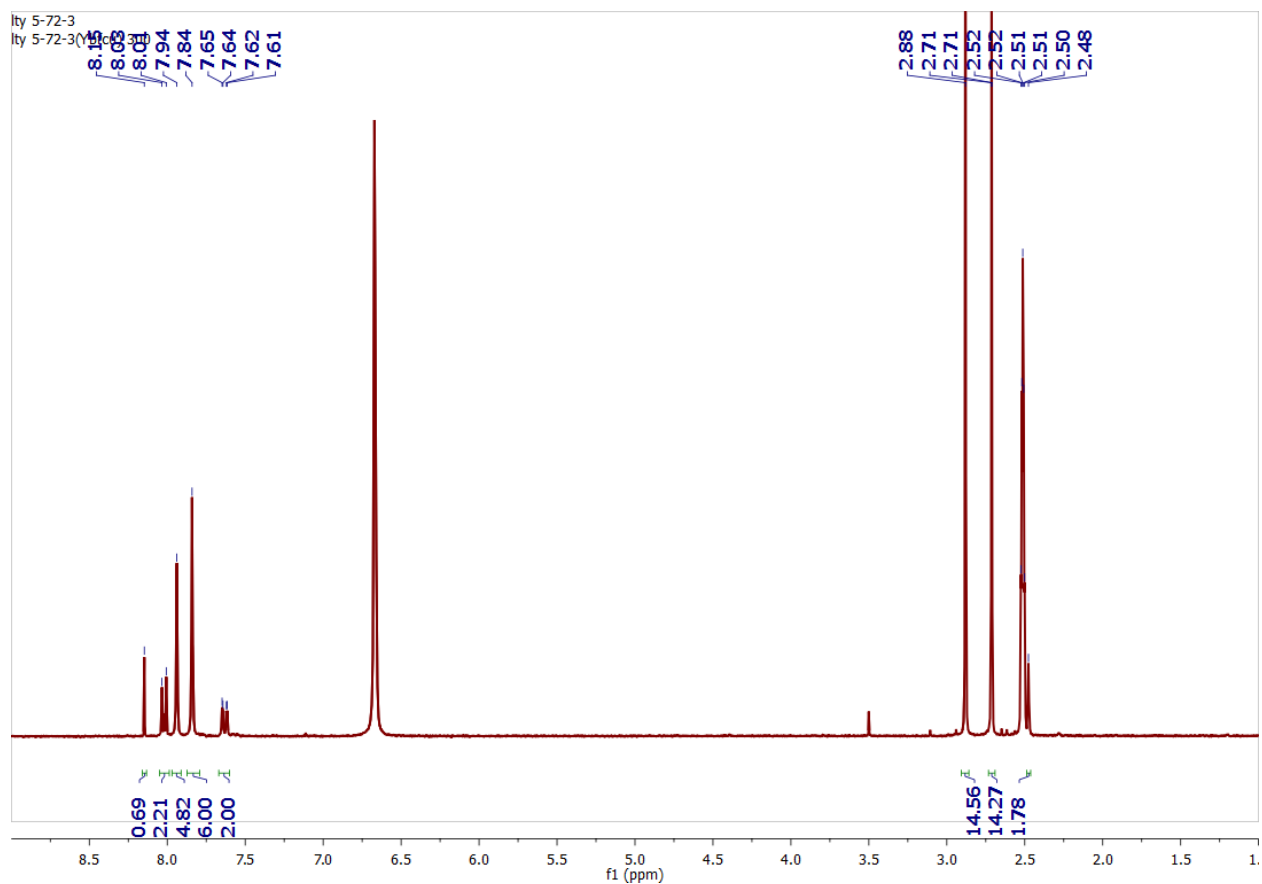


**Figure 3.4** Solution  $^1\text{H}$  NMR spectrum of acid digested Yb-NH<sub>2</sub>-TPDC sample. Singlet peaks at 1.78 ppm and 8.15 ppm indicate the presence of dimethyl ammonium(DMA). The ratio of DMA:NH<sub>2</sub>-TPDC is determined to be 1:3.

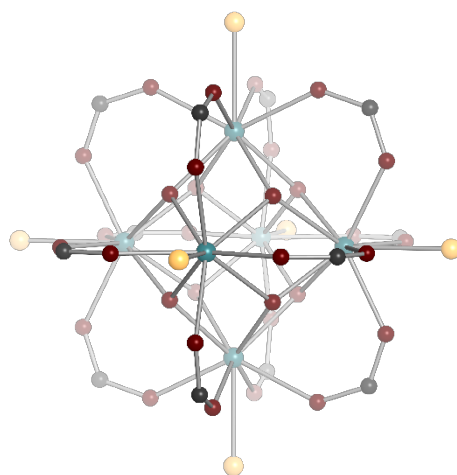


**Figure 3.5**  $[\text{Yb}_6(\text{OH})_8(\text{COO})_{12}(\text{Solvent})_6]^{2-}$  SBU (Yb<sup>3+</sup>, teal spheres; C, grey spheres; O atoms on carboxylates and  $\mu_3$ -OH groups, red spheres; O atoms from coordinating solvent molecules, yellow spheres).

Thermogravimetric analysis (TGA) of Yb-NH<sub>2</sub>-TPDC (Figure 3.6) showed a steep weight loss below 120 °C corresponding to evaporation of solvent guests and a more gradual weight loss after 120 °C. The lack of a well-defined plateau in the TGA curve signifies poor thermal stability above 120 °C. Yb-NH<sub>2</sub>-TPDC was successfully activated under vacuum at room temperature without losing crystallinity (Figure 3.7) after stepwise solvent exchange with dichloromethane and n-pentane.<sup>177</sup> N<sub>2</sub> adsorption analysis of activated Yb-NH<sub>2</sub>-TPDC at 77K yielded a type I isotherm (Figure 3.8) from which the Brunauer–Emmett–Teller (BET) surface area of 2370 m<sup>2</sup>/g was determined.

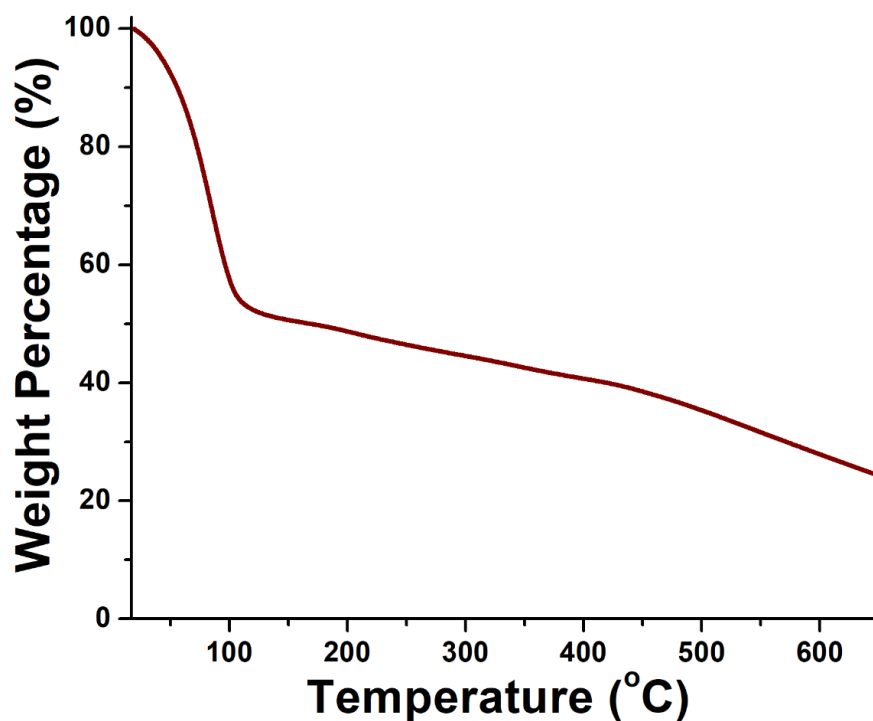


**Figure 3.6** TGA curve of as-synthesized Yb-NH<sub>2</sub>-TPDC.

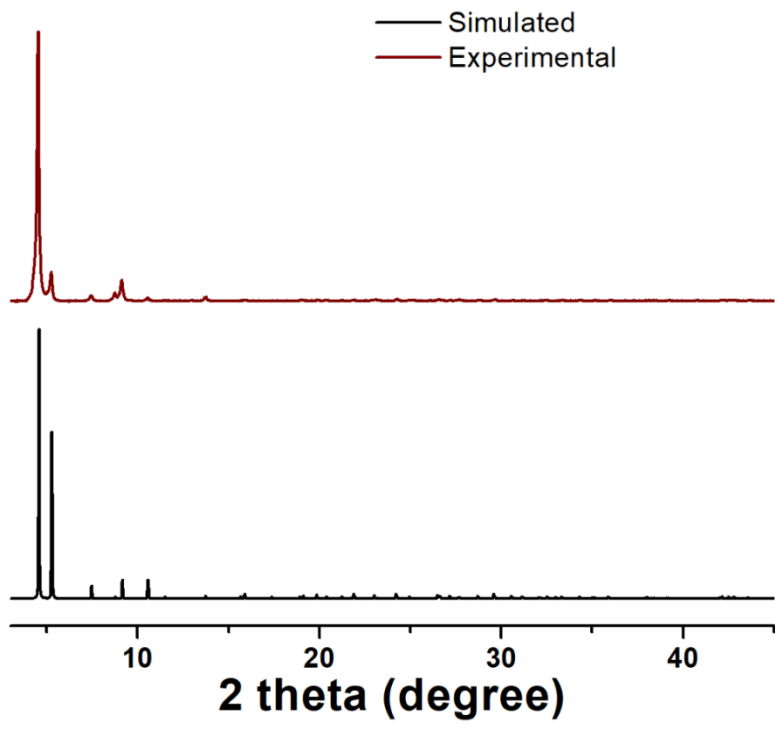


Figure 3.7 Experimental PXRD pattern of activated Yb-NH<sub>2</sub>-TPDC and simulated PXRD pattern of Yb-NH<sub>2</sub>-TPDC (black).

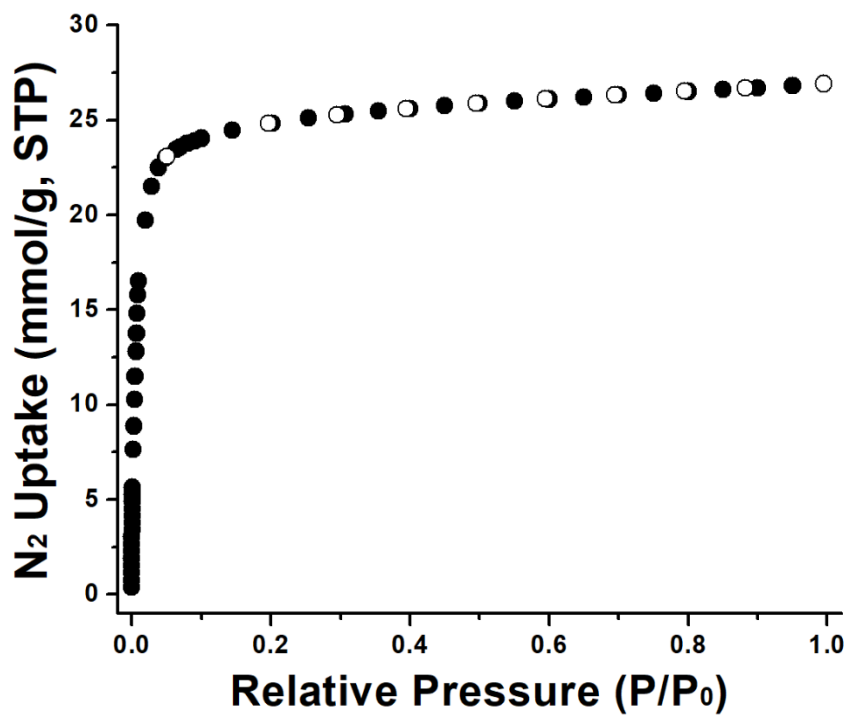
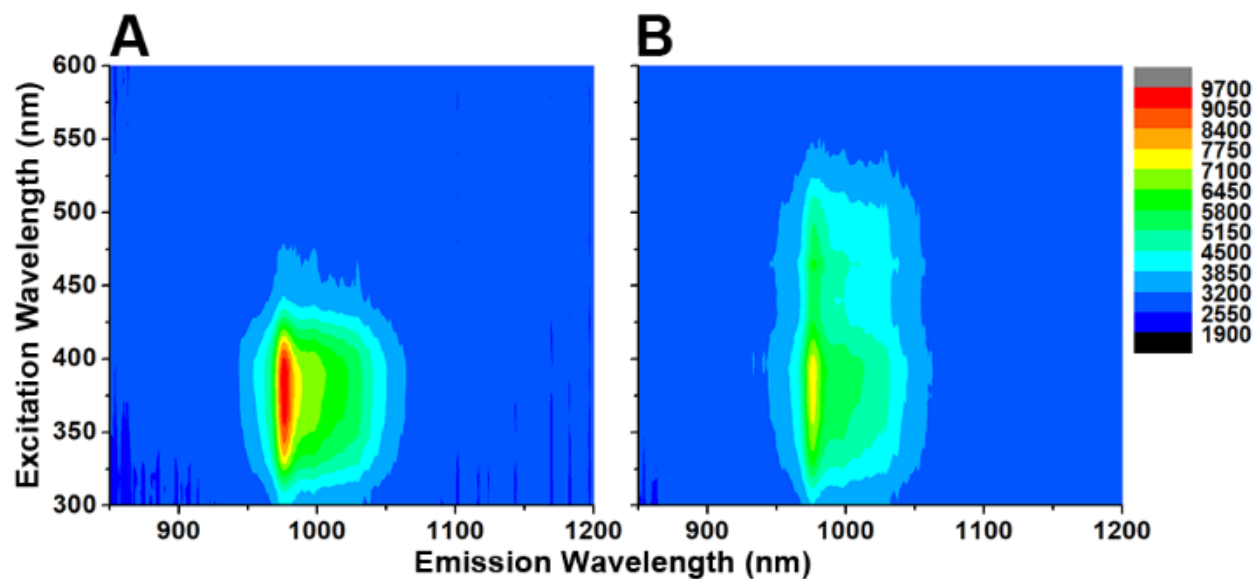
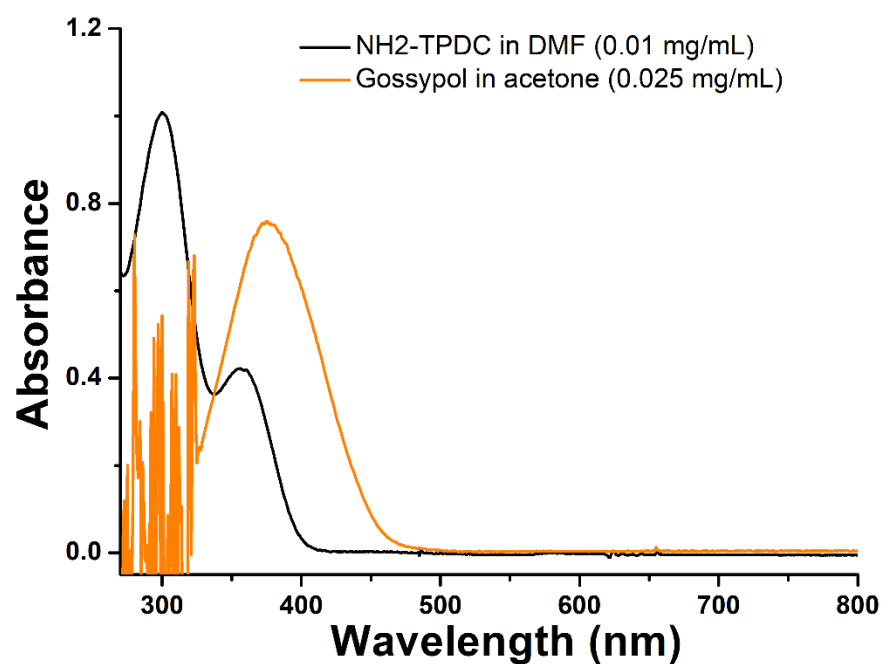


Figure 3.8 N<sub>2</sub> isotherm at 77K of activated Yb-NH<sub>2</sub>-TPDC. Brunauer–Emmett–Teller (BET) surface area: 2370 m<sup>2</sup>/g.

In the absence of gossypol, a solid Yb-NH<sub>2</sub>-TPDC sample under acetone, when excited between 300-475 nm, exhibited the characteristic Yb<sup>3+</sup> NIR emission band at 940 – 1060 nm corresponding to <sup>2</sup>F<sub>5/2</sub> → <sup>2</sup>F<sub>7/2</sub> transition of Yb<sup>3+</sup> (Figure 3.9A). Since Yb<sup>3+</sup> does not have electronic levels that can be excited with ultraviolet or visible light, the Yb<sup>3+</sup> PL of Yb-NH<sub>2</sub>-TPDC must be due to the “antenna effect” of the NH<sub>2</sub>-TPDC linker. Notably, the excitation band of Yb-NH<sub>2</sub>-TPDC (300 - 475 nm) was red-shifted in comparison to the UV-vis absorption spectrum of H<sub>2</sub>-NH<sub>2</sub>-TPDC in solution, which showed two bands centered at 300 nm and 360 nm and no significant absorption at wavelengths above 410 nm (Figure 3.10, black line). We have observed similar effects in a different MOF.<sup>178</sup> This large discrepancy may be due to confinement effects, where the MOF architecture forces molecules to adopt different conformations than those in solution. Intriguingly, incubating Yb-NH<sub>2</sub>-TPDC with gossypol led to a red-shift of the long wavelength edge of excitation band of Yb<sup>3+</sup> PL from 475 nm as observed in the blank sample to 550 nm (Figure 3.9B). Compared to the blank sample, a decrease in Yb<sup>3+</sup> PL intensity in the presence of gossypol was also noted when Yb-NH<sub>2</sub>-TPDC was excited between 340 and 400 nm. We ascribe this to the attenuation of incident light caused by the strong light absorption of gossypol in solution in this range (Figure 3.10, orange line). The above results indicate that under excitation between 475 nm and 550 nm, the Yb<sup>3+</sup> PL of Yb-NH<sub>2</sub>-TPDC can be switched on from a complete non-emissive state in response to the presence of gossypol.



**Figure 3.9** Excitation-Emission maps of Yb-NH<sub>2</sub>-TPDC (A) in the absence of gossypol and (B) in the presence of gossypol.



**Figure 3.10** UV-vis spectra of H<sub>2</sub>-NH<sub>2</sub>-TPDC/DMF solution (0.01 mg/mL, black), and gossypol/acetone solution (0.025 mg/mL, orange). The noisy feature from 270-300 nm of gossypol spectrum is due to acetone absorption.

We studied the kinetics of Yb<sup>3+</sup> PL of Yb-NH<sub>2</sub>-TPDC in response to gossypol. Specifically, 1 mL of gossypol/acetone solution (25 μg/mL, 50 μg/mL, 75 μg/mL, 100 μg/mL) was added to 2

mL of acetone suspension containing 2.5 mg of Yb-NH<sub>2</sub>-TPDC powder in a standard macro fluorescence cuvette. Yb<sup>3+</sup> PL was immediately monitored for 300 min under 485 nm excitation light. Figure 3.11A shows the evolution of Yb<sup>3+</sup> PL intensity at 976 nm as a function time, where data points at 0 min represent PL intensity measured immediately after the addition of gossypol solutions. Upon addition of gossypol, Yb<sup>3+</sup> emission gradually increased over 300 min. The slow increase of PL intensity was likely due to the hindered diffusion of the bulky gossypol into Yb-NH<sub>2</sub>-TPDC. With an equal amount of incubation time, stronger Yb<sup>3+</sup> PL intensity correlates with higher gossypol concentration in the 25 - 100 μg/mL range (Figure 3.11A, B). At 300 min, Yb<sup>3+</sup> PL intensity follows a linear dependence with gossypol concentration between 25 μg/mL and 100 μg/mL (Figure 3.11B inset), and therefore is suitable for quantification of gossypol in this concentration range. In the absence of gossypol, no appreciable Yb<sup>3+</sup> emission was observed. The limit of detection for gossypol was determined to be 25 μg/mL (~32 ppm in acetone solution) with a S/N of 7. No reliable Yb<sup>3+</sup> emission was detected when gossypol solutions of lower concentrations were tested. We note that the actual minimum detectable gossypol concentration was 8.3 μg/mL (~11 ppm in acetone solution), because the 1 mL of 25 μg/mL gossypol solution was diluted into 3 mL in cuvette. Despite the relatively slow response, Yb-NH<sub>2</sub>-TPDC is a promising sensor for practical detection and quantification of gossypol in terms of its limit of detection.

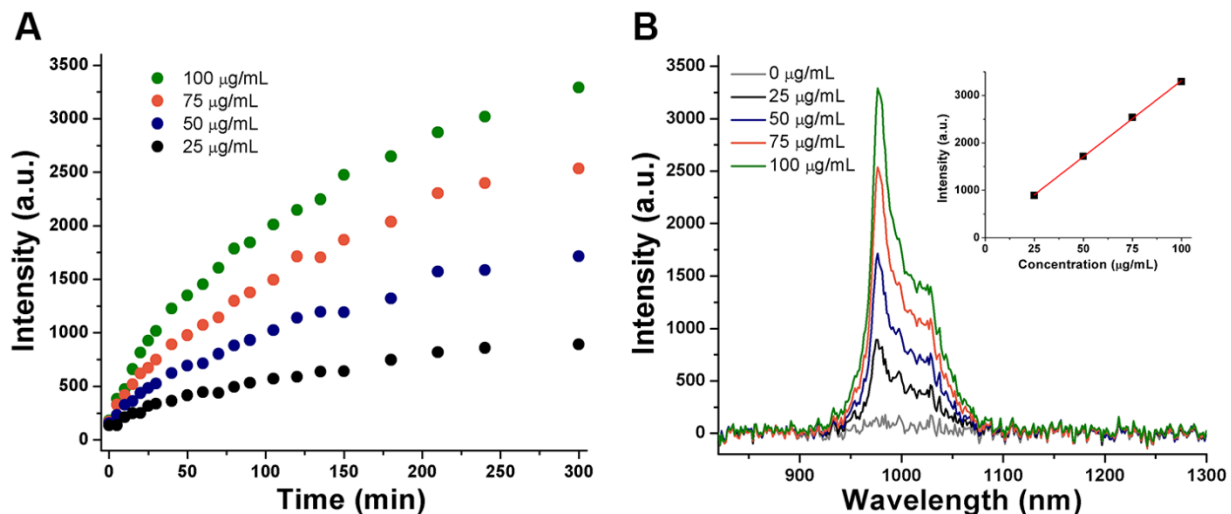


**Figure 3.11** Gossypol sensing experiments using Yb-NH<sub>2</sub>-TPDC. (A) kinetics of Yb<sup>3+</sup> PL of Yb-NH<sub>2</sub>-TPDC in response to gossypol solutions of different concentrations (100 µg/mL, green; 75 µg/mL, orange; 50 µg/mL, blue; 25 µg/mL, black); (B) emission spectra of Yb-NH<sub>2</sub>-TPDC samples in response to different gossypol concentrations at 300 min (100 µg/mL, green; 75 µg/mL, orange; 50 µg/mL, blue; 25 µg/mL, black; blank, grey; calibration curve, inset).

Interference from background molecules present in realistic samples, such as cottonseed oil and cotton meals, may hamper gossypol detection and quantification. To evaluate the selectivity of Yb-NH<sub>2</sub>-TPDC as a sensor for gossypol, we further investigated whether Yb<sup>3+</sup> PL excited at 485 nm can be turned on by substances commonly present in the context of gossypol detection. Refined cottonseed oil solution (100 mg/mL), palmitic acid solution (1 mg/mL), linoleic acid solution (1 mg/mL), and  $\alpha$ -tocopherol solution (1 mg/mL) did not induce Yb<sup>3+</sup> PL (white bars in Figure 3.12). Presumably, Yb<sup>3+</sup> PL cannot be sensitized by these substances, because they do not absorb visible light (Figures 3.13 and 3.14) or they cannot modulate the absorption of NH<sub>2</sub>-TPDC linkers. Apart from producing interfering signals, interferants could also block the interactions between the target analyte and sensor. For instance, background molecules could adsorb to Yb-NH<sub>2</sub>-TPDC more favorably than gossypol and prevent gossypol from switching on Yb<sup>3+</sup> luminescence. To assess the gossypol detection performance of Yb-NH<sub>2</sub>-TPDC in the presence of

background substances, Yb<sup>3+</sup> PL intensity at 976 nm in response to gossypol (100 μg/mL) without interferents was compared to PL intensity in the presence of cottonseed oil (100 mg/mL), palmitic acid (1 mg/mL), linoleic acid (1 mg/mL), and α-tocopherol (1 mg/mL) (grey bars in Figure 3.12), respectively. Although the concentrations of all tested interferents were at least 10 times higher than gossypol, the PL intensities of Yb-NH<sub>2</sub>-TPDC are largely unaffected. Overall, the Yb<sup>3+</sup> PL of Yb-NH<sub>2</sub>-TPDC is selectively turned on by gossypol.

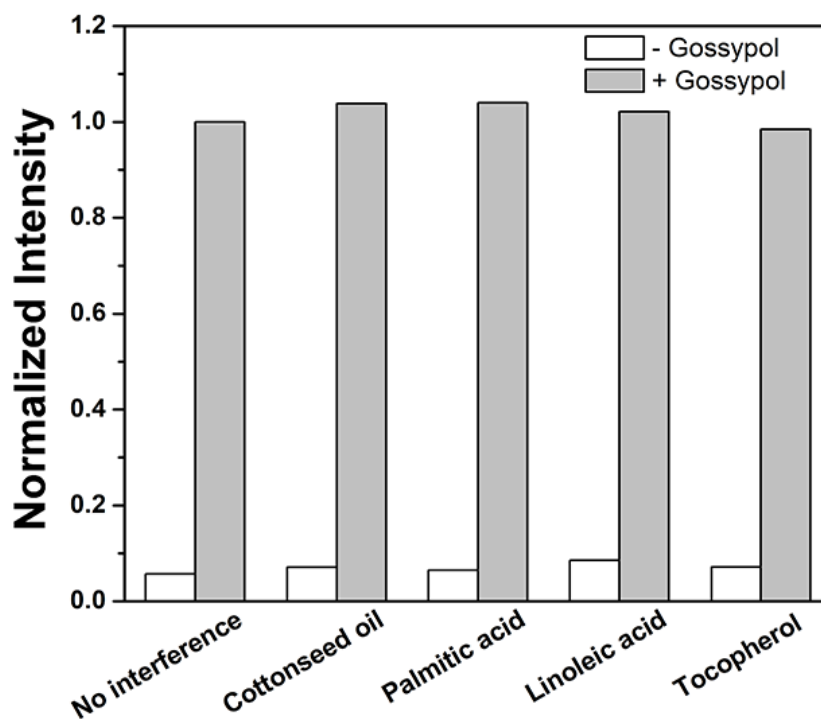


**Figure 3.12** Yb<sup>3+</sup> PL of Yb-NH<sub>2</sub>-TPDC samples in the presence of interferants (with gossypol, grey bars; without gossypol, white bars).

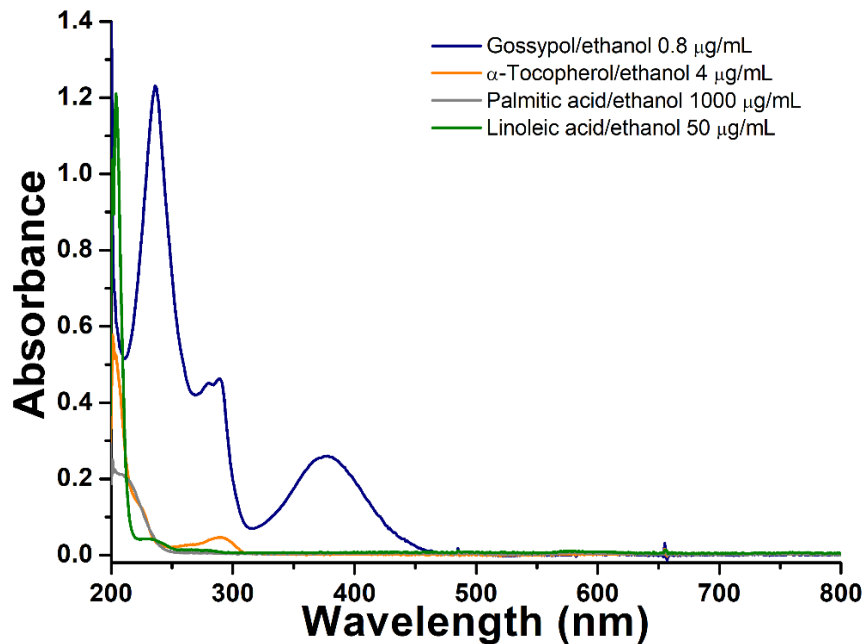


Figure 3.13 UV-vis spectra of gossypol/ethanol (0.8  $\mu\text{g/mL}$ , blue),  $\alpha$ -tocopherol/ethanol (4  $\mu\text{g/mL}$ , orange), palmitic acid/ethanol (1000  $\mu\text{g/mL}$ , grey) and linoleic acid/ethanol (50  $\mu\text{g/mL}$ , green). Spectrum of cottonseed oil/ethanol was not collected because cottonseed oil is insoluble in ethanol.

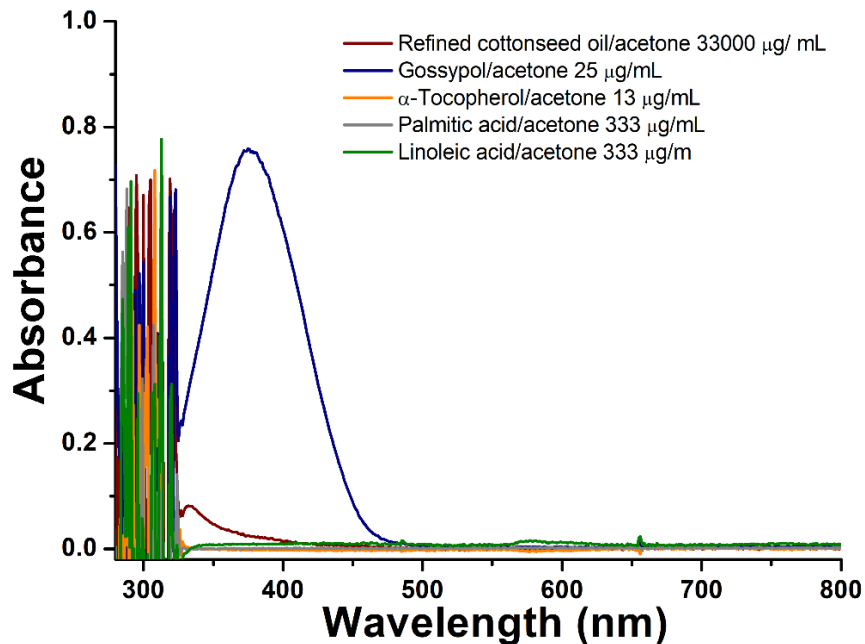
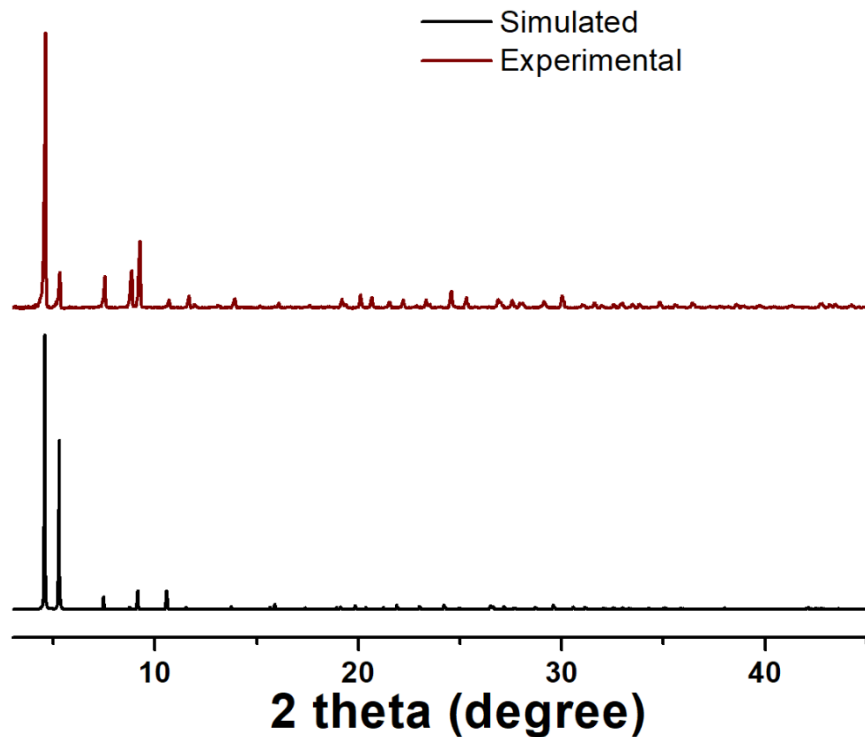
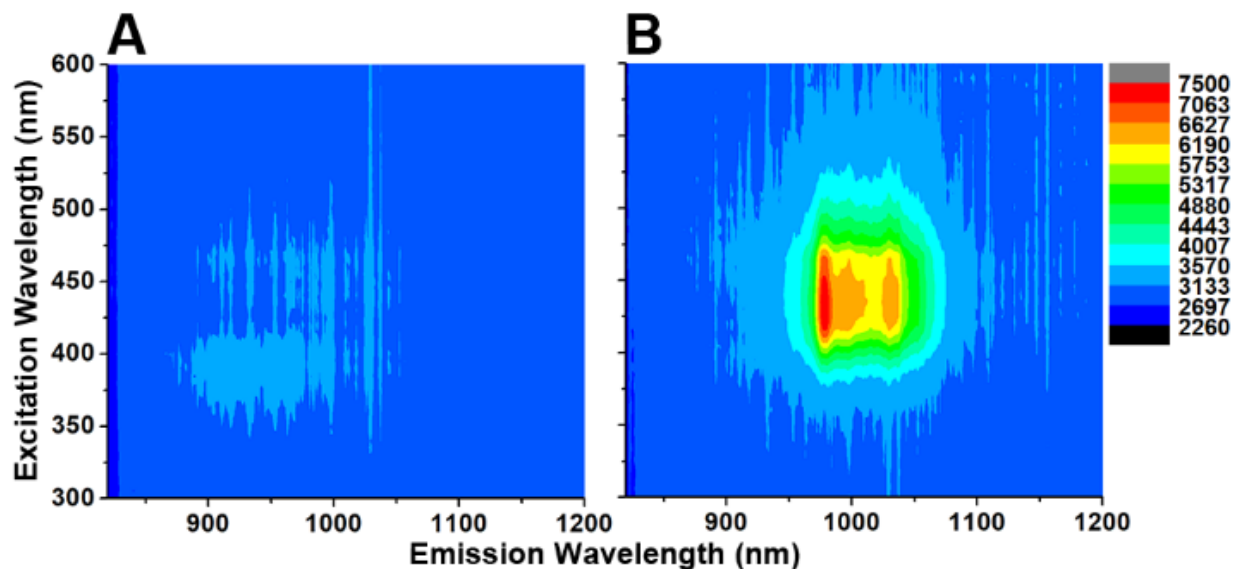


Figure 3.14 UV-Vis spectra of cottonseed oil/acetone solution (33000  $\mu\text{g/mL}$ , red), gossypol/acetone (25  $\mu\text{g/mL}$ , blue),  $\alpha$ -tocopherol/acetone (13  $\mu\text{g/mL}$ , orange), palmitic acid/acetone (333  $\mu\text{g/mL}$ , grey) and linoleic acid/acetone (333  $\mu\text{g/mL}$ , green). The noisy features between 280 nm and 330 nm are due to acetone absorption.

As discussed earlier, two mechanisms are likely responsible for the “turn-on” response of Yb-NH<sub>2</sub>-TPDC PL at 485 nm excitation in the presence of gossypol: 1) gossypol can function as an effective sensitizer for Yb<sup>3+</sup> luminescence on its own, or 2) gossypol can red-shift the absorption band of the NH<sub>2</sub>-TPDC linker, the integral sensitizer in Yb-NH<sub>2</sub>-TPDC, by formation of Schiff base products with a larger  $\pi$  system. To determine the operative mechanism, Yb-NO<sub>2</sub>-TPDC was synthesized using 2'-nitro-1,1':4',1''-terphenyl-4,4''-dicarboxylic acid (H<sub>2</sub>-NO<sub>2</sub>-TPDC) as a linker. Yb-NO<sub>2</sub>-TPDC and Yb-NH<sub>2</sub>-TPDC are isorecticular, as confirmed by PXRD (Figure 3.15). Lacking -NH<sub>2</sub> groups, Yb-NO<sub>2</sub>-TPDC cannot react with gossypol to form Schiff base products. In the absence of gossypol, the NO<sub>2</sub>-TPDC linker does not sensitize Yb<sup>3+</sup> PL at any excitation wavelengths (Figure 3.16A). Incubating Yb-NO<sub>2</sub>-TPDC with gossypol solution, however, led to strong Yb<sup>3+</sup> PL with excitation wavelengths spanning from 350 nm to 600 nm (Figure 3.16B). Significantly, these experiments indicate, for the first time, that gossypol is an effective sensitizer for Yb<sup>3+</sup> PL. We note further that no sign of Schiff base formation was observed after reacting Yb-NH<sub>2</sub>-TPDC with gossypol using our previously reported method (see 3.4.10 EXPERIMENTAL SECTION).<sup>174</sup> Therefore, we conclude that the “turn-on” response of Yb<sup>3+</sup> PL at 485 nm excitation is mainly due to the “antenna” effect of gossypol. As “antenna”, gossypol can sensitize Yb<sup>3+</sup> PL of both Yb-NH<sub>2</sub>-TPDC and Yb-NO<sub>2</sub>-TPDC at excitation wavelengths greater than 525 nm, while gossypol in solution does not exhibit absorption above 480 nm. The large discrepancy between the gossypol excitation range in the MOF and its absorption band in solution resembles our previous observation with NH<sub>2</sub>-TPDC linker, and may also be attributed to confinement effects.



**Figure 3.15** Experimental PXRD pattern of as-synthesized Yb-NO<sub>2</sub>-TPDC (red), and Simulated PXRD pattern of Yb-NH<sub>2</sub>-TPDC (black) based on its crystal structure. The close match between the two PXRD patterns indicates Yb-NO<sub>2</sub>-TPDC is a isorecticular MOF of Yb-NH<sub>2</sub>-TPDC.



**Figure 3.16** Excitation-Emission Maps of Yb-NO<sub>2</sub>-TPDC (A) in the absence of gossypol and (B) in the presence of gossypol.

With strong evidence supporting that gossypol is an effective sensitizer for  $\text{Yb}^{3+}$  PL, we further explored other Ln materials for gossypol detection. Since gossypol can form complexes with  $\text{Ln}^{3+}$  ions in solution,<sup>173</sup> we were particularly interested to test whether simple and commercially available  $\text{Ln}^{3+}$  salts can be used as “turn-on” sensors for gossypol. Indeed,  $\text{YbCl}_3 \cdot 6\text{H}_2\text{O}$  solution exhibited intense  $\text{Yb}^{3+}$  PL upon addition of gossypol. The excitation-emission map of  $\text{YbCl}_3 \cdot 6\text{H}_2\text{O}$  solution after 5 min incubation with gossypol (Figure 3.17) showed that  $\text{Yb}^{3+}$  PL can be observed upon excitation from 330 nm to 480 nm.

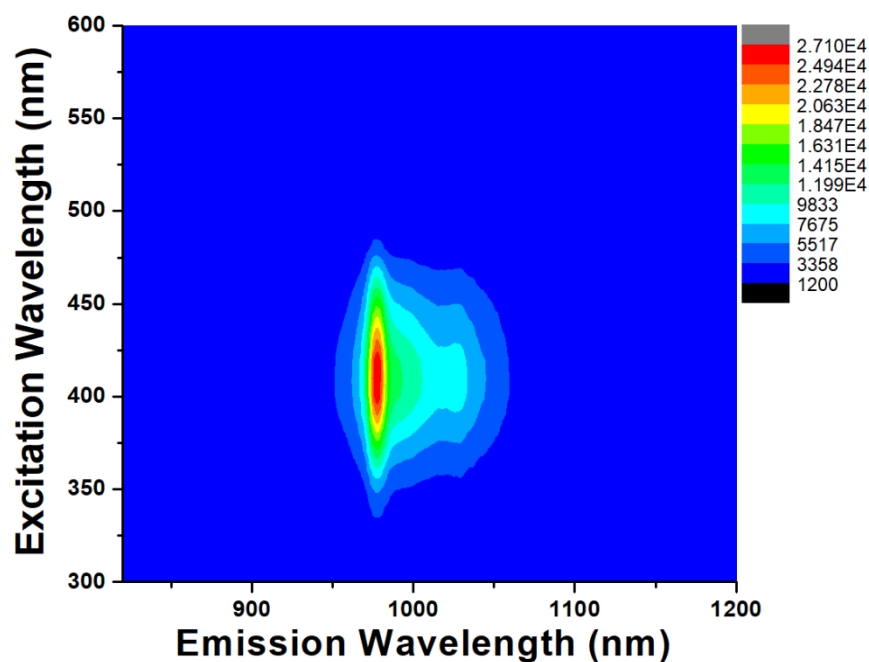


**Figure 3.17** Excitation-Emission map of  $\text{YbCl}_3 \cdot 6\text{H}_2\text{O}$  solution in the presence of gossypol.

Compared to  $\text{Yb-NH}_2\text{-TPDC}$ , the response time of  $\text{YbCl}_3 \cdot 6\text{H}_2\text{O}$  is significantly faster, likely because gossypol molecules can readily access and coordinate  $\text{Yb}^{3+}$  ions in solution without overcoming the diffusion barriers posed by MOF pores. To determine the detection range of  $\text{YbCl}_3 \cdot 6\text{H}_2\text{O}$ , emission spectra were collected 5 minutes after 1 mL of gossypol/acetone solution (0  $\mu\text{g/mL}$ , 0.5  $\mu\text{g/mL}$ , 1  $\mu\text{g/mL}$ , 3  $\mu\text{g/mL}$ , 5  $\mu\text{g/mL}$ , 7  $\mu\text{g/mL}$ , 10  $\mu\text{g/mL}$ , 25  $\mu\text{g/mL}$ , 50  $\mu\text{g/mL}$ ) was added to 2 mL of  $\text{YbCl}_3 \cdot 6\text{H}_2\text{O}/\text{DMF}$  solution (1 mg/mL) (Figure 3.18). No emission was

observed for the sample with acetone blank, while  $\text{Yb}^{3+}$  emission was observed for all samples containing gossypol. The limit of detection was determined to be  $0.5 \mu\text{g/mL}$  (0.64 ppm) with a S/N of 10. The PL intensity at 976 nm follows a linear dependence with the concentration of gossypol solution between  $0.5 \mu\text{g/mL}$  and  $10 \mu\text{g/mL}$  and approached saturation at higher concentrations (Figure 3.19).

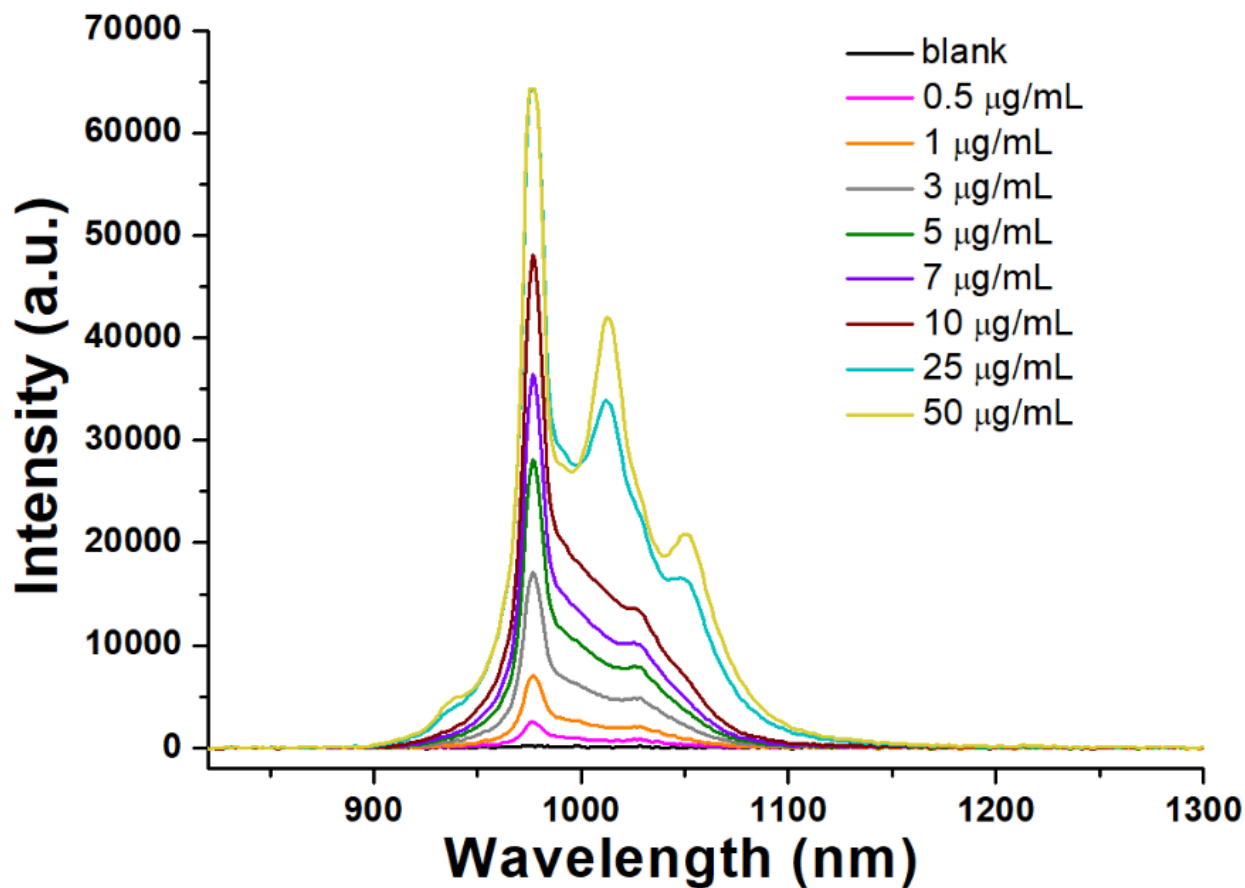


**Figure 3.18** Emission spectra of  $\text{YbCl}_3$  solution in the presence of gossypol at various concentrations. Excitation: 400 nm.

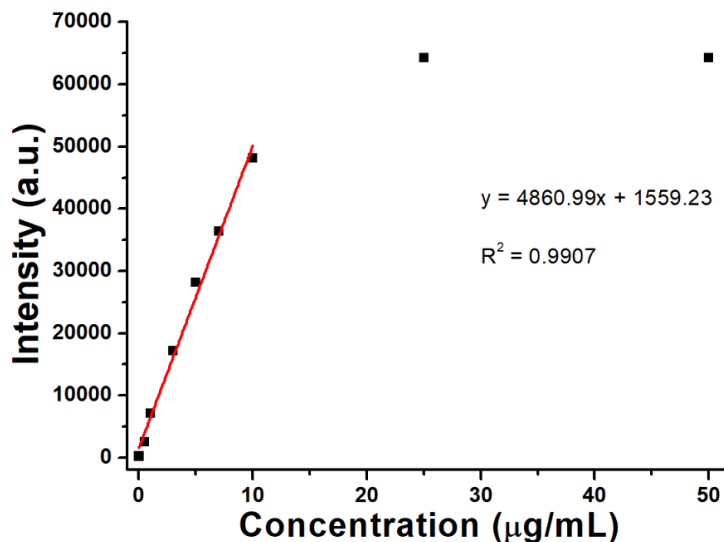


**Figure 3.19** Emission intensities at 976 nm of  $\text{YbCl}_3$  solution in the presence of various gossypol concentration.

In addition, we discovered that the  $\text{Nd}^{3+}$  PL of  $\text{NdCl}_3 \cdot 6\text{H}_2\text{O}$  at 1056 nm can also be used for gossypol detection in a similar fashion (Figures 3.20 and 3.21). Arguably,  $\text{Yb-NH}_2\text{-TPDC}$  and  $\text{YbCl}_3 \cdot 6\text{H}_2\text{O}$  are complimentary and allow for detection and quantification of gossypol at different concentration ranges: from 0.5  $\mu\text{g/mL}$  to 10  $\mu\text{g/mL}$  using  $\text{YbCl}_3 \cdot 6\text{H}_2\text{O}$ , and from 25 to 100  $\mu\text{g/mL}$  using  $\text{Yb-NH}_2\text{-TPDC}$ . In addition,  $\text{Yb-NH}_2\text{-TPDC}$  can be advantageous for integration into solid state devices, whereas  $\text{YbCl}_3 \cdot 6\text{H}_2\text{O}$  provides a simple way to rapidly and sensitively detect gossypol in solution.

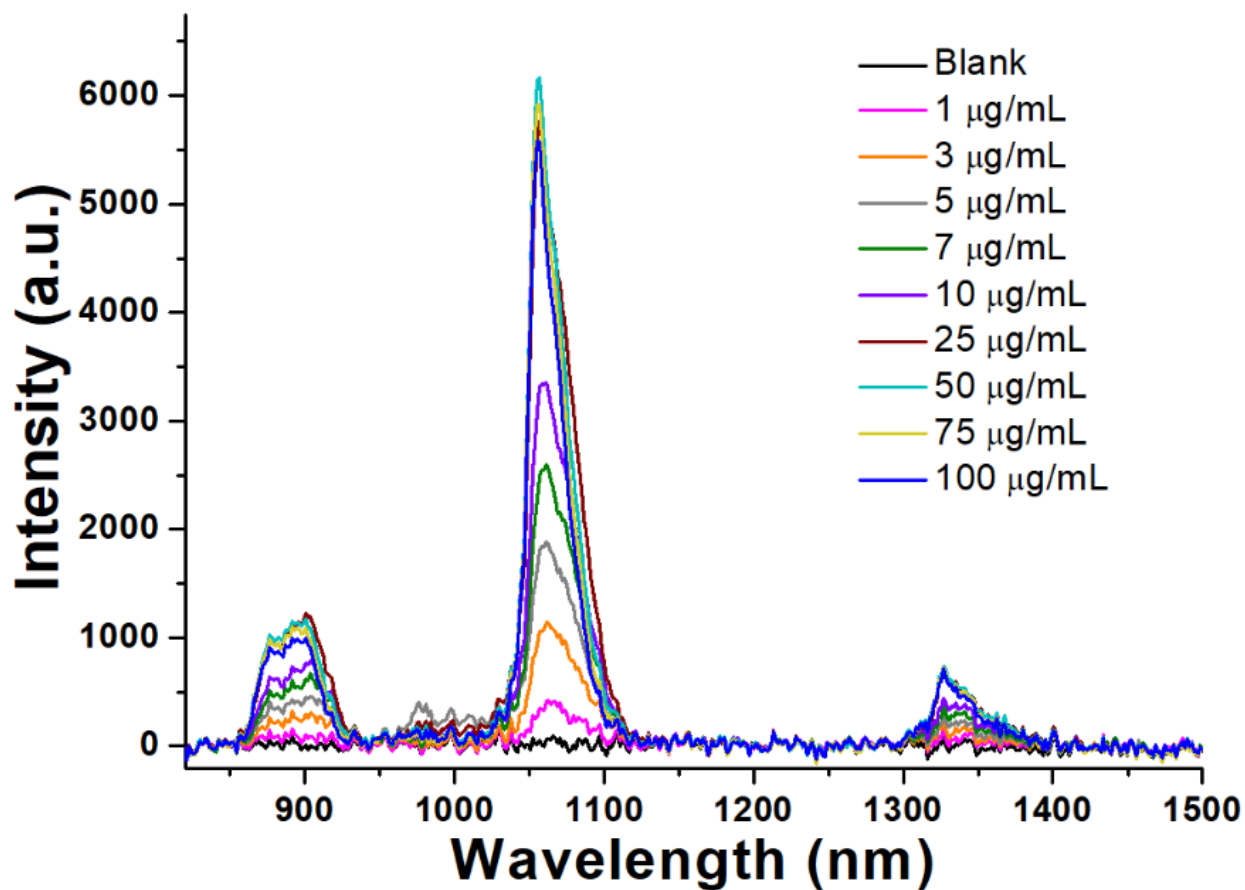


Figure 3.20 Emission spectra of  $\text{NdCl}_3$  solution in the presence of gossypol at various concentrations. Excitation:

400 nm.

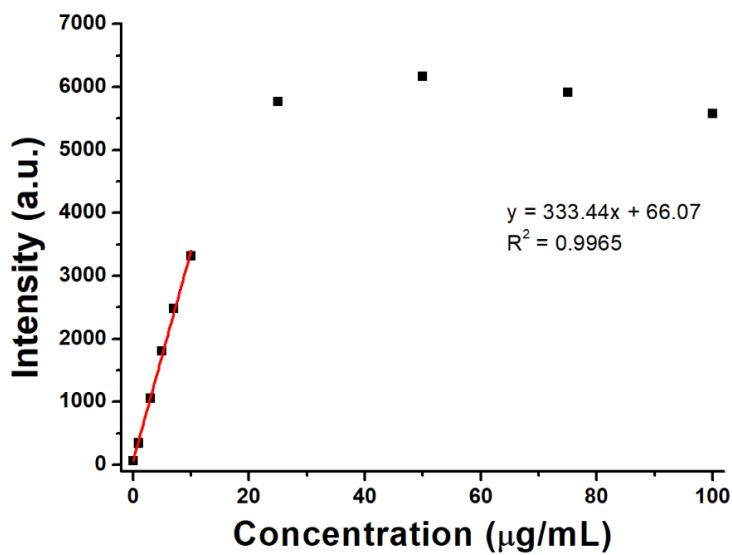


Figure 3.21 Emission intensities at 1056 nm of  $\text{NdCl}_3$  solution in the presence of various gossypol concentration.

### 3.3 CONCLUSIONS

In summary, we discovered that gossypol, a toxic molecule that concerns the cotton industry, can effectively sensitize  $\text{Yb}^{3+}$  and  $\text{Nd}^{3+}$  NIR PL. Leveraging this discovery, we demonstrate the first examples of luminescence “turn-on” detection of gossypol using Ln MOFs an Ln salts and achieve highly selective, fast-responding, and sensitive sensing of gossypol in acetone solution with a concentration of 0.5 – 100  $\mu\text{g/mL}$ . We envision that this general sensing approach will be applicable to the detection of a wide variety of aromatic molecules, including pharmaceuticals, pesticides, and other contaminants that be present in water and food.

### 3.4 EXPERIMENTAL SECTION

#### 3.4.1 General materials and methods

All purchased chemicals were used without further purification except where otherwise noted. Refined cottonseed oil, gossypol, palmitic acid, linoleic acid,  $\alpha$ -tocopherol were purchased from sigma-aldrich. Nanopure water (18.1  $\text{M}\Omega$ ) was obtained from a Barnstead Diamond<sup>TM</sup> water purification system.

PXRD patterns were collected using a Bruker AXS D8 Discover powder diffractometer at 40 kV, 40 mA for Cu  $\text{K}\alpha$ , ( $\lambda = 1.5406 \text{ \AA}$ ) from 3 to 45° at a step size of 0.02°. The data were analyzed using the EVA program from the Bruker Powder Analysis Software package. The simulated powder patterns were calculated using Mercury 3.8 and CIF files.

SCXRD experiments were performed on a Bruker X8 Prospector Ultra diffractometer equipped with an Apex II CCD detector and an I $\mu$ S micro-focus Cu K $\alpha$  X-ray source ( $\lambda = 1.54178$  Å). Data were collected at 230 K under N<sub>2</sub> flow and integrated by Bruker program SAINT. Empirical absorption correction was applied using program SADABS. The structure was solved with direct method using SHELXT and refined by full-matrix least-squares on F<sup>2</sup> using SHELXL<sup>138, 179</sup> in Olex2.<sup>137</sup>

<sup>1</sup>H NMR spectra were collected using Bruker Avance III 300 MHz spectrometers. Chemical shifts are in parts per million (ppm) using the residual solvent peak (DMSO-d<sub>6</sub>) as references.

TGA were performed using a TGA Q500 thermal analysis system under a N<sub>2</sub> atmosphere from room temperature to 650 °C at a ramping rate of 5 °C /min.

Solution UV–vis absorption spectra were collected using an Agilent 8453 UV–vis spectrometer equipped with deuterium and tungsten lamps.

PL data were collected using a Horiba Jobin-Yvon NanoLog spectrofluorometer with a 450 W xenon source, double excitation monochromators, and a Symphony II InGaAs array detector. Excitation gratings were blazed at 330 nm with 1200 grooves/mm and emission gratings blazed at 780 nm with 100 grooves/mm. All measurements were obtained with an 830 nm long-pass filter at ambient temperature.

### **3.4.2 Synthesis of 3,3''-diamino-1,1':4',1''-terphenyl-4,4''-dicarboxylic acid (H<sub>2</sub>-NH<sub>2</sub>-**

#### **TPDC)**

3,3''-Diamino-1,1':4',1''-terphenyl-4,4''-dicarboxylic acid was synthesized using previously reported conditions.<sup>174</sup>

### 3.4.3 Synthesis of 2'-nitro-1,1':4',1''-terphenyl-4,4''-dicarboxylic acid (H<sub>2</sub>-NO<sub>2</sub>-TPDC)

2'-Nitro-1,1':4',1''-terphenyl-4,4''-dicarboxylic acid was synthesized using previously reported conditions.<sup>180</sup>

### 3.4.4 Synthesis of Yb-NH<sub>2</sub>-TPDC

Stock solutions of H<sub>2</sub>-NH<sub>2</sub>-TPDC (0.05 M) and YbCl<sub>3</sub>·6H<sub>2</sub>O (0.05 M) and 2,6-difluorobenzoic acid (1 M) in DMF were prepared. A mixture of concentrated hydrochloric acid/DMF (1/2.3 v/v) was prepared. To a 20 mL Pyrex vial was added H<sub>2</sub>-NH<sub>2</sub>-TPDC solution (1.5 mL, 0.05 M), YbCl<sub>3</sub>·6H<sub>2</sub>O (0.75 mL, 0.05 M), 2,6-difluorobenzoic acid (0.75 mL, 1 M), nanopure H<sub>2</sub>O (0.15 mL) and concentrated hydrochloric acid/DMF (0.2 mL) sequentially. The vial was tightly capped and heated in a 120 °C isothermal oven for 14 hours. The vial was then removed from oven and cooled down naturally to room temperature. Crystals were collected after centrifugation and washed with fresh DMF (3x, 2 mL each time). Formula: [Yb<sub>6</sub>(OH)<sub>8</sub>(C<sub>20</sub>H<sub>14</sub>N<sub>2</sub>O<sub>4</sub>)<sub>6</sub>(H<sub>2</sub>O)<sub>6</sub>] · 2(C<sub>2</sub>H<sub>8</sub>N) · 17DMF · 6H<sub>2</sub>O; Yield: 15 mg. Anal. calcd. (%): C, 43.76; H, 5.27; N, 9.04; Found (%): C, 43.09; H, 4.68; N, 9.32.

### 3.4.5 Sample activation and N<sub>2</sub> gas adsorption experiment of Yb-NH<sub>2</sub>-TPDC

Two batches of as-synthesized Yb-NH<sub>2</sub>-TPDC were prepared (*vide supra*) and combined in a 20 mL Pyrex vial after thoroughly washed with DMF. Solvent exchange was performed with dichloromethane and then n-pentane using a slightly modified procedure from the literature report.<sup>177</sup> To perform solvent exchange, most of existing solvent in the sample vial was first

removed using a glass pipette with enough solvent left to submerge the MOF sample. Then vial was then replenished with fresh solvent. This solvent exchange procedure was performed every 20 min, with dichloromethane (6 mL each time) for the first 5 cycles and then n-pentane (12 mL each time) for another 5 times. After the last solvent exchange cycle with n-pentane, the solvent was removed by pipetting followed by drying under argon flow. The MOF sample was then evacuated on a Micromeritics Smart VacPrep at room temperature for 21 hours to obtain 29.4 mg of activated sample. N<sub>2</sub> isotherm of MOF samples were collected at 77K on a Micromeritics 3Flex instrument.

#### **3.4.6 Excitation-Emission maps of Yb-NH<sub>2</sub>-TPDC samples**

Excitation-Emission maps of Yb-NH<sub>2</sub>-TPDC samples with and without gossypol were measured using an integration sphere on solid MOF samples stored under acetone in quartz capillary tubes. The excitation wavelength was scanned from 300 to 700 nm in 5 nm increments, and the emission was detected between 820 to 1580 nm with 1.5 nm increments. Slit widths were set at 10 nm for both excitation and emission. An integration time of 10 s was used for each emission spectrum.

The Yb-NH<sub>2</sub>-TPDC samples was prepared using the procedure below: two samples each containing 2.5 mg of activated Yb-NH<sub>2</sub>-TPDC were incubated respectively with acetone (1 mL) and gossypol/acetone solution (0.1 mg/mL, 1mL) in 1.5 mL centrifuge tubes at 20 °C for 44 hours using a thermal mixer at 1000 rpm. After the incubation time, the MOF crystals were centrifuged and transferred to custom-made quartz tubes with 0.5 mL of the incubation solvent or solution. The quartz tubes were sealed with parafilm to prevent solvent evaporation.

### 3.4.7 Sensing experiments using Yb-NH<sub>2</sub>-TPDC

A slurry containing three batches of as-synthesized Yb-NH<sub>2</sub>-TPDC (approx. 45 mg) and 0.5 mL of DMF was ground with a mortar and pestle for 20 min to reduce the size of Yb-NH<sub>2</sub>-TPDC crystals. Grinding without DMF would cause Yb-NH<sub>2</sub>-TPDC to lose crystallinity. The ground sample was then solvent exchanged with dichloromethane and n-pentane in a 5 mL sample vial. To perform solvent exchange, the sample vial was loaded in a 50 mL centrifuge tube as secondary container and centrifuged at 3000 rpm for 3 min to form a sample pellet at the bottom the vial. Most of supernatant was removed using a glass pipette with enough solvent left to ensure the MOF sample was submerged. After the vial was replenished with fresh solvent, MOF sample was redispersed via vortexing. This solvent exchange procedure was performed every 20 min, with dichloromethane (4 mL each time) for 5 times and then n-pentane (4 mL each time) for 5 times. After the last solvent exchange cycle with n-pentane, the solvent was removed by pipetting followed by drying under argon flow. After evacuating under Schlenk vacuum for 1 hour, the Yb-NH<sub>2</sub>-TPDC sample was ready for sensing experiments.

For gossypol sensing experiments, 2.5 mg of Yb-NH<sub>2</sub>-TPDC was dispersed with 2 mL of acetone in a standard fluorescence macro cuvette equipped with a PTFE stopper (Fireflysci type 21 macro cuvette, light path: 10 mm x 10 mm). 1 mL of gossypol/acetone solution (0 µg/mL, 25 µg/mL, 50 µg/mL, 75 µg/mL, 100 µg/mL) was then added to the MOF suspension. The cuvette was tightly capped, mounted on top of a thermomixer (Eppendorf Thermomixer R Mixer) using a custom-made sample holder and incubated at room temperature with 500 rpm mixing frequency. Emission spectra of each sample was followed over 300 min. The cuvette was vigorously shaken with hand and emission spectra were immediately collected. The emission spectra were obtained using 485 nm excitation wavelength. The emission was detected between 820 to 1580 nm with 1.5

nm increments. Slit widths were set at 10 nm for both excitation and emission. An integration time of 1 s was used for each emission spectrum.

For gossypol sensing interference experiments, 1 mL of 2.5 mg/mL Yb-NH<sub>2</sub>-TPDC in acetone was mixed with 1 mL of acetone (blank) or gossypol/acetone solution (100 µg/mL) and 1 mL of interferant acetone solution, including: cottonseed oil (100 mg/mL), palmitic acid (1 mg/mL), linoleic acid (1 mg/mL) and  $\alpha$ -tocopherol (1 mg/mL). The mixture was incubated on top of a thermomixer (Eppendorf Thermomixer R Mixer) in a 15 mL centrifuge tube at room temperature for 300 min with 500 rpm mixing frequency and then transferred to a standard fluorescence macro cuvette equipped with a PTFE stopper (Fireflysci type 21 macro cuvette, light path: 10 mm x 10 mm). The cuvette was vigorously shaken with hand and emission spectra were immediately collected. The emission spectra were obtained using 485 nm excitation wavelength. The emission was detected between 820 to 1580 nm with 1.5 nm increments. Slit widths were set at 10 nm for both excitation and emission. An integration time of 1 s was used for each emission spectrum.

### 3.4.8 Synthesis of Yb-NO<sub>2</sub>-TPDC

Stock solutions of H<sub>2</sub>-NO<sub>2</sub>-TPDC (0.05 M) and YbCl<sub>3</sub>·6H<sub>2</sub>O (0.05 M) and 2,6-difluorobenzoic acid (1 M) in DMF were prepared. To a 4 mL Pyrex vial equipped with a PTFE cap was added H<sub>2</sub>-NO<sub>2</sub>TPDC solution (0.3 mL, 0.05 M), YbCl<sub>3</sub>·6H<sub>2</sub>O (0.15 mL, 0.05 M), 2,6-difluorobenzoic acid (0.25 mL, 1 M) sequentially. The vial was tightly capped and heated in a 100 °C isothermal oven for 40 hours. The vial was then removed from oven and cooled down naturally to room temperature. Crystals were collected after centrifugation and washed with fresh DMF (3x, 1 mL each time). Yield: 2.3 mg.

### 3.4.9 Excitation-Emission maps of Yb-NO<sub>2</sub>-TPDC samples

Excitation-Emission maps of Yb-NO<sub>2</sub>-TPDC samples with and without gossypol were measured using an integration sphere on solid MOF samples stored under acetone in quartz capillary tubes. The excitation wavelength was scanned from 300 to 700 nm in 5 nm increments, and the emission was detected between 820 to 1580 nm with 1.5 nm increments. Slit widths were set at 10 nm for both excitation and emission. An integration time of 10 s was used for each emission spectrum.

The Yb-NO<sub>2</sub>-TPDC samples was prepared using the procedure below: two samples containing 6 mg of as-synthesized Yb-NO<sub>2</sub>-TPDC were first washed with acetone (4 times, 1 mL each time), and then incubated respectively with acetone (1 mL) and gossypol/acetone solution (0.1 mg/mL, 1mL) in 1.5 mL centrifuge tubes at 20 °C for 44 hours using a thermomixer (Eppendorf Thermomixer R Mixer) with 1000 rpm mixing frequency. After the incubation time, the MOF crystals were centrifuged and transferred to quartz tubes with 0.5 mL of the incubation solvent or solution. The quartz tubes were sealed with parafilm to prevent solvent evaporation. Excitation-Emission maps were collected once all MOF crystals settled to the bottom of the quartz tubes.

### 3.4.10 LC-MS experiments

Yb-NH<sub>2</sub>-TPDC (5.7 mg) was incubated in gossypol/acetone solution (0.1 mg/mL, 2 mL) at 20 °C for 44 hours on a thermomixer (Eppendorf Thermomixer R Mixer) at room temperature with 500 rpm mixing frequency. After incubation, the MOF crystals were washed with ethanol (3 times, 3 mL each time). To the washed MOF crystals were then added NaBH<sub>4</sub>/EtOH solution (10

mg/mL, 3 mL) in a Pyrex vial. The mixture was allowed to react at room temperature for 18 hrs. The solid in the mixture was separated via centrifugation and then washed with fresh EtOH (3 times, 1 mL each time). To the solid was then added aqueous HCl solution (1 M, 1 mL). After sonicating for 5 min, the mixture was centrifuged, and supernatant removed. The precipitate was then dissolved in MeOH (1 mL). The MeOH solution was then submitted to LC-MS.

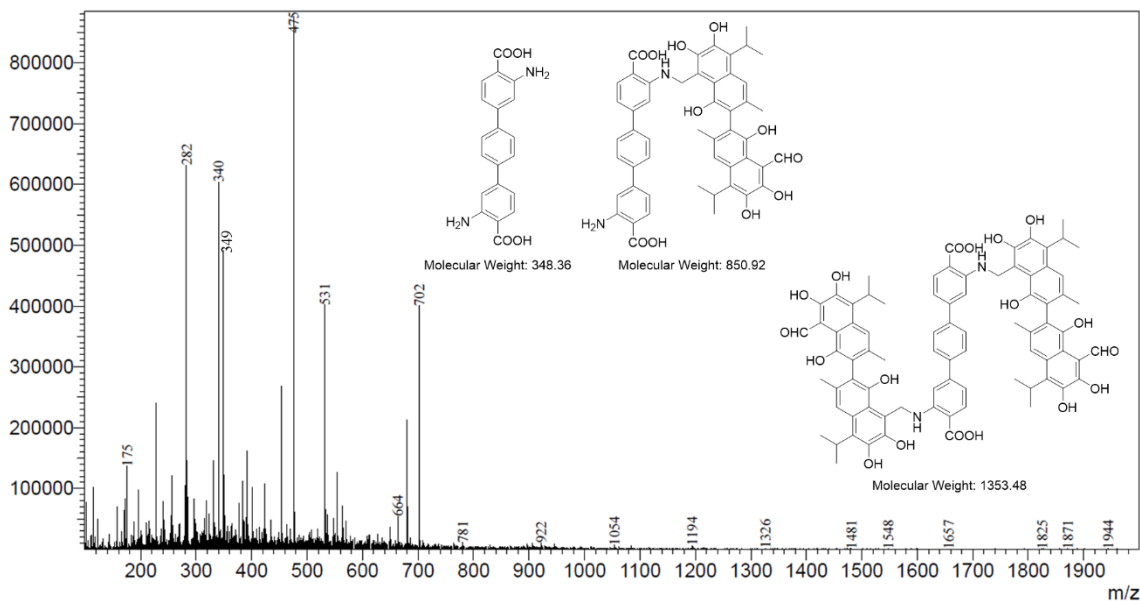


**Figure 3.22** Mass spectrum (ESI+). The  $[M+H]^+$  peak for  $NH_2$ -TPDC linker ( $m/z = 349$ ) was observed along with additional peaks. However, no peaks corresponding to the two possible reduced Schiff base products were identified.

Yb-NH<sub>2</sub>-TPDC MOF (2.5 mg) was incubated with gossypol acetone solution (0.1 mg/mL, 1mL) at room temperature for 42 hrs. The supernatant was collected and examined with LC-MS using ESI<sup>-</sup> mode. Mass spectrometry data indicate that gossypol molecules in solution were intact after incubation with MOF in acetone for 42 hours.

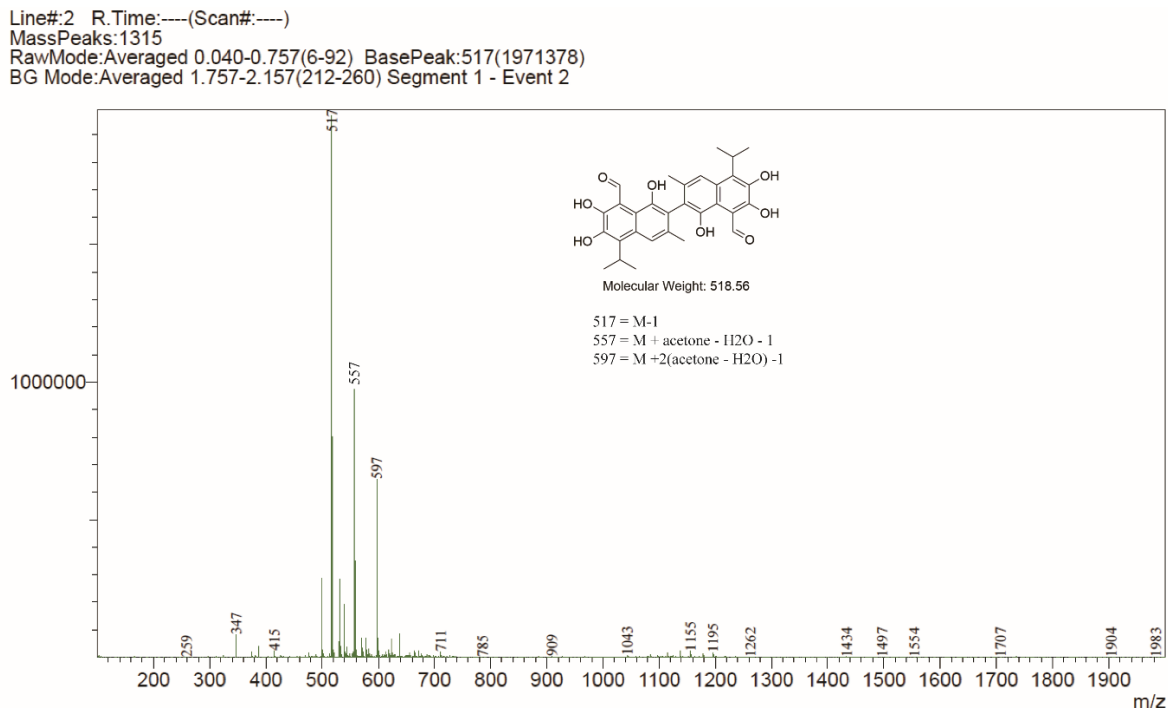


**Figure 3.23** Mass spectrum (ESI<sup>-</sup>) of gossypol solution after incubating with MOF Yb-NH<sub>2</sub>-TPDC. The three peaks with m/z = 517, m/z = 557, m/z = 597 correspond respectively to [M-H]<sup>-</sup>, [M+acetone-H<sub>2</sub>O-H]<sup>-</sup> and [M+2(acetone-H<sub>2</sub>O)-H]<sup>-</sup>.

### 3.4.11 Excitation-Emission map of YbCl<sub>3</sub>•6H<sub>2</sub>O sample in the presence of gossypol

Excitation-Emission maps of YbCl<sub>3</sub> in the presence of gossypol were measured on a solution sample in a macro cuvette. The excitation wavelength was scanned from 300 to 700 nm in 10 nm increments, and the emission was detected between 820 to 1580 nm with 1.5 nm

increments. Slit widths were set at 10 nm for both excitation and emission. An integration time of 1 s was used for each emission spectrum.

The sample was prepared using the procedure below:  $\text{YbCl}_3 \cdot 6\text{H}_2\text{O}$  (2.3 mg) was dissolved in DMF (2 mL) in a standard fluorescence macro cuvette equipped with a PTFE stopper (Fireflysci type 21 macro cuvette, light path: 10 mm x 10 mm). Gossypol/acetone solution (0.005 mg/mL, 1 mL) was added to the cuvette. The mixture was incubated at room temperature for 5 minutes before excitation-emission map was collected.

### **3.4.12 Gossypol sensing experiments using $\text{YbCl}_3$**

A stock solution of 1 mg/mL  $\text{YbCl}_3 \cdot 6\text{H}_2\text{O}$  in DMF was prepared by dissolving  $\text{YbCl}_3 \cdot 6\text{H}_2\text{O}$  (30.7 mg) in DMF (30.7 mL) in a 40 mL Pyrex vial. In each sensing experiment, 2 mL of the  $\text{YbCl}_3 \cdot 6\text{H}_2\text{O}$  solution (1 mg/mL) was added in a standard fluorescence macro cuvette equipped with a PTFE stopper (Fireflysci type 21 macro cuvette, light path: 10 mm x 10 mm). 1 mL of gossypol/acetone solution (0  $\mu\text{g/mL}$ , 0.5  $\mu\text{g/mL}$ , 1  $\mu\text{g/mL}$ , 3  $\mu\text{g/mL}$ , 5  $\mu\text{g/mL}$ , 7  $\mu\text{g/mL}$ , 10  $\mu\text{g/mL}$ , 25  $\mu\text{g/mL}$ , 50  $\mu\text{g/mL}$ ) was then added to the cuvette. The cuvette was capped and incubated at room temperature for 5 min on top of a thermomixer (Eppendorf Thermomixer R Mixer) with 500 rpm mixing frequency before emission spectra were collected. The emission spectra were obtained using 400 nm excitation wavelength. The emission was detected between 820 to 1580 nm with 1.5 nm increments. Slit widths were set at 10 nm for both excitation and emission. An integration time of 1 s was used for each emission spectrum.

### 3.4.13 Gossypol sensing experiments using NdCl<sub>3</sub>

A stock solution of 1 mg/mL NdCl<sub>3</sub>•6H<sub>2</sub>O in DMF was prepared by dissolving NdCl<sub>3</sub>•6H<sub>2</sub>O (23.1 mg) in DMF (23.1 mL) in a 40 mL Pyrex vial. In each sensing experiment, 2 mL of the NdCl<sub>3</sub>•6H<sub>2</sub>O solution (1 mg/mL) was added in a standard fluorescence macro cuvette equipped with a PTFE stopper (Fireflysci type 21 macro cuvette, light path: 10 mm x 10 mm). 1 mL of gossypol/acetone solution (0 µg/mL, 1 µg/mL, 3 µg/mL, 5 µg/mL, 7 µg/mL, 10 µg/mL, 25 µg/mL, 50 µg/mL, 75 µg/mL, 100 µg/mL) was then added to the cuvette. The cuvette was capped and incubated at room temperature for 5 min on top of a thermomixer at 500 rpm before emission spectra were collected. The cuvette was capped and incubated at room temperature for 5 min on top of a thermomixer (Eppendorf Thermomixer R Mixer) with 500 rpm mixing frequency before emission spectra were collected. The emission spectra were obtained using 400 nm excitation wavelength. The emission was detected between 820 to 1580 nm with 1.5 nm increments. Slit widths were set at 10 nm for both excitation and emission. An integration time of 1 s was used for each emission spectrum.

## 4.0 MULTIVARIATE STRATIFIED METAL-ORGANIC FRAMEWORKS: DIVERSIFICATION USING DOMAIN BUILDING BLOCKS

This chapter is adapted and reprinted in part with permission from: **Tian-Yi Luo**; Chong Liu; Xing Yee Gan, Patrick F. Muldoon; Nathan A. Diemler; Jill E. Millstone; Nathaniel L. Rosi. Multivariate Stratified Metal–Organic Frameworks: Diversification Using Domain Building Blocks. *Journal of the American Chemical Society* **2019**, *141* (5), 2161-2168. Copyright 2019 American Chemical Society.

Tian-Yi Luo (Tianyi Luo) and Nathaniel L. Rosi designed the experiments. Tian-Yi Luo carried out most of the MOF synthesis and characterization. Chong Liu synthesized a MOF linker and collected UV-Vis spectra of nanoparticle-MOF composites. Xing Yee Gan synthesized Au and Cu<sub>2-x</sub>Se nanoparticles. Patrick F. Muldoon contributed to optimization of MOF syntheses. Nathan A. Diemler helped collect STEM-HAADF and EDS data of nanoparticle-MOF composites. Tian-Yi Luo and Nathaniel L. Rosi wrote the manuscript. All authors made comments on the manuscript.

### 4.1 INTRODUCTION

Reticular chemistry enables rational placement and organization of molecules in periodic three-dimensional space.<sup>181</sup> The metal-organic framework (MOF) is one embodiment of reticular chemistry and its basic principles.<sup>12</sup> MOF structures and properties are defined by the connectivity and organization of their constituent metal nodes and organic linkers, which are considered the

basic building blocks for MOF construction. A virtually unparalleled degree of structural and compositional diversity can be achieved within MOFs by varying and mixing these building blocks.<sup>182</sup> Such diversity is perhaps best manifest in multivariate (MTV) MOFs, wherein a plurality of metal and molecular building blocks is anchored periodically in 3-D space.<sup>66, 80</sup> Building block identities and disposition code for aggregate properties not necessarily achievable with simple MOFs containing only one type of metal node or linker. MTV-MOFs signal the importance of compositional diversity and represent an important milestone in the path toward increased MOF complexity.

Here we introduce ‘domain building blocks’ (DBBs) into the MOF lexicon and define them as distinct structural or compositional regions within a MOF. As such, each DBB is itself a MOF and necessarily consist of collections of periodically connected metal nodes and organic linkers. DBBs should be considered modular and the placement and organization of domains within a MOF material may code for properties and function. Further, in addition to the metal node and linker building blocks, the DBB is an additional multiplier for increasing MOF diversity and complexity.<sup>183</sup> Just as in biology where collections of organelles work together to define cellular function, collections of DBBs comprising a MOF could each have distinct properties or functions that, when integrated, would define system properties and functions. We can therefore predict that MOFs constructed from DBBs may ultimately be able to perform sequences of operations and complex tasks.

In this study, we highlight stratified MOFs (hereafter abbreviated ‘sMOFs’) and use them to illustrate how DBBs can significantly expand MOF diversity beyond what is achievable when considering only metal ion and linker building blocks. sMOFs are multivariate MOF crystals consisting of two or more concentrically organized domains (strata). The multivariate nature is

defined by the sequence of different strata *and* the different component metal ions and linkers comprising the different strata. In principle, an infinite number of concentric MOF strata can be present in one sMOF crystal. The properties of sMOFs are not simply defined by the sum of the properties of individual strata. When different strata are combined together, synergy may emerge. The combination and sequence of different strata are unique variables that can significantly affect the overall properties of the whole crystal.

A basis set of only a few possible domains can give rise to numerous sMOFs with different properties. Consider, for example, the MOF domains that can be prepared with  $M$  number of metal ions and  $L$  number linkers (Figure 4.1). If each domain can only consist of a single metal and linker, there are  $M \times L$  possible distinct domain compositions. In MOF chemistry, it is perfectly reasonable to synthesize isostructural domains with three different metals and linkers; in this case, we can envision preparing 9 compositionally distinct domains each with 1 type of metal and 1 type of linker (Figure 4.1A). We can next calculate the number of different multivariate sMOFs that could be constructed using this basis set of 9 domains. The simplest sMOF architecture is the binary domain core-shell system. The number of possible strata (domain) sequences in the multivariate family of core-shell MOFs would be  $[M \times L] \times [(M \times L) - 1]^{(S-1)}$ , where  $S$  is the number of strata. This formula accounts for and eliminates materials where both strata have identical composition, which by definition are not sMOFs. Of course, core-shell and other similar binary domain MOFs are well-established.<sup>72, 184-190</sup> A basis set of 9 different domains can be used to construct 72 binary domain core-shell MOFs, each having distinct domain composition and sequence. These different possibilities are represented by intersection points in a 2D coordinate system where each axis represents a stratum (black points at the bottom of Figure 4.1B). The *ica* binary domain variant is illustrated, where 'i' is the core domain and 'a' is the shell domain.

Significantly less explored are classes of sMOFs with more than 2 strata.<sup>185, 191-193</sup> Here, the formula for calculating the number of possible strata sequences in an sMOF with ' $S$ ' strata still applies, and we emphasize that it only accounts for those sMOFs in which adjacent strata have different compositions. If an sMOF contains adjacent strata with identical composition, the number of strata would be reduced by 1, and therefore it would not qualify as an sMOF with  $S$  strata. With this in mind, MOFs with three strata ( $S = 3$ ) constructed from our basis set of 9 domains can have 576 distinct sequences. These different possibilities can be visualized as coordinates in a 3D coordinate system where each axis represents one stratum (all points except the black points of Figure 4.1B;  $iCaCe$  is illustrated). The number of possible sMOF sequences grows exponentially as  $S$  increases: 36,864 unique strata sequences are possible in quinary domain sMOFs!

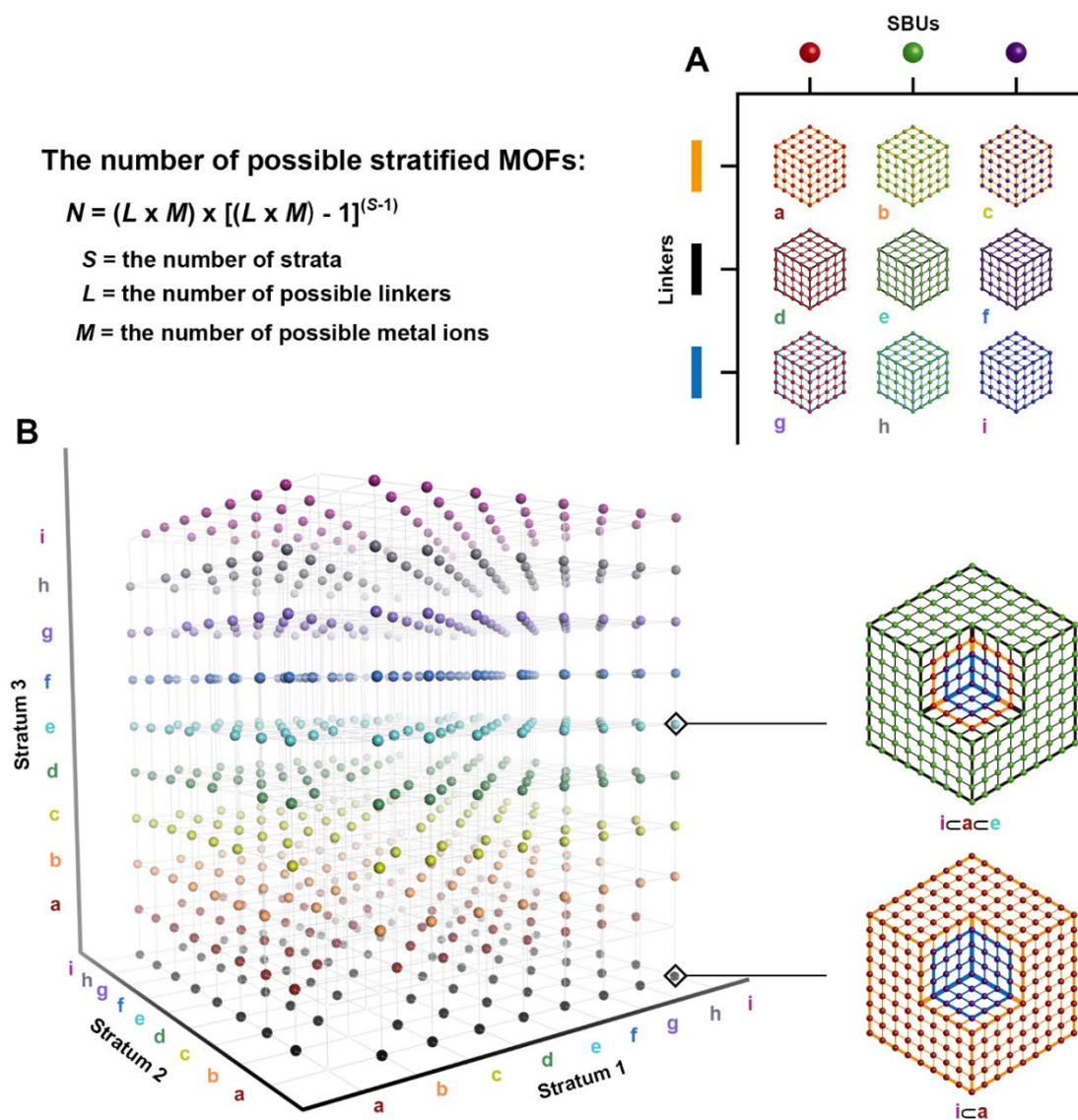


**Figure 4.1** Illustration of increased diversity and complexity in MTV sMOFs using domain building blocks.

In this work, we build a diverse library of UiO-67<sup>36</sup> (UiO, University of Oslo) sMOFs. We demonstrate systematic control over the combination and sequence of multiple domains. Ten different sMOFs containing up to three strata are synthesized via stepwise epitaxial growth. We demonstrate that individual strata can be specifically post-synthetically addressed and manipulated. The UiO-67 MOF and its analogues with **fcu** topology are an excellent platform for building a library of sMOFs due to their rich compositional diversity. The **fcu** MOFs features

highly stable  $M_6(OH)_4O_4(COO)_{12}$  ( $M = Zr(IV), Hf(IV), Ce(IV)$ ), or  $M_6(OH)_8(COO)_{12}^{2+}$  ( $M =$  Lanthanides (III)) secondary building units (SBUs) connected by dicarboxylate linkers, representing a rare example where the MOF structure is both amenable to a large number of different metal ions and organic functional groups without significant difference in lattice parameters.<sup>36, 94, 97-98</sup> These features potentially allow multiple domains to be integrated in a single particle via epitaxial growth. This new platform of multi-domain UiO-based MOF materials and the strategies outlined for their synthesis will lead to new opportunities in catalysis, separations, and sensing as well as the design of individual multi-domain MOF crystals that can simultaneously perform multiple functions.

## 4.2 RESULTS AND DISCUSSION

To examine feasibility and identify suitable reaction conditions, we first targeted sMOF particles having a UiO-67(Zr) core and a UiO-67(Hf) shell, denoted as UiO-67(Zr)@UiO-67(Hf). The distinct metal compositions in the core and shell would permit characterization of the stratified architecture using energy dispersive X-ray spectroscopy (EDS). Discrete truncated octahedral UiO-67(Zr) seed crystals having an average diameter of  $351 \pm 51$  nm (Figure 4.2A, C; PXRD pattern is shown in Figure 4.18 of 4.3 EXPERIMENTAL SECTION) were dispersed in a crystal growth solution prepared by dissolving  $Hf(O^iPr)_4$ , 1,1'-biphenyl-4,4'-dicarboxylic acid (H<sub>2</sub>-BPDC), and acetic acid in dimethylformamide (DMF) and then allowed to react at room temperature with gentle stirring. Product crystals (PXRD pattern is shown in Figure 4.19 of 4.3 EXPERIMENTAL SECTION) were collected, copiously washed with DMF, and then characterized using transmission electron microscopy (TEM) and scanning electron microscopy

EDS (SEM-EDS). TEM images show that the product MOF crystallites remain discrete through the reaction and the average diameter of crystallites increases to  $555\pm 70$  nm (Figure 4.2B, C). EDS line-scan data across single MOF particles (Figure 4.3) clearly show the formation of a binary domain sMOF with a core-shell architecture, as signified by the different line-scan profiles of Zr and Hf. The highest content of Hf is observed on the edge of a particle, while Zr is most concentrated in the center, confirming the formation of the target  $\text{UiO-67(Zr)}\subset\text{UiO-67(Hf)}$  sMOF particles. The stratified architecture of  $\text{UiO-67(Zr)}\subset\text{UiO-67(Hf)}$  is further confirmed by SEM-EDS mapping data (Figure 4.3), where Hf was detected at the entire area of a sMOF particle while Zr was only detected in the core. During epitaxial growth processes, homogeneous nucleation is often a competing reaction pathway that leads to undesired byproduct, in this case isolated  $\text{UiO-67(Hf)}$  particles. To evaluate the percentage of stratified MOF particles and homogeneous nucleation products, we examined 54 random crystallites using SEM-EDS line-scan. All particles examined were stratified crystals, indicating that homogeneous MOF nucleation is suppressed using the reported reaction conditions. To the best of our knowledge, this represents the first example of a multi-domain UiO-based MOF in which the domains are topologically identical.

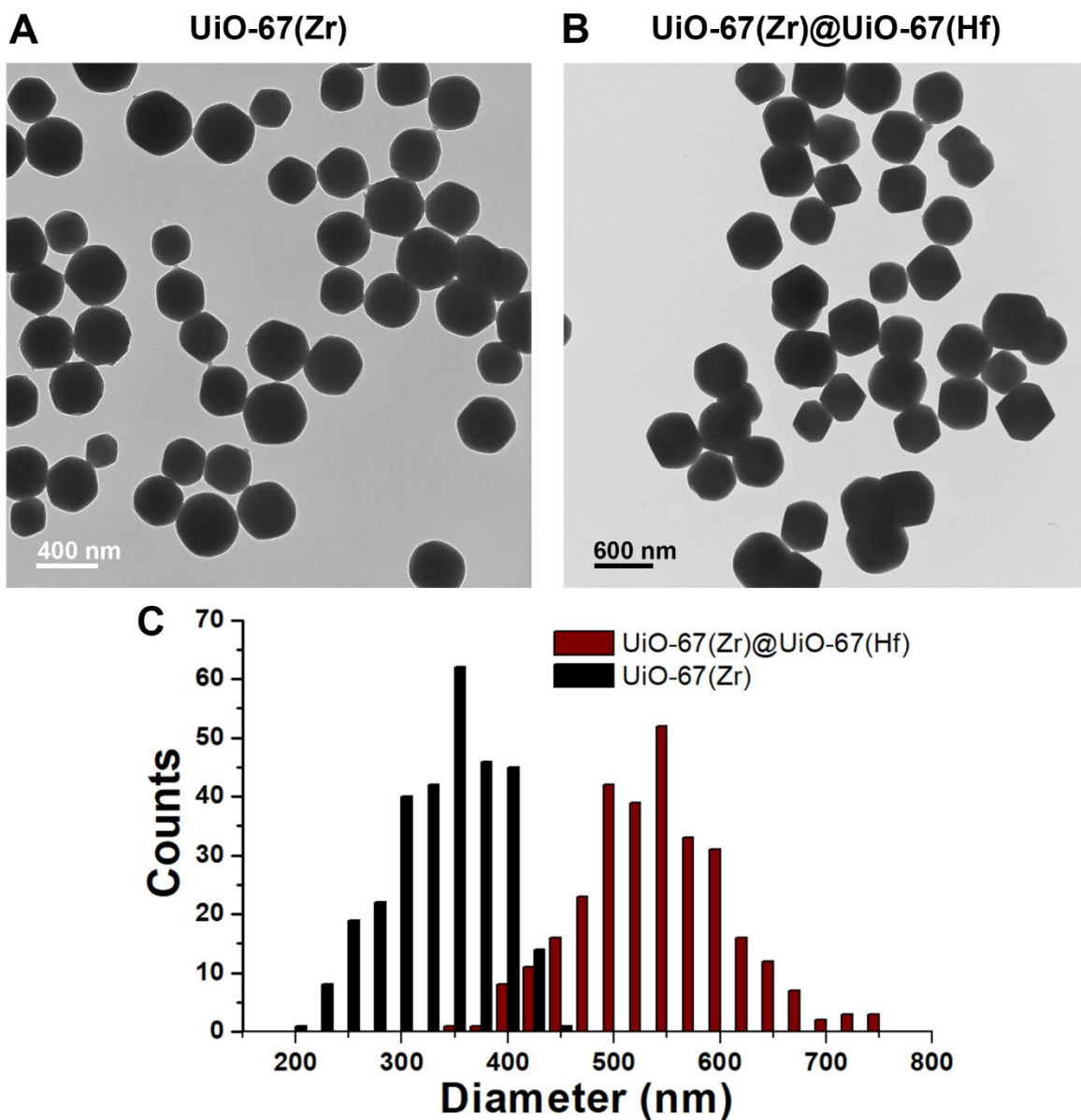


**Figure 4.2** (A) TEM image of UiO-67(Zr) seed crystallites with an average diameter of  $351 \pm 51$  nm; (B) TEM image of UiO-67(Zr)@UiO-67(Hf) crystallites with a diameter of  $555 \pm 70$  nm ; (C) size distributions (based on 300 counts) of UiO-67(Zr) seed crystallites (black) and UiO-67(Zr)@UiO-67(Hf) crystallites (red).

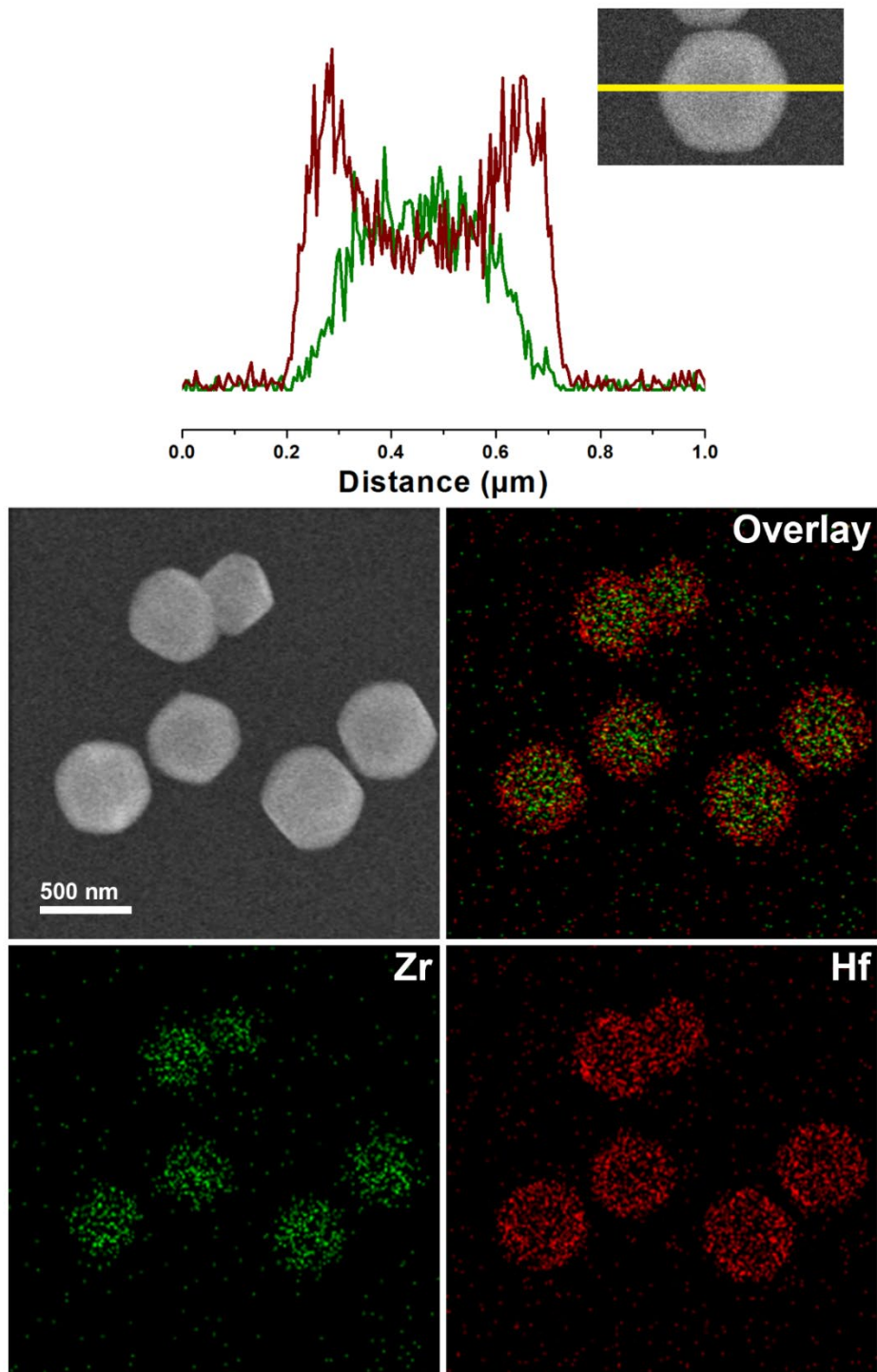


**Figure 4.3** SEM-EDS line-scan and mapping data of UiO-67(Zr)/UiO-67(Hf) (Zr, green; Hf, red). EDS line-scan and map data were generated using Zr L $\alpha$ 1 line at 2.0 keV, Hf M $\alpha$ 1 line at 1.6 keV.

Because spatial control of stratified domains may be important for controlling MOF functions in catalysis or separations, we next targeted UiO-67(Hf)@UiO-67(Zr), which has a reversed stratum order. Here, UiO-67(Hf) seed crystallites (PXRD pattern is shown in Figure 4.20 of 4.3 EXPERIMENTAL SECTION) were dispersed in a DMF solution containing  $Zr(O^iPr)_4$ ,  $H_2$ -BPDC, and acetic acid for epitaxial growth. An outer UiO-67(Zr) stratum encased the UiO-67(Hf) seeds to afford UiO-67(Hf)@UiO-67(Zr) (PXRD pattern is shown in Figure 4.21 of 4.3 EXPERIMENTAL SECTION), as evidenced by both EDS line-scan and mapping data (Figure 4.4).

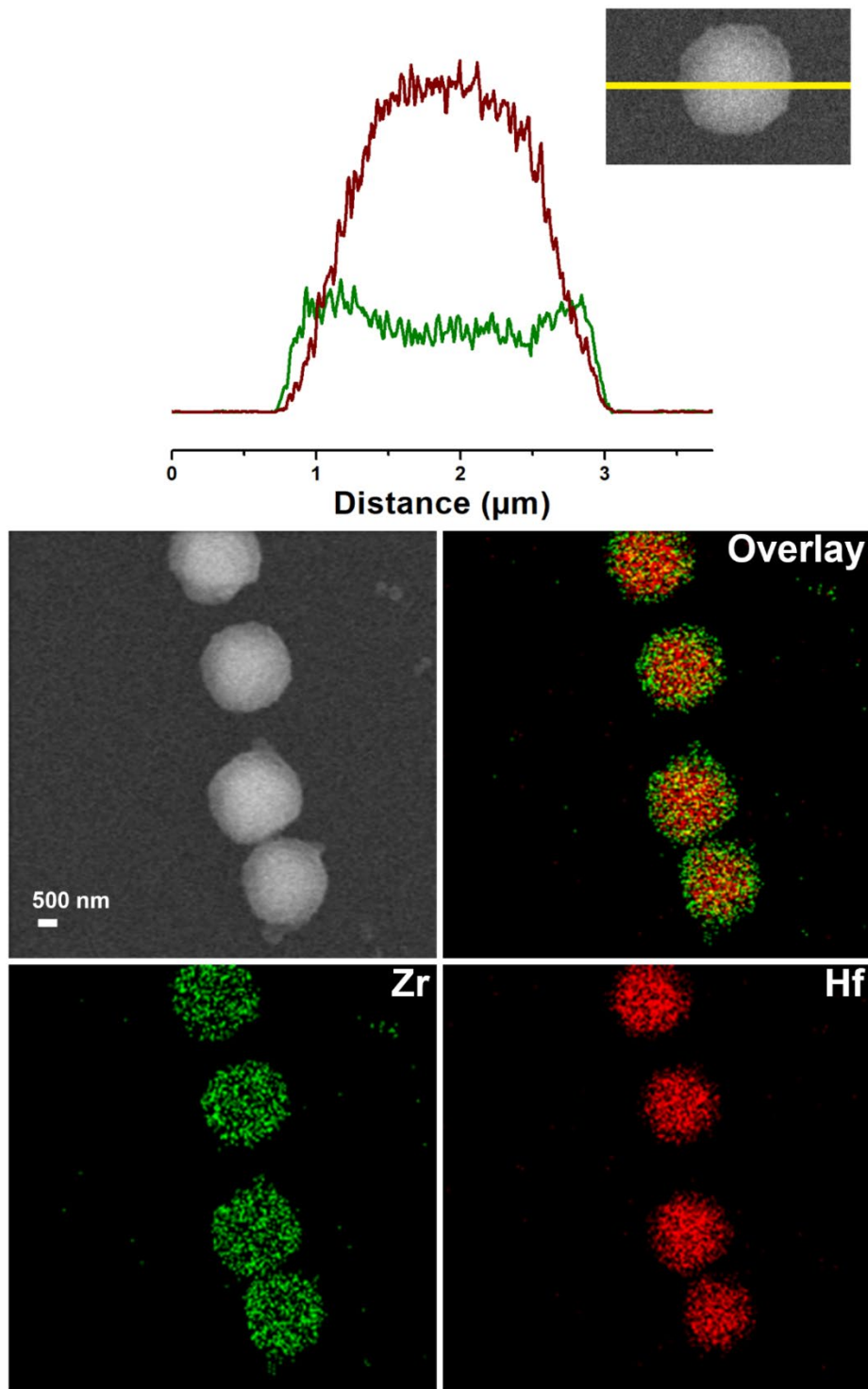


**Figure 4.4** SEM-EDS line-scan and mapping data of UiO-67(Hf)@UiO-67(Zr) (Zr, green; Hf, red). EDS line-scan and map data were generated using Zr L $\alpha$ 1 line at 2.0 keV, Hf M $\alpha$ 1 line at 1.6 keV.

We next sought to create a diverse family of UiO-67 sMOF particles by systematically altering different parameters such as organic functional groups, inorganic composition, and number of domains. The former can be controlled by using different functionalized linkers for each step of epitaxial growth. However, the epitaxial growth process could potentially be complicated by competing linker exchange processes.<sup>57, 59, 67, 194-195</sup> We envisioned two different scenarios. If the formation of a new stratum on seed particles outpaces the linker exchange process, the desired sMOF product may be obtained. Conversely, if linker exchange occurs at a much faster rate than stratum growth, uniform mixing of linkers throughout MOF particles is more likely, unless the linker exchange process is diffusion controlled whereby linker exchange at the MOF particle surface would occur faster than linker exchange near the particle center.<sup>195</sup> We performed a series of experiments to investigate if differentially functionalized strata can be established in the UiO-67 platform.

To visualize the distribution of functional groups in MOF particles after epitaxial growth, we introduced 2-iodo-1,1'-biphenyl-4,4'-dicarboxylic acid (H<sub>2</sub>-I-BPDC) to the synthesis of sMOFs. In this case, the distribution of iodo groups would be directly observable via EDS. We first aimed to synthesize I-UiO-67(Zr)⊂UiO-67(Hf). An outer UiO-67(Hf) stratum was grown onto octahedral I-UiO-67(Zr) seeds with an average edge length of 290 ± 19 nm (Figure 4.5A, C; PXRD PATTERN is shown in Figure 4.22 of 4.3 EXPERIMENTAL SECTION). The average edge length of the product crystallites was 371 ± 20 nm (Figure 4.5B, C; PXRD PATTERN and solution <sup>1</sup>H NMR are shown in Figures 4.23 and 4.24 of 4.3 EXPERIMENTAL SECTION), strongly supporting epitaxial growth over homogeneous nucleation. EDS line-scan and mapping data (Figure 4.6) show that Zr and I are localized in the core stratum, while Hf is mainly distributed

in the surface stratum, supporting the formation of two differentially functionalized domains within a single MOF particle.

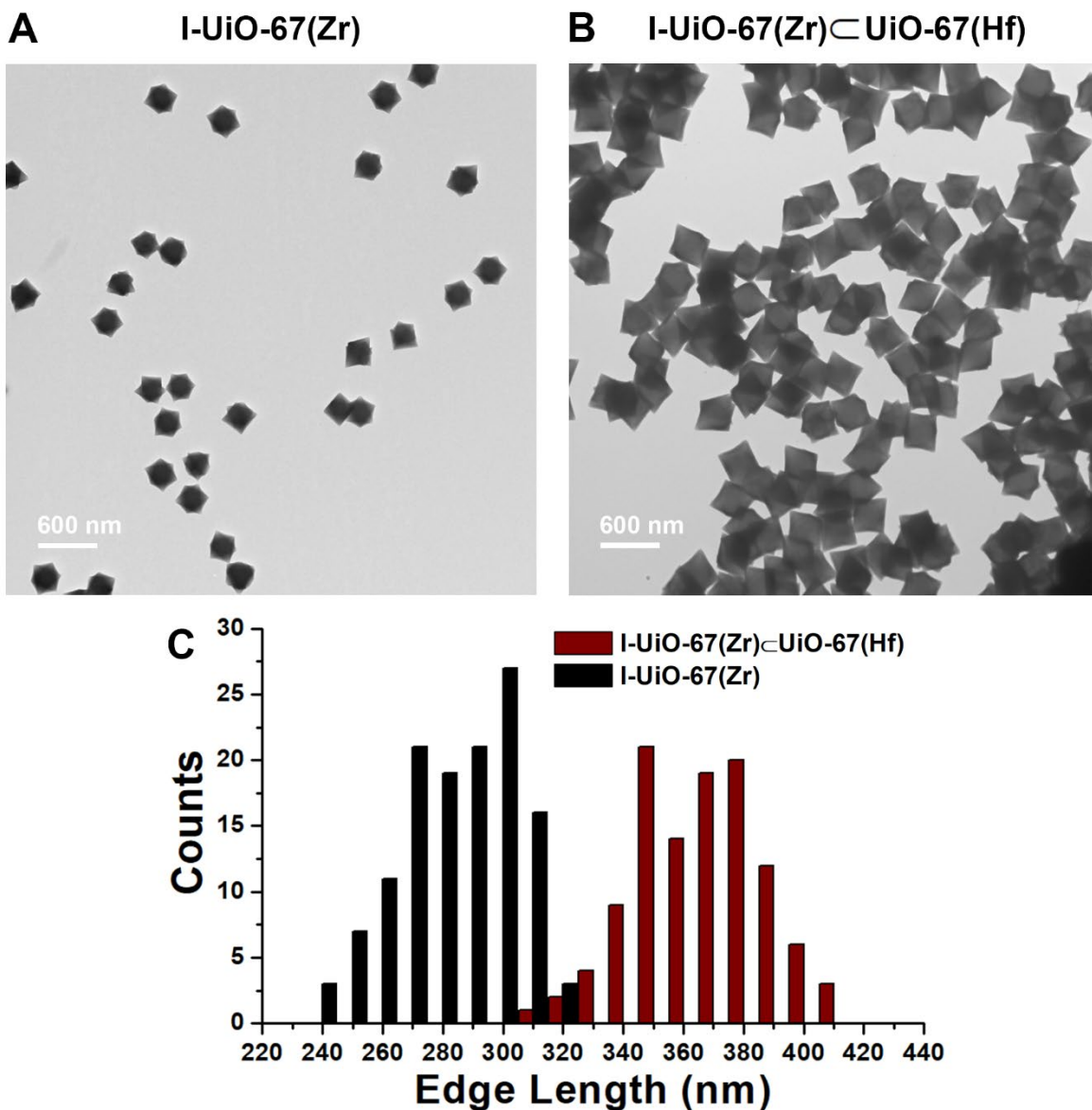


**Figure 4.5** (A) TEM image of octahedral I-UiO-67(Zr) seed crystallites with an average edge length of  $290 \pm 19$  nm; (B) TEM image of octahedral I-UiO-67(Zr)⊂UiO-67(Hf) crystallites with an average edge length of  $371 \pm 20$  nm; (C) size distributions (based on 100 counts) of I-UiO-67(Zr) seed crystallites (black) and I-UiO-67(Zr)⊂UiO-67(Hf) crystallites (red).

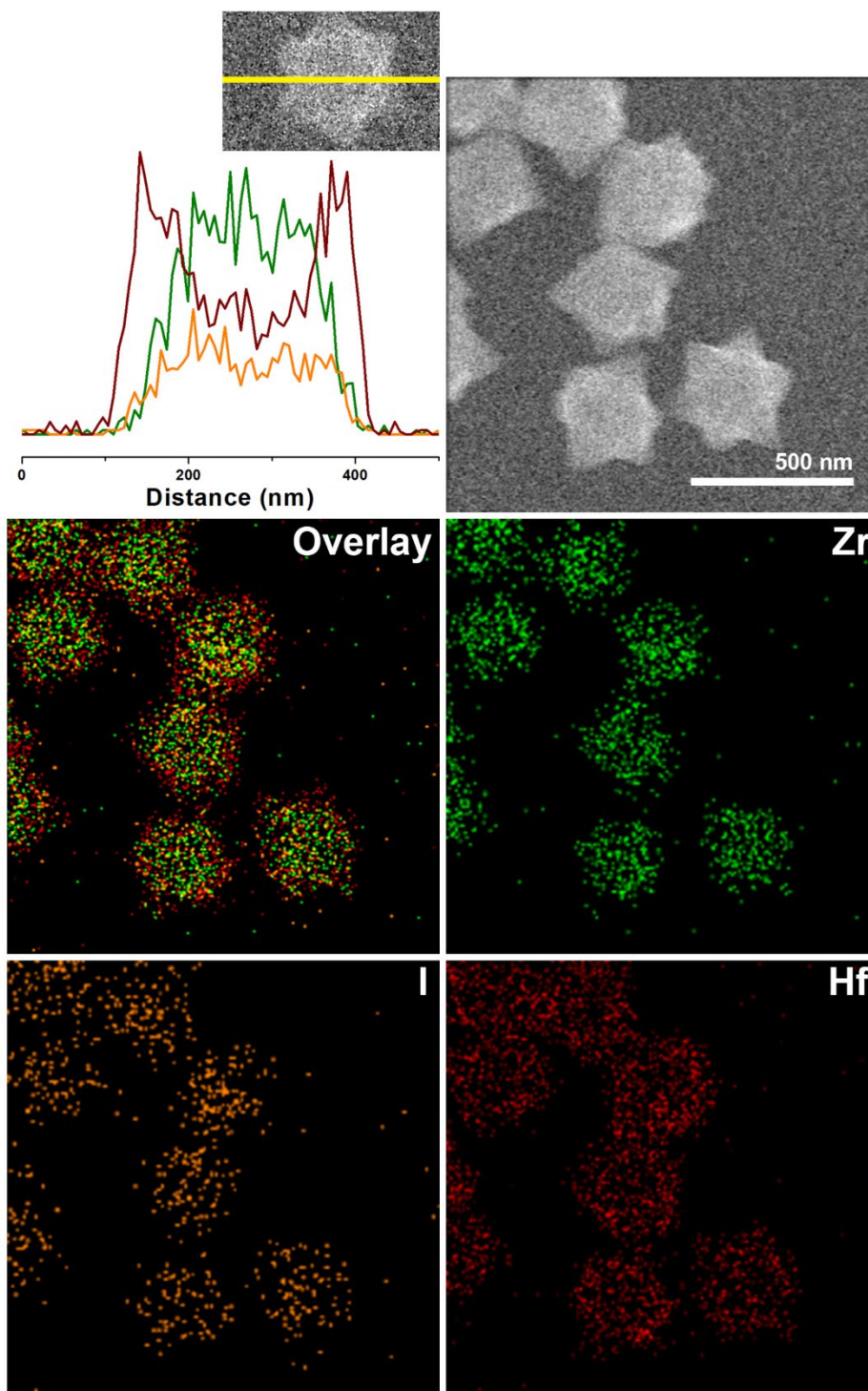


**Figure 4.6** SEM-EDS line-scan and mapping data of I-Uio-67(Zr)@Uio-67(Hf) (Zr, green; I, orange; Hf, red). EDS line-scan and map data were generated using Zr L $\alpha$ 1 line at 2.0 keV, Hf M $\alpha$ 1 line at 1.6 keV, and I L $\alpha$ 1 at 3.9 keV.

We next aimed to synthesize stratified homometallic MOF particles containing differentially functionalized strata.  $\text{NH}_2\text{-UiO-67(Zr)}\subset\text{I-UiO-67(Zr)}$  was chosen as a target, and  $\text{I-UiO-67(Zr)}$  was grown epitaxially onto  $\text{NH}_2\text{-UiO-67(Zr)}$  seeds (PXRD patterns and  $^1\text{H NMR}$  are shown in Figure 4.25 – 4.27 of 4.3 EXPERIMENTAL SECTION). EDS line-scan data of the product crystallites indicate higher iodine content on the edge than at the center (Figure 4.7), supporting a shell and a core that are mainly functionalized with  $-\text{I}$  and  $-\text{NH}_2$ , respectively. It is worth noting that the color of the crystal growth solution changed from almost colorless at the outset of epitaxial growth to slightly yellow at the end of the reaction, indicative of linker exchange between the yellow 2-amino-1,1'-biphenyl-4,4'-dicarboxylate ( $\text{NH}_2\text{-BPDC}$ ) linkers in  $\text{NH}_2\text{-UiO-67(Zr)}$  seeds with the colorless  $\text{I-BPDC}$  in solution. We and others have observed that core-shell and gradient structures can be directly obtained via diffusion-controlled ligand exchange processes on large MOF crystals.<sup>180, 195</sup> Therefore, we further investigated whether formation of  $\text{NH}_2\text{-UiO-67}\subset\text{I-UiO-67}$  could result solely from linker exchange.  $\text{NH}_2\text{-UiO-67(Zr)}$  crystals were subjected to reaction conditions free of Zr precursor but otherwise identical to the previous epitaxial growth conditions. Under these conditions, the epitaxial growth pathway is eliminated, and linker exchange becomes the only route toward multi-domain crystallites. Proton nuclear magnetic resonance ( $^1\text{H NMR}$ ) data of the digested product shows the presence of both  $\text{NH}_2\text{-BPDC}$  and  $\text{I-BPDC}$ , indicating partial linker exchange (Figure 4.28 of 4.3 EXPERIMENTAL SECTION). EDS line-scan data of the product crystallites (Figure 4.8) reveal a different distribution profile of iodine compared to Figure 4.7, indicating relatively even mixing of the two different linkers throughout the crystals. Therefore, we conclude that epitaxial growth is responsible for the formation of differentially functionalized strata in this case.

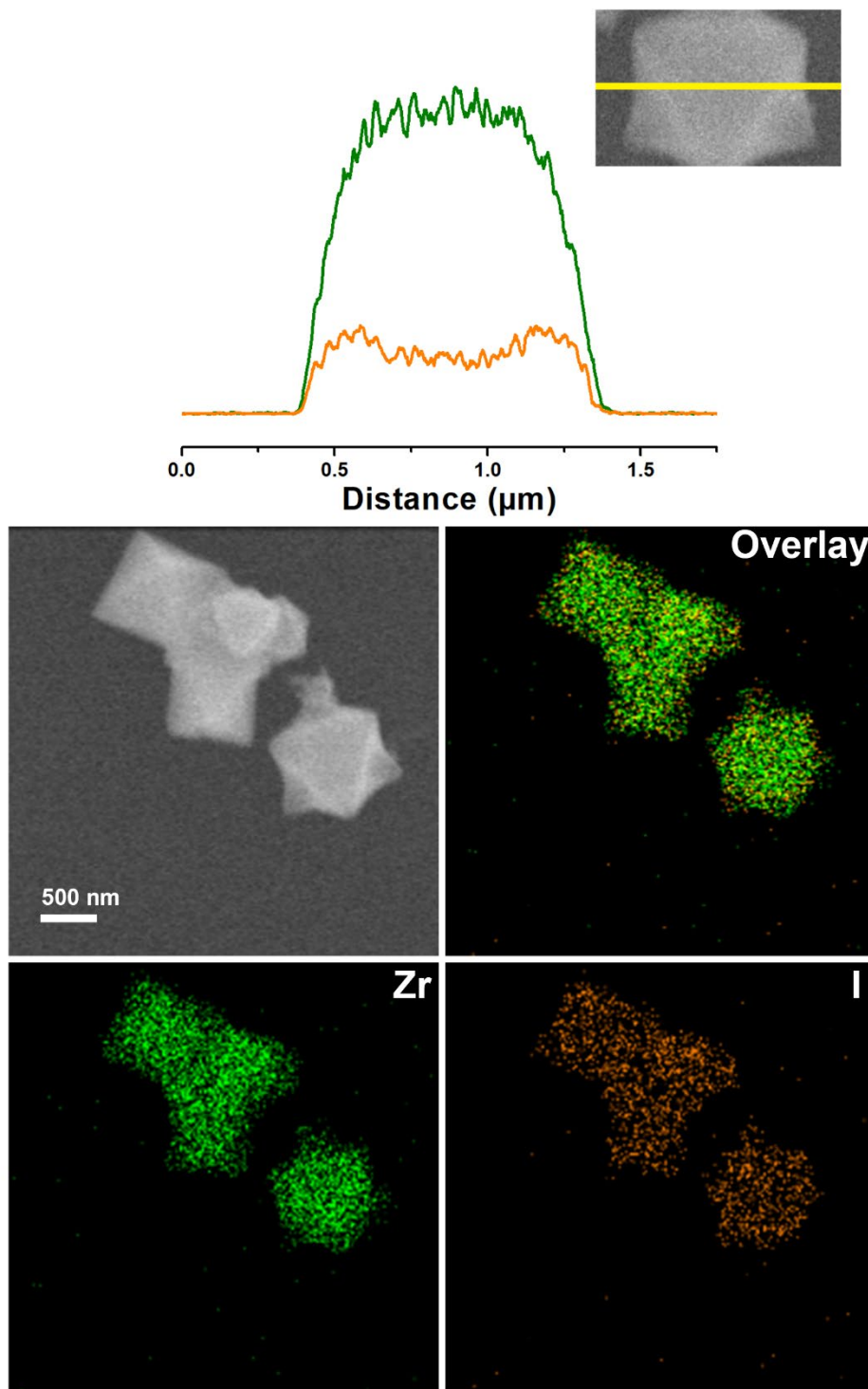


**Figure 4.7** SEM-EDS line-scan and mapping data of  $\text{NH}_2\text{-UiO-67(Zr)}@I\text{-UiO-67(Zr)}$  (Zr, green; I, orange). EDS line-scan and map data were generated using Zr  $L\alpha_1$  line at 2.0 keV, and I  $L\alpha_1$  at 3.9 keV.

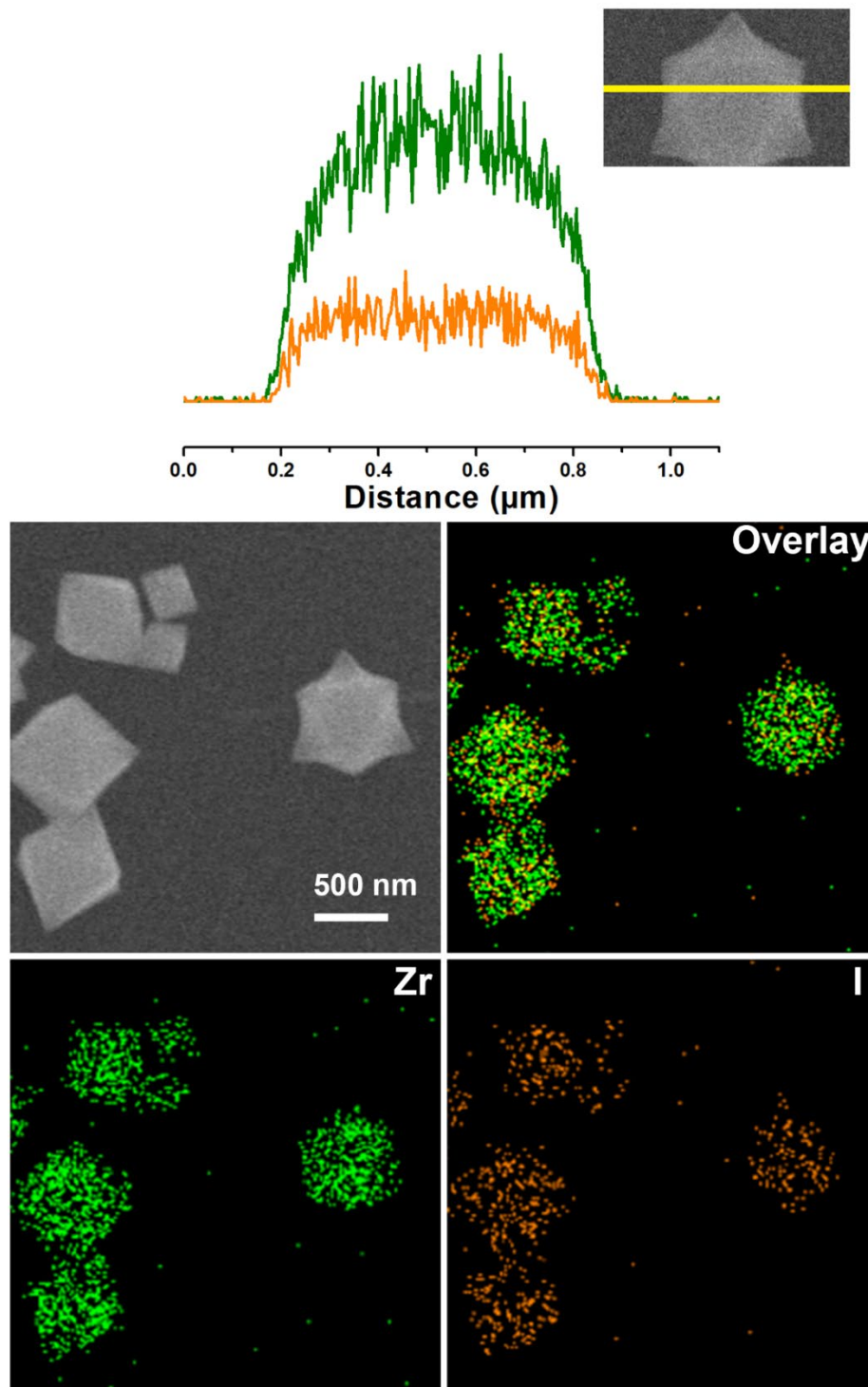


**Figure 4.8** SEM-EDS line-scan and mapping data of crystallites formed after a linker exchange reaction between  $\text{NH}_2\text{-UiO-67(Zr)}$  and  $\text{H}_2\text{-I-BPDC}$  (Zr, green; I, orange). EDS line-scan and map data were generated using Zr  $L\alpha_1$  line at 2.0 keV, and I  $L\alpha_1$  at 3.9 keV.

UiO-67 sMOFs with more than two domains can be synthesized by conducting multiple steps of epitaxial growth using different reaction precursors. As a proof of principle, we prepared and characterized ternary domain sMOF particles featuring three concentric strata, denoted respectively as UiO-67(Zr)⊂UiO-67(Hf)⊂UiO-67(Zr) (Figure 4.9, PXRD Pattern is shown in Figure 4.29 of 4.3 EXPERIMENTAL SECTION) and I-UiO-67(Zr)⊂UiO-67(Hf)⊂NH<sub>2</sub>-UiO-67(Zr) (Figure 4.10, PXRD pattern and <sup>1</sup>H NMR are shown in Figure 4.30-4.31 of 4.3 EXPERIMENTAL SECTION). EDS line-scan data confirm the concentric distribution of the three domains. Successful growth of the third stratum in both cases can be corroborated by the appearance of ‘shoulder’ features in the Zr line scan data which are not present in the parent core-shell starting materials (Figures 4.3 and 4.6) used for preparing these ternary domain sMOFs. These sMOFs represent 2 out of the 150 different possible ternary domain sMOF sequences achievable by combining BPDC, NH<sub>2</sub>-BPDC, I-BPDC and M<sub>6</sub>O<sub>4</sub>(OH)<sub>4</sub>(COO)<sub>12</sub> (M = Zr(IV), Hf(IV)). I-UiO-67(Zr)⊂UiO-67(Hf)⊂NH<sub>2</sub>-UiO-67(Zr) is one of the most compositionally complex MOFs prepared to date, containing 5 different components<sup>42-43, 133, 196-198</sup> organized in three different domains, and it clearly demonstrates the degree of structural and compositional complexity that can be achieved using domain building blocks. In principle, additional strata could be grown in subsequent steps to achieve even higher order domain MOFs with higher levels of compositional complexity.

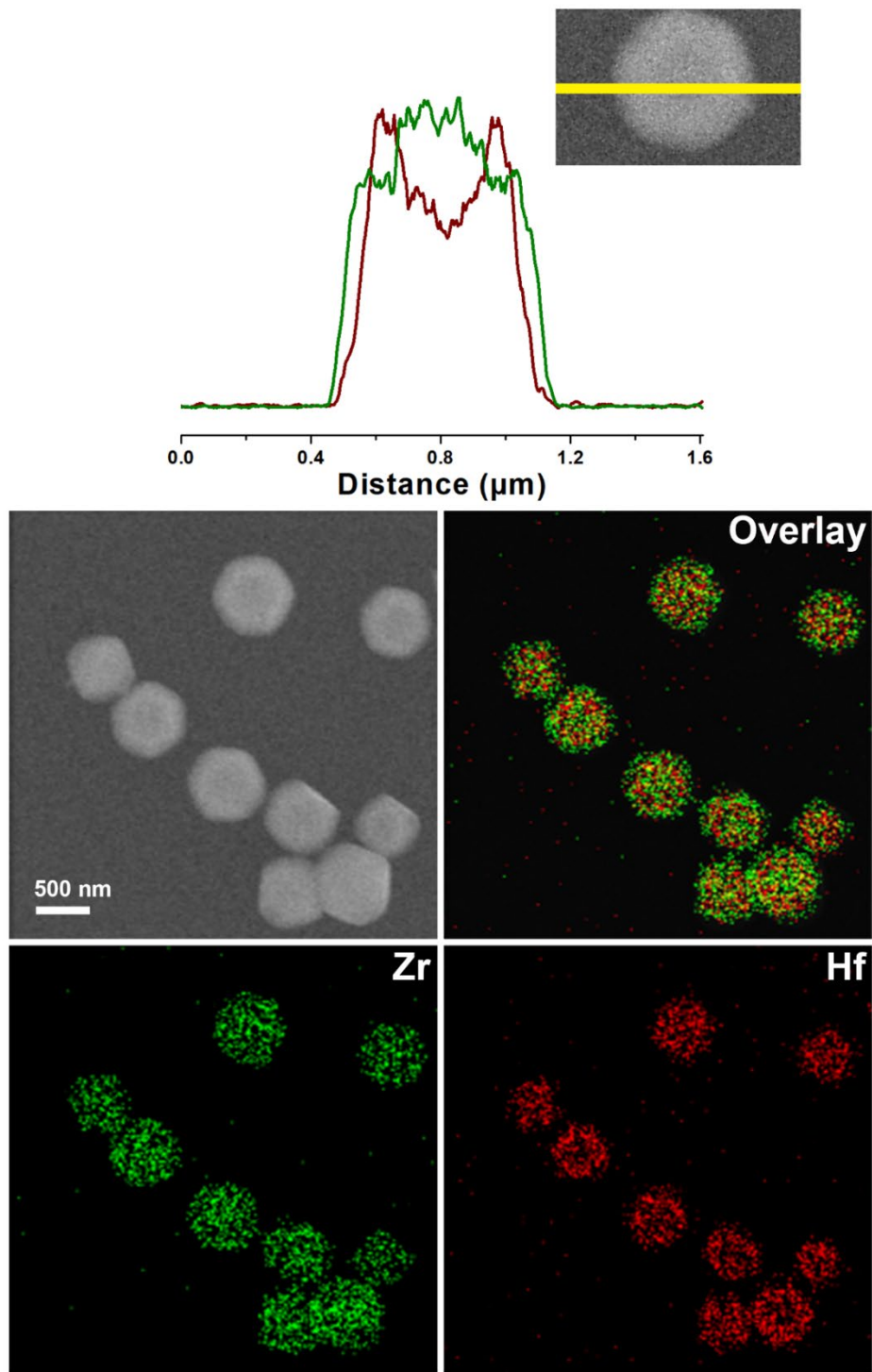


**Figure 4.9** SEM-EDS characterization of UiO-67(Zr)@UiO-67(Hf)@UiO-67(Zr) (Zr, green; Hf, red). EDS line-scan and map data were generated using Zr L $\alpha$ 1 line at 2.0 keV, and Hf M $\alpha$ 1 line at 1.6 keV.

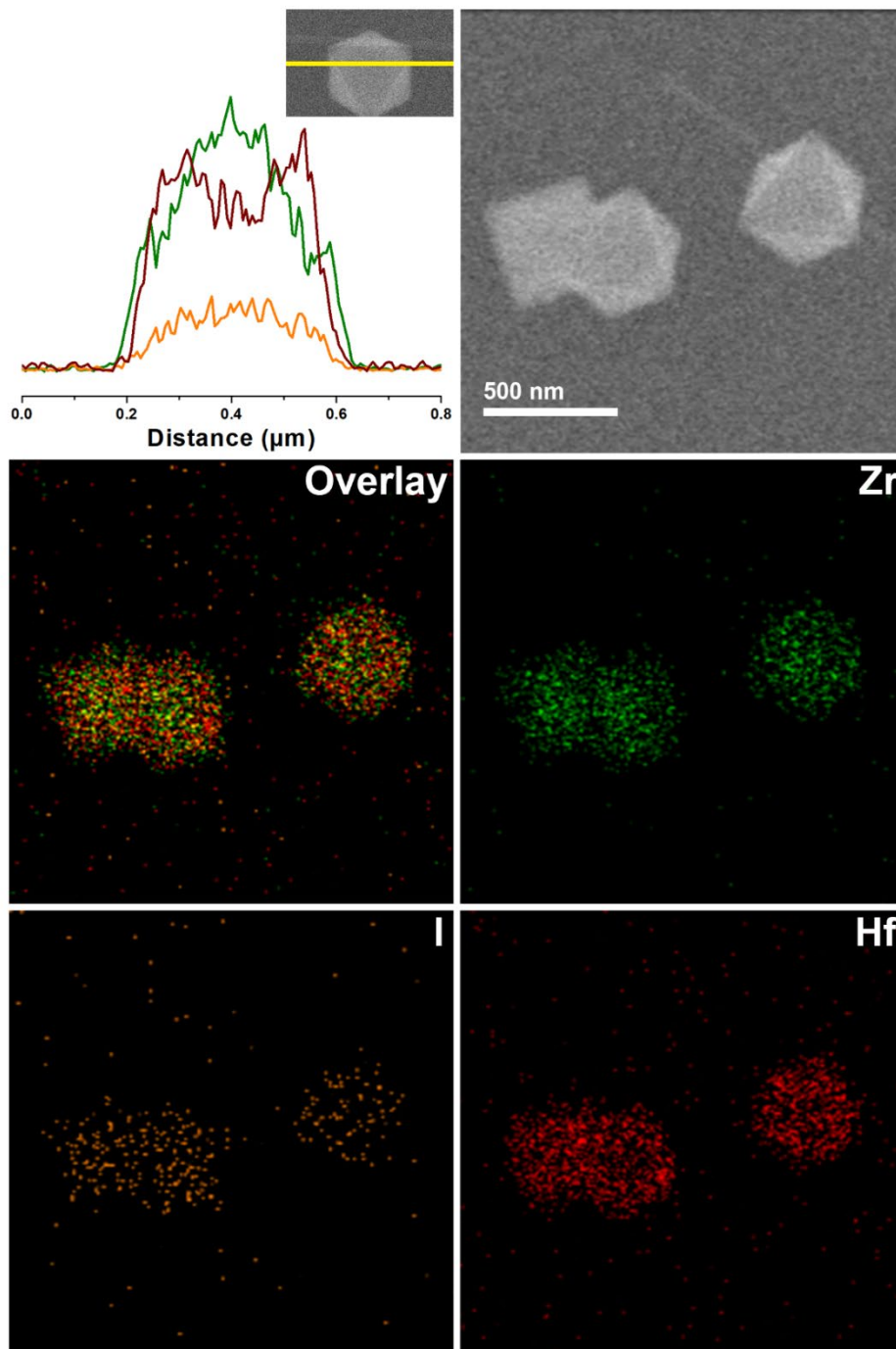


**Figure 4.10** SEM-EDS characterization of I-UiO-67(Zr)@UiO-67(Hf)@NH<sub>2</sub>-UiO-67(Zr) (Zr, green; I, orange; Hf, red). EDS line-scan and map data were generated using Zr L $\alpha$ 1 line at 2.0 keV, Hf M $\alpha$ 1 line at 1.6 keV, and I L $\alpha$ 1 at 3.9 keV.

We recognize that the structural integrity of sMOFs may eventually be compromised by linker exchange reactions as an increasing number of cycles of epitaxial growth are applied. The sMOFs, featuring well defined domains, may be considered kinetic products of MTV-MOFs. Given enough time for linker exchange reactions to proceed, MTV-MOFs with more evenly mixed linkers may form, as they may be entropically favored. Therefore, suppressing linker exchange during epitaxial growth is critically important in the synthesis of sMOFs. We hypothesized that linker exchange can be suppressed by judiciously choosing organic linkers with proper steric demand. When the linker molecules in the epitaxial growth solution are too large to enter the pores of MOF seed crystallites, the competing linker exchange process can be limited to the external surface, which is expected to be slow and does not negate the formation of stratified domains. Once the epitaxial growth is initiated, linker exchange reactions on the crystallite surface would be halted, as the internal strata may no longer be accessible to linkers in solution. To test this hypothesis, we prepared seed crystallites, denoted as Bpy-UiO-67(Zr) (PXRD pattern is shown in Figure 4.32 of 4.3 EXPERIMENTAL SECTION), using 2,2'-bipyridine-5,5'-dicarboxylic acid (H<sub>2</sub>-BpyDC) and ZrCl<sub>4</sub> as the precursors. Epitaxial growth reactions on Bpy-UiO-67(Zr) seeds were then performed using H<sub>2</sub>BPDC and a H<sub>2</sub>-NH<sub>2</sub>-BPDC derivative functionalized with a Boc-Proline residue<sup>199</sup> (H<sub>2</sub>-Pro-BPDC), respectively, two linkers with significantly different steric demand. The strata integrity of the resulting sMOFs, denoted as Bpy-UiO-67(Zr)⊂UiO-67(Zr) and Bpy-UiO-67(Zr)⊂Pro-UiO-67(Zr) (PXRD patterns, <sup>1</sup>H NMR and TEM images are shown in Figures 4.33-4.36 of 4.3 EXPERIMENTAL SECTION), was evaluated by probing the spatial distribution of BpyDC linkers in the crystallites. To visualize the spatial distribution of BpyDC, we performed postsynthetic metalation reactions on sMOFs with PdCl<sub>2</sub>(CH<sub>3</sub>CN)<sub>2</sub> in acetonitrile. Control experiments were also performed to ensure that Pd (II) specifically binds to BpyDC

(Figures 4.37-4.38 of 4.3 EXPERIMENTAL SECTION). The spatial distribution of Pd within the crystallites should reflect the location of the BpyDC linkers.

The metalated sMOFs, denoted as BpyPd-UiO-67(Zr)⊂UiO-67(Zr) and BpyPd-UiO-67(Zr)⊂Pro-UiO-67(Zr) (Figures 4.39-4.42 of 4.3 EXPERIMENTAL SECTION), visualized using scanning transmission electron microscopy high angle annular dark field imaging (STEM-HAADF), clearly exhibited two distinct strata, with bright core domains and darker shell domains (Figure 4.11A, C). STEM-EDS data of BpyPd-UiO-67(Zr)⊂UiO-67(Zr) further revealed an appreciable amount of Pd present in the outer stratum with an abrupt increase in Pd content across the interface of the two strata (Figures 4.11B and 4.12). In this case, when BPDC linker is used for epitaxial growth, it can readily diffuse into the seed crystal and displace BpyDC via linker exchange. The displaced BpyDC in solution can then incorporate into the growing outer stratum via epitaxial growth or linker exchange. Although BpyPd-UiO-67(Zr)⊂UiO-67(Zr) have largely differentially functionalized domains, a non-trivial degree of linker exchange ostensibly occurred. In contrast, EDS data of BpyPd-UiO-67(Zr)⊂Pro-UiO-67(Zr) show almost no Pd present in the outer stratum (Figures 4.11D and 4.13). We can infer from these data that very little linker exchange occurs during the epitaxial growth in this case. The suppression of linker exchange can be attributed to the steric bulk of the H<sub>2</sub>-Pro-BPDC linker. Based on the above results, we contend that undesirable linker exchange pathways can be successfully suppressed by judicious selection of linkers in sMOF syntheses. Significantly, we also note that the Pd metalation studies indicate that sMOFs can be designed to selectively incorporate or adsorb chemical species at specific domains within a MOF crystal and demonstrate that different domains can be designed for different tasks or functions.

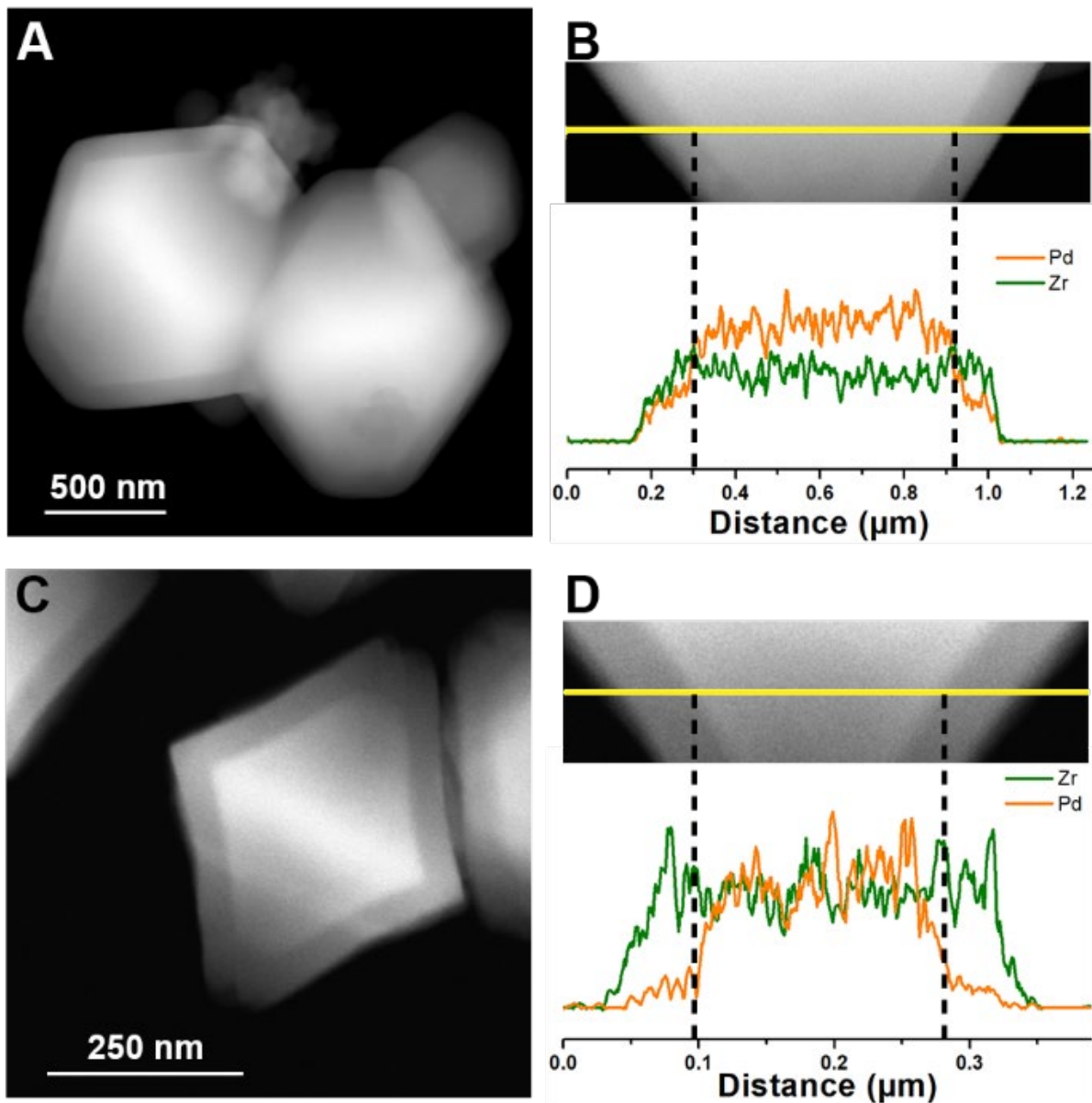
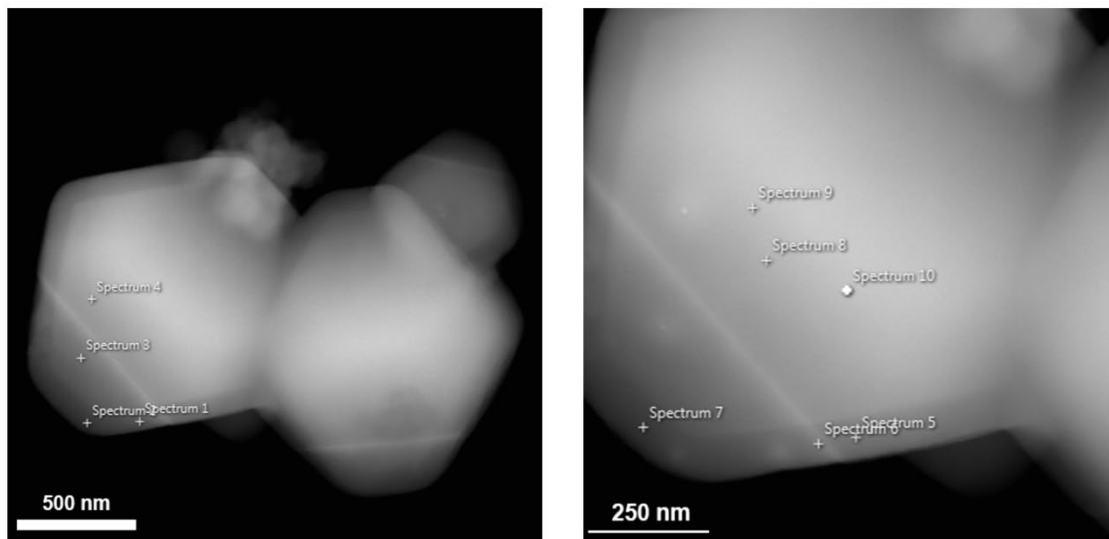
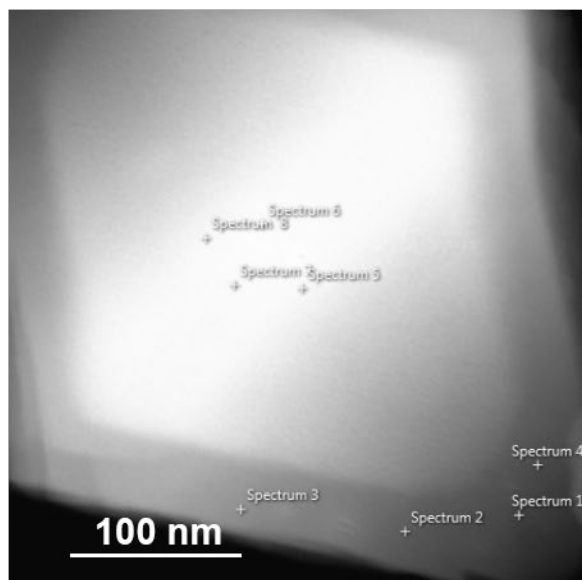


**Figure 4.11** Characterization of BpyPd-UiO-67(Zr)⊂UiO-67(Zr) and BpyPd-UiO-67(Zr)⊂Pro-UiO-67(Zr). STEM-HAADF image of BpyPd-UiO-67(Zr)⊂UiO-67(Zr) (A); STEM-EDS line-scan data of BpyPd-UiO-67(Zr)⊂UiO-67(Zr) (B); STEM-HAADF image of BpyPd-UiO-67(Zr)⊂Pro-UiO-67(Zr) (C); STEM-EDS line-scan data of BpyPd-UiO-67(Zr)⊂Pro-UiO-67(Zr) (D). EDS line-scan data were generated using Zr K $\alpha$ 1 line at 15.7 keV and Pd L $\alpha$ 1 line at 2.8 keV.



Site number	Site Location	Zr/Pd Ratio
1	Shell	1: 0.201
2	Shell	1: 0.206
3	Core	1: 0.535
4	Core	1: 0.725
5	Shell	1: 0.222
6	Shell	1: 0.211
7	Shell	1: 0.199
8	Core	1: 0.831
9	Core	1: 0.819
10	Core	1: 0.989

**Figure 4.12** Zr:Pd ratios at different points in a BpyPd-UiO-67(Zr)@UiO-67(Zr) crystal determined from STEM-EDS spectra using Zr K $\alpha$ 1 at 15.7 keV and Pd L $\alpha$ 1 at 2.8 keV.



Site number	Point Location	Pd/Zr Ratio
1	Shell	0:1
2	Shell	0:1
3	Shell	0.08:1
4	Shell	0:1
5	Core	0.62:1
6	Core	0.85:1
7	Core	0.84:1
8	Core	0.75:1

**Figure 4.13** Pd:Zr ratios at different points in a BpyPd-UiO-67(Zr)@UiO-67(Zr) crystal determined from STEM-EDS spectra using Zr K $\alpha$ 1 at 15.7 keV and Pd L $\alpha$ 1 at 2.8 keV.

In sMOFs, each domain is a functional module. Inner modules are encapsulated by outer modules. This modular design can be further developed to incorporate other types of functional modules beyond MOFs, such as nanoparticles (NPs).<sup>200-201</sup> An attractive feature of existing MOF syntheses is their compatibility with various substrates and surfaces, which allows for preparation of composite hybrid materials.<sup>200-202</sup> We were therefore motivated to challenge the syntheses reported herein to determine whether they could be used to construct sMOF architectures around NPs. The resulting composite materials with NPs embedded within sMOFs could potentially have more sophisticated functions. Here we show that three different kinds of plasmonic nanoparticles

(50 nm  $\text{Cu}_{2-x}\text{Se}$  NPs ( $x = 0.75$ ), 13 nm Au NPs, and 40 nm Ag NPs) (TEM images are shown in Figures 4.43-4.45 of 4.3 EXPERIMENTAL SECTION) can be encapsulated in  $\text{UiO-67(Zr)}\subset\text{UiO-67(Hf)}$ . Encapsulation was achieved by adding polyvinylpyrrolidone (PVP)-coated NPs to the  $\text{UiO-67(Zr)}$  synthesis solution followed by epitaxial growth of a  $\text{UiO-67(Hf)}$  outer stratum (Figures 4.14-4.16; PXRD patterns and TEM images are shown in Figure 4.46-4.54 of 4.3 EXPERIMENTAL SECTION).<sup>203</sup> The successful encapsulation of NPs in stratified MOF composites was confirmed by STEM-HAADF images and STEM-EDS mapping (Figures 4.14-4.16). To the best of our knowledge, the  $\text{Cu}_{2-x}\text{Se}\subset\text{UiO-67(Zr)}\subset\text{UiO-67(Hf)}$  reported here is the first demonstration that pre-synthesized metal chalcogenide nanoparticles can be encapsulated in UiO MOFs. In addition, the plasmonic properties of Au NPs and Ag NPs were retained after encapsulation, as evidenced by the UV/vis spectra of  $\text{Au}\subset\text{UiO-67(Zr)}\subset\text{UiO-67(Hf)}$  and  $\text{Ag}\subset\text{UiO-67(Zr)}\subset\text{UiO-67(Hf)}$  (Figure 4.17).

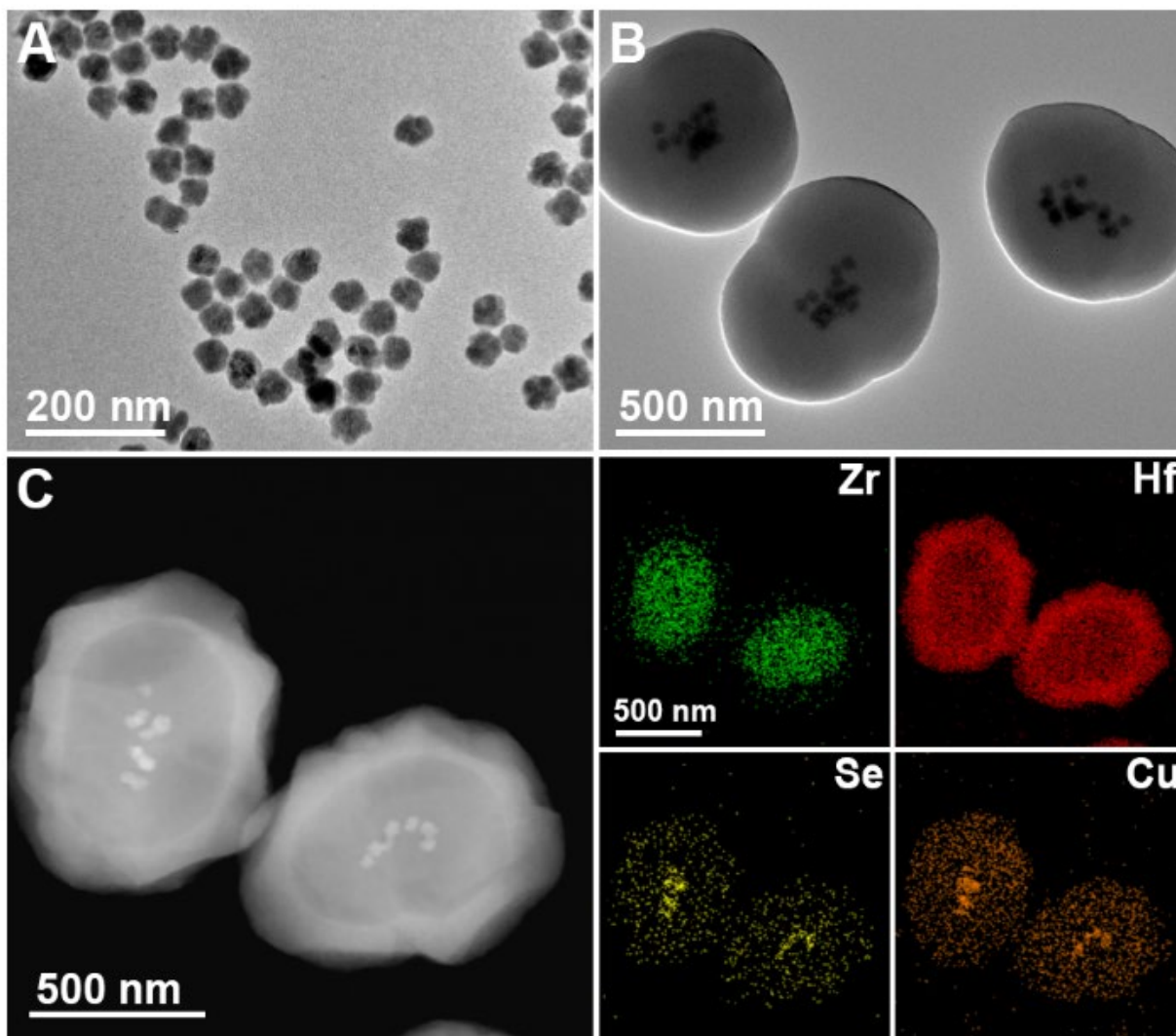


**Figure 4.14** Characterization of  $\text{Cu}_{2-x}\text{Se}@UiO-67(\text{Zr})@UiO-67(\text{Hf})$ . TEM image of  $\text{Cu}_{2-x}\text{Se}$  nanoparticles (A); TEM image of  $\text{Cu}_{2-x}\text{Se}@UiO-67(\text{Zr})$  (B); STEM-EDS mapping of  $\text{Cu}_{2-x}\text{Se}@UiO-67(\text{Zr})@UiO-67(\text{Hf})$  (C). EDS Maps were generated using Zr  $\text{K}\alpha_1$  line at 15.7 keV, Hf  $\text{M}\alpha_1$  line at 1.6 keV, Cu  $\text{L}\alpha_1$  line at 0.9 keV and Se  $\text{K}\alpha_1$  line at 11.2 keV.

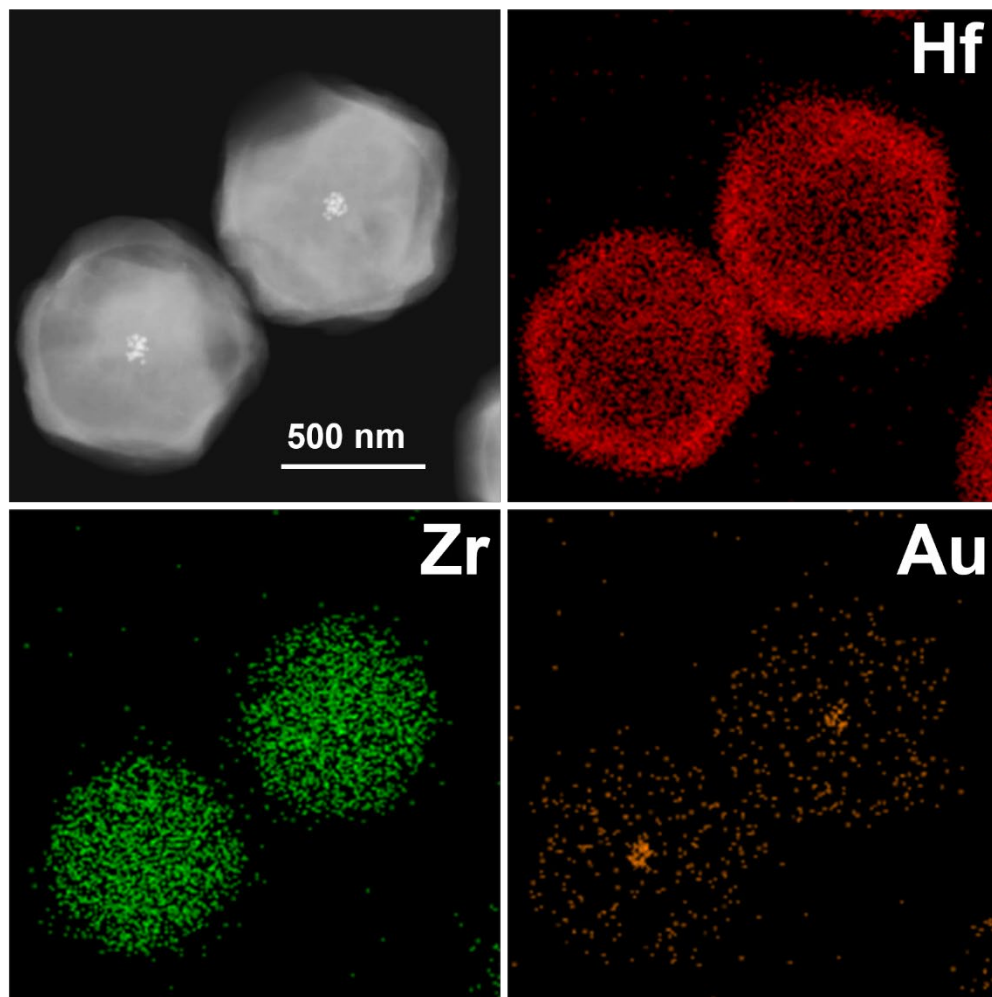


**Figure 4.15** STEM-EDS characterization of Au@UiO-67(Zr)@UiO-67(Hf). EDS map data were generated using Zr K $\alpha$ 1 line at 15.7 keV, Hf M $\alpha$ 1 line at 1.6 keV, and Au L $\alpha$ 1 line at 9.7 keV.

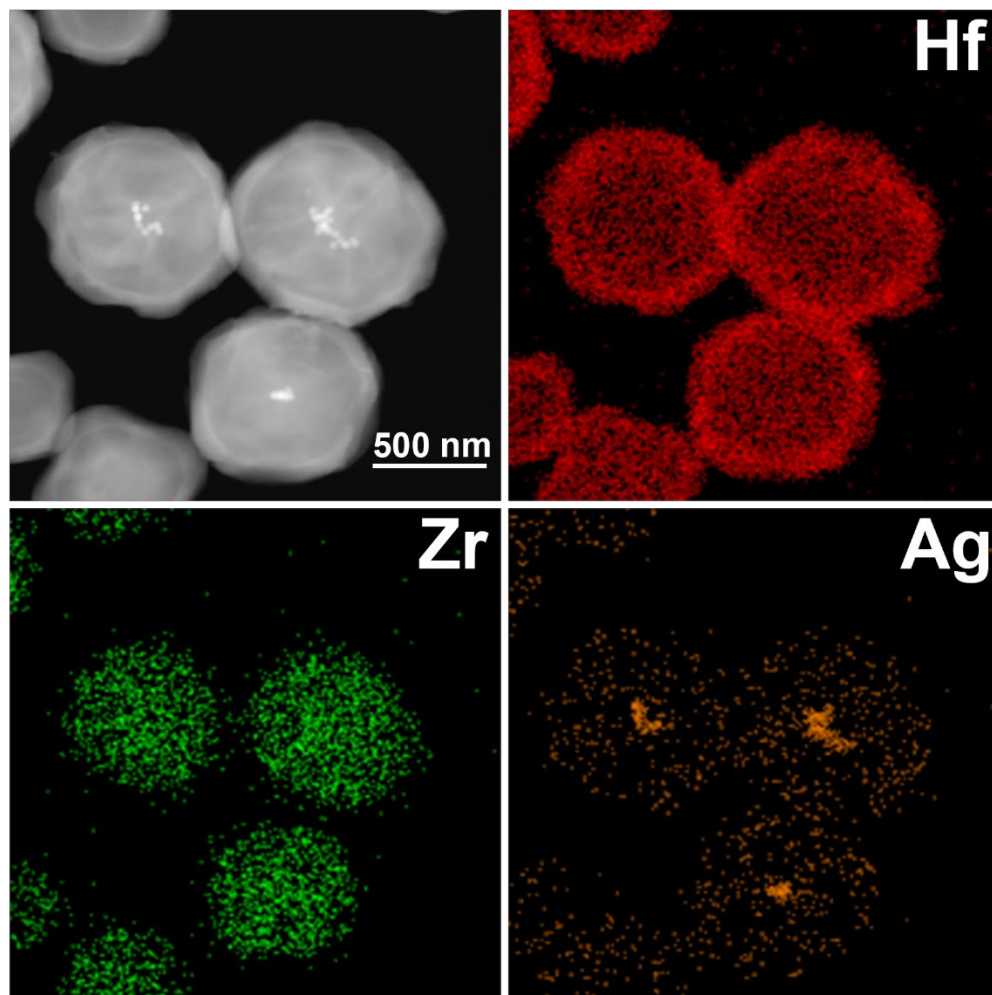


**Figure 4.16** STEM-EDS characterization of Ag@UiO-67(Zr)@UiO-67(Hf). EDS map data were generated using Zr K $\alpha$ 1 line at 15.7 keV, Hf M $\alpha$ 1 line at 1.6 keV, and Ag L $\alpha$ 1 line at 3.0 keV.

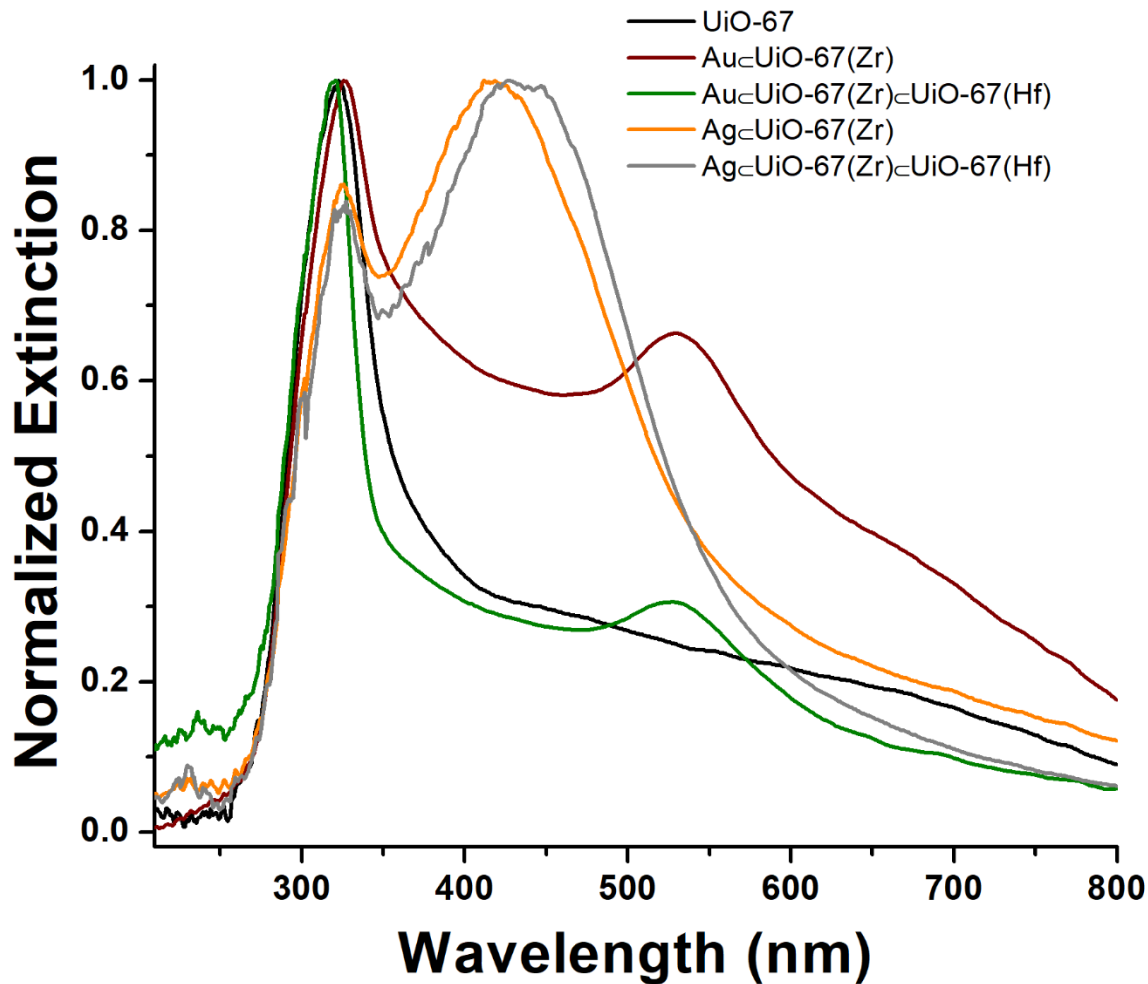


**Figure 4.17** Extinction spectra of UiO-67(Zr) (black), Au@UiO-67(Zr) (red), Au@UiO-67(Zr)@UiO-67(Hf) (green), Ag@UiO-67(Zr) (orange) and Ag@UiO-67(Zr)@UiO-67(Hf) (grey) samples drop cast on glass slides.

### 4.3 CONCLUSIONS

The structural, compositional, and functional diversity of MOFs can be exponentially increased by considering the ‘domain’ as a modular building block. We envision that MOFs with a plurality of distinct functional domains could perform integrated series of tasks or could serve as

highly selective filters for capturing and concentrating target analytes at specific domains. In all cases, domain distribution and sequence within a MOF crystal will code for function.

## 4.4 EXPERIMENTAL SECTION

### 4.4.1 General methods

Powder X-ray diffraction patterns were collected using a Bruker AXS D8 Discover powder diffractometer at 40 kV, 40 mA for Cu K $\alpha$  ( $\lambda = 1.5406 \text{ \AA}$ ) with a scan speed of 0.20 sec/step from 3 to 45° at a step size of 0.02°. The data were analyzed using the EVA program from the Bruker Powder Analysis Software package. The simulated powder patterns were calculated using Mercury 3.8 based on MOF crystal structures.

<sup>1</sup>H NMR spectra were obtained using Bruker Avance III 300/400/500 MHz spectrometers. Chemical shifts are in parts per million (ppm) using the residual solvent peak (CDCl<sub>3</sub>, DMSO-*d*<sub>6</sub>, or D<sub>2</sub>O) as references. MOF samples were digested with DMSO-*d*<sub>6</sub> and a small amount of hydrofluoric acid 48%, or K<sub>3</sub>PO<sub>4</sub> and D<sub>2</sub>O.

Scanning electron microscopy – energy dispersive X-ray spectroscopy (SEM-EDS) analyses were conducted using ZEISS Sigma 500 VP scanning electron microscope equipped with Oxford Aztec X-EDS. Samples were dispersed in ethanol, and drop cast on TEM grids (Ted Pella Inc 200 mesh carbon film copper grids Catalog No. NC0733370). The TEM grids were dried under ambient conditions before SEM-EDS studies. An STEM sample holder was used to mount the TEM grids. Secondary electron images and EDS data of the samples were collected at a working distance of 8.5 mm and an accelerating voltage of 20 kV. The EDS was acquired using 1024

channels from 0 to 20 keV. Elemental maps were collected for 10-15 minutes with a pixel dwell time of 100  $\mu$ s and a pixel resolution of 1024x1024. Zirconium maps and line-scans were obtained using the Zr L $\alpha$ 1 line intensity at 2.0 keV. Hafnium maps and line-scans were obtained using the Hf M $\alpha$ 1 line intensity at 1.6 keV. Iodine maps and line-scans were obtained using the I L $\alpha$ 1 intensity at 3.9 keV.

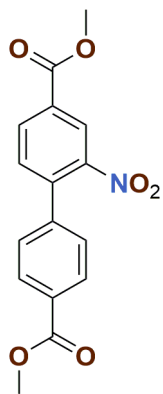
Transmission electron microscopy (TEM) images used to determine size distributions of MOF crystallites were collected on an FEI Morgagni 268 operated at 80 kV with an AMT side mount CCD camera system. TEM images of NPs and NPs@MOF composites were collected on a JEOL JEM-2100F equipped with a Gatan Orius camera operated at 200 kV or a Hitachi 9500 ETEM equipped with a Gatan Orius camera operated at 300 kV. High angle annular dark field (HAADF) imaging and scanning transmission electron microscopy - energy dispersive X-ray spectroscopy (STEM-EDS) studies were conducted on a JEOL JEM-2100F. The EDS was acquired using 1024 channels from 0 to 20 keV. Elemental maps were collected for 10-15 minutes with a pixel dwell time of 100  $\mu$ s and a pixel resolution of 1024x1024. Zirconium maps and line-scans were obtained using the Zr K $\alpha$ 1 line intensity at 15.7 keV. Hafnium maps and line-scans were obtained using the Hf M $\alpha$ 1 line intensity at 1.6 keV. Palladium maps and line-scans were obtained using the Pd L $\alpha$ 1 line intensity at 2.8 keV. Chlorine maps were obtained using the Cl K $\alpha$ 1 line intensity at 2.6 keV. Copper maps were obtained using the Cu L $\alpha$ 1 line intensity at 0.9 keV. Selenium maps were obtained using the Se K $\alpha$ 1 line intensity at 11.2 keV. Silver maps were obtained using the Ag L $\alpha$ 1 line intensity at 3.0 keV. Gold maps were obtained using the Au L $\alpha$ 1 line intensity at 9.7 keV. Samples were dispersed in ethanol or acetonitrile, and drop cast on TEM grids (Ted Pella Inc 200 mesh carbon film copper grids Catalog No. NC0733370, or Ni grids for

$\text{Cu}_{2-x}\text{Se}@\text{UiO}-67(\text{Zr})@\text{UiO}-67(\text{Hf})$ ). The TEM grids were dried under ambient conditions before TEM and STEM-EDS analyses.

Solution UV/vis spectra of Au and Ag nanoparticles were collected on an Agilent 8453 UV/Vis spectrometer equipped with deuterium and tungsten lamps. Solution UV/vis/NIR extinction spectrum of  $\text{Cu}_{2-x}\text{Se}$  nanoparticles were collected on a Cary 5000 spectrophotometer (Agilent Inc.). UV/vis extinction spectra of NPs@MOF samples were collected on a CRAIC QDI 2010 microspectrophotometer. Samples dispersed in ethanol was drop cast on glass slides, and dried under ambient conditions to form a sample film. Spectra were collected on a  $19 \times 19 \mu\text{m}^2$  sampling area.

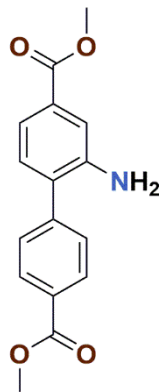
#### 4.4.2 Syntheses and characterization of MOF linkers

##### 4.4.2.1 Dimethyl 2-nitro-1, 1'-biphenyl-4,4'-dicarboxylate (1)



Compound 1 was synthesized according to literature conditions.<sup>46</sup>

#### 4.4.2.2 Dimethyl 2-amino-1, 1'-biphenyl-4,4'-dicarboxylate (2)



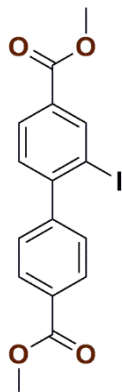
To a 100 mL schlenk flask equipped with a stir bar, were added compound **1** (710 mg, 2 mmol), 10 wt. % palladium on carbon (70 mg) and ethyl acetate (30 mL). The schlenk flask was quickly evacuated on a schlenk line and then backfilled with argon gas. This evacuation and backfill process was repeated for 3 times. The schlenk flask was then evacuated and attached to a H<sub>2</sub> balloon. The reaction mixture was stirred at room temperature under H<sub>2</sub> atmosphere and monitored via thin layer chromatography (TLC). After 6 hours, the reaction was stopped by removing Pd catalyst via vacuum filtration through a celite cake. The filtrate was concentrated *in vacuo* to yield light yellow solid compound **2** (570 mg, 93%). Compound **2** was used without further purification. <sup>1</sup>H NMR (400 MHz, CDCl<sub>3</sub>) δ 8.13 (m, 2H), 7.55 (m, 2H), 7.48 (dd, J = 7.9, 1.4 Hz, 1H), 7.45 (d, J = 1.4 Hz, 1H), 7.18 (d, J = 7.9 Hz, 1H), 3.95 (s, 3H), 3.92 (s, 3H), 3.86 (s, 2H).

#### 4.4.2.3 2-Amino-1, 1'-biphenyl-4,4'-dicarboxylic acid (3)



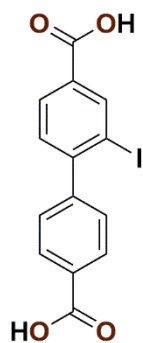
Compound **3** was synthesized using compound **2** as starting material based on literature conditions.<sup>1</sup> <sup>1</sup>H NMR (500 MHz, DMSO-*d*<sub>6</sub>) δ 12.83 (s, 2H), 8.01 (d, J = 8.5 Hz, 2H), 7.58 (d, J = 8.5 Hz, 2H), 7.41 (d, J = 1.5 Hz, 1H), 7.20 (dd, J = 7.5, 1.5 Hz, 1H), 7.11 (d, J = 7.5 Hz, 1H), 5.17 (s, 2H).

#### 4.4.2.4 Dimethyl 2-iodo-1, 1'-biphenyl-4,4'-dicarboxylate (4)



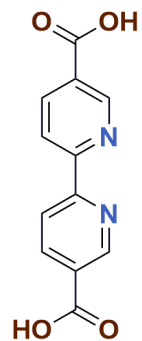
Compound **2** (790 mg, 2.77 mmol) was suspended and stirred in 15% hydrochloric acid (10 mL). NaNO<sub>2</sub> (220 mg, 3.2 mmol) dissolved in H<sub>2</sub>O (3 mL) was added dropwise to the suspension at 0 °C. After stirring at 0 °C for 10 min, NaI (500 mg, 3.3 mmol) dissolved in H<sub>2</sub>O (3 mL) was added dropwise to the reaction mixture. The reaction was then heated in oil bath at 60 °C for 20 min. Upon cooling down to room temperature, the reaction mixture was poured into iced water (50 mL). The aqueous solution was extracted with ethyl acetate (150 mL, 3x). The combined organic phase was washed with 10% Na<sub>2</sub>SO<sub>3</sub> (50 mL, 2x) and brine (50 mL, 1x). The organic phase was dried over Na<sub>2</sub>SO<sub>4</sub> and concentrated *in vacuo* to obtain the crude product. The crude product was purified via silica gel column chromatography (hexanes:DCM = 1:1) to yield off-white solid compound **4** (600 mg, 54%). <sup>1</sup>H NMR (400 MHz, DMSO-*d*<sub>6</sub>) δ 8.50 (d, J = 1.6 Hz, 1H), 8.06 (m, 3H), 7.52 (m, 3H), 3.90 (s, 6H).

#### 4.4.2.5 2-Iodo-1, 1'-biphenyl-4,4'-dicarboxylic acid (5)



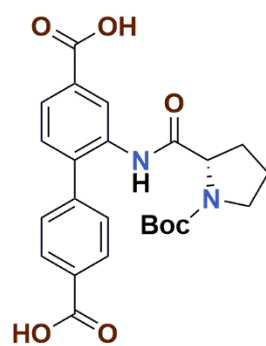
Compound **4** (600 mg, 1.50 mmol) was dissolved in a 1:1 mixture of THF/MeOH (30 mL). To the solution of compound **4**, was added 1 M NaOH aqueous solution (15 mL). The reaction mixture was stirred at room temperature for 24 hours and then concentrated *in vacuo* to remove THF and MeOH. The aqueous residue was then acidified with 1 M HCl solution until the pH of solution reached ~2 and a white slurry formed. The slurry was stirred for 30 min. After vacuum filtration, solid precipitate was collected and washed with water (150 mL, 3x). The off-white solid was dried under vacuum to obtain compound **5** (500 mg, 90%). Compound **5** was used without further purification. <sup>1</sup>H NMR (500 MHz, DMSO-*d*<sub>6</sub>) δ 13.21 (s, 2H), 8.48 (d, J = 2.0 Hz, 1H), 8.02 (m, 3H), 7.48 (m, 3H).

#### 4.4.2.6 2,2'-Bipyridine-5,5'-dicarboxylic acid (6)



Compound 6 was synthesized according to literature conditions.<sup>204</sup>

#### 4.4.2.7 (S)-2-(1-(tert-butoxycarbonyl)pyrrolidine-2-carboxamido)-1,1'-biphenyl-4,4'-dicarboxylic acid (7)



Compound 7 was synthesized according to literature conditions.<sup>199</sup>

### 4.4.3 Syntheses and characterization of stratified MOFs

#### 4.4.3.1 Synthesis of UiO-67(Zr) seed crystallites

0.4 M solution of  $Zr(O^iPr)_4$  in  $CH_3COOH$  was prepared by mixing  $Zr(O^iPr)_4$  70 wt. % in *n*-propanol (187.2 mg, 0.4 mmol) with  $CH_3COOH$  (1 mL). A 0.02 M solution of 1, 1'-biphenyl-4,4'-dicarboxylic acid ( $H_2$ -BPDC) in DMF was prepared by heating a mixture of  $H_2$ -BPDC (19.4 mg, 0.08 mmol) and DMF (4 mL) on a stir plate at 150 °C until complete dissolution. To a 20 mL Pyrex vial were added in sequence  $CH_3COOH$  (0.3 mL), 0.4 M  $Zr(O^iPr)_4$  solution (0.05 mL, 0.02 mmol), DMF (4 mL) and 0.02 M  $H_2$ -BPDC solution (1 mL, 0.02 mmol). The vial was tightly capped and heated at 65 °C for 0.5 h in an isothermal oven to yield turbid suspension. The suspension was centrifuged at 10000 rpm for 2 min to obtain white precipitate. The precipitate was washed with fresh DMF (4 mL, 4x) and used immediately for the next step.

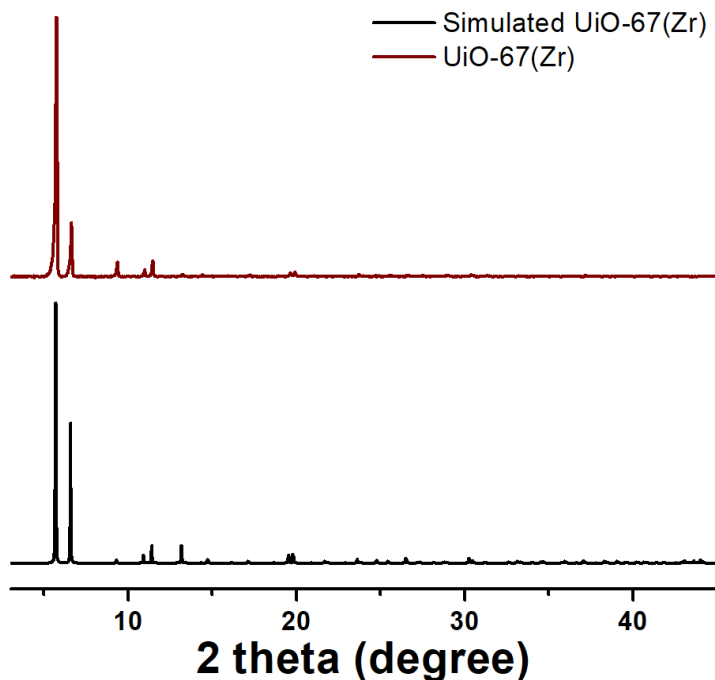


**Figure 4.18** Simulated PXRD pattern of UiO-67(Zr) (black) and experimental PXRD pattern of as-synthesized UiO-67(Zr) seed crystallites (red).

#### 4.4.3.2 Synthesis of UiO-67(Zr)⊂UiO-67(Hf)

A 0.02 M solution of H<sub>2</sub>-BPDC in DMF was prepared by heating a mixture of H<sub>2</sub>-BPDC (19.4 mg, 0.08 mmol) and DMF (4 mL) on a stir plate at 150 °C until complete dissolution. Hf(O<sup>*i*</sup>Pr)<sub>4</sub>•<sup>*i*</sup>PrOH (19 mg, 0.04 mmol) and CH<sub>3</sub>COOH (0.7 mL) was mixed in a 20 mL Pyrex vial. After the mixture was sonicated for 3 min, DMF (3.2 mL) and 0.02 M H<sub>2</sub>-BPDC solution (2 mL, 0.04 mmol) was added. The mixture was vortexed and incubated at 65 °C in an isothermal oven for 1 h. The reaction suspension was then centrifuged at 10000 rpm for 2 min to obtain white precipitate and clear supernatant. The clear supernatant was carefully collected in a 20 mL Pyrex vial. UiO-67(Zr) seed crystals (*vide supra*) was dispersed in 1 mL DMF and added to the vial. The mixture was stirred with a magnetic stir bar (60 rpm) at 25 °C. After 19 hours the reaction suspension was centrifuged at 10000 rpm for 2 min to obtain white precipitate product. The product was then washed with fresh DMF (4 mL, 4x).

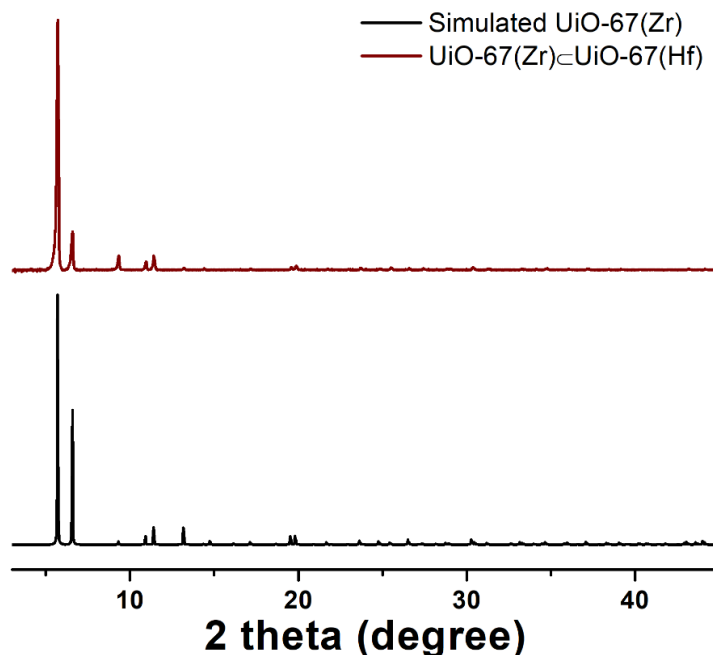


**Figure 4.19** Simulated PXR D pattern of UiO-67(Zr) (black) and experimental PXR D pattern of as-synthesized UiO-67(Zr)⊂UiO-67(Hf) (red).

#### 4.4.3.3 Synthesis of UiO-67(Hf) seed crystallites

A 0.02 M solution of H<sub>2</sub>-BPDC in DMF was prepared by heating a mixture of H<sub>2</sub>-BPDC (19.4 mg, 0.08 mmol) and DMF (4 mL) on a stir plate at 150 °C until complete dissolution. Hf(O<sup>*i*</sup>Pr)<sub>4</sub>·<sup>*i*</sup>PrOH (76 mg, 0.16 mmol) and CH<sub>3</sub>COOH (2.8 mL) was mixed in a 40 mL pyrex vial. After the mixture was sonicated for 3 min, DMF (13.8 mL) and 0.02 M H<sub>2</sub>-BPDC solution (8 mL, 0.16 mmol) was added. The mixture was vortexed and allowed to react at 25 °C. After 24 h, the reaction suspension was centrifuged to obtain white precipitate. The precipitate was washed with fresh DMF (16 mL, 4x), dispersed in 2 mL DMF and used immediately as seeds to prepare stratified MOFs.

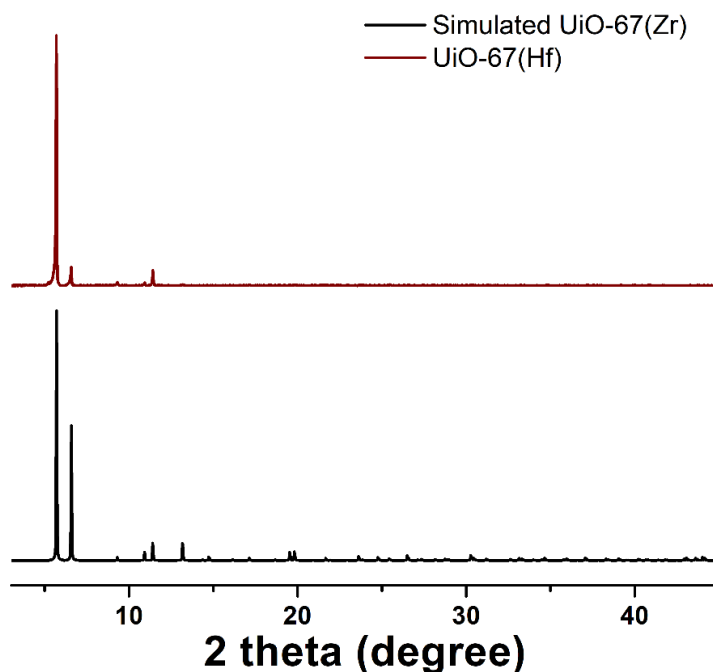


**Figure 4.20** Simulated PXRD pattern of UiO-67(Zr) (black) and experimental PXRD pattern of as-synthesized UiO-67(Hf) seed crystallites (red).

#### 4.4.3.4 Synthesis of UiO-67(Hf)⊂UiO-67(Zr)

0.4 M solution of  $Zr(O^iPr)_4$  in  $CH_3COOH$  was prepared by mixing  $Zr(O^iPr)_4$  70 wt. % in *n*-propanol (187.2 mg, 0.4 mmol) with  $CH_3COOH$  (1 mL). A 0.02 M solution of  $H_2$ -BPDC in DMF was prepared by heating a mixture of  $H_2$ -BPDC (19.4 mg, 0.08 mmol) and DMF (4 mL) on a stir plate at 150 °C until complete dissolution. To a 20 mL Pyrex vial were added in sequence  $CH_3COOH$  (0.6 mL), 0.4 M  $Zr(O^iPr)_4$  solution in  $CH_3COOH$  (0.1 mL, 0.04 mmol), DMF (3 mL) and 0.02 M  $H_2$ -BPDC solution (2 mL, 0.04 mmol). The vial was tightly capped and vortexed for 10 seconds. The reaction was allowed to proceed at room temperature for 50 min, at which point, a murky suspension was formed. After centrifugation at 10,000 rpm to remove the precipitate, supernatant was collected in a new 20 mL vial. To the supernatant was added 1 mL of DMF suspension of UiO-67(Hf) seed crystals prepared previously (*vide supra*). The mixture was stirred with a magnetic stir bar (60 rpm) at room temperature for 18 hrs. After centrifugation at 10,000 rpm, white precipitate was collected and washed with DMF (16 mL, 4x).

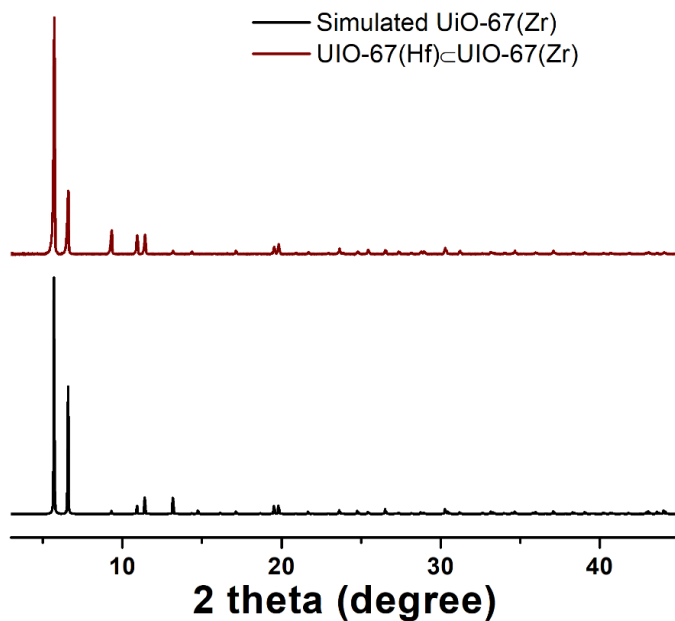


**Figure 4.21** Simulated PXR D pattern of UiO-67(Zr) (black) and experimental PXR D pattern of as-synthesized UiO-67(Hf)⊂UiO-67(Zr) (red).

#### 4.4.3.5 Synthesis of I-UiO-67(Zr) seed crystallites

0.4 M solution of  $Zr(O^iPr)_4$  in  $CH_3COOH$  was prepared by mixing  $Zr(O^iPr)_4$  70 wt. % in *n*-propanol (187.2 mg, 0.4 mmol) with  $CH_3COOH$  (1 mL). 0.015 M solution of 2-iodo-1, 1'-biphenyl-4,4'-dicarboxylic acid ( $H_2$ -I-BPDC) in DMF was prepared by dissolving  $H_2$ -I-BPDC (16.2 mg, 0.045 mmol) in DMF (3 mL). To a 40 mL Pyrex vial were added in sequence  $CH_3COOH$  (1.05 mL), 0.4 M  $Zr(O^iPr)_4$  solution (0.15 mL, 0.06 mmol), DMF (9 mL) and 0.015 M  $H_2$ -I-BPDC solution (3 mL, 0.045 mmol). The vial was tightly capped and heated at 65 °C in an isothermal oven for 3.5 h to yield turbid suspension. The suspension was centrifuged at 10000 rpm for 2 min to obtain white precipitate. The precipitate was washed with fresh DMF (16 mL, 4x).

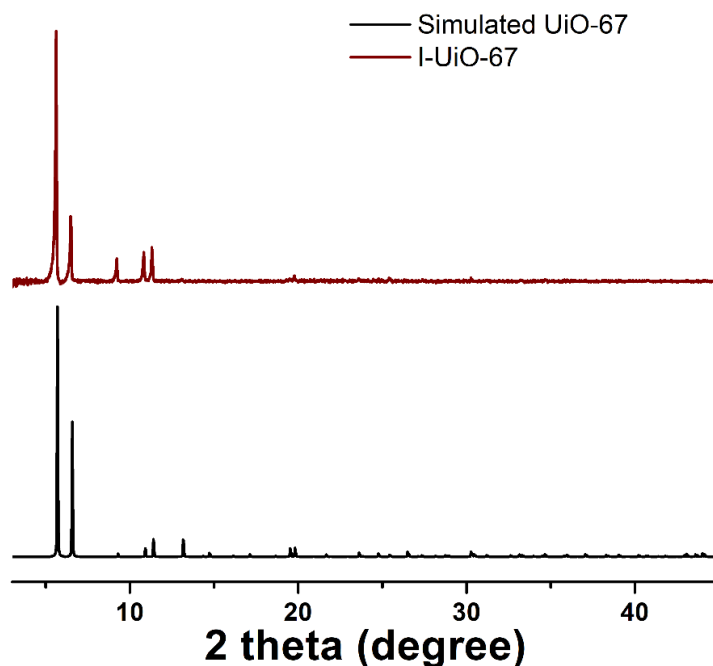


**Figure 4.22** Simulated PXRD pattern of UiO-67(Zr) (black) and experimental PXRD pattern of as-synthesized I-UiO-67(Zr) seed crystallites (red).

#### 4.4.3.6 Synthesis of I-UiO-67(Zr)⊂UiO-67(Hf)

0.02 M solution of H<sub>2</sub>-BPDC in DMF was prepared by heating a mixture of H<sub>2</sub>-BPDC (19.4 mg, 0.08 mmol) and DMF (4 mL) on a stir plate at 150 °C until complete dissolution. Hf(O<sup>*i*</sup>Pr)<sub>4</sub>·<sup>*i*</sup>PrOH (19 mg, 0.04 mmol) and CH<sub>3</sub>COOH (0.7 mL) was mixed in a 20 mL Pyrex vial. After the mixture was sonicated for 3 min, DMF (3.2 mL) and 0.02 M H<sub>2</sub>-BPDC solution (2 mL, 0.04 mmol) was added. The mixture was vortexed and incubated at 65 °C in an isothermal oven for 50 min. The reaction suspension was then centrifuged at 10000 rpm for 2 min to obtain white precipitate and clear supernatant. The clear supernatant was carefully collected in a 20 mL Pyrex vial. I-UiO-67(Zr) seed crystals previously (*vide supra*) prepared was added to the supernatant in the vial. The mixture was allowed to react at 25 °C for 14 h. The reaction suspension was centrifuged at 10000 rpm for 2 min to obtain white precipitate product. The product was then washed with fresh DMF (16 mL, 4x) and dispersed in 5 mL fresh DMF.

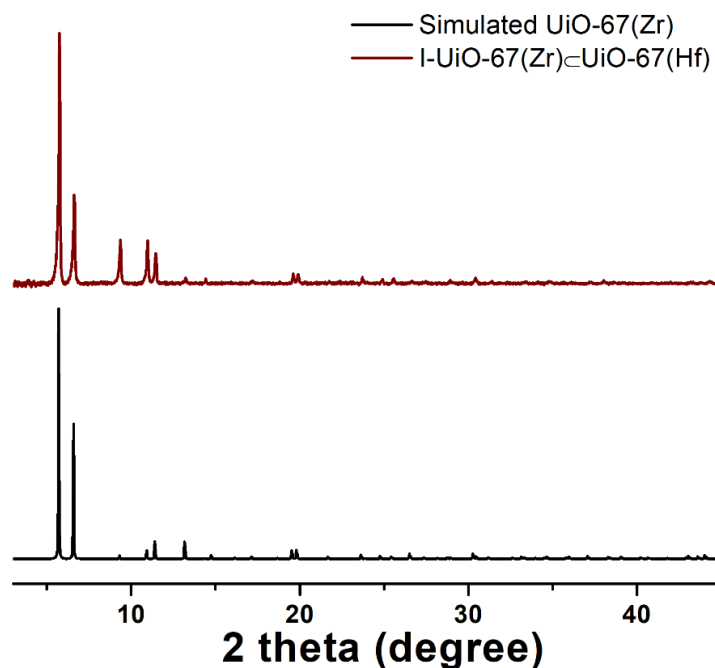


**Figure 4.23** Simulated PXRD pattern of UiO-67(Zr) (black) and PXRD pattern of as-synthesized I-UiO-67(Zr)⊂UiO-67(Hf) (red).

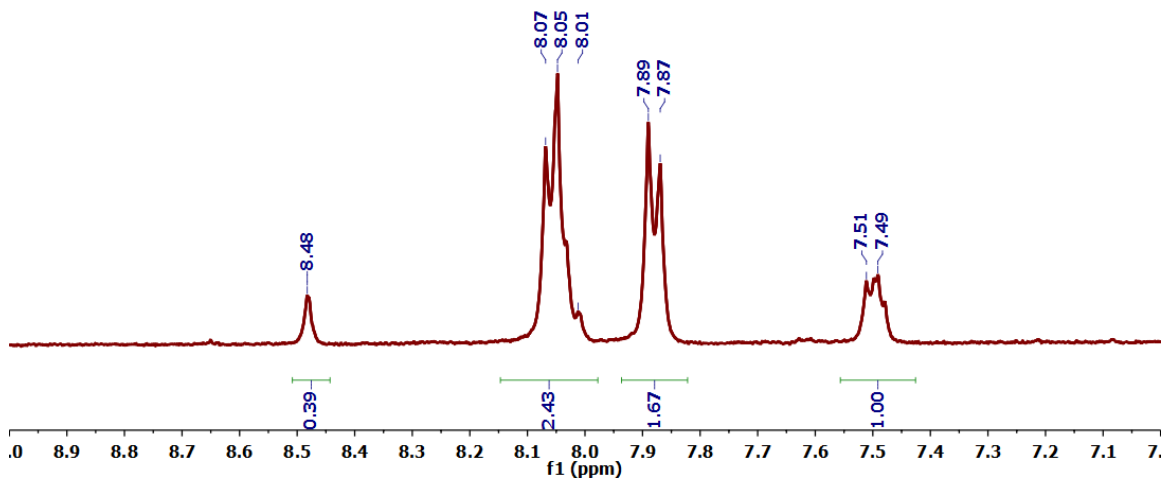


**Figure 4.24** <sup>1</sup>H NMR of acid digested I-UiO-67(Zr) c UiO-67(Hf) in DMSO-d<sub>6</sub> showing an approximate I-BPDC : BPDC ratio of 1:1.25.

#### 4.4.3.7 Synthesis of NH<sub>2</sub>-UiO-67(Zr) seed crystallites

0.4 M solution of Zr(O<sup>*n*</sup>Pr)<sub>4</sub> in CH<sub>3</sub>COOH was prepared by mixing Zr(O<sup>*n*</sup>Pr)<sub>4</sub> 70 wt. % in *n*-propanol (187.2 mg, 0.4 mmol) with CH<sub>3</sub>COOH (1 mL). A 0.02 M solution of 2-amino-1, 1'-biphenyl-4,4'-dicarboxylic acid (H<sub>2</sub>-NH<sub>2</sub>-BPDC) in DMF was prepared by dissolving H<sub>2</sub>-NH<sub>2</sub>-BPDC (15.4 mg, 0.06 mmol) in DMF (3 mL). To a 40 mL Pyrex vial were added in sequence CH<sub>3</sub>COOH (0.6 mL), 0.4 M Zr(O<sup>*n*</sup>Pr)<sub>4</sub> solution (0.15 mL, 0.06 mmol), DMF (15 mL) and 0.02 M H<sub>2</sub>-NH<sub>2</sub>-BPDC solution (3 mL, 0.06 mmol). The vial was tightly capped and heated at 65 °C in an isothermal oven for 16 h to yield turbid yellow suspension. The suspension was centrifuged at 10000 rpm for 2 min to obtain yellow precipitate. The precipitate was washed with fresh DMF (16 mL, 4x) and dispersed in DMF (3 mL).

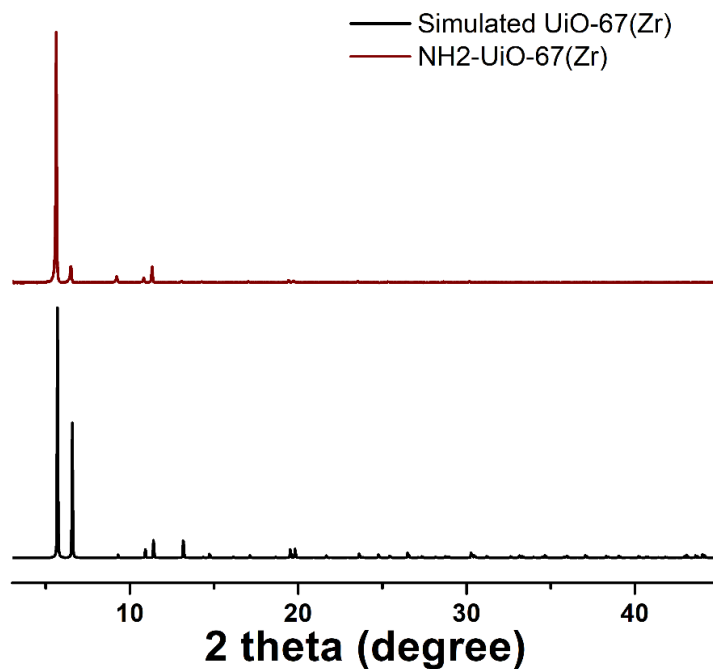


**Figure 4.25** Simulated PXRD pattern based on UiO-67(Zr) (black) and experimental PXRD pattern of as-synthesized NH<sub>2</sub>-UiO-67(Zr) seed crystallites (red).

#### 4.4.3.8 Synthesis of NH<sub>2</sub>-UiO-67(Zr)⊂I-UiO-67(Zr)

0.4 M solution of Zr(O<sup>n</sup>Pr)<sub>4</sub> in CH<sub>3</sub>COOH was prepared by mixing Zr(O<sup>n</sup>Pr)<sub>4</sub> 70 wt. % in *n*-propanol (187.2 mg, 0.4 mmol) with CH<sub>3</sub>COOH (1 mL). A 0.015 M solution of H<sub>2</sub>-I-BPDC in DMF was prepared by dissolving H<sub>2</sub>-I-BPDC (16.2 mg, 0.045 mmol) in DMF (3 mL). To a 20 mL Pyrex vial were added in sequence CH<sub>3</sub>COOH (0.30 mL), 0.4 M Zr(O<sup>n</sup>Pr)<sub>4</sub> solution (0.05 mL, 0.02 mmol), DMF (2 mL), 0.015 M H<sub>2</sub>-I-BPDC solution (1 mL, 0.015 mmol) and 1 mL of DMF suspension of the NH<sub>2</sub>-UiO-67(Zr) seed crystals (*vide supra*). The mixture was stirred with a magnetic stir bar (60 rpm) at 25 °C for 5 h. The suspension was centrifuged at 10000 rpm for 2 min to obtain yellow precipitate. The precipitate was washed with fresh DMF (4 mL, 4x) and used immediately for characterization and further reactions.

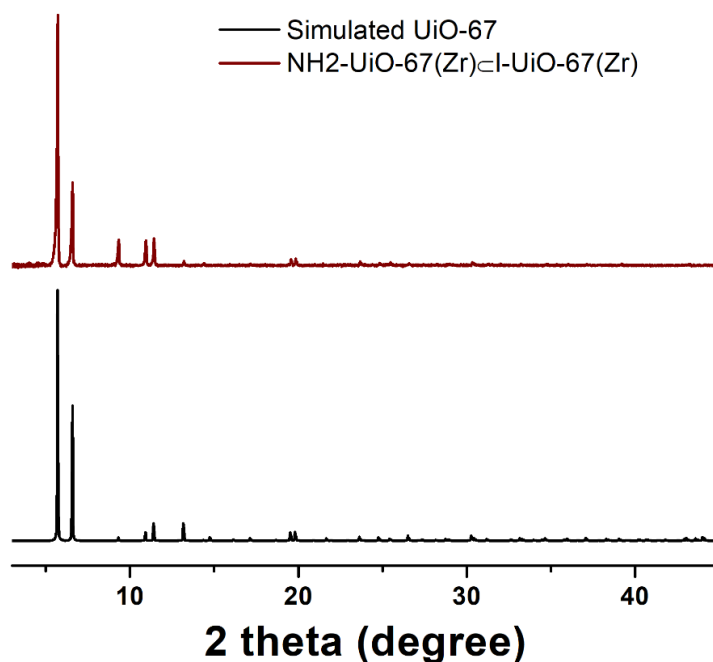


**Figure 4.26** Simulated PXRD pattern of UiO-67(Zr) (black) and experimental PXRD pattern of as-synthesized NH<sub>2</sub>-UiO-67(Zr)⊂I-UiO-67(Zr) (red).

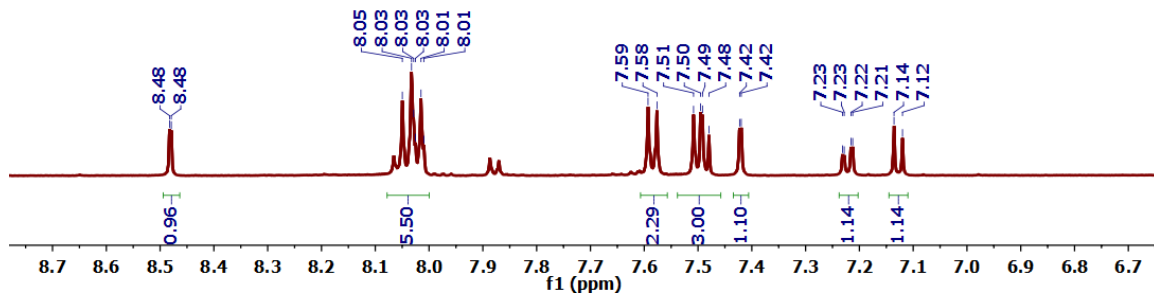


**Figure 4.27**  $^1\text{H}$  NMR of acid digested  $\text{NH}_2\text{-UiO-67(Zr)}\subset\text{I-UiO-67(Zr)}$  in  $\text{DMSO-d}_6$  showing an approximate I-BPDC :  $\text{NH}_2\text{-BPDC}$  ratio of 1:1.15.

#### 4.4.3.9 Linker exchange experiment using NH<sub>2</sub>-UiO-67(Zr) and H<sub>2</sub>-I-BPDC

A 0.015 M solution of H<sub>2</sub>-I-BPDC in DMF was prepared by dissolving H<sub>2</sub>-I-BPDC (16.2 mg, 0.045 mmol) in DMF (3 mL). To a 20 mL Pyrex vial were added in sequence CH<sub>3</sub>COOH (0.35 mL), DMF (2 mL), 0.015 M H<sub>2</sub>-I-BPDC solution (1 mL, 0.015 mmol) and 1 mL of DMF suspension of the NH<sub>2</sub>-UiO-67(Zr) seed crystals (*vide supra*). The mixture was stirred with a magnetic stir bar (60 rpm) at 25 °C for 5 h. The suspension was centrifuged at 10000 rpm for 2 min to obtain yellow precipitate. The precipitate was washed with fresh DMF (4x) and used immediately for characterization and further reactions.

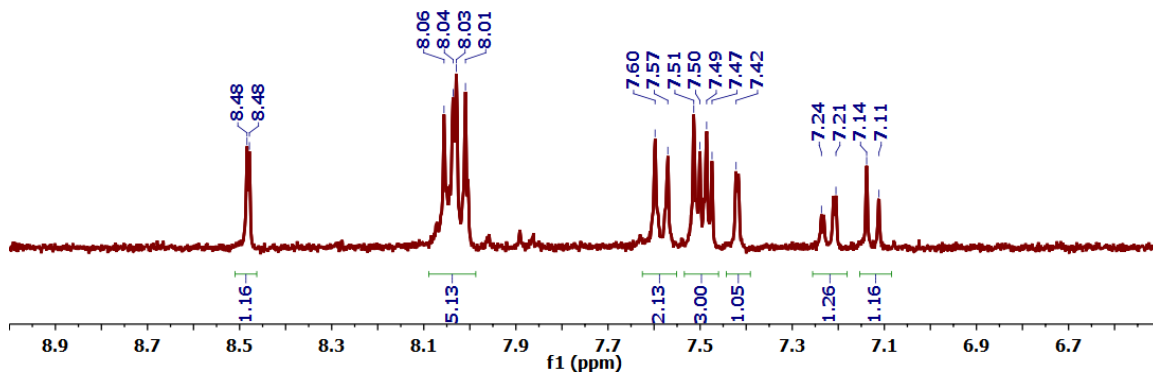


**Figure 4.28** <sup>1</sup>H NMR of acid digested NH<sub>2</sub>-UiO-67(Zr)⊂I-UiO-67(Zr) in DMSO-d<sub>6</sub> showing an approximate I-BPDC : NH<sub>2</sub>-BPDC ratio of 1:1.2.

#### 4.4.3.10 Synthesis of UiO-67(Zr)⊂UiO-67(Hf)⊂UiO-67(Zr)

0.4 M solution of  $Zr(O^iPr)_4$  in  $CH_3COOH$  was prepared by mixing  $Zr(O^iPr)_4$  70 wt. % in *n*-propanol (187.2 mg, 0.4 mmol) with  $CH_3COOH$  (1 mL). A 0.02 M solution of  $H_2$ -BPDC in DMF was prepared by mixing  $H_2$ -BPDC (19.4 mg, 0.08 mmol) with DMF (4 mL) followed by heating on a stir plate at 150 °C until complete dissolution. To a 20 mL Pyrex vial were added in sequence  $CH_3COOH$  (0.6 mL), 0.4 M  $Zr(O^iPr)_4$  solution in  $CH_3COOH$  (0.1 mL, 0.04 mmol), DMF (3 mL) and 0.02 M  $H_2$ -BPDC solution (2 mL, 0.04 mmol). The vial was tightly capped and vortexed for 10 seconds. The reaction was allowed to proceed at room temperature for 50 min, at which point, a murky suspension was formed. After centrifugation at 10,000 rpm to remove the precipitate, supernatant was collected in a new 20 mL vial. To the supernatant was added UiO-67(Zr)⊂UiO-67(Hf) crystals prepared previously (*vide supra*). The mixture was stirred with a magnetic stir bar (200 rpm) at room temperature for 5.5 hrs. After centrifugation at 10,000 rpm, white precipitate was collected and washed with DMF (16 mL, 4x).

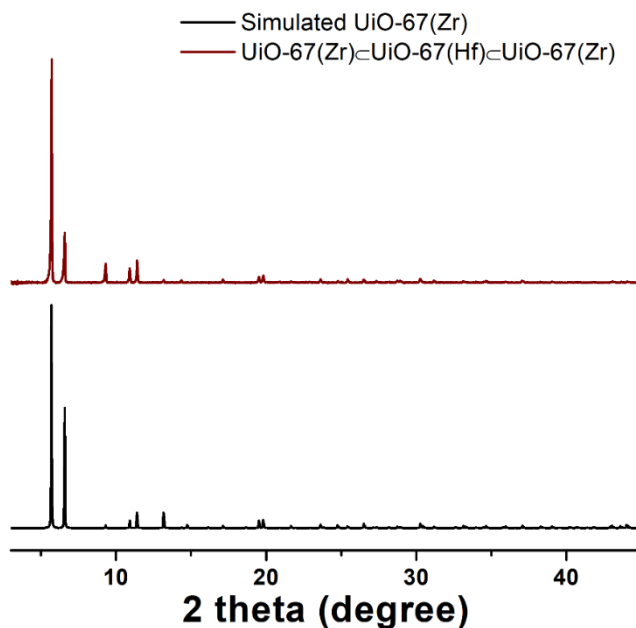


**Figure 4.29** Simulated PXRD pattern of UiO-67(Zr) (black) and experimental PXRD pattern of as-synthesized UiO-67(Zr)⊂UiO-67(Hf)⊂UiO-67(Zr) (red).

#### 4.4.3.11 Synthesis of I-UiO-67(Zr)⊂UiO-67(Hf)⊂NH<sub>2</sub>-UiO-67(Zr)

0.4 M solution of Zr(O<sup>n</sup>Pr)<sub>4</sub> in CH<sub>3</sub>COOH was prepared by mixing Zr(O<sup>n</sup>Pr)<sub>4</sub> 70 wt. % in *n*-propanol (187.2 mg, 0.4 mmol) with CH<sub>3</sub>COOH (1 mL). A 0.02 M solution of H<sub>2</sub>-NH<sub>2</sub>-BPDC in DMF was prepared by dissolving H<sub>2</sub>-NH<sub>2</sub>-BPDC (10.3 mg, 0.04 mmol) with DMF (2 mL). To a 20 mL Pyrex vial were added in sequence CH<sub>3</sub>COOH (0.25 mL), 0.4 M Zr(O<sup>n</sup>Pr)<sub>4</sub> solution (0.05 mL, 0.02 mmol), 3 mL of the DMF suspension of I-UiO-67(Zr) ⊂UiO-67(Hf) prepared previously (*vide supra*) and 0.02 M H<sub>2</sub>-BPDC solution (1 mL, 0.02 mmol). The vial was tightly capped and allowed to stand at room temperature for 14 hrs. After centrifugation of the resulting suspension at 10000 rpm for 2 min, pale yellow precipitate was obtained. The precipitate was washed with fresh DMF (16 mL, 4x) before characterization.

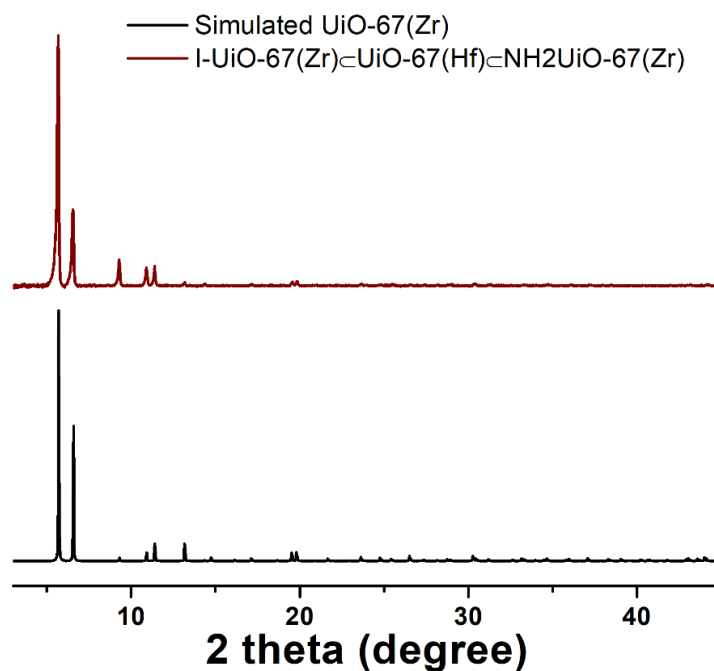


**Figure 4.30** Simulated PXRD pattern of UiO-67(Zr) (black) and experimental PXRD pattern of as-synthesized I-UiO-67(Zr)⊂UiO-67(Hf)⊂NH<sub>2</sub>-UiO-67(Zr) (red).

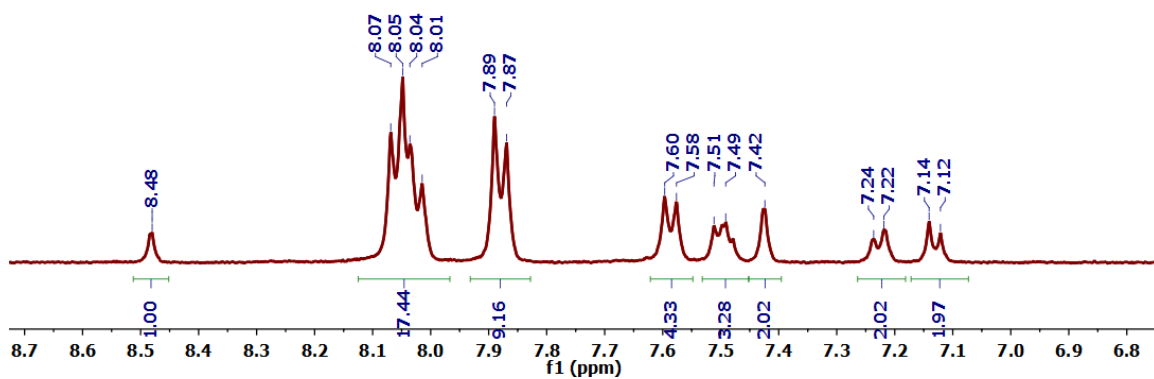


**Figure 4.31**  $^1\text{H}$  NMR of acid digested I-UiO-67(Zr)@UiO-67(Hf)@NH<sub>2</sub>-UiO-67(Zr) in DMSO-d<sub>6</sub> showing an approximate I-BPDC : BPDC : NH<sub>2</sub>-BPDC ratio of 1 : 2.29 : 2.

#### 4.4.3.12 Synthesis of Bpy-UiO-67(Zr) seed crystallites

Bpy-UiO-67(Zr) seed crystallites were prepared using one of the conditions below.

**Condition I:** Bpy-UiO-67(Zr) was synthesized using modified literature conditions.<sup>4</sup> To a 20 mL Pyrex vial was added 2 2'-bipyridine-5 5'-dicarboxylic acid (H<sub>2</sub>-BpyDC) (12.2 mg, 0.05 mmol) and 2 mL of DMF. The mixture was sonicated for 30 min to form a suspension. Acetic acid (0.2 mL) and ZrCl<sub>4</sub> (11.7 mg, 0.05 mmol) were then added to the vial. After sonication for 10 min, the vial was placed in a 120 °C oven for 24 hours. The reaction suspension was then centrifuged at 10,000 rpm for 3 min to obtain white precipitate. The precipitate was washed with fresh DMF (16 mL, 4x) and suspended in DMF (1 mL).

**Condition II:** To a 20 mL Pyrex vial was added ZrCl<sub>4</sub> (9.8 mg, 0.04 mmol), DMF (10 mL), CH<sub>3</sub>COOH (0.5 mL) and H<sub>2</sub>-BpyDC (9.3 mg, 0.04 mmol). After sonication for 5 min, the vial was placed in in a 100 °C for 6.5 hours. The reaction suspension was then centrifuged at 10,000 rpm for 3 min to obtain white precipitate. The precipitate was washed with fresh DMF (16 mL, 4x) and dispersed in DMF (1 mL).

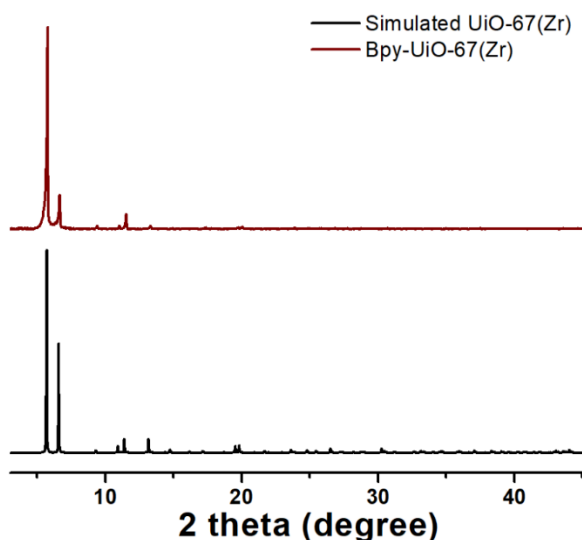


**Figure 4.32** Simulated PXRD pattern of UiO-67(Zr) (black) and experimental PXRD pattern of as-synthesized Bpy-UiO-67(Zr) seed crystallites (red).

#### 4.4.3.13 Synthesis of Bpy-UiO-67(Zr)⊂UiO-67(Zr)

0.4 M solution of  $Zr(O^iPr)_4$  in  $CH_3COOH$  was prepared by mixing  $Zr(O^iPr)_4$  70 wt. % in *n*-propanol (187.2 mg, 0.4 mmol) with  $CH_3COOH$  (1 mL). A 0.02 M solution of  $H_2$ -BPDC in DMF was prepared by heating a mixture of  $H_2$ -BPDC (19.4 mg, 0.08 mmol) and DMF (4 mL) on a stir plate at 150 °C until complete dissolution. To a 20 mL Pyrex vial were added in sequence  $CH_3COOH$  (0.3 mL), 0.4 M  $Zr(O^iPr)_4$  solution in  $CH_3COOH$  (0.05 mL, 0.02 mmol), DMF (3 mL) and 0.02 M  $H_2$ -BPDC solution (1 mL, 0.02 mmol) and DMF suspension of Bpy-UiO-67(Zr) (1 mL) prepared previously (condition I, *vide supra*). The mixture was vortexed for 10 seconds and stirred at 200 rpm and room temperature for 2 h. After centrifugation at 10,000 rpm for 3 min, Bpy-UiO-67(Zr)⊂UiO-67(Zr) was obtained as white precipitate. The precipitate was copiously washed with fresh DMF (4 mL, 4x) and acetonitrile (4 mL, 4x) and suspended in 1 mL acetonitrile.

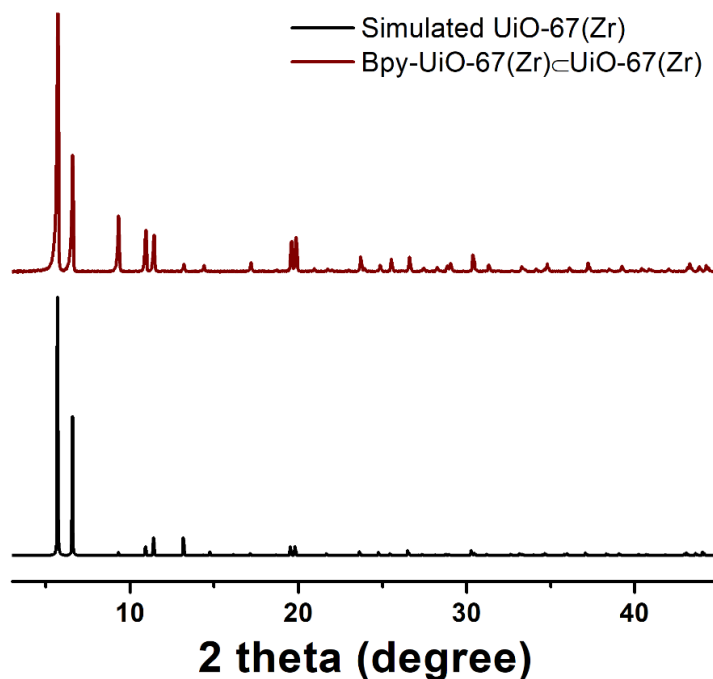


**Figure 4.33** Simulated PXRD pattern of UiO-67(Zr) (black) and experimental PXRD pattern of as-synthesized Bpy-UiO-67(Zr)⊂UiO-67(Zr) (red).

#### 4.4.3.14 Synthesis of Bpy-UiO-67(Zr)⊂Pro-UiO-67(Zr)

0.4 M solution of  $Zr(O^iPr)_4$  in  $CH_3COOH$  was prepared by mixing  $Zr(O^iPr)_4$  70 wt. % in *n*-propanol (187.2 mg, 0.4 mmol) with  $CH_3COOH$  (1 mL). A 0.02 M solution of (S)-2-(1-(tert-butoxycarbonyl)pyrrolidine-2-carboxamido)-1,1'-biphenyl-4,4'-dicarboxylic acid linker ( $H_2$ -Pro-BPDC) in DMF was prepared by dissolving  $H_2$ -Pro-BPDC (36 mg, 0.08 mmol) in DMF (4 mL). To a 20 mL Pyrex vial were added in sequence  $CH_3COOH$  (0.4 mL), 0.4 M  $Zr(O^iPr)_4$  solution in  $CH_3COOH$  (0.1 mL, 0.04 mmol), DMF (7 mL) and 0.02 M  $H_2$ -Pro-BPDC solution (2 mL, 0.04 mmol) and DMF suspension of Bpy-UiO-67(Zr) (1 mL) prepared previously (condition II, *vide supra*). The mixture was vortexed for 10 seconds and stirred with a magnetic stir bar (50 rpm) in a 65 °C oil bath for 5.5 hours. The reaction was cooled down to room temperature and centrifuged at 10,000 rpm for 3 min to obtain Bpy-UiO-67(Zr)⊂Pro-UiO-67(Zr) as a white precipitate. The precipitate was copiously washed with fresh DMF (4 mL, 4x) and acetonitrile (4 mL, 4x) and evacuated under schlenk line vacuum for 2 hours.

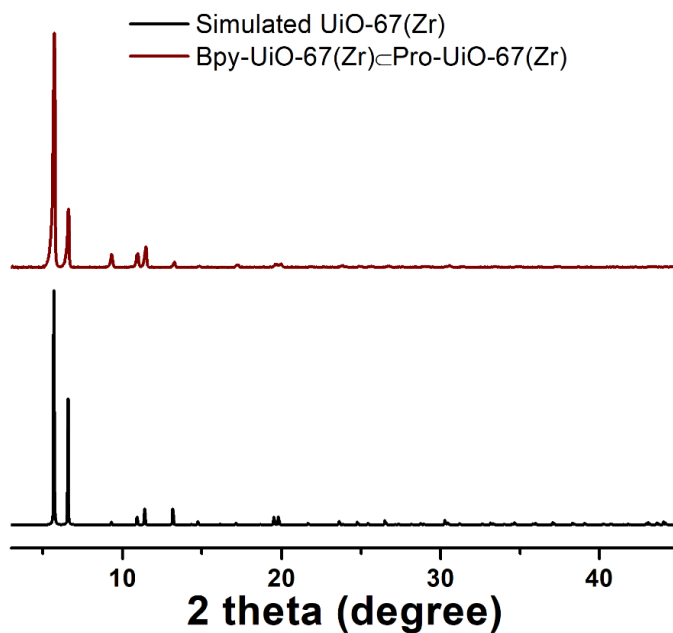


**Figure 4.34** Simulated PXRD pattern of UiO-67(Zr) (black) and experimental PXRD pattern of as-synthesized Bpy-UiO-67(Zr)⊂Pro-UiO-67(Zr) (red).

lty 6-158 500H  
lty 6-158 500H

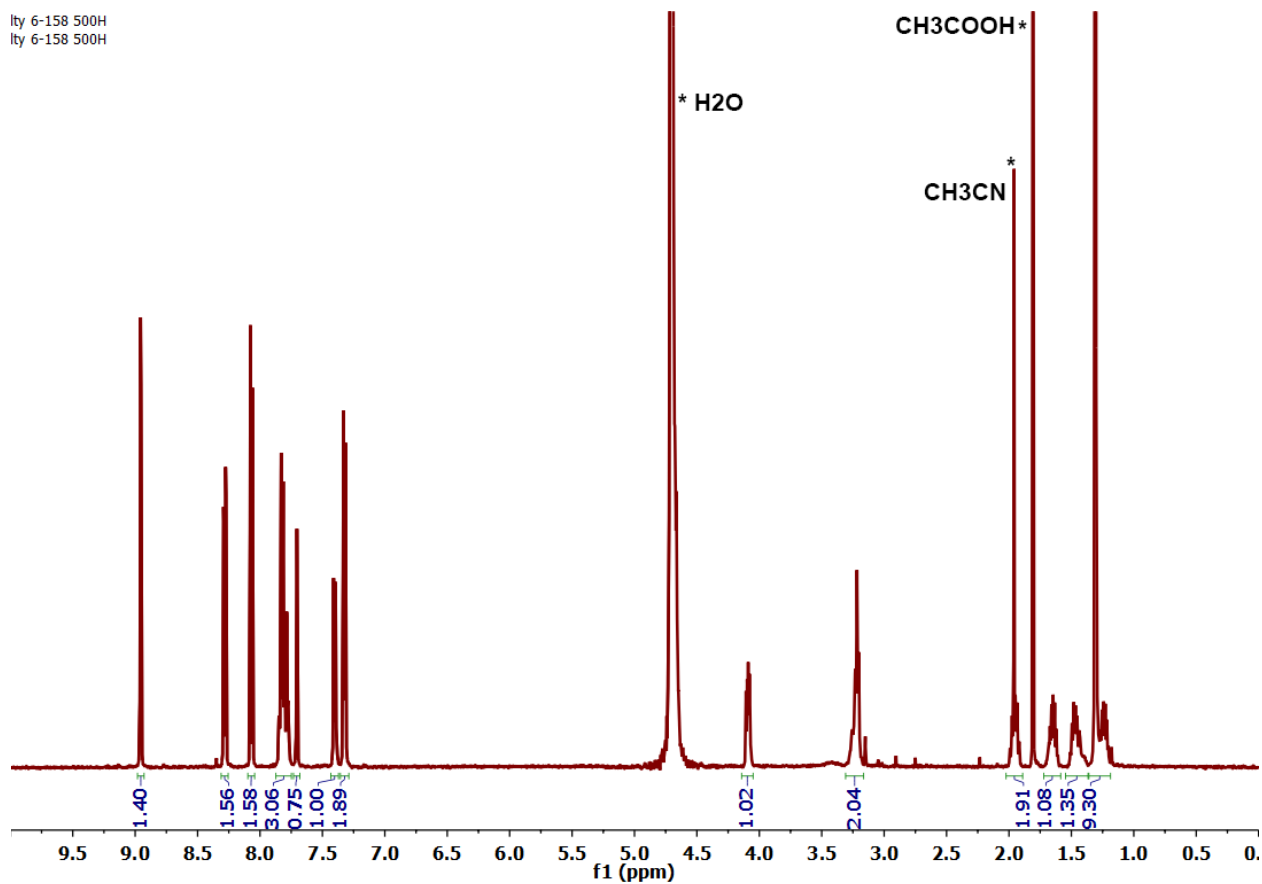


**Figure 4.35**  $^1\text{H}$  NMR of digested Bpy-UiO-67(Zr)@Pro-UiO-67(Hf) in  $\text{K}_3\text{PO}_4/\text{D}_2\text{O}$  showing an approximate BpyDC : Pro-BPDC ratio of 1:1.25.

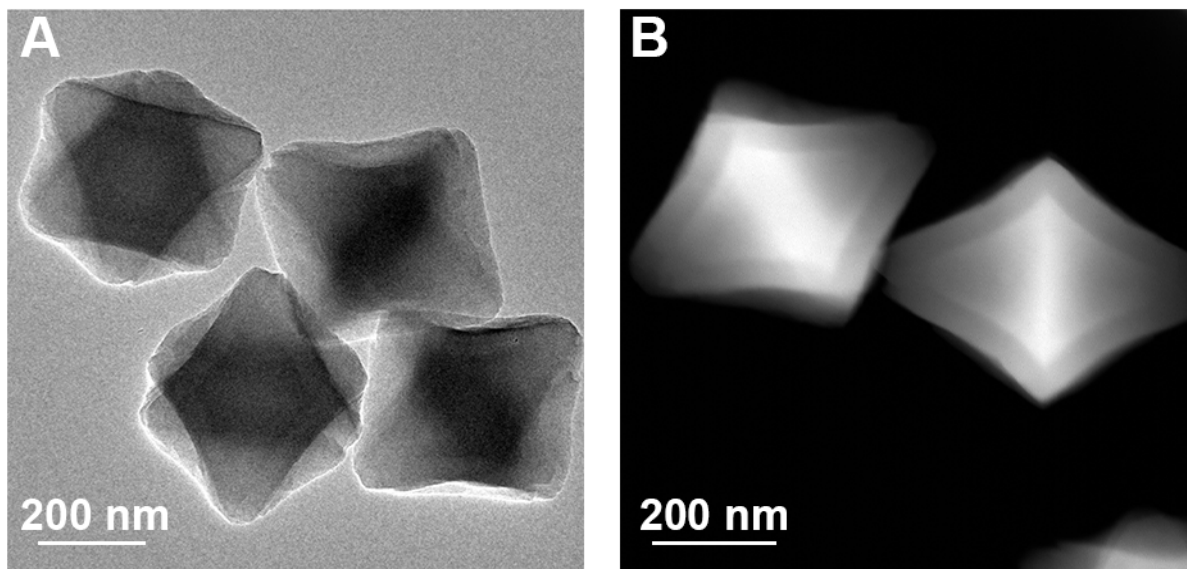


**Figure 4.36** TEM image (A) and STEM-HAADF image (B) of Bpy-UiO-67(Zr)@Pro-UiO-67(Zr).

#### 4.4.3.15 UiO-67(Zr) metalation control experiment

Bis(acetonitrile)dichloropalladium(II) (15.6 mg, 0.06 mmol) was dissolved in 3 mL acetonitrile in a 4 mL pyrex vial. The Bis(acetonitrile)dichloropalladium(II) solution was then mixed with 1 mL acetonitrile suspension of UiO-67(Zr) (~ 3 mg, ~0.009 mmol BPDC). The mixture was placed at room temperature for 24 hours. After centrifugation at 10,000 rpm for 2 min and copiously wash with acetonitrile (6 mL, 6x), white precipitate was collected and examined by STEM-EDS.

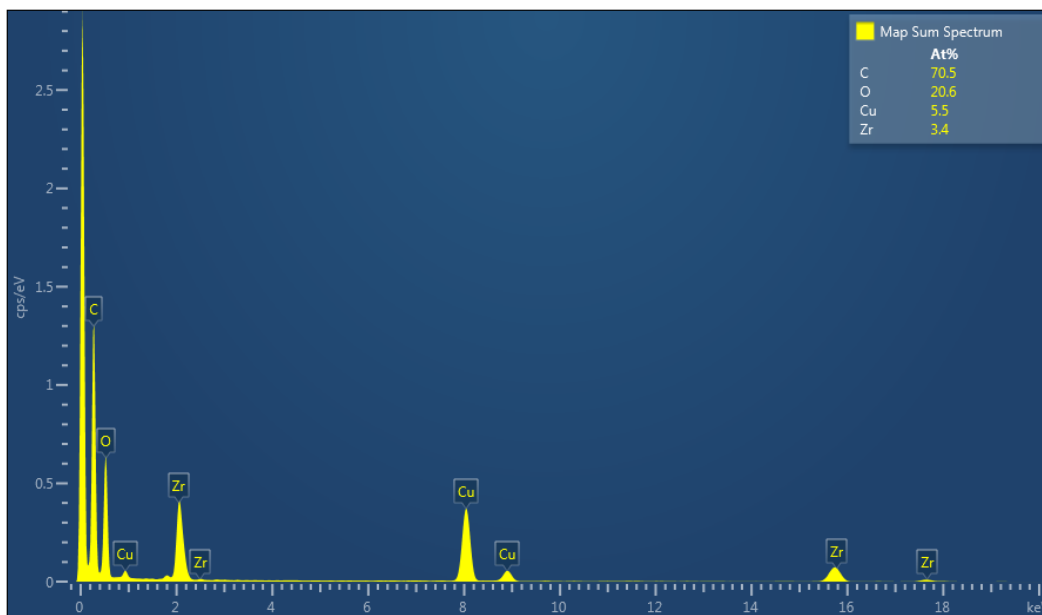
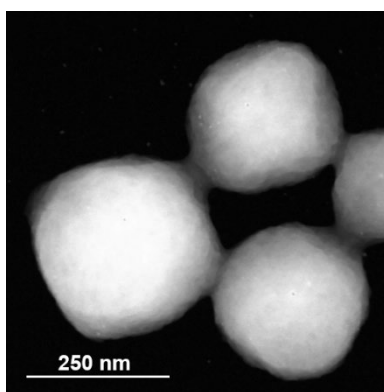


**Figure 4.37** STEM-HAADF Image of UiO-67(Zr) (top) and EDS sum spectrum (bottom) of the entire image area after soaking with  $\text{PdCl}_2(\text{CH}_3\text{CN})_2$  solution and thorough washing.

#### 4.4.3.16 Pro-UiO-67(Zr) metalation control experiment

0.4 M solution of  $Zr(O^iPr)_4$  in  $CH_3COOH$  was prepared by mixing  $Zr(O^iPr)_4$  70 wt. % in *n*-propanol (187.2 mg, 0.4 mmol) with  $CH_3COOH$  (1 mL). A 0.02 M solution of  $H_2$ -Pro-BPDC in DMF was prepared by dissolving  $H_2$ -Pro-BPDC (18 mg, 0.04 mmol) in DMF (2 mL). To a 20 mL Pyrex vial were added in sequence  $CH_3COOH$  (0.2 mL), 0.4 M  $Zr(O^iPr)_4$  solution (0.05 mL, 0.02 mmol), DMF (4 mL) and 0.02 M  $H_2$ -Pro-BPDC solution (1 mL, 0.02 mmol). The vial was tightly capped and heated at 65 °C for 9 hours in an isothermal oven to yield turbid suspension. The suspension was centrifuged at 10000 rpm for 2 min to obtain Pro-UiO-67(Zr) as off-white precipitate. The precipitate was washed with fresh DMF (4 mL, 4x) and acetonitrile (4 mL, 4x), and then evacuated under vacuum for 1 h.

Bis(acetonitrile)dichloropalladium(II) (2.6 mg, 0.01 mmol) was dissolved in 1 mL acetonitrile in a 4 mL pyrex vial. The Bis(acetonitrile)dichloropalladium(II) solution was then mixed with 0.5 mL acetonitrile suspension of Pro-UiO-67(Zr) (~ 4 mg, ~0.007 mmol BPDC). The mixture was placed at room temperature for 24 h. After centrifugation at 10,000 rpm for 2 min and copiously wash with acetonitrile (6 mL, 6x), white precipitate was collected and examined by STEM-EDS.

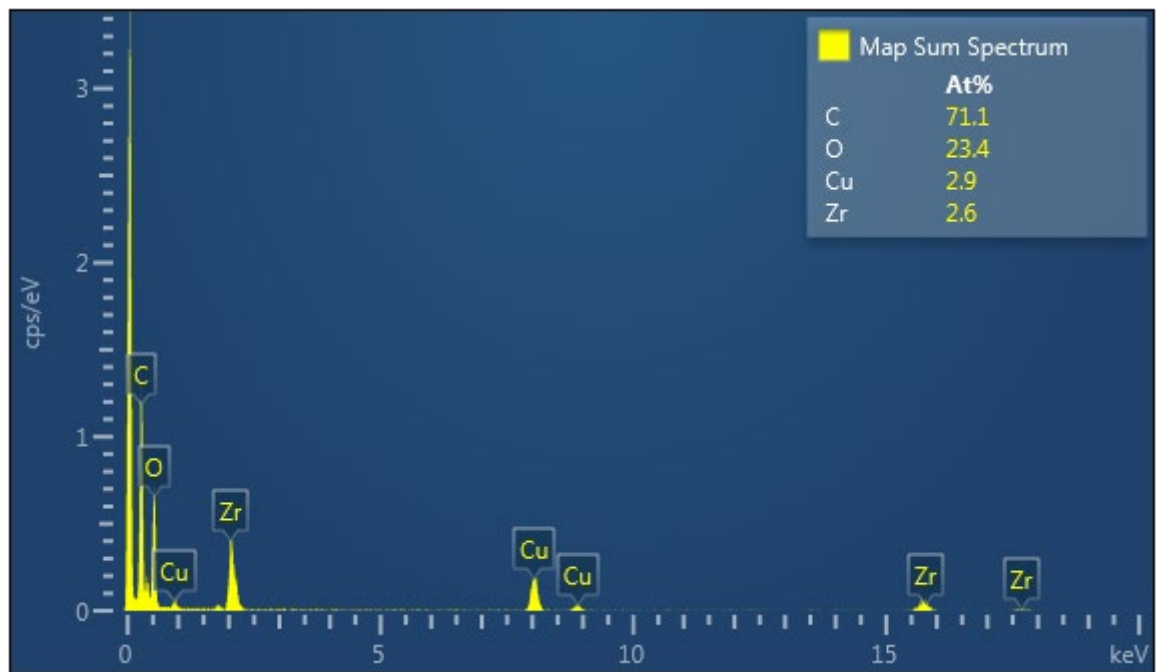
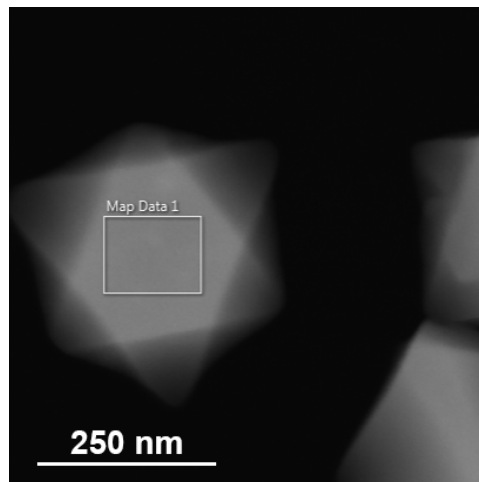


**Figure 4.38** STEM-HAADF Image of Pro-UiO-67(Zr) (top) and EDS sum spectrum (bottom) of the surveyed area after soaking with  $\text{PdCl}_2(\text{CH}_3\text{CN})_2$  solution and thorough washing.

#### 4.4.3.17 Synthesis of BpyPd-UiO-67(Zr)⊂UiO-67(Zr)

Bis(acetonitrile)dichloropalladium(II) (10.4 mg, 0.04 mmol) was dissolved in 3 mL acetonitrile in a 4 mL Pyrex vial. The Bis(acetonitrile)dichloropalladium(II) solution was then mixed with 1 mL acetonitrile suspension of Bpy-UiO-67(Zr)⊂UiO-67(Zr) (~0.033 mmol BpyDC) prepared previously (*vide supra*). The mixture was placed at room temperature for 24 h. After centrifugation at 10,000 rpm for 2 min and copiously wash with acetonitrile (6 mL, 6x), yellow precipitate was collected.

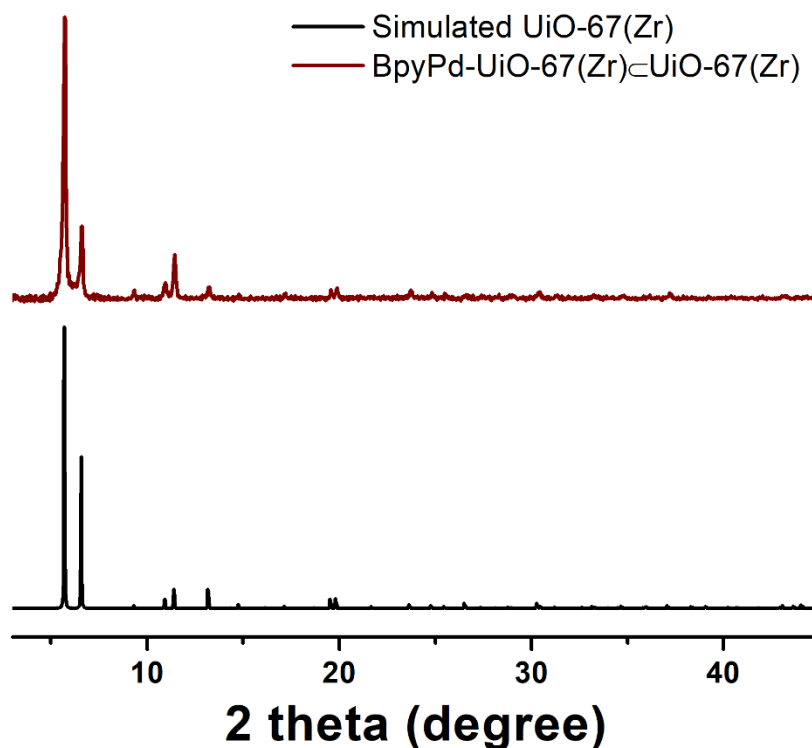


**Figure 4.39** Simulated PXRD pattern of UiO-67(Zr) (black) and experimental PXRD pattern of as-synthesized BpyPd-UiO-67(Zr)⊂UiO-67(Zr) (red).

#### 4.4.3.18 Synthesis of BpyPd-UiO-67(Zr)⊂Pro-UiO-67(Zr)

Bpy-UiO-67(Zr)⊂Pro-UiO-67(Zr) (34.4 mg, containing ~ 0.03 mmol bipyridine linker) was suspended in 1 mL acetonitrile. Bis(acetonitrile)dichloropalladium(II) (7.5 mg, 0.031 mmol) dissolved in acetonitrile (6 mL) was added to the MOF suspension. The mixture was allowed to react at room temperature for 24 h and then centrifuged at 10,000 rpm for 2 min. The yellow precipitate was collected and profusely washed with acetonitrile (6 mL, 6x).

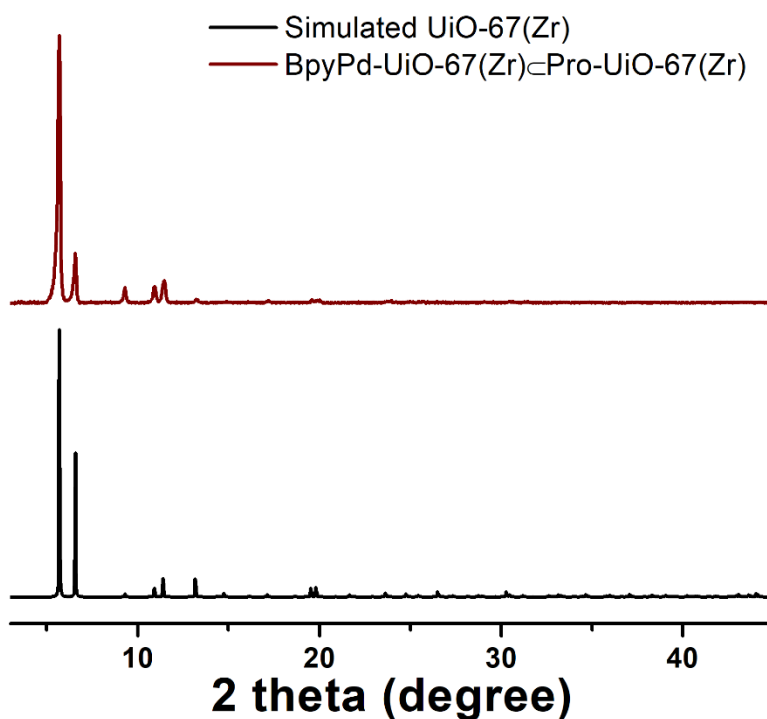


**Figure 4.40** Simulated PXRD pattern of UiO-67(Zr) and experimental PXRD pattern of as-synthesized BpyPd-UiO-67(Zr)⊂Pro-UiO-67(Zr) (red).

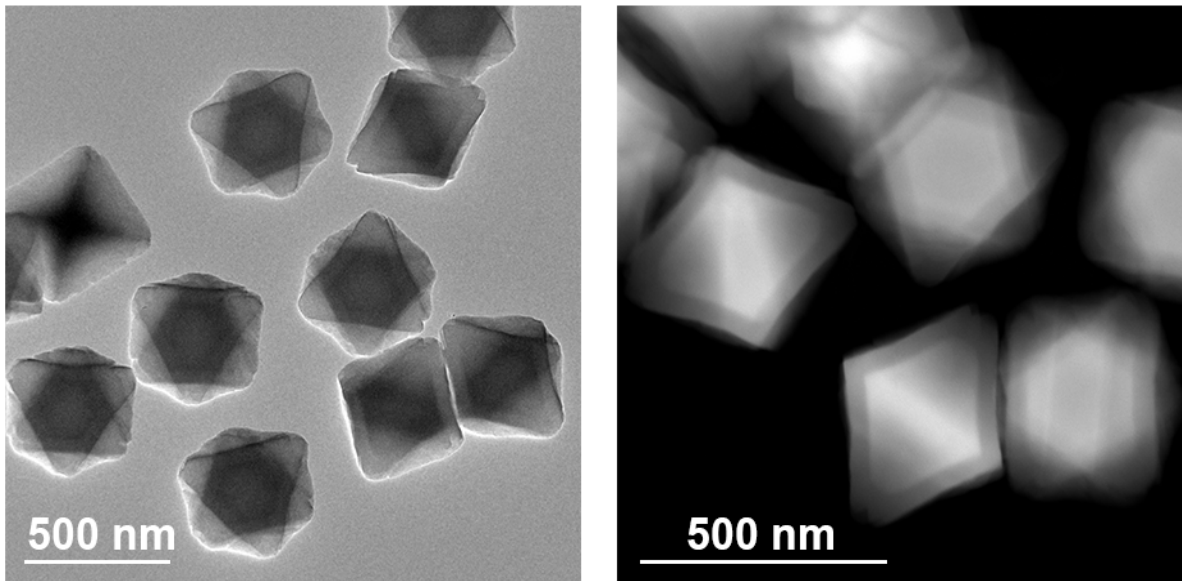


**Figure 4.41** TEM and STEM-HAADF images of BpyPd-UiO-67(Zr)@Pro-UiO-67(Zr).

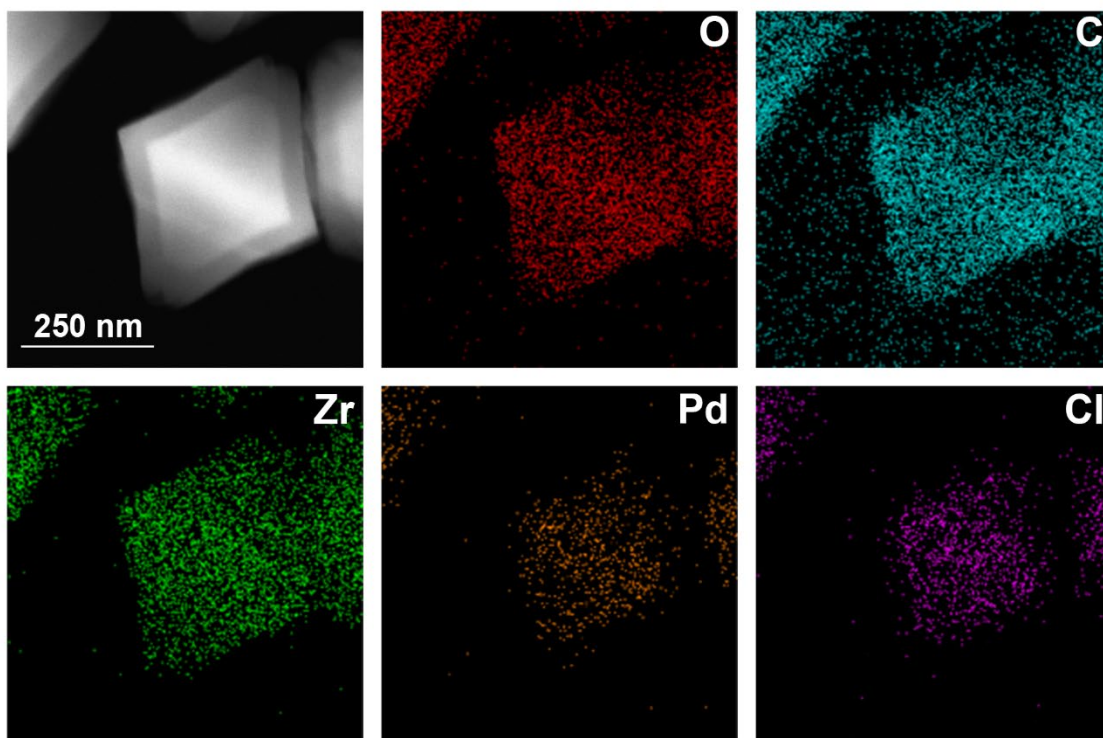


**Figure 4.42** STEM-EDS mapping data of BpyPd-UiO-67(Zr)@Pro-UiO-67(Zr).

#### 4.4.4 Characterization of nanoparticle samples

##### 4.4.4.1 Au nanoparticles with 55 kDa PVP

Au nanoparticle samples were provided by Xing Yee Gan from Millstone Group.

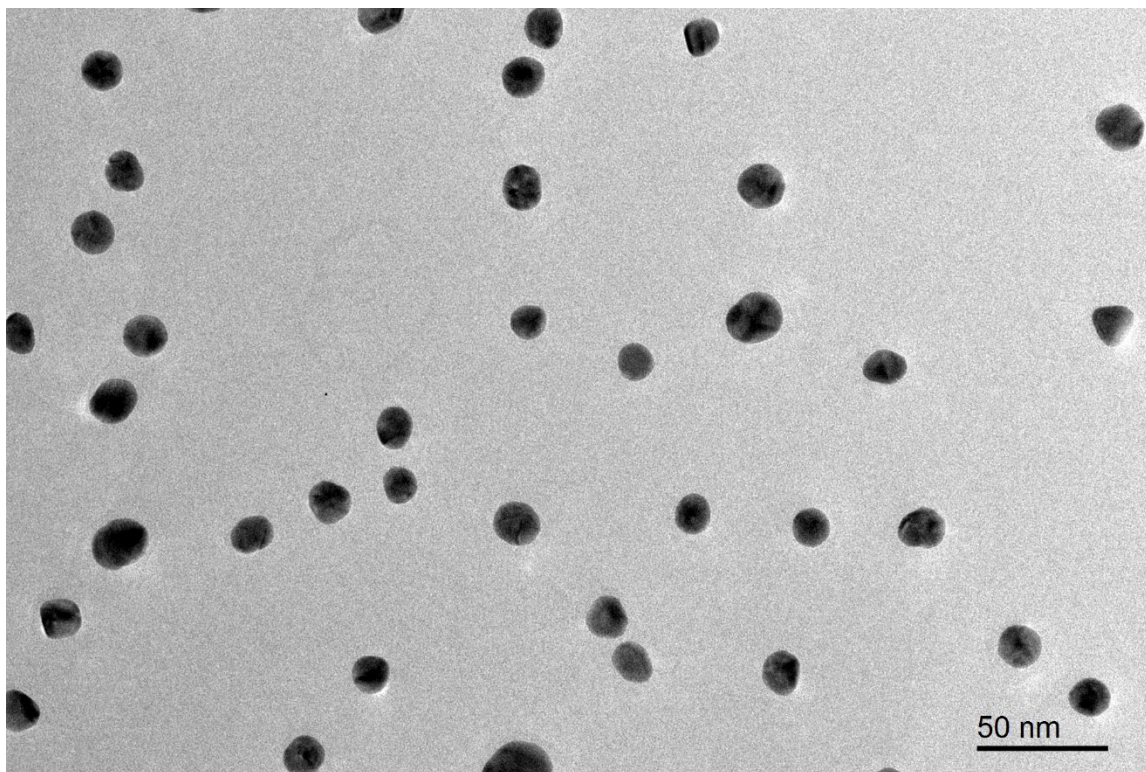


**Figure 4.43** TEM images of 13 nm 55 kDa PVP capped Au nanoparticles.

##### 4.4.4.2 40 kDa PVP capped Ag nanoparticles

40 nm 40 kDa PVP capped Ag nanoparticles was purchased from VWR as a dried powder (#103369-674 NanoXact Silver Nanospheres, Dried Powder). Ag nanoparticles were dissolved in DMF before MOF encapsulation reactions.

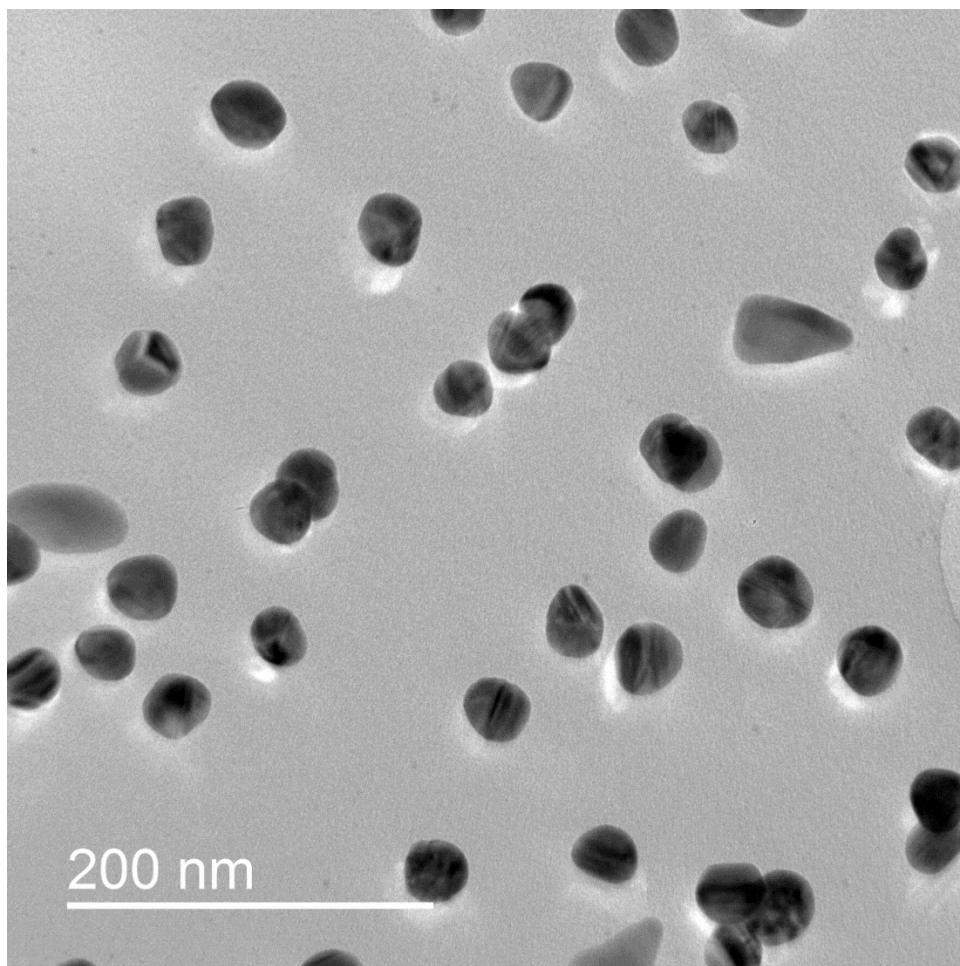


**Figure 4.44** TEM image of 40 nm Ag nanoparticles capped with 40 kDa PVP.

#### 4.4.4.3 55 kDa PVP capped $\text{Cu}_{2-x}\text{Se}$ ( $x=0.75$ ) nanoparticles

$\text{Cu}_{2-x}\text{Se}$  nanoparticle samples were provided by Xing Yee Gan from Millstone Group.

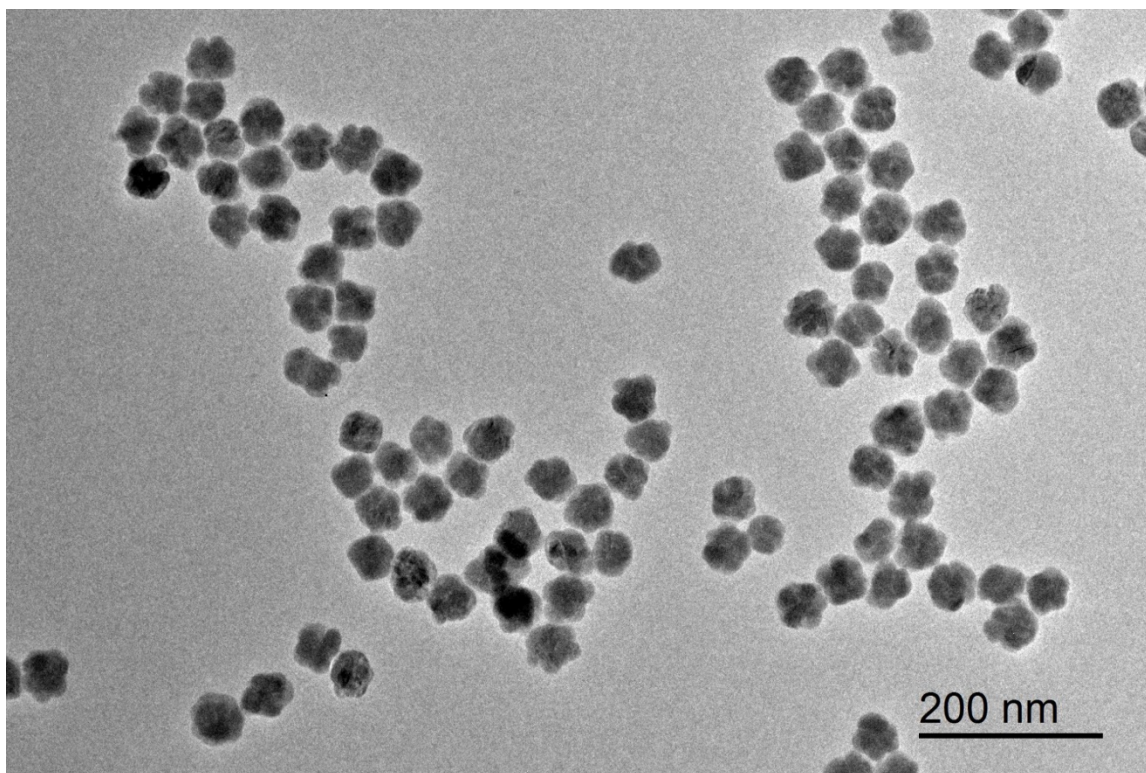


**Figure 4.45** TEM image of  $\text{Cu}_{2-x}\text{Se}$  nanoparticles capped with 55 kDa.

#### 4.4.5 Syntheses and characterization of NPs@MOF composites

##### 4.4.5.1 Synthesis of Au@UiO-67

0.4 M solution of  $\text{Zr}(\text{O}^i\text{Pr})_4$  in  $\text{CH}_3\text{COOH}$  was prepared by mixing  $\text{Zr}(\text{O}^i\text{Pr})_4$  70 wt. % in *n*-propanol (187.2 mg, 0.4 mmol) with  $\text{CH}_3\text{COOH}$  (1 mL). A 0.02 M solution of  $\text{H}_2\text{-BPDC}$  in DMF was prepared by heating a mixture of  $\text{H}_2\text{-BPDC}$  (19.4 mg, 0.08 mmol) and DMF (4 mL) on a stir plate at 150 °C until complete dissolution. DMF solution of 13 nm Au nanoparticles capped with 55 kDa PVP was prepared such that the optical density was 0.132 at 521 nm upon dilution by 25 times. To a 20 mL Pyrex vial were added in sequence  $\text{CH}_3\text{COOH}$  (0.3 mL), 0.4 M  $\text{Zr}(\text{O}^i\text{Pr})_4$

solution (0.05 mL, 0.02 mmol), DMF (4 mL) and 0.02 M H<sub>2</sub>-BPDC solution (1 mL, 0.02 mmol), Au nanoparticle solution (0.2 mL) . The vial was tightly capped and heated at 65 °C in an isothermal oven for 30 min to yield pink turbid suspension. The suspension was centrifuged at 10000 rpm for 2 min to obtain pink precipitate. The precipitate was washed with fresh DMF (16mL, 4x) and used immediately for the next step.

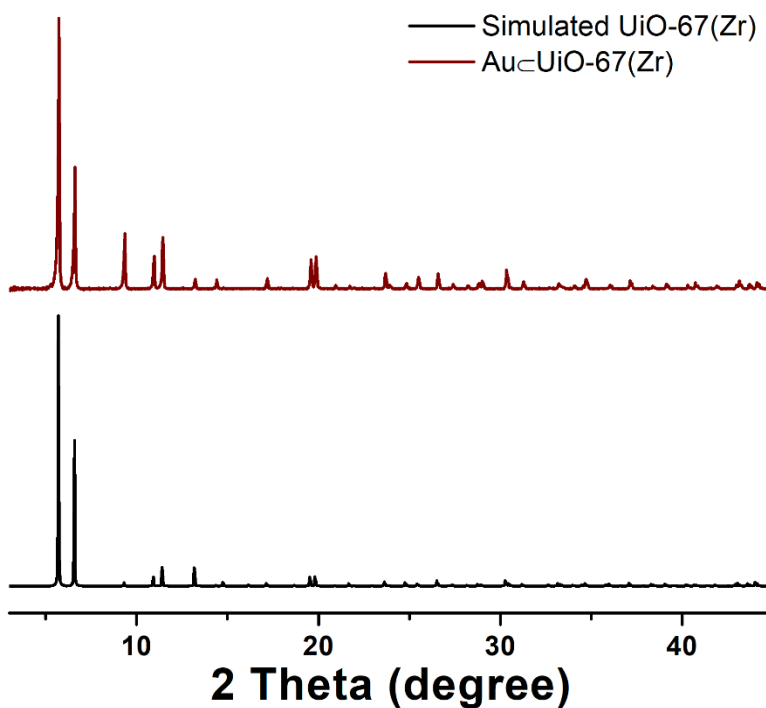


**Figure 4.46** Simulated PXRD pattern of UiO-67(Zr) (black) and PXRD pattern of as-synthesized Au@UiO-67(Zr) (red).

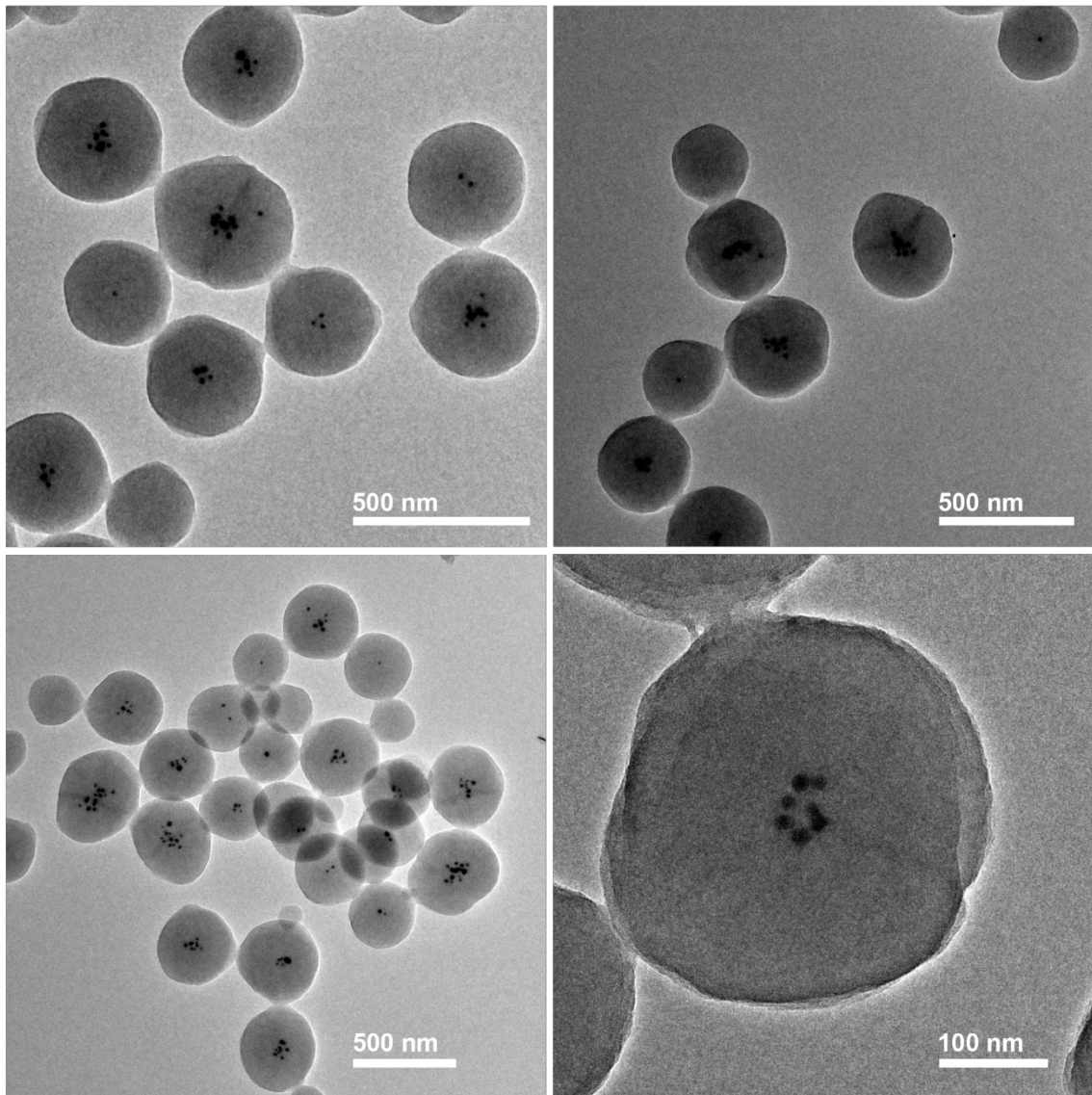


**Figure 4.47** TEM images of Au@UiO-67(Zr).

#### 4.4.5.2 Synthesis of Au $\subset$ UiO-67(Zr) $\subset$ UiO-67(Hf)

0.02 M solution of H<sub>2</sub>-BPDC in DMF was prepared by heating a mixture of H<sub>2</sub>-BPDC (19.4 mg, 0.08 mmol) and DMF (4 mL) on a stir plate at 150 °C until complete dissolution. Hf(O<sup>*i*</sup>Pr)<sub>4</sub>•<sup>*i*</sup>PrOH (19 mg, 0.04 mmol) and CH<sub>3</sub>COOH (0.7 mL) was mixed in a 20 mL Pyrex vial. After the mixture was sonicated for 3 min, DMF (3.2 mL) and 0.02 M H<sub>2</sub>-BPDC solution (2 mL, 0.04 mmol) was added. The mixture was vortexed and incubated at 65 °C in an isothermal oven for 50 min. The reaction suspension was then centrifuged at 10000 rpm for 2 min to obtain white precipitate and clear supernatant. The clear supernatant (3 mL) was used to disperse Au $\subset$ UiO-67(Zr) prepared previously (*vide supra*) by vortexing and sonication. The reaction was allowed to proceed at 25 °C without stirring for 19 hours. the reaction suspension was centrifuged at 10000 rpm for 2 min to obtain pink precipitate. The product was then washed with fresh DMF (16mL, 4x) before further characterization or reactions.

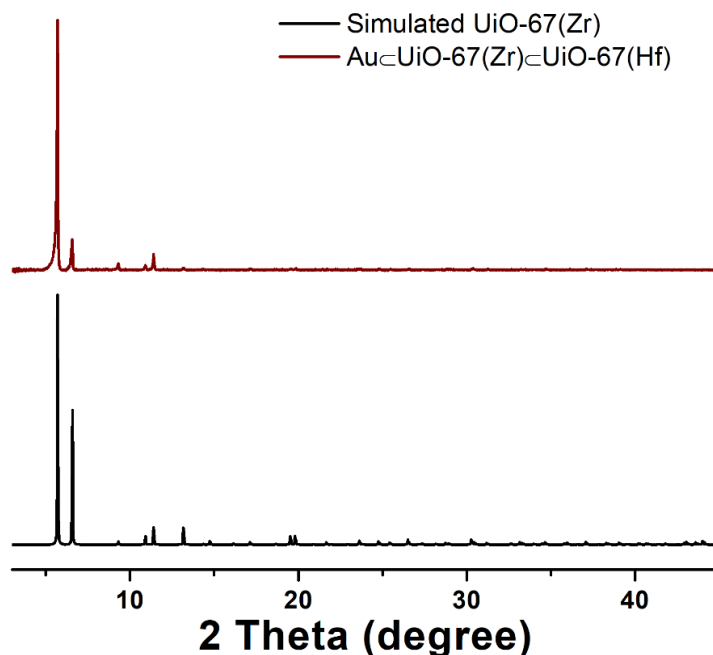


**Figure 4.48** Simulated PXRD pattern of UiO-67(Zr) (black) and experimental PXRD pattern of as-synthesized Au $\subset$ UiO-67(Zr) $\subset$ UiO-67(Hf) (red).

#### 4.4.5.3 Synthesis of Ag@UiO-67(Zr)

0.4 M solution of  $Zr(O^iPr)_4$  in  $CH_3COOH$  was prepared by mixing  $Zr(O^iPr)_4$  70 wt. % in *n*-propanol (187.2 mg, 0.4 mmol) with  $CH_3COOH$  (1 mL). A 0.02 M solution of  $H_2$ -BPDC in DMF was prepared by heating a mixture of  $H_2$ -BPDC (19.4 mg, 0.08 mmol) and DMF (4 mL) on a stir plate at 150 °C until complete dissolution. DMF solution of 40 nm Ag nanoparticles capped with 40k PVP was prepared such that the optical density was ~0.37 at 439 nm upon dilution by 10 times. To a 20 mL Pyrex vial were added in sequence  $CH_3COOH$  (0.3 mL), 0.4 M  $Zr(O^iPr)_4$  solution (0.05 mL, 0.02 mmol), DMF (1.6 mL), 0.02 M  $H_2$ -BPDC solution (1 mL, 0.02 mmol) and Ag nanoparticle solution (0.8 mL). The vial was tightly capped and heated at 65 °C for 15 min in an isothermal oven to yield turbid suspension. The suspension was centrifuged at 10000 rpm for 2 min to obtain dark yellow precipitate. The precipitate was washed with fresh DMF (16mL, 4x) and used immediately for the next step.

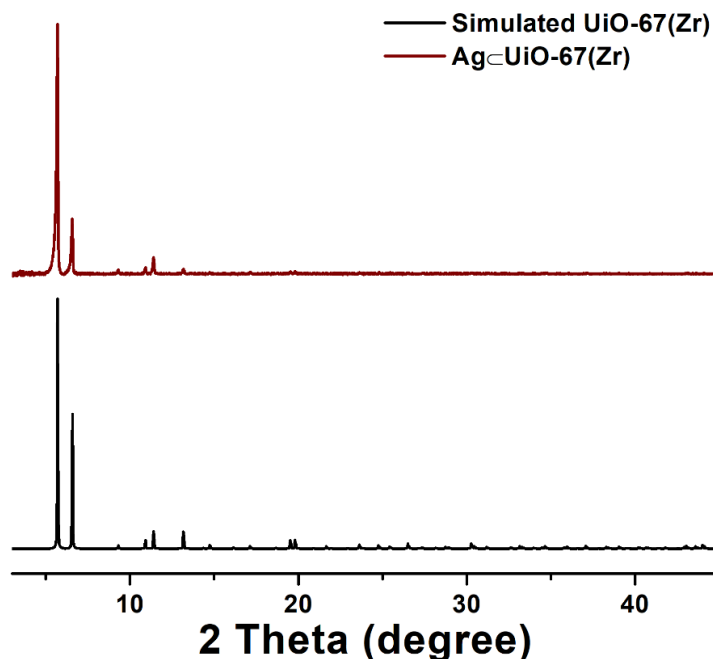


**Figure 4.49** Simulated PXRD pattern based on UiO-67(Zr) crystal structure and PXRD pattern of as-synthesized Ag@UiO-67(Zr) (red).

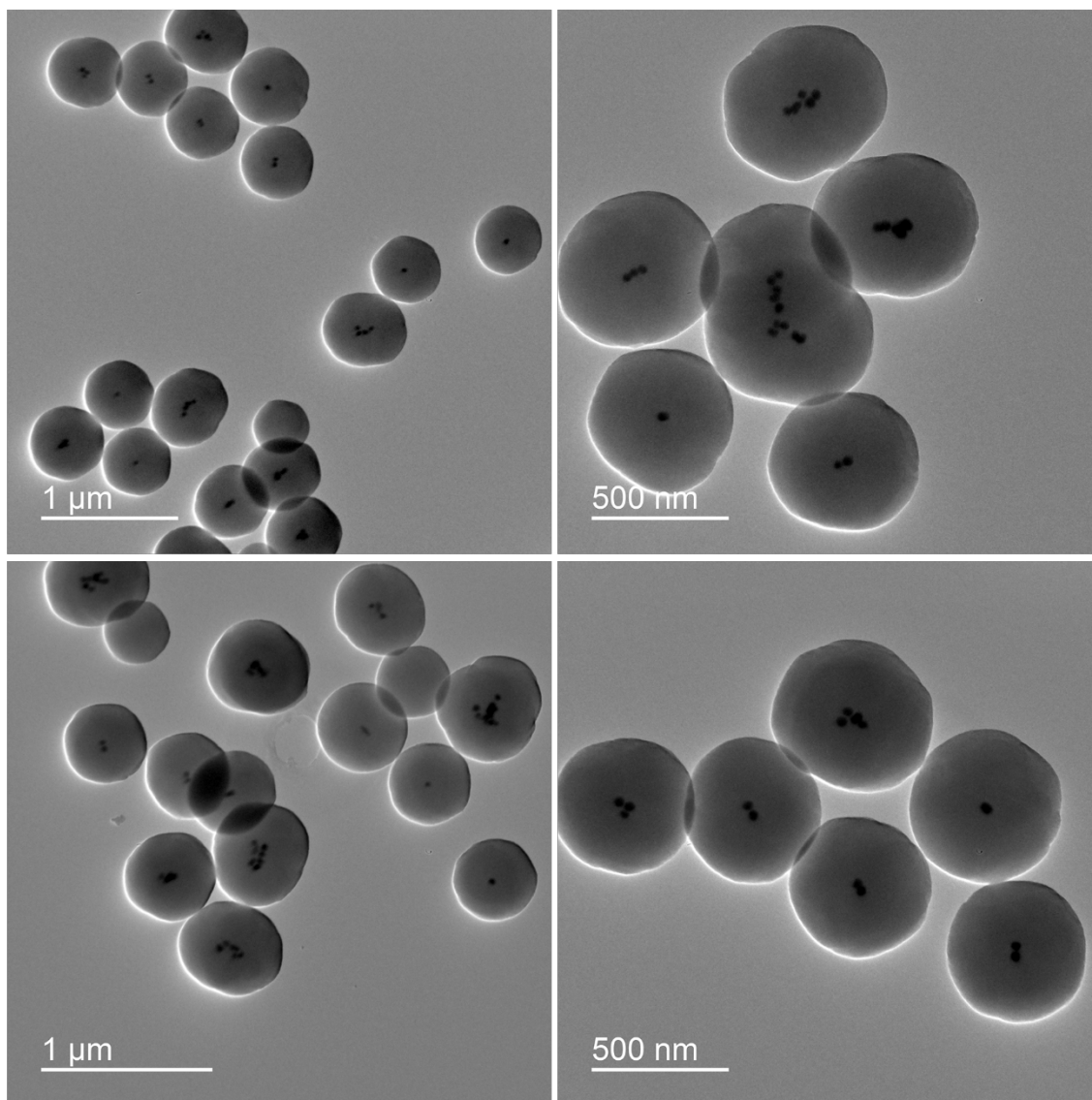


**Figure 4.50** TEM images of Ag@UiO-67(Zr).

#### 4.4.5.4 Synthesis of Ag@UiO-67(Zr)@UiO-67(Hf)

0.02 M solution of H<sub>2</sub>-BPDC in DMF was prepared by heating a mixture of H<sub>2</sub>-BPDC (19.4 mg, 0.08 mmol) and DMF (4 mL) on a stir plate at 150 °C until complete dissolution. Hf(O<sup>*i*</sup>Pr)<sub>4</sub>·<sup>*i*</sup>PrOH (19 mg, 0.04 mmol) and CH<sub>3</sub>COOH (0.7 mL) was mixed in a 20 mL Pyrex vial. After the mixture was sonicated for 3 min, DMF (3.2 mL) and 0.02 M H<sub>2</sub>-BPDC solution (2 mL,

0.04 mmol) was added. The mixture was vortexed and incubated at 65 °C in an isothermal oven for 50 min. The reaction suspension was then centrifuged at 10000 rpm for 2 min to obtain white precipitate and clear supernatant. The clear supernatant (3 mL) was used to disperse Ag $\subset$ UiO-67(Zr) prepared previously (*vide supra*) by vortexing and sonication. The reaction was allowed to proceed at 25 °C without stirring for 8 h. the reaction suspension was centrifuged at 10000 rpm for 2 min to obtain yellow precipitate. The product was then washed with fresh DMF (16mL, 4x) before further characterization or reactions.

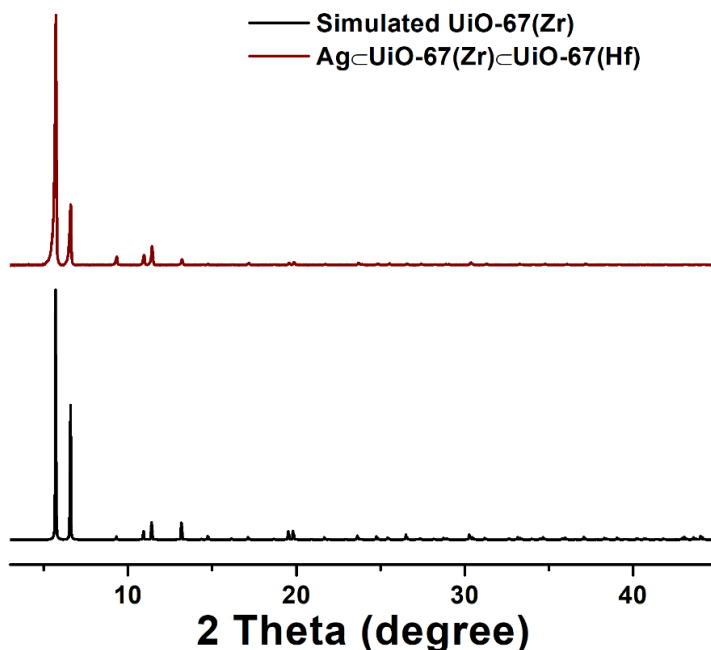


**Figure 4.51** Simulated PXRD pattern based on UiO-67(Zr) crystal structure (black) and PXRD pattern of as-synthesized Ag $\subset$ UiO-67(Zr) $\subset$ UiO-67(Hf) (red).

#### 4.4.5.5 Synthesis of Cu<sub>2-x</sub>Se $\subset$ UiO-67(Zr)

0.4 M solution of Zr(O<sup>n</sup>Pr)<sub>4</sub> in CH<sub>3</sub>COOH was prepared by mixing Zr(O<sup>n</sup>Pr)<sub>4</sub> 70 wt. % in *n*-propanol (187.2 mg, 0.4 mmol) with CH<sub>3</sub>COOH (1 mL). A 0.02 M solution of H<sub>2</sub>-BPDC in DMF was prepared by mixing H<sub>2</sub>-BPDC (19.4 mg, 0.08 mmol) with DMF (4 mL) followed by

heating on a stir plate at 150 °C until complete dissolution. EtOH solution of 50 nm  $\text{Cu}_{2-x}\text{Se}$  nanoparticles capped with 55 kDa PVP was prepared with optical density 0.2 at 1085 nm. To a 20 mL Pyrex vial were added in sequence  $\text{CH}_3\text{COOH}$  (1.2 mL), 0.4 M  $\text{Zr}(\text{O}^i\text{Pr})_4$  solution (0.2 mL, 0.08 mmol), DMF (4 mL), 0.02 M  $\text{H}_2\text{-BPDC}$  solution (4 mL, 0.08 mmol), and  $\text{Cu}_{2-x}\text{Se}$  nanoparticle EtOH solution (optical density  $\sim 0.20$  at 1085 nm, 8 mL). The reaction was tightly capped and allowed to reaction at room temperature for 40 min to yield turbid suspension. The suspension was centrifuged at 10000 rpm for 2 min to obtain dark green precipitate. The precipitate was washed with fresh DMF (16mL, 4x) and used immediately for the next step.

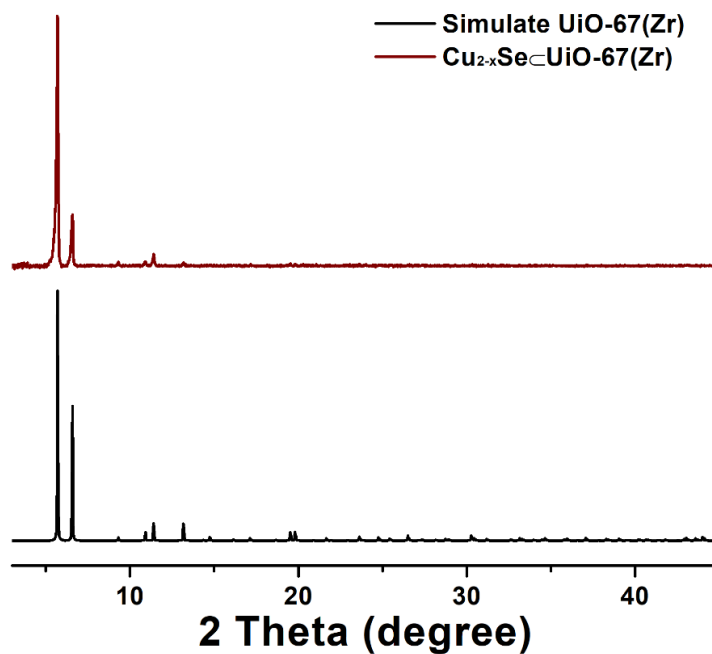


**Figure 4.52** Simulated PXRD pattern based on UiO-67(Zr) crystal structure and PXRD pattern of as-synthesized  $\text{Cu}_{2-x}\text{Se}@UiO-67(\text{Zr})$  (red).

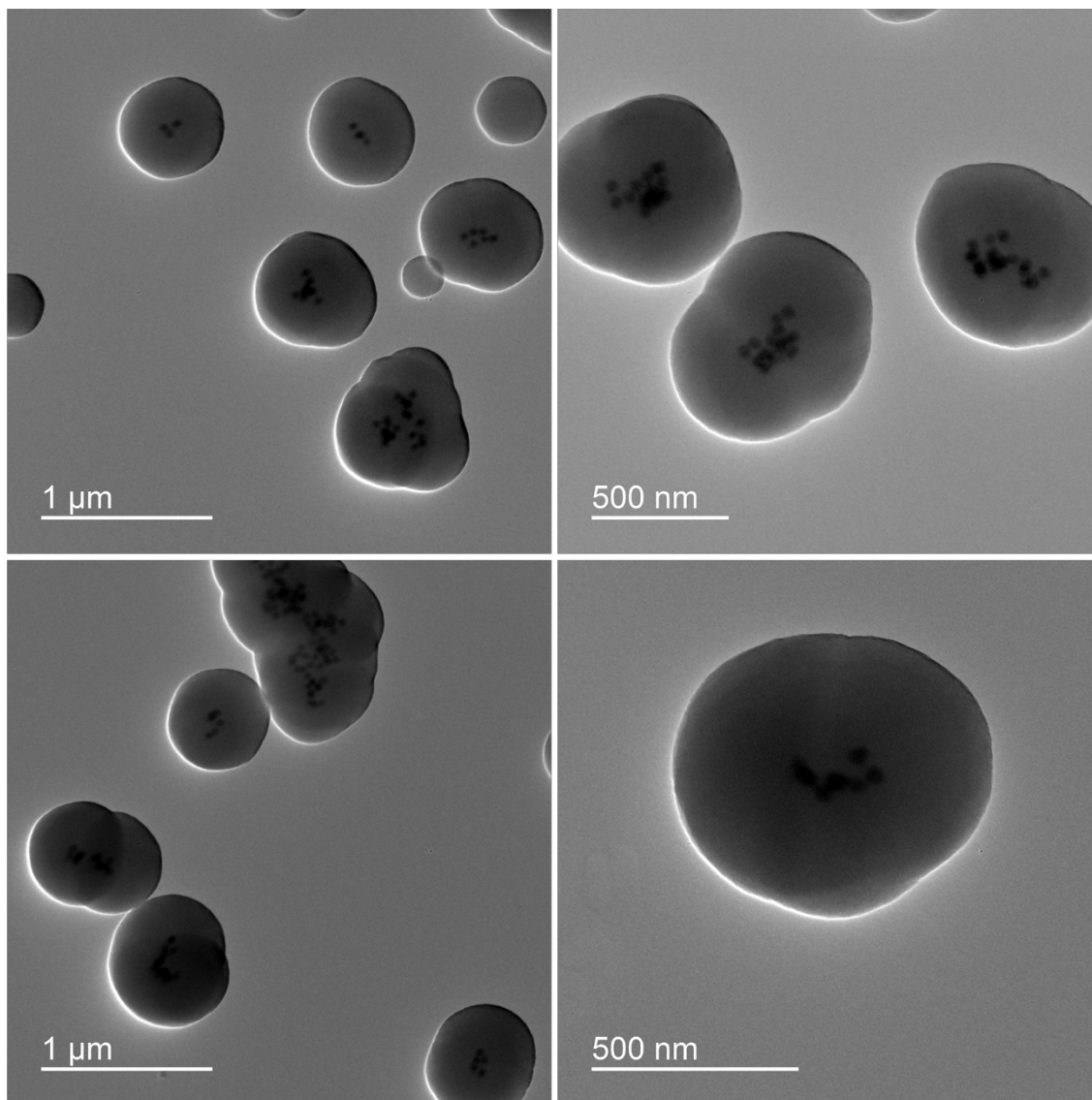


**Figure 4.53** TEM images of  $\text{Cu}_{2-x}\text{Se}@\text{UiO}-67(\text{Zr})$ .

#### 4.4.5.6 Synthesis of $\text{Cu}_{2-x}\text{Se}@\text{UiO}-67(\text{Zr})@\text{UiO}-67(\text{Hf})$

0.02 M solution of  $\text{H}_2\text{-BPDC}$  in DMF was prepared by heating a mixture of  $\text{H}_2\text{-BPDC}$  (19.4 mg, 0.08 mmol) and DMF (4 mL) on a stir plate at 150 °C until complete dissolution.  $\text{Hf}(\text{O}^i\text{Pr})_4 \cdot i\text{PrOH}$  (19 mg, 0.04 mmol) and  $\text{CH}_3\text{COOH}$  (0.7 mL) was mixed in a 20 mL Pyrex vial. After the mixture was sonicated for 3 min, DMF (3.2 mL) and 0.02 M  $\text{H}_2\text{-BPDC}$  solution (2 mL,

0.04 mmol) was added. The mixture was vortexed and incubated at 65 °C in an isothermal oven for 50 min. The reaction suspension was then centrifuged at 10000 rpm for 2 min to obtain white precipitate and clear supernatant. The clear supernatant (3 mL) was used to disperse  $\text{Cu}_{2-x}\text{Se}@\text{UiO}-67(\text{Zr})$  prepared previously (*vide supra*) by brief vortexing and sonication. The reaction was allowed to proceed at 25 °C without stirring for 6 h. the reaction suspension was centrifuged at 10000 rpm for 2 min to obtain grey precipitate. The product was then washed with fresh DMF (16mL, 4x) before further characterization or reactions.

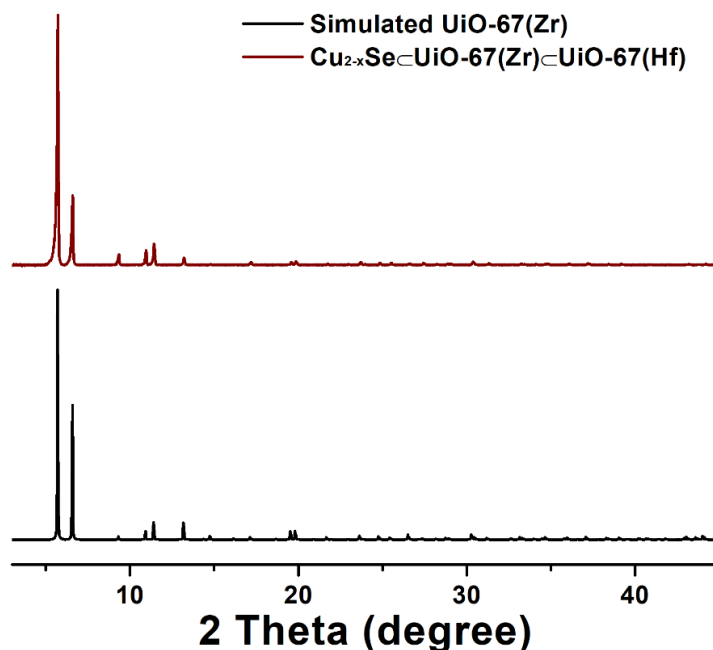


**Figure 4.54** Simulated PXRD pattern based on UiO-67(Zr) crystal structure and PXRD pattern of as-synthesized  $\text{Cu}_{2-x}\text{Se}@\text{UiO}-67(\text{Zr})@\text{UiO}-67(\text{Hf})$  (red).

## 5.0 DESIGN, SYNTHESIS AND CHARACTERIZATION OF METAL-ORGANIC FRAMEWORKS FOR ENHANCED SORPTION OF CHEMICAL WARFARE AGENT SIMULANTS

This chapter is adapted and reprinted in part with permission from: Jonathan P. Ruffley; Isabella Goodenough; **Tian-Yi Luo**; Melissandre Richard; Eric Borguet; Nathaniel L. Rosi; J. Karl Johnson. Design, Synthesis, and Characterization of Metal–Organic Frameworks for Enhanced Sorption of Chemical Warfare Agent Simulants. *The Journal of Physical Chemistry C* **2019**, *123* (32), 19748-19758. Copyright 2019 American Chemical Society.

Jonathan P. Ruffley, Isabella Goodenough and **Tian-Yi Luo** (Tianyi Luo) contributed equally to this work. Tian-Yi Luo conducted MOF synthesis and characterization. Jonathan P. Ruffley performed theoretical modeling. Isabella Goodenough and Melissandre Richard conducted temperature programmed desorption experiments. All authors participated in experiment design, data interpretation and manuscript writing.

### 5.1 INTRODUCTION

Chemical warfare agents (CWAs) are a persistent and evolving threat. Therefore, continued development of mitigation and defense technologies is necessary. Currently, a combination of high-efficiency particulate air (HEPA) media and activated carbon impregnated with materials

capable of reacting with volatile species is used in respirators to protect against exposure to CWAs.<sup>205-207</sup> While highly effective in capturing a variety of deadly species, microporous carbon-based materials suffer from limited selectivity to CWAs due to their ill-defined pore sizes, shapes, and pore chemistry.<sup>208</sup> In addition, the lack of catalytic activity in purely carbonaceous sorbents (e.g., activated carbon) results in the potential re-emission of CWAs.<sup>209-210</sup>

Key features of an ideal reactive sorbent material for CWA removal include high capacity and selectivity towards CWAs, the ability to convert CWAs into benign products, stability under a variety of conditions for a long period of time, and the ability to regenerate the sorbent and catalyst. To this end, metal-organic frameworks (MOFs) have many advantages. Compared to porous carbons, many MOFs have not only larger surface areas for high adsorption capacity, but also well-defined pores required for high selectivity.<sup>211-212</sup> Further, MOF pore dimensions and chemistry can be systematically modified by adjusting the size and functional groups of organic linkers, which can significantly affect MOF-adsorbate interactions and potentially lead to enhanced selectivity for specific adsorbates.<sup>213-214</sup>

A variety of MOFs have been examined for CWA simulant adsorption and destruction.<sup>215-220</sup> Computational and experimental methods demonstrate that MOFs degrade CWAs and less hazardous CWA simulant molecules in acidic/basic/neutral solutions,<sup>215-216,221-224</sup> under ambient conditions,<sup>225-226</sup> catalytically,<sup>215-216, 221-224, 226-228</sup> non-catalytically,<sup>225</sup> when impregnated into other materials such as textiles,<sup>224, 228-229</sup> and when doped or impregnated with other materials, such as Lewis bases.<sup>223, 227</sup>

In this work we focus on the UiO family of MOFs.<sup>36</sup> These MOFs consist of  $Zr_6O_4(OH)_4(COO)_{12}$  secondary building units (SBUs) interconnected by linear dicarboxylate ligands and are known for their exceptional thermal, mechanical, and chemical stability.<sup>36, 230-231</sup>

By introducing functional groups to the ligands pre-synthesis, a variety of variations of these MOFs have been synthesized while maintaining excellent stability properties.<sup>49, 232-234</sup>

Recently, Wang et al. reported that dimethyl methylphosphonate (DMMP), an adsorption simulant for sarin, can be adsorbed by non-functionalized Zr-based MOFs via both reversible physisorption and irreversible chemisorption.<sup>225</sup> However, there have been relatively few studies of the interactions of CWAs or CWA simulants with functionalized MOFs.<sup>235</sup> Our hypothesis is that different functional groups incorporated into MOF linkers can be used to tune the adsorption strength of CWAs. At the outset, it is not obvious that CWA or simulant adsorption strengths can be controlled through modifying the linker with different functional groups because these molecules typically interact strongly with the SBU rather than the linker.<sup>225, 236</sup> However, the strong guest-SBU interactions are typically due to the presence of defects, such as missing linkers;<sup>225, 236-237</sup> we assume that in relatively defect-free MOFs the sorbent-sorbate interactions can be tuned by introducing functional groups on the linker.

This work examines the adsorption of DMMP in functionalized UiO-67 with the goal of identifying functional groups that impart enhanced MOF-DMMP binding. We use a variety of experimental and computational methods to probe three functionalized UiO-67 MOFs, determining the nature of their interactions with DMMP. The studies and conclusions presented herein will inform our design of stratified MOFs<sup>238</sup> containing specific domains that selectively concentrate CWAs and others that reject undesired background molecules and/or enhance the removal of CWA degradation products.

## 5.2 RESULTS AND DISCUSSION

### 5.2.1 Functional group selection

We selected UiO-67 (see Figure 1.8 in Chapter 1 for crystal structure of UiO-67) as the platform MOF for our studies because its pore windows are sufficiently large to permit facile diffusion of CWAs and their simulants.<sup>225</sup> We confined our search for functional groups to a subset of those that have already been incorporated within UiO MOFs.<sup>232, 239-241</sup> Specifically, we considered the ligands shown in Figure 5.1, including 1,1'-biphenyl-4,4'-dicarboxylate (BPDC) and its derivatives with different substituents at the 2-position, such as -CH<sub>3</sub>, -SH, -NH<sub>2</sub>, -N<sub>3</sub>, -NO<sub>2</sub>, -Br, and -Cl. We denote the corresponding UiO-67 analogue MOFs as UiO-67-X, where X represents the functional moiety.

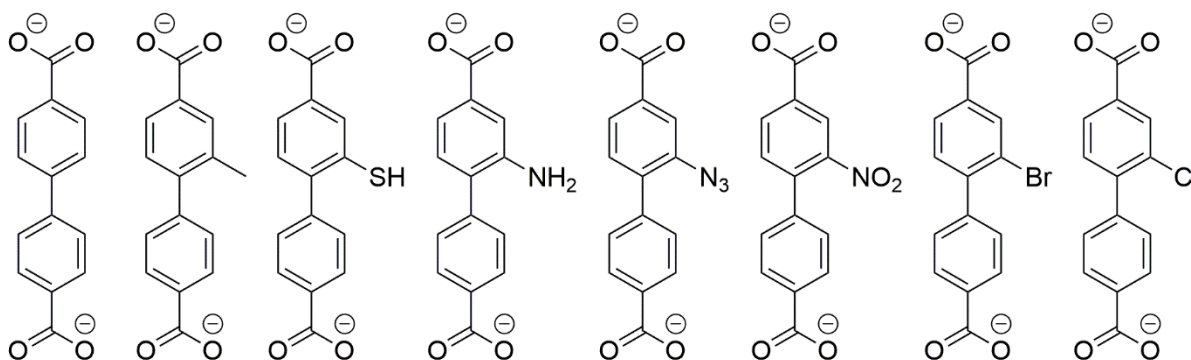


**Figure 5.1** Ligands computationally screened to create a UiO-67 family MOF (from left to right: BPDC, CH<sub>3</sub>-BPDC, SH-BPDC, NH<sub>2</sub>-BPDC, N<sub>3</sub>-BPDC, NO<sub>2</sub>-BPDC, Br-BPDC, Cl-BPDC).

### 5.2.2 DFT calculations

Density functional theory (DFT) calculations were performed with ideal primitive cells of UiO-67 and UiO-67-X ( $X = \text{CH}_3, \text{SH}, \text{NH}_2, \text{N}_3, \text{NO}_2, \text{Br}, \text{and Cl}$ ) crystal structures and a single gas phase DMMP molecule to assess the influence of different functional groups on the binding energies for DMMP. The calculated binding energies of the most favorable binding configurations are compared in Figure 5.2a. Functional groups in UiO-67 analogues lead to different binding affinity to DMMP with the order from weakest to strongest binding being  $\text{H} < \text{SH} < \text{Cl} \sim \text{NO}_2 < \text{N}_3 < \text{CH}_3 < \text{Br} < \text{NH}_2$ . Examination of the energy local minima of DMMP and the MOF crystal structures further reveals that DMMP interacts with the confluence of linkers around the SBU of the MOF in each case. The geometries of the most favorable binding configurations with DMMP for three MOFs - UiO-67, UiO-67-CH<sub>3</sub>, and UiO-67-NH<sub>2</sub> - are shown in Figure 5.2b-d. It is important to note that the DMMP does not interact directly with the SBU in the absence of missing linker defects, as can be seen from the closest pairwise interactions between DMMP and the framework coming from O atoms on DMMP interacting with H atoms on the linkers (Figure 5.2b-d). According to DFT calculations, UiO-67, UiO-67-CH<sub>3</sub>, and UiO-67-NH<sub>2</sub> have the weakest, intermediate, and strongest binding for DMMP among all the computationally examined UiO-67 analogues. we decided to further examine these three MOFs experimentally to validate the effects of functional groups on UiO-67 MOFs' binding affinity to DMMP.

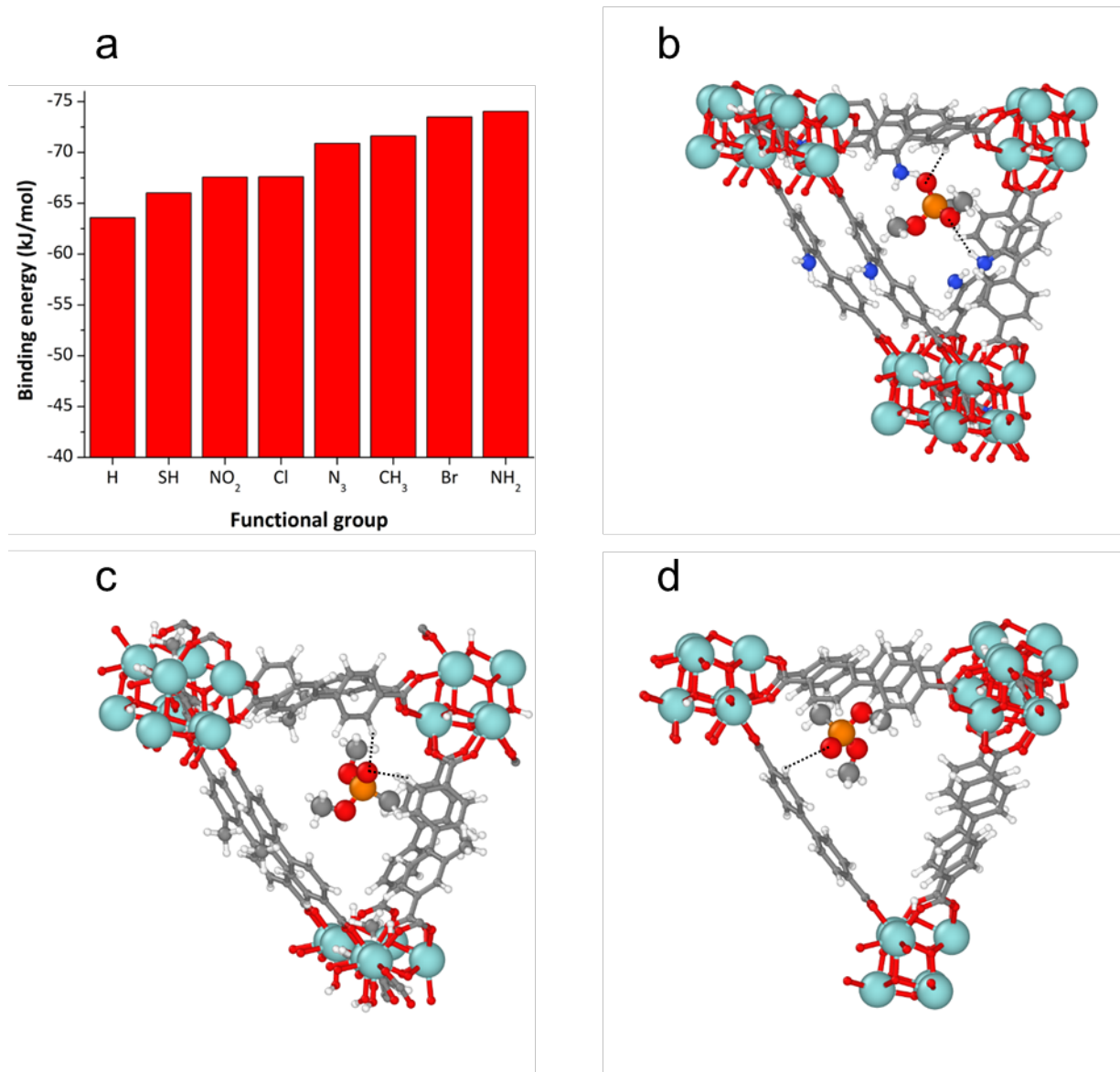


**Figure 5.2** (a) Crystal binding energies computed from CP2K DFT calculations. (b) Optimal binding geometry of DMMP with UiO-67-NH<sub>2</sub>. Dashed lines indicate hydrogen bonds of 2.34 Å (top) and 2.45 Å (bottom). (c) Optimal binding geometry of DMMP with UiO-67-CH<sub>3</sub>. Dashed lines indicate hydrogen bonds of 2.28 Å (vertical) and 2.40 Å (horizontal). (d) Optimal binding geometry of DMMP with UiO-67. Dashed line indicates hydrogen bond of 2.76 Å. For panels (b), (c), and (d), Zr shown in light blue, oxygen shown in red, carbon shown in gray, nitrogen shown in blue, hydrogen shown in white. Visualizations created with OVITO.<sup>242</sup>

### 5.2.3 MOF synthesis and characterization

Although UiO-67-X crystal structures are usually described as having each  $Zr_6O_4(OH)_4$  inorganic SBU coordinated with twelve carboxylates real UiO MOFs samples are often prone to missing linker defects with the actual number of coordinating carboxylates per SBU lower than twelve. As a result, Lewis acidic open coordination sites on  $Zr_6O_4(OH)_4$  SBUs are often present in UiO MOFs, which have been shown to strongly interact with DMMP molecules.<sup>225</sup> Therefore, the presence of a large amount of missing linker defects very likely would interfere our experimental validation of the functional groups' effects on DMMP binding predicted by DFT calculations. To minimize the influence of sample defects on DMMP-MOF interaction, UiO-67 samples with low defects are needed for this study.

UiO MOFs are usually synthesized in DMF solution solvothermally by reacting Zr(IV) metal precursors with dicarboxylic acid linker precursors in the presence of an excess amount of acidic modulator. Typical modulators used include inorganic acids or monocarboxylic acids, such as hydrochloric acid, formic acid, acetic acid and benzoic acid. The use of excess reaction modulator improves the crystallinity and reproducibility of UiO MOF products likely by modulating the crystallization process and making it more reversible. Previous works investigating the interaction between UiO MOFs and CWA simulant molecules were mostly conducted with highly defective UiO MOF samples with evidence indicating only eight coordinating carboxylates per  $Zr_6O_4(OH)_4$  SBU in some cases, instead of twelve.<sup>47</sup> These samples were mostly prepared using a standard synthesis modulated by hydrochloric acid.<sup>47</sup> The high concentration of defects in these samples are probably caused by the presence of a large amount of water (from hydrochloric acid) or strong acidity of HCl under the synthetic conditions. To produce low-defect UiO-67-X samples, glacial acetic acid, a monocarboxylic acid modulator with weaker acidity and no water

present, was used to modulate the syntheses of UiO-67 and UiO-67-X (CH<sub>3</sub>, NH<sub>2</sub>). To assess the level of defects in the synthesized UiO-67-X samples, N<sub>2</sub> gas adsorption isotherms at 77 K were collected to extrapolate BET surface areas, which were then compared with theoretical surface areas simulated using ideal crystal structures. A large discrepancy between experimental BET surface areas with the theoretical values would indicate poor sample quality, although a close match of the two does not necessarily mean the samples are defect-free. The C, H, N elemental compositions of samples with surface areas close to theoretical values were then analyzed to derive sample formulae to further estimate the level of defects in samples. An ideal sample without defect should have a formula of Zr<sub>6</sub>O<sub>4</sub>(OH)<sub>4</sub>(BPDC-X)<sub>6</sub>, while a defective MOF sample presumably can be formulated as Zr<sub>6</sub>O<sub>4</sub>(OH)<sub>4</sub>(BPDC-X)<sub>6-x</sub>(OH)<sub>2x</sub>(H<sub>2</sub>O)<sub>2x</sub> where a larger x value would indicate more defects in the sample.

The synthesis conditions, such as reaction temperature, Zr precursors and concentrations of reagents, were optimized for UiO-67, UiO-67-NH<sub>2</sub> and UiO-67-CH<sub>3</sub>. The optimized syntheses yielded relatively monodispersed discrete crystallites (Figure 5.3). The phase purity of the highly crystalline MOF samples was verified by their powder X-ray diffraction (PXRD) patterns, which show good agreement with the PXRD pattern simulated from single crystal diffraction data of UiO-67 (Figure 5.4). To determine the optimal sample activation conditions for N<sub>2</sub> adsorption experiments and the TPD experiments, thermogravimetric analysis (TGA) was used to examine the thermal stability of the three UiO-67 MOF analogues. TGA plots of all three as-synthesized samples (Figure 5.5) showed steep initial weight losses below 150°C corresponding to the evaporation of solvent guests. Solvent guest in UiO-67 accounted for a greater percentage of the initial sample weight than that of UiO-NH<sub>2</sub> and UiO-67-Me, indicating UiO-67 was more porous than UiO-67-Me and UiO-67-NH<sub>2</sub> due to the lack of functional groups. Negligible weight loss was

observed between 150°C and 400°C for all three UiO-67 analogues, indicating all three samples may be thermally stable up to 400°C.

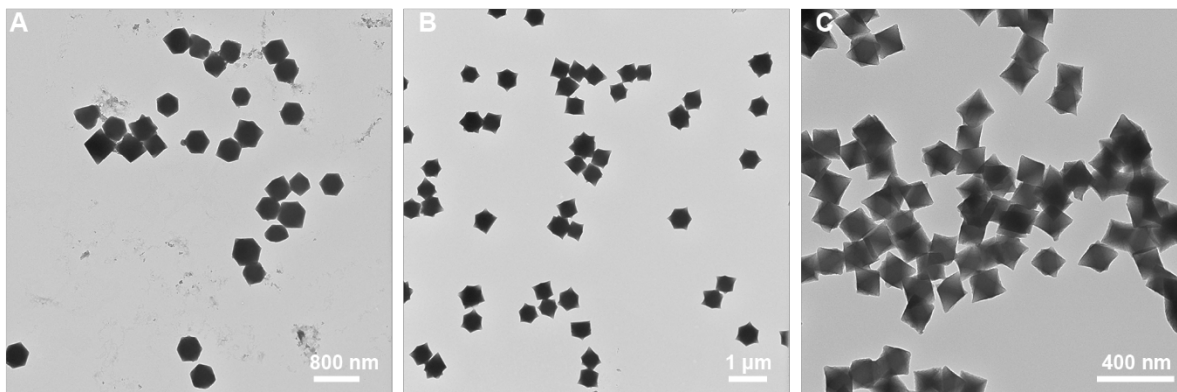


**Figure 5.3** TEM images of (A) UiO-67 crystals, (B) UiO-67-CH<sub>3</sub> crystals and (C) UiO-67-NH<sub>2</sub> crystals.

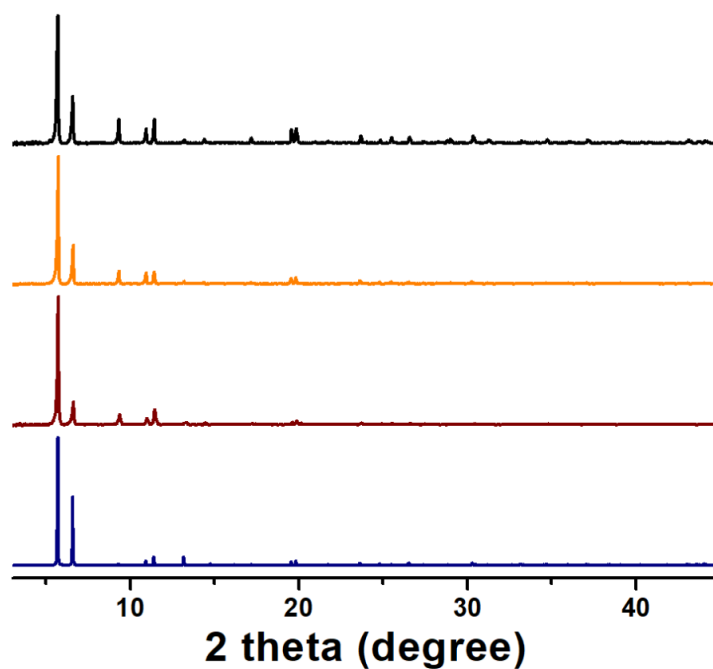


**Figure 5.4** PXRD patterns of as-synthesized UiO-67 (black), as-synthesized UiO-67-NH<sub>2</sub> (orange) and as-synthesized UiO-67-CH<sub>3</sub> (red) in comparison with simulated PXRD pattern based on the UiO-67 crystal structure (blue).

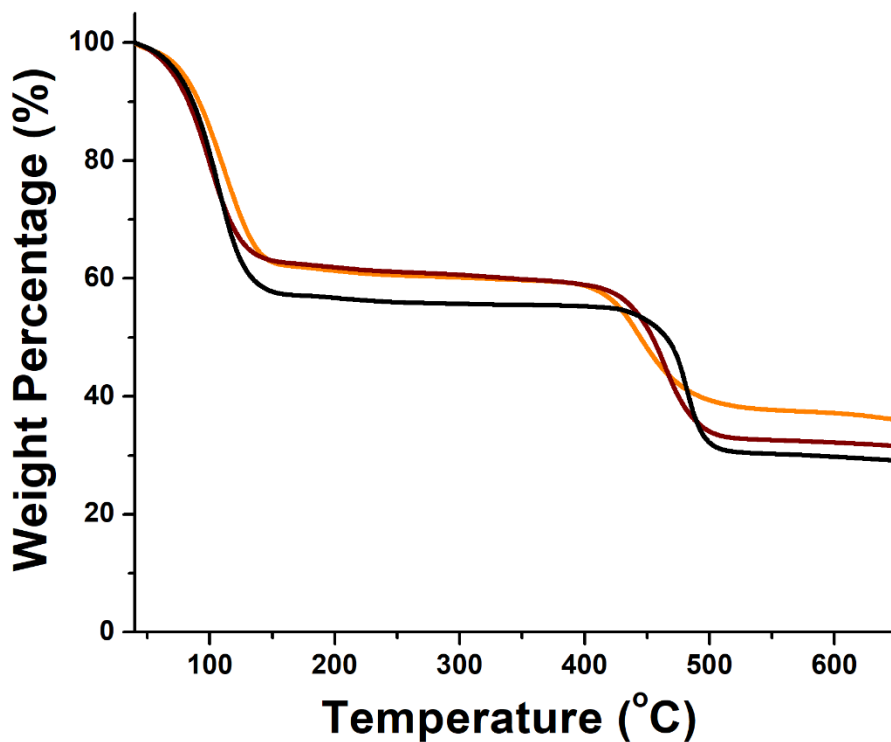


**Figure 5.5** Thermogravimetric analyses of as-synthesized UiO-67 (black), UiO-67-CH<sub>3</sub> (red), and UiO-67-NH<sub>2</sub> (orange).

Upon activation under vacuum at 100°C to remove solvent, UiO-67, UiO-67-NH<sub>2</sub> and UiO-67-CH<sub>3</sub> samples exhibit type I N<sub>2</sub> isotherms at 77 K (Figure 5.6), as expected for a microporous material.<sup>243</sup> For each MOF, N<sub>2</sub> isotherms at 77K of two or three independent batches were measured and showed very good reproducibility (Figure 5.7). Experimental BET surface areas are in good agreement with geometric surface areas calculated with ideal crystal structures as well as BET surface areas calculated from simulated N<sub>2</sub> isotherms (Figure 5.8). This good agreement in surface areas indicates that effects of missing linker defects present in the actual samples<sup>237, 241</sup> are likely small. In addition, pore size distribution data extracted from experimental N<sub>2</sub> isotherm data showed the presence of mainly two distinct types of pores, with pore widths of 13 Å and 16 Å, in UiO-67, UiO-67-NH<sub>2</sub> and UiO-67-CH<sub>3</sub> samples (Figure 5.9). They correspond to the tetrahedral and octahedral cavities in these MOFs. For UiO-67, a small amount of a third type of cavity with pore width of 18 Å was also observed (Figure 5.9), which could be a sign of defects as missing

linker defects lead to larger cavities in MOFs. According to C, H, N microanalysis data of the MOF samples after solvent removal, UiO-67-NH<sub>2</sub>, UiO-67-CH<sub>3</sub> and UiO-67 can be formulated as Zr<sub>6</sub>O<sub>4</sub>(OH)<sub>4</sub>(BPDC-NH<sub>2</sub>)<sub>5.5</sub>(OH)(H<sub>2</sub>O), Zr<sub>6</sub>O<sub>4</sub>(OH)<sub>4</sub>(BPDC-CH<sub>3</sub>)<sub>5.2</sub>(OH)<sub>1.6</sub>(H<sub>2</sub>O)<sub>1.6</sub>, and Zr<sub>6</sub>O<sub>4</sub>(OH)<sub>4</sub>(BPDC)<sub>5.6</sub>(OH)<sub>0.8</sub>(H<sub>2</sub>O)<sub>0.8</sub>, respectively. Compared to the formula of an ideal UiO-67 sample, which is Zr<sub>6</sub>O<sub>4</sub>(OH)<sub>4</sub>(BPDC-X)<sub>6</sub>, the synthesized MOF samples contain slightly fewer linkers. However, the microanalysis formulae indicate that the number of defects is similar in each sample. Therefore, comparison of experimental results between samples should still reflect the effect of different functional groups. It is also worth noting that these MOF samples contain significantly fewer defects (on average one carboxylate is missing per inorganic SBU) than MOF samples previously used in CWA studies that were synthesized with hydrochloric acid as modulator (on average, four carboxylates are missing).<sup>47</sup>

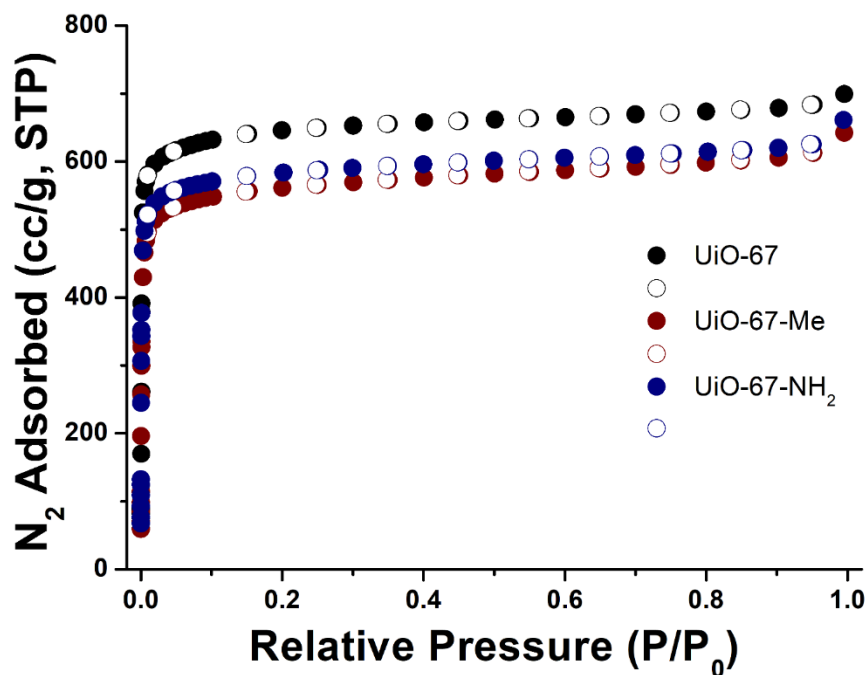


**Figure 5.6** Experimental N<sub>2</sub> isotherms at 77 K of UiO-67 (black), UiO-67-Me (red) and UiO-NH<sub>2</sub> (blue). Solid circle and open circles represent adsorption and desorption data points respectively.

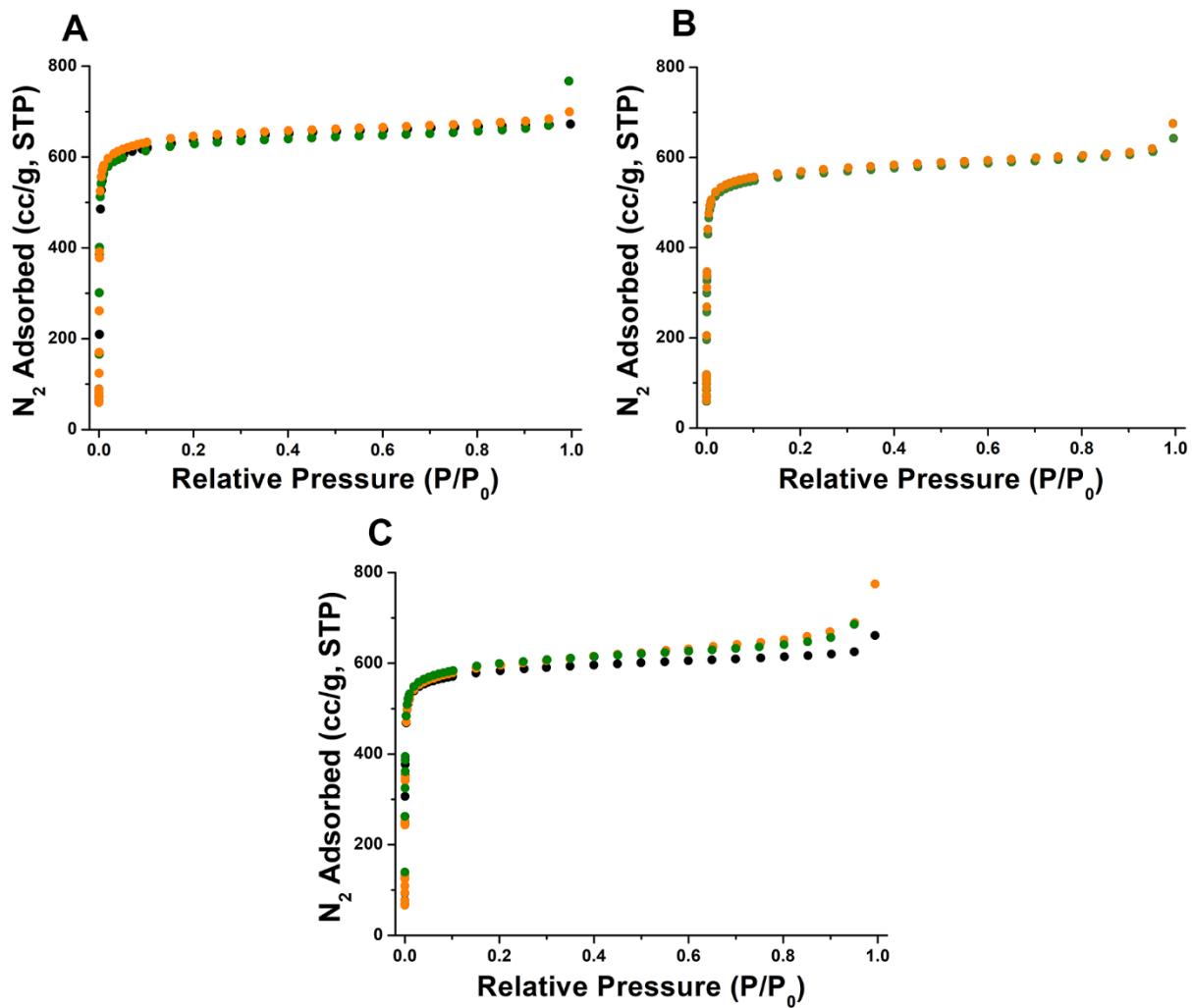


**Figure 5.7** Reproducible N<sub>2</sub> adsorption isotherms at 77 K collected with multiple independent sample batches of (a) UiO-67, (b) UiO-67-Me and (c) UiO-67-NH<sub>2</sub>. Orange, black and green data points represent different sample batches.

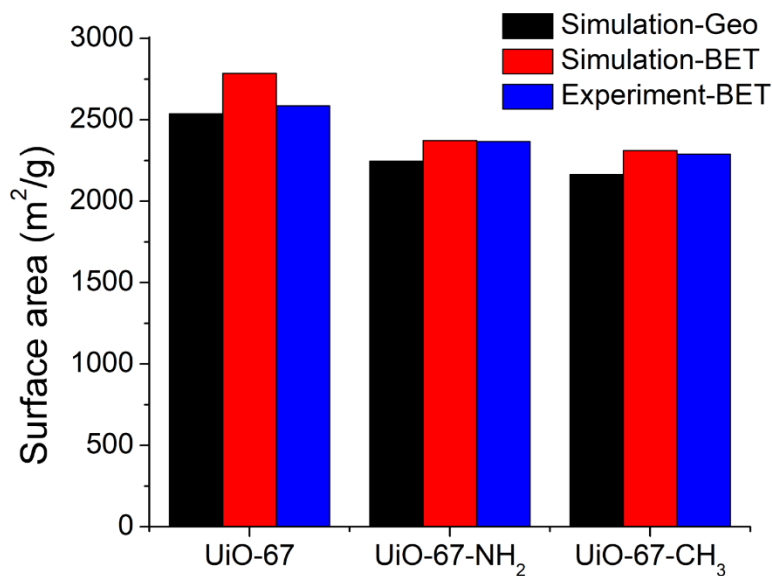


**Figure 5.8** Surface areas for the synthesized MOFs computed from simulations and from experimental BET measurements based on N<sub>2</sub> isotherms at 77 K. The data shown as black bars were computed from a geometric algorithm involving rolling an argon atom over the surface of the MOF. The data shown as red bars were computed from applying the BET equation to simulated N<sub>2</sub> isotherms at 77 K. The blue bars represent BET surface areas from experimental N<sub>2</sub> isotherms at 77 K (Figure 6.5). Overall, the agreement is very good between the experiments and simulations.

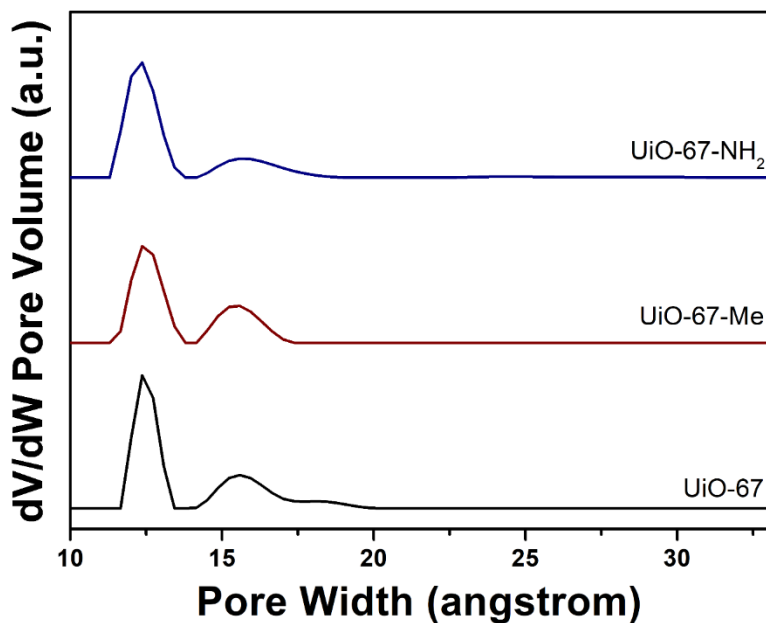


**Figure 5.9** DFT pore size distribution of UiO-67 (black), UiO-67-Me (red), and UiO-67-NH<sub>2</sub> (blue) simulated using experimental isotherm data in Figure 5.6.

#### 5.2.4 Experimental binding of DMMP to the UiO-67-X series MOFs

To investigate the strength and nature of adsorbate interactions with the UiO-67 and UiO-67 (X = CH<sub>3</sub>, NH<sub>2</sub>) MOFs, temperature programmed desorption (TPD) experiments were performed by monitoring the m/z = 15, 79, 94 and 109 DMMP molecular ion fragments as the MOF samples were heated under vacuum (from a base pressure < 1×10<sup>-9</sup> Torr) following analyte exposure. Similar temperature profiles shown in Figure 5.10, were obtained for all tracked masses for each exposure (1000 – 8000 L), providing evidence for molecular desorption of DMMP from the different UiO-67-X MOFs investigated in this study. This result suggests that association of DMMP with the MOF occurs primarily through physisorption. Previously, DMMP decomposition has been reported upon interaction with UiO-67 through hydrolysis of a single P-OCH<sub>3</sub> bond forming the chemisorbed Zr-bound product, methyl methylphosphonic acid (MMPA), and methanol.<sup>225</sup> The lack of any significant evolution of methanol (m/z = 32), as indicated by the molecular ion fragment (m/=32) provides further evidence of DMMP physisorption, rather than chemisorption.<sup>244-245</sup> This lack of chemisorption and reaction of DMMP is likely due to the low level of defects in our materials, combined with the absence of significant amounts of adsorbed water.

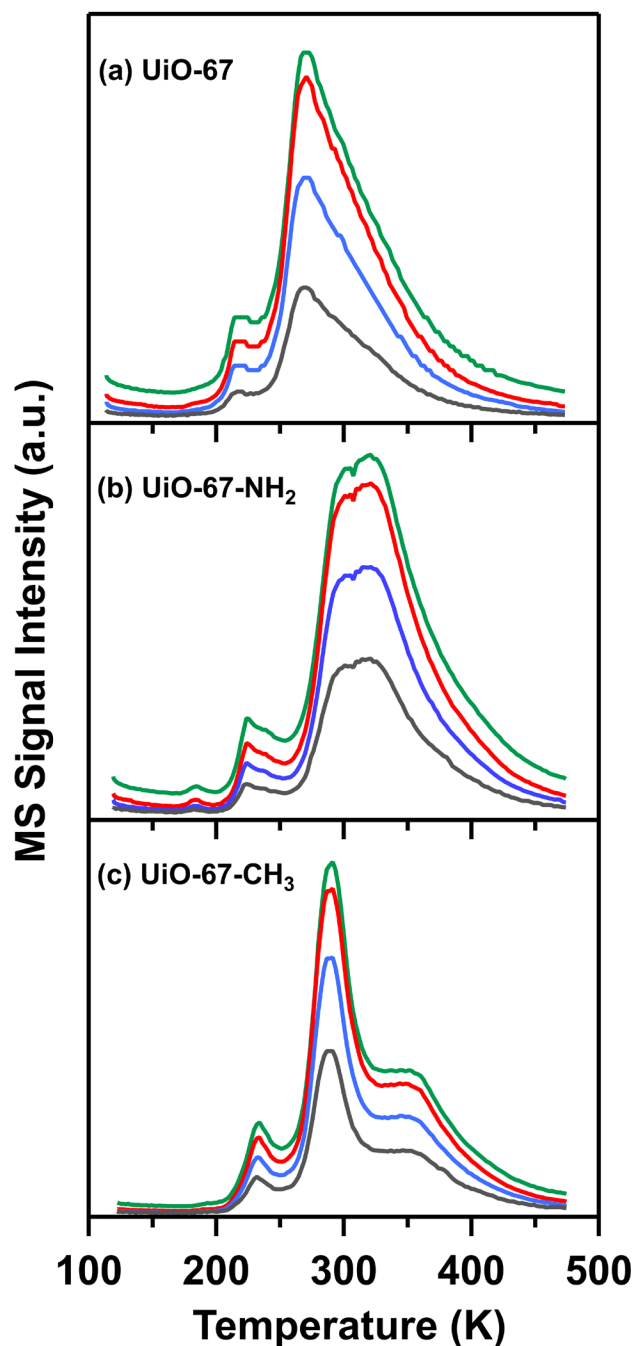


**Figure 5.10** Mass spectra temperature profiles showing all mass fragments:  $m/z = 15$  (green),  $m/z = 79$  (red),  $m/z = 94$  (blue) and  $m/z = 109$  (gray). All DMMP fragments share similar profiles indicating molecular desorption of DMMP. Note:  $m/z = 109$  was multiplied by 3 for improved resolution.

The positions of each of the multiple peaks in the DMMP TPD spectra, shown in Figure 5.11, reflect the binding energy for the associated adsorption sites on the MOF. All spectra are

shown for the  $m/z = 79$  molecular ion, which is assigned to  $\text{PO}_2\text{CH}_4^+$ .<sup>245-246</sup> At the lowest DMMP exposure (1000 L), two desorption sites were observed for all three MOFs. The first site (**M**) ( $T < 230$  K) evolved with a seemingly common leading edge and non-symmetric peak shape with successive increases in exposure. This behavior typically reflects a process following zero-order kinetics, otherwise known as multilayer (**M**) desorption.<sup>247-248</sup> The second, higher temperature site is more intense relative to the **M**-site and presents with a slightly non-symmetrical peak shape. We assign this feature to strongly (**S**) physisorbed DMMP within the MOF. Increasing exposure beyond 2000 L leads to the appearance of a third, intermediate site, which we designate as weakly (**W**) physisorbed DMMP. For UiO-67-NH<sub>2</sub> and UiO-67, **W**- and **S**-physisorbed sites evolve as a single convoluted feature whereas for UiO-67-CH<sub>3</sub>, the **W**- and **S**-sites are distinct, well-resolved features in the TPD (Figure 5.11). We interpret **S**-site desorption to be DMMP bound to the most easily accessible sites within the interior pore space. As exposure is increased, the saturation of higher energy sites (**S**) allows for DMMP to populate lower energy binding sites, and thus the evolution of the **W**-site.

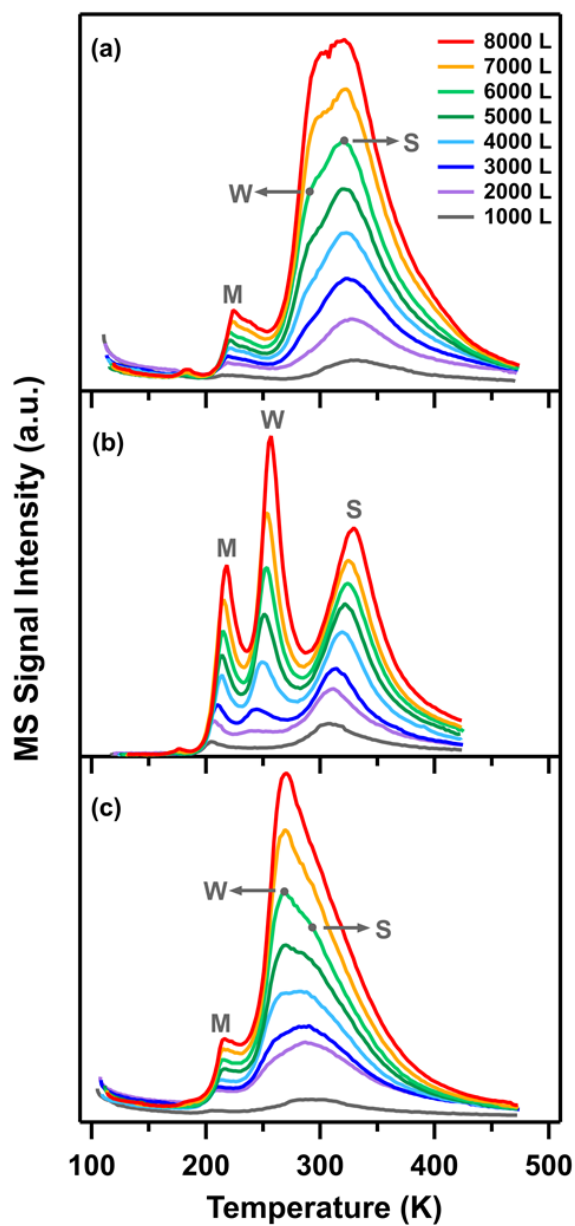


**Figure 5.11** Thermal desorption profiles as a function of DMMP exposure for (a) UiO-67-NH<sub>2</sub>, (b) UiO-67-CH<sub>3</sub> and (c) UiO-67. Spectra are shown for increasing exposure from 1000 L (gray) to 8000 L (red). Desorption sites are characterized by increasing temperature: (M) multilayer, (W) weakly physisorbed and (S) strongly physisorbed.

At the lowest DMMP exposure (1000 L), the **W**-site is not observed, as seen in Figure 5.12. The peak desorption temperature of the **S**-site of UiO-67-NH<sub>2</sub> (335 K) is greater than UiO-67-CH<sub>3</sub> (307 K) and UiO-67 (260 K). The desorption profiles for 1000 L DMMP exposure suggest the

relative binding strength for the S-site as: UiO-67-NH<sub>2</sub> > UiO-67-CH<sub>3</sub> > UiO-67 (Figure 6.11). The binding energies for the physisorbed DMMP species can be extrapolated from the peak desorption temperatures at low exposure (1000 L) using the Redhead analysis method.<sup>249</sup> Extracted energies from the S-site yield values of 87 kJ/mol, 81 kJ/mol and 76 kJ/mol, respectively (Table 5.1). The energy trend compares quite favorably with the binding energies calculated from DFT on the periodic crystal, with the DFT weaker binding than the experiments by around 10 kJ/mol.

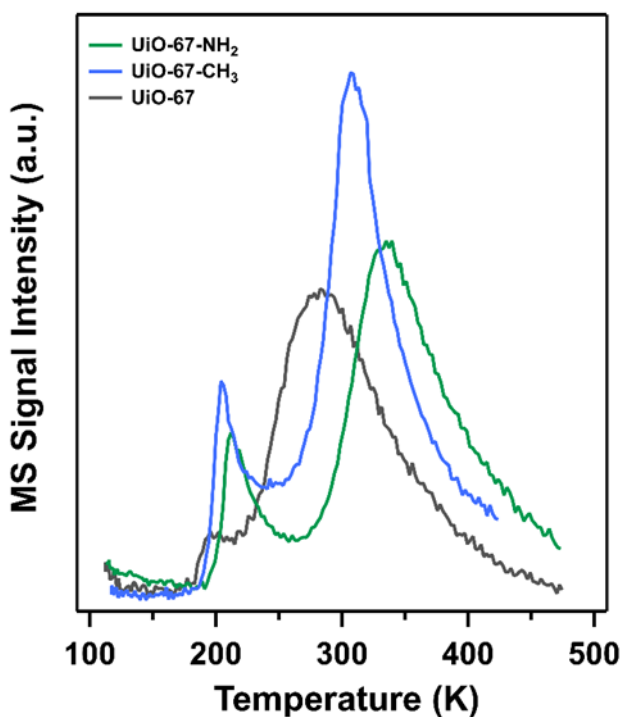


**Figure 5.12** Thermal desorption profiles at 1000 L DMMP exposure for UiO-67-NH<sub>2</sub> (green), UiO-67-CH<sub>3</sub> (blue) and UiO-67 (black).

**Table 5.1** Kinetic parameters extracted from desorption profiles following 1000 L DMMP on UiO-67-X, along with DFT predictions of the negative of the binding energies.

MOF	* $T_{\text{des}}$ (K)	$E_{\text{des}}$ (kJ/mol)	$E_{\text{DFT}}$ (kJ/mol)
UiO-67-NH <sub>2</sub>	334	87 ± 2.0	74
UiO-67-CH <sub>3</sub>	307	81 ± 0.5	71
UiO-67	260	76 ± 2.0	64

\* $T_{\text{des}}$  shown for single TPD spectra at 1000 L DMMP exposure with a heating rate of 2.2 K/s.

Infrared spectroscopy as a function of exposure provides additional information on the uptake of DMMP by the MOF, the inter-adsorbate and/or adsorbate-MOF interactions, as well as the nature of the DMMP adsorption sites. Initial IR profiles for all UiO-67-X share similar spectrum characteristics yielding several well-defined features previously assigned for low-defect and highly crystalline structures (Figure 5.13, black).<sup>250-252</sup>

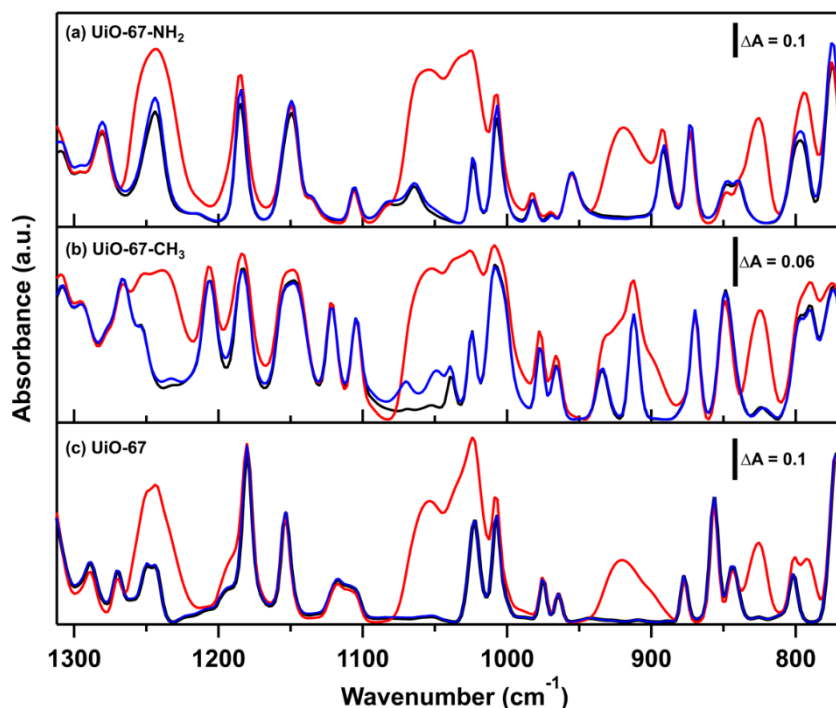


**Figure 5.13** FTIR spectra of the fingerprint region for (a) UiO-67-NH<sub>2</sub>, (b) UiO-67-CH<sub>3</sub> and (c) UiO-67 showing the initial MOF before DMMP exposure (black), after 9000 L DMMP exposure (red), and after thermal treatment to 473 K (blue). All spectra were collected at 100 K and baseline corrected.

Upon exposure (9000 L), several bands characteristic of DMMP evolve within the 1300 cm<sup>-1</sup> – 800 cm<sup>-1</sup> region (Figure 5.13, red), while the features associated with the clean MOF remain unperturbed (Figure 5.13, black). For the UiO-67 spectrum, bands centered at 1245 cm<sup>-1</sup>, 1054 cm<sup>-1</sup>, 1024 cm<sup>-1</sup> and 920 cm<sup>-1</sup> are assigned to P=O stretching, asymmetric and symmetric O-C stretching, and P-CH<sub>3</sub> bending of DMMP in the MOF, respectively (Figure 5.13, red).<sup>250-253</sup> Exposure at 100 K leads to a significant (30 – 40 cm<sup>-1</sup>) redshift for  $\nu(\text{P}=\text{O})$  and  $\nu(\text{O}-\text{C})$  modes

compared to gaseous DMMP, while the remaining DMMP spectral features remain largely unaffected, suggesting that coordination occurs primarily through the phosphoryl oxygen and/or the methoxy moieties. This observation is in qualitative agreement with the highest binding energy configurations observed in Figure 5.2, where the closest distances between DMMP and framework atoms involves O atoms within DMMP interacting with H atoms of the framework. Chemisorption of DMMP on Zr-based MOFs has been identified by a large shift in the phosphoryl stretching frequency from  $1276\text{ cm}^{-1}$  to  $1188\text{ cm}^{-1}$ .<sup>225</sup> In the present work, the phosphoryl stretch only shifts to  $1245\text{ cm}^{-1}$ , indicating a weaker (physisorption) interaction. This could be due to the relatively low density of defects in the MOFs synthesized in this work, because chemisorption of DMMP on the SBU requires the presence of undercoordinated Zr sites not available in non-defective UiO-67.

Temperature dependent IR experiments record DMMP-MOF interactions as samples are heated following DMMP exposure. Complete removal of DMMP is observed by 473 K for UiO-67 and UiO-67-NH<sub>2</sub> (Figure 5.13a, c), as evidenced by the disappearance of characteristic DMMP features described previously and recovery of pristine MOF spectral features. The recovery of the clean MOF spectra upon cooling to 100 K indicates completely reversible adsorption of DMMP on both UiO-67 and UiO-67-NH<sub>2</sub>. However, for UiO-67-CH<sub>3</sub>, spectral features potentially consistent with adsorbed DMMP are observed at  $1070\text{ cm}^{-1}$  and  $1049\text{ cm}^{-1}$  following thermal treatment to 473 K (Figure 5.13b). These features may be associated with asymmetric and symmetric methoxy stretch modes,  $\nu(\text{O-C})$ . During exposure at 100 K, these features were observed at  $1050\text{ cm}^{-1}$  and  $1030\text{ cm}^{-1}$ . The shift towards higher frequency, essentially the gas phase values, suggests residual gas-phase-like DMMP in UiO-67-CH<sub>3</sub> after thermal treatment. We do not have an explanation for this feature, but we note that it is not consistent with chemisorbed DMMP.

### 5.3 CONCLUSIONS

Density functional theory has been used to predict ligand functional groups that yield differential uptake of DMMP in a UiO-67 family MOFs. Three functionalized MOFs were synthesized based on DFT predictions of differential binding energies. TPD experiments showed that the functionalized MOFs indeed exhibit the same order of adsorption affinities for DMMP predicted from DFT calculations. Consistent with the TPD studies discussed above, FT-IR showed no evidence of decomposition reactions of DMMP with any of the MOFs, in contrast to other literature accounts, though a small amount of DMMP persists for UiO-67-CH<sub>3</sub>, even after heating to 473 K. These results demonstrate that functionalized MOF domains with differential affinity for CWAs can be fabricated, providing a foundation on which stratified MOFs for CWA capture may be based. Our calculations and experiments predict that a stratified MOF consisting of UiO-67-NH<sub>2</sub>⊂UiO-67-CH<sub>3</sub>⊂UiO-67 will show an equilibrium concentration gradient of DMMP induced by the differential binding of DMMP. Assuming a Boltzmann distribution the ratio of concentrations is predicted to be about 55:17:1 in the UiO-67-NH<sub>2</sub>, UiO-67-CH<sub>3</sub> and UiO-67 strata, respectively, based on the DFT energies (Table 5.1) at a temperature of 300 K. Thus, even these modest differences in binding energies can result in significant concentration enhancement in a target stratum of a stratified MOF.

## 5.4 EXPERIMENTAL SECTION

### 5.4.1 DFT calculations of DMMP binding energies

The functionalized linkers were incorporated into perfect UiO-67 primitive cells. The atom positions (included in the SI), using lattice parameters of relaxed UiO-67 ( $a = b = c = 19.1 \text{ \AA}$ ,  $\alpha = \beta = \gamma = 60^\circ$ ) were then relaxed using DFT as implemented in CP2K.<sup>254-256</sup> The lattice parameters of each MOF were not relaxed because it has been shown that there is minimal difference between the parameters of functionalized ligand MOFs.<sup>257</sup> The Goedecker-Teter-Hutter pseudopotentials<sup>258</sup> were used with the DZVP-MOLOPT-SR basis set,<sup>259</sup> and Grimme's dispersion correction<sup>260</sup> was applied. The cutoff and relative cutoff were 400 Ry and 50 Ry, respectively. The DIIS orbital transformation minimizer<sup>256</sup> and LBFGS optimizer<sup>261</sup> were used. These settings were used for all other CP2K calculations in this work. A single gas phase DMMP molecule was also relaxed using this procedure to compute binding energies. The resulting energies were then used to calculate binding energies via eq (1).

$$\bullet \quad \Delta E_{\text{bind}} = E_{AB} - E_A - E_B \quad (1)$$

Note that  $\Delta E_{\text{bind}}$  is negative if binding is favorable.

The ground state of a single DMMP molecule in the various UiO-67-X MOFs was estimated using the following procedure: A single DMMP molecule was randomly placed into the octahedral pore of each primitive cell. Ab initio molecular dynamics (AIMD) simulations in the canonical ensemble were carried out on the periodic system at a temperature of 1000 K using the GLE thermostat.<sup>262-263</sup> The AIMD simulations were run for 7.5 ps, using a timestep of 0.5 fs. The coordinates of the AIMD simulations were saved every 100 timesteps and the sampled geometries were relaxed in CP2K to their local minima. The lowest energy structure identified was used in eq

(1) to compute the binding energy for each functionalized MOF. Strongest binding energy structures for each MOF were then retested by substituting functional groups for all other MOFs into these structures as additional configurations to test.

## **5.4.2 MOF synthesis and characterization**

### **5.4.2.1 Synthesis of 2-amino-1,1'-biphenyl-4,4'-dicarboxylic acid**

2-Amino-1,1'-biphenyl-4,4'-dicarboxylic acid was synthesized according to literature conditions.<sup>67</sup>

### **5.4.2.2 Synthesis of 2-methyl-1,1'-biphenyl-4,4'-dicarboxylic acid**

2-Methyl-1,1'-biphenyl-4,4'-dicarboxylic acid was synthesized according to literature conditions.<sup>264</sup>

### **5.4.2.3 Synthesis of UiO-67**

A stock solution of 1,1'-biphenyl-4,4'-dicarboxylic acid (H<sub>2</sub>-BPDC) (0.04 M) in DMF was first prepared by dissolving BPDC (106.6 mg, 0.44 mmol) in DMF (11 mL) in a loosely capped 20 mL vial. To facilitate the dissolution of H<sub>2</sub>-BPDC, the vial was heated on a ceramic stir plate at ~150°C until clear solution was formed. The solution was cooled to room temperature. To a flame-dried 250 mL round-bottom flask was added ZrCl<sub>4</sub> (93.2 mg, 0.4 mmol), DMF (43 mL) and acetic acid (7 mL). The reaction mixture was sonicated for 1 min before the flask was capped by a septum and heated in oil bath at 120°C for 10 min. 0.04 M BPDC stock solution (10 mL, 0.4 mmol) was then added to the reaction mixture. The mixture was heated in oil bath at 120°C for 5 hours to yield cloudy suspension. After cooling to room temperature, the reaction mixture was

centrifuged at 3000 rpm for 15 min to yield white precipitate. The precipitate was washed with fresh DMF (120 mL, 3x). Formula:  $Zr_6(OH)_4O_4(C_{14}H_8O_4)_{5.6}(OH)_{0.8}(H_2O)_{0.8}$ ; Calc: C, 45.88; H, 2.51; N, 0.00; Found: C, 45.72; H, 2.04; N, 0.00.

#### 5.4.2.4 Synthesis of UiO-67-CH<sub>3</sub>

To a flame-dried 250 mL round-bottom flask was added  $ZrCl_4$  (46.6 mg, 0.2 mmol), DMF (50 mL) and acetic acid (2.5 mL). The reaction mixture was sonicated for 1 min before the flask was capped by a septum and heated in oil bath at 100°C for 10 min. 2-methyl-1,1'-biphenyl-4,4'-dicarboxylic acid ( $H_2-CH_3-BPDC$ ) (51.2 mg, 0.2 mmol) was then added to the reaction mixture. The mixture was sonicated for 1 min and heated in oil bath at 100°C for 14.5 hours to yield a cloudy suspension. After cooling to room temperature, the reaction mixture was centrifuged at 3000 rpm for 15 min to yield white precipitate. The precipitate was washed with fresh DMF (120 mL, 3x). Formula:  $Zr_6O_4(OH)_4(C_{15}H_{10}O_4)_{5.2}(OH)_{1.6}(H_2O)_{1.6}$ ; Calc: C, 45.53; H, 2.98; N, 0.00; Found: C, 45.26; H, 2.52; N, 0.19.

#### 5.4.2.5 Synthesis of UiO-67-NH<sub>2</sub>

0.4 M solution of  $Zr(O^iPr)_4$  in  $CH_3COOH$  was prepared by mixing  $Zr(O^iPr)_4$  70 wt. % in 1-propanol (187.2 mg, 0.04 mmol) with  $CH_3COOH$  (1 mL). To a 40 mL Pyrex vial were added acetic acid (1.2 mL) To a 40 mL Pyrex vial were added in sequence  $CH_3COOH$  (1.2 mL), 0.4 M  $Zr(O^iPr)_4$  solution (0.3 mL, 0.12 mmol), DMF (24 mL) and 2-amino-1,1'-biphenyl-4,4'-dicarboxylic acid ( $H_2-NH_2-BPDC$ ) (30.9 mg, 0.12 mmol). After sonication for 1 min, the tightly capped vial was heated at 65°C in an isothermal oven for 16 h to yield a turbid yellow suspension. The mixture was centrifuged at 3000 rpm for 15 min to obtain yellow precipitate. The precipitate

was washed with fresh DMF (120 mL, 3x). Formula:  $Zr_6O_4(OH)_4(C_{14}NH_9O_4)_{5.5}(OH)(H_2O)$ ; Calc: C, 43.66; H, 2.69; N, 3.64; Found: C, 43.24; H, 2.32; N, 3.52.

#### **5.4.2.6 Powder x-ray diffraction**

Powder X-ray diffraction (PXRD) patterns were collected using a Bruker AXS D8 Discover powder diffractometer at 40 kV, 40 mA for Cu K $\alpha$  ( $\lambda = 1.5406 \text{ \AA}$ ) with a scan speed of 0.10 s/step from 3° to 45° at a step size of 0.02°. The data were analyzed using the EVA program from the Bruker Powder Analysis Software package. The simulated powder patterns were calculated using Mercury 3.8, based on crystal structures of corresponding MOFs.

#### **5.4.2.7 N<sub>2</sub> gas adsorption**

N<sub>2</sub> gas adsorption experiments were performed using a Quantachrome Autosorb-1 instrument. MOF samples suspended in dimethyl formamide (DMF) were centrifuged at 5000 rpm for 3 min. After the removal of supernatant, the precipitate was evacuated on a Schlenk line for 20 min. The powdery sample was then activated by heating under vacuum at an outgassing station on a Quantachrome Autosorb-1 instrument in three sequential stages: 50°C for 1 hour, 90°C for 2 hours and 100°C for 15 hours. N<sub>2</sub> adsorption isotherms at 77 K were then collected.

#### **5.4.2.8 C, H, N elemental microanalyses**

C, H, N elemental microanalyses were performed by the University of Illinois, Department of Chemistry Microanalytical Laboratory using a Perkin-Elmer 240 Elemental Analyzer and an Exeter Analytical CE440. Prior to analysis, MOF samples were activated under vacuum on an Autosorb AS-1 (vide supra) and shipped to the microanalytical laboratory.

#### 5.4.2.9 Thermogravimetric analyses

Thermogravimetric analyses (TGA) were performed using a TGA Q500 thermal analysis system under a nitrogen atmosphere from room temperature to 650°C at a ramping rate of 5°C/min. Transmission electron microscopy (TEM) imaging was conducted on an FEI Morgagni 268 operated at 80 kV and equipped with an AMT side mount CCD camera system. TEM samples were prepared by drop casting 3  $\mu$ L of ethanol suspension of MOF sample onto a 3 mm diameter copper grid with Carbon/Formvar coating. The grid was then air-dried before TEM imaging.

#### 5.4.2.10 Simulated surface areas

Simulated surface areas were calculated for each MOF using a Lennard-Jones 12-6 argon model<sup>265</sup> following an accessible surface area procedure<sup>266</sup> and compared to Brunauer-Emmett-Teller (BET)<sup>267</sup> surface areas calculated from nitrogen isotherms at 77 K. These nitrogen isotherms were compared to isotherms simulated within the grand canonical Monte Carlo (GCMC) approach, as implemented in RASPA.<sup>268</sup> The potential used for nitrogen was taken from the literature.<sup>269</sup>

#### 5.4.2.11 TPD-MS and TP-IR

TPD-MS and TP-IR experiments were performed in an ultra-high vacuum (UHV) instrument described previously.<sup>270</sup> Briefly, a stainless steel UHV chamber was evacuated using a turbomolecular pump backed by a mechanical pump providing a base pressure of less than  $5 \times 10^{-9}$  Torr after bakeout. MOF samples were deposited onto a clean 25  $\mu$ m tungsten grid (AlfaAesar) braced to a copper sample manipulator. A fast-response K-type thermocouple (Omega) was spot-welded directly onto the W grid to monitor sample temperature. This design allowed for rapid cooling of the sample to cryogenic temperatures of  $\sim 100$  K and resistive heating up to 1400 K using direct current from a power supply (Model # SCR 10-80, Electronic Measurements Inc.).

The MOF samples, dispersed in DMF, were first centrifuged at 14,000 rpm for 5 min after which the supernatant solvent was removed. The wet MOF paste (~2 mg) was placed onto the W grid using a spatula, and the paste adhered to the grid naturally as it dried. The sample was positioned in the center of the mesh as a disk of 6-8 mm diameter and thickness about 25-50  $\mu\text{m}$  to provide uniform coverage with no apparent holes and introduced into the UHV chamber. The resulting optical density evaluated by FTIR was on the order of 1. The chamber was baked out over a period of 18-24 hours, during which the temperature of the sample and chamber reached a maximum of 373 K. Sample activation was achieved post-bakeout by holding UiO-67 and UiO-67-NH<sub>2</sub> samples at 473 K for 1 hour. UiO-67-CH<sub>3</sub> was held at 473 K for IR experiments and 423 K for 1 hour for TPD experiments, because activation of UiO-67-CH<sub>3</sub> at 473 K resulted in reproducibility issues that were not seen for the other MOFs.

DMMP (97% Sigma Aldrich) vapor was dosed to the sample by backfilling the UHV chamber through a leak valve (Varian). The purity of DMMP was verified, after having undergone 5 freeze-pump-thaw cycles, using a shielded residual gas analyzer (RGA) (AccuQuad RGA 300, Stanford Research Systems) installed in the UHV chamber. Desired exposures of DMMP were achieved by dosing at a suitable constant pressure (typically  $5 \times 10^{-6}$  Torr), monitored with a nude ion gauge (Duniway iridium filament), for the time required to achieve the desired exposure, measured in Langmuir, L, where 1 L = exposure of  $10^{-6}$  Torr for 1 s. After DMMP adsorption at 100 K, the sample temperature was ramped at 2 K/s from 100 K to 473 K (423 K for UiO-67-CH<sub>3</sub>). The most abundant mass fragments of DMMP ( $m/z = 15, 79, 94, \text{ and } 109$ ) were monitored as a function of temperature during the TPD-MS experiment. A custom program written in LabVIEW, using drivers for commercial components, was used to control the heating process, monitor temperature and pressure, and track the evolution of selected mass fragments. To monitor

DMMP integrity and purity, the mass spectra in the range 1-130 amu were collected prior to experiments (Figure 5.14).

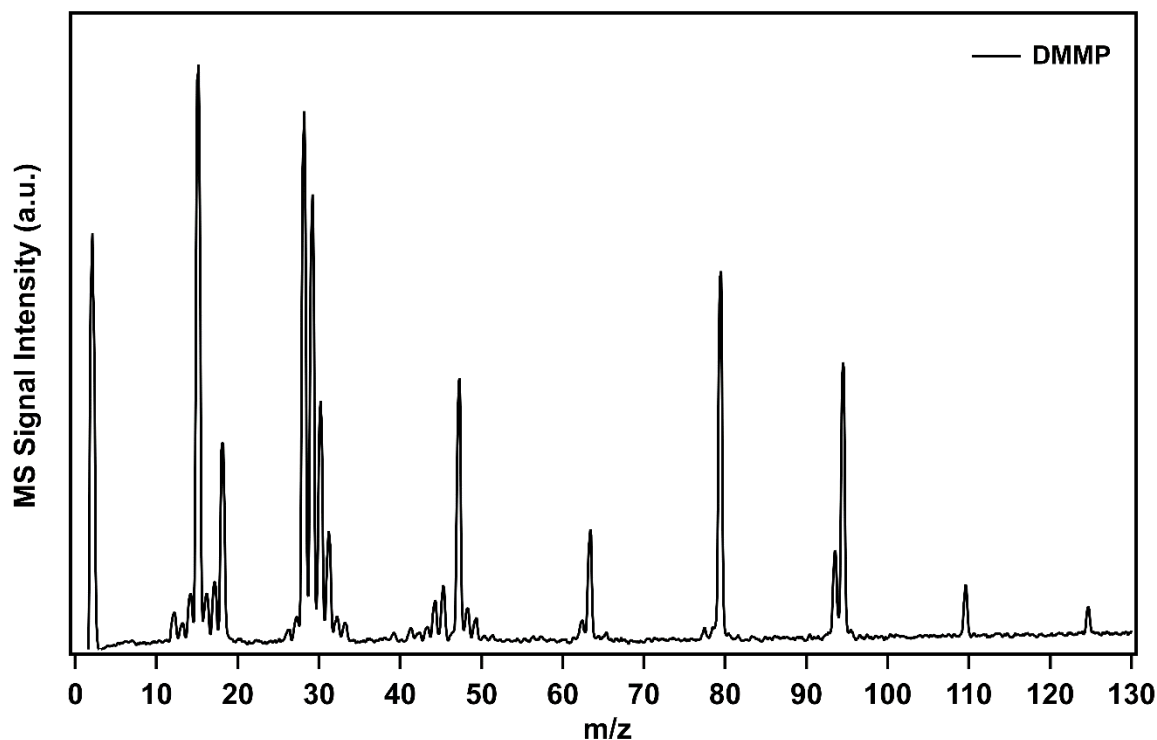


**Figure 5.14** Full DMMP mass spectrum after purification via consecutive freeze-pump-thaw cycles.

In situ IR was used to monitor changes in the MOF samples induced by DMMP by collecting spectra in real time using an FTIR spectrometer (Tensor 27, Bruker) via OPUS 7.5 software (Bruker). Spectra were recorded in transmission mode between 400-4000  $\text{cm}^{-1}$  using a room temperature DLaTGS detector with 4  $\text{cm}^{-1}$  resolution and an average of 16 scans (6 mm aperture and 10 kHz scan velocity). Before each experiment, a 64-scan background spectrum was collected using the bare W mesh as the sample reference.

## APPENDIX A CRYSTALLOGRAPHIC TABLES FOR CHAPTER 2

**Table A1** Fractional atomic coordinates ( $\times 10^4$ ) and equivalent isotropic displacement parameters ( $\text{\AA}^2 \times 10^3$ ) for MOF-1114(Gd).  $U_{\text{eq}}$  is defined as 1/3 of the trace of the orthogonalised UIJ tensor.

Atom	<i>x</i>	<i>y</i>	<i>z</i>	<b>U(eq)</b>
Gd1	2014.1(2)	2985.9(2)	2985.9(2)	38.2(6)
O2	2152(3)	2152(3)	2848(3)	41(3)
O3S	1504(3)	3496(3)	3496(3)	81(5)
O1	2218(3)	2782(3)	3749(4)	177(10)
C1	2500	2500	3972(8)	160(20)
C2	2500	2500	4499(7)	138(16)
C3	2808(5)	2192(5)	4760(6)	144(11)
N1	3126(15)	1874(15)	4556(17)	120(30)
O5S	5000	5000	5000	360(100)
O4S	1449(13)	2458(14)	3551(13)	119(16)

**Table A2** Anisotropic displacement parameters ( $\text{\AA}^2 \times 10^3$ ) for MOF-1114(Gd). The anisotropic displacement factor exponent takes the form:  $-2\pi^2[h2a^*2U11+2hka^*b^*U12+\dots]$ .

Atom	U <sub>11</sub>	U <sub>22</sub>	U <sub>33</sub>	U <sub>23</sub>	U <sub>13</sub>	U <sub>12</sub>
Gd1	38.2(6)	38.2(6)	38.2(6)	-4.1(2)	4.1(2)	4.1(2)
O2	41(3)	41(3)	41(3)	2(3)	2(3)	-2(3)
O3S	81(5)	81(5)	81(5)	-17(5)	17(5)	17(5)
O1	249(15)	249(15)	33(5)	0(4)	0(4)	188(17)
C1	230(30)	230(30)	34(12)	0	0	170(30)
C2	190(30)	190(30)	25(10)	0	0	130(30)
C3	196(17)	196(17)	41(9)	0(6)	0(6)	130(20)
N1	180(40)	180(40)	20(30)	12(17)	-12(17)	100(50)
O4S	130(20)	90(30)	130(20)	20(20)	-50(30)	-20(20)

**Table A3** Bond lengths for MOF-1114(Gd).

Atom	Atom	Length/ $\text{\AA}$	Atom	Atom	Length/ $\text{\AA}$
Gd1	Gd1 <sup>1</sup>	3.8290(17)	Gd1	O4S	2.67(5)
Gd1	Gd1 <sup>2</sup>	3.8290(17)	O2	Gd1 <sup>2</sup>	2.386(5)
Gd1	O2 <sup>1</sup>	2.386(5)	O2	Gd1 <sup>1</sup>	2.386(5)
Gd1	O2 <sup>2</sup>	2.386(5)	O1	C1	1.273(15)
Gd1	O2	2.386(5)	C1	O1 <sup>1</sup>	1.272(15)
Gd1	O3S	2.460(17)	C1	C2	1.47(3)
Gd1	O1 <sup>3</sup>	2.273(11)	C2	C3 <sup>1</sup>	1.42(2)
Gd1	O1	2.273(11)	C2	C3	1.42(2)
Gd1	O1 <sup>4</sup>	2.273(11)	C3	C3 <sup>5</sup>	1.34(3)
Gd1	O4S <sup>3</sup>	2.67(5)	C3	N1	1.37(6)
Gd1	O4S <sup>4</sup>	2.67(5)			

<sup>1</sup>1/2-X,1/2-Y,+Z; <sup>2</sup>+X,1/2-Y,1/2-Z; <sup>3</sup>1/2-Z,1/2-X,+Y; <sup>4</sup>1/2-Y,+Z,1/2-X; <sup>5</sup>+X,+Y,1-Z

**Table A4** Bond angles for MOF-1114(Gd).

Atom	Atom	Atom	Angle/°	Atom	Atom	Atom	Angle/°
Gd1 <sup>1</sup>	Gd1	Gd1 <sup>2</sup>	60.0	O1 <sup>4</sup>	Gd1	O2 <sup>2</sup>	82.3(3)
O2 <sup>1</sup>	Gd1	Gd1 <sup>1</sup>	36.63(16)	O1 <sup>3</sup>	Gd1	O2 <sup>1</sup>	82.3(3)
O2 <sup>1</sup>	Gd1	Gd1 <sup>2</sup>	76.8(3)	O1 <sup>3</sup>	Gd1	O3S	75.5(3)
O2	Gd1	Gd1 <sup>1</sup>	36.63(16)	O1 <sup>4</sup>	Gd1	O3S	75.5(3)
O2 <sup>2</sup>	Gd1	Gd1 <sup>2</sup>	36.63(16)	O1	Gd1	O3S	75.5(3)
O2	Gd1	Gd1 <sup>2</sup>	36.63(16)	O1 <sup>3</sup>	Gd1	O1 <sup>4</sup>	113.9(3)
O2 <sup>2</sup>	Gd1	Gd1 <sup>1</sup>	76.8(3)	O1 <sup>3</sup>	Gd1	O1	113.9(3)
O2	Gd1	O2 <sup>1</sup>	70.1(5)	O1 <sup>4</sup>	Gd1	O1	113.9(3)
O2	Gd1	O2 <sup>2</sup>	70.1(5)	O1 <sup>4</sup>	Gd1	O4S	144.2(10)
O2 <sup>1</sup>	Gd1	O2 <sup>2</sup>	70.1(5)	O1 <sup>3</sup>	Gd1	O4S	57.18(11)
O2 <sup>1</sup>	Gd1	O3S	138.4(3)	O1 <sup>3</sup>	Gd1	O4S <sup>4</sup>	144.2(10)
O2 <sup>2</sup>	Gd1	O3S	138.4(3)	O1	Gd1	O4S	57.18(11)
O2	Gd1	O3S	138.4(3)	O1	Gd1	O4S <sup>4</sup>	57.18(11)
O2 <sup>1</sup>	Gd1	O4S <sup>3</sup>	69.7(10)	O1	Gd1	O4S <sup>3</sup>	144.2(10)
O2	Gd1	O4S <sup>3</sup>	125.5(7)	O1 <sup>4</sup>	Gd1	O4S <sup>3</sup>	57.18(11)
O2 <sup>2</sup>	Gd1	O4S <sup>3</sup>	125.5(7)	O1 <sup>4</sup>	Gd1	O4S <sup>4</sup>	57.18(11)
O2 <sup>2</sup>	Gd1	O4S <sup>4</sup>	69.7(10)	O1 <sup>3</sup>	Gd1	O4S <sup>3</sup>	57.18(11)
O2	Gd1	O4S <sup>4</sup>	125.5(7)	O4S	Gd1	Gd1 <sup>1</sup>	91.5(8)
O2 <sup>1</sup>	Gd1	O4S <sup>4</sup>	125.5(7)	O4S <sup>4</sup>	Gd1	Gd1 <sup>2</sup>	91.5(8)
O2 <sup>2</sup>	Gd1	O4S	125.5(7)	O4S <sup>4</sup>	Gd1	Gd1 <sup>1</sup>	146.5(10)
O2 <sup>1</sup>	Gd1	O4S	125.5(7)	O4S <sup>3</sup>	Gd1	Gd1 <sup>2</sup>	146.5(10)
O2	Gd1	O4S	69.7(10)	O4S	Gd1	Gd1 <sup>2</sup>	91.5(8)
O3S	Gd1	Gd1 <sup>2</sup>	144.735(1)	O4S <sup>3</sup>	Gd1	Gd1 <sup>1</sup>	91.5(8)
O3S	Gd1	Gd1 <sup>1</sup>	144.7	O4S	Gd1	O4S <sup>4</sup>	107.6(10)
O3S	Gd1	O4S <sup>3</sup>	68.7(10)	O4S	Gd1	O4S <sup>3</sup>	107.6(10)
O3S	Gd1	O4S	68.7(10)	O4S <sup>4</sup>	Gd1	O4S <sup>3</sup>	107.6(10)
O3S	Gd1	O4S <sup>4</sup>	68.7(10)	Gd1	O2	Gd1 <sup>2</sup>	106.7(3)
O1 <sup>3</sup>	Gd1	Gd1 <sup>2</sup>	119.0(3)	Gd1	O2	Gd1 <sup>1</sup>	106.7(3)
O1 <sup>3</sup>	Gd1	Gd1 <sup>1</sup>	69.3(3)	Gd1 <sup>1</sup>	O2	Gd1 <sup>2</sup>	106.7(3)
O1	Gd1	Gd1 <sup>1</sup>	119.0(3)	C1	O1	Gd1	140.0(12)
O1	Gd1	Gd1 <sup>2</sup>	69.3(3)	O1 <sup>2</sup>	C1	O1	121(2)
O1 <sup>4</sup>	Gd1	Gd1 <sup>2</sup>	119.0(3)	O1	C1	C2	119.3(10)

O1 <sup>4</sup>	Gd1	Gd1 <sup>1</sup>	119.0(3)	O1 <sup>2</sup>	C1	C2	119.3(10)
O1	Gd1	O2	82.3(3)	C3	C2	C1	120.9(10)
O1 <sup>3</sup>	Gd1	O2	82.3(3)	C3 <sup>2</sup>	C2	C1	120.9(10)
O1 <sup>4</sup>	Gd1	O2 <sup>1</sup>	82.3(3)	C3	C2	C3 <sup>2</sup>	118(2)
O1	Gd1	O2 <sup>1</sup>	146.1(5)	C3 <sup>5</sup>	C3	C2	120.9(10)
O1	Gd1	O2 <sup>2</sup>	82.3(3)	C3 <sup>5</sup>	C3	N1	114(2)
O1 <sup>4</sup>	Gd1	O2	146.1(5)	N1	C3	C2	125(2)
O1 <sup>3</sup>	Gd1	O2 <sup>2</sup>	146.1(4)				

<sup>1</sup>+X,1/2-Y,1/2-Z; <sup>2</sup>1/2-X,1/2-Y,+Z; <sup>3</sup>1/2-Z,1/2-X,+Y; <sup>4</sup>1/2-Y,+Z,1/2-X; <sup>5</sup>+X,+Y,1-Z

**Table A5** Torsion angles for MOF-1114(Gd).

A	B	C	D	Angle/°	A	B	C	D	Angle/°
Gd1	O1	C1	O1 <sup>1</sup>	0.000(6)	O1 <sup>1</sup>	C1	C2	C3	0.000(6)
Gd1	O1	C1	C2	180.000(3)	C1	C2	C3	C3 <sup>2</sup>	180.000(3)
O1 <sup>1</sup>	C1	C2	C3 <sup>1</sup>	180.000(5)	C1	C2	C3	N1	0.000(11)
O1	C1	C2	C3	180.000(5)	C3 <sup>1</sup>	C2	C3	C3 <sup>2</sup>	0.000(7)
O1	C1	C2	C3 <sup>1</sup>	0.000(6)	C3 <sup>1</sup>	C2	C3	N1	180.000(10)

<sup>1</sup>1/2-X,1/2-Y,+Z; <sup>2</sup>+X,+Y,1-Z

**Table A6** Hydrogen atom coordinates ( $\text{\AA} \times 10^4$ ) and isotropic displacement parameters ( $\text{\AA}^2 \times 10^3$ ) for MOF-1114(Gd).

Atom	x	y	z	U(eq)
H1A	3305	1695	4737	149
H1B	3147	1853	4245	149

**Table A7** Atomic occupancy for MOF-1114(Gd).

Atom	Occupancy	Atom	Occupancy	Atom	Occupancy
N1	0.25	H1A	0.25	H1B	0.25
O4S	0.3333				

**Table A8** Fractional atomic coordinates ( $\times 10^4$ ) and equivalent isotropic displacement parameters ( $\text{\AA}^2 \times 10^3$ ) for MOF-1130(Dy).  $U_{eq}$  is defined as 1/3 of the trace of the orthogonalised UIJ tensor.

Atom	<i>x</i>	<i>y</i>	<i>z</i>	<i>U(eq)</i>
Dy1	531.9(6)	2154.2(6)	2720.4(3)	17.1(4)
Dy2	-508.0(6)	2078.4(6)	3693.3(3)	18.2(4)
Dy3	933.9(6)	669.0(6)	3537.6(4)	20.7(4)
Dy4	-855.3(6)	667.1(6)	2828.6(4)	22.4(4)
O1	654(6)	1941(7)	3444(4)	15.9(17)
O2	-641(7)	1938(7)	2975(4)	15.9(17)
O3	426(8)	902(7)	2844(4)	23(3)
O4	-334(6)	843(7)	3532(4)	15.9(17)
O5	313(8)	3318(9)	2947(5)	39(4)
O6	-330(7)	3261(9)	3505(5)	33(4)
O7	-547(11)	9496(10)	3082(6)	54(5)
O8	678(13)	9512(10)	3211(6)	66(6)
O9	1147(12)	1198(11)	4186(6)	65(6)
O10	402(10)	2119(12)	4258(5)	56(5)
O11	3734(11)	3691(10)	7234(5)	52(5)
O12	4623(10)	2864(11)	7134(5)	53(5)
O13	1986(10)	1148(12)	3303(7)	73(6)
O14	1823(8)	2145(10)	2914(5)	44(4)
O15	8206(8)	1989(10)	3496(5)	44(4)
O16	8068(8)	1040(10)	3089(5)	44(4)
O17	-1052(8)	2832(9)	4195(5)	37(4)
O18	-1028(11)	1505(12)	4267(6)	67(5)
O19	-3871(11)	3415(11)	7155(5)	58(5)
O20	-3971(11)	2112(12)	7198(6)	66(5)
O61S	431(12)	-171(12)	4031(7)	77(6)
O71S	1978(14)	-67(12)	3848(9)	103(9)
O81S	-361(13)	-42(13)	2277(7)	79(6)
O91S	-1853(11)	-86(11)	2520(7)	72(6)
N3	1458(12)	8289(14)	3326(13)	119(13)
N4	-890(20)	4525(15)	3749(13)	143(16)
N5	4586(16)	2230(20)	6402(9)	127(14)

N8	-2810(30)	3890(30)	6700(15)	200(20)
N81S	150(30)	-360(40)	1717(17)	108(16)
N91S	-2490(40)	-1180(30)	2382(18)	114(18)
C1	-11(12)	3617(15)	3229(8)	38(5)
C2	4(11)	4464(5)	3256(6)	45(6)
C3	464(10)	4836(7)	3009(5)	50(6)
C4	482(10)	5601(7)	3011(5)	53(6)
C5	41(11)	5993(5)	3259(6)	49(6)
C6	-419(11)	5621(8)	3506(6)	76(8)
C7	-437(11)	4856(8)	3505(6)	77(8)
C8	63(9)	6826(6)	3253(7)	57(6)
C9	742(7)	7192(8)	3284(7)	65(7)
C10	761(7)	7954(8)	3255(8)	71(7)
C11	101(9)	8351(6)	3195(7)	58(6)
C12	-579(7)	7985(8)	3164(7)	63(7)
C13	-598(7)	7223(8)	3193(7)	68(7)
C14	64(16)	9158(13)	3169(9)	45(7)
C15	-1188(16)	2239(18)	4398(9)	59(6)
C16	-1610(20)	2301(15)	4774(7)	141(12)
C17	-1764(19)	1695(13)	5011(8)	141(12)
C18	-2110(20)	1789(14)	5369(8)	138(12)
C19	-2310(20)	2490(15)	5489(8)	133(12)
C20	-2160(20)	3097(13)	5252(8)	146(13)
C21	-1810(20)	3002(13)	4895(8)	153(13)
C22	-2665(17)	2556(16)	5889(7)	100(9)
C23	-3080(17)	1980(13)	6028(8)	110(10)
C24	-3415(17)	2053(14)	6391(8)	109(10)
C25	-3334(19)	2703(17)	6616(7)	124(11)
C26	-2920(20)	3280(14)	6477(9)	133(11)
C27	-2585(18)	3206(14)	6114(9)	120(11)
C28	-3740(20)	2780(20)	7012(10)	75(7)
C29	938(17)	1747(19)	4371(8)	50(8)
C30	1408(9)	1952(10)	4784(4)	53(6)
C31	1237(9)	2579(9)	5000(5)	65(7)
C32	1661(10)	2763(9)	5366(5)	61(7)

C33	2256(10)	2321(10)	5515(4)	58(7)
C34	2428(9)	1694(10)	5300(5)	73(8)
C35	2004(10)	1510(9)	4934(5)	66(7)
C36	2707(9)	2535(12)	5919(4)	61(7)
C37	2391(7)	2962(13)	6209(5)	76(8)
C38	2810(9)	3157(12)	6574(5)	74(8)
C39	3545(8)	2924(12)	6650(4)	54(6)
C40	3861(7)	2498(12)	6360(5)	65(7)
C41	3443(9)	2303(11)	5994(5)	59(7)
C42	4016(16)	3203(15)	7035(8)	45(6)
C43	2232(13)	1696(16)	3126(8)	44(6)
C44	3077(6)	1791(13)	3163(6)	62(7)
C45	3419(7)	2096(12)	2839(5)	77(5)
C46	4192(8)	2113(13)	2856(5)	77(5)
C47	4623(6)	1825(13)	3196(6)	63(7)
C48	4281(8)	1521(14)	3519(5)	92(9)
C49	3509(8)	1504(13)	3503(5)	77(5)
C50	5448(6)	1715(12)	3218(6)	62(7)
C51	5781(7)	1369(12)	2904(5)	67(7)
C52	6553(8)	1330(11)	2922(5)	70(7)
C53	6991(6)	1637(11)	3253(6)	51(5)
C54	6658(8)	1984(12)	3567(5)	77(8)
C55	5886(8)	2023(12)	3550(5)	72(7)
C56	7795(13)	1575(15)	3272(8)	42(5)
C81S	-190(50)	100(50)	1980(20)	91(14)
C82S	100(60)	-1050(60)	1820(20)	110(20)
C83S	540(70)	-50(60)	1350(30)	150(30)
C91S	-1920(50)	-790(40)	2470(30)	97(15)
C92S	-2360(60)	-1890(50)	2270(40)	140(30)
C93S	-3230(60)	-950(50)	2390(40)	160(30)
N1A	7040(20)	2300(30)	3910(11)	120(20)
N2A	3024(16)	2440(20)	2508(11)	145(19)
N6A	650(20)	3070(20)	4896(12)	110(20)
N7A	-1600(40)	970(20)	4922(16)	130(20)
N61S	40(20)	-1260(20)	4245(17)	93(13)

C61S	560(30)	-810(30)	4156(19)	88(12)
C62S	-720(30)	-1070(30)	4240(30)	110(20)
C63S	150(30)	-2020(30)	4340(20)	88(16)
N1B	6760(30)	990(30)	2588(17)	63(16)
N2B	3210(30)	1230(40)	3844(14)	100(30)
N6B	2230(30)	858(19)	4759(13)	90(20)
N7B	-1680(40)	3650(30)	4689(17)	190(30)

**Table A9** Anisotropic displacement parameters ( $\text{\AA}^2 \times 10^3$ ) for MOF-1130(Dy). The anisotropic displacement factor exponent takes the form:  $-2\pi^2[h2a^*2U11+2hka^*b^*U12+\dots]$ .

Atom	U <sub>11</sub>	U <sub>22</sub>	U <sub>33</sub>	U <sub>23</sub>	U <sub>13</sub>	U <sub>12</sub>
Dy1	13.1(7)	19.0(7)	19.6(7)	3.8(5)	3.3(5)	-1.0(5)
Dy2	10.9(7)	21.9(7)	22.1(7)	-1.4(5)	4.0(5)	-1.7(5)
Dy3	11.4(7)	19.6(7)	29.3(7)	5.1(6)	-5.8(5)	0.4(5)
Dy4	15.5(7)	17.9(7)	31.5(8)	-0.8(6)	-8.7(5)	-3.6(5)
O1	5(4)	20(4)	23(4)	4(4)	-1(3)	3(3)
O2	5(4)	20(4)	23(4)	4(4)	-1(3)	3(3)
O3	26(8)	23(8)	20(8)	-5(6)	1(6)	3(7)
O4	5(4)	20(4)	23(4)	4(4)	-1(3)	3(3)
O5	21(8)	48(9)	52(8)	18(7)	16(6)	6(7)
O6	7(7)	51(9)	42(8)	-8(7)	6(6)	-12(7)
O7	57(13)	38(10)	61(12)	-2(9)	-22(10)	18(10)
O8	100(18)	27(10)	72(14)	18(10)	14(12)	7(12)
O9	92(16)	44(12)	48(12)	0(10)	-51(11)	9(11)
O10	17(9)	110(17)	42(11)	-20(11)	3(8)	11(11)
O11	69(10)	55(10)	25(9)	-5(7)	-27(7)	7(8)
O12	60(10)	75(11)	20(8)	-8(8)	-12(7)	4(8)
O13	23(9)	90(12)	110(15)	50(11)	22(10)	4(8)
O14	18(8)	65(10)	50(10)	16(8)	11(7)	0(7)
O15	8(6)	63(9)	62(9)	-14(8)	12(6)	-1(6)
O16	14(7)	58(9)	60(10)	-8(7)	8(6)	-7(6)
O17	25(8)	49(8)	38(9)	-3(7)	7(7)	4(7)
O18	56(12)	74(9)	72(12)	18(8)	19(10)	-11(8)

O19	60(12)	83(11)	37(10)	-13(8)	31(9)	-4(9)
O20	61(12)	91(11)	54(11)	-21(8)	36(10)	2(9)
O61S	63(12)	68(12)	100(16)	42(11)	7(12)	-7(10)
O71S	79(16)	54(14)	170(30)	33(15)	-40(17)	-5(13)
O81S	95(16)	89(15)	56(13)	-29(12)	22(11)	16(13)
O91S	52(12)	47(10)	113(17)	-11(11)	-12(11)	-14(9)
N3	61(10)	39(12)	250(40)	7(15)	-28(12)	-3(8)
N4	210(30)	32(11)	220(30)	-2(13)	160(30)	4(13)
N5	58(10)	230(30)	81(16)	-80(20)	-35(10)	54(15)
N8	290(50)	160(20)	160(30)	-70(20)	130(30)	-60(30)
N81S	150(40)	110(30)	66(19)	-22(18)	40(20)	40(30)
N91S	90(20)	52(15)	190(40)	-13(19)	-50(30)	-19(14)
C1	6(9)	57(11)	53(9)	4(8)	8(7)	-4(8)
C2	57(12)	17(8)	64(13)	-1(7)	16(10)	3(7)
C3	67(13)	20(7)	67(13)	-3(7)	20(11)	-1(7)
C4	76(14)	20(7)	65(13)	-1(7)	20(11)	0(7)
C5	66(13)	23(8)	57(13)	-4(7)	8(10)	4(8)
C6	110(16)	27(8)	100(16)	-2(8)	49(14)	5(8)
C7	106(15)	24(8)	109(16)	-3(8)	61(14)	7(8)
C8	52(9)	30(8)	86(18)	-4(9)	-8(10)	6(6)
C9	51(9)	29(8)	110(20)	0(9)	-9(10)	7(6)
C10	55(8)	28(8)	120(20)	1(9)	-18(9)	6(6)
C11	54(8)	24(8)	91(18)	-2(9)	-17(9)	5(6)
C12	55(9)	30(8)	99(19)	-4(10)	-15(10)	4(6)
C13	51(9)	29(8)	120(20)	-3(10)	-8(10)	4(6)
C14	43(17)	21(14)	69(19)	13(13)	-10(14)	-18(15)
C15	40(13)	72(9)	63(13)	17(8)	-8(10)	-8(9)
C16	220(30)	132(18)	88(17)	14(13)	80(20)	47(19)
C17	210(30)	133(18)	86(17)	14(13)	74(19)	41(18)
C18	210(30)	129(18)	87(17)	13(13)	72(19)	35(19)
C19	200(30)	128(18)	82(17)	15(13)	77(19)	30(20)
C20	230(30)	127(18)	98(18)	16(13)	100(20)	38(19)
C21	240(30)	131(18)	101(18)	19(13)	110(20)	45(18)
C22	120(20)	109(17)	79(16)	-7(12)	35(15)	19(16)
C23	140(20)	116(17)	83(16)	-12(13)	41(16)	8(16)

C24	140(20)	115(17)	81(16)	-12(12)	41(16)	10(16)
C25	160(30)	122(17)	97(17)	-22(13)	58(17)	-5(17)
C26	180(30)	124(17)	106(17)	-26(13)	73(17)	-11(16)
C27	150(20)	118(17)	99(17)	-20(12)	57(17)	1(16)
C28	81(17)	92(11)	61(14)	-22(9)	46(13)	-3(10)
C29	39(19)	70(20)	39(16)	-11(16)	6(14)	-39(18)
C30	51(11)	82(12)	23(9)	-8(8)	-12(8)	-1(9)
C31	62(12)	94(13)	33(10)	-20(9)	-26(9)	11(10)
C32	57(12)	90(13)	30(10)	-17(9)	-23(9)	8(10)
C33	52(12)	87(13)	31(10)	-12(9)	-19(9)	4(10)
C34	70(13)	98(14)	44(11)	-20(10)	-26(10)	14(11)
C35	62(12)	92(13)	39(10)	-16(9)	-22(9)	8(10)
C36	43(9)	97(17)	39(10)	-18(10)	-17(7)	7(10)
C37	44(10)	130(20)	46(10)	-34(12)	-26(8)	23(11)
C38	43(9)	127(19)	45(10)	-33(12)	-25(7)	19(11)
C39	35(8)	93(16)	31(9)	-8(10)	-16(7)	3(9)
C40	41(8)	109(17)	41(9)	-20(10)	-16(7)	8(9)
C41	41(9)	94(16)	37(9)	-16(10)	-15(7)	6(10)
C42	54(11)	48(12)	30(11)	-7(9)	-17(8)	-12(8)
C43	13(10)	69(12)	53(13)	18(9)	14(8)	3(8)
C44	15(8)	83(16)	88(11)	9(11)	7(6)	0(8)
C45	11(5)	122(13)	97(10)	29(9)	7(5)	0(6)
C46	11(5)	122(13)	97(10)	29(9)	7(5)	0(6)
C47	9(8)	88(17)	91(12)	14(11)	2(7)	-5(8)
C48	18(7)	150(20)	109(13)	46(14)	7(7)	0(8)
C49	11(5)	122(13)	97(10)	29(9)	7(5)	0(6)
C50	26(8)	75(16)	87(13)	-12(11)	12(7)	-2(8)
C51	15(7)	96(18)	90(13)	-26(12)	6(7)	-6(8)
C52	17(7)	102(17)	90(11)	-30(11)	6(6)	-5(7)
C53	16(6)	65(13)	75(10)	-9(9)	9(5)	-7(6)
C54	30(7)	111(18)	91(11)	-33(12)	13(7)	-2(8)
C55	29(8)	93(18)	94(13)	-25(12)	11(7)	-2(8)
C56	14(6)	59(10)	54(11)	-5(8)	10(6)	-6(6)
C81S	110(30)	100(20)	60(15)	-24(15)	31(17)	20(20)
C82S	150(50)	110(30)	50(30)	-25(18)	30(30)	30(20)

C83S	220(60)	130(30)	110(30)	0(30)	100(40)	50(40)
C91S	80(20)	47(12)	150(40)	-13(14)	-40(20)	-14(11)
C92S	90(30)	59(16)	240(70)	-30(30)	-50(40)	-16(17)
C93S	90(20)	80(30)	300(80)	-40(40)	-40(30)	-14(15)
N1A	33(14)	200(50)	120(20)	-90(30)	7(12)	4(16)
N2A	29(13)	260(40)	150(20)	110(30)	5(11)	9(15)
N6A	110(30)	140(30)	70(20)	-60(20)	-70(20)	60(20)
N7A	190(60)	134(19)	80(30)	11(15)	50(30)	40(20)
N61S	64(15)	74(14)	140(30)	53(15)	13(16)	-9(12)
C61S	58(15)	71(13)	140(30)	52(14)	11(16)	-7(11)
C62S	63(16)	70(20)	200(60)	60(30)	22(19)	-10(13)
C63S	60(20)	73(14)	130(40)	48(17)	10(20)	-10(13)
N1B	14(15)	90(40)	84(16)	-20(20)	4(11)	-2(15)
N2B	15(18)	170(70)	110(20)	50(30)	6(13)	-4(19)
N6B	100(30)	110(20)	60(20)	-40(20)	-50(20)	40(20)
N7B	330(70)	140(20)	140(30)	27(18)	160(40)	50(20)

**Table A10** Bond lengths for MOF-1130(Dy).

Atom	Atom	Length/Å	Atom	Atom	Length/Å
Dy1	Dy2	3.8489(15)	N91S	C92S	1.37(11)
Dy1	Dy3	3.8102(16)	N91S	C93S	1.41(12)
Dy1	Dy4	3.7256(16)	C1	C2	1.54(3)
Dy1	O1	2.377(12)	C2	C3	1.3900
Dy1	O2	2.384(12)	C2	C7	1.3900
Dy1	O3	2.323(14)	C3	C4	1.3900
Dy1	O5	2.289(17)	C4	C5	1.3900
Dy1	O12 <sup>1</sup>	2.388(16)	C5	C6	1.3900
Dy1	O14	2.351(15)	C5	C8	1.515(15)
Dy1	O19 <sup>2</sup>	2.457(17)	C6	C7	1.3900
Dy1	O20 <sup>2</sup>	2.408(17)	C8	C9	1.3900
Dy1	C28 <sup>2</sup>	2.77(3)	C8	C13	1.3900
Dy2	Dy3	3.7233(16)	C9	C10	1.3900
Dy2	Dy4	3.8158(16)	C10	C11	1.3900

Dy2	O1	2.338(12)	C11	C12	1.3900
Dy2	O2	2.343(13)	C11	C14	1.47(3)
Dy2	O4	2.335(13)	C12	C13	1.3900
Dy2	O6	2.268(16)	C15	C16	1.52(4)
Dy2	O10	2.339(18)	C16	C17	1.3900
Dy2	O15 <sup>3</sup>	2.349(14)	C16	C21	1.3900
Dy2	O17	2.417(15)	C17	C18	1.3900
Dy2	O18	2.414(18)	C17	N7A	1.390(19)
Dy2	C15	2.73(3)	C18	C19	1.3900
Dy3	Dy4	3.7737(15)	C19	C20	1.3900
Dy3	O1	2.381(13)	C19	C22	1.52(2)
Dy3	O3	2.389(13)	C20	C21	1.3900
Dy3	O4	2.308(12)	C21	N7B	1.39(3)
Dy3	O8 <sup>4</sup>	2.38(2)	C22	C23	1.3900
Dy3	O9	2.32(2)	C22	C27	1.3900
Dy3	O13	2.291(17)	C23	C24	1.3900
Dy3	O61S	2.457(19)	C24	C25	1.3900
Dy3	O71S	2.44(2)	C25	C26	1.3900
Dy4	O2	2.383(13)	C25	C28	1.56(3)
Dy4	O3	2.348(14)	C26	C27	1.3900
Dy4	O4	2.408(12)	C28	Dy1 <sup>8</sup>	2.77(3)
Dy4	O7 <sup>4</sup>	2.331(17)	C29	C30	1.56(3)
Dy4	O11 <sup>1</sup>	2.318(16)	C30	C31	1.3900
Dy4	O16 <sup>3</sup>	2.301(15)	C30	C35	1.3900
Dy4	O81S	2.454(19)	C31	C32	1.3900
Dy4	O91S	2.399(19)	C31	N6A	1.40(2)
O5	C1	1.26(3)	C32	C33	1.3900
O6	C1	1.29(3)	C33	C34	1.3900
O7	Dy4 <sup>5</sup>	2.331(17)	C33	C36	1.524(14)
O7	C14	1.27(3)	C34	C35	1.3900
O8	Dy3 <sup>5</sup>	2.38(2)	C35	N6B	1.398(18)
O8	C14	1.28(3)	C36	C37	1.3900
O9	C29	1.24(4)	C36	C41	1.3900
O10	C29	1.21(4)	C37	C38	1.3900
O11	Dy4 <sup>6</sup>	2.317(16)	C38	C39	1.3900

O11	C42	1.24(3)	C39	C40	1.3900
O12	Dy1 <sup>6</sup>	2.388(16)	C39	C42	1.53(3)
O12	C42	1.27(3)	C40	C41	1.3900
O13	C43	1.25(3)	C43	C44	1.53(3)
O14	C43	1.26(3)	C44	C45	1.3900
O15	Dy2 <sup>7</sup>	2.349(14)	C44	C49	1.3900
O15	C56	1.24(3)	C45	C46	1.3900
O16	Dy4 <sup>7</sup>	2.301(15)	C45	N2A	1.38(2)
O16	C56	1.27(3)	C46	C47	1.3900
O17	C15	1.30(3)	C47	C48	1.3900
O18	C15	1.44(4)	C47	C50	1.496(15)
O19	Dy1 <sup>8</sup>	2.457(17)	C48	C49	1.3900
O19	C28	1.28(4)	C49	N2B	1.383(18)
O20	Dy1 <sup>8</sup>	2.408(17)	C50	C51	1.3900
O20	C28	1.43(4)	C50	C55	1.3900
O61S	C61S	1.25(5)	C51	C52	1.3900
O81S	C81S	1.09(8)	C52	C53	1.3900
O91S	C91S	1.30(7)	C52	N1B	1.34(6)
N3	C10	1.394(17)	C53	C54	1.3900
N4	C7	1.34(3)	C53	C56	1.45(3)
N5	C40	1.39(3)	C54	C55	1.3900
N8	C26	1.33(5)	C54	N1A	1.381(19)
N81S	C81S	1.38(10)	N61S	C61S	1.30(6)
N81S	C82S	1.29(12)	N61S	C62S	1.42(5)
N81S	C83S	1.55(12)	N61S	C63S	1.42(5)
N91S	C91S	1.26(9)			

<sup>1</sup>-1/2+X,1/2-Y,-1/2+Z; <sup>2</sup>1/2+X,1/2-Y,-1/2+Z; <sup>3</sup>-1+X,+Y,+Z; <sup>4</sup>+X,-1+Y,+Z; <sup>5</sup>+X,1+Y,+Z; <sup>6</sup>1/2+X,1/2-Y,1/2+Z; <sup>7</sup>1+X,+Y,+Z; <sup>8</sup>-1/2+X,1/2-Y,1/2+Z

**Table A11** Bond angles for MOF-1130(Dy).

Atom	Atom	Atom	Angle/°	Atom	Atom	Atom	Angle/°
Dy3	Dy1	Dy2	58.17(3)	O7 <sup>4</sup>	Dy4	O2	141.9(5)
Dy4	Dy1	Dy2	60.47(3)	O7 <sup>4</sup>	Dy4	O3	87.7(6)
Dy4	Dy1	Dy3	60.09(3)	O7 <sup>4</sup>	Dy4	O4	74.2(5)
O1	Dy1	Dy2	35.0(3)	O7 <sup>4</sup>	Dy4	O81S	71.8(7)
O1	Dy1	Dy3	36.8(3)	O7 <sup>4</sup>	Dy4	O91S	76.6(7)
O1	Dy1	Dy4	77.5(3)	O11 <sup>1</sup>	Dy4	Dy1	73.5(4)
O1	Dy1	O2	67.9(4)	O11 <sup>1</sup>	Dy4	Dy2	107.1(4)
O1	Dy1	O12 <sup>1</sup>	141.0(5)	O11 <sup>1</sup>	Dy4	Dy3	133.8(5)
O1	Dy1	O19 <sup>2</sup>	132.3(5)	O11 <sup>1</sup>	Dy4	O2	73.2(5)
O1	Dy1	O20 <sup>2</sup>	142.0(6)	O11 <sup>1</sup>	Dy4	O3	99.0(6)
O1	Dy1	C28 <sup>2</sup>	146.1(8)	O11 <sup>1</sup>	Dy4	O4	142.1(5)
O2	Dy1	Dy2	35.1(3)	O11 <sup>1</sup>	Dy4	O7 <sup>4</sup>	143.2(6)
O2	Dy1	Dy3	75.6(3)	O11 <sup>1</sup>	Dy4	O81S	76.2(7)
O2	Dy1	Dy4	38.6(3)	O11 <sup>1</sup>	Dy4	O91S	77.0(7)
O2	Dy1	O12 <sup>1</sup>	73.4(5)	O16 <sup>3</sup>	Dy4	Dy1	115.0(4)
O2	Dy1	O19 <sup>2</sup>	131.7(6)	O16 <sup>3</sup>	Dy4	Dy2	67.1(4)
O2	Dy1	O20 <sup>2</sup>	138.3(6)	O16 <sup>3</sup>	Dy4	Dy3	118.4(4)
O2	Dy1	C28 <sup>2</sup>	144.0(9)	O16 <sup>3</sup>	Dy4	O2	76.5(5)
O3	Dy1	Dy2	76.5(3)	O16 <sup>3</sup>	Dy4	O3	143.7(5)
O3	Dy1	Dy3	36.6(3)	O16 <sup>3</sup>	Dy4	O4	82.7(5)
O3	Dy1	Dy4	37.3(3)	O16 <sup>3</sup>	Dy4	O7 <sup>4</sup>	108.6(7)
O3	Dy1	O1	70.7(4)	O16 <sup>3</sup>	Dy4	O11 <sup>1</sup>	87.1(7)
O3	Dy1	O2	71.7(4)	O16 <sup>3</sup>	Dy4	O81S	144.0(7)
O3	Dy1	O12 <sup>1</sup>	93.6(6)	O16 <sup>3</sup>	Dy4	O91S	72.3(7)
O3	Dy1	O14	92.5(5)	O81S	Dy4	Dy1	90.8(6)
O3	Dy1	O19 <sup>2</sup>	76.5(6)	O81S	Dy4	Dy2	148.2(6)
O3	Dy1	O20 <sup>2</sup>	135.1(6)	O81S	Dy4	Dy3	95.6(6)
O3	Dy1	C28 <sup>2</sup>	104.0(9)	O91S	Dy4	Dy1	149.0(6)
O5	Dy1	Dy2	69.6(4)	O91S	Dy4	Dy2	138.8(6)
O5	Dy1	Dy3	117.1(4)	O91S	Dy4	Dy3	144.6(5)
O5	Dy1	Dy4	120.0(4)	O91S	Dy4	O4	132.7(6)
O5	Dy1	O1	80.3(5)	O91S	Dy4	O81S	73.0(8)

O5	Dy1	O2	81.4(5)	Dy1	O1	Dy3	106.4(5)
O5	Dy1	O3	146.1(5)	Dy2	O1	Dy1	109.4(5)
O5	Dy1	O12 <sup>1</sup>	98.3(6)	Dy2	O1	Dy3	104.2(5)
O5	Dy1	O14	96.9(6)	Dy2	O2	Dy1	109.0(5)
O5	Dy1	O19 <sup>2</sup>	137.3(6)	Dy2	O2	Dy4	107.7(5)
O5	Dy1	O20 <sup>2</sup>	78.8(6)	Dy4	O2	Dy1	102.8(5)
O5	Dy1	C28 <sup>2</sup>	109.9(9)	Dy1	O3	Dy3	107.9(5)
O12 <sup>1</sup>	Dy1	Dy2	107.8(4)	Dy1	O3	Dy4	105.8(5)
O12 <sup>1</sup>	Dy1	Dy3	128.0(5)	Dy4	O3	Dy3	105.6(5)
O12 <sup>1</sup>	Dy1	Dy4	69.7(4)	Dy2	O4	Dy4	107.1(5)
O12 <sup>1</sup>	Dy1	O19 <sup>2</sup>	73.3(6)	Dy3	O4	Dy2	106.6(5)
O12 <sup>1</sup>	Dy1	O20 <sup>2</sup>	73.6(7)	Dy3	O4	Dy4	106.3(5)
O12 <sup>1</sup>	Dy1	C28 <sup>2</sup>	71.2(9)	C1	O5	Dy1	138.0(15)
O14	Dy1	Dy2	109.4(4)	C1	O6	Dy2	138.6(15)
O14	Dy1	Dy3	72.2(4)	C14	O7	Dy4 <sup>5</sup>	133.8(17)
O14	Dy1	Dy4	128.8(4)	C14	O8	Dy3 <sup>5</sup>	128.3(19)
O14	Dy1	O1	75.2(5)	C29	O9	Dy3	138.0(18)
O14	Dy1	O2	142.8(5)	C29	O10	Dy2	134.3(18)
O14	Dy1	O12 <sup>1</sup>	142.7(6)	C42	O11	Dy4 <sup>6</sup>	133.3(17)
O14	Dy1	O19 <sup>2</sup>	72.5(6)	C42	O12	Dy1 <sup>6</sup>	135.7(16)
O14	Dy1	O20 <sup>2</sup>	76.3(6)	C43	O13	Dy3	143.1(17)
O14	Dy1	C28 <sup>2</sup>	71.6(9)	C43	O14	Dy1	131.4(15)
O19 <sup>2</sup>	Dy1	Dy2	153.0(5)	C56	O15	Dy2 <sup>7</sup>	136.0(15)
O19 <sup>2</sup>	Dy1	Dy3	99.2(4)	C56	O16	Dy4 <sup>7</sup>	141.6(15)
O19 <sup>2</sup>	Dy1	Dy4	96.6(5)	C15	O17	Dy2	89.1(17)
O19 <sup>2</sup>	Dy1	C28 <sup>2</sup>	27.4(9)	C15	O18	Dy2	86.2(15)
O20 <sup>2</sup>	Dy1	Dy2	148.3(5)	C28	O19	Dy1 <sup>8</sup>	90.1(18)
O20 <sup>2</sup>	Dy1	Dy3	146.0(5)	C28	O20	Dy1 <sup>8</sup>	88.6(15)
O20 <sup>2</sup>	Dy1	Dy4	140.5(5)	C61S	O61S	Dy3	137(3)
O20 <sup>2</sup>	Dy1	O19 <sup>2</sup>	58.6(7)	C81S	O81S	Dy4	134(5)
O20 <sup>2</sup>	Dy1	C28 <sup>2</sup>	31.2(9)	C91S	O91S	Dy4	132(4)
C28 <sup>2</sup>	Dy1	Dy2	178.9(8)	C81S	N81S	C83S	121(8)
C28 <sup>2</sup>	Dy1	Dy3	122.8(8)	C82S	N81S	C81S	112(7)
C28 <sup>2</sup>	Dy1	Dy4	119.3(8)	C82S	N81S	C83S	127(7)
Dy3	Dy2	Dy1	60.39(3)	C91S	N91S	C92S	116(8)

Dy3	Dy2	Dy4	60.06(3)	C91S	N91S	C93S	126(8)
Dy4	Dy2	Dy1	58.16(3)	C92S	N91S	C93S	118(7)
O1	Dy2	Dy1	35.6(3)	O5	C1	O6	124(2)
O1	Dy2	Dy3	38.3(3)	O5	C1	C2	117.8(19)
O1	Dy2	Dy4	75.9(3)	O6	C1	C2	118(2)
O1	Dy2	O2	69.2(4)	C3	C2	C1	117.4(13)
O1	Dy2	O10	72.3(5)	C3	C2	C7	120.0
O1	Dy2	O15 <sup>3</sup>	142.4(5)	C7	C2	C1	122.5(13)
O1	Dy2	O17	137.4(5)	C2	C3	C4	120.0
O1	Dy2	O18	131.1(6)	C3	C4	C5	120.0
O1	Dy2	C15	143.2(7)	C4	C5	C8	119.2(13)
O2	Dy2	Dy1	35.8(3)	C6	C5	C4	120.0
O2	Dy2	Dy3	77.9(3)	C6	C5	C8	120.8(12)
O2	Dy2	Dy4	36.5(3)	C7	C6	C5	120.0
O2	Dy2	O15 <sup>3</sup>	73.8(5)	N4	C7	C2	122.5(15)
O2	Dy2	O17	136.9(5)	N4	C7	C6	117.5(15)
O2	Dy2	O18	136.0(6)	C6	C7	C2	120.0
O2	Dy2	C15	147.6(7)	C9	C8	C5	120.1(13)
O4	Dy2	Dy1	76.1(3)	C9	C8	C13	120.0
O4	Dy2	Dy3	36.4(3)	C13	C8	C5	119.8(13)
O4	Dy2	Dy4	37.1(3)	C8	C9	C10	120.0
O4	Dy2	O1	70.9(4)	C9	C10	N3	116.9(15)
O4	Dy2	O2	70.9(4)	C9	C10	C11	120.0
O4	Dy2	O10	96.2(6)	C11	C10	N3	122.9(15)
O4	Dy2	O15 <sup>3</sup>	91.3(5)	C10	C11	C14	124.0(15)
O4	Dy2	O17	140.4(5)	C12	C11	C10	120.0
O4	Dy2	O18	80.3(6)	C12	C11	C14	116.0(15)
O4	Dy2	C15	112.1(8)	C11	C12	C13	120.0
O6	Dy2	Dy1	69.4(4)	C12	C13	C8	120.0
O6	Dy2	Dy3	119.7(3)	O7	C14	O8	120(2)
O6	Dy2	Dy4	117.0(4)	O7	C14	C11	122(2)
O6	Dy2	O1	81.4(5)	O8	C14	C11	118(2)
O6	Dy2	O2	80.5(5)	O17	C15	Dy2	62.4(14)
O6	Dy2	O4	145.5(5)	O17	C15	O18	124(3)
O6	Dy2	O10	94.3(7)	O17	C15	C16	119(3)

O6	Dy2	O15 <sup>3</sup>	98.9(6)	O18	C15	Dy2	62.0(14)
O6	Dy2	O17	74.0(5)	O18	C15	C16	116(2)
O6	Dy2	O18	134.1(6)	C16	C15	Dy2	176(2)
O6	Dy2	C15	102.4(8)	C17	C16	C15	122.4(19)
O10	Dy2	Dy1	106.6(4)	C17	C16	C21	120.0
O10	Dy2	Dy3	71.6(5)	C21	C16	C15	117.5(19)
O10	Dy2	Dy4	130.7(5)	C16	C17	N7A	126(2)
O10	Dy2	O2	141.4(5)	C18	C17	C16	120.0
O10	Dy2	O15 <sup>3</sup>	144.3(6)	C18	C17	N7A	114(2)
O10	Dy2	O17	75.5(6)	C19	C18	C17	120.0
O10	Dy2	O18	72.6(7)	C18	C19	C20	120.0
O10	Dy2	C15	71.0(7)	C18	C19	C22	117.3(19)
O15 <sup>3</sup>	Dy2	Dy1	109.1(4)	C20	C19	C22	122.7(19)
O15 <sup>3</sup>	Dy2	Dy3	126.8(4)	C21	C20	C19	120.0
O15 <sup>3</sup>	Dy2	Dy4	70.6(4)	C16	C21	N7B	125(2)
O15 <sup>3</sup>	Dy2	O17	76.5(5)	C20	C21	C16	120.0
O15 <sup>3</sup>	Dy2	O18	74.4(7)	C20	C21	N7B	115(2)
O15 <sup>3</sup>	Dy2	C15	73.8(7)	C23	C22	C19	121(2)
O17	Dy2	Dy1	143.4(4)	C23	C22	C27	120.0
O17	Dy2	Dy3	145.1(4)	C27	C22	C19	119(2)
O17	Dy2	Dy4	146.5(4)	C22	C23	C24	120.0
O17	Dy2	C15	28.5(8)	C25	C24	C23	120.0
O18	Dy2	Dy1	156.2(5)	C24	C25	C28	119(2)
O18	Dy2	Dy3	98.1(5)	C26	C25	C24	120.0
O18	Dy2	Dy4	103.6(5)	C26	C25	C28	121(2)
O18	Dy2	O17	60.2(7)	N8	C26	C25	121(3)
O18	Dy2	C15	31.8(8)	N8	C26	C27	119(3)
C15	Dy2	Dy1	171.5(7)	C25	C26	C27	120.0
C15	Dy2	Dy3	124.7(6)	C26	C27	C22	120.0
C15	Dy2	Dy4	129.8(7)	O19	C28	Dy1 <sup>8</sup>	62.4(13)
Dy2	Dy3	Dy1	61.44(3)	O19	C28	O20	123(2)
Dy2	Dy3	Dy4	61.19(3)	O19	C28	C25	120(3)
Dy4	Dy3	Dy1	58.84(3)	O20	C28	Dy1 <sup>8</sup>	60.3(12)
O1	Dy3	Dy1	36.8(3)	O20	C28	C25	117(3)
O1	Dy3	Dy2	37.5(3)	C25	C28	Dy1 <sup>8</sup>	177(3)

O1	Dy3	Dy4	76.4(3)	O9	C29	C30	116(3)
O1	Dy3	O3	69.5(4)	O10	C29	O9	125(2)
O1	Dy3	O8 <sup>4</sup>	140.5(6)	O10	C29	C30	118(3)
O1	Dy3	O61S	126.9(6)	C31	C30	C29	120.2(17)
O1	Dy3	O71S	136.9(6)	C31	C30	C35	120.0
O3	Dy3	Dy1	35.5(3)	C35	C30	C29	119.8(17)
O3	Dy3	Dy2	78.5(3)	C30	C31	C32	120.0
O3	Dy3	Dy4	36.8(3)	C30	C31	N6A	127.1(16)
O3	Dy3	O61S	126.7(6)	C32	C31	N6A	112.9(16)
O3	Dy3	O71S	133.9(8)	C31	C32	C33	120.0
O4	Dy3	Dy1	77.2(3)	C32	C33	C36	118.8(11)
O4	Dy3	Dy2	36.9(3)	C34	C33	C32	120.0
O4	Dy3	Dy4	37.8(3)	C34	C33	C36	121.2(11)
O4	Dy3	O1	70.6(4)	C35	C34	C33	120.0
O4	Dy3	O3	71.6(4)	C30	C35	N6B	126.8(16)
O4	Dy3	O8 <sup>4</sup>	88.3(7)	C34	C35	C30	120.0
O4	Dy3	O9	91.3(6)	C34	C35	N6B	113.2(16)
O4	Dy3	O61S	70.1(6)	C37	C36	C33	120.6(12)
O4	Dy3	O71S	143.1(7)	C37	C36	C41	120.0
O8 <sup>4</sup>	Dy3	Dy1	107.4(5)	C41	C36	C33	119.4(12)
O8 <sup>4</sup>	Dy3	Dy2	124.2(6)	C38	C37	C36	120.0
O8 <sup>4</sup>	Dy3	Dy4	67.1(5)	C37	C38	C39	120.0
O8 <sup>4</sup>	Dy3	O3	72.3(6)	C38	C39	C40	120.0
O8 <sup>4</sup>	Dy3	O61S	71.1(8)	C38	C39	C42	119.1(15)
O8 <sup>4</sup>	Dy3	O71S	78.9(8)	C40	C39	C42	120.7(15)
O9	Dy3	Dy1	110.2(5)	N5	C40	C39	125.1(15)
O9	Dy3	Dy2	69.1(5)	N5	C40	C41	114.9(15)
O9	Dy3	Dy4	127.6(5)	C41	C40	C39	120.0
O9	Dy3	O1	74.2(5)	C40	C41	C36	120.0
O9	Dy3	O3	143.2(5)	O11	C42	O12	127(2)
O9	Dy3	O8 <sup>4</sup>	141.3(7)	O11	C42	C39	116(2)
O9	Dy3	O61S	72.5(8)	O12	C42	C39	116(2)
O9	Dy3	O71S	78.5(9)	O13	C43	O14	124(2)
O13	Dy3	Dy1	66.6(5)	O13	C43	C44	117(2)
O13	Dy3	Dy2	113.5(5)	O14	C43	C44	120(2)

O13	Dy3	Dy4	118.8(5)	C45	C44	C43	120.1(14)
O13	Dy3	O1	76.1(6)	C45	C44	C49	120.0
O13	Dy3	O3	82.4(6)	C49	C44	C43	119.5(14)
O13	Dy3	O4	143.1(6)	C46	C45	C44	120.0
O13	Dy3	O8 <sup>4</sup>	108.4(8)	N2A	C45	C44	122.7(16)
O13	Dy3	O9	94.6(9)	N2A	C45	C46	117.1(16)
O13	Dy3	O61S	146.0(7)	C45	C46	C47	120.0
O13	Dy3	O71S	73.5(8)	C46	C47	C50	124.2(13)
O61S	Dy3	Dy1	147.3(5)	C48	C47	C46	120.0
O61S	Dy3	Dy2	91.6(5)	C48	C47	C50	115.2(13)
O61S	Dy3	Dy4	92.9(5)	C47	C48	C49	120.0
O71S	Dy3	Dy1	139.6(7)	C48	C49	C44	120.0
O71S	Dy3	Dy2	147.1(8)	N2B	C49	C44	123(2)
O71S	Dy3	Dy4	145.9(6)	N2B	C49	C48	117(2)
O71S	Dy3	O61S	73.1(8)	C51	C50	C47	121.8(14)
Dy1	Dy4	Dy2	61.36(3)	C51	C50	C55	120.0
Dy1	Dy4	Dy3	61.07(3)	C55	C50	C47	118.0(14)
Dy3	Dy4	Dy2	58.76(3)	C50	C51	C52	120.0
O2	Dy4	Dy1	38.6(3)	C53	C52	C51	120.0
O2	Dy4	Dy2	35.8(3)	N1B	C52	C51	110(2)
O2	Dy4	Dy3	76.4(3)	N1B	C52	C53	130(2)
O2	Dy4	O4	68.9(4)	C52	C53	C54	120.0
O2	Dy4	O81S	126.3(7)	C52	C53	C56	119.4(15)
O2	Dy4	O91S	137.5(6)	C54	C53	C56	120.6(15)
O3	Dy4	Dy1	36.9(3)	C55	C54	C53	120.0
O3	Dy4	Dy2	77.0(3)	N1A	C54	C53	124.7(19)
O3	Dy4	Dy3	37.6(3)	N1A	C54	C55	115.3(19)
O3	Dy4	O2	71.3(4)	C54	C55	C50	120.0
O3	Dy4	O4	70.6(4)	O15	C56	O16	120(2)
O3	Dy4	O81S	71.3(7)	O15	C56	C53	121(2)
O3	Dy4	O91S	143.9(6)	O16	C56	C53	118(2)
O4	Dy4	Dy1	78.0(3)	O81S	C81S	N81S	126(9)
O4	Dy4	Dy2	35.8(3)	N91S	C91S	O91S	130(8)
O4	Dy4	Dy3	36.0(3)	C61S	N61S	C62S	124(2)
O4	Dy4	O81S	129.2(6)	C61S	N61S	C63S	125(2)

O7 <sup>4</sup>	Dy4	Dy1	123.9(5)	C63S	N61S	C62S	111(4)
O7 <sup>4</sup>	Dy4	Dy2	109.7(4)	O61S	C61S	N61S	124(3)
O7 <sup>4</sup>	Dy4	Dy3	68.0(4)				

<sup>1</sup>-1/2+X,1/2-Y,-1/2+Z; <sup>2</sup>1/2+X,1/2-Y,-1/2+Z; <sup>3</sup>-1+X,+Y,+Z; <sup>4</sup>+X,-1+Y,+Z; <sup>5</sup>+X,1+Y,+Z; <sup>6</sup>1/2+X,1/2-Y,1/2+Z; <sup>7</sup>1+X,+Y,+Z; <sup>8</sup>-1/2+X,1/2-Y,1/2+Z

**Table A12** Torsion angles for MOF-1130(Dy).

A	B	C	D	Angle/°	A	B	C	D	Angle/°
Dy1	O5	C1	O6	2(4)	C20	C19	C22	C23	153(2)
Dy1	O5	C1	C2	179.4(14)	C20	C19	C22	C27	-25(4)
Dy1 <sup>1</sup>	O12	C42	O11	4(5)	C21	C16	C17	C18	0.0
Dy1 <sup>1</sup>	O12	C42	C39	-169.0(16)	C21	C16	C17	N7A	179(3)
Dy1	O14	C43	O13	-4(4)	C22	C19	C20	C21	178(4)
Dy1	O14	C43	C44	173.4(16)	C22	C23	C24	C25	0.0
Dy1 <sup>2</sup>	O19	C28	O20	1(3)	C23	C22	C27	C26	0.0
Dy1 <sup>2</sup>	O19	C28	C25	-180(3)	C23	C24	C25	C26	0.0
Dy1 <sup>2</sup>	O20	C28	O19	-1(3)	C23	C24	C25	C28	178(3)
Dy1 <sup>2</sup>	O20	C28	C25	180(3)	C24	C25	C26	N8	-177(5)
Dy2	O6	C1	O5	2(4)	C24	C25	C26	C27	0.0
Dy2	O6	C1	C2	-175.0(14)	C24	C25	C28	O19	-159(3)
Dy2	O10	C29	O9	1(4)	C24	C25	C28	O20	20(4)
Dy2	O10	C29	C30	-178.4(15)	C25	C26	C27	C22	0.0
Dy2 <sup>3</sup>	O15	C56	O16	1(4)	C26	C25	C28	O19	19(5)
Dy2 <sup>3</sup>	O15	C56	C53	173.3(16)	C26	C25	C28	O20	-162(2)
Dy2	O17	C15	O18	-2(3)	C27	C22	C23	C24	0.0
Dy2	O17	C15	C16	-176(3)	C28	C25	C26	N8	6(5)
Dy2	O18	C15	O17	2(3)	C28	C25	C26	C27	-177(3)
Dy2	O18	C15	C16	176(2)	C29	C30	C31	C32	-179.4(19)
Dy3 <sup>4</sup>	O8	C14	O7	40(4)	C29	C30	C31	N6A	2(3)
Dy3 <sup>4</sup>	O8	C14	C11	-144.1(19)	C29	C30	C35	C34	179.4(19)
Dy3	O9	C29	O10	15(5)	C29	C30	C35	N6B	-2(3)
Dy3	O9	C29	C30	-165.6(18)	C30	C31	C32	C33	0.0
Dy3	O13	C43	O14	-20(5)	C31	C30	C35	C34	0.0
Dy3	O13	C43	C44	163(2)	C31	C30	C35	N6B	178(3)
Dy3	O61S	C61S	N61S	-143(5)	C31	C32	C33	C34	0.0

Dy4 <sup>4</sup>	O7	C14	O8	16(4)	C31	C32	C33	C36	-180(2)
Dy4 <sup>4</sup>	O7	C14	C11	-159.4(18)	C32	C33	C34	C35	0.0
Dy4 <sup>1</sup>	O11	C42	O12	7(4)	C32	C33	C36	C37	25(2)
Dy4 <sup>1</sup>	O11	C42	C39	-179.8(15)	C32	C33	C36	C41	-154.8(13)
Dy4 <sup>3</sup>	O16	C56	O15	-27(4)	C33	C34	C35	C30	0.0
Dy4 <sup>3</sup>	O16	C56	C53	160.1(17)	C33	C34	C35	N6B	-179(2)
Dy4	O81S	C81S	N81S	173(4)	C33	C36	C37	C38	-180(2)
Dy4	O91S	C91S	N91S	164(6)	C33	C36	C41	C40	180(2)
O5	C1	C2	C3	-9(3)	C34	C33	C36	C37	-154.7(13)
O5	C1	C2	C7	168.6(16)	C34	C33	C36	C41	26(2)
O6	C1	C2	C3	168.2(16)	C35	C30	C31	C32	0.0
O6	C1	C2	C7	-14(3)	C35	C30	C31	N6A	-179(3)
O9	C29	C30	C31	176.7(19)	C36	C33	C34	C35	180(2)
O9	C29	C30	C35	-3(3)	C36	C37	C38	C39	0.0
O10	C29	C30	C31	-4(3)	C37	C36	C41	C40	0.0
O10	C29	C30	C35	176.4(19)	C37	C38	C39	C40	0.0
O13	C43	C44	C45	147(2)	C37	C38	C39	C42	174(2)
O13	C43	C44	C49	-27(3)	C38	C39	C40	N5	-180(3)
O14	C43	C44	C45	-31(3)	C38	C39	C40	C41	0.0
O14	C43	C44	C49	155(2)	C38	C39	C42	O11	-8(3)
O17	C15	C16	C17	-179(2)	C38	C39	C42	O12	166.0(19)
O17	C15	C16	C21	-3(4)	C39	C40	C41	C36	0.0
O18	C15	C16	C17	7(4)	C40	C39	C42	O11	166.4(19)
O18	C15	C16	C21	-177(2)	C40	C39	C42	O12	-20(3)
N3	C10	C11	C12	-174(3)	C41	C36	C37	C38	0.0
N3	C10	C11	C14	5(3)	C42	C39	C40	N5	6(3)
N5	C40	C41	C36	180(3)	C42	C39	C40	C41	-174(2)
N8	C26	C27	C22	177(5)	C43	C44	C45	C46	-173(2)
C1	C2	C3	C4	178(2)	C43	C44	C45	N2A	12(3)
C1	C2	C7	N4	2(3)	C43	C44	C49	C48	173(2)
C1	C2	C7	C6	-178(2)	C43	C44	C49	N2B	-10(4)
C2	C3	C4	C5	0.0	C44	C45	C46	C47	0.0
C3	C2	C7	N4	-180(3)	C45	C44	C49	C48	0.0
C3	C2	C7	C6	0.0	C45	C44	C49	N2B	177(3)
C3	C4	C5	C6	0.0	C45	C46	C47	C48	0.0

C3	C4	C5	C8	-179.4(19)	C45	C46	C47	C50	171(2)
C4	C5	C6	C7	0.0	C46	C47	C48	C49	0.0
C4	C5	C8	C9	-47(2)	C46	C47	C50	C51	-49(2)
C4	C5	C8	C13	128.9(15)	C46	C47	C50	C55	126.4(16)
C5	C6	C7	N4	180(3)	C47	C48	C49	C44	0.0
C5	C6	C7	C2	0.0	C47	C48	C49	N2B	-177(3)
C5	C8	C9	C10	176(2)	C47	C50	C51	C52	175(2)
C5	C8	C13	C12	-176(2)	C47	C50	C55	C54	-175(2)
C6	C5	C8	C9	133.2(15)	C48	C47	C50	C51	122.5(16)
C6	C5	C8	C13	-50(2)	C48	C47	C50	C55	-62.6(19)
C7	C2	C3	C4	0.0	C49	C44	C45	C46	0.0
C8	C5	C6	C7	179.4(19)	C49	C44	C45	N2A	-175(2)
C8	C9	C10	N3	174(3)	C50	C47	C48	C49	-171(2)
C8	C9	C10	C11	0.0	C50	C51	C52	C53	0.0
C9	C8	C13	C12	0.0	C50	C51	C52	N1B	-179(2)
C9	C10	C11	C12	0.0	C51	C50	C55	C54	0.0
C9	C10	C11	C14	179(2)	C51	C52	C53	C54	0.0
C10	C11	C12	C13	0.0	C51	C52	C53	C56	178(2)
C10	C11	C14	O7	174(2)	C52	C53	C54	C55	0.0
C10	C11	C14	O8	-1(3)	C52	C53	C54	N1A	180(3)
C11	C12	C13	C8	0.0	C52	C53	C56	O15	161(2)
C12	C11	C14	O7	-7(3)	C52	C53	C56	O16	-26(3)
C12	C11	C14	O8	178(2)	C53	C54	C55	C50	0.0
C13	C8	C9	C10	0.0	C54	C53	C56	O15	-20(3)
C14	C11	C12	C13	-179(2)	C54	C53	C56	O16	152.5(19)
C15	C16	C17	C18	176(3)	C55	C50	C51	C52	0.0
C15	C16	C17	N7A	-5(4)	C56	C53	C54	C55	-178(2)
C15	C16	C21	C20	-176(3)	C56	C53	C54	N1A	1(3)
C15	C16	C21	N7B	3(4)	C82S	N81S	C81S	O81S	15(9)
C16	C17	C18	C19	0.0	C83S	N81S	C81S	O81S	-165(9)
C17	C16	C21	C20	0.0	C92S	N91S	C91S	O91S	168(10)
C17	C16	C21	N7B	179(3)	C93S	N91S	C91S	O91S	-11(11)
C17	C18	C19	C20	0.0	N1A	C54	C55	C50	-180(2)
C17	C18	C19	C22	-178(3)	N2A	C45	C46	C47	175(2)
C18	C19	C20	C21	0.0	N6A	C31	C32	C33	179(2)

C18	C19	C22	C23	-28(3)	N7A	C17	C18	C19	-179(3)
C18	C19	C22	C27	153(2)	C62S	N61S	C61S	O61S	-5(11)
C19	C20	C21	C16	0.0	C63S	N61S	C61S	O61S	172(6)
C19	C20	C21	N7B	-179(3)	N1B	C52	C53	C54	179(3)
C19	C22	C23	C24	-179(3)	N1B	C52	C53	C56	-3(3)
C19	C22	C27	C26	179(3)					

<sup>1</sup>1/2+X,1/2-Y,1/2+Z; <sup>2</sup>-1/2+X,1/2-Y,1/2+Z; <sup>3</sup>1+X,+Y,+Z; <sup>4</sup>+X,1+Y,+Z

**Table A13** Hydrogen atom coordinates ( $\text{\AA}\times 10^4$ ) and isotropic displacement parameters ( $\text{\AA}^2\times 10^3$ ) for MOF-1130(Dy).

Atom	x	y	z	U(eq)
H3A	1854	8021	3385	142
H3B	1496	8765	3311	142
H4A	-1158	4788	3901	172
H4B	-915	4048	3756	172
H5A	4746	1968	6207	152
H5B	4881	2334	6623	152
H8A	-2994	3930	6935	236
H8B	-2547	4248	6611	236
H3	762	4571	2841	61
H4	793	5853	2843	63
H6	-718	5886	3675	92
H9	1189	6923	3325	78
H12	-1026	8253	3123	75
H13	-1058	6975	3172	81
H18	-2215	1379	5529	165
H20	-2288	3571	5334	175
H23	-3134	1540	5876	132
H24	-3695	1664	6485	131
H27	-2304	3596	6020	144
H32	1545	3187	5511	73
H34	2830	1396	5401	87
H37	1894	3119	6158	91
H38	2596	3445	6770	89

H41	3657	2015	5798	71
H46	4423	2319	2637	92
H48	4573	1326	3750	111
H51	5484	1161	2680	80
H55	5661	2257	3762	86
H81S	-279	585	1885	109
H82A	295	-1111	2105	158
H82B	373	-1349	1644	158
H82C	-425	-1190	1787	158
H83A	223	304	1202	222
H83B	648	-452	1169	222
H83C	1008	181	1457	222
H91S	-1467	-1052	2499	116
H92A	-2117	-1895	2021	205
H92B	-2834	-2150	2225	205
H92C	-2050	-2132	2491	205
H93A	-3316	-788	2662	238
H93B	-3567	-1353	2305	238
H93C	-3333	-543	2195	238
H1AA	6798	2510	4096	143
H1AB	7526	2298	3940	143
H2AA	3260	2660	2322	174
H2AB	2539	2446	2486	174
H6AA	345	3000	4675	134
H6AB	589	3451	5053	134
H7AA	-1723	617	5084	158
H7AB	-1387	863	4703	158
H61S	1055	-974	4188	106
H62A	-786	-754	4476	168
H62B	-1018	-1515	4264	168
H62C	-888	-817	3988	168
H63A	456	-2241	4140	133
H63B	-324	-2270	4323	133
H63C	406	-2073	4614	133
H1BA	7225	931	2557	76

H1BB	6417	819	2402	76
H2BA	3495	1072	4056	116
H2BB	2724	1205	3846	116
H6BA	2610	613	4880	112
H6BB	2003	697	4530	112
H7BA	-1810	4071	4786	229
H7BB	-1460	3638	4462	229

**Table A14** Atomic occupancy for MOF-1130(Dy).

<b>Atom</b>	<b>Occupancy</b>	<b>Atom</b>	<b>Occupancy</b>	<b>Atom</b>	<b>Occupancy</b>
N81S	0.46(4)	N91S	0.46(4)	C81S	0.46(4)
H81S	0.46(4)	C82S	0.46(4)	H82A	0.4625
H82B	0.4625	H82C	0.4625	C83S	0.46(4)
H83A	0.4625	H83B	0.4625	H83C	0.4625
C91S	0.46(4)	H91S	0.46(4)	C92S	0.46(4)
H92A	0.4558	H92B	0.4558	H92C	0.4558
C93S	0.46(4)	H93A	0.4558	H93B	0.4558
H93C	0.4558	N1A	0.58(4)	H1AA	0.58(4)
H1AB	0.58(4)	N2A	0.83(4)	H2AA	0.83(4)
H2AB	0.83(4)	N6A	0.56(4)	H6AA	0.56(4)
H6AB	0.56(4)	N7A	0.48(5)	H7AA	0.48(5)
H7AB	0.48(5)	N61S	0.66(4)	C61S	0.66(4)
H61S	0.66(4)	C62S	0.66(4)	H62A	0.6583
H62B	0.6583	H62C	0.6583	C63S	0.66(4)
H63A	0.6583	H63B	0.6583	H63C	0.6583
N1B	0.42(4)	H1BA	0.42(4)	H1BB	0.42(4)
N2B	0.17(4)	H2BA	0.17(4)	H2BB	0.17(4)
N6B	0.44(4)	H6BA	0.44(4)	H6BB	0.44(4)
N7B	0.52(5)	H7BA	0.52(5)	H7BB	0.52(5)

**Table A15** Fractional atomic coordinates ( $\times 10^4$ ) and equivalent isotropic displacement parameters ( $\text{\AA}^2 \times 10^3$ ) for MOF-1131(Yb).  $U_{eq}$  is defined as 1/3 of the trace of the orthogonalised UIJ tensor.

Atom	<i>x</i>	<i>y</i>	<i>z</i>	U(eq)
C1	3797(16)	2240(12)	9336(10)	96(15)
C2	4446(8)	2281(16)	9341(9)	142(12)
C3	4735(10)	2818(14)	9395(11)	147(12)
C4	5323(10)	2826(11)	9395(11)	151(13)
C5	5624(8)	2297(12)	9342(7)	147(13)
C6	5336(10)	1760(11)	9288(11)	151(13)
C7	4747(10)	1752(14)	9287(12)	155(13)
C8	6586(12)	1857(18)	9518(13)	250(20)
C9	7175(11)	1867(15)	9517(14)	250(20)
C10	7461(10)	2326(13)	9341(10)	240(20)
C11	7158(11)	2775(16)	9165(14)	250(20)
C12	6569(11)	2765(18)	9166(13)	250(20)
C13	6283(10)	2306(18)	9342(8)	240(20)
C14	8376(7)	1798(9)	9276(7)	113(10)
C15	8087(6)	2331(11)	9340(7)	106(10)
C16	8386(7)	2855(10)	9409(7)	104(10)
C17	8975(7)	2848(8)	9414(7)	101(9)
C18	9264(6)	2315(9)	9350(8)	97(9)
C19	8965(7)	1790(8)	9281(8)	111(10)
C20	9924(9)	2303(9)	9334(10)	84(9)
C21	855(16)	1909(16)	8492(9)	92(8)
C22	552(11)	2096(14)	8147(5)	123(10)
C23	636(14)	1743(14)	7843(7)	147(12)
C24	361(14)	1882(14)	7522(6)	155(13)
C25	2(9)	2375(11)	7505(5)	153(13)
C26	-83(13)	2729(13)	7809(6)	151(13)
C27	193(14)	2590(16)	8129(5)	138(12)
C28	-283(13)	2547(15)	7142(6)	210(18)
C29	-132(15)	2248(18)	6828(8)	212(17)
C30	-420(15)	2363(18)	6508(7)	220(17)
C31	-860(10)	2778(12)	6502(6)	198(14)

C32	-1011(14)	3078(17)	6816(8)	203(16)
C33	-723(16)	2962(19)	7136(7)	215(17)
C34	-1165(9)	2902(11)	6156(5)	175(13)
C35	-1056(13)	2548(14)	5856(6)	166(14)
C36	-1347(15)	2651(16)	5536(5)	143(12)
C37	-1746(11)	3108(14)	5515(5)	116(11)
C38	-1855(13)	3462(15)	5816(7)	138(13)
C39	-1565(13)	3359(14)	6136(6)	165(14)
C40	-2116(18)	3187(17)	5194(10)	102(13)
C41	2848(19)	1905(19)	8487(13)	130(20)
C42	3174(17)	2033(19)	8138(6)	176(16)
C43	3546(18)	2515(19)	8117(7)	184(16)
C44	3822(17)	2640(16)	7795(8)	188(16)
C45	3725(16)	2283(16)	7494(6)	185(16)
C46	3352(17)	1801(18)	7515(7)	189(16)
C47	3077(17)	1676(17)	7837(8)	186(16)
C48	4016(13)	2371(14)	7141(7)	218(18)
C49	4563(15)	2600(20)	7162(6)	224(18)
C50	4873(13)	2690(20)	6849(8)	213(18)
C51	4636(13)	2557(17)	6516(6)	197(17)
C52	4090(14)	2330(20)	6495(6)	206(17)
C53	3779(12)	2240(20)	6807(8)	215(18)
C54	4969(12)	2703(14)	6174(5)	119(12)
C55	5425(12)	3097(15)	6188(5)	128(12)
C56	5721(11)	3233(15)	5875(6)	123(11)
C57	5560(11)	2976(15)	5549(5)	96(10)
C58	5104(12)	2582(15)	5536(5)	114(11)
C59	4809(11)	2445(14)	5848(6)	124(12)
C60	5882(14)	3124(14)	5207(9)	47(8)
C61	-2960(30)	5192(16)	4345(7)	134(10)
C62	-2980(20)	5824(7)	4344(8)	137(10)
C63	-3031(19)	6150(11)	4662(7)	141(11)
C64	-3043(18)	6773(10)	4651(7)	141(12)
C65	-3007(18)	7071(7)	4323(8)	139(12)
C66	-2959(19)	6744(11)	4005(7)	148(13)

C67	-2950(20)	6121(11)	4016(7)	157(12)
C68	-3046(13)	7755(8)	4337(9)	128(12)
C69	-3410(13)	8039(12)	4576(9)	126(11)
C70	-3439(13)	8662(12)	4584(8)	131(12)
C71	-3103(13)	9001(8)	4354(9)	132(12)
C72	-2739(14)	8716(12)	4115(9)	147(13)
C73	-2711(14)	8093(12)	4107(9)	141(12)
C74	-3107(11)	9662(7)	4325(9)	105(9)
C75	-2604(9)	9984(10)	4307(9)	111(10)
C76	-2612(8)	10607(10)	4328(8)	90(8)
C77	-3124(11)	10908(7)	4367(8)	69(6)
C78	-3628(8)	10586(10)	4384(8)	91(8)
C79	-3619(9)	9963(10)	4363(8)	100(9)
C80	-3153(14)	11606(13)	4355(9)	54(5)
O1	3569(9)	1717(14)	9309(8)	87(9)
O2	3523(9)	2736(11)	9350(6)	64(6)
O3	10149(8)	1779(10)	9321(6)	66(6)
O4	10208(8)	2789(12)	9352(6)	75(7)
O5	2928(10)	2267(16)	8744(7)	101(10)
O6	2567(13)	1423(13)	8504(7)	100(10)
O7	5740(8)	2848(10)	4923(6)	53(5)
O8	6239(10)	3554(11)	5223(5)	71(7)
O9	775(8)	2255(12)	8754(5)	67(6)
O10	1190(12)	1477(15)	8477(6)	109(9)
O11	-2416(11)	3654(11)	5174(6)	78(7)
O12	-2018(9)	2872(11)	4919(6)	69(6)
O13	-2914(15)	4887(10)	4649(7)	110(9)
O14	-2990(19)	4890(11)	4039(7)	146(12)
O15	-2658(8)	11862(9)	4344(6)	57(5)
O16	-3622(7)	11871(8)	4357(4)	37(4)
O17	-3718(6)	3794(7)	4343(3)	22(4)
O18	-3123(6)	12941(8)	4702(4)	30(4)
O19	2437(7)	1187(9)	9324(4)	45(5)
O20	1873(6)	2055(7)	8987(4)	28(4)
O21S	-3115(12)	4596(10)	5366(6)	87(8)

O22S	-4010(14)	4611(13)	4825(9)	132(11)
O23S	-3991(15)	4559(18)	3778(8)	148(12)
O24S	-3180(14)	4573(14)	3314(6)	112(9)
Yb1	2651.3(5)	2190.8(7)	9342.4(3)	35.6(4)
Yb2	-3935.0(5)	12801.5(7)	4347.7(3)	34.3(4)
Yb3	-3152.3(6)	3969.4(7)	4836.5(3)	39.6(4)
Yb4	-3152.0(6)	3945.5(7)	3841.7(3)	40.5(5)
N1A	4380(30)	3390(30)	9440(20)	160(20)
N1B	4460(30)	1150(40)	9190(30)	180(30)
N2	9242(15)	3390(20)	9513(14)	157(19)
N3A	6220(30)	3590(40)	5932(16)	160(30)
N3B	4950(30)	2350(50)	5235(17)	160(30)
N4A	3610(40)	2900(40)	8415(17)	200(30)
N4B	2740(50)	1150(50)	7830(20)	200(30)
N5A	70(30)	2990(40)	8440(17)	170(30)
N5B	800(40)	1090(50)	7880(20)	160(20)
N6A	-2080(20)	10930(30)	4310(30)	100(20)
N6B	-4197(18)	10820(20)	4327(17)	108(17)
N7A	-3100(40)	5860(30)	4987(16)	150(20)
N7B	-2830(60)	5890(30)	3680(18)	180(30)
N8	-1240(20)	2300(20)	5255(10)	180(20)
N9S	-4500(30)	5550(30)	4810(20)	133(18)
C100	-4150(40)	5180(40)	4920(20)	128(16)
C101	-4640(40)	5540(40)	4450(30)	150(30)
C102	-4530(40)	6140(40)	4960(20)	140(30)

---

**Table A16** Anisotropic displacement parameters ( $\text{\AA}^2 \times 10^3$ ) for MOF-1131(Yb). The anisotropic displacement factor exponent takes the form:  $-2\pi^2[h2a^*2U11+2hka^*b^*U12+\dots]$ .

Atom	U <sub>11</sub>	U <sub>22</sub>	U <sub>33</sub>	U <sub>23</sub>	U <sub>13</sub>	U <sub>12</sub>
C1	50(30)	170(60)	70(30)	10(30)	3(19)	0(30)
C2	47(14)	150(20)	230(30)	-20(20)	12(16)	6(13)
C3	55(14)	150(20)	240(30)	-20(20)	11(17)	3(13)
C4	56(14)	150(20)	250(30)	-20(20)	11(17)	2(13)
C5	54(14)	150(20)	230(30)	-20(20)	9(16)	4(13)
C6	52(14)	150(20)	250(30)	-20(20)	11(18)	6(13)
C7	54(14)	150(20)	260(30)	-20(20)	9(18)	7(13)
C8	48(17)	280(40)	410(50)	80(40)	-20(20)	-10(20)
C9	48(17)	290(40)	410(50)	80(40)	-10(20)	-10(20)
C10	40(17)	280(40)	400(50)	80(40)	-10(20)	0(20)
C11	42(16)	290(40)	420(50)	90(40)	-10(20)	0(20)
C12	44(16)	290(40)	420(50)	100(40)	-10(20)	0(20)
C13	41(17)	280(40)	390(50)	80(40)	-10(20)	-10(20)
C14	47(12)	130(20)	160(30)	-17(17)	13(13)	-2(11)
C15	52(12)	130(20)	140(20)	-8(18)	19(12)	-1(11)
C16	52(11)	130(20)	130(20)	-8(17)	21(13)	0(11)
C17	53(11)	128(19)	120(20)	-10(15)	22(12)	0(11)
C18	49(11)	128(19)	110(20)	-12(15)	18(11)	-1(11)
C19	49(11)	130(19)	160(30)	-18(16)	13(13)	-2(11)
C20	52(11)	130(20)	70(20)	0(20)	16(11)	1(12)
C21	81(16)	144(17)	51(9)	-26(10)	-43(10)	27(13)
C22	126(19)	190(20)	57(9)	-32(10)	-58(11)	63(16)
C23	170(20)	210(20)	65(10)	-45(12)	-73(12)	92(19)
C24	170(30)	220(30)	67(11)	-43(13)	-76(13)	100(20)
C25	160(30)	220(30)	72(13)	-41(14)	-75(15)	90(20)
C26	170(20)	220(20)	71(12)	-38(13)	-70(15)	90(20)
C27	150(20)	200(20)	67(12)	-36(12)	-65(13)	82(18)
C28	230(30)	310(40)	95(16)	-38(19)	-80(18)	130(30)
C29	220(30)	320(40)	95(16)	-42(19)	-100(18)	150(30)
C30	220(30)	340(40)	93(15)	-45(18)	-88(16)	170(30)
C31	200(20)	320(30)	77(12)	-31(15)	-74(14)	150(20)

C32	210(30)	320(40)	80(13)	-31(17)	-60(15)	140(30)
C33	240(30)	320(40)	87(14)	-34(18)	-79(16)	140(30)
C34	180(20)	270(30)	71(11)	-39(13)	-63(13)	140(20)
C35	180(20)	250(30)	69(12)	-30(14)	-58(14)	130(20)
C36	160(20)	200(20)	63(11)	-26(13)	-48(13)	110(19)
C37	124(19)	170(20)	49(10)	-26(12)	-48(12)	77(17)
C38	140(20)	210(30)	63(11)	-47(14)	-58(13)	90(20)
C39	170(20)	250(30)	71(12)	-51(15)	-69(13)	120(20)
C40	120(20)	140(30)	48(13)	-24(16)	-42(14)	60(20)
C41	90(30)	210(60)	100(40)	-50(40)	60(30)	-80(40)
C42	190(30)	260(30)	75(15)	-41(18)	97(18)	-100(20)
C43	200(30)	270(30)	83(15)	-39(18)	93(18)	-110(20)
C44	210(30)	280(40)	83(16)	-40(18)	94(19)	-110(30)
C45	200(30)	280(40)	82(16)	-41(18)	94(19)	-100(30)
C46	210(30)	280(40)	81(15)	-47(19)	100(18)	-110(30)
C47	210(30)	270(30)	80(15)	-48(18)	101(18)	-110(20)
C48	160(20)	420(50)	76(14)	20(20)	63(16)	-90(30)
C49	170(20)	430(50)	75(14)	30(20)	62(16)	-100(30)
C50	150(20)	420(50)	69(14)	30(20)	56(16)	-90(30)
C51	140(20)	390(50)	63(14)	20(20)	59(16)	-80(30)
C52	140(20)	400(50)	73(14)	20(20)	60(15)	-80(30)
C53	160(20)	410(50)	76(14)	20(20)	66(16)	-90(30)
C54	114(19)	190(30)	51(11)	7(14)	31(12)	-49(19)
C55	130(20)	210(30)	45(11)	3(14)	34(12)	-67(19)
C56	121(18)	210(30)	44(10)	3(14)	31(12)	-62(18)
C57	79(16)	160(30)	43(10)	11(13)	26(11)	-24(16)
C58	99(18)	190(30)	51(10)	5(14)	32(11)	-49(18)
C59	111(18)	210(30)	53(11)	1(15)	36(12)	-59(19)
C60	70(20)	15(16)	60(20)	-9(16)	36(18)	0(17)
C61	290(30)	26(9)	88(11)	0(8)	-19(14)	-4(12)
C62	280(30)	26(8)	103(12)	0(8)	-29(15)	-5(11)
C63	290(30)	32(10)	104(12)	-2(8)	-31(16)	1(14)
C64	290(40)	31(11)	103(14)	-1(9)	-32(18)	0(14)
C65	280(40)	32(12)	106(14)	2(10)	-30(20)	-3(15)
C66	310(40)	34(11)	105(14)	3(9)	-35(18)	-2(15)

C67	330(30)	34(11)	109(13)	3(9)	-24(16)	-2(15)
C68	160(30)	44(13)	180(30)	31(16)	10(20)	11(15)
C69	160(30)	42(13)	180(30)	32(16)	10(20)	11(15)
C70	170(30)	42(13)	180(30)	33(16)	20(20)	12(16)
C71	170(30)	41(13)	180(30)	33(16)	30(20)	12(15)
C72	190(30)	46(13)	200(30)	31(17)	50(20)	12(16)
C73	180(30)	44(13)	200(30)	31(17)	30(20)	10(16)
C74	93(12)	58(11)	160(30)	0(12)	24(15)	2(9)
C75	89(12)	52(10)	190(30)	3(12)	25(14)	8(9)
C76	74(9)	51(10)	140(20)	5(11)	20(10)	10(8)
C77	73(9)	47(8)	86(17)	7(8)	13(9)	6(7)
C78	76(9)	57(10)	140(20)	0(11)	20(10)	-1(8)
C79	91(12)	56(10)	150(20)	0(12)	23(13)	0(9)
C80	45(7)	51(8)	64(14)	4(9)	10(8)	5(7)
O1	26(13)	100(20)	140(20)	-40(19)	3(13)	1(13)
O2	51(14)	54(15)	88(17)	-2(13)	-2(12)	6(12)
O3	45(13)	68(17)	86(16)	-22(13)	8(11)	9(12)
O4	22(11)	110(20)	89(16)	9(16)	8(10)	-13(13)
O5	66(16)	180(30)	61(16)	-21(18)	33(13)	-36(18)
O6	120(20)	90(20)	100(20)	-33(16)	72(18)	-34(18)
O7	55(13)	47(13)	56(13)	-9(12)	12(10)	-16(11)
O8	102(18)	62(17)	48(13)	-12(12)	34(12)	5(15)
O9	57(12)	109(15)	35(8)	-4(9)	-31(8)	9(11)
O10	108(17)	157(17)	62(12)	-39(12)	-54(12)	47(14)
O11	107(19)	72(17)	56(14)	-7(13)	-47(13)	19(15)
O12	65(14)	83(18)	58(14)	-3(13)	-23(11)	23(13)
O13	230(30)	24(10)	78(11)	-5(8)	2(14)	15(14)
O14	330(40)	23(11)	87(12)	1(9)	-19(15)	-13(16)
O15	37(7)	35(9)	98(15)	-1(10)	11(7)	17(7)
O16	38(7)	40(9)	33(9)	3(8)	9(6)	-3(7)
O17	29(7)	32(10)	5(6)	-2(5)	2(5)	15(6)
O18	12(8)	61(13)	18(8)	-8(9)	0(6)	-12(8)
O19	50(11)	61(15)	25(10)	-2(9)	-10(8)	-9(10)
O20	27(8)	24(10)	34(9)	-3(8)	-18(6)	-7(7)
O21S	160(20)	49(15)	56(14)	-26(12)	12(14)	22(15)

O22S	160(20)	88(18)	150(20)	-60(17)	-30(20)	80(17)
O23S	168(16)	180(30)	97(14)	61(16)	4(12)	81(17)
O24S	180(20)	105(19)	50(10)	29(11)	-8(11)	4(16)
Yb1	27.5(8)	46.2(10)	33.2(8)	2.9(7)	5.9(6)	-4.7(7)
Yb2	26.2(8)	45.9(10)	30.7(8)	-1.4(7)	5.6(6)	-1.8(7)
Yb3	55.1(10)	40.8(10)	22.8(8)	-4.1(7)	4.1(7)	4.3(8)
Yb4	61.5(10)	39.5(10)	20.5(8)	4.1(7)	4.5(7)	2.2(8)
N1A	60(20)	150(30)	280(70)	-20(30)	10(30)	3(16)
N1B	50(20)	150(30)	330(70)	-40(30)	10(30)	7(17)
N2	80(30)	120(40)	270(60)	10(40)	20(30)	-10(20)
N3A	160(30)	280(60)	40(20)	0(20)	32(18)	-120(40)
N3B	140(40)	270(50)	56(13)	-10(20)	44(16)	-110(40)
N4A	240(50)	280(50)	90(20)	-50(30)	100(30)	-120(40)
N4B	230(60)	280(40)	80(30)	-50(30)	110(30)	-120(40)
N5A	210(50)	230(40)	74(18)	-50(20)	-70(20)	110(40)
N5B	200(60)	210(20)	70(20)	-54(16)	-100(30)	100(20)
N6A	75(12)	52(19)	180(60)	10(20)	19(15)	8(12)
N6B	78(11)	58(18)	190(50)	-10(20)	9(14)	-1(11)
N7A	310(70)	44(19)	109(15)	4(12)	-30(20)	0(20)
N7B	390(80)	30(20)	112(15)	4(13)	-10(20)	-10(30)
N8	230(40)	250(30)	80(15)	-47(19)	-69(19)	160(30)
N9S	150(30)	90(20)	160(30)	-70(20)	-50(30)	80(20)
C100	140(30)	90(20)	150(30)	-70(20)	-50(30)	79(19)
C101	200(60)	100(30)	170(30)	-70(20)	-70(30)	100(40)
C102	150(50)	90(20)	170(40)	-70(20)	-60(40)	90(30)

---

**Table A17** Bond lengths for MOF-1131(Yb).

Atom	Atom	Length/Å	Atom	Atom	Length/Å
C1	C2	1.54(4)	C61	O14	1.32(3)
C1	O1	1.29(2)	C62	C63	1.3900
C1	O2	1.28(2)	C62	C67	1.3900
C1	Yb1	2.71(4)	C63	C64	1.3900
C2	C3	1.3900	C63	N7A	1.37(5)
C2	C7	1.3900	C64	C65	1.3900
C3	C4	1.3900	C65	C66	1.3900
C3	N1A	1.54(6)	C65	C68	1.53(2)
C4	C5	1.3900	C66	C67	1.3900
C5	C6	1.3900	C67	N7B	1.37(5)
C5	C13	1.56(3)	C68	C69	1.3900
C6	C7	1.3900	C68	C73	1.3900
C7	N1B	1.54(6)	C69	C70	1.3900
C8	C9	1.3900	C70	C71	1.3900
C8	C13	1.3900	C71	C72	1.3900
C9	C10	1.3900	C71	C74	1.48(2)
C10	C11	1.3900	C72	C73	1.3900
C10	C15	1.48(3)	C74	C75	1.3900
C11	C12	1.3900	C74	C79	1.3900
C12	C13	1.3900	C75	C76	1.3900
C14	C15	1.3900	C76	C77	1.3900
C14	C19	1.3900	C76	N6A	1.46(4)
C15	C16	1.3900	C77	C78	1.3900
C16	C17	1.3900	C77	C80	1.56(3)
C17	C18	1.3900	C78	C79	1.3900
C17	N2	1.41(5)	C78	N6B	1.46(4)
C18	C19	1.3900	C80	O15	1.30(3)
C18	C20	1.559(18)	C80	O16	1.26(3)
C20	O3	1.28(2)	O1	Yb1	2.41(2)
C20	O4	1.28(2)	O2	Yb1	2.39(2)
C20	Yb2 <sup>1</sup>	2.70(2)	O3	Yb2 <sup>1</sup>	2.36(2)
C21	C22	1.52(4)	O4	Yb2 <sup>1</sup>	2.41(2)

C21	O9	1.26(2)	O5	Yb1	2.32(2)
C21	O10	1.25(2)	O6	Yb4 <sup>2</sup>	2.27(2)
C22	C23	1.3900	O7	Yb2 <sup>3</sup>	2.28(2)
C22	C27	1.3900	O8	Yb3 <sup>4</sup>	2.24(2)
C23	C24	1.3900	O9	Yb2 <sup>5</sup>	2.307(18)
C23	N5B	1.51(10)	O10	Yb4 <sup>2</sup>	2.26(3)
C24	C25	1.3900	O11	Yb3	2.25(2)
C25	C26	1.3900	O12	Yb1 <sup>6</sup>	2.28(2)
C25	C28	1.55(3)	O13	Yb3	2.23(2)
C26	C27	1.3900	O14	Yb4	2.26(3)
C27	N5A	1.49(7)	O15	Yb1 <sup>7</sup>	2.23(2)
C28	C29	1.3900	O16	Yb2	2.201(18)
C28	C33	1.3900	O17	Yb2 <sup>8</sup>	2.271(16)
C29	C30	1.3900	O17	Yb3	2.294(14)
C30	C31	1.3900	O17	Yb4	2.321(13)
C31	C32	1.3900	O18	Yb1 <sup>7</sup>	2.288(13)
C31	C34	1.50(3)	O18	Yb2	2.341(14)
C32	C33	1.3900	O18	Yb3 <sup>9</sup>	2.347(18)
C34	C35	1.3900	O19	Yb1	2.29(2)
C34	C39	1.3900	O19	Yb3 <sup>2</sup>	2.387(16)
C35	C36	1.3900	O19	Yb4 <sup>2</sup>	2.281(17)
C36	C37	1.3900	O20	Yb1	2.278(15)
C36	N8	1.33(4)	O20	Yb2 <sup>5</sup>	2.357(15)
C37	C38	1.3900	O20	Yb4 <sup>2</sup>	2.295(16)
C37	C40	1.49(4)	O21S	Yb3	2.41(2)
C38	C39	1.3900	O22S	Yb3	2.48(3)
C40	O11	1.26(2)	O22S	C100	1.35(7)
C40	O12	1.26(2)	O23S	Yb4	2.42(3)
C41	C42	1.54(4)	O24S	Yb4	2.41(2)
C41	O5	1.26(3)	Yb1	O12 <sup>2</sup>	2.28(2)
C41	O6	1.26(3)	Yb1	O15 <sup>5</sup>	2.23(2)
C42	C43	1.3900	Yb1	O18 <sup>5</sup>	2.288(13)
C42	C47	1.3900	Yb1	Yb2 <sup>5</sup>	3.7446(16)
C43	C44	1.3900	Yb1	Yb3 <sup>2</sup>	3.698(2)
C43	N4A	1.41(6)	Yb1	Yb4 <sup>2</sup>	3.665(2)

C44	C45	1.3900	Yb2	C20 <sup>10</sup>	2.70(2)
C45	C46	1.3900	Yb2	O3 <sup>10</sup>	2.36(2)
C45	C48	1.50(2)	Yb2	O4 <sup>10</sup>	2.41(2)
C46	C47	1.3900	Yb2	O7 <sup>11</sup>	2.28(2)
C47	N4B	1.41(6)	Yb2	O9 <sup>7</sup>	2.307(18)
C48	C49	1.3900	Yb2	O17 <sup>9</sup>	2.271(16)
C48	C53	1.3900	Yb2	O20 <sup>7</sup>	2.357(16)
C49	C50	1.3900	Yb2	Yb1 <sup>7</sup>	3.7446(16)
C50	C51	1.3900	Yb2	Yb3 <sup>9</sup>	3.668(2)
C51	C52	1.3900	Yb2	Yb4 <sup>9</sup>	3.670(2)
C51	C54	1.53(2)	Yb3	O8 <sup>12</sup>	2.24(2)
C52	C53	1.3900	Yb3	O18 <sup>8</sup>	2.347(18)
C54	C55	1.3900	Yb3	O19 <sup>6</sup>	2.387(16)
C54	C59	1.3900	Yb3	Yb1 <sup>6</sup>	3.698(2)
C55	C56	1.3900	Yb3	Yb2 <sup>8</sup>	3.668(2)
C56	C57	1.3900	Yb3	Yb4	3.6935(16)
C56	N3A	1.44(7)	Yb4	O6 <sup>6</sup>	2.27(2)
C57	C58	1.3900	Yb4	O10 <sup>6</sup>	2.26(3)
C57	C60	1.52(3)	Yb4	O19 <sup>6</sup>	2.281(17)
C58	C59	1.3900	Yb4	O20 <sup>6</sup>	2.295(16)
C58	N3B	1.28(7)	Yb4	Yb1 <sup>6</sup>	3.665(2)
C60	O7	1.26(4)	Yb4	Yb2 <sup>8</sup>	3.670(2)
C60	O8	1.28(4)	N9S	C100	1.23(9)
C61	C62	1.41(4)	N9S	C101	1.37(10)
C61	O13	1.32(3)	N9S	C102	1.45(9)

<sup>1</sup>3/2+X,3/2-Y,1/2+Z; <sup>2</sup>1/2+X,1/2-Y,1/2+Z; <sup>3</sup>1+X,-1+Y,+Z; <sup>4</sup>1+X,+Y,+Z; <sup>5</sup>1/2+X,3/2-Y,1/2+Z; <sup>6</sup>-1/2+X,1/2-Y,-1/2+Z; <sup>7</sup>-1/2+X,3/2-Y,-1/2+Z; <sup>8</sup>+X,-1+Y,+Z; <sup>9</sup>+X,1+Y,+Z; <sup>10</sup>-3/2+X,3/2-Y,-1/2+Z; <sup>11</sup>-1+X,1+Y,+Z; <sup>12</sup>-1+X,+Y,+Z

**Table A18** Bond angles for MOF-1131(Yb).

Atom	Atom	Atom	Angle/°	Atom	Atom	Atom	Angle/°
C2	C1	Yb1	178(3)	O12 <sup>2</sup>	Yb1	O2	74.3(8)
O1	C1	C2	118(3)	O12 <sup>2</sup>	Yb1	O5	143.6(8)
O1	C1	Yb1	63.1(19)	O12 <sup>2</sup>	Yb1	O18 <sup>5</sup>	73.5(6)
O2	C1	C2	117(3)	O12 <sup>2</sup>	Yb1	O19	92.5(7)
O2	C1	O1	125(3)	O12 <sup>2</sup>	Yb1	Yb2 <sup>5</sup>	109.5(5)
O2	C1	Yb1	62.0(18)	O12 <sup>2</sup>	Yb1	Yb3 <sup>2</sup>	70.5(6)
C3	C2	C1	123(2)	O12 <sup>2</sup>	Yb1	Yb4 <sup>2</sup>	127.5(6)
C3	C2	C7	120.0	O15 <sup>5</sup>	Yb1	C1	106.7(7)
C7	C2	C1	117(2)	O15 <sup>5</sup>	Yb1	O1	135.0(9)
C2	C3	N1A	118(3)	O15 <sup>5</sup>	Yb1	O2	78.5(8)
C4	C3	C2	120.0	O15 <sup>5</sup>	Yb1	O5	91.6(10)
C4	C3	N1A	122(3)	O15 <sup>5</sup>	Yb1	O12 <sup>2</sup>	99.5(8)
C3	C4	C5	120.0	O15 <sup>5</sup>	Yb1	O18 <sup>5</sup>	81.8(6)
C4	C5	C6	120.0	O15 <sup>5</sup>	Yb1	O19	148.1(6)
C4	C5	C13	120.0(7)	O15 <sup>5</sup>	Yb1	O20	82.2(7)
C6	C5	C13	120.0(7)	O15 <sup>5</sup>	Yb1	Yb2 <sup>5</sup>	70.7(5)
C7	C6	C5	120.0	O15 <sup>5</sup>	Yb1	Yb3 <sup>2</sup>	119.4(5)
C2	C7	N1B	123(4)	O15 <sup>5</sup>	Yb1	Yb4 <sup>2</sup>	119.1(5)
C6	C7	C2	120.0	O18 <sup>5</sup>	Yb1	C1	144.2(9)
C6	C7	N1B	117(3)	O18 <sup>5</sup>	Yb1	O1	134.0(9)
C9	C8	C13	120.0	O18 <sup>5</sup>	Yb1	O2	138.5(7)
C8	C9	C10	120.0	O18 <sup>5</sup>	Yb1	O5	142.7(7)
C9	C10	C15	119.6(8)	O18 <sup>5</sup>	Yb1	O19	73.5(6)
C11	C10	C9	120.0	O18 <sup>5</sup>	Yb1	Yb2 <sup>5</sup>	36.5(4)
C11	C10	C15	120.4(8)	O18 <sup>5</sup>	Yb1	Yb3 <sup>2</sup>	37.6(4)
C12	C11	C10	120.0	O18 <sup>5</sup>	Yb1	Yb4 <sup>2</sup>	78.1(4)
C11	C12	C13	120.0	O19	Yb1	C1	105.1(7)
C8	C13	C5	120.2(13)	O19	Yb1	O1	76.7(9)
C12	C13	C5	119.8(13)	O19	Yb1	O2	133.3(8)
C12	C13	C8	120.0	O19	Yb1	O5	96.0(10)
C15	C14	C19	120.0	O19	Yb1	Yb2 <sup>5</sup>	77.5(5)
C14	C15	C10	119.1(8)	O19	Yb1	Yb3 <sup>2</sup>	38.7(4)

C16	C15	C10	120.9(8)	O19	Yb1	Yb4 <sup>2</sup>	36.6(4)
C16	C15	C14	120.0	O20	Yb1	C1	143.5(9)
C15	C16	C17	120.0	O20	Yb1	O1	129.3(8)
C16	C17	N2	116.0(19)	O20	Yb1	O2	140.0(7)
C18	C17	C16	120.0	O20	Yb1	O5	71.7(7)
C18	C17	N2	123.9(19)	O20	Yb1	O12 <sup>2</sup>	143.9(7)
C17	C18	C19	120.0	O20	Yb1	O18 <sup>5</sup>	71.1(5)
C17	C18	C20	120.9(7)	O20	Yb1	O19	71.1(6)
C19	C18	C20	119.0(7)	O20	Yb1	Yb2 <sup>5</sup>	36.8(4)
C18	C19	C14	120.0	O20	Yb1	Yb3 <sup>2</sup>	77.3(4)
C18	C20	Yb2 <sup>1</sup>	175(2)	O20	Yb1	Yb4 <sup>2</sup>	36.9(4)
O3	C20	C18	115.6(16)	Yb3 <sup>2</sup>	Yb1	Yb2 <sup>5</sup>	59.05(4)
O3	C20	Yb2 <sup>1</sup>	60.6(13)	Yb4 <sup>2</sup>	Yb1	Yb2 <sup>5</sup>	59.37(4)
O4	C20	C18	120.5(15)	Yb4 <sup>2</sup>	Yb1	Yb3 <sup>2</sup>	60.21(4)
O4	C20	O3	124(2)	C20 <sup>10</sup>	Yb2	Yb1 <sup>7</sup>	175.1(5)
O4	C20	Yb2 <sup>1</sup>	63.2(13)	C20 <sup>10</sup>	Yb2	Yb3 <sup>9</sup>	124.8(6)
O9	C21	C22	114(2)	C20 <sup>10</sup>	Yb2	Yb4 <sup>9</sup>	123.6(6)
O10	C21	C22	118(2)	O3 <sup>10</sup>	Yb2	C20 <sup>10</sup>	28.3(5)
O10	C21	O9	127(3)	O3 <sup>10</sup>	Yb2	O4 <sup>10</sup>	56.5(8)
C23	C22	C21	117.3(18)	O3 <sup>10</sup>	Yb2	Yb1 <sup>7</sup>	156.2(5)
C23	C22	C27	120.0	O3 <sup>10</sup>	Yb2	Yb3 <sup>9</sup>	101.5(6)
C27	C22	C21	122.7(18)	O3 <sup>10</sup>	Yb2	Yb4 <sup>9</sup>	99.6(5)
C22	C23	C24	120.0	O4 <sup>10</sup>	Yb2	C20 <sup>10</sup>	28.2(5)
C22	C23	N5B	121(3)	O4 <sup>10</sup>	Yb2	Yb1 <sup>7</sup>	147.2(6)
C24	C23	N5B	114(3)	O4 <sup>10</sup>	Yb2	Yb3 <sup>9</sup>	143.5(5)
C23	C24	C25	120.0	O4 <sup>10</sup>	Yb2	Yb4 <sup>9</sup>	143.7(6)
C24	C25	C28	119.8(8)	O7 <sup>11</sup>	Yb2	C20 <sup>10</sup>	71.5(9)
C26	C25	C24	120.0	O7 <sup>11</sup>	Yb2	O3 <sup>10</sup>	73.1(7)
C26	C25	C28	120.1(8)	O7 <sup>11</sup>	Yb2	O4 <sup>10</sup>	74.5(7)
C27	C26	C25	120.0	O7 <sup>11</sup>	Yb2	O9 <sup>7</sup>	143.0(7)
C22	C27	N5A	124(3)	O7 <sup>11</sup>	Yb2	O18	75.2(6)
C26	C27	C22	120.0	O7 <sup>11</sup>	Yb2	O20 <sup>7</sup>	143.5(6)
C26	C27	N5A	116(3)	O7 <sup>11</sup>	Yb2	Yb1 <sup>7</sup>	110.2(5)
C29	C28	C25	119.8(14)	O7 <sup>11</sup>	Yb2	Yb3 <sup>9</sup>	71.0(5)
C29	C28	C33	120.0	O7 <sup>11</sup>	Yb2	Yb4 <sup>9</sup>	128.4(5)

C33	C28	C25	119.9(14)	O9 <sup>7</sup>	Yb2	C20 <sup>10</sup>	71.7(9)
C30	C29	C28	120.0	O9 <sup>7</sup>	Yb2	O3 <sup>10</sup>	73.3(8)
C29	C30	C31	120.0	O9 <sup>7</sup>	Yb2	O4 <sup>10</sup>	74.4(8)
C30	C31	C34	119.6(13)	O9 <sup>7</sup>	Yb2	O18	141.5(6)
C32	C31	C30	120.0	O9 <sup>7</sup>	Yb2	O20 <sup>7</sup>	72.7(6)
C32	C31	C34	120.4(13)	O9 <sup>7</sup>	Yb2	Yb1 <sup>7</sup>	106.7(5)
C33	C32	C31	120.0	O9 <sup>7</sup>	Yb2	Yb3 <sup>9</sup>	131.1(6)
C32	C33	C28	120.0	O9 <sup>7</sup>	Yb2	Yb4 <sup>9</sup>	72.4(6)
C35	C34	C31	119.5(8)	O16	Yb2	C20 <sup>10</sup>	104.7(6)
C35	C34	C39	120.0	O16	Yb2	O3 <sup>10</sup>	133.0(7)
C39	C34	C31	120.5(8)	O16	Yb2	O4 <sup>10</sup>	76.6(7)
C36	C35	C34	120.0	O16	Yb2	O7 <sup>11</sup>	98.2(7)
C37	C36	C35	120.0	O16	Yb2	O9 <sup>7</sup>	93.5(8)
N8	C36	C35	119(2)	O16	Yb2	O17 <sup>9</sup>	147.3(6)
N8	C36	C37	121(2)	O16	Yb2	O18	80.9(6)
C36	C37	C38	120.0	O16	Yb2	O20 <sup>7</sup>	82.2(5)
C36	C37	C40	121.8(17)	O16	Yb2	Yb1 <sup>7</sup>	70.6(4)
C38	C37	C40	117.7(17)	O16	Yb2	Yb3 <sup>9</sup>	119.5(5)
C37	C38	C39	120.0	O16	Yb2	Yb4 <sup>9</sup>	119.5(4)
C38	C39	C34	120.0	O17 <sup>9</sup>	Yb2	C20 <sup>10</sup>	108.0(6)
O11	C40	C37	118(2)	O17 <sup>9</sup>	Yb2	O3 <sup>10</sup>	79.6(6)
O12	C40	C37	118(3)	O17 <sup>9</sup>	Yb2	O4 <sup>10</sup>	136.1(7)
O12	C40	O11	121(3)	O17 <sup>9</sup>	Yb2	O7 <sup>11</sup>	92.2(6)
O5	C41	C42	116(3)	O17 <sup>9</sup>	Yb2	O9 <sup>7</sup>	96.5(7)
O5	C41	O6	126(4)	O17 <sup>9</sup>	Yb2	O18	72.0(6)
O6	C41	C42	118(3)	O17 <sup>9</sup>	Yb2	O20 <sup>7</sup>	71.4(5)
C43	C42	C41	121(2)	O17 <sup>9</sup>	Yb2	Yb1 <sup>7</sup>	76.7(4)
C43	C42	C47	120.0	O17 <sup>9</sup>	Yb2	Yb3 <sup>9</sup>	36.8(4)
C47	C42	C41	119(2)	O17 <sup>9</sup>	Yb2	Yb4 <sup>9</sup>	37.4(3)
C42	C43	C44	120.0	O18	Yb2	C20 <sup>10</sup>	146.7(8)
C42	C43	N4A	120(3)	O18	Yb2	O3 <sup>10</sup>	136.1(7)
C44	C43	N4A	120(3)	O18	Yb2	O4 <sup>10</sup>	138.8(7)
C45	C44	C43	120.0	O18	Yb2	O20 <sup>7</sup>	68.9(5)
C44	C45	C46	120.0	O18	Yb2	Yb1 <sup>7</sup>	35.5(3)
C44	C45	C48	124(2)	O18	Yb2	Yb3 <sup>9</sup>	38.6(4)

C46	C45	C48	116(2)	O18	Yb2	Yb4 <sup>9</sup>	77.5(4)
C45	C46	C47	120.0	O20 <sup>7</sup>	Yb2	C20 <sup>10</sup>	144.0(8)
C42	C47	N4B	126(3)	O20 <sup>7</sup>	Yb2	O3 <sup>10</sup>	131.8(6)
C46	C47	C42	120.0	O20 <sup>7</sup>	Yb2	O4 <sup>10</sup>	139.3(7)
C46	C47	N4B	114(3)	O20 <sup>7</sup>	Yb2	Yb1 <sup>7</sup>	35.4(4)
C49	C48	C45	115(2)	O20 <sup>7</sup>	Yb2	Yb3 <sup>9</sup>	77.2(4)
C49	C48	C53	120.0	O20 <sup>7</sup>	Yb2	Yb4 <sup>9</sup>	37.3(4)
C53	C48	C45	125(2)	Yb3 <sup>9</sup>	Yb2	Yb1 <sup>7</sup>	59.84(4)
C48	C49	C50	120.0	Yb3 <sup>9</sup>	Yb2	Yb4 <sup>9</sup>	60.44(4)
C51	C50	C49	120.0	Yb4 <sup>9</sup>	Yb2	Yb1 <sup>7</sup>	59.24(4)
C50	C51	C52	120.0	O8 <sup>12</sup>	Yb3	O11	90.6(9)
C50	C51	C54	119(2)	O8 <sup>12</sup>	Yb3	O17	93.9(7)
C52	C51	C54	121(2)	O8 <sup>12</sup>	Yb3	O18 <sup>8</sup>	75.6(7)
C53	C52	C51	120.0	O8 <sup>12</sup>	Yb3	O19 <sup>6</sup>	146.0(8)
C52	C53	C48	120.0	O8 <sup>12</sup>	Yb3	O21S	74.8(9)
C55	C54	C51	120(2)	O8 <sup>12</sup>	Yb3	O22S	73.9(11)
C55	C54	C59	120.0	O8 <sup>12</sup>	Yb3	Yb1 <sup>6</sup>	111.2(6)
C59	C54	C51	120(2)	O8 <sup>12</sup>	Yb3	Yb2 <sup>8</sup>	72.6(6)
C54	C55	C56	120.0	O8 <sup>12</sup>	Yb3	Yb4	129.7(6)
C55	C56	N3A	114(3)	O11	Yb3	O17	146.7(7)
C57	C56	C55	120.0	O11	Yb3	O18 <sup>8</sup>	77.9(7)
C57	C56	N3A	125(3)	O11	Yb3	O19 <sup>6</sup>	87.0(8)
C56	C57	C58	120.0	O11	Yb3	O21S	72.6(9)
C56	C57	C60	120(2)	O11	Yb3	O22S	145.0(9)
C58	C57	C60	120(2)	O11	Yb3	Yb1 <sup>6</sup>	70.2(6)
C59	C58	C57	120.0	O11	Yb3	Yb2 <sup>8</sup>	116.1(6)
N3B	C58	C57	120(3)	O11	Yb3	Yb4	123.3(6)
N3B	C58	C59	120(3)	O13	Yb3	O8 <sup>12</sup>	137.9(9)
C58	C59	C54	120.0	O13	Yb3	O11	105.3(11)
O7	C60	C57	117(3)	O13	Yb3	O17	93.1(8)
O7	C60	O8	125(3)	O13	Yb3	O18 <sup>8</sup>	145.2(7)
O8	C60	C57	117(3)	O13	Yb3	O19 <sup>6</sup>	74.8(8)
O13	C61	C62	121(3)	O13	Yb3	O21S	73.4(9)
O14	C61	C62	120(3)	O13	Yb3	O22S	70.9(12)
O14	C61	O13	118(3)	O13	Yb3	Yb1 <sup>6</sup>	110.9(7)

C63	C62	C61	122(2)	O13	Yb3	Yb2 <sup>8</sup>	128.5(7)
C63	C62	C67	120.0	O13	Yb3	Yb4	72.6(6)
C67	C62	C61	118(2)	O17	Yb3	O18 <sup>8</sup>	71.5(5)
C62	C63	C64	120.0	O17	Yb3	O19 <sup>6</sup>	71.2(5)
N7A	C63	C62	121(3)	O17	Yb3	O21S	140.1(7)
N7A	C63	C64	119(3)	O17	Yb3	O22S	67.1(8)
C63	C64	C65	120.0	O17	Yb3	Yb1 <sup>6</sup>	77.5(3)
C64	C65	C66	120.0	O17	Yb3	Yb2 <sup>8</sup>	36.3(4)
C64	C65	C68	116(2)	O17	Yb3	Yb4	37.1(3)
C66	C65	C68	124(2)	O18 <sup>8</sup>	Yb3	O19 <sup>6</sup>	70.7(6)
C67	C66	C65	120.0	O18 <sup>8</sup>	Yb3	O21S	137.5(7)
C66	C67	C62	120.0	O18 <sup>8</sup>	Yb3	O22S	125.7(9)
N7B	C67	C62	129(4)	O18 <sup>8</sup>	Yb3	Yb1 <sup>6</sup>	36.5(3)
N7B	C67	C66	110(4)	O18 <sup>8</sup>	Yb3	Yb2 <sup>8</sup>	38.5(4)
C69	C68	C65	121(3)	O18 <sup>8</sup>	Yb3	Yb4	76.9(4)
C69	C68	C73	120.0	O19 <sup>6</sup>	Yb3	O21S	135.6(8)
C73	C68	C65	119(3)	O19 <sup>6</sup>	Yb3	O22S	123.3(9)
C70	C69	C68	120.0	O19 <sup>6</sup>	Yb3	Yb1 <sup>6</sup>	36.9(5)
C71	C70	C69	120.0	O19 <sup>6</sup>	Yb3	Yb2 <sup>8</sup>	78.2(5)
C70	C71	C72	120.0	O19 <sup>6</sup>	Yb3	Yb4	36.7(4)
C70	C71	C74	126(2)	O21S	Yb3	O22S	73.0(9)
C72	C71	C74	114(2)	O21S	Yb3	Yb1 <sup>6</sup>	142.3(6)
C73	C72	C71	120.0	O21S	Yb3	Yb2 <sup>8</sup>	146.1(7)
C72	C73	C68	120.0	O21S	Yb3	Yb4	145.4(6)
C75	C74	C71	121(2)	O22S	Yb3	Yb1 <sup>6</sup>	144.6(7)
C75	C74	C79	120.0	O22S	Yb3	Yb2 <sup>8</sup>	89.4(7)
C79	C74	C71	119(2)	O22S	Yb3	Yb4	89.6(7)
C76	C75	C74	120.0	Yb2 <sup>8</sup>	Yb3	Yb1 <sup>6</sup>	61.11(4)
C75	C76	C77	120.0	Yb2 <sup>8</sup>	Yb3	Yb4	59.81(4)
C75	C76	N6A	119(4)	Yb4	Yb3	Yb1 <sup>6</sup>	59.46(4)
C77	C76	N6A	121(4)	O6 <sup>6</sup>	Yb4	O17	145.7(8)
C76	C77	C78	120.0	O6 <sup>6</sup>	Yb4	O19 <sup>6</sup>	86.1(9)
C76	C77	C80	121(2)	O6 <sup>6</sup>	Yb4	O20 <sup>6</sup>	76.1(8)
C78	C77	C80	119(2)	O6 <sup>6</sup>	Yb4	O23S	139.9(10)
C77	C78	N6B	126(3)	O6 <sup>6</sup>	Yb4	O24S	77.2(10)

C79	C78	C77	120.0	O6 <sup>6</sup>	Yb4	Yb1 <sup>6</sup>	69.1(7)
C79	C78	N6B	112(3)	O6 <sup>6</sup>	Yb4	Yb2 <sup>8</sup>	114.3(7)
C78	C79	C74	120.0	O6 <sup>6</sup>	Yb4	Yb3	124.2(8)
O15	C80	C77	114(2)	O10 <sup>6</sup>	Yb4	O6 <sup>6</sup>	91.8(12)
O16	C80	C77	121(3)	O10 <sup>6</sup>	Yb4	O17	91.4(8)
O16	C80	O15	126(3)	O10 <sup>6</sup>	Yb4	O19 <sup>6</sup>	146.2(9)
C1	O1	Yb1	89(2)	O10 <sup>6</sup>	Yb4	O20 <sup>6</sup>	75.7(9)
C1	O2	Yb1	90(2)	O10 <sup>6</sup>	Yb4	O23S	67.4(13)
C20	O3	Yb2 <sup>1</sup>	91.0(14)	O10 <sup>6</sup>	Yb4	O24S	74.8(10)
C20	O4	Yb2 <sup>1</sup>	88.6(15)	O10 <sup>6</sup>	Yb4	Yb1 <sup>6</sup>	111.6(8)
C41	O5	Yb1	129(3)	O10 <sup>6</sup>	Yb4	Yb2 <sup>8</sup>	70.8(7)
C41	O6	Yb4 <sup>2</sup>	137(2)	O10 <sup>6</sup>	Yb4	Yb3	127.0(7)
C60	O7	Yb2 <sup>3</sup>	135.7(18)	O14	Yb4	O6 <sup>6</sup>	113.0(13)
C60	O8	Yb3 <sup>4</sup>	134.9(19)	O14	Yb4	O10 <sup>6</sup>	134.1(13)
C21	O9	Yb2 <sup>5</sup>	131(2)	O14	Yb4	O17	88.4(10)
C21	O10	Yb4 <sup>2</sup>	137(2)	O14	Yb4	O19 <sup>6</sup>	76.4(10)
C40	O11	Yb3	136(2)	O14	Yb4	O20 <sup>6</sup>	145.5(8)
C40	O12	Yb1 <sup>6</sup>	137(2)	O14	Yb4	O23S	69.0(15)
C61	O13	Yb3	136(2)	O14	Yb4	O24S	74.1(10)
C61	O14	Yb4	140(2)	O14	Yb4	Yb1 <sup>6</sup>	113.1(9)
C80	O15	Yb1 <sup>7</sup>	135.1(17)	O14	Yb4	Yb2 <sup>8</sup>	124.4(8)
C80	O16	Yb2	137.7(18)	O14	Yb4	Yb3	70.3(7)
Yb2 <sup>8</sup>	O17	Yb3	106.9(6)	O17	Yb4	O23S	71.7(8)
Yb2 <sup>8</sup>	O17	Yb4	106.1(5)	O17	Yb4	O24S	136.3(8)
Yb3	O17	Yb4	106.3(6)	O17	Yb4	Yb1 <sup>6</sup>	77.9(4)
Yb1 <sup>7</sup>	O18	Yb2	108.0(6)	O17	Yb4	Yb2 <sup>8</sup>	36.5(4)
Yb1 <sup>7</sup>	O18	Yb3 <sup>9</sup>	105.8(6)	O17	Yb4	Yb3	36.6(4)
Yb2	O18	Yb3 <sup>9</sup>	103.0(6)	O19 <sup>6</sup>	Yb4	O17	72.7(5)
Yb1	O19	Yb3 <sup>2</sup>	104.4(7)	O19 <sup>6</sup>	Yb4	O20 <sup>6</sup>	71.0(6)
Yb4 <sup>2</sup>	O19	Yb1	106.5(7)	O19 <sup>6</sup>	Yb4	O23S	130.3(9)
Yb4 <sup>2</sup>	O19	Yb3 <sup>2</sup>	104.6(7)	O19 <sup>6</sup>	Yb4	O24S	136.7(9)
Yb1	O20	Yb2 <sup>5</sup>	107.8(6)	O19 <sup>6</sup>	Yb4	Yb1 <sup>6</sup>	36.9(5)
Yb1	O20	Yb4 <sup>2</sup>	106.6(6)	O19 <sup>6</sup>	Yb4	Yb2 <sup>8</sup>	79.3(5)
Yb4 <sup>2</sup>	O20	Yb2 <sup>5</sup>	104.2(6)	O19 <sup>6</sup>	Yb4	Yb3	38.7(4)
C100	O22S	Yb3	138(4)	O20 <sup>6</sup>	Yb4	O17	71.6(5)

C1	Yb1	Yb2 <sup>5</sup>	177.4(6)	O20 <sup>6</sup>	Yb4	O23S	126.3(11)
C1	Yb1	Yb3 <sup>2</sup>	123.2(7)	O20 <sup>6</sup>	Yb4	O24S	139.1(8)
C1	Yb1	Yb4 <sup>2</sup>	122.6(7)	O20 <sup>6</sup>	Yb4	Yb1 <sup>6</sup>	36.6(4)
O1	Yb1	C1	28.4(5)	O20 <sup>6</sup>	Yb4	Yb2 <sup>8</sup>	38.5(4)
O1	Yb1	Yb2 <sup>5</sup>	154.2(7)	O20 <sup>6</sup>	Yb4	Yb3	77.2(4)
O1	Yb1	Yb3 <sup>2</sup>	100.5(8)	O23S	Yb4	Yb1 <sup>6</sup>	149.6(7)
O1	Yb1	Yb4 <sup>2</sup>	97.7(7)	O23S	Yb4	Yb2 <sup>8</sup>	91.6(9)
O2	Yb1	C1	28.3(5)	O23S	Yb4	Yb3	94.9(7)
O2	Yb1	O1	56.6(9)	O24S	Yb4	O23S	64.7(10)
O2	Yb1	Yb2 <sup>5</sup>	149.1(6)	O24S	Yb4	Yb1 <sup>6</sup>	145.7(8)
O2	Yb1	Yb3 <sup>2</sup>	142.5(6)	O24S	Yb4	Yb2 <sup>8</sup>	143.9(8)
O2	Yb1	Yb4 <sup>2</sup>	143.2(6)	O24S	Yb4	Yb3	143.6(7)
O5	Yb1	C1	72.8(10)	Yb1 <sup>6</sup>	Yb4	Yb2 <sup>8</sup>	61.39(4)
O5	Yb1	O1	74.1(10)	Yb1 <sup>6</sup>	Yb4	Yb3	60.33(4)
O5	Yb1	O2	74.2(9)	Yb2 <sup>8</sup>	Yb4	Yb3	59.75(4)
O5	Yb1	Yb2 <sup>5</sup>	106.8(6)	C100	N9S	C101	119(7)
O5	Yb1	Yb3 <sup>2</sup>	132.2(8)	C100	N9S	C102	121(7)
O5	Yb1	Yb4 <sup>2</sup>	73.3(8)	C101	N9S	C102	111(7)
O12 <sup>2</sup>	Yb1	C1	70.8(10)	N9S	C100	O22S	135(8)
O12 <sup>2</sup>	Yb1	O1	73.6(9)				

<sup>1</sup>3/2+X,3/2-Y,1/2+Z; <sup>2</sup>1/2+X,1/2-Y,1/2+Z; <sup>3</sup>1+X,-1+Y,+Z; <sup>4</sup>1+X,+Y,+Z; <sup>5</sup>1/2+X,3/2-Y,1/2+Z; <sup>6</sup>-1/2+X,1/2-Y,-1/2+Z; <sup>7</sup>-1/2+X,3/2-Y,-1/2+Z; <sup>8</sup>+X,-1+Y,+Z; <sup>9</sup>+X,1+Y,+Z; <sup>10</sup>-3/2+X,3/2-Y,-1/2+Z; <sup>11</sup>-1+X,1+Y,+Z; <sup>12</sup>-1+X,+Y,+Z

Table A19 Torsion angles for MOF-1131(Yb).

A	B	C	D	Angle/°	A	B	C	D	Angle/°
C1	C2	C3	C4	-180(3)	C50	C51	C52	C53	0.0
C1	C2	C3	N1A	-2(5)	C50	C51	C54	C55	-16(3)
C1	C2	C7	C6	180(3)	C50	C51	C54	C59	165(2)
C1	C2	C7	N1B	6(7)	C51	C52	C53	C48	0.0
C2	C1	O1	Yb1	179(3)	C51	C54	C55	C56	-179(3)
C2	C1	O2	Yb1	-179(3)	C51	C54	C59	C58	179(3)
C2	C3	C4	C5	0.0	C52	C51	C54	C55	160(3)
C3	C2	C7	C6	0.0	C52	C51	C54	C59	-20(3)
C3	C2	C7	N1B	-173(7)	C53	C48	C49	C50	0.0
C3	C4	C5	C6	0.0	C54	C51	C52	C53	-176(3)
C3	C4	C5	C13	179.9(11)	C54	C55	C56	C57	0.0
C4	C5	C6	C7	0.0	C54	C55	C56	N3A	-173(6)
C4	C5	C13	C8	138(3)	C55	C54	C59	C58	0.0
C4	C5	C13	C12	-42(3)	C55	C56	C57	C58	0.0
C5	C6	C7	C2	0.0	C55	C56	C57	C60	-180(3)
C5	C6	C7	N1B	174(6)	C56	C57	C58	C59	0.0
C6	C5	C13	C8	-42(3)	C56	C57	C58	N3B	179(7)
C6	C5	C13	C12	138(3)	C56	C57	C60	O7	176(2)
C7	C2	C3	C4	0.0	C56	C57	C60	O8	-10(4)
C7	C2	C3	N1A	178(5)	C57	C58	C59	C54	0.0
C8	C9	C10	C11	0.0	C57	C60	O7	Yb2 <sup>5</sup>	-175(2)
C8	C9	C10	C15	-180(3)	C57	C60	O8	Yb3 <sup>6</sup>	178(2)
C9	C8	C13	C5	-180.0(18)	C58	C57	C60	O7	-4(4)
C9	C8	C13	C12	0.0	C58	C57	C60	O8	170(2)
C9	C10	C11	C12	0.0	C59	C54	C55	C56	0.0
C9	C10	C15	C14	44(3)	C60	C57	C58	C59	180(3)
C9	C10	C15	C16	-135(3)	C60	C57	C58	N3B	-1(7)
C10	C11	C12	C13	0.0	C61	C62	C63	C64	179(5)
C10	C15	C16	C17	179(2)	C61	C62	C63	N7A	-5(7)
C11	C10	C15	C14	-136(3)	C61	C62	C67	C66	-179(5)
C11	C10	C15	C16	46(3)	C61	C62	C67	N7B	-7(9)
C11	C12	C13	C5	180.0(17)	C62	C61	O13	Yb3	154(4)

C11	C12	C13	C8	0.0	C62	C61	O14	Yb4	-164(4)
C13	C5	C6	C7	-179.9(11)	C62	C63	C64	C65	0.0
C13	C8	C9	C10	0.0	C63	C62	C67	C66	0.0
C14	C15	C16	C17	0.0	C63	C62	C67	N7B	172(9)
C15	C10	C11	C12	180(3)	C63	C64	C65	C66	0.0
C15	C14	C19	C18	0.0	C63	C64	C65	C68	178(3)
C15	C16	C17	C18	0.0	C64	C65	C66	C67	0.0
C15	C16	C17	N2	-175(3)	C64	C65	C68	C69	-38(3)
C16	C17	C18	C19	0.0	C64	C65	C68	C73	142(2)
C16	C17	C18	C20	177(3)	C65	C66	C67	C62	0.0
C17	C18	C19	C14	0.0	C65	C66	C67	N7B	-173(7)
C17	C18	C20	O3	171(2)	C65	C68	C69	C70	180(2)
C17	C18	C20	O4	-5(4)	C65	C68	C73	C72	-180(2)
C18	C20	O3	Yb2 <sup>1</sup>	-176(2)	C66	C65	C68	C69	140(3)
C18	C20	O4	Yb2 <sup>1</sup>	176(3)	C66	C65	C68	C73	-40(3)
C19	C14	C15	C10	-179(2)	C67	C62	C63	C64	0.0
C19	C14	C15	C16	0.0	C67	C62	C63	N7A	177(6)
C19	C18	C20	O3	-12(4)	C68	C65	C66	C67	-177(4)
C19	C18	C20	O4	171(3)	C68	C69	C70	C71	0.0
C20	C18	C19	C14	-177(3)	C69	C68	C73	C72	0.0
C21	C22	C23	C24	179(3)	C69	C70	C71	C72	0.0
C21	C22	C23	N5B	25(6)	C69	C70	C71	C74	177(2)
C21	C22	C27	C26	-178(3)	C70	C71	C72	C73	0.0
C21	C22	C27	N5A	1(6)	C70	C71	C74	C75	136(2)
C22	C21	O9	Yb2 <sup>2</sup>	176(2)	C70	C71	C74	C79	-36(3)
C22	C21	O10	Yb4 <sup>3</sup>	169(3)	C71	C72	C73	C68	0.0
C22	C23	C24	C25	0.0	C71	C74	C75	C76	-171(3)
C23	C22	C27	C26	0.0	C71	C74	C79	C78	172(3)
C23	C22	C27	N5A	179(6)	C72	C71	C74	C75	-47(2)
C23	C24	C25	C26	0.0	C72	C71	C74	C79	142(2)
C23	C24	C25	C28	177.2(15)	C73	C68	C69	C70	0.0
C24	C25	C26	C27	0.0	C74	C71	C72	C73	-178(2)
C24	C25	C28	C29	-7(3)	C74	C75	C76	C77	0.0
C24	C25	C28	C33	168(2)	C74	C75	C76	N6A	180(5)
C25	C26	C27	C22	0.0	C75	C74	C79	C78	0.0

C25	C26	C27	N5A	-179(5)	C75	C76	C77	C78	0.0
C25	C28	C29	C30	174(2)	C75	C76	C77	C80	-174(3)
C25	C28	C33	C32	-174.5(19)	C76	C77	C78	C79	0.0
C26	C25	C28	C29	170(2)	C76	C77	C78	N6B	-162(4)
C26	C25	C28	C33	-15(3)	C76	C77	C80	O15	-7(4)
C27	C22	C23	C24	0.0	C76	C77	C80	O16	173(2)
C27	C22	C23	N5B	-153(6)	C77	C78	C79	C74	0.0
C28	C25	C26	C27	-177.2(15)	C77	C80	O15	Yb1 <sup>7</sup>	-177.5(19)
C28	C29	C30	C31	0.0	C77	C80	O16	Yb2	179.6(17)
C29	C28	C33	C32	0.0	C78	C77	C80	O15	179(2)
C29	C30	C31	C32	0.0	C78	C77	C80	O16	-1(4)
C29	C30	C31	C34	179.7(7)	C79	C74	C75	C76	0.0
C30	C31	C32	C33	0.0	C80	C77	C78	C79	174(3)
C30	C31	C34	C35	8(3)	C80	C77	C78	N6B	12(4)
C30	C31	C34	C39	-173(2)	O1	C1	C2	C3	-175(3)
C31	C32	C33	C28	0.0	O1	C1	C2	C7	5(5)
C31	C34	C35	C36	178.6(9)	O1	C1	O2	Yb1	3(4)
C31	C34	C39	C38	-178.6(9)	O2	C1	C2	C3	7(5)
C32	C31	C34	C35	-172(2)	O2	C1	C2	C7	-173(3)
C32	C31	C34	C39	6(3)	O2	C1	O1	Yb1	-3(4)
C33	C28	C29	C30	0.0	O3	C20	O4	Yb2 <sup>1</sup>	0(4)
C34	C31	C32	C33	-179.7(7)	O4	C20	O3	Yb2 <sup>1</sup>	0(4)
C34	C35	C36	C37	0.0	O5	C41	C42	C43	2(7)
C34	C35	C36	N8	-179(5)	O5	C41	C42	C47	-176(4)
C35	C34	C39	C38	0.0	O5	C41	O6	Yb4 <sup>3</sup>	26(9)
C35	C36	C37	C38	0.0	O6	C41	C42	C43	-172(4)
C35	C36	C37	C40	-172(3)	O6	C41	C42	C47	10(7)
C36	C37	C38	C39	0.0	O6	C41	O5	Yb1	4(8)
C36	C37	C40	O11	-171(3)	O7	C60	O8	Yb3 <sup>6</sup>	-9(5)
C36	C37	C40	O12	-8(6)	O8	C60	O7	Yb2 <sup>5</sup>	12(5)
C37	C38	C39	C34	0.0	O9	C21	C22	C23	178(3)
C37	C40	O11	Yb3	-166(2)	O9	C21	C22	C27	-3(5)
C37	C40	O12	Yb1 <sup>4</sup>	-174(2)	O9	C21	O10	Yb4 <sup>3</sup>	-3(8)
C38	C37	C40	O11	16(6)	O10	C21	C22	C23	5(5)
C38	C37	C40	O12	179(3)	O10	C21	C22	C27	-177(3)

C39	C34	C35	C36	0.0	O10	C21	O9	Yb2 <sup>2</sup>	-11(7)
C40	C37	C38	C39	173(3)	O11	C40	O12	Yb1 <sup>4</sup>	-12(7)
C41	C42	C43	C44	-178(5)	O12	C40	O11	Yb3	31(7)
C41	C42	C43	N4A	-2(7)	O13	C61	C62	C63	-8(8)
C41	C42	C47	C46	178(5)	O13	C61	C62	C67	171(4)
C41	C42	C47	N4B	-7(9)	O13	C61	O14	Yb4	15(10)
C42	C41	O5	Yb1	-170(3)	O14	C61	C62	C63	171(4)
C42	C41	O6	Yb4 <sup>3</sup>	-161(3)	O14	C61	C62	C67	-10(8)
C42	C43	C44	C45	0.0	O14	C61	O13	Yb3	-25(9)
C43	C42	C47	C46	0.0	O15	C80	O16	Yb2	0(5)
C43	C42	C47	N4B	175(9)	O16	C80	O15	Yb1 <sup>7</sup>	2(5)
C43	C44	C45	C46	0.0	Yb3	O22S	C100	N9S	150(10)
C43	C44	C45	C48	-178(3)	N1A	C3	C4	C5	-178(5)
C44	C45	C46	C47	0.0	N2	C17	C18	C19	175(3)
C44	C45	C48	C49	31(3)	N2	C17	C18	C20	-8(4)
C44	C45	C48	C53	-150(3)	N3A	C56	C57	C58	173(6)
C45	C46	C47	C42	0.0	N3A	C56	C57	C60	-7(6)
C45	C46	C47	N4B	-176(8)	N3B	C58	C59	C54	-179(7)
C45	C48	C49	C50	179.3(8)	N4A	C43	C44	C45	-175(7)
C45	C48	C53	C52	-179.2(8)	N5B	C23	C24	C25	155(6)
C46	C45	C48	C49	-147(3)	N6A	C76	C77	C78	-180(5)
C46	C45	C48	C53	32(3)	N6A	C76	C77	C80	6(5)
C47	C42	C43	C44	0.0	N6B	C78	C79	C74	165(3)
C47	C42	C43	N4A	175(7)	N7A	C63	C64	C65	-177(6)
C48	C45	C46	C47	178(3)	N8	C36	C37	C38	179(5)
C48	C49	C50	C51	0.0	N8	C36	C37	C40	6(5)
C49	C48	C53	C52	0.0	C101	N9S	C100	O22S	-33(18)
C49	C50	C51	C52	0.0	C102	N9S	C100	O22S	-177(10)
C49	C50	C51	C54	176(3)					

<sup>1</sup>3/2+X,3/2-Y,1/2+Z; <sup>2</sup>1/2+X,3/2-Y,1/2+Z; <sup>3</sup>1/2+X,1/2-Y,1/2+Z; <sup>4</sup>-1/2+X,1/2-Y,-1/2+Z; <sup>5</sup>1+X,-1+Y,+Z; <sup>6</sup>1+X,+Y,+Z; <sup>7</sup>-1/2+X,3/2-Y,-1/2+Z

**Table A20** Hydrogen atom coordinates ( $\text{\AA}\times 10^4$ ) and isotropic displacement parameters ( $\text{\AA}^2\times 10^3$ ) for MOF-1131(Yb).

Atom	<i>x</i>	<i>y</i>	<i>z</i>	U(eq)
H4	5518	3189	9432	181
H6	5539	1403	9252	181
H8	6393	1547	9637	295
H9	7380	1564	9636	296
H11	7351	3085	9046	302
H12	6364	3068	9047	303
H14	8173	1443	9229	136
H16	8191	3216	9452	125
H19	9160	1430	9238	134
H24	418	1643	7317	186
H26	-326	3063	7797	181
H29	165	1967	6832	254
H30	-317	2161	6296	264
H32	-1308	3358	6812	244
H33	-826	3164	7348	257
H35	-786	2239	5870	200
H38	-2126	3771	5802	165
H39	-1639	3599	6339	198
H44	4074	2965	7781	226
H46	3286	1559	7311	227
H49	4723	2693	7388	269
H50	5243	2849	6864	256
H52	3930	2236	6269	247
H53	3410	2080	6793	258
H55	5534	3271	6408	153
H59	4500	2179	5839	149
H64	-3075	6994	4866	169
H66	-2935	6946	3783	178
H69	-3637	7811	4731	151
H70	-3685	8855	4746	157
H72	-2512	8945	3959	176

H73	-2464	7900	3945	169
H75	-2258	9781	4281	134
H79	-3960	9746	4375	120
H1AA	4548	3739	9464	196
H1AB	4012	3375	9437	196
H1BA	4662	842	9134	213
H1BB	4090	1130	9183	213
H2A	9608	3404	9538	188
H2B	9040	3711	9550	188
H3AA	6449	3662	5754	194
H3AB	6292	3738	6145	194
H3BA	4659	2106	5228	188
H3BB	5131	2432	5039	188
H4AA	3419	2841	8611	241
H4AB	3844	3205	8402	241
H4BA	2723	936	7633	235
H4BB	2556	1040	8020	235
H5AA	-161	3292	8413	205
H5AB	231	2926	8648	205
H5BA	842	931	8090	193
H5BB	850	875	7685	193
H6AA	-1761	10738	4286	124
H6AB	-2075	11323	4322	124
H6BA	-4479	10582	4286	129
H6BB	-4255	11210	4334	129
H7AA	-3106	5475	4996	184
H7AB	-3124	6074	5184	184
H7BA	-2780	6136	3499	214
H7BB	-2814	5508	3648	214
H8A	-1428	2355	5054	221
H8B	-993	2016	5271	221
H100	-3931	5329	5107	154
H10A	-4311	5454	4304	232
H10B	-4792	5934	4379	232
H10C	-4931	5239	4403	232

H10D	-4362	6145	5195	204
H10E	-4924	6268	4973	204
H10F	-4327	6421	4803	204

**Table A21** Atomic occupancy for MOF-1131(Yb).

<b>Atom</b>	<b>Occupancy</b>	<b>Atom</b>	<b>Occupancy</b>	<b>Atom</b>	<b>Occupancy</b>
N1A	0.56(5)	H1AA	0.56(5)	H1AB	0.56(5)
N1B	0.44(5)	H1BA	0.44(5)	H1BB	0.44(5)
N3A	0.52(5)	H3AA	0.52(5)	H3AB	0.52(5)
N3B	0.48(5)	H3BA	0.48(5)	H3BB	0.48(5)
N4A	0.58(5)	H4AA	0.58(5)	H4AB	0.58(5)
N4B	0.42(5)	H4BA	0.42(5)	H4BB	0.42(5)
N5A	0.56(5)	H5AA	0.56(5)	H5AB	0.56(5)
N5B	0.44(5)	H5BA	0.44(5)	H5BB	0.44(5)
N6A	0.39(4)	H6AA	0.39(4)	H6AB	0.39(4)
N6B	0.61(4)	H6BA	0.61(4)	H6BB	0.61(4)
N7A	0.57(5)	H7AA	0.57(5)	H7AB	0.57(5)
N7B	0.43(5)	H7BA	0.43(5)	H7BB	0.43(5)
N9S	0.56(4)	C100	0.56(4)	H100	0.56(4)
C101	0.56(4)	H10A	0.56(4)	H10B	0.56(4)
H10C	0.56(4)	C102	0.56(4)	H10D	0.56(4)
H10E	0.56(4)	H10F	0.56(4)		

**Table A22** Fractional atomic coordinates ( $\times 10^4$ ) and equivalent isotropic displacement parameters ( $\text{\AA}^2 \times 10^3$ ) for MOF-1115(Tb). Ueq is defined as 1/3 of the trace of the orthogonalised UIJ tensor.

Atom	x	y	z	U(eq)
Tb1	6547.9(4)	6547.9(4)	1547.9(4)	74(2)
Tb2	6548.9(4)	6548.9(4)	5951.1(4)	73(2)
O1	6427(4)	6427(4)	5477(4)	310(20)
O3	6466(4)	6034(4)	6034(4)	51(8)
O5S	6865(4)	6865(4)	5635(4)	137(14)
O4	6473(6)	6027(6)	1473(6)	102(11)
O2	6426(3)	6426(3)	2027(3)	245(16)
O7S	6878(4)	6878(4)	1878(4)	114(11)
O6S	6170(11)	6920(13)	5580(13)	150(30)
O8S	6909(15)	6251(13)	1909(15)	190(40)
C1	6250	6250	5339(9)	320(30)
C2	6250	6250	5014(8)	320(20)
C3	6439(4)	6439(4)	4854(6)	320(20)
C4	6434(4)	6434(4)	4543(6)	330(20)
C5	6250	6250	4374(8)	330(30)
C11	6250	6250	2182(9)	290(18)
C12	6250	6250	2486(10)	313(19)
C13	6068(4)	6068(4)	2646(7)	330(18)
C14	6060(4)	6060(4)	2961(7)	340(20)
C15	6250	6250	3103(9)	340(30)
C21	6250	6250	4046(8)	180(30)
C22	6057(4)	6443(4)	3892(7)	300(40)
C23	6066(4)	6434(4)	3578(7)	270(40)
C24	6250	6250	3426(9)	240(40)
C25	5883(7)	6617(7)	3407(6)	340(40)
C26	5684(6)	6816(6)	3546(8)	370(40)
C27	5674(6)	6826(6)	3860(8)	630(80)
C28	5859(7)	6641(7)	4032(6)	350(40)
N1	5868(6)	5868(6)	2527(12)	340(30)
N2	6638(6)	6638(6)	4983(12)	310(30)

**Table A23** Anisotropic displacement parameters ( $\text{\AA}^2 \times 10^3$ ) for MOF-1115(Tb). The anisotropic displacement factor exponent takes the form:  $-2\pi^2[h2a^2U_{11}+2hka*b*U_{12}+\dots]$ .

Atom	U <sub>11</sub>	U <sub>22</sub>	U <sub>33</sub>	U <sub>23</sub>	U <sub>13</sub>	U <sub>12</sub>
Tb1	74(2)	74(2)	74(2)	-6.3(9)	-6.3(9)	-6.3(9)
Tb2	73(2)	73(2)	73(2)	8.6(9)	8.6(9)	-8.6(9)
O1	440(40)	440(40)	49(18)	41(14)	41(14)	-250(50)
O3	51(8)	51(8)	51(8)	6(10)	-6(10)	-6(10)
O5S	137(14)	137(14)	137(14)	36(13)	36(13)	-36(13)
O4	102(11)	102(11)	102(11)	-35(17)	35(17)	-35(17)
O2	340(30)	340(30)	54(14)	-20(7)	-20(7)	-280(30)
O7S	114(11)	114(11)	114(11)	3(13)	3(13)	3(13)
O6S	80(50)	190(50)	190(50)	-160(60)	70(40)	-70(40)
O8S	230(60)	120(60)	230(60)	90(40)	30(70)	90(40)
C1	440(40)	440(40)	60(20)	0	0	-360(50)
C2	450(30)	450(30)	70(20)	0	0	-330(40)
C3	450(30)	450(30)	69(19)	7(8)	7(8)	-320(30)
C4	460(30)	460(30)	72(19)	3(8)	3(8)	-310(40)
C5	460(40)	460(40)	70(30)	0	0	-310(40)
C11	390(30)	390(30)	84(19)	0	0	-310(30)
C12	430(30)	430(30)	81(18)	0	0	-310(30)
C13	450(30)	450(30)	92(18)	5(7)	5(7)	-330(30)
C14	460(30)	460(30)	88(18)	3(8)	3(8)	-330(30)
C15	460(40)	460(40)	90(30)	0	0	-320(40)
C21	220(40)	220(40)	90(40)	0	0	-80(50)
C22	330(50)	330(50)	230(60)	-10(50)	10(50)	-60(60)
C23	340(50)	340(50)	130(50)	-20(40)	20(40)	-150(60)
C24	300(60)	300(60)	120(60)	0	0	-100(70)
C25	430(60)	430(60)	170(50)	40(50)	-40(50)	-150(70)
C26	410(50)	410(50)	290(70)	-30(40)	30(40)	70(70)
C27	610(80)	610(80)	680(120)	-60(60)	60(60)	20(90)
C28	480(60)	480(60)	100(40)	-90(40)	90(40)	-190(70)
N1	480(50)	480(50)	80(30)	8(10)	8(10)	-370(50)
N2	430(50)	430(50)	70(30)	7(10)	7(10)	-310(50)

Table A24 Bond lengths for MOF-1115(Tb).

Atom	Atom	Length/Å	Atom	Atom	Length/Å
Tb1	Tb1 <sup>1</sup>	3.780(5)	O2	C11	1.317(14)
Tb1	Tb1 <sup>2</sup>	3.780(5)	C1	O1 <sup>3</sup>	1.281(17)
Tb1	O4	2.384(18)	C1	C2	1.46(2)
Tb1	O4 <sup>3</sup>	2.384(18)	C2	C3 <sup>3</sup>	1.396(18)
Tb1	O4 <sup>1</sup>	2.384(18)	C2	C3	1.396(19)
Tb1	O2 <sup>4</sup>	2.282(15)	C3	C4	1.394(18)
Tb1	O2 <sup>5</sup>	2.282(15)	C3	N2	1.39(2)
Tb1	O2	2.282(15)	C4	C5	1.391(19)
Tb1	O7S	2.57(3)	C5	C4 <sup>3</sup>	1.391(19)
Tb1	O8S <sup>5</sup>	2.65(7)	C5	C21	1.47(2)
Tb1	O8S <sup>4</sup>	2.65(7)	C11	O2 <sup>3</sup>	1.317(14)
Tb1	O8S	2.65(7)	C11	C12	1.36(5)
Tb2	Tb2 <sup>3</sup>	3.793(5)	C12	C13 <sup>3</sup>	1.361(14)
Tb2	Tb2 <sup>6</sup>	3.793(5)	C12	C13	1.361(14)
Tb2	O1 <sup>7</sup>	2.265(15)	C13	C14	1.415(18)
Tb2	O1 <sup>8</sup>	2.265(15)	C13	N1	1.38(2)
Tb2	O1	2.265(15)	C14	C15	1.362(14)
Tb2	O3	2.370(12)	C15	C14 <sup>3</sup>	1.362(14)
Tb2	O3 <sup>6</sup>	2.370(12)	C15	C24	1.45(2)
Tb2	O3 <sup>3</sup>	2.370(12)	C21	C22 <sup>3</sup>	1.403(14)
Tb2	O5S	2.46(3)	C21	C22	1.403(14)
Tb2	O6S <sup>8</sup>	2.90(8)	C22	C23	1.412(17)
Tb2	O6S	2.90(8)	C22	C28	1.41(2)
Tb2	O6S <sup>7</sup>	2.90(8)	C23	C24	1.351(17)
O1	C1	1.281(17)	C23	C25	1.39(2)
O3	Tb2 <sup>3</sup>	2.371(12)	C24	C23 <sup>3</sup>	1.351(17)
O3	Tb2 <sup>6</sup>	2.371(12)	C25	C26	1.407(19)
O4	Tb1 <sup>1</sup>	2.384(18)	C26	C27	1.409(18)
O4	Tb1 <sup>3</sup>	2.384(18)	C27	C28	1.40(2)

<sup>1</sup>+X,5/4-Y,1/4-Z; <sup>2</sup>5/4-X,+Y,1/4-Z; <sup>3</sup>5/4-X,5/4-Y,+Z; <sup>4</sup>1/2+Z,+X,-1/2+Y; <sup>5</sup>+Y,1/2+Z,-1/2+X; <sup>6</sup>+X,5/4-Y,5/4-Z; <sup>7</sup>+Y,5/4-Z,5/4-X; <sup>8</sup>5/4-Z,+X,5/4-Y

**Table A25** Bond angles for MOF-1115(Tb).

Atom	Atom	Atom	Angle/°	Atom	Atom	Atom	Angle/°
Tb1 <sup>1</sup>	Tb1	Tb1 <sup>2</sup>	60.0	O1	Tb2	O6S <sup>8</sup>	145.8(12)
O4 <sup>2</sup>	Tb1	Tb1 <sup>1</sup>	37.6(6)	O1 <sup>7</sup>	Tb2	O6S <sup>7</sup>	57.20(18)
O4 <sup>3</sup>	Tb1	Tb1 <sup>2</sup>	78.5(10)	O1 <sup>7</sup>	Tb2	O6S <sup>8</sup>	57.20(18)
O4	Tb1	Tb1 <sup>1</sup>	78.5(10)	O1 <sup>8</sup>	Tb2	O6S	57.20(18)
O4	Tb1	Tb1 <sup>2</sup>	37.6(6)	O1	Tb2	O6S	57.20(18)
O4 <sup>2</sup>	Tb1	Tb1 <sup>2</sup>	37.6(6)	O1 <sup>8</sup>	Tb2	O6S <sup>8</sup>	57.20(18)
O4 <sup>3</sup>	Tb1	Tb1 <sup>1</sup>	37.6(6)	O3 <sup>3</sup>	Tb2	Tb2 <sup>6</sup>	77.2(7)
O4	Tb1	O4 <sup>2</sup>	72.7(15)	O3 <sup>6</sup>	Tb2	Tb2 <sup>6</sup>	36.9(4)
O4	Tb1	O4 <sup>3</sup>	72.7(16)	O3 <sup>3</sup>	Tb2	Tb2 <sup>3</sup>	36.9(4)
O4 <sup>2</sup>	Tb1	O4 <sup>3</sup>	72.7(16)	O3	Tb2	Tb2 <sup>3</sup>	36.9(4)
O4 <sup>3</sup>	Tb1	O7S	136.8(10)	O3	Tb2	Tb2 <sup>6</sup>	36.9(4)
O4	Tb1	O7S	136.8(10)	O3 <sup>6</sup>	Tb2	Tb2 <sup>3</sup>	77.2(7)
O4 <sup>2</sup>	Tb1	O7S	136.8(10)	O3 <sup>3</sup>	Tb2	O3 <sup>6</sup>	70.8(11)
O4 <sup>3</sup>	Tb1	O8S <sup>4</sup>	127.9(12)	O3 <sup>3</sup>	Tb2	O3	70.8(11)
O4 <sup>3</sup>	Tb1	O8S <sup>5</sup>	71(2)	O3 <sup>6</sup>	Tb2	O3	70.8(11)
O4	Tb1	O8S <sup>4</sup>	127.9(12)	O3 <sup>3</sup>	Tb2	O5S	138.0(7)
O4 <sup>2</sup>	Tb1	O8S	127.9(12)	O3	Tb2	O5S	138.0(7)
O4 <sup>3</sup>	Tb1	O8S	127.9(12)	O3 <sup>6</sup>	Tb2	O5S	138.0(7)
O4 <sup>2</sup>	Tb1	O8S <sup>5</sup>	127.9(12)	O3	Tb2	O6S	123.9(7)
O4 <sup>2</sup>	Tb1	O8S <sup>4</sup>	71(2)	O3 <sup>3</sup>	Tb2	O6S <sup>7</sup>	123.9(7)
O4	Tb1	O8S	71(2)	O3 <sup>6</sup>	Tb2	O6S <sup>8</sup>	66.9(12)
O4	Tb1	O8S <sup>5</sup>	127.9(12)	O3	Tb2	O6S <sup>7</sup>	66.9(12)
O2	Tb1	Tb1 <sup>2</sup>	119.8(4)	O3 <sup>6</sup>	Tb2	O6S	123.9(7)
O2 <sup>5</sup>	Tb1	Tb1 <sup>2</sup>	119.8(4)	O3 <sup>6</sup>	Tb2	O6S <sup>7</sup>	123.9(7)
O2	Tb1	Tb1 <sup>1</sup>	119.8(4)	O3	Tb2	O6S <sup>8</sup>	123.9(7)
O2 <sup>4</sup>	Tb1	Tb1 <sup>1</sup>	119.8(4)	O3 <sup>3</sup>	Tb2	O6S	66.9(12)
O2 <sup>5</sup>	Tb1	Tb1 <sup>1</sup>	70.2(5)	O3 <sup>3</sup>	Tb2	O6S <sup>8</sup>	123.9(7)
O2 <sup>4</sup>	Tb1	Tb1 <sup>2</sup>	70.2(5)	O5S	Tb2	Tb2 <sup>6</sup>	144.734(4)
O2	Tb1	O4 <sup>3</sup>	82.2(7)	O5S	Tb2	Tb2 <sup>3</sup>	144.734(2)
O2 <sup>5</sup>	Tb1	O4 <sup>3</sup>	82.2(7)	O5S	Tb2	O6S <sup>8</sup>	71.1(10)
O2 <sup>5</sup>	Tb1	O4 <sup>2</sup>	82.2(7)	O5S	Tb2	O6S <sup>7</sup>	71.1(10)
O2	Tb1	O4 <sup>2</sup>	148.7(11)	O5S	Tb2	O6S	71.1(10)

O2 <sup>4</sup>	Tb1	O4	82.2(7)	O6S <sup>8</sup>	Tb2	Tb2 <sup>3</sup>	144.2(10)
O2 <sup>5</sup>	Tb1	O4	148.7(11)	O6S <sup>8</sup>	Tb2	Tb2 <sup>6</sup>	89.5(9)
O2 <sup>4</sup>	Tb1	O4 <sup>3</sup>	148.7(11)	O6S	Tb2	Tb2 <sup>6</sup>	144.2(10)
O2	Tb1	O4	82.2(7)	O6S <sup>7</sup>	Tb2	Tb2 <sup>6</sup>	89.5(9)
O2 <sup>4</sup>	Tb1	O4 <sup>2</sup>	82.2(7)	O6S	Tb2	Tb2 <sup>3</sup>	89.5(9)
O2	Tb1	O2 <sup>5</sup>	113.1(4)	O6S <sup>7</sup>	Tb2	Tb2 <sup>3</sup>	89.5(9)
O2 <sup>5</sup>	Tb1	O2 <sup>4</sup>	113.1(4)	O6S	Tb2	O6S <sup>8</sup>	110.0(10)
O2	Tb1	O2 <sup>4</sup>	113.1(4)	O6S <sup>8</sup>	Tb2	O6S <sup>7</sup>	110.0(10)
O2 <sup>5</sup>	Tb1	O7S	74.5(5)	O6S	Tb2	O6S <sup>7</sup>	110.0(10)
O2	Tb1	O7S	74.5(5)	C1	O1	Tb2	139(3)
O2 <sup>4</sup>	Tb1	O7S	74.5(5)	Tb2	O3	Tb2 <sup>6</sup>	106.3(8)
O2 <sup>5</sup>	Tb1	O8S	139.9(19)	Tb2	O3	Tb2 <sup>3</sup>	106.3(8)
O2 <sup>4</sup>	Tb1	O8S <sup>4</sup>	56.68(19)	Tb2 <sup>3</sup>	O3	Tb2 <sup>6</sup>	106.3(8)
O2	Tb1	O8S <sup>4</sup>	139.9(19)	Tb1	O4	Tb1 <sup>3</sup>	104.9(11)
O2	Tb1	O8S <sup>5</sup>	56.7(2)	Tb1 <sup>2</sup>	O4	Tb1 <sup>3</sup>	104.9(11)
O2	Tb1	O8S	56.7(2)	Tb1	O4	Tb1 <sup>2</sup>	104.9(11)
O2 <sup>5</sup>	Tb1	O8S <sup>4</sup>	56.68(19)	C11	O2	Tb1	142(2)
O2 <sup>4</sup>	Tb1	O8S <sup>5</sup>	139.9(19)	O1	C1	O1 <sup>3</sup>	122(4)
O2 <sup>4</sup>	Tb1	O8S	56.68(19)	O1	C1	C2	119(2)
O2 <sup>5</sup>	Tb1	O8S <sup>5</sup>	56.7(2)	O1 <sup>3</sup>	C1	C2	119(2)
O7S	Tb1	Tb1 <sup>2</sup>	144.734(4)	C3	C2	C1	120.9(17)
O7S	Tb1	Tb1 <sup>1</sup>	144.734(1)	C3 <sup>3</sup>	C2	C1	120.9(17)
O7S	Tb1	O8S <sup>5</sup>	65.4(18)	C3 <sup>3</sup>	C2	C3	118(3)
O7S	Tb1	O8S <sup>4</sup>	65.4(18)	C4	C3	C2	120(3)
O7S	Tb1	O8S	65.4(18)	N2	C3	C2	125(3)
O8S <sup>5</sup>	Tb1	Tb1 <sup>1</sup>	94.4(16)	N2	C3	C4	116(3)
O8S	Tb1	Tb1 <sup>2</sup>	94.4(16)	C5	C4	C3	124(3)
O8S <sup>5</sup>	Tb1	Tb1 <sup>2</sup>	149.9(18)	C4 <sup>3</sup>	C5	C4	114(3)
O8S	Tb1	Tb1 <sup>1</sup>	149.9(18)	C4 <sup>3</sup>	C5	C21	123.0(17)
O8S <sup>4</sup>	Tb1	Tb1 <sup>1</sup>	94.4(16)	C4	C5	C21	123.0(17)
O8S <sup>4</sup>	Tb1	Tb1 <sup>2</sup>	94.4(16)	O2 <sup>3</sup>	C11	O2	116(4)
O8S <sup>5</sup>	Tb1	O8S <sup>4</sup>	104(2)	O2	C11	C12	121.9(19)
O8S <sup>5</sup>	Tb1	O8S	104(2)	O2 <sup>3</sup>	C11	C12	121.9(19)
O8S <sup>4</sup>	Tb1	O8S	104(2)	C11	C12	C13	122(2)
Tb2 <sup>3</sup>	Tb2	Tb2 <sup>6</sup>	60.002(1)	C11	C12	C13 <sup>3</sup>	122(2)

O1 <sup>7</sup>	Tb2	Tb2 <sup>6</sup>	70.0(6)	C13 <sup>3</sup>	C12	C13	116(4)
O1	Tb2	Tb2 <sup>6</sup>	119.6(5)	C12	C13	C14	124(3)
O1 <sup>8</sup>	Tb2	Tb2 <sup>6</sup>	119.6(5)	C12	C13	N1	125(3)
O1	Tb2	Tb2 <sup>3</sup>	70.0(6)	N1	C13	C14	111(3)
O1 <sup>8</sup>	Tb2	Tb2 <sup>3</sup>	119.6(5)	C15	C14	C13	116(3)
O1 <sup>7</sup>	Tb2	Tb2 <sup>3</sup>	119.6(5)	C14 <sup>3</sup>	C15	C14	124(4)
O1 <sup>8</sup>	Tb2	O1	113.3(5)	C14 <sup>3</sup>	C15	C24	118.0(19)
O1 <sup>8</sup>	Tb2	O1 <sup>7</sup>	113.3(5)	C14	C15	C24	118.0(19)
O1 <sup>7</sup>	Tb2	O1	113.3(5)	C22 <sup>3</sup>	C21	C5	119.5(18)
O1 <sup>7</sup>	Tb2	O3 <sup>6</sup>	82.7(6)	C22	C21	C5	119.5(18)
O1	Tb2	O3 <sup>6</sup>	147.3(10)	C22 <sup>3</sup>	C21	C22	121(4)
O1 <sup>8</sup>	Tb2	O3	147.3(9)	C21	C22	C23	117(3)
O1 <sup>7</sup>	Tb2	O3 <sup>3</sup>	147.3(9)	C21	C22	C28	124(3)
O1 <sup>8</sup>	Tb2	O3 <sup>6</sup>	82.7(6)	C28	C22	C23	118.7(11)
O1	Tb2	O3 <sup>3</sup>	82.7(6)	C24	C23	C22	123(3)
O1 <sup>8</sup>	Tb2	O3 <sup>3</sup>	82.7(6)	C24	C23	C25	116(3)
O1	Tb2	O3	82.7(6)	C25	C23	C22	121.1(11)
O1 <sup>7</sup>	Tb2	O3	82.7(6)	C23 <sup>3</sup>	C24	C15	120.4(19)
O1	Tb2	O5S	74.7(6)	C23	C24	C15	120.4(19)
O1 <sup>8</sup>	Tb2	O5S	74.7(6)	C23	C24	C23 <sup>3</sup>	119(4)
O1 <sup>7</sup>	Tb2	O5S	74.7(6)	C23	C25	C26	120.2(12)
O1	Tb2	O6S <sup>7</sup>	57.20(18)	C25	C26	C27	119.0(11)
O1 <sup>7</sup>	Tb2	O6S	145.8(12)	C28	C27	C26	120.7(11)
O1 <sup>8</sup>	Tb2	O6S <sup>7</sup>	145.8(12)	C27	C28	C22	120.2(12)

<sup>1</sup>5/4-X,+Y,1/4-Z; <sup>2</sup>+X,5/4-Y,1/4-Z; <sup>3</sup>5/4-X,5/4-Y,+Z; <sup>4</sup>1/2+Z,+X,-1/2+Y; <sup>5</sup>+Y,1/2+Z,-1/2+X; <sup>6</sup>+X,5/4-Y,5/4-Z; <sup>7</sup>5/4-Z,+X,5/4-Y; <sup>8</sup>+Y,5/4-Z,5/4-X

**Table A26** Torsion angles for MOF-1115(Tb).

<b>A</b>	<b>B</b>	<b>C</b>	<b>D</b>	<b>Angle/°</b>	<b>A</b>	<b>B</b>	<b>C</b>	<b>D</b>	<b>Angle/°</b>
Tb1	O2	C11	O2 <sup>1</sup>	0.000(8)	C13 <sup>1</sup>	C12	C13	C14	0.000(8)
Tb1	O2	C11	C12	180.000(4)	C13 <sup>1</sup>	C12	C13	N1	180.000(7)
Tb2	O1	C1	O1 <sup>1</sup>	0.001(10)	C13	C14	C15	C14 <sup>1</sup>	0.000(4)
Tb2	O1	C1	C2	180.000(6)	C13	C14	C15	C24	180.000(2)
O1	C1	C2	C3 <sup>1</sup>	180.000(3)	C14	C15	C24	C23	-90.000(10)
O1 <sup>1</sup>	C1	C2	C3	180.000(3)	C14 <sup>1</sup>	C15	C24	C23	90.000(12)
O1	C1	C2	C3	0.000(3)	C14	C15	C24	C23 <sup>1</sup>	90.000(12)
O1 <sup>1</sup>	C1	C2	C3 <sup>1</sup>	0.000(3)	C14 <sup>1</sup>	C15	C24	C23 <sup>1</sup>	-90.000(10)
O2	C11	C12	C13 <sup>1</sup>	0.000(6)	C21	C22	C23	C24	0.001(11)
O2 <sup>1</sup>	C11	C12	C13 <sup>1</sup>	180.000(5)	C21	C22	C23	C25	180.001(9)
O2	C11	C12	C13	180.000(5)	C21	C22	C28	C27	179.999(11)
O2 <sup>1</sup>	C11	C12	C13	0.000(6)	C22 <sup>1</sup>	C21	C22	C23	-0.001(12)
C1	C2	C3	C4	180.000(4)	C22 <sup>1</sup>	C21	C22	C28	180.000(11)
C1	C2	C3	N2	0.000(8)	C22	C23	C24	C15	179.999(12)
C2	C3	C4	C5	0.000(6)	C22	C23	C24	C23 <sup>1</sup>	0.00(2)
C3 <sup>1</sup>	C2	C3	C4	0.000(6)	C22	C23	C25	C26	0.000(9)
C3 <sup>1</sup>	C2	C3	N2	180.000(5)	C23	C22	C28	C27	0.000(14)
C3	C4	C5	C4 <sup>1</sup>	0.000(8)	C23	C25	C26	C27	0.00(2)
C3	C4	C5	C21	180.000(5)	C24	C23	C25	C26	179.999(8)
C4 <sup>1</sup>	C5	C21	C22 <sup>1</sup>	-90.001(5)	C25	C23	C24	C15	0.000(8)
C4	C5	C21	C22 <sup>1</sup>	89.999(4)	C25	C23	C24	C23 <sup>1</sup>	180.000(14)
C4 <sup>1</sup>	C5	C21	C22	89.999(4)	C25	C26	C27	C28	0.000(17)
C4	C5	C21	C22	-90.001(5)	C26	C27	C28	C22	0.000(10)
C5	C21	C22	C23	179.999(8)	C28	C22	C23	C24	180.001(9)
C5	C21	C22	C28	0.000(10)	C28	C22	C23	C25	0.000(16)
C11	C12	C13	C14	180.000(3)	N1	C13	C14	C15	180.000(4)
C11	C12	C13	N1	0.000(4)	N2	C3	C4	C5	180.000(4)
C12	C13	C14	C15	0.000(7)					

<sup>1</sup>5/4-X,5/4-Y,+Z

**Table A27** Hydrogen atom coordinates ( $\text{\AA}\times 10^4$ ) and isotropic displacement parameters ( $\text{\AA}^2\times 10^3$ ) for MOF-1115(Tb).

<b>Atom</b>	<b><i>x</i></b>	<b><i>y</i></b>	<b><i>z</i></b>	<b>U(eq)</b>
H4	6563	6563	4441	401
H14	5932	5932	3066	406
H25	5892	6608	3198	412
H26	5560	6940	3431	441
H27	5542	6958	3955	756
H28	5850	6650	4241	420
H1A	5851	5851	2334	414
H1B	5759	5759	2644	414
H2A	6750	6750	4870	375
H2B	6651	6651	5176	375

**Table A28** Atomic occupancy for MOF-1115(Tb).

<b>Atom</b>	<b><i>Occupancy</i></b>	<b>Atom</b>	<b><i>Occupancy</i></b>	<b>Atom</b>	<b><i>Occupancy</i></b>
O6S	0.3333	O8S	0.3333	N1	0.5
H1A	0.5	H1B	0.5	N2	0.5
H2A	0.5	H2B	0.5		

## APPENDIX B CRYSTALLOGRAPHIC TABLES FOR CHAPTER 3

**Table B1** Fractional atomic coordinates ( $\times 10^4$ ) and equivalent isotropic displacement parameters ( $\text{\AA}^2 \times 10^3$ ) for Yb-NH<sub>2</sub>-TPDC. U<sub>eq</sub> is defined as 1/3 of the trace of the orthogonalised UIJ tensor.

Atom	x	y	z	U(eq)
Yb1	5000	5000	4193.3(4)	44.8(9)
O1	4387(4)	5000	3891(4)	82(4)
O2	5375(2)	5375(2)	4625(2)	25(3)
N1	4200(15)	5000	3148(14)	280(60)
C1	4014(6)	5000	4014(6)	101(8)
C2	3712(6)	5000	3712(6)	128(9)
C3	3803(8)	5000	3308(6)	165(10)
C4	3505(8)	5000	3023(9)	199(12)
C5	3108(10)	5000	3108(10)	228(15)
C6	2788(11)	5000	2788(11)	266(18)
C7	2924(12)	5000	2398(8)	300(20)
O1S	5000	5000	3420(40)	140(60)

**Table B2** Anisotropic displacement parameters ( $\text{\AA}^2 \times 10^3$ ) for Yb-NH<sub>2</sub>-TPDC. The anisotropic displacement factor exponent takes the form:  $-2\pi^2[h2a^*2U11+2hka^*b^*U12+\dots]$ .

Atom	U11	U22	U33	U23	U13	U12
Yb1	51.4(10)	51.4(10)	31.7(11)	0	0	0
O1	79(7)	102(10)	65(8)	0	-38(6)	0
O2	25(3)	25(3)	25(3)	1(3)	1(3)	-1(3)
N1	100(40)	680(180)	60(30)	0	-30(30)	0
C1	81(7)	140(20)	81(7)	0	-35(8)	0
C2	101(8)	180(20)	101(8)	0	-55(10)	0
C3	135(13)	260(30)	100(9)	0	-51(10)	0
C4	145(14)	330(30)	117(12)	0	-69(13)	0
C5	142(13)	400(40)	142(13)	0	-67(14)	0
C6	157(16)	480(50)	157(16)	0	-81(18)	0
C7	180(30)	560(50)	156(17)	0	-80(18)	0

**Table B3** Bond lengths for Yb-NH<sub>2</sub>-TPDC.

Atom	Atom	Length/Å	Atom	Atom	Length/Å
Yb1	Yb11	3.818(2)	O2	Yb13	2.289(4)
Yb1	Yb12	3.818(2)	N1	C3	1.43(6)
Yb1	Yb13	3.818(2)	C1	O19	1.313(18)
Yb1	O14	2.288(12)	C1	C2	1.43(4)
Yb1	O15	2.288(12)	C2	C3	1.384(18)
Yb1	O16	2.288(12)	C2	C39	1.384(18)
Yb1	O1	2.288(12)	C3	C4	1.378(18)
Yb1	O27	2.289(4)	C4	C5	1.360(18)
Yb1	O2	2.289(4)	C5	C49	1.360(18)
Yb1	O28	2.289(4)	C5	C6	1.51(6)
Yb1	O26	2.289(4)	C6	C7	1.383(19)
Yb1	O1S	2.57(14)	C6	C79	1.383(19)
O1	C1	1.313(19)	C7	C710	1.52(6)
O2	Yb12	2.289(4)			

1+Z,+X,+Y; 21-Y,1-Z,1-X; 31-Z,1-X,1-Y; 41-Y,1-X,+Z; 5+Y,+X,+Z; 61-X,1-Y,+Z; 7+X,1-Y,+Z; 81-X,+Y,+Z; 9+Z,1-Y,+X; 101/2-Z,+Y,1/2-X

**Table B4** Bond angles for Yb-NH<sub>2</sub>-TPDC.

Atom	Atom	Atom	Angle/°	Atom	Atom	Atom	Angle/°
Yb11	Yb1	Yb12	90.002(1)	O2	Yb1	Yb11	33.49(13)
Yb11	Yb1	Yb13	60.0	O25	Yb1	Yb12	33.49(13)
Yb13	Yb1	Yb12	60.001(1)	O28	Yb1	Yb12	86.7(3)
O14	Yb1	Yb13	161.3(4)	O25	Yb1	Yb13	86.7(3)
O15	Yb1	Yb12	161.3(4)	O28	Yb1	Yb13	86.7(3)
O14	Yb1	Yb11	108.2(2)	O27	Yb1	Yb11	86.7(3)
O14	Yb1	Yb12	108.2(2)	O2	Yb1	Yb13	33.49(13)
O1	Yb1	Yb11	161.3(4)	O27	Yb1	Yb13	33.49(13)
O16	Yb1	Yb12	108.2(2)	O28	Yb1	Yb11	33.49(13)
O15	Yb1	Yb11	71.2(4)	O27	Yb1	O2	66.6(3)
O1	Yb1	Yb12	71.3(4)	O25	Yb1	O2	101.8(6)
O15	Yb1	Yb13	108.2(2)	O27	Yb1	O28	101.8(6)
O16	Yb1	Yb11	108.2(2)	O28	Yb1	O25	66.6(3)
O1	Yb1	Yb13	108.2(2)	O28	Yb1	O2	66.6(3)
O16	Yb1	Yb13	71.2(4)	O27	Yb1	O25	66.6(3)
O14	Yb1	O15	78.7(3)	O27	Yb1	O1S	129.1(3)
O16	Yb1	O1	78.7(3)	O28	Yb1	O1S	129.1(3)
O16	Yb1	O15	78.7(3)	O25	Yb1	O1S	129.1(3)
O15	Yb1	O1	127.5(7)	O2	Yb1	O1S	129.1(3)
O14	Yb1	O16	127.5(7)	O1S	Yb1	Yb13	134.999(3)
O14	Yb1	O1	78.7(3)	O1S	Yb1	Yb11	134.999(9)

O16	Yb1	O25	140.45(19)	O1S	Yb1	Yb12	134.999(9)
O14	Yb1	O25	77.7(4)	C1	O1	Yb1	135.4(14)
O14	Yb1	O27	140.45(19)	Yb1	O2	Yb11	113.0(3)
O16	Yb1	O27	77.7(4)	Yb1	O2	Yb13	113.0(3)
O14	Yb1	O28	77.7(4)	Yb13	O2	Yb11	113.0(3)
O1	Yb1	O27	77.7(4)	O19	C1	O1	127(3)
O1	Yb1	O28	140.45(19)	O1	C1	C2	116.7(13)
O16	Yb1	O28	140.45(19)	O19	C1	C2	116.7(13)
O1	Yb1	O25	77.7(4)	C3	C2	C1	122.3(17)
O15	Yb1	O2	77.7(4)	C39	C2	C1	122.3(17)
O14	Yb1	O2	140.45(19)	C39	C2	C3	115(3)
O15	Yb1	O25	140.45(19)	C2	C3	N1	125(3)
O15	Yb1	O28	77.7(4)	C4	C3	N1	114(3)
O16	Yb1	O2	77.7(4)	C4	C3	C2	121(3)
O1	Yb1	O2	140.45(19)	C5	C4	C3	124(4)
O15	Yb1	O27	140.45(19)	C49	C5	C4	114(5)
O15	Yb1	O1S	63.7(4)	C4	C5	C6	123(2)
O1	Yb1	O1S	63.7(4)	C49	C5	C6	123(2)
O16	Yb1	O1S	63.7(4)	C79	C6	C5	116(3)
O14	Yb1	O1S	63.7(4)	C7	C6	C5	116(3)
O27	Yb1	Yb12	33.49(13)	C79	C6	C7	128(6)
O2	Yb1	Yb12	86.7(3)	C6	C7	C710	116(3)
O25	Yb1	Yb11	86.7(3)				

11-Z,1-X,1-Y; 2+Z,+X,+Y; 31-Y,1-Z,1-X; 4+Y,+X,+Z; 51-X,1-Y,+Z; 61-Y,1-X,+Z; 71-X,+Y,+Z; 8+X,1-Y,+Z; 9+Z,1-Y,+X; 101/2-Z,+Y,1/2-X

**Table B5** Torsion angles for Yb-NH<sub>2</sub>-TPDC.

A	B	C	D	Angle/°	A	B	C	D	Angle/°
Yb1	O1	C1	O11	0.000(4)	C31	C2	C3	N1	180.000(4)
Yb1	O1	C1	C2	180.000(2)	C31	C2	C3	C4	0.000(3)
O11	C1	C2	C31	0.000(4)	C3	C4	C5	C41	0.000(4)
O11	C1	C2	C3	180.000(3)	C3	C4	C5	C6	180.000(3)
O1	C1	C2	C31	180.000(3)	C41	C5	C6	C7	180.000(4)
O1	C1	C2	C3	0.000(4)	C41	C5	C6	C71	0.000(5)
N1	C3	C4	C5	180.000(3)	C4	C5	C6	C71	180.000(4)
C1	C2	C3	N1	0.000(5)	C4	C5	C6	C7	0.000(4)
C1	C2	C3	C4	180.000(3)	C5	C6	C7	C72	180.000(3)
C2	C3	C4	C5	0.000(4)	C71	C6	C7	C72	0.000(6)

1+Z,1-Y,+X; 21/2-Z,+Y,1/2-X

**Table B6** Hydrogen atom coordinates ( $\text{\AA}\times 10^4$ ) and isotropic displacement parameters ( $\text{\AA}^2\times 10^3$ ) for Yb-NH<sub>2</sub>-TPDC.

Atom	<i>x</i>	<i>Y</i>	<i>z</i>	U(eq)
H1A	4237	5000	2891	334
H1B	4405	5000	3308	334
H4	3582	5000	2753	238
H7	3197	5000	2335	358

**Table B7** Atomic occupancy for Yb-NH<sub>2</sub>-TPDC.

Atom	<i>Occupancy</i>	Atom	<i>Occupancy</i>	Atom	<i>Occupancy</i>
N1	0.5	H1A	0.5	H1B	0.5
O1S	0.31(9)				

## BIBLIOGRAPHY

1. Ogba, O. M.; Warner, N. C.; O'Leary, D. J.; Grubbs, R. H., Recent advances in ruthenium-based olefin metathesis. *Chemical Society Reviews* **2018**, *47*, 4510-4544.
2. Nedelcu, G.; Protesescu, L.; Yakunin, S.; Bodnarchuk, M. I.; Grotevent, M. J.; Kovalenko, M. V., Fast Anion-Exchange in Highly Luminescent Nanocrystals of Cesium Lead Halide Perovskites (CsPbX<sub>3</sub>, X = Cl, Br, I). *Nano Letters* **2015**, *15*, 5635-5640.
3. Liu, H.; Tanaka, T.; Urabe, Y.; Kataura, H., High-Efficiency Single-Chirality Separation of Carbon Nanotubes Using Temperature-Controlled Gel Chromatography. *Nano Letters* **2013**, *13*, 1996-2003.
4. Chang, H.-H.; Murphy, C. J., Mini Gold Nanorods with Tunable Plasmonic Peaks beyond 1000 nm. *Chemistry of Materials* **2018**, *30*, 1427-1435.
5. Yaghi, O. M.; Li, G.; Li, H., Selective binding and removal of guests in a microporous metal-organic framework. *Nature* **1995**, *378*, 703-706.
6. Yaghi, O. M.; Li, H., Hydrothermal Synthesis of a Metal-Organic Framework Containing Large Rectangular Channels. *Journal of the American Chemical Society* **1995**, *117*, 10401-10402.
7. Rowsell, J. L. C.; Yaghi, O. M., Metal-organic frameworks: a new class of porous materials. *Microporous and Mesoporous Materials* **2004**, *73*, 3-14.
8. Seth, S.; Matzger, A. J., Metal-Organic Frameworks: Examples, Counterexamples, and an Actionable Definition. *Crystal Growth & Design* **2017**, *17*, 4043-4048.
9. Eddaoudi, M.; Moler, D. B.; Li, H.; Chen, B.; Reineke, T. M.; O'Keeffe, M.; Yaghi, O. M., Modular Chemistry: Secondary Building Units as a Basis for the Design of Highly Porous and Robust Metal-Organic Carboxylate Frameworks. *Accounts of Chemical Research* **2001**, *34*, 319-330.
10. Li, H.; Eddaoudi, M.; O'Keeffe, M.; Yaghi, O. M., Design and synthesis of an exceptionally stable and highly porous metal-organic framework. *Nature* **1999**, *402*, 276-279.
11. Chui, S. S.-Y.; Lo, S. M.-F.; Charmant, J. P. H.; Orpen, A. G.; Williams, I. D., A Chemically Functionalizable Nanoporous Material [Cu<sub>3</sub>(TMA)<sub>2</sub>(H<sub>2</sub>O)<sub>3</sub>]<sub>n</sub>. *Science* **1999**, *283*, 1148-1150.
12. Yaghi, O. M.; O'Keeffe, M.; Ockwig, N. W.; Chae, H. K.; Eddaoudi, M.; Kim, J., Reticular synthesis and the design of new materials. *Nature* **2003**, *423*, 705.

13. Suh, M. P.; Park, H. J.; Prasad, T. K.; Lim, D.-W., Hydrogen Storage in Metal–Organic Frameworks. *Chemical Reviews* **2012**, *112*, 782-835.
14. Sumida, K.; Rogow, D. L.; Mason, J. A.; McDonald, T. M.; Bloch, E. D.; Herm, Z. R.; Bae, T.-H.; Long, J. R., Carbon Dioxide Capture in Metal–Organic Frameworks. *Chemical Reviews* **2012**, *112*, 724-781.
15. Li, J.-R.; Kuppler, R. J.; Zhou, H.-C., Selective gas adsorption and separation in metal–organic frameworks. *Chemical Society Reviews* **2009**, *38*, 1477-1504.
16. Drake, T.; Ji, P.; Lin, W., Site Isolation in Metal–Organic Frameworks Enables Novel Transition Metal Catalysis. *Accounts of Chemical Research* **2018**, *51*, 2129-2138.
17. Huang, Y.-B.; Liang, J.; Wang, X.-S.; Cao, R., Multifunctional metal–organic framework catalysts: synergistic catalysis and tandem reactions. *Chemical Society Reviews* **2017**, *46*, 126-157.
18. Zeng, L.; Guo, X.; He, C.; Duan, C., Metal–Organic Frameworks: Versatile Materials for Heterogeneous Photocatalysis. *ACS Catalysis* **2016**, *6*, 7935-7947.
19. Yoon, M.; Srirambalaji, R.; Kim, K., Homochiral Metal–Organic Frameworks for Asymmetric Heterogeneous Catalysis. *Chemical Reviews* **2012**, *112*, 1196-1231.
20. Chen, B.; Xiang, S.; Qian, G., Metal–Organic Frameworks with Functional Pores for Recognition of Small Molecules. *Accounts of Chemical Research* **2010**, *43*, 1115-1124.
21. Karmakar, A.; Samanta, P.; Desai, A. V.; Ghosh, S. K., Guest-Responsive Metal–Organic Frameworks as Scaffolds for Separation and Sensing Applications. *Accounts of Chemical Research* **2017**, *50*, 2457-2469.
22. Furukawa, H.; Ko, N.; Go, Y. B.; Aratani, N.; Choi, S. B.; Choi, E.; Yazaydin, A. Ö.; Snurr, R. Q.; O’Keeffe, M.; Kim, J.; Yaghi, O. M., Ultrahigh Porosity in Metal-Organic Frameworks. *Science* **2010**, *329*, 424-428.
23. Hönicke, I. M.; Senkowska, I.; Bon, V.; Baburin, I. A.; Bönisch, N.; Raschke, S.; Evans, J. D.; Kaskel, S., Balancing Mechanical Stability and Ultrahigh Porosity in Crystalline Framework Materials. *Angewandte Chemie International Edition* **2018**, *57*, 13780-13783.
24. Farha, O. K.; Eryazici, I.; Jeong, N. C.; Hauser, B. G.; Wilmer, C. E.; Sarjeant, A. A.; Snurr, R. Q.; Nguyen, S. T.; Yazaydin, A. Ö.; Hupp, J. T., Metal–Organic Framework Materials with Ultrahigh Surface Areas: Is the Sky the Limit? *Journal of the American Chemical Society* **2012**, *134*, 15016-15021.
25. Medishetty, R.; Zaręba, J. K.; Mayer, D.; Samoć, M.; Fischer, R. A., Nonlinear optical properties, upconversion and lasing in metal–organic frameworks. *Chemical Society Reviews* **2017**, *46*, 4976-5004.

26. Coronado, E.; Mínguez Espallargas, G., Dynamic magnetic MOFs. *Chemical Society Reviews* **2013**, *42*, 1525-1539.
27. Sun, L.; Campbell, M. G.; Dincă, M., Electrically Conductive Porous Metal–Organic Frameworks. *Angewandte Chemie International Edition* **2016**, *55*, 3566-3579.
28. Cui, W.-G.; Hu, T.-L.; Bu, X.-H., Metal-Organic Framework Materials for the Separation and Purification of Light Hydrocarbons. *Advanced Materials* **2019**, *0*, 1806445.
29. Wang, H.; Li, J., Microporous metal-organic frameworks for adsorptive separation of C5-C6 alkane isomers. *Accounts of Chemical Research* **2019**, *52*, 1968-1978.
30. O’Keeffe, M.; Yaghi, O. M., Deconstructing the Crystal Structures of Metal–Organic Frameworks and Related Materials into Their Underlying Nets. *Chemical Reviews* **2012**, *112*, 675-702.
31. O’Keeffe, M.; Eddaoudi, M.; Li, H.; Reineke, T.; Yaghi, O. M., Frameworks for Extended Solids: Geometrical Design Principles. *Journal of Solid State Chemistry* **2000**, *152*, 3-20.
32. Moghadam, P. Z.; Rogge, S. M. J.; Li, A.; Chow, C.-M.; Wieme, J.; Moharrami, N.; Aragonés-Anglada, M.; Conduit, G.; Gomez-Gualdrón, D. A.; Van Speybroeck, V.; Fairen-Jimenez, D., Structure-Mechanical Stability Relations of Metal-Organic Frameworks via Machine Learning. *Matter* **2019**, *1*, 219-234.
33. Feng, D.; Gu, Z.-Y.; Li, J.-R.; Jiang, H.-L.; Wei, Z.; Zhou, H.-C., Zirconium-Metalloporphyrin PCN-222: Mesoporous Metal–Organic Frameworks with Ultrahigh Stability as Biomimetic Catalysts. *Angewandte Chemie International Edition* **2012**, *51*, 10307-10310.
34. Deria, P.; Gómez-Gualdrón, D. A.; Hod, I.; Snurr, R. Q.; Hupp, J. T.; Farha, O. K., Framework-Topology-Dependent Catalytic Activity of Zirconium-Based (Porphinato)zinc(II) MOFs. *Journal of the American Chemical Society* **2016**, *138*, 14449-14457.
35. Férey, G.; Serre, C.; Mellot-Draznieks, C.; Millange, F.; Surblé, S.; Dutour, J.; Margiolaki, I., A Hybrid Solid with Giant Pores Prepared by a Combination of Targeted Chemistry, Simulation, and Powder Diffraction. *Angewandte Chemie International Edition* **2004**, *43*, 6296-6301.
36. Cavka, J. H.; Jakobsen, S.; Olsbye, U.; Guillou, N.; Lamberti, C.; Bordiga, S.; Lillerud, K. P., A New Zirconium Inorganic Building Brick Forming Metal Organic Frameworks with Exceptional Stability. *Journal of the American Chemical Society* **2008**, *130*, 13850-13851.
37. Chae, H. K.; Kim, J.; Friedrichs, O. D.; O’Keeffe, M.; Yaghi, O. M., Design of Frameworks with Mixed Triangular and Octahedral Building Blocks Exemplified by the Structure of [Zn<sub>4</sub>O(TCA)<sub>2</sub>] Having the Pyrite Topology. *Angewandte Chemie International Edition* **2003**, *42*, 3907-3909.

38. Chae, H. K.; Siberio-Pérez, D. Y.; Kim, J.; Go, Y.; Eddaoudi, M.; Matzger, A. J.; O'Keeffe, M.; Yaghi, O. M.; Materials, D.; Discovery, G., A route to high surface area, porosity and inclusion of large molecules in crystals. *Nature* **2004**, *427*, 523-527.
39. Chen, Z.; Xiang, S.; Liao, T.; Yang, Y.; Chen, Y.-S.; Zhou, Y.; Zhao, D.; Chen, B., A New Multidentate Hexacarboxylic Acid for the Construction of Porous Metal–Organic Frameworks of Diverse Structures and Porosities. *Crystal Growth & Design* **2010**, *10*, 2775-2779.
40. Grünker, R.; Bon, V.; Heerwig, A.; Klein, N.; Müller, P.; Stoeck, U.; Baburin, I. A.; Mueller, U.; Senkovska, I.; Kaskel, S., Dye Encapsulation Inside a New Mesoporous Metal–Organic Framework for Multifunctional Solvatochromic-Response Function. *Chemistry – A European Journal* **2012**, *18*, 13299-13303.
41. Grünker, R.; Senkovska, I.; Biedermann, R.; Klein, N.; Lohe, M. R.; Müller, P.; Kaskel, S., A highly porous flexible Metal–Organic Framework with corundum topology. *Chemical Communications* **2011**, *47*, 490-492.
42. Klein, N.; Senkovska, I.; Gedrich, K.; Stoeck, U.; Henschel, A.; Mueller, U.; Kaskel, S., A Mesoporous Metal–Organic Framework. *Angewandte Chemie International Edition* **2009**, *48*, 9954-9957.
43. Koh, K.; Wong-Foy, A. G.; Matzger, A. J., A Porous Coordination Copolymer with over 5000 m<sup>2</sup>/g BET Surface Area. *Journal of the American Chemical Society* **2009**, *131*, 4184-4185.
44. Sun, D.; Collins, D. J.; Ke, Y.; Zuo, J.-L.; Zhou, H.-C., Construction of Open Metal–Organic Frameworks Based on Predesigned Carboxylate Isomers: From Achiral to Chiral Nets. *Chemistry – A European Journal* **2006**, *12*, 3768-3776.
45. Eddaoudi, M.; Kim, J.; Rosi, N.; Vodak, D.; Wachter, J.; O'Keeffe, M.; Yaghi, O. M., Systematic Design of Pore Size and Functionality in Isorecticular MOFs and Their Application in Methane Storage. *Science* **2002**, *295*, 469-472.
46. Deng, H.; Grunder, S.; Cordova, K. E.; Valente, C.; Furukawa, H.; Hmadeh, M.; Gándara, F.; Whalley, A. C.; Liu, Z.; Asahina, S.; Kazumori, H.; O'Keeffe, M.; Terasaki, O.; Stoddart, J. F.; Yaghi, O. M., Large-Pore Apertures in a Series of Metal-Organic Frameworks. *Science* **2012**, *336*, 1018-1023.
47. Katz, M. J.; Brown, Z. J.; Colón, Y. J.; Siu, P. W.; Scheidt, K. A.; Snurr, R. Q.; Hupp, J. T.; Farha, O. K., A facile synthesis of UiO-66, UiO-67 and their derivatives. *Chemical Communications* **2013**, *49*, 9449-9451.

48. Wang, B.; Huang, H.; Lv, X.-L.; Xie, Y.; Li, M.; Li, J.-R., Tuning CO<sub>2</sub> Selective Adsorption over N<sub>2</sub> and CH<sub>4</sub> in UiO-67 Analogues through Ligand Functionalization. *Inorganic Chemistry* **2014**, *53*, 9254-9259.
49. Kutzscher, C.; Nickerl, G.; Senkovska, I.; Bon, V.; Kaskel, S., Proline Functionalized UiO-67 and UiO-68 Type Metal–Organic Frameworks Showing Reversed Diastereoselectivity in Aldol Addition Reactions. *Chemistry of Materials* **2016**, *28*, 2573-2580.
50. Butova, V. V.; Budnyk, A. P.; Guda, A. A.; Lomachenko, K. A.; Bugaev, A. L.; Soldatov, A. V.; Chavan, S. M.; Øien-Ødegaard, S.; Olsbye, U.; Lillerud, K. P.; Atzori, C.; Bordiga, S.; Lamberti, C., Modulator Effect in UiO-66-NDC (1,4-Naphthalenedicarboxylic Acid) Synthesis and Comparison with UiO-67-NDC Isorecticular Metal–Organic Frameworks. *Crystal Growth & Design* **2017**, *17*, 5422-5431.
51. Park, S.; Song, H.; Ko, N.; Kim, C.; Kim, K.; Lee, E., SuFEx in Metal–Organic Frameworks: Versatile Postsynthetic Modification Tool. *ACS Applied Materials & Interfaces* **2018**, *10*, 33785-33789.
52. Das, A.; Anbu, N.; Sk, M.; Dhakshinamoorthy, A.; Biswas, S., Highly Active Urea-Functionalized Zr(IV)-UiO-67 Metal–Organic Framework as Hydrogen Bonding Heterogeneous Catalyst for Friedel–Crafts Alkylation. *Inorganic Chemistry* **2019**, *58*, 5163-5172.
53. Wang, K.; Huang, H.; Zhou, X.; Wang, Q.; Li, G.; Shen, H.; She, Y.; Zhong, C., Highly Chemically Stable MOFs with Trifluoromethyl Groups: Effect of Position of Trifluoromethyl Groups on Chemical Stability. *Inorganic Chemistry* **2019**, *58*, 5725-5732.
54. Ruffley, J. P.; Goodenough, I.; Luo, T.-Y.; Richard, M.; Borguet, E.; Rosi, N. L.; Johnson, J. K., Design, Synthesis, and Characterization of Metal–Organic Frameworks for Enhanced Sorption of Chemical Warfare Agent Simulants. *The Journal of Physical Chemistry C* **2019**, *123*, 19748-19758.
55. Karagiari, O.; Bury, W.; Mondloch, J. E.; Hupp, J. T.; Farha, O. K., Solvent-Assisted Linker Exchange: An Alternative to the De Novo Synthesis of Unattainable Metal–Organic Frameworks. *Angewandte Chemie International Edition* **2014**, *53*, 4530-4540.
56. Cohen, S. M., Postsynthetic Methods for the Functionalization of Metal–Organic Frameworks. *Chemical Reviews* **2012**, *112*, 970-1000.
57. Kim, M.; Cahill, J. F.; Fei, H.; Prather, K. A.; Cohen, S. M., Postsynthetic Ligand and Cation Exchange in Robust Metal–Organic Frameworks. *Journal of the American Chemical Society* **2012**, *134*, 18082-18088.
58. Fei, H.; Cahill, J. F.; Prather, K. A.; Cohen, S. M., Tandem Postsynthetic Metal Ion and Ligand Exchange in Zeolitic Imidazolate Frameworks. *Inorganic Chemistry* **2013**, *52*, 4011-4016.

59. Li, T.; Kozlowski, M. T.; Doud, E. A.; Blakely, M. N.; Rosi, N. L., Stepwise Ligand Exchange for the Preparation of a Family of Mesoporous MOFs. *Journal of the American Chemical Society* **2013**, *135*, 11688-11691.
60. Gross, A. F.; Sherman, E.; Mahoney, S. L.; Vajo, J. J., Reversible Ligand Exchange in a Metal–Organic Framework (MOF): Toward MOF-Based Dynamic Combinatorial Chemical Systems. *The Journal of Physical Chemistry A* **2013**, *117*, 3771-3776.
61. Park, J.; Feng, D.; Zhou, H.-C., Structure-Assisted Functional Anchor Implantation in Robust Metal–Organic Frameworks with Ultralarge Pores. *Journal of the American Chemical Society* **2015**, *137*, 1663-1672.
62. Wang, Z.; Cohen, S. M., Postsynthetic Covalent Modification of a Neutral Metal–Organic Framework. *Journal of the American Chemical Society* **2007**, *129*, 12368-12369.
63. Burrows, A. D.; Frost, C. G.; Mahon, M. F.; Richardson, C., Post-Synthetic Modification of Tagged Metal–Organic Frameworks. *Angewandte Chemie International Edition* **2008**, *47*, 8482-8486.
64. Gadzikwa, T.; Lu, G.; Stern, C. L.; Wilson, S. R.; Hupp, J. T.; Nguyen, S. T., Covalent surface modification of a metal–organic framework: selective surface engineering via Cu-catalyzed Huisgen cycloaddition. *Chemical Communications* **2008**, 5493-5495.
65. Liu, C.; Li, T.; Rosi, N. L., Strain-Promoted “Click” Modification of a Mesoporous Metal–Organic Framework. *Journal of the American Chemical Society* **2012**, *134*, 18886-18888.
66. Deng, H.; Doonan, C. J.; Furukawa, H.; Ferreira, R. B.; Towne, J.; Knobler, C. B.; Wang, B.; Yaghi, O. M., Multiple Functional Groups of Varying Ratios in Metal-Organic Frameworks. *Science* **2010**, *327*, 846-850.
67. Liu, C.; Luo, T.-Y.; Feura, E. S.; Zhang, C.; Rosi, N. L., Orthogonal Ternary Functionalization of a Mesoporous Metal–Organic Framework via Sequential Postsynthetic Ligand Exchange. *Journal of the American Chemical Society* **2015**, *137*, 10508-10511.
68. Garibay, S. J.; Wang, Z.; Tanabe, K. K.; Cohen, S. M., Postsynthetic Modification: A Versatile Approach Toward Multifunctional Metal-Organic Frameworks. *Inorganic Chemistry* **2009**, *48*, 7341-7349.
69. Das, S.; Kim, H.; Kim, K., Metathesis in Single Crystal: Complete and Reversible Exchange of Metal Ions Constituting the Frameworks of Metal–Organic Frameworks. *Journal of the American Chemical Society* **2009**, *131*, 3814-3815.
70. Brozek, C. K.; Dincă, M.,  $\text{Ti}^{3+}$ -,  $\text{V}^{2+/3+}$ -,  $\text{Cr}^{2+/3+}$ -,  $\text{Mn}^{2+}$ -, and  $\text{Fe}^{2+}$ -Substituted MOF-5 and Redox Reactivity in Cr- and Fe-MOF-5. *Journal of the American Chemical Society* **2013**, *135*, 12886-12891.

71. Mohamed, M. H.; Yang, Y.; Li, L.; Zhang, S.; Ruffley, J. P.; Jarvi, A. G.; Saxena, S.; Vesper, G.; Johnson, J. K.; Rosi, N. L., Designing Open Metal Sites in Metal–Organic Frameworks for Paraffin/Olefin Separations. *Journal of the American Chemical Society* **2019**, *141*, 13003-13007.
72. Song, X.; Kim, T. K.; Kim, H.; Kim, D.; Jeong, S.; Moon, H. R.; Lah, M. S., Post-Synthetic Modifications of Framework Metal Ions in Isostructural Metal–Organic Frameworks: Core–Shell Heterostructures via Selective Transmetalations. *Chemistry of Materials* **2012**, *24*, 3065-3073.
73. Sudik, A. C.; Côté, A. P.; Yaghi, O. M., Metal–Organic Frameworks Based on Trigonal Prismatic Building Blocks and the New “acs” Topology. *Inorganic Chemistry* **2005**, *44*, 2998-3000.
74. Carson, F.; Su, J.; Platero-Prats, A. E.; Wan, W.; Yun, Y.; Samain, L.; Zou, X., Framework Isomerism in Vanadium Metal–Organic Frameworks: MIL-88B(V) and MIL-101(V). *Crystal Growth & Design* **2013**, *13*, 5036-5044.
75. Hong, K.; Bak, W.; Moon, D.; Chun, H., Bistable and Porous Metal–Organic Frameworks with Charge-Neutral acs Net Based on Heterometallic  $M_3O(CO_2)_6$  Building Blocks. *Crystal Growth & Design* **2013**, *13*, 4066-4070.
76. Goesten, M. G.; Magusin, P. C. M. M.; Pidko, E. A.; Mezari, B.; Hensen, E. J. M.; Kapteijn, F.; Gascon, J., Molecular Promoting of Aluminum Metal–Organic Framework Topology MIL-101 by N,N-Dimethylformamide. *Inorganic Chemistry* **2014**, *53*, 882-887.
77. Schoedel, A.; Zaworotko, M. J.,  $[M_3(\mu_3-O)(O_2CR)_6]$  and related trigonal prisms: versatile molecular building blocks for crystal engineering of metal–organic material platforms. *Chemical Science* **2014**, *5*, 1269-1282.
78. Wang, K.; Feng, D.; Liu, T.-F.; Su, J.; Yuan, S.; Chen, Y.-P.; Bosch, M.; Zou, X.; Zhou, H.-C., A Series of Highly Stable Mesoporous Metalloporphyrin Fe-MOFs. *Journal of the American Chemical Society* **2014**, *136*, 13983-13986.
79. Zhao, X.; Bu, X.; Zhai, Q.-G.; Tran, H.; Feng, P., Pore Space Partition by Symmetry-Matching Regulated Ligand Insertion and Dramatic Tuning on Carbon Dioxide Uptake. *Journal of the American Chemical Society* **2015**, *137*, 1396-1399.
80. Liu, Q.; Cong, H.; Deng, H., Deciphering the Spatial Arrangement of Metals and Correlation to Reactivity in Multivariate Metal–Organic Frameworks. *Journal of the American Chemical Society* **2016**, *138*, 13822-13825.
81. Reinares-Fisac, D.; Aguirre-Díaz, L. M.; Iglesias, M.; Snejko, N.; Gutiérrez-Puebla, E.; Monge, M. Á.; Gándara, F., A Mesoporous Indium Metal–Organic Framework: Remarkable Advances in Catalytic Activity for Strecker Reaction of Ketones. *Journal of the American Chemical Society* **2016**, *138*, 9089-9092.

82. Zhai, Q.-G.; Bu, X.; Zhao, X.; Mao, C.; Bu, F.; Chen, X.; Feng, P., Advancing Magnesium–Organic Porous Materials through New Magnesium Cluster Chemistry. *Crystal Growth & Design* **2016**, *16*, 1261-1267.
83. Zhao, X.; Bu, X.; Nguyen, E. T.; Zhai, Q.-G.; Mao, C.; Feng, P., Multivariable Modular Design of Pore Space Partition. *Journal of the American Chemical Society* **2016**, *138*, 15102-15105.
84. Chandrasekhar, P.; Savitha, G.; Moorthy, J. N., Robust MOFs of “tsg” Topology Based on Trigonal Prismatic Organic and Metal Cluster SBUs: Single Crystal to Single Crystal Postsynthetic Metal Exchange and Selective CO<sub>2</sub> Capture. *Chemistry – A European Journal* **2017**, *23*, 7297-7305.
85. Peng, L.; Asgari, M.; Mieville, P.; Schouwink, P.; Bulut, S.; Sun, D. T.; Zhou, Z.; Pattison, P.; van Beek, W.; Queen, W. L., Using Predefined M<sub>3</sub>(μ<sub>3</sub>-O) Clusters as Building Blocks for an Isostructural Series of Metal–Organic Frameworks. *ACS Applied Materials & Interfaces* **2017**, *9*, 23957-23966.
86. Nowacka, A.; Briantais, P.; Prestipino, C.; Llabrés i Xamena, F. X., Facile “green” aqueous synthesis of mono- and bimetallic trimesate metalorganic frameworks. *Crystal Growth & Design* **2019**, *19*, 4981-4989.
87. Feldblyum, J. I.; Liu, M.; Gidley, D. W.; Matzger, A. J., Reconciling the Discrepancies between Crystallographic Porosity and Guest Access As Exemplified by Zn-HKUST-1. *Journal of the American Chemical Society* **2011**, *133*, 18257-18263.
88. Kozachuk, O.; Yusenko, K.; Noei, H.; Wang, Y.; Walleck, S.; Glaser, T.; Fischer, R. A., Solvothermal growth of a ruthenium metal–organic framework featuring HKUST-1 structure type as thin films on oxide surfaces. *Chemical Communications* **2011**, *47*, 8509-8511.
89. Kramer, M.; Schwarz, U.; Kaskel, S., Synthesis and properties of the metal-organic framework Mo<sub>3</sub>(BTC)<sub>2</sub> (TUDMOF-1). *Journal of Materials Chemistry* **2006**, *16*, 2245-2248.
90. Maniam, P.; Stock, N., Investigation of Porous Ni-Based Metal–Organic Frameworks Containing Paddle-Wheel Type Inorganic Building Units via High-Throughput Methods. *Inorganic Chemistry* **2011**, *50*, 5085-5097.
91. Murray, L. J.; Dinca, M.; Yano, J.; Chavan, S.; Bordiga, S.; Brown, C. M.; Long, J. R., Highly-Selective and Reversible O<sub>2</sub> Binding in Cr<sub>3</sub>(1,3,5-benzenetricarboxylate)<sub>2</sub>. *Journal of the American Chemical Society* **2010**, *132*, 7856-7857.
92. Xie, L.; Liu, S.; Gao, C.; Cao, R.; Cao, J.; Sun, C.; Su, Z., Mixed-Valence Iron(II, III) Trimesates with Open Frameworks Modulated by Solvents. *Inorganic Chemistry* **2007**, *46*, 7782-7788.

93. Zhang, L.; Tan, Y.-f.; Lin, F.; Chen, H.; You, J.-j.; Lai, A.-n.; Jiang, X.-y.; Chen, W.-Z.; Lu, C.-Z., Synthesis, structure and luminescence property of a cadmium-organic framework based on 6-connected paddle-wheel building units and btc ligands. *Inorganic Chemistry Communications* **2018**, *93*, 83-86.
94. deKrafft, K. E.; Boyle, W. S.; Burk, L. M.; Zhou, O. Z.; Lin, W., Zr- and Hf-based nanoscale metal-organic frameworks as contrast agents for computed tomography. *Journal of Materials Chemistry* **2012**, *22*, 18139-18144.
95. Falaise, C.; Volkringer, C.; Loiseau, T., Mixed Formate-Dicarboxylate Coordination Polymers with Tetravalent Uranium: Occurrence of Tetranuclear {U<sub>4</sub>O<sub>4</sub>} and Hexanuclear {U<sub>6</sub>O<sub>4</sub>(OH)<sub>4</sub>} Motifs. *Crystal Growth & Design* **2013**, *13*, 3225-3231.
96. Knope, K. E.; Wilson, R. E.; Vasiliu, M.; Dixon, D. A.; Soderholm, L., Thorium(IV) Molecular Clusters with a Hexanuclear Th Core. *Inorganic Chemistry* **2011**, *50*, 9696-9704.
97. Lammert, M.; Wharmby, M. T.; Smolders, S.; Bueken, B.; Lieb, A.; Lomachenko, K. A.; Vos, D. D.; Stock, N., Cerium-based metal organic frameworks with UiO-66 architecture: synthesis, properties and redox catalytic activity. *Chemical Communications* **2015**, *51*, 12578-12581.
98. Xue, D.-X.; Cairns, A. J.; Belmabkhout, Y.; Wojtas, L.; Liu, Y.; Alkordi, M. H.; Eddaoudi, M., Tunable Rare-Earth fcu-MOFs: A Platform for Systematic Enhancement of CO<sub>2</sub> Adsorption Energetics and Uptake. *Journal of the American Chemical Society* **2013**, *135*, 7660-7667.
99. Serre, C.; Millange, F.; Thouvenot, C.; Gardant, N.; Pellé, F.; Férey, G., Synthesis, characterisation and luminescent properties of a new three-dimensional lanthanide trimesate: M((C<sub>6</sub>H<sub>3</sub>)-(CO<sub>2</sub>)<sub>3</sub>) (M = Y, Ln) or MIL-78. *Journal of Materials Chemistry* **2004**, *14*, 1540-1543.
100. Eliseeva, S. V.; Bünzli, J.-C. G., Lanthanide luminescence for functional materials and bio-sciences. *Chemical Society Reviews* **2010**, *39*, 189-227.
101. Huang, Y.-G.; Jiang, F.-L.; Hong, M.-C., Magnetic lanthanide-transition-metal organic-inorganic hybrid materials: From discrete clusters to extended frameworks. *Coordination Chemistry Reviews* **2009**, *253*, 2814-2834.
102. Cui, Y.; Chen, B.; Qian, G., Lanthanide metal-organic frameworks for luminescent sensing and light-emitting applications. *Coordination Chemistry Reviews* **2014**, *273-274*, 76-86.
103. Foucault-Collet, A.; Gogick, K. A.; White, K. A.; Villette, S.; Pallier, A.; Collet, G.; Kieda, C.; Li, T.; Geib, S. J.; Rosi, N. L.; Petoud, S., Lanthanide near infrared imaging in living cells with Yb<sup>3+</sup> nano metal organic frameworks. *Proceedings of the National Academy of Sciences* **2013**, *110*, 17199-17204.

104. Woodruff, D. N.; Winpenny, R. E. P.; Layfield, R. A., Lanthanide Single-Molecule Magnets. *Chemical Reviews* **2013**, *113*, 5110-5148.
105. Zhang, J.; Badger, P. D.; Geib, S. J.; Petoud, S., Sensitization of Near-Infrared-Emitting Lanthanide Cations in Solution by Tropolonate Ligands. *Angewandte Chemie International Edition* **2005**, *44*, 2508-2512.
106. Petoud, S.; Cohen, S. M.; Bünzli, J.-C. G.; Raymond, K. N., Stable Lanthanide Luminescence Agents Highly Emissive in Aqueous Solution: Multidentate 2-Hydroxyisophthalamide Complexes of Sm<sup>3+</sup>, Eu<sup>3+</sup>, Tb<sup>3+</sup>, Dy<sup>3+</sup>. *Journal of the American Chemical Society* **2003**, *125*, 13324-13325.
107. Bünzli, J.-C. G.; Piguet, C., Taking advantage of luminescent lanthanide ions. *Chemical Society Reviews* **2005**, *34*, 1048-1077.
108. Weissman, S. I., Intramolecular Energy Transfer The Fluorescence of Complexes of Europium. *The Journal of Chemical Physics* **1942**, *10*, 214-217.
109. An, J.; Shade, C. M.; Chengelis-Czegan, D. A.; Petoud, S.; Rosi, N. L., Zinc-Adeninate Metal–Organic Framework for Aqueous Encapsulation and Sensitization of Near-infrared and Visible Emitting Lanthanide Cations. *Journal of the American Chemical Society* **2011**, *133*, 1220-1223.
110. White, K. A.; Chengelis, D. A.; Gogick, K. A.; Stehman, J.; Rosi, N. L.; Petoud, S., Near-Infrared Luminescent Lanthanide MOF Barcodes. *Journal of the American Chemical Society* **2009**, *131*, 18069-18071.
111. White, K. A.; Chengelis, D. A.; Zeller, M.; Geib, S. J.; Szakos, J.; Petoud, S.; Rosi, N. L., Near-infrared emitting ytterbium metal-organic frameworks with tunable excitation properties. *Chemical Communications* **2009**, 4506-4508.
112. Uh, H.; Petoud, S., Novel antennae for the sensitization of near infrared luminescent lanthanide cations. *Comptes Rendus Chimie* **2010**, *13*, 668-680.
113. Weissleder, R., A clearer vision for in vivo imaging. *Nature Biotechnology* **2001**, *19*, 316-317.
114. Pansare, V. J.; Hejazi, S.; Faenza, W. J.; Prud'homme, R. K., Review of Long-Wavelength Optical and NIR Imaging Materials: Contrast Agents, Fluorophores, and Multifunctional Nano Carriers. *Chemistry of Materials* **2012**, *24*, 812-827.
115. Martinić, I.; Eliseeva, S. V.; Petoud, S., Near-infrared emitting probes for biological imaging: Organic fluorophores, quantum dots, fluorescent proteins, lanthanide(III) complexes and nanomaterials. *Journal of Luminescence* **2017**, *189*, 19-43.
116. Cui, Y.; Yue, Y.; Qian, G.; Chen, B., Luminescent Functional Metal–Organic Frameworks. *Chemical Reviews* **2012**, *112*, 1126-1162.

117. Hu, Z.; Deibert, B. J.; Li, J., Luminescent metal–organic frameworks for chemical sensing and explosive detection. *Chemical Society Reviews* **2014**, *43*, 5815-5840.
118. Allendorf, M. D.; Bauer, C. A.; Bhakta, R. K.; Houk, R. J. T., Luminescent metal–organic frameworks. *Chemical Society Reviews* **2009**, *38*, 1330-1352.
119. He, C.; Liu, D.; Lin, W., Nanomedicine Applications of Hybrid Nanomaterials Built from Metal–Ligand Coordination Bonds: Nanoscale Metal–Organic Frameworks and Nanoscale Coordination Polymers. *Chemical Reviews* **2015**, *115*, 11079-11108.
120. McKinlay, A. C.; Morris, R. E.; Horcajada, P.; Férey, G.; Gref, R.; Couvreur, P.; Serre, C., BioMOFs: Metal–Organic Frameworks for Biological and Medical Applications. *Angewandte Chemie International Edition* **2010**, *49*, 6260-6266.
121. Bai, Y.; Dou, Y.; Xie, L.-H.; Rutledge, W.; Li, J.-R.; Zhou, H.-C., Zr-based metal–organic frameworks: design, synthesis, structure, and applications. *Chemical Society Reviews* **2016**, *45*, 2327-2367.
122. Guillerm, V.; WeselińskiŁukasz, J.; Belmabkhout, Y.; Cairns, A. J.; D'Elia, V.; WojtasŁukasz; Adil, K.; Eddaoudi, M., Discovery and introduction of a (3,18)-connected net as an ideal blueprint for the design of metal–organic frameworks. *Nature Chemistry* **2014**, *6*, 673-680.
123. Alezi, D.; Peedikakkal, A. M. P.; Weseliński, Ł. J.; Guillerm, V.; Belmabkhout, Y.; Cairns, A. J.; Chen, Z.; Wojtas, Ł.; Eddaoudi, M., Quest for Highly Connected Metal–Organic Framework Platforms: Rare-Earth Polynuclear Clusters Versatility Meets Net Topology Needs. *Journal of the American Chemical Society* **2015**, *137*, 5421-5430.
124. Wu, Y.; Morton, S.; Kong, X.; Nichol, G. S.; Zheng, Z., Hydrolytic synthesis and structural characterization of lanthanide-acetylacetonato/hydroxo cluster complexes - A systematic study. *Dalton Transactions* **2011**, *40*, 1041-1046.
125. Kong, X.-J.; Long, L.-S.; Zheng, L.-S.; Wang, R.; Zheng, Z., Hydrolytic Synthesis and Structural Characterization of Lanthanide Hydroxide Clusters Supported by Nicotinic Acid. *Inorganic Chemistry* **2009**, *48*, 3268-3273.
126. Wang, R.; Selby, H. D.; Liu, H.; Carducci, M. D.; Jin, T.; Zheng, Z.; Anthis, J. W.; Staples, R. J., Halide-Templated Assembly of Polynuclear Lanthanide-Hydroxo Complexes. *Inorganic Chemistry* **2002**, *41*, 278-286.
127. Wang, R.; Liu, H.; Carducci, M. D.; Jin, T.; Zheng, C.; Zheng, Z., Lanthanide Coordination with  $\alpha$ -Amino Acids under Near Physiological pH Conditions: Polymetallic Complexes Containing the Cubane-Like  $[\text{Ln}_4(\mu_3\text{-OH})_4]^{8+}$  Cluster Core. *Inorganic Chemistry* **2001**, *40*, 2743-2750.
128. Zheng, Z., Ligand-controlled self-assembly of polynuclear lanthanide-oxo/hydroxo complexes: from synthetic serendipity to rational supramolecular design. *Chemical Communications* **2001**, 2521-2529.

129. Wang, R.; Zheng, Z.; Jin, T.; Staples, R. J., Coordination Chemistry of Lanthanides at “High” pH: Synthesis and Structure of the Pentadecanuclear Complex of Europium(III) with Tyrosine. *Angewandte Chemie International Edition* **1999**, *38*, 1813-1815.
130. Wu, P.; He, C.; Wang, J.; Peng, X.; Li, X.; An, Y.; Duan, C., Photoactive Chiral Metal–Organic Frameworks for Light-Driven Asymmetric  $\alpha$ -Alkylation of Aldehydes. *Journal of the American Chemical Society* **2012**, *134*, 14991-14999.
131. Yi, X.; Bernot, K.; Calvez, G.; Daiguebonne, C.; Guillou, O., 3D Organization of Dysprosium Cubanes. *European Journal of Inorganic Chemistry* **2013**, *2013*, 5879-5885.
132. Savard, D.; Lin, P.-H.; Burchell, T. J.; Korobkov, I.; Wernsdorfer, W.; Clérac, R.; Murugesu, M., Two-Dimensional Networks of Lanthanide Cubane-Shaped Dumbbells. *Inorganic Chemistry* **2009**, *48*, 11748-11754.
133. Tu, B.; Pang, Q.; Ning, E.; Yan, W.; Qi, Y.; Wu, D.; Li, Q., Heterogeneity within a Mesoporous Metal–Organic Framework with Three Distinct Metal-Containing Building Units. *Journal of the American Chemical Society* **2015**, *137*, 13456-13459.
134. All MOF materials in this paper were assigned through Berkeley Global Science Institute submission request, <http://globalscience.berkeley.edu/netcentre>.
135. Della Rocca, J.; Liu, D.; Lin, W., Nanoscale Metal–Organic Frameworks for Biomedical Imaging and Drug Delivery. *Accounts of Chemical Research* **2011**, *44*, 957-968.
136. Dolgoplova, E. A.; Rice, A. M.; Smith, M. D.; Shustova, N. B., Photophysics, Dynamics, and Energy Transfer in Rigid Mimics of GFP-based Systems. *Inorganic Chemistry* **2016**, *55*, 7257-7264.
137. Dolomanov, O. V.; Bourhis, L. J.; Gildea, R. J.; Howard, J. A. K.; Puschmann, H., OLEX2: a complete structure solution, refinement and analysis program. *Journal of Applied Crystallography* **2009**, *42*, 339-341.
138. Sheldrick, G., A short history of SHELX. *Acta Crystallographica Section A* **2008**, *64*, 112-122.
139. Fennell Jr., J. F.; Liu, S. F.; Azzarelli, J. M.; Weis, J. G.; Rochat, S.; Mirica, K. A.; Ravnsbæk, J. B.; Swager, T. M., Nanowire Chemical/Biological Sensors: Status and a Roadmap for the Future. *Angewandte Chemie International Edition* **2016**, *55*, 1266-1281.
140. Rocha, J.; Carlos, L. D.; Paz, F. A. A.; Ananias, D., Luminescent multifunctional lanthanides-based metal–organic frameworks. *Chemical Society Reviews* **2011**, *40*, 926-940.
141. Cable, M. L.; Kirby, J. P.; Sorasaene, K.; Gray, H. B.; Ponce, A., Bacterial Spore Detection by [Tb<sup>3+</sup>(macrocycle)(dipicolinate)] Luminescence. *Journal of the American Chemical Society* **2007**, *129*, 1474-1475.

142. Cable, M. L.; Kirby, J. P.; Gray, H. B.; Ponce, A., Enhancement of Anion Binding in Lanthanide Optical Sensors. *Accounts of Chemical Research* **2013**, *46*, 2576-2584.
143. Hao, J.-N.; Yan, B., A water-stable lanthanide-functionalized MOF as a highly selective and sensitive fluorescent probe for Cd<sup>2+</sup>. *Chemical Communications* **2015**, *51*, 7737-7740.
144. Karmakar, A.; Samanta, P.; Dutta, S.; Ghosh, S. K., Fluorescent “Turn-on” Sensing Based on Metal-organic Frameworks (MOFs). *Chemistry – An Asian Journal* DOI: 10.1002/asia.201901168.
145. Li, Y.; Zhang, S.; Song, D., A Luminescent Metal–Organic Framework as a Turn-On Sensor for DMF Vapor. *Angewandte Chemie International Edition* **2013**, *52*, 710-713.
146. Tan, H.; Liu, B.; Chen, Y., Lanthanide Coordination Polymer Nanoparticles for Sensing of Mercury(II) by Photoinduced Electron Transfer. *ACS Nano* **2012**, *6*, 10505-10511.
147. Yu, Y.; Ma, J.-P.; Dong, Y.-B., Luminescent humidity sensors based on porous Ln<sup>3+</sup>-MOFs. *CrystEngComm* **2012**, *14*, 7157-7160.
148. Zhao, B.; Chen, X.-Y.; Cheng, P.; Liao, D.-Z.; Yan, S.-P.; Jiang, Z.-H., Coordination Polymers Containing 1D Channels as Selective Luminescent Probes. *Journal of the American Chemical Society* **2004**, *126*, 15394-15395.
149. Parker, D.; Kanthi Senanayake, P.; A. Gareth Williams, J., Luminescent sensors for pH, pO<sub>2</sub>, halide and hydroxide ions using phenanthridine as a photosensitiser in macrocyclic europium and terbium complexes. *Journal of the Chemical Society, Perkin Transactions 2* **1998**, 2129-2140.
150. Fent, K.; Weston, A. A.; Caminada, D., Ecotoxicology of human pharmaceuticals. *Aquatic Toxicology* **2006**, *76*, 122-159.
151. Richardson, S. D., Water Analysis: Emerging Contaminants and Current Issues. *Analytical Chemistry* **2007**, *79*, 4295-4324.
152. Liu, S.; Fu, Y.; Xiong, C.; Liu, Z.; Zheng, L.; Yan, F., Detection of Bisphenol A Using DNA-Functionalized Graphene Field Effect Transistors Integrated in Microfluidic Systems. *ACS Applied Materials & Interfaces* **2018**, *10*, 23522-23528.
153. López-Tocón, I.; Otero, J. C.; Arenas, J. F.; Garcia-Ramos, J. V.; Sanchez-Cortes, S., Multicomponent Direct Detection of Polycyclic Aromatic Hydrocarbons by Surface-Enhanced Raman Spectroscopy Using Silver Nanoparticles Functionalized with the Viologen Host Lucigenin. *Analytical Chemistry* **2011**, *83*, 2518-2525.
154. Wu, L.; Qu, X., Cancer biomarker detection: recent achievements and challenges. *Chemical Society Reviews* **2015**, *44*, 2963-2997.

155. Gadelha, I. C. N.; Fonseca, N. B. S.; Oloris, S. C. S.; Melo, M. M.; M., I.; Soto-Blanco, B., Gossypol Toxicity from Cottonseed Products. *The Scientific World Journal* **2014**, *2014*, 11.
156. GB 2716-2018, Hygienic Standard for Edible Vegetable Oils.
157. Directive 2002/32/EC of the European Parliament And of the Council.
158. Boatner, C. H.; Caravella, M.; Kyame, L., Quantitative Determination of Extractable Gossypol in Cottonseed and Cotton seed Meal A Spectrophotometric Method. *Industrial & Engineering Chemistry Analytical Edition* **1944**, *16*, 566-572.
159. Smith, F. H., Spectrophotometric Method for Estimating Gossypol in Crude Cottonseed Oil. *Industrial & Engineering Chemistry Analytical Edition* **1946**, *18*, 41-43.
160. Admasu, A.; Chandravanshi, B. S., Spectrophotometric determination of total gossypol in cottonseeds and cottonseed meals. *Analytical Chemistry* **1984**, *56*, 30-32.
161. Botsoglou, N. A., Determination of "free" gossypol in cottonseed and cottonseed meals by second-derivative ultraviolet spectrophotometry. *Journal of Agricultural and Food Chemistry* **1991**, *39*, 478-482.
162. Hron Sr., R. J.; Kuk, M. S.; Wan, P. J., Quick method for estimating free gossypol in cottonseed, meals, collets, and extracted meals. *Journal of the American Oil Chemists' Society* **1996**, *73*, 199-202.
163. Abou-Donia, S. A.; Lasker, J. M.; Abou-Donia, M. B., High-performance liquid chromatographic analysis of gossypol. *Journal of Chromatography A* **1981**, *206*, 606-610.
164. Nomeir, A. A.; Abou-Donia, M. B., Gossypol: High-performance liquid chromatographic analysis and stability in various solvents. *Journal of the American Oil Chemists Society* **1982**, *59*, 546-549.
165. Hron, R. J.; Kim, H. L.; Calhoun, M. C.; Fisher, G. S., Determination of (+)-, (-)-, and total gossypol in cottonseed by high-performance liquid chromatography. *Journal of the American Oil Chemists' Society* **1999**, *76*, 1351-1355.
166. Lee, K.-J.; Dabrowski, K., High-performance liquid chromatographic determination of gossypol and gossypolone enantiomers in fish tissues using simultaneous electrochemical and ultraviolet detectors. *Journal of Chromatography B* **2002**, *779*, 313-319.
167. Hron Sr., R. J.; Kuk, M. S.; Abraham, G., Determination of free and total gossypol by high performance liquid chromatography. *Journal of the American Oil Chemists' Society* **1990**, *67*, 182-187.
168. Mirghani, M. E. S.; Che Man, Y. B., A new method for determining gossypol in cottonseed oil by FTIR spectroscopy. *Journal of the American Oil Chemists' Society* **2003**, *80*, 625-628.

169. Li, C.; Zhao, T.; Li, C.; Mei, L.; Yu, E.; Dong, Y.; Chen, J.; Zhu, S., Determination of gossypol content in cottonseeds by near infrared spectroscopy based on Monte Carlo uninformative variable elimination and nonlinear calibration methods. *Food Chemistry* **2017**, *221*, 990-996.
170. Zhao, C.; Wu, D., Rapid detection assay for the molecular imprinting of gossypol using a two-layer PMAA/SiO<sub>2</sub> bulk structure with a piezoelectric imprinting sensor. *Sensors and Actuators B: Chemical* **2013**, *181*, 104-113.
171. Xu, S.; Zhou, K.; Fang, D.; Ma, L., Highly Sensitive and Selective Fluorescent Detection of Gossypol Based on BSA-Stabilized Copper Nanoclusters. *Molecules* **2018**, *24*, 95.
172. Marciniak, B.; Kozubek, H.; Koput, J.; Paszyc, S., Spectroscopic and Photochemical Studies of Gossypol in Solution. *Zeitschrift für Naturforschung A* **1990**, *45*, 179-183.
173. Brzezinski, B.; Rozwadowski, J.; Marciniak, B.; Paszyc, S., Spectroscopic study of gossypol-lanthanide cation complexes in acetonitrile solution. *Journal of Molecular Structure* **1997**, *435*, 275-279.
174. Luo, T.-Y.; Liu, C.; Eliseeva, S. V.; Muldoon, P. F.; Petoud, S.; Rosi, N. L., Rare Earth pcu Metal–Organic Framework Platform Based on RE<sub>4</sub>(μ<sub>3</sub>-OH)<sub>4</sub>(COO)<sub>6</sub><sup>2+</sup> Clusters: Rational Design, Directed Synthesis, and Deliberate Tuning of Excitation Wavelengths. *Journal of the American Chemical Society* **2017**, *139*, 9333-9340.
175. Guo, Z.; Xu, H.; Su, S.; Cai, J.; Dang, S.; Xiang, S.; Qian, G.; Zhang, H.; O’Keeffe, M.; Chen, B., A robust near infrared luminescent ytterbium metal–organic framework for sensing of small molecules. *Chemical Communications* **2011**, *47*, 5551-5553.
176. Honkeldieva, M.; Kunafiev, R.; Hamidov, H. I., Redetermined structure of gossypol (P3 polymorph). *Acta Crystallographica Section E* **2015**, *71*, o442-o443.
177. Ma, J.; Kalenak, A. P.; Wong-Foy, A. G.; Matzger, A. J., Rapid Guest Exchange and Ultra-Low Surface Tension Solvents Optimize Metal–Organic Framework Activation. *Angewandte Chemie International Edition* **2017**, *56*, 14618-14621.
178. White, K. A.; Chengelis, D. A.; Zeller, M.; Geib, S. J.; Szakos, J.; Petoud, S.; Rosi, N. L., Near-infrared emitting ytterbium metal–organic frameworks with tunable excitation properties. *Chemical Communications* **2009**, 4506-4508.
179. Sheldrick, G., Crystal structure refinement with SHELXL. *Acta Crystallographica Section C* **2015**, *71*, 3-8.
180. Liu, C.; Zeng, C.; Luo, T.-Y.; Merg, A. D.; Jin, R.; Rosi, N. L., Establishing Porosity Gradients within Metal–Organic Frameworks Using Partial Postsynthetic Ligand Exchange. *Journal of the American Chemical Society* **2016**, *138*, 12045-12048.

181. Ockwig, N. W.; Delgado-Friedrichs, O.; O'Keeffe, M.; Yaghi, O. M., Reticular Chemistry: Occurrence and Taxonomy of Nets and Grammar for the Design of Frameworks. *Accounts of Chemical Research* **2005**, *38*, 176-182.
182. Furukawa, H.; Cordova, K. E.; O'Keeffe, M.; Yaghi, O. M., The Chemistry and Applications of Metal-Organic Frameworks. *Science* **2013**, *341*, 1230444.
183. Very recently, a similar concept was proposed for MOF-on-MOF heterostructures consisting of lattice mismatched MOFs: Feng, L.; Yuan, S.; Li, J.-L.; Wang, K.-Y.; Day, G. S.; Zhang, P.; Wang, Y.; Zhou, H.-C. Uncovering Two Principles of Multivariate Hierarchical Metal–Organic Framework Synthesis via Retrosynthetic Design. *ACS Central Science* **2018**, *4*, 1719-1726.
184. Furukawa, S.; Hirai, K.; Nakagawa, K.; Takashima, Y.; Matsuda, R.; Tsuruoka, T.; Kondo, M.; Haruki, R.; Tanaka, D.; Sakamoto, H.; Shimomura, S.; Sakata, O.; Kitagawa, S., Heterogeneously Hybridized Porous Coordination Polymer Crystals: Fabrication of Heterometallic Core–Shell Single Crystals with an In-Plane Rotational Epitaxial Relationship. *Angewandte Chemie* **2009**, *121*, 1798-1802.
185. Koh, K.; Wong-Foy, A. G.; Matzger, A. J., MOF@MOF: microporous core–shell architectures. *Chemical Communications* **2009**, 6162-6164.
186. Li, T.; Sullivan, J. E.; Rosi, N. L., Design and Preparation of a Core–Shell Metal–Organic Framework for Selective CO<sub>2</sub> Capture. *Journal of the American Chemical Society* **2013**, *135*, 9984-9987.
187. Tang, J.; Salunkhe, R. R.; Liu, J.; Torad, N. L.; Imura, M.; Furukawa, S.; Yamauchi, Y., Thermal Conversion of Core–Shell Metal–Organic Frameworks: A New Method for Selectively Functionalized Nanoporous Hybrid Carbon. *Journal of the American Chemical Society* **2015**, *137*, 1572-1580.
188. Lee, H. J.; Cho, Y. J.; Cho, W.; Oh, M., Controlled Isotropic or Anisotropic Nanoscale Growth of Coordination Polymers: Formation of Hybrid Coordination Polymer Particles. *ACS Nano* **2013**, *7*, 491-499.
189. Pan, M.; Zhu, Y.-X.; Wu, K.; Chen, L.; Hou, Y.-J.; Yin, S.-Y.; Wang, H.-P.; Fan, Y.-N.; Su, C.-Y., Epitaxial Growth of Hetero-Ln-MOF Hierarchical Single Crystals for Domain- and Orientation-Controlled Multicolor Luminescence 3D Coding Capability. *Angewandte Chemie* **2017**, *129*, 14774-14778.
190. Yang, X.; Yuan, S.; Zou, L.; Drake, H.; Zhang, Y.; Qin, J.; Alsalme, A.; Zhou, H.-C., One-Step Synthesis of Hybrid Core–Shell Metal–Organic Frameworks. *Angewandte Chemie International Edition* **2018**, *57*, 3927-3932.
191. Zhan, G.; Zeng, H. C., Hydrogen spillover through Matryoshka-type (ZIFs@)<sub>n-1</sub>ZIFs nanocubes. *Nature Communications* **2018**, *9*, 3778.

192. Schmitt, S.; Silvestre, M.; Tsotsalas, M.; Winkler, A.-L.; Shahnas, A.; Grosjean, S.; Laye, F.; Gliemann, H.; Lahann, J.; Bräse, S.; Franzreb, M.; Wöll, C., Hierarchically Functionalized Magnetic Core/Multishell Particles and Their Postsynthetic Conversion to Polymer Capsules. *ACS Nano* **2015**, *9*, 4219-4226.
193. Liu, X.-Y.; Zhang, F.; Goh, T.-W.; Li, Y.; Shao, Y.-C.; Luo, L.; Huang, W.; Long, Y.-T.; Chou, L.-Y.; Tsung, C.-K., Using a Multi-Shelled Hollow Metal–Organic Framework as a Host to Switch the Guest-to-Host and Guest-to-Guest Interactions. *Angewandte Chemie International Edition* **2018**, *57*, 2110-2114.
194. Burnett, B. J.; Barron, P. M.; Hu, C.; Choe, W., Stepwise Synthesis of Metal–Organic Frameworks: Replacement of Structural Organic Linkers. *Journal of the American Chemical Society* **2011**, *133*, 9984-9987.
195. Boissonnault, J. A.; Wong-Foy, A. G.; Matzger, A. J., Core–Shell Structures Arise Naturally During Ligand Exchange in Metal–Organic Frameworks. *Journal of the American Chemical Society* **2017**, *139*, 14841-14844.
196. Liu, L.; Konstas, K.; Hill, M. R.; Telfer, S. G., Programmed Pore Architectures in Modular Quaternary Metal–Organic Frameworks. *Journal of the American Chemical Society* **2013**, *135*, 17731-17734.
197. An, J.; Farha, O. K.; Hupp, J. T.; Pohl, E.; Yeh, J. I.; Rosi, N. L., Metal-adeninate vertices for the construction of an exceptionally porous metal-organic framework. *Nature Communications* **2012**, *3*, 604.
198. Muldoon, P. F.; Liu, C.; Miller, C. C.; Koby, S. B.; Gamble Jarvi, A.; Luo, T.-Y.; Saxena, S.; O’Keeffe, M.; Rosi, N. L., Programmable Topology in New Families of Heterobimetallic Metal–Organic Frameworks. *Journal of the American Chemical Society* **2018**, *140*, 6194-6198.
199. Lun, D. J.; Waterhouse, G. I. N.; Telfer, S. G., A General Thermolabile Protecting Group Strategy for Organocatalytic Metal–Organic Frameworks. *Journal of the American Chemical Society* **2011**, *133*, 5806-5809.
200. Yang, Q.; Xu, Q.; Jiang, H.-L., Metal–organic frameworks meet metal nanoparticles: synergistic effect for enhanced catalysis. *Chemical Society Reviews* **2017**, *46*, 4774-4808.
201. Hu, P.; Morabito, J. V.; Tsung, C.-K., Core–Shell Catalysts of Metal Nanoparticle Core and Metal–Organic Framework Shell. *ACS Catalysis* **2014**, *4*, 4409-4419.
202. Zacher, D.; Schmid, R.; Wöll, C.; Fischer, R. A., Surface Chemistry of Metal–Organic Frameworks at the Liquid–Solid Interface. *Angewandte Chemie International Edition* **2011**, *50*, 176-199.
203. Lu, G.; Li, S.; Guo, Z.; Farha, O. K.; Hauser, B. G.; Qi, X.; Wang, Y.; Wang, X.; Han, S.; Liu, X.; DuChene, J. S.; Zhang, H.; Zhang, Q.; Chen, X.; Ma, J.; Loo, S. C. J.; Wei, W. D.;

- Yang, Y.; Hupp, J. T.; Huo, F., Imparting functionality to a metal–organic framework material by controlled nanoparticle encapsulation. *Nature Chemistry* **2012**, *4*, 310-316.
204. Rama, G.; Ardá, A.; Maréchal, J.-D.; Gamba, I.; Ishida, H.; Jiménez-Barbero, J.; Vázquez, M. E.; Vázquez López, M., Stereoselective Formation of Chiral Metallopeptides. *Chemistry – A European Journal* **2012**, *18*, 7030-7035.
205. Jacoby, M., Building A Better Gas Mask. *C&EN* **2014**, *92*, 34-38.
206. Morrison, R. W. In *Overview of current collective protection filtration technology*, NBC Defense Collective Protection Conference, 2002.
207. Prasad, G.; Singh, B.; Vijayaraghavan, R., Respiratory protection against chemical and biological warfare agents. *Defence Science Journal* **2008**, *58*, 686.
208. Bobbitt, N. S.; Mendonca, M. L.; Howarth, A. J.; Islamoglu, T.; Hupp, J. T.; Farha, O. K.; Snurr, R. Q., Metal–organic frameworks for the removal of toxic industrial chemicals and chemical warfare agents. *Chemical Society Reviews* **2017**, *46*, 3357-3385.
209. Linders, M. J. G.; Baak, P. J.; van Bokhoven, J. J. G. M., Exploratory Investigation of the Risk of Desorption from Activated Carbon Filters in Respiratory Protective Devices. *Industrial & Engineering Chemistry Research* **2007**, *46*, 4034-4039.
210. *Adsorption and Desorption of Chemical Warfare Agents on Activated Carbon: Impact of Temperature and Relative Humidity*; U.S. Environmental Protection Agency: Washington D.C., 2014.
211. Liao, P.-Q.; Huang, N.-Y.; Zhang, W.-X.; Zhang, J.-P.; Chen, X.-M., Controlling guest conformation for efficient purification of butadiene. *Science* **2017**, *356*, 1193-1196.
212. Herm, Z. R.; Wiers, B. M.; Mason, J. A.; van Baten, J. M.; Hudson, M. R.; Zajdel, P.; Brown, C. M.; Masciocchi, N.; Krishna, R.; Long, J. R., Separation of Hexane Isomers in a Metal-Organic Framework with Triangular Channels. *Science* **2013**, *340*, 960-964.
213. Li, T.; Chen, D.-L.; Sullivan, J. E.; Kozlowski, M. T.; Johnson, J. K.; Rosi, N. L., Systematic modulation and enhancement of CO<sub>2</sub>: N<sub>2</sub> selectivity and water stability in an isorecticular series of bio-MOF-11 analogues. *Chemical Science* **2013**, *4*, 1746-1755.
214. Fracaroli, A. M.; Furukawa, H.; Suzuki, M.; Dodd, M.; Okajima, S.; Gándara, F.; Reimer, J. A.; Yaghi, O. M., Metal–Organic Frameworks with Precisely Designed Interior for Carbon Dioxide Capture in the Presence of Water. *Journal of the American Chemical Society* **2014**, *136*, 8863-8866.
215. Ploskonka, A. M.; DeCoste, J. B., Tailoring the Adsorption and Reaction Chemistry of the Metal–Organic Frameworks UiO-66, UiO-66-NH<sub>2</sub>, and HKUST-1 via the Incorporation of Molecular Guests. *ACS Applied Materials & Interfaces* **2017**, *9*, 21579-21585.

216. de Koning, M. C.; van Grol, M.; Breijaert, T., Degradation of Paraoxon and the Chemical Warfare Agents VX, Tabun, and Soman by the Metal–Organic Frameworks UiO-66-NH<sub>2</sub>, MOF-808, NU-1000, and PCN-777. *Inorganic Chemistry* **2017**, *56*, 11804-11809.
217. Liu, Y.; Howarth, A. J.; Hupp, J. T.; Farha, O. K., Selective Photooxidation of a Mustard-Gas Simulant Catalyzed by a Porphyrinic Metal–Organic Framework. *Angewandte Chemie International Edition* **2015**, *54*, 9001-9005.
218. Liu, Y.; Buru, C. T.; Howarth, A. J.; Mahle, J. J.; Buchanan, J. H.; DeCoste, J. B.; Hupp, J. T.; Farha, O. K., Efficient and selective oxidation of sulfur mustard using singlet oxygen generated by a pyrene-based metal–organic framework. *Journal of Materials Chemistry A: Materials for Energy and Sustainability* **2016**, *4*, 13809-13813.
219. Bromberg, L.; Klichko, Y.; Chang, E. P.; Speakman, S.; Straut, C. M.; Wilusz, E.; Hatton, T. A., Alkylaminopyridine-Modified Aluminum Aminoterephthalate Metal-Organic Frameworks As Components of Reactive Self-Detoxifying Materials. *ACS Applied Materials & Interfaces* **2012**, *4*, 4595-4602.
220. Mondloch, J. E.; Katz, M. J.; Isley Iii, W. C.; Ghosh, P.; Liao, P.; Bury, W.; Wagner, G. W.; Hall, M. G.; DeCoste, J. B.; Peterson, G. W.; Snurr, R. Q.; Cramer, C. J.; Hupp, J. T.; Farha, O. K., Destruction of chemical warfare agents using metal–organic frameworks. *Nature Materials* **2015**, *14*, 512-516.
221. Katz, M. J.; Mondloch, J. E.; Totten, R. K.; Park, J. K.; Nguyen, S. T.; Farha, O. K.; Hupp, J. T., Simple and Compelling Biomimetic Metal–Organic Framework Catalyst for the Degradation of Nerve Agent Simulants. *Angewandte Chemie International Edition* **2014**, *53*, 497-501.
222. Katz, M. J.; Moon, S.-Y.; Mondloch, J. E.; Beyzavi, M. H.; Stephenson, C. J.; Hupp, J. T.; Farha, O. K., Exploiting parameter space in MOFs: a 20-fold enhancement of phosphate-ester hydrolysis with UiO-66-NH<sub>2</sub>. *Chemical Science* **2015**, *6*, 2286-2291.
223. Gil-San-Millan, R.; López-Maya, E.; Hall, M.; Padial, N. M.; Peterson, G. W.; DeCoste, J. B.; Rodríguez-Albelo, L. M.; Oltra, J. E.; Barea, E.; Navarro, J. A. R., Chemical Warfare Agents Detoxification Properties of Zirconium Metal–Organic Frameworks by Synergistic Incorporation of Nucleophilic and Basic Sites. *ACS Applied Materials & Interfaces* **2017**, *9*, 23967-23973.
224. Zhao, J.; Lee, D. T.; Yaga, R. W.; Hall, M. G.; Barton, H. F.; Woodward, I. R.; Oldham, C. J.; Walls, H. J.; Peterson, G. W.; Parsons, G. N., Ultra-Fast Degradation of Chemical Warfare Agents Using MOF–Nanofiber Kebabs. *Angewandte Chemie International Edition* **2016**, *55*, 13224-13228.
225. Wang, G.; Sharp, C.; Plonka, A. M.; Wang, Q.; Frenkel, A. I.; Guo, W.; Hill, C.; Smith, C.; Kollar, J.; Troya, D.; Morris, J. R., Mechanism and Kinetics for Reaction of the Chemical Warfare Agent Simulant, DMMP(g), with Zirconium(IV) MOFs: An Ultrahigh-Vacuum and DFT Study. *The Journal of Physical Chemistry C* **2017**, *121*, 11261-11272.

226. DeCoste, J. B.; Rossin, J. A.; Peterson, G. W., Hierarchical Pore Development by Plasma Etching of Zr-Based Metal–Organic Frameworks. *Chemistry - A European Journal* **2015**, *21*, 18029-18032.
227. Mondal, S. S.; Holdt, H.-J., Breaking Down Chemical Weapons by Metal–Organic Frameworks. *Angewandte Chemie International Edition* **2016**, *55*, 42-44.
228. Lee, D. T.; Zhao, J.; Oldham, C. J.; Peterson, G. W.; Parsons, G. N., UiO-66-NH<sub>2</sub> Metal–Organic Framework (MOF) Nucleation on TiO<sub>2</sub>, ZnO, and Al<sub>2</sub>O<sub>3</sub> Atomic Layer Deposition-Treated Polymer Fibers: Role of Metal Oxide on MOF Growth and Catalytic Hydrolysis of Chemical Warfare Agent Simulants. *ACS Applied Materials & Interfaces* **2017**, *9*, 44847-44855.
229. López-Maya, E.; Montoro, C.; Rodríguez-Albelo, L. M.; Aznar Cervantes, S. D.; Lozano-Pérez, A. A.; Cenís, J. L.; Barea, E.; Navarro, J. A. R., Textile/Metal–Organic-Framework Composites as Self-Detoxifying Filters for Chemical-Warfare Agents. *Angewandte Chemie International Edition* **2015**, *54*, 6790-6794.
230. DeCoste, J. B.; Peterson, G. W.; Jasuja, H.; Glover, T. G.; Huang, Y.-g.; Walton, K. S., Stability and degradation mechanisms of metal–organic frameworks containing the Zr<sub>6</sub>O<sub>4</sub>(OH)<sub>4</sub> secondary building unit. *Journal of Materials Chemistry A* **2013**, *1*, 5642-5650.
231. Valenzano, L.; Civalleri, B.; Chavan, S.; Bordiga, S.; Nilsen, M. H.; Jakobsen, S.; Lillerud, K. P.; Lamberti, C., Disclosing the Complex Structure of UiO-66 Metal Organic Framework: A Synergic Combination of Experiment and Theory. *Chemistry of Materials* **2011**, *23*, 1700-1718.
232. Kandiah, M.; Nilsen, M. H.; Usseglio, S.; Jakobsen, S.; Olsbye, U.; Tilset, M.; Larabi, C.; Quadrelli, E. A.; Bonino, F.; Lillerud, K. P., Synthesis and Stability of Tagged UiO-66 Zr-MOFs. *Chemistry of Materials* **2010**, *22*, 6632-6640.
233. Biswas, S.; Van Der Voort, P., A General Strategy for the Synthesis of Functionalised UiO-66 Frameworks: Characterisation, Stability and CO<sub>2</sub> Adsorption Properties. *European Journal of Inorganic Chemistry* **2013**, *2013*, 2154-2160.
234. Øien-Ødegaard, S.; Bouchevreau, B.; Hylland, K.; Wu, L.; Blom, R.; Grande, C.; Olsbye, U.; Tilset, M.; Lillerud, K. P., UiO-67-type Metal–Organic Frameworks with Enhanced Water Stability and Methane Adsorption Capacity. *Inorganic Chemistry* **2016**, *55*, 1986-1991.
235. Peterson, G. W.; Destefano, M. R.; Garibay, S. J.; Ploskonka, A.; McEntee, M.; Hall, M.; Karwacki, C. J.; Hupp, J. T.; Farha, O. K., Optimizing Toxic Chemical Removal through Defect-Induced UiO-66-NH<sub>2</sub> Metal–Organic Framework. *Chemistry - A European Journal* **2017**, *23*, 15913-15916.
236. Moon, S.-Y.; Wagner, G. W.; Mondloch, J. E.; Peterson, G. W.; DeCoste, J. B.; Hupp, J. T.; Farha, O. K., Effective, Facile, and Selective Hydrolysis of the Chemical Warfare

- Agent VX Using Zr<sub>6</sub>-Based Metal–Organic Frameworks. *Inorganic Chemistry* **2015**, *54*, 10829-10833.
237. Trickett, C. A.; Gagnon, K. J.; Lee, S.; Gándara, F.; Bürgi, H.-B.; Yaghi, O. M., Definitive Molecular Level Characterization of Defects in UiO-66 Crystals. *Angewandte Chemie International Edition* **2015**, *54*, 11162-11167.
238. Luo, T.-Y.; Liu, C.; Gan, X. Y.; Muldoon, P. F.; Diemler, N. A.; Millstone, J. E.; Rosi, N. L., Multivariate Stratified Metal–Organic Frameworks: Diversification Using Domain Building Blocks. *Journal of the American Chemical Society* **2019**, *141*, 2161-2168.
239. Vermoortele, F.; Vandichel, M.; Van de Voorde, B.; Ameloot, R.; Waroquier, M.; Van Speybroeck, V.; De Vos, D. E., Electronic Effects of Linker Substitution on Lewis Acid Catalysis with Metal–Organic Frameworks. *Angewandte Chemie International Edition* **2012**, *51*, 4887-4890.
240. Kim, M.; Cahill, J. F.; Su, Y.; Prather, K. A.; Cohen, S. M., Postsynthetic ligand exchange as a route to functionalization of ‘inert’ metal–organic frameworks. *Chemical Science* **2012**, *3*, 126-130.
241. DeStefano, M. R.; Islamoglu, T.; Garibay, S. J.; Hupp, J. T.; Farha, O. K., Room-Temperature Synthesis of UiO-66 and Thermal Modulation of Densities of Defect Sites. *Chemistry of Materials* **2017**, *29*, 1357-1361.
242. Stukowski, A., Visualization and analysis of atomistic simulation data with OVITO—the Open Visualization Tool. *Modelling and Simulation in Materials Science and Engineering* **2009**, *18*, 015012.
243. Thommes, M.; Kaneko, K.; Neimark Alexander, V.; Olivier James, P.; Rodriguez-Reinoso, F.; Rouquerol, J.; Sing Kenneth, S. W., Physisorption of gases, with special reference to the evaluation of surface area and pore size distribution (IUPAC Technical Report). In *Pure and Applied Chemistry*, 2015; Vol. 87, p 1051.
244. Holtzclaw, J. R.; Wyatt, J. R.; Campana, J. E., Structure and fragmentation of dimethyl methylphosphonate and trimethyl phosphite. *Organic Mass Spectrometry* **1985**, *20*, 90-97.
245. Smentkowski, V. S.; Hagans, P.; Yates, J. T., Study of the catalytic destruction of dimethyl methylphosphonate(DMMP): oxidation over molybdenum(110). *The Journal of Physical Chemistry* **1988**, *92*, 6351-6357.
246. Gutsev, G. L.; Ampadu Boateng, D.; Jena, P.; Tibbetts, K. M., A Theoretical and Mass Spectrometry Study of Dimethyl Methylphosphonate: New Isomers and Cation Decay Channels in an Intense Femtosecond Laser Field. *The Journal of Physical Chemistry A* **2017**, *121*, 8414-8424.
247. Burke, D. J.; Wolff, A. J.; Edridge, J. L.; Brown, W. A., The adsorption and desorption of ethanol ices from a model grain surface. *The Journal of Chemical Physics* **2008**, *128*, 104702.

248. Green, S. D.; Bolina, A. S.; Chen, R.; Collings, M. P.; Brown, W. A.; McCoustra, M. R. S., Applying laboratory thermal desorption data in an interstellar context: sublimation of methanol thin films. *Monthly Notices of the Royal Astronomical Society* **2009**, *398*, 357-367.
249. Redhead, P. A., Thermal desorption of gases. *Vacuum* **1962**, *12*, 203-211.
250. Bertilsson, L.; Engquist, I.; Liedberg, B., Interaction of Dimethyl Methylphosphonate with Alkanethiolate Monolayers Studied by Temperature-Programmed Desorption and Infrared Spectroscopy. *The Journal of Physical Chemistry B* **1997**, *101*, 6021-6027.
251. Moss, J. A.; Szczepankiewicz, S. H.; Park, E.; Hoffmann, M. R., Adsorption and Photodegradation of Dimethyl Methylphosphonate Vapor at TiO<sub>2</sub> Surfaces. *The Journal of Physical Chemistry B* **2005**, *109*, 19779-19785.
252. Rusu, C. N.; Yates, J. T., Adsorption and Decomposition of Dimethyl Methylphosphonate on TiO<sub>2</sub>. *The Journal of Physical Chemistry B* **2000**, *104*, 12292-12298.
253. Hung, W.-C.; Wang, J.-C.; Wu, K.-H., Adsorption and decomposition of dimethyl methylphosphonate (DMMP) on expanded graphite/metal oxides. *Applied Surface Science* **2018**, *444*, 330-335.
254. Frigo, M.; Johnson, S. G., The Design and Implementation of FFTW3. *Proceedings of the IEEE* **2005**, *93*, 216-231.
255. VandeVondele, J.; Krack, M.; Mohamed, F.; Parrinello, M.; Chassaing, T.; Hutter, J., Quickstep: Fast and accurate density functional calculations using a mixed Gaussian and plane waves approach. *Computer Physics Communications* **2005**, *167*, 103-128.
256. VandeVondele, J.; Hutter, J., An efficient orbital transformation method for electronic structure calculations. *The Journal of Chemical Physics* **2003**, *118*, 4365-4369.
257. Ye, J.; Johnson, J. K., Screening Lewis Pair Moieties for Catalytic Hydrogenation of CO<sub>2</sub> in Functionalized UiO-66. *ACS Catalysis* **2015**, *5*, 6219-6229.
258. Goedecker, S.; Teter, M.; Hutter, J., Separable dual-space Gaussian pseudopotentials. *Physical Review B* **1996**, *54*, 1703-1710.
259. VandeVondele, J.; Hutter, J., Gaussian basis sets for accurate calculations on molecular systems in gas and condensed phases. *The Journal of Chemical Physics* **2007**, *127*, 114105.
260. Grimme, S.; Antony, J.; Ehrlich, S.; Krieg, H., A consistent and accurate ab initio parametrization of density functional dispersion correction (DFT-D) for the 94 elements H-Pu. *The Journal of Chemical Physics* **2010**, *132*, 154104.
261. Liu, D. C.; Nocedal, J., On the limited memory BFGS method for large scale optimization. *Mathematical Programming* **1989**, *45*, 503-528.

262. Ceriotti, M.; Bussi, G.; Parrinello, M., Langevin Equation with Colored Noise for Constant-Temperature Molecular Dynamics Simulations. *Physical Review Letters* **2009**, *102*, 020601.
263. Ceriotti, M.; Bussi, G.; Parrinello, M., Nuclear Quantum Effects in Solids Using a Colored-Noise Thermostat. *Physical Review Letters* **2009**, *103*, 030603.
264. Yuan, S.; Zou, L.; Li, H.; Chen, Y.-P.; Qin, J.; Zhang, Q.; Lu, W.; Hall, M. B.; Zhou, H.-C., Flexible Zirconium Metal-Organic Frameworks as Bioinspired Switchable Catalysts. *Angewandte Chemie International Edition* **2016**, *55*, 10776-10780.
265. Rowley, L. A.; Nicholson, D.; Parsonage, N. G., Monte Carlo grand canonical ensemble calculation in a gas-liquid transition region for 12-6 Argon. *Journal of Computational Physics* **1975**, *17*, 401-414.
266. Düren, T.; Millange, F.; Férey, G.; Walton, K. S.; Snurr, R. Q., Calculating Geometric Surface Areas as a Characterization Tool for Metal–Organic Frameworks. *The Journal of Physical Chemistry C* **2007**, *111*, 15350-15356.
267. Brunauer, S.; Emmett, P. H.; Teller, E., Adsorption of Gases in Multimolecular Layers. *Journal of the American Chemical Society* **1938**, *60*, 309-319.
268. Dubbeldam, D.; Calero, S.; Ellis, D. E.; Snurr, R. Q., RASPA: molecular simulation software for adsorption and diffusion in flexible nanoporous materials. *Molecular Simulation* **2016**, *42*, 81-101.
269. Potoff, J. J.; Siepmann, J. I., Vapor–liquid equilibria of mixtures containing alkanes, carbon dioxide, and nitrogen. *AIChE Journal* **2001**, *47*, 1676-1682.
270. Kwon, S.; Vidic, R.; Borguet, E., The effect of surface chemical functional groups on the adsorption and desorption of a polar molecule, acetone, from a model carbonaceous surface, graphite. *Surface Science* **2003**, *522*, 17-26.